

2022

The Synthesis and Biological Assessment of Novel Ursolic Acid Derivatives as Potential Chemotherapeutic Agents for Cancer

Julie Rose Mae Mondala

Technological University Dublin, jrmondala23@gmail.com

Follow this and additional works at: <https://arrow.tudublin.ie/sfehthes>



Part of the [Environmental Health Commons](#), and the [Medicine and Health Sciences Commons](#)

Recommended Citation

Mondala, J. R. M. (2022). The Synthesis and Biological Assessment of Novel Ursolic Acid Derivatives as Potential Chemotherapeutic Agents for Cancer. Technological University Dublin. DOI: 10.21427/RG1V-6C66

This Theses, Ph.D is brought to you for free and open access by the School of Food Science and Environmental Health at ARROW@TU Dublin. It has been accepted for inclusion in Theses by an authorized administrator of ARROW@TU Dublin. For more information, please contact arrow.admin@tudublin.ie, aisling.coyne@tudublin.ie, gerard.connolly@tudublin.ie.



This work is licensed under a [Creative Commons Attribution-NonCommercial-Share Alike 4.0 License](#)
Funder: Technological University Dublin

The Synthesis and Biological Assessment of Novel Ursolic Acid Derivatives as Potential Chemotherapeutic Agents for Cancer



Thesis submitted to the Technological University Dublin in fulfilment of the
requirements for PhD examination

Julie Rose Mae Mondala, BSc

School of Food Science and Environmental Health

Technological University Dublin

City Campus

Grangegorman, Dublin 7

2022

Supervisors: Professor James F. Curtin

Dr Denis O'Shea

Professor Michael Devereux

Dr Gemma K. Kinsella

ABSTRACT

Glioblastoma (GBM) is considered to be the most biologically aggressive type of brain tumour accounting for approximately 48% of all malignant primary brain tumours. GBM patients diagnosed have poor prognosis with a low five-year survival rate of <10%, highlighting the need for novel and more effective treatment for these tumours. Ursolic acid (UA), a natural bioactive compound has shown anti-cancer activities both *in vitro* and *in vivo* against various malignant cell lines. Our previous research has demonstrated that UA has a significant anti-cancer activity in GBM over conventional chemotherapeutic agents used to treat GBM. However, UA has low solubility, limiting bioavailability in humans and targeted delivery of UA has proven difficult to date. Folic acid, which binds to folate receptor with high affinity, was used for folate targeted drug delivery for GBM due to evidences that folate receptor is highly expressed in the brain, and has low expression in normal cells.

The aim of this study was to develop novel UA derivatives to enhance its bioavailability. Nine novel UA derivatives: three different diamine linkers, with Boc-protected and deprotected ends, and with folic acid were designed and synthesized to improve compound activity and/or delivery. The structures of the newly synthesised compounds were confirmed using mass spectrometry, FTIR, ¹H NMR and ¹³C NMR. The structural activity relationship (SAR) of UA and novel UA derivatives that were designed to improve its activity and bioavailability (predicted ADMET profile) were explored, and molecular docking studies against proposed targets – FOLR1 and/or VRK1 were utilised, with an in-depth analysis of predicted interactions. The cytotoxic activity was determined using alamarBlue™ cell viability assay in a panel of cancer cell lines and normal cells. It

was found that the conjugation of folic acid to UA decreased its cytotoxic activity. Interestingly, our study showed that the Boc-protected compounds have delayed cytotoxicity in comparison to deprotected compounds, which are more evident in U-251 MG and A431 cell lines using 2D cell culture assay. Whereas in 3D cell culture, only deprotected compounds exhibited an activity. The deprotected novel UA derivatives also retained the inherent anti-proliferative and anti-migratory effect of UA in U-251 MG cells. The synergistic studies focusing on the cell membrane damage performed showed that novel UA derivatives (**7 – 12**) may have a protective effect when exposed to radioactivity. In addition, the initial inhibitor studies suggests that compounds **8** and **10** at longer timepoint, may trigger multiple cell demise pathway. Based on these preliminary results, this study provides a new insight into using novel UA derivatives and a possible MOA for their anti-cancer effect.

DECLARATION

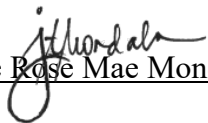
I certify that this thesis which I now submit for examination for the award of Doctor of Philosophy, is entirely my own work and has not been taken from the work of others, save and to the extent that such work has been cited and acknowledged within the text of my work.

This thesis was prepared according to the regulations for graduate study by research of the Technological University Dublin and has not been submitted in whole or in part for another award in any other third level institution.

The work reported on in this thesis conforms to the principles and requirements of the TU Dublin's guidelines for ethics in research.

TU Dublin has permission to keep, lend or copy this thesis in whole or in part, on condition that any such use of the material of the thesis be duly acknowledged.

Signature:


Julie Rose Mae Mondala

Candidate

Date: 11 November 2022

ACKNOWLEDGEMENTS

I would like to express my profound gratitude to Prof James Curtin for all the trust and support I have received over the years. I started my PhD application when I was still working in Canada and I appreciate the times he needed to adjust according to my schedule just to draft the research proposal. I would also like to express my great appreciation to Dr Denis O'Shea, Prof Michael Devereux and Dr Gemma Kinsella for their support and patience. I am beyond lucky and blessed for having four amazing supervisors, that despite their busy schedules, have never failed to show their support and guidance. Words are not enough to thank you all for giving me the opportunity to work and learn from you. I've learned so much from all of you and I wouldn't be the researcher I am today if not because of you all. Your endless support, guidance, advice and contribution to the project has been unequivocal, and I'm really grateful for that.

I would like to acknowledge the Fiosraigh Dean of Graduate Students Scholarship Award from TU Dublin for supporting this research project. Thank you also to all the research collaborations over the past years, especially to Dr Brijesh Tiwari of Teagasc, Ashtown for all the opportunity.

A huge thank you to all my colleagues, friends and staff in FSEH and ESHI for all the help and support they have offered me for the past years. I will forever treasure the endless laughter and fun, especially all the coffee breaks we shared together. Special thanks to Noel Grace for always being there to help; you're always a life saver. I would also like to thank all the lab technicians in ESHI especially to Claudio, Natasha, Tara and Ola for the scientific support in cell culture and for the great times. Thank you to Martin Kitson for

his help with NMR. Furthermore, thank you to all the porters in Marlborough St for all the patience in looking after me and waiting for me at times I stay late in the lab. My heartfelt gratitude to Dr Aisling Crowley and Dr Ajay Pal for taking the time in sharing their knowledge and skills; I wouldn't have survived without you. I would also like to thank Dr Gary Hessman of Trinity College Dublin for helping me with mass spectrometry.

Thank you so much to the Research Committee in FSEH for the opportunity to be a member for few years, it certainly was a great experience for me. In ESHI, thank you to those who helped, supported and balanced my life; I really won't make it if not because of you all. Thank you to Rory, TJ, Jamie, Aaron, Brian and Tadgh for their help with my random concerns. To research friends who turned to be friends for life - Janith, Kalpani, Sam, Ekene, Harshitha, Chitanya, Rajeev, Andressa, Sebnem, Rocky, Eline, Sean, Dia, Ajay, Kate, Gouri and Albert, thank you is not enough for keeping me sane all throughout. To more international food trips and coffee breaks in the future. Thank you to all my amazing friends for checking up on me and reminded me to relax especially to Toby, Yeqi, Gemmae, Robert, JC, Ephraim, Nestle and Kuya Adong. Special thanks to my best friend, Kimberly, for listening to all my rants in life. Of course, thank you to now my fiancé, King Adrian, for your endless love and support (and most importantly your unbelievable patience and understanding) throughout the years.

Behind the big smiles I have are longing for the loved ones I lost while doing the PhD. To my dear friend Mikka, thank you for pushing and believing in me in pursuing this PhD. To my Grandma Rosita, Mang how I miss your smile that always made my day and all your stories of how proud you are of me. Lastly, to my dearest Grandpa Segundo who

is the reason why I grew up dreaming to be a Cancer Researcher, words cannot express the pain in my heart that I won't be able to physically hand the diploma that is meant for you. I miss you all everyday. I know you all guided me in finishing this PhD. Thank you my guardian angels, for being my everyday strength. I hope you are all proud of me up there. You are all forever in my heart. I love you!

I am beyond blessed to have a big and very supportive family. My heartfelt gratitude to all my family around the globe for believing in me from the very start. You are all my strength and motivation. To my siblings, Tricia Mae and Rey Segrid, guys how will I survive life without you two? Thank you so much for your patience and understanding, endless love and support, and for dragging me out of the house to have random joyrides to de-stress. I would like to give my deepest appreciation and love to my Papa Rey and Mama Luc, who did everything to give us a better life and education. Thank you for all your hardwork, sacrifices, unwavering encouragement and support that have been the beacon of all my achievements. I will never make it here if not because of you. I promise to always make you proud. All the trainings and things you taught me are definitely worth it. Thank you for shaping me into the woman I am today.

Thank you our dear Lord God for the knowledge, wisdom and strength you bestowed upon me. All glory and honour is yours.

"I can do all things through Christ who strengthens me." -Philippians 4:13

SYMBOLS & ABBREVIATIONS

$(\text{CH}_3\text{CO})_2\text{O}$	Acetic anhydride
$(\text{COCl})_2$	Oxalyl chloride
5-methyl THF	5-methyltetrahydrofolic acid
ADME	Absorption Distribution Metabolism and Excretion
ADT	AutoDock Tools
AMT	Absorptive-Mediated Transcytosis
ATP	Adenosine Triphosphate
BBB	Blood brain barrier
BBTB	Blood-brain Tumour Barrier
BCNU	Carmustine
BCS	Biopharmaceutical Classification System
Boc_2O	Di- <i>tert</i> -butyl dicarbonate
BOILED-Egg	Brain Or IntestinaL Estimated permeation
CBTRUS	Central Brain Tumour Registry of United States
CCNB1	Cyclin B1
CCNU	Lomustine
CHCl_3	Chloroform
CNS	Central Nervous System
COX-2	Cyclooxygenase-2
CrO_3	Chromium Trioxide
CYS	Cystamine bis-hydrochloride
DAVLBH	Desacetylvinblastine Hydrazide
DCC	N,N'-dicyclohexylcarbodiimide

DCM	Dichloromethane
DCU	Dicyclohexylurea
DDR	DNA Damage Response
DHF	Dihydrofolate
DHFR	Dihydrofolate Reductase
DIPEA	<i>N,N</i> -diisopropylethylamine
DMAP	4-dimethylaminopyridine
DMF	Dimethylformamide
DMSO	Dimethyl Sulfoxide
DNA	Deoxyribonucleic acid
EDA	Ethylenediamine
EDC	1-ethyl-3-(3-dimethylaminopropyl)carbodiimide
EDEA	2, 2'-(ethylenedioxy)bis(ethylamine)
EGFR	Epidermal Growth Factor Receptor
EGFR/MAPK	Epidermal Growth Factor Receptor/Mitogen-Activated Protein Kinase
EMA	European Medicines Agency
EtOAc	Ethyl Acetate
EtOH	Ethanol
FA	Folic Acid
FDA	Food and Drug Administration
FITC	Fluorescein Isothiocyanate
FR	Folate Receptor
FT-IR	Fourier Transform Infrared Spectroscopy
FUA	Folate-Ursolic Acid

GBM	Glioblastoma Multiforme
GPI	Glycosylphosphatidylinositol
GSH	Glutathione
HATU	1-[Bis(dimethylamino)methylene]-1H-1,2,3-triazolo[4,5-b]pyridinium 3-oxide hexafluorophosphate
HBA	Hydrogen Bond Acceptor
HBD	Hydrogen Bond Donor
HCl	Hydrochloric Acid
HIA	Human Intestinal Absorption
HOBt	Hydroxybenzotriazole
HPLC	High Performance Liquid Chromatography
IARC	International Agency for Research on Cancer
IDH	Isocitrate Dehydrogenase
JNK	c-Jun N-terminal kinase
LC-MS	Liquid Chromatography Mass Spectrometry
LMP	Lysosome Associated Membrane Permeability
LOH	Loss of Heterozygosity
m-CPBA	meta-Chloroperoxybenzoic acid
mAB	Monoclonal Antibody
MDM2	Mouse Double Minute 2
MeOH	Methanol
MGMT	O-6 Methylguanine Methyltransferase
MOMP	Mitochondrial Outer Membrane Permeabilization
MW	Molecular Weight
N ₂	Nitrogen

Na ₂ SO ₄	Sodium Sulphate
NCRI	National Cancer Registry of Ireland
NF-κB	Nuclear Factor-κB
NHS	N-hydroxysuccinimide
NMR	Nuclear Magnetic Resonance
NSCLC	Non-small Cell Lung Cancer
OAt	<i>O</i> -acyl(tetramethyl)
P-gp	Permeability Glycoprotein
PABA	<i>para</i> -aminobenzoic Acid
PCC	Pyridinium chlorochromate
PCFT	Proton-Coupled Folate Transporter
PDB	Protein Data Bank
PDGFA	Platelet-derived Growth Factor Receptor Alpha
PEG	Polyethylene glycol
PI3K	Phosphoinositol-3-kinase
PLK1	Polo-like Kinase 1
PTEN	Phosphatase and Tensin Homolog
RB	Retinoblastoma
RCSB	Research Collaboratory for Structural Bioinformatics
RFC	Reduced Folate Carrier
RME	Receptor-Mediated Endocytosis
RMSD	Root Mean Square Deviation
RNA	Ribonucleic Acid
ROS	Reactive Oxygen Species
RP-HPLC	Reversed-Phase High Performance Liquid Chromatography

RTK	Receptor Tyrosine Kinase
SAR	Structural Activity Relationship
SEM	Standard Error of Means
STAT 3	Signal Transducer and Activator of Transcription 3
TEA	Triethylamine
TFA	Trifluoroacetic Acid
THF	Tetrahydrofolate
THFR	Tetrahydrofuran
TiCl ₃	Titanium (III) chloride
TLC	Thin Layer Chromatography
TMS	Trimethylsilane
TMT	Transporter-Mediated Transcytosis
TMZ	Temozolomide
TP53	Tumour Protein 53
TPSA	Topological Polar Surface Area
TRAIL	Tumour Necrosis Factor-Related Apoptosis-Inducing Ligand
UA	Ursolic Acid
UA NL	Ursolic Acid Nano-Liposomes
VEGF	Vascular Endothelial Growth Factor
VRK1	Vaccinia-Related Kinase
WHO	World Health Organisation

TABLE OF CONTENTS

ABSTRACT	i
DECLARATION	iii
ACKNOWLEDGEMENTS	iv
SYMBOLS & ABBREVIATIONS	vii
TABLE OF CONTENTS	xii
LIST OF FIGURES	xxii
LIST OF SCHEMES	xxxvii
LIST OF TABLES	xxxix
CHAPTER 1. INTRODUCTION	1
1.1 Introduction to Cancer	2
1.1.1 The Hallmarks of Cancer	4
1.2 Chemotherapy	9
1.2.1 Novel Chemotherapeutic Drugs	11
1.3 Glioblastoma Multiforme (GBM)	13
1.3.1 Primary and Secondary Glioblastoma	14
1.3.2 Epidemiology of Glioblastoma	16
1.3.3 Glioblastoma Core Signalling Pathways (Gliomagenesis)	18
1.3.4 Current Therapeutic Strategies in Glioblastoma	20
1.3.4.1 Surgery	21
1.3.4.2 Radiotherapy	22

1.3.4.3	Chemotherapy	22
1.4	Drug Delivery Barriers in Brain Cancer	24
1.4.1	Drug Delivery for Brain Cancer	27
1.4.2	Targeted Therapy/Targeted Drug Delivery	28
1.4.2.1	Folate Targeted Drug Delivery	31
1.5	Folic Acid as a Targeting Ligand	33
1.5.1	The Folate Receptor	37
1.5.2	The Mechanism of Folate Uptake <i>via</i> the Folate Receptor	41
1.6	Ursolic Acid	43
1.6.1	UA on the Hallmarks of Cancer	45
1.6.2	Pharmacokinetic Study of Ursolic Acid	49
1.6.3	Molecular Targets of UA	51
1.6.4	Modifications to UA and their impact on cytotoxicity	55
	PROJECT RATIONALE	62
	Research Questions	64
	Aims and Objectives	66
	CHAPTER 2. RESULTS AND DISCUSSION 1	68
2.0	The Synthesis of Novel UA and FUA Derivatives	69
2.1	The comparison of UA Hunan and UA Sigma	70
2.1.1	Chemical comparison of UA Hunan and UA Sigma	70
2.1.2	Biological comparison of UA Hunan and UA Sigma	72

2.2	The Synthesis of Novel Folate-Ursolic Acid (FUA) Conjugates	74
2.2.1	The <i>N</i> -Boc protection of diamine functional linkers (Step 1)	78
2.2.2	Conjugation of <i>N</i> -Boc-Ethylenediamine with Folate (Step 2a)	82
2.2.3	Deprotection of <i>N</i> -Boc-Ethylenediamine-Folate (Step 2b)	86
2.2.4	Attempted conjugation of UA with Folate-Ethylenediamine (Step 2c)	89
2.3	An alternative approach to the synthesis of the Folate-Ursolic Acid (FUA) compounds	93
2.3.1	Conjugation of <i>N</i> -Boc diamines with Ursolic Acid (Step 3a)	93
2.3.2	The Deprotection of <i>N</i> -Boc Diamine UA conjugates (Step 3b)	103
2.3.3	The conjugation of Ursolic Acid diamine with Folic Acid (Step 3c)	106
2.4	Summary	109
CHAPTER 3. RESULTS AND DISCUSSION 2		110
3.0	The Activity of Novel FUA Derivatives	111
3.1	The <i>in silico</i> studies of Novel FUA Derivatives	112
3.1.1	SwissADME Bioavailability Radar	114
3.1.2	Physicochemical Properties of Novel FUA Derivatives	114
3.1.3	BBB penetration, Bioavailability and Synthetic Accessibility of Novel FUA Derivatives	117
3.2	The Pharmacodynamic Studies of Novel FUA Derivatives	120
3.2.1	The Molecular Docking of Novel FUA Derivatives to Folate Receptor	120
3.2.1.1	Visualization and interaction analysis	122
3.2.2.2	Docking Studies of novel FUA derivatives (13 – 15) with FR α	126

3.2.2	The Molecular Docking of Novel FUA Derivatives to VRK1	134
3.2.2.1	Visualization and interaction analysis	136
3.2.2.2	Docking Studies of novel FUA derivatives (13 – 15) with VRK1	137
3.3	The chemotherapeutic potential of Novel FUA Derivatives	150
3.3.1	Novel FUA derivatives in different cell lines (folate free medium)	151
3.3.2	Novel FUA derivatives in different cell lines and media	155
3.3.3	Novel FUA derivatives with methotrexate control in selected cell lines	158
3.3.4	Novel FUA derivatives inhibit cytotoxicity of Ursolic Acid	160
3.3.5	Ultrasound assisted delivery of novel FUA derivatives	162
3.3.6	Increased Concentration of Novel FUA derivatives	164
3.4	Summary	166
CHAPTER 4. RESULTS AND DISCUSSION 3		167
4.0	The Activity of Boc and Deprotected Conjugates	168
4.1	The activity of Boc-protected and deprotected UA-linkers	170
4.1.1	Cytotoxic Activity of Linkers	173
4.2	The <i>in-silico</i> studies of Novel FUA Derivatives	174
4.2.1	SwissADME Bioavailability Radar	174
4.2.2	Predicted Physicochemical Properties of Novel UA Derivatives	177
4.2.3	BBB penetration, Bioavailability and Synthetic Accessibility of Novel UA Derivatives	178
4.3	The Pharmacodynamic Studies of Novel FUA Derivatives	182

4.3.1	The Molecular Docking of Novel UA Derivatives in VRK1	182
4.4	Cytotoxicity of novel UA derivatives	196
4.4.1	Cell Viability of novel UA derivatives in different cancer cell lines	196
4.4.2	Novel UA Derivatives Induced Cell Membrane Damage	202
4.4.3	Novel UA Derivatives Induced Mitochondrial Membrane Depolarisation	205
4.5	Stability of novel UA derivatives	207
4.5.1	Stability in Cell Culture Medium	208
4.5.2	Investigation of possible enzymatic activity of N-Boc protected compounds	209
4.6	Collective cell migration in novel UA derivatives	211
4.7	Effect of Novel UA Derivatives to Cell Membrane Damage	216
4.7.1	Cytotoxicity curve of TMZ	217
4.7.2	Cytotoxicity Curve of UV-Vis	218
4.7.3	Synergistic effect of TMZ and novel UA derivatives	219
4.7.4	Synergistic effect of UV-Vis and novel UA derivatives	223
4.8	Cell proliferation of novel UA derivatives	225
4.8.1	Determining cell count using haemocytometer	226
4.8.2	Carboxy-fluorescein succinimidyl ester (CFSE) Cell Proliferation Dye	230
4.9	Cell death mechanism(s) of novel UA derivatives	235
4.10	<i>In Vitro</i> Cytotoxicity Assay in 3D cell culture model	241
4.11	Summary	246

CHAPTER 5. GENERAL DISCUSSION	249
CHAPTER 6. CONCLUSION & FUTURE WORK	265
6.1 Conclusion and Future Work	266
6.1.1 Conclusion	266
6.2 Future Work	268
CHAPTER 7. EXPERIMENTAL	271
7.1 Experimental Methods and Instrumentation	272
7.2 UA Purification	273
7.2.1 Recrystallisation	273
7.2.2 Thin Layer Chromatography (TLC)	273
7.2.3 Column Chromatography	273
7.2.4 Reverse Phase High Performance Liquid Chromatography	274
7.3 <i>N</i> -Boc protection of diamines linkers	274
7.3.1 <i>N</i> -Boc protection of Ethylenediamine (1)	274
7.3.2 <i>N</i> -Boc protection of cystamine dihydrochloride (2)	275
7.3.3 <i>N</i> -Boc protection of 2,2'-(ethylenedioxy)bis(ethylamine) (3)	276
7.4 The attempted conjugation of Folate-Ethylenediamine linker to UA	277
7.4.1 Synthesis of <i>N</i> -Boc-EDA-FA (4)	277
7.4.2 Synthesis of FA-EDA (deprotection) (5)	278
7.4.3 Synthesis of FA-EDA-UA (6)	279
7.5 The conjugation of UA diamine with FA	280

7.5.1	The attempted conjugation of <i>N</i> -Boc-EDA with UA	280
7.5.1.1	<i>N</i> -Boc-EDA-UA with DCC/NHS	280
7.5.1.2	<i>N</i> -Boc-EDA-UA with EDC/HOBt	281
7.5.2	The conjugation of <i>N</i> -Boc protected diamine linkers with UA	282
7.5.2.1	Synthesis of <i>N</i> -Boc-EDA-UA (7)	282
7.5.2.2	Synthesis of <i>N</i> -Boc-CYS-UA (8)	283
7.5.2.3	Synthesis of <i>N</i> -Boc-EDEA-UA (9)	284
7.5.3	The deprotection of <i>N</i> -Boc protected Diamine linkers with Ursolic Acid	285
7.5.3.1	Synthesis of UA-EDA (10)	285
7.5.3.2	Synthesis of UA-CYS (11)	286
7.5.3.3	Synthesis of UA-EDEA (12)	287
7.5.4	The conjugation of Ursolic Acid diamine with Folic Acid	288
7.5.4.1	Synthesis of UA-EDA-FA (13)	288
7.5.4.2	Synthesis of UA-CYS-FA (14)	289
7.5.4.3	Synthesis of UA-EDEA-FA (15)	290
7.6	Pharmacokinetics	291
7.7	Pharmacodynamics	291
7.7.1	Computational tools and software	291
7.7.2	Protein Structures	292
7.7.3	Ligand Structures	293
7.7.4	Molecular Docking	293
7.8	Cell Culture	294
7.8.1	Cell culture conditions	294

7.8.2	Cytotoxicity	295
7.8.3	Cell Viability Assay	296
7.9	Ultrasound Treatment	297
7.10	Flow Cytometry	297
7.11	Inhibitor Studies	299
7.12	Stability of Novel UA Derivatives	300
7.13	Cell Membrane Damage Assay	301
7.14	Cell Proliferation Assay	302
7.15	Collective Cell Migration Assay	303
7.16	3D Cell Culture Assay	304
7.17	Data Analysis	305
7.18	Statistical Analysis	305
	PROFESSIONAL DEVELOPMENT	306
	Publications	307
	Structured PhD Modules	308
	Conferences and Seminars Attended	309
	REFERENCES	311

APPENDICES	364
A.1 COA of UA Hunan	365
A.2 UA Hunan	366
A.3 UA Sigma	369
A.4 <i>N</i> -Boc Ethylenediamine (1)	371
A.4 <i>N</i> -Boc cystamine dihydrochloride (2)	373
A.5 <i>N</i> -Boc 2,2'-(ethylenedioxy)bis(ethylamine) (3)	375
A.6 <i>N</i> -Boc-ethylenediamine-folate (4)	377
A.7 Folate-Ethylenediamine (5)	378
A.8 Folate-Ethylenediamine-UA (6)	379
A.9 <i>N</i> -Boc-ethylenediamine-Ursolic Acid (DCC/NHS)	380
A.10 <i>N</i> -Boc-ethylenediamine-Ursolic Acid (EDC/HOBt)	381
A.11 <i>N</i> -Boc-ethylenediamine-Ursolic Acid (7)	382
A.12 <i>N</i> -Boc-cystamine dihydrochloride-Ursolic Acid (8)	384
A.13 <i>N</i> -Boc-2,2'-(ethylenedioxy)bis(ethylamine)-Ursolic Acid (9)	386
A.14 UA-Ethylenediamine (10)	388
A.15 UA-Cystamine dihydrochloride (11)	390
A.16 UA- <i>N</i> -Boc-2,2'-(ethylenedioxy)bis(ethylamine) (12)	392
A.17 Ursolic Acid-Ethylenediamine-Folate (13)	394
A.18 Ursolic Acid- Cystamine dihydrochloride -Folate (14)	396
A.19 Ursolic Acid-Ethylenediamine-Folate (15)	398

A.20 Canonical SMILES of UA and Compounds (7 – 15)	400
A.21 Re-docking studies of E8V to VRK1 (PDB ID: 6BU6)	401
A.22 Docking studies of UA bound to FR α	403
A.23 Docking studies of FA bound to VRK1	404
A.24 IC ₅₀ of UA in different cell lines under different folate conditions	405
A.25 NOAEL concentrations of novel UA derivatives (7 – 12)	406
A.26 Comparison of novel FUA derivatives in different folate in media	407
A.27 IC ₅₀ of UA in different cell lines under different folate conditions	409

LIST OF FIGURES

Figure 1. Graphical overview of incidence and mortality rates of different cancers worldwide in 2020	3
Figure 2. The Hallmarks of Cancer (modified from Hanahan and Weinberg, 2011; Hanahan 2022).	5
Figure 3. The chemical structures of Arsphenamine, Aminopterin and Methotrexate.	9
Figure 4. The chemical structures of vincristine and procarbazine.	10
Figure 5. Plant derived anti-cancer agents: Four main classes of natural products.	12
Figure 6. Distribution of Primary Brain and Other CNS Tumours by Behaviours (Five-Year Total of 431,773; Annual Average Cases of 86,355), CBTRUS Statistical Report: US Cancer Statistics - NPCR and SEER, 2014–2018 (Ostrom <i>et al.</i> , 2021).	17
Figure 7. Structures of different chemotherapeutic alkylating agents for GBM treatment.	24
Figure 8. Schematic representation of the healthy blood-brain barrier (BBB) and blood-brain tumour barrier (BBTB) (modified from Raucher, Dragojevic and Ryu, 2018). Image created with BioRender.com.	26
Figure 9. A schematic of several strategies for brain cancer drug delivery of therapeutic agents. Cell-penetrating peptides (CPP); nanoparticles (NPs); receptor-mediated transport (RMT) (adapted from Zhang <i>et al.</i> , 2015)	28
Figure 10. Typical structure of receptor-directed drug delivery system (modified from Leamon and Reddy, 2004). Image created using ChemDraw Professional 16.0.	31
Figure 11. The chemical structure of folic acid highlighting the three core components: pteridine ring, para-aminobenzoic acid (PABA), and the glutamate moiety. The α and γ COOH functionalization are indicated.	34

- Figure 12.** The 3D interaction map of folic acid bound to FR α (PDB ID: 4LRH) found by Chen and his colleagues (image adapted from Chen *et al.*, 2013). 40
- Figure 13.** Uptake of folate-drug conjugates. The folate-drug conjugate is taken up by cells by binding of folate to the folate receptor. Invagination of the plasma membrane results in receptor mediated endocytosis. The acidic pH (~5) results in dissociation of the drug cargo and the folate receptor is recycled to the cell surface once more (modified from Hilgenbrink and Low, 2005). Image created using ChemDraw Professional 16.0. 42
- Figure 14.** The chemical structure of ursolic acid. Numbers indicate the different carbons present and letters indicate the different rings. 44
- Figure 15.** The current of knowledge of the molecular mechanism of action of UA in cancer cells. Red - downregulated; green – upregulated. 48
- Figure 16.** The 3D interaction map UA bound to VRK1 (PDB ID: 6AC9) showing residues essential for ligand binding (Image obtained from Kim *et al.*, 2015). 52
- Figure 17.** The 3D interaction map of UA bound to (A) Akt1/protein kinase B (PDB ID: 3OCB) and (B) MDM2/E₃ ubiquitin-protein ligase (PDB ID: 4HG7) (Image obtained from Frolova *et al.*, 2019) 53
- Figure 18.** The 3D interaction map of UA bound to (A) PLK1 (PDB ID: 2RKU) and (B) CCNB1 (PDB ID: 6GU3) The green structure represents the small molecule compound, and the red structure represents the binding site of the compound to the hub proteins. (Image obtained from Zhang *et al.*, 2021) 54
- Figure 19.** UA derivatives modifying ring A by Tu *et al* (2009). 55
- Figure 20.** UA derivatives modifying C3 and C28 of Meng *et al* (2009). 57
- Figure 21.** UA derivatives modifying C3 and C28 of Ma *et al* (2005). 58

Figure 22. Cytotoxicity of UA Hunan vs UA Sigma on (A) U-251 MG and (B) SW480 cell lines after 48 hours treatment.	72
Figure 23. The structures of the novel FUA compounds (functionalised linkers highlighted in red). (A) ethylenediamine linker (B) disulphide linker (C) ethereal oxygen linker.	74
Figure 24. <i>N</i> -Boc protected diamines 1-3 .	78
Figure 25. The aliphatic CH ₂ group (linker) and boc group of diamine linker for ¹³ CNMR interpretation.	80
Figure 26. The proposed structure of <i>N</i> -Boc ethylenediamine-folate conjugate 4 .	83
Figure 27. <i>N</i> -Boc-ethylenediamine folate conjugate 4 illustrating numbering scheme for ¹ HNMR analysis.	85
Figure 28. <i>N</i> -Boc-ethylenediamine folate conjugate illustrating numbering scheme for ¹³ CNMR analysis.	86
Figure 29. Folate ethylenediamine conjugate 5 illustrating the numbering scheme for ¹ HNMR analysis.	87
Figure 30. The dialysis method used to obtain compound 6 .	89
Figure 31. The intended structure of compound 6 , its numbering scheme for ¹ HNMR analysis, and the actual ¹ HNMR spectrum obtained.	91
Figure 32. The proposed structures of <i>N</i> -Boc diamine-UA conjugates 7 – 9 .	97
Figure 33. <i>N</i> -Boc diamine UA conjugates illustrating numbering scheme for ¹ HNMR and ¹³ CNMR analysis.	99
Figure 34. The proposed structures of deprotected <i>N</i> -Boc diamine-UA conjugates 10 – 12 .	103
Figure 35. The deprotected <i>N</i> -Boc diamine UA conjugates illustrating numbering scheme for ¹ HNMR analysis.	105

Figure 36. General structure of the FUA conjugates **13 - 15** illustrating numbering scheme for ¹HNMR analysis. 107

Figure 37. The bioavailability radar (pink area exhibits optimal range of particular property) of UA and novel FUA derivatives **13 – 15** evaluated using SwissADME. Lipophilicity (LIPO): XLOGP3 between -0.7 and +5.0; molecular weight (SIZE): MW between 150 and 500 g/mol; polarity (POLAR) TPSA between 20 Å² and 130 Å²; Solubility (INSOLU): log S not higher than 6; Saturation (INSATU): fraction of carbons in sp³ hybridization between 0.25 and 1; and flexibility (FLEX): no more than 9 rotatable bonds. 115

Figure 38. The 3D crystal structure of the FR α -folic acid complex (PDB code: 4LRH), denoting the chains (A-H) that were recrystallised by Chen *et al.* (2013). Chain A is zoomed in showing the co-crystallised ligand and the sphere indicating the binding pocket. Image generated in BIOVIA DS Client Visualizer 2020 and PyMOL™ v2.4.1. 121

Figure 40. (A) The superimposed 3D images of folic acid - 4LRH (cyan) and docked folic acid ligand (green) showing residues essential for ligand binding. The 2D diagram of (B) folic acid – 4LRH, and (C) docked to folic acid FR α (PDB ID: 4LRH). The 3D image was visualised and rendered in PyMOL™ v2.4.1. The 2D interaction map was generated in BIOVIA DS Client visualizer 2020. 123

Figure 41. The folic acid docked to FR α surface showing (a) charge distribution surface (b) hydrogen bond donor/acceptor and (c) hydrophobicity (images generated are our own results analysed using BIOVIA DS Client Visualizer 2020). 124

Figure 43. The 3D overlay of folic acid (green), compound **13** (blue), compound **14** (magenta) and compound **15** (yellow) docked to FR (PDB ID: 4LRH). The image was generated in PyMOL™ v2.4.1. 127

Figure 44. The (A) 3D image and (b) 2D interaction map of compound **13** docked to FR α (PDB ID: 4LRH). The 3D image was analysed and rendered in PyMOLTM v2.4.1 and the 2D interaction map was generated in BIOVIA DS Visualizer 2020. 128

Figure 45. The (A) 3D image and (b) 2D interaction map of compound **14** docked to FR α (PDB ID: 4LRH). The 3D image was analysed and rendered in PyMOLTM v2.4.1 and the 2D interaction map was generated in BIOVIA DS Visualizer 2020. 130

Figure 46. The (A) 3D image and (b) 2D interaction map of compound **15** docked to FR α (PDB ID: 4LRH). The 3D image was analysed and rendered in PyMOLTM v2.4.1 and the 2D interaction map was generated in BIOVIA DS Visualizer 2020. 132

Figure 45. The 3D crystal structure of VRK1-bis-difluorophenol-aminopyridine complex (PDB: 6BU6), denoting the chains (A-D) that were recrystallised by Couñago *et al* (2017). Chain A is zoomed in showing the co-crystallized ligand and the binding pocket. Image generated in BIOVIA DS Client Visualizer 2020 and PyMOLTM v2.4.1. 135

Figure 49. The superimposed 3D images of E8V - 6BU6 (green) and docked ligand (cyan) showing residues essential for ligand binding. Images were visualised and rendered in PyMOL v2.4.1. 136

Figure 50. The UA docked to VRK1 surface showing (a) charge distribution surface (b) hydrogen bond donor/acceptor and (c) hydrophobicity. Images generated are our own results analysed using BIOVIA DS Visualizer 2020. 138

Figure 51. The superimposed 3D image of 6BU6 ligand E8V (green) and UA (cyan). Image was visualised and rendered in PyMOLTM v2.4.1. 139

Figure 52. The (A) 3D image and (b) 2D interaction map of UA docked to VRK1 (PDB ID: 6BU6). The 3D image was analysed and rendered in PyMOLTM v2.4.1 and the 2D interaction map was generated in BIOVIA DS Visualizer 2020. 141

Figure 53. The 3D overlay of UA (green), compound **13** (blue), compound **14** (magenta) and compound **15** (yellow) docked to VRK1 (PDB ID: 6BU6). The image was generated in PyMOL™ v2.4.1. 143

Figure 54. The (A) 3D image and (b) 2D interaction map of compound **13** docked to VRK1 (PDB ID: 6BU6). The 3D image was analysed and rendered in PyMOL™ v2.4.1 and the 2D interaction map was generated in BIOVIA DS Visualizer 2020. 144

Figure 55. The (A) 3D image and (b) 2D interaction map of compound **14** docked to VRK1 (PDB ID: 6BU6). The 3D image was analysed and rendered in PyMOL™ v2.4.1 and the 2D interaction map was generated in BIOVIA DS Visualizer 2020. 146

Figure 56. The (A) 3D image and (b) 2D interaction map of compound **15** docked to VRK1 (PDB ID: 6BU6). The 3D image was analysed and rendered in PyMOL™ v2.4.1 and the 2D interaction map was generated in BIOVIA DS Visualizer 2020. 148

Figure 57. Cytotoxicity of novel FUA derivatives (**13 – 15**) in cancer cells. An initial concentration of 100 µM in culture medium was added to cells and serially diluted to different concentrations (100 µM to 3.125 µM). AlamarBlue cell viability assay was then carried out following treatment for 48 and 144 hours. Data shown were normalised to the untreated control and are shown as the % mean ± SEM. Statistical analysis was carried out using non-linear regression analysis and Two-way ANOVA with Bonferroni post-tests, (n = 3) (*P<0.0001). 154

Figure 58. Cytotoxicity of novel FUA derivatives (**13 – 15**) in cancer cells (low folate medium). An initial concentration of 100 µM in culture medium was added to cells and serially diluted to different concentrations (100 µM to 3.125 µM). AlamarBlue cell viability assay was then carried out following treatment for 48 and 144 hours. Data shown were normalised to the untreated control and are shown as the % mean ± SEM. Statistical

analysis was carried out using non-linear regression analysis and Two-way ANOVA with Bonferroni post-tests, (n = 3) (*P<0.0001). 156

Figure 59. Cytotoxicity of novel FUA derivatives (**13 – 15**) in cancer cells (medium folate medium). An initial concentration of 100 μM in culture medium was added to cells and serially diluted to different concentrations (100 μM to 3.125 μM). AlamarBlue cell viability assay was then carried out following treatment for 48 and 144 hours. Data shown were normalised to the untreated control and are shown as the % mean \pm SEM. Statistical analysis was carried out using non-linear regression analysis and Two-way ANOVA with Bonferroni post-tests, (n = 3) (*P<0.0001). 157

Figure 60. Methotrexate activity in different cancer cells. An initial concentration of 100 μM in culture medium was added to cells and serially diluted to different concentrations (100 μM to 3.125 μM). AlamarBlue cell viability assay was then carried out following treatment for 48 and 144 hours. Data shown were normalised to the untreated control and are shown as the % mean \pm SEM. Statistical analysis was carried out using non-linear regression analysis and Two-way ANOVA with Bonferroni post-tests, (n = 3) (*P<0.0001). 159

Figure 61. Inhibitory studies of novel FUA derivatives (**13 – 15**) with Ursolic Acid. U-251 MG cells were treated with different concentrations of FA and novel FUA derivatives (40 μM to 5 μM) and co-treated with 10 or 20 μM UA. AlamarBlue cell viability assay was then carried out following treatment for 48 and 144 hours. Data shown were normalised to the untreated control and are shown as the % mean \pm SEM (n=3). 161

Figure 62. Ultrasound assisted delivery of novel FUA derivatives (**13 – 15**). An initial concentration of 100 μM in culture medium was added to cells and serially diluted to different concentrations (100 μM to 3.125 μM). Cells were then treated with water bath ultrasound at 25 kHz, and temperature was maintained at <35 $^{\circ}\text{C}$. AlamarBlue cell

viability assay was then carried out following treatment for 48 and 144 hours. Data shown were normalised to the untreated control and are shown as the % mean \pm SEM. Statistical analysis was carried out using non-linear regression analysis and Two-way ANOVA with Bonferroni post-tests, (n = 3) (*P<0.0001). 163

Figure 63. Cytotoxic activity of novel FUA derivatives (**13 – 15**) at higher concentration. An initial concentration of 1000 μ M in culture medium was added to cells and serially diluted to different concentrations (1000 μ M to 31.25 μ M). AlamarBlue cell viability assay was then carried out following treatment for 48 and 144 hours. Data shown were normalised to the untreated control and are shown as the % mean \pm SEM. Statistical analysis was carried out using non-linear regression analysis and Two-way ANOVA with Bonferroni post-tests, (n = 3) (*P<0.0001). 165

Figure 64. Cytotoxic activity of intermediates (novel UA derivatives **7 – 12**) in U-251 MG cells. An initial concentration of 100 μ M in culture medium was added to cells and serially diluted to different concentrations (100 μ M to 3.125 μ M). AlamarBlue cell viability assay was then carried out following treatment for 48 and 144 hours. Data shown were normalised to the untreated control and are shown as the % mean \pm SEM, (n = 3). 172

Figure 65. Cytotoxicity of Linkers. An initial concentration of 100 μ M in culture medium was added to cells and serially diluted to different concentrations (100 μ M to 3.125 μ M). AlamarBlue cell viability assay was then carried out following treatment for 48 and 144 hours. Data shown were normalised to the untreated control and are shown as the % mean \pm SEM, (n = 3). 173

Figure 66. The bioavailability radar (pink area exhibits optimal range of particular property) of UA and novel UA derivatives (**7 – 12**) evaluated using SwissADME. Lipophilicity (LIPO): XLOGP3 between -0.7 and +5.0; molecular weight (SIZE): MW

between 150 and 500 g/mol; polarity (POLAR) TPSA between 20 Å² and 130 Å²; Solubility (INSOLU): log S not higher than 6; Saturation (INSATU): fraction of carbons in sp³ hybridization between 0.25 and 1; and flexibility (FLEX): no more than 9 rotatable bonds. 175

Figure 67. The predicted BOILED-Egg diagram of UA and novel UA derivatives (**7 – 12**) obtained from SwissADME tool for the evaluation of passive human gastrointestinal absorption (HIA), brain penetration (BBB) and P-glycoprotein activity in presence of the molecule (P-gp). Note that in the remarks, 1 molecule is out of range – compound **8**. 180

Figure 68. The structures of the novel UA derivatives (**7 – 12**) with Boc-protected (R1) and deprotected (R2) ends. All compounds structures drawn using ChemDraw Professional v16.0. 168

Figure 69. The 3D overlay of UA (green), compound **7** (blue), compound **10** (magenta), compound **8** (yellow), compound **11** (orange), compound **9** (raspberry) and compound **12** (grey) docked to VRK1 (PDB ID: 6BU6). The image was generated in PyMOL™ v2.4.1. 185

Figure 70. The (A) 3D image and (b) 2D interaction map of compound **7** docked to VRK1 (PDB ID: 6BU6). The 3D image was analysed and rendered in PyMOL™ v2.4.1 and the 2D interaction map was generated in BIOVIA DS Visualizer 2020. 187

Figure 71. The (A) 3D image and (b) 2D interaction map of compound **10** docked to VRK1 (PDB ID: 6BU6). The 3D image was analysed and rendered in PyMOL™ v2.4.1 and the 2D interaction map was generated in BIOVIA DS Visualizer 2020. 188

Figure 72. The (A) 3D image and (b) 2D interaction map of compound **8** docked to VRK1 (PDB ID: 6BU6). The 3D image was analysed and rendered in PyMOL™ v2.4.1 and the 2D interaction map was generated in BIOVIA DS Visualizer 2020. 190

Figure 73. The (A) 3D image and (b) 2D interaction map of compound **11** docked to VRK1 (PDB ID: 6BU6). The 3D image was analysed and rendered in PyMOL™ v2.4.1 and the 2D interaction map was generated in BIOVIA DS Visualizer 2020. 191

Figure 74. The (A) 3D image and (b) 2D interaction map of compound **9** docked to VRK1 (PDB ID: 6BU6). The 3D image was analysed and rendered in PyMOL™ v2.4.1 and the 2D interaction map was generated in BIOVIA DS Visualizer 2020. 193

Figure 75. The (A) 3D image and (b) 2D interaction map of compound **12** docked to VRK1 (PDB ID: 6BU6). The 3D image was analysed and rendered in PyMOL™ v2.4.1 and the 2D interaction map was generated in BIOVIA DS Visualizer 2020. 194

Figure 76. Heatmap of the IC₅₀ of novel UA derivatives (**7 – 12**) in different cell lines. The colours indicate the IC₅₀ values of the UA and novel UA derivatives from 0 – 50 µM; green being the most cytotoxic and red as the least cytotoxic. An initial concentration of 100 µM in culture medium was added to cells and serially diluted to different concentrations (100 µM to 3.125 µM). AlamarBlue cell viability assay was then carried out following treatment for 48 and 144 hours. Data shown were normalised to the untreated control and are shown as the % mean ± SEM (standard error of the mean). Statistical analysis was carried out using non-linear regression analysis (n = 3) and mean IC₅₀ values in µM are plotted in a heatmap. 200

Figure 77. Cell membrane damage of novel UA derivatives using PI. U-251 MG cells were treated with 10 µM of UA or novel UA derivatives (**7 – 12**) or 0.05% DMSO (NC - negative control) or 20% DMSO (positive control) for (A, C) 48 hr and (B, D) 6 days. Cells were stained with 0.5 µg/ml propidium iodide for 5 mins and analysed by flow cytometry. (A, B) dot plot analyse in CytExpert software and (C, D) Bar graph of the % cell viability of compounds plotted using Graphpad Prism 9. Statistical analysis was

carried out using One-Way ANOVA with Bonferroni post-test (**P ≤ 0.01, ****P ≤ 0.0001). 203

Figure 78. Mitochondrial membrane depolarisation. U-251 MG cells were treated with 10 µM of UA or novel UA derivatives (**7 – 12**) or 0.05% DMSO (NC – negative control) or 0.1% H₂O₂ (positive control) for 48 and 144 hours. Cells were loaded with 2.5 µg/ml JC-1 dye for 5 mins and analysed by flow cytometry. (A, B) dot plot analyse using CytExpert software and (C, D) Bar graph of the % cell viability of compounds plotted using Graphpad Prism 9. Statistical analysis was carried out using One-Way ANOVA with Bonferroni post-test (*P ≤ 0.05, ****P ≤ 0.0001). 207

Figure 79. Stability of Boc-protected compound in cell culture medium. Compounds **7** and **10** were investigated by incubating 100 µM of the compounds in culture medium and incubated at 37 °C for 144 hours. After which time, was added to cells and serially diluted to 3.125 µM. AlamarBlue cell viability assay was carried out following treatment for 48 hours (A) and 144 hours (B). Data shown were normalised to the untreated control and are shown as the % mean ± SEM. Statistical analysis was carried out using Two-way ANOVA with Bonferroni post-test, (n = 3) (****P ≤ 0.0001). 208

Figure 80. Enzymatic activity of Boc-protected compound. U-251 MG cells were extracted by freeze-thawing (FT). Then, compounds were added to the FT cells and pre-incubated at 37 °C or ice for 1 hour; negative control with compounds in PBS was pre-incubated at 37 °C for 1 hour. AlamarBlue cell viability assay was carried out following treatment for 48 and 144 hours. Data shown were normalised to the untreated control and are shown as the % mean ± SEM. Statistical analysis was carried out using Two-way ANOVA with Bonferroni post-tests, (n = 3) (****P ≤ 0.0001). 210

Figure 81. Inhibitor studies of novel UA derivatives (**7 – 12**). U-251 MG cells were pre-treated with 10 µM E-64, 12.5 µM SP600125 and 25 µM zVAD-fmk for 1 hour. Cells

were then treated with IC_{50} of compounds determined for each timepoint. Then incubated for (A) 48 and (B) 144 hours, analysed by AlamarBlue. Data shown was normalised to the untreated control and are shown as the % mean \pm S.E.M (n=3). Statistical analysis was carried out using Two-Way ANOVA with Bonferroni's post-test (*P \leq 0.05, **P \leq 0.01, ***P \leq 0.001, ****P \leq 0.0001). 238

Figure 82. Collective Cell Migration of novel UA derivatives (7 – 12) in U-251 MG cells. Scratch assay was performed and cells were treated with sub-toxic concentration of each compounds. (A) Demonstrates the transformation process using Fiji software to analyse % size of scratch over time. (B) Scratch area analysis recorded every hour for 7 hours using 10X zoom using the Tucsen camera (ISH500) mounted Optika XDS-2 trinocular inverse microscope. Fiji software was used to analyse and calculate total scratch area. Statistical analysis was carried out using simple linear regression. (C) Rate of closure was calculated using the slope of the line and statistical analysis was carried out using One-Way ANOVA with Bonferroni's post-test (ns, not significant P > 0.05, ****P \leq 0.0001). All statistical analysis was performed using Graphpad Prism 9.0. Data are shown as the mean \pm S.E.M. of three independent experiments (n=3). 214

Figure 83. TMZ Dose Response Curve in U-251 MG cells. U-251 MG cells were exposed to TMZ at varying concentrations (0 – 500 μ M). Cells were also treated with a vehicle control of 0.5% DMSO. After 48 and 144 hours, cells were analysed using AlamarBlue cell viability assay. Data shown was normalised to the untreated control and are shown as the % mean \pm S.E.M (n=3). Statistical analysis was carried out using non-linear regression using Prism 9 statistical software. 218

Figure 84. UV-Vis Dose Response Curve in U-251 MG cells. U-251 MG cells were exposed to UV light at different timepoints. Cells were then incubated for (A) 48 hours and (B) 144 hours, and analysed by AlamarBlue. Data shown was normalised to the

untreated control and are shown as the % mean \pm S.E.M (n=3). Statistical analysis was carried out using non-linear regression. 219

Figure 85. Synergistic activity of UA and low dose of TMZ. (A) U-251 MG cells treated with and without 15 μ M TMZ as controls. (B) U-251 MG cells pre-treated with 5-20 μ M UA for 1 hour, after which 15 μ M TMZ was added to the wells. Cells were incubated for 48 and 144 hours, and analysed by AlamarBlue. Data shown was normalised to the untreated control and are shown as the % mean \pm S.E.M (n=3). Statistical analysis was carried out using Two-Way ANOVA with Bonferroni post-test (ns, not significant $P > 0.05$) (* $P \leq 0.05$, **** $P \leq 0.0001$). 220

Figure 86. Synergistic activity of Boc-protected compounds (7 – 9) and low dose of TMZ. U-251 MG cells were pre-treated with 5-20 μ M (A, B) compound 7; (C, D) compound 8; (E, F) compound 9 for 1 hour, after which 15 μ M TMZ was added to the wells. Cells were incubated for 48 and 144 hours, and analysed by AlamarBlue. Data shown was normalised to the untreated control and are shown as the % mean \pm S.E.M (n=3). Statistical analysis was carried out using Two-Way ANOVA with Bonferroni post-test (** $P \leq 0.01$, *** $P \leq 0.001$). 221

Figure 87. Synergistic activity of deprotected compounds (10 – 12) and low dose of TMZ. U-251 MG cells were pre-treated with 5-20 μ M (A, B) compound 10; (C, D) compound 11; (E, F) compound 12 for 1 hour, after which 15 μ M TMZ was added to the wells. Cells were incubated for 48 and 144 hours, and analysed by AlamarBlue. Data shown was normalised to the untreated control and are shown as the % mean \pm S.E.M (n=3). Statistical analysis was carried out using Two-Way ANOVA with Bonferroni post-test (**** $P \leq 0.0001$). 222

Figure 88. Combination of Compounds and low dose of UV-Vis. U-251 MG cells were pre-treated with NOAEL concentrations of compounds for 1 hour. After which was

exposed to UV for 10 and 15 seconds. Cells were then incubated for 144 hours and analysed by AlamarBlue. Data shown was normalised to the untreated control (NC) and 1 minute UV treatment (PC) and are shown as the % mean \pm S.E.M (n=3). Statistical analysis was carried out using One-Way ANOVA with Bonferroni post-test (**P \leq 0.01, ****P \leq 0.0001). 224

Figure 89. Cell proliferation seeding density. Cell Proliferation Measurement after 96 hours using haemocytometer in cells/ml. U-251 MG cells were seeded in a 96-well plate with 1.5×10^3 , 3×10^3 and 5×10^3 cells/well (100 μ l final volume), and incubated for 24, 48, 72 and 96 hours. Cells were dislodged and counted using a haemocytometer, for each timepoint. Concentration per ml was calculated and plotted in Graphpad Prism 9. Data are shown as the mean \pm S.E.M. of three independent experiments (n=3). 227

Figure 90. Cell Proliferation Measurement after 96 hours using haemocytometer in cells/ml. U-251 MG cells were seeded in a 96-well plate with 3×10^3 cells/well (100 μ l final volume), treated with vehicle control (0.1% DMSO), NOAEL concentration of UA and novel UA derivatives (7 – 12), and incubated for 24, 48, 72 and 96 hours. Cells were dislodged and counted using a haemocytometer, for each timepoint. Concentration per ml was calculated and plotted in Graphpad Prism 9. Data are shown as the mean \pm S.E.M. of three independent experiments (n=3). Statistical analysis was carried out using Two-Way ANOVA with Bonferroni post-test (**P \leq 0.01, ****P \leq 0.0001). 229

Figure 91. Histograms of CFSE proliferation of (A) vehicle control (NC; 0.1% DMSO), (B) positive control (PC; 20% DMSO), and (C) UA in U-251 MG cells. Shown are the gating strategy conducted; determination of live and dead cells using PI – P2 (live cells), P3 (dead cells); cell proliferation; cell proliferation population of live cells; cell proliferation of dead cells. 231

Figure 92. Histograms of CFSE proliferation of novel UA derivatives, compounds (A) 7, (B) 8, (C) 9, (D) 10, (E) 11, and (F) 12 in U-251 MG cells. Shown are the gating strategy conducted; determination of live and dead cells using PI – P2 (live cells), P3 (dead cells); cell proliferation; cell proliferation population of live cells; cell proliferation of dead cells. 232

Figure 93. Cell proliferation and cell death of novel UA derivatives (7 – 12) in U-251 MG cells. (A) Dot plot of cell proliferation, co-stained with PI analysed using CytExpert software; and bar graph of the % (B) cell viability and (C) cell death of compounds plotted using Graphpad Prism 9. Statistical analysis was carried out using One-Way ANOVA with Bonferroni post-test (*P ≤ 0.05, **P ≤ 0.01, ***P ≤ 0.001, ****P ≤ 0.0001). 234

Figure 94. Novel UA derivatives (7 – 12) in U-251 MG and A431 cells using 3D cell model. (A) Heatmap of the IC₅₀ of Novel UA derivatives. Initial concentration of 100 μM in culture medium was added to cells and serially diluted to different concentrations, as indicated. Alamar blue cell viability assay was then carried out following treatment for 48 and 144 hours. Statistical analysis was carried out using non-linear regression analysis, (n = 3). Images of (B) U-251 MG cells and (C) A431 cells. Captured using Optika XDS-2 trinocular inverse microscope equipped with a microscope Camera ISH500. 244

LIST OF SCHEMES

Scheme 1. Folic acid is reduced to dihydrofolic acid (DHF), which is in turn reduced to tetrahydrofolic acid (THF) in reactions mediated by dihydrofolate reductase (DHFR). 5-Methyltetrahydrofolic acid (5-methylTHF) is the major folate found in blood 36

Scheme 2. Schematic diagram of the ring A modification of UA. Reagents and conditions: (a) CrO_3 , H_2SO_4 , DMF; (b) m-CPBA, CHCl_3 ; (c) KOH, MeOH; (d) H_2SO_4 , MeOH (Tu *et al.*, 2009). * CrO_3 – chromium trioxide, m-CPBA – meta-Chloroperoxybenzoic acid. 56

Scheme 3. Schematic diagram of C3 and C28 modification of UA. Reagents and conditions: (a) and (d) $(\text{CH}_3\text{CO})_2\text{O}$, DMAP, THFR, RT; (b) $(\text{COCl})_2$, CH_2Cl_2 , RT; (c) $\text{NH}_2\text{-ROH}$, Et_3N , RT (Meng *et al.*, 2009). * $(\text{CH}_3\text{CO})_2\text{O}$ – acetic anhydride, DMAP- 4-dimethylaminopyridine, THFR – tetrahydrofuran, $(\text{COCl})_2$ – oxalyl chloride. 57

Scheme 4. Schematic diagram of the modification at C3 and C28 (compounds **E – H**). Reagents and conditions: (a) PCC; (b) NH_2OH ; (c) NaBH_3CN , TiCl_3 (Ma *et al.*, 2005) *PCC – pyridinium chlorochromate, NH_2OH – hydroxylamine, NaBH_3CN – sodium cyanoborohydride, TiCl_3 – titanium (III) chloride. 59

Scheme 5. A schematic of the synthesis of the novel FUA derivatives (based on similar synthetic procedures from the literature). The synthesis of novel FUA compounds B and C were conjugated using a similar approach. 76

Scheme 6. A schematic of the initial approach carried out to synthesise novel FUA derivatives. The first attempt was to conjugate FA to UA. 77

Scheme 7. The *N*-Boc protection of diamines where $\text{R} = (\text{CH}_2)_2\text{NH}_2$, $(\text{CH}_2)_2\text{SS}(\text{CH}_2)_2\text{NH}_2$ and $(\text{CH}_2)_2\text{O}(\text{CH}_2)_2\text{O}(\text{CH}_2)_2\text{NH}_2$ (Common Organic Chemistry, 2020). 79

Scheme 8. The conjugation of <i>N</i> -Boc protected diamines to folic acid (Trindade et al., 2014).	84
Scheme 9. The Boc deprotection of <i>N</i> -Boc ethylenediamine folate.	88
Scheme 10. A schematic of the initial approach to conjugating UA to FUA to generate novel FUA conjugates. This attempt uses carbodiimide chemistry with two most common coupling reagents – DCC/NHS and EDC/HOBt.	96
Scheme 11. The conjugation of <i>N</i> -Boc protected diamines to ursolic acid (Liu et al., 2018).	98
Scheme 12. The Boc deprotection of UA-diamine.	104

LIST OF TABLES

Table 1. The classification of astrocytic tumours by WHO (Louis et al., 2016).	13
Table 2. Some published UA modifications and anti-cancer activities. Cell lines used below are A549, H460 and H322 (human lung); HCT-116 (colorectal); MCF-7, FR-2, SUM149PT, HCC1937 and Bcap-37 (breast); THP-1 (human monocytic), MGC803 (gastric); LKB1 and HepG2 (liver); T24 (urinary bladder); U87, GBM02 and GBM95 (GBM); and HT-29 (colon) cancer cell lines.	60
Table 3. Key ¹ HNMR and ¹³ CNMR resonances for UA Hunan and UA Sigma.	71
Table 4. Cytotoxicity evaluation summary of two different UA origins obtained from natural sources.	73
Table 5. A summary of the synthetic steps undertaken for the synthesis of novel FUA derivatives.	75
Table 6. ¹ HNMR resonances for <i>N</i> -Boc protected diamines 1 – 3 . The integration and peak splitting are shown in brackets.	80
Table 7. ¹³ CNMR resonances for <i>N</i> -Boc protected diamines 1 – 3 .	81
Table 8. Mass spectroscopy results of <i>N</i> -Boc protected diamines 1 – 3 .	81
Table 9. Summary of other failed attempts to conjugate ursolic acid with the folate-ethylenediamine (6).	92
Table 10. Key ¹ HNMR resonances for <i>N</i> -Boc diamine-UA 7 – 9 . The integration and peak splitting are shown in brackets.	100
Table 11. Key ¹³ CNMR resonances for <i>N</i> -Boc diamine-UA 7 – 9 .	101
Table 12. Mass spectroscopy result of <i>N</i> -Boc diamine UA 7 – 9 .	102
Table 13. Key ¹ HNMR resonances for deprotected <i>N</i> -Boc diamine-UA 10 – 12 . The integration and peak splitting are shown in brackets.	105
Table 14. Mass spectroscopy result of deprotected <i>N</i> -Boc diamine UA 10 – 12 .	106

Table 15. Mass spectroscopy result of FUA compound 13 – 15 .	108
Table 16. Physicochemical and pharmacokinetic properties, and drug-likeness predictions of novel FUA derivatives using SwissADME. Colours are represented as: within the predicted range (green), slightly above the predicted range (orange), and out of predicted range (red).	113
Table 17. Summary of the molecular docking results for FA and the novel FUA derivatives with FR α (PDB: 4LRH). HB – hydrogen bond.	133
Table 18. Summary of the molecular docking results for folic acid and the novel FUA derivatives with VRK1 (PDB: 6BU6). HB – hydrogen bond.	150
Table 19. The IC ₅₀ of novel FUA derivatives at high concentrations.	164
Table 20. The IC ₅₀ Cytotoxicity of novel UA derivatives in U-251 MG cells.	171
Table 21. Physicochemical and pharmacokinetic properties, and drug-likeness predictions of Novel UA Derivatives. Colours are represented as: within the predicted range (green), slightly above the predicted range (orange), and out of predicted range (red).	176
Table 22. Number of docking poses and predicted binding affinity of novel UA derivatives.	183
Table 23. Summary of the molecular docking results for UA and the novel UA derivatives with VRK1 (PDB: 6BU6). HB – hydrogen bond.	195
Table 24. IC ₅₀ of novel UA derivatives (7 – 12) on different cancer cell lines and normal cell line. The colours are in comparison to UA cytotoxicity of UA – green (enhanced), orange (slightly decreased, <5) and red (decreased, >5).	201
Table 25. The calculated rate of gap closure with statistical difference (Bonferroni's post-test) analysis for UA and novel UA derivatives (7 - 12). NC – negative control; NS – not significant.	215

Table 26. The 2D and 3D cell culture IC ₅₀ of novel UA derivatives (7 – 12) in U-251 MG and A431 cell lines. The colours are in comparison to the cytotoxicity of UA – green (enhanced) and red (decreased).	245
Table 27. The binding pocket centre co-ordinates obtained from ADT and the grid box dimensions.	294
Table 28. Modules completed as part of the structured PhD - ¹ Discipline Specific Skills and ² Employability Skills. The required 40 credits for structured PhD has been fully completed.	308
Table 29. Extracurricular activities undertaken.	309

CHAPTER 1

INTRODUCTION

1.1 Introduction to Cancer

The World Health Organisation (WHO) defined cancer – also called neoplasm and malignant tumour, as an uncontrolled and erratic growth of cells that can be altered by a number of different internal and external environmental factors. In some cases, a cancer cell could become malignant and can spread throughout the body, invading various body tissues. Cancer ranks as one of the leading causes of mortality and is an important barrier to increasing life expectancy worldwide. Hence, early detection, correct diagnosis and effective treatment is crucial to prolong the life expectancy of diagnosed patients (WHO, 2022).

The International Agency for Research on Cancer (IARC) in GLOBOCAN cancer statistics survey 2020, estimated 19.3 million new cases and almost 10.0 million deaths from cancer worldwide (**Figure 1**; Ferlay *et al.*, 2021). In addition, global cancer burden is projected to rise to 47% or 28.4 million new cases in 2040 (Ferlay *et al.*, 2021; Sung *et al.*, 2021). GLOBOCAN 2020 reported that the leading cause of cancer death is lung cancer (18.0% of total cancer deaths), followed by colorectal (9.4%), liver (8.3%), stomach (7.7%), and female breast (6.9%) cancers (Sung *et al.*, 2021). Europe accounts for 22.8% of total cancer cases and 19.6% deaths in the GLOBOCAN 2020 report, despite having only one-tenth of global population (Ferlay *et al.*, 2021). In Ireland, cancer is the most common cause of death, accounting for approximately 30% of deaths every year (National Cancer Registry Ireland, 2022). There were an estimated 45,753 new cases reported in 2020, and the most common cancers diagnosed are lung, bowel, breast, prostate and skin cancers (Irish Cancer Society, 2022).

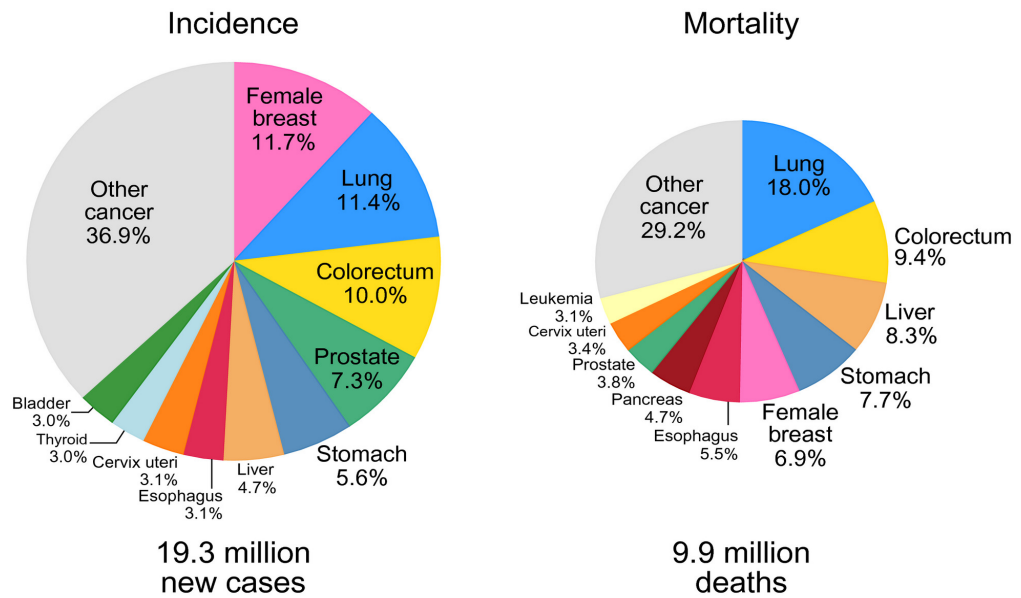


Figure 1. Graphical overview of incidence and mortality rates of different cancers worldwide in 2020 (Sung *et al.*, 2021).

Central nervous system (CNS) cancer represents a substantial morbidity and mortality worldwide. GLOBOCAN statistics 2020 reported that there were 308, 102 (1.6%) cases and 251, 329 (2.5%) brain and CNS cancer deaths globally (Sung *et al.*, 2021). The Central Brain Tumour Registry of United States (CBTRUS) reported that there were 24.25 per 100, 000 cases, with an average annual mortality rate of 4.43 per 100, 000 and a five-year relative survival rate of 66.9% between 2014 and 2018, of malignant brain and other CNS tumours (Ostrom *et al.*, 2021). Furthermore, Europe accounts for 21.8% of incidence and 21.4% of mortality worldwide, with 23.6% of 5-year prevalence in 2020 (The Global Cancer Observatory, 2020). In Ireland, brain and CNS cancer accounts for 3.5% of cancer mortalities between 2014 and 2016 (NCRI, 2019). The average survival rate in Ireland for primary malignant brain cancer is poor, having an unchanged five-year net survival of 19%, similar to figures in the UK (NCRI, 2019).

1.1.1 The Hallmarks of Cancer

In the year 2000, Hanahan and Weinberg published their influential review: the hallmarks of cancer, detailing six alterations essential for malignant growth: self-sufficiency in growth signals, insensitivity to growth-inhibitory signals, limitless replicative potential, evading apoptosis, sustained angiogenesis, and tissue invasion and metastasis (Hanahan and Weinberg, 2000). This concept has been revisited in 2011, introducing two emerging hallmarks based on the progress within the previous decade – reprogramming energy metabolism and evasion by cancer cells; and two enabling characteristics – genomic instability and inflammation (Hanahan and Weinberg, 2011). The two emerging hallmarks added in 2021 are now considered as core hallmarks. Recently, Hanahan (2022) recognised the impact of their study and from research in the past decade, he proposed additional new hallmarks and enabling characteristics – unlocking phenotypic plasticity, non-mutational epigenetic reprogramming, polymorphic microbiome, and senescent cells (Hanahan, 2022). The concept of ‘Hallmarks of cancer’ became an essential resource for cancer researchers, providing a comprehensive foundation for studying and understanding cancer biology. The following sections are the summary of each of the hallmarks to understand the architecture behind the diversity of cancer development (Figure 2).

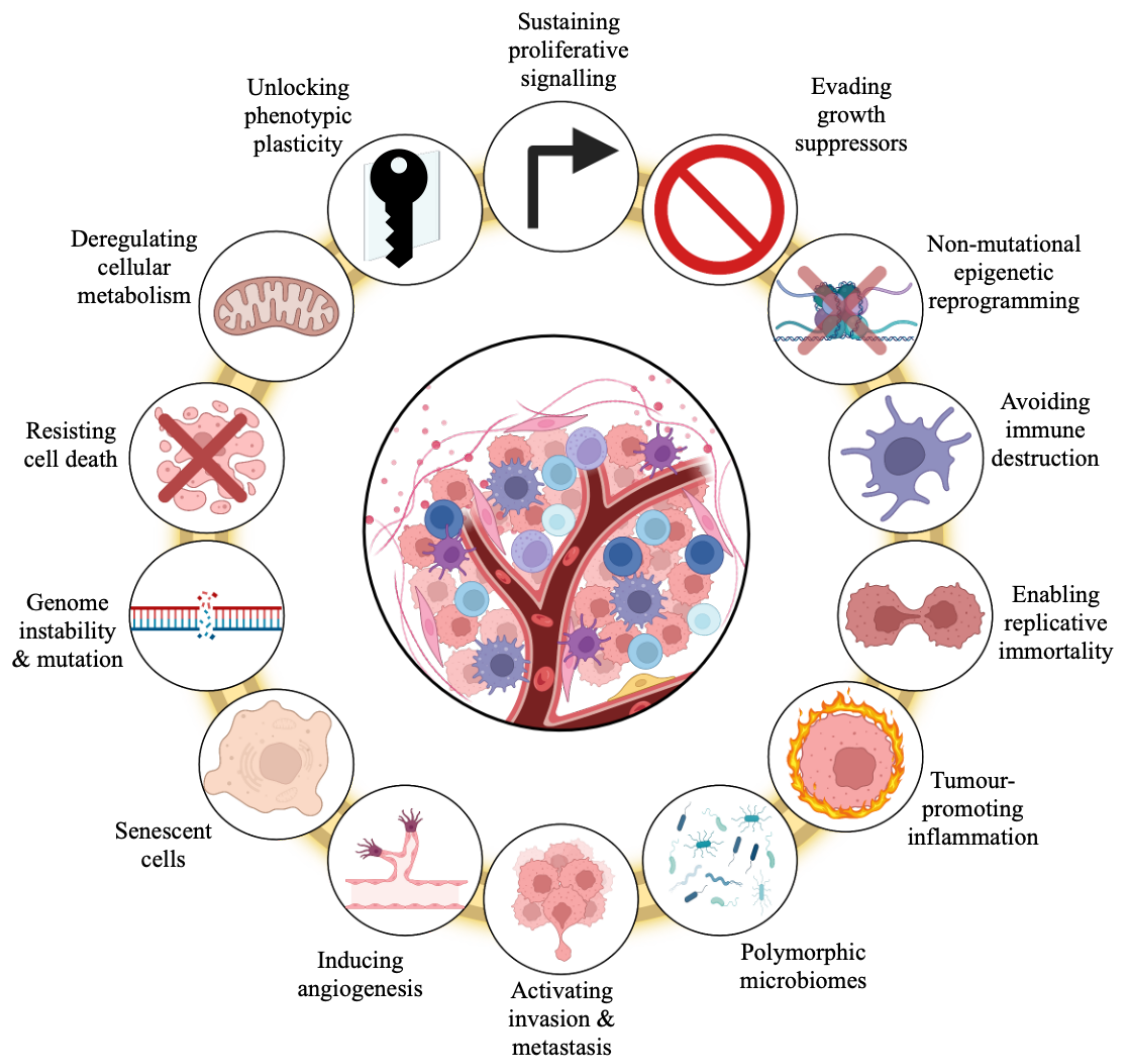


Figure 2. The Hallmarks of Cancer (modified from Hanahan and Weinberg, 2011; Hanahan 2022). Figure created with BioRender.com.

One of the most prominent characteristics of a cancer cell is its **Sustained Proliferative Signalling** in the absence of external stimuli. Tumour cells have the capability to sustain proliferative signalling in multiple ways: (1) They produce their own growth factors and the corresponding receptor results in autocrine stimulation. (2) They may send paracrine signals to stimulate normal, tumour-associated stroma, producing various growth factors to support cancer cells. (3) Receptor signalling could be deregulated or growth factor receptor levels could be elevated, making cancer cells hyperresponsive. (4) Lastly, cancer

cells could become independent from growth factors, because of downstream signalling pathway activation or disruption of negative-feedback mechanisms (Hanahan and Weinberg, 2011; Gutschner and Diederichs, 2012).

The ability to **Evade Growth Suppression** is a highly complementary hallmark capability for sustaining proliferative signalling in cancer cells. There are two canonical suppressors, tumour protein 53 (TP53) and retinoblastoma (RB), each operating as nodes within regulatory circuits. The TP53 receives inputs from stress and abnormality, stopping cell cycle progression until system is back to normal. RB protein receives signal from extracellular and intracellular sources, determining whether a cell should undertake a growth and division cycle (Hanahan and Weinberg, 2011; Hanahan and Weinberg, 2000).

Programmed Cell Death, or apoptosis, is one of the defences of the body against cancer cells. Apoptosis can be induced by various external as well as internal stimuli and several studies have shown how highly malignant cancers can attenuate apoptosis and become therapy resistant. Another pathway that is activated by stress signal is autophagy, and has been found to be activated in cancer cells (Elmore, 2007; Gutschner and Diederichs, 2012).

Most cells/normal cells go through a limited number of **Growth-and-Division** cycles due to senescence and cell death. Conversely, cancer cells need unlimited replicative potential in order to form tumours, essentially becoming **immortal**. There were evidence indicating that telomeres protecting the ends of chromosomes, are involved in the capability for unlimited proliferation. Telomeres are known to shorten every cell division,

until a critically short length triggers cell death. About 90% of immortalised cells, including cancers, have the ability to increase their telomere length due to a mutation in telomerase (Bryan *et al*, 1997; Blasco, 2005).

Cancer cells require oxygen and nutrients in order to grow and proliferate. The formation of new blood vessels to supply these elements to the cells through a process called **Angiogenesis**. Regulatory mechanisms in the cell normally controls the process of angiogenesis. Cancer cells show activation of the angiogenetic pathway, leading to formation of blood vessels supplying the tumour. An “angiogenic switch” is also turned on during tumour progression, which leads to continuous sprouting of new vessels that help to sustain tumour growth (Hanahan and Weinberg, 2011; Hanahan and Folkman, 1996).

The process of **Invasion and Metastasis** is a cascade of changes in the cell. This invasion and metastasis cascade is comprised of multiple biological changes that allow cancer cells to invade into healthy tissues, followed by intravasation into nearby blood and lymphatic vessels. During the transit of cells through the lymph and blood system, cancer cells must escape immune surveillance and show anchorage-independent growth and survival (Talmadge and Fidler, 2010; Gutschner and Diederichs, 2012).

The two **Enabling Characteristics** added in 2011 confers the “functional capabilities that allow cancer cells to survive, proliferate, and disseminate” (Hanahan and Weinberg, 2011). The first characteristic, genomic instability, facilitates a higher than normal mutation rate and aberrations in the genome. Whereas, the second one is highly infiltrated

with the cells of the immune system and a picture has emerged whereby immune cells promote tumour progression (Hanahan and Weinberg, 2011).

The two **Emerging Hallmarks** that emerged are part of the core cancer framework that was originally created in the year 2000 (Hanahan and Weinberg, 2000). The reprogramming of energy metabolism supports proliferation. Whereas, evading immune destruction is the ability of cancer cells to escape the surveillance and attack by the body's immune system. The latter's concept is particularly important in light of emerging treatments that aim to harness the strength of the immune system to attack tumours (Hanahan and Weinberg, 2011; Azvolinsky, 2011).

Recent addition to emerging hallmark suggested that **phenotypic plasticity** enables various disruptions of cellular differentiation which is integral to cancer pathogenesis. Hanahan (2022) notes that cellular plasticity is not a “novel invention” in cancer, but rather a malignant twist on existing mechanisms that some normal cells can activate to repair and regenerate normal tissues. The two new enabling characteristics indicates that global changes in **epigenetic** landscape are recognised as a common feature of many cancers. Reproducing what happens during normal embryogenesis and development in cancer cells can reprogram a large number of gene-regulation networks to alter gene expression. The profound contribution of a vast array of **microorganisms** to human health has been found to have protective or deleterious effects on cancer development and progression. In addition, the new edition also acknowledges the importance of **senescent cells** as instrumental components of tumour microenvironment. The role of cellular senescence in cancer is now well recognised, and was found that it can stimulate tumour development and malignant progression (Hanahan, 2022).

1.2 Chemotherapy

Cancer chemotherapy has already been proven as a widely effective treatment and has profoundly influenced the survival of cancer patients. The famous German chemist, Paul Ehrlich, first coined the term “chemotherapy” in the early 1900s. He defined it as a use of chemical to treat infectious diseases, for example, arsphenamine (Salvarsan; **Figure 3**) to treat syphilis (Ehrlich, 1900). In 1948, Dr Sidney Farber demonstrated that aminopterin (**Figure 3**), a synthetic derivative of the B-vitamin folic acid, produced remission in children with acute leukemia by blocking the uptake of folic acid and consequently arresting DNA replication. The drug was improved due to difficult synthesis of aminopterin, resulting in the generation of methotrexate (**Figure 3**), an antifolate drug still widely used today and the first drug to cure choriocarcinoma (Galmarini *et al.*, 2012; Strebhardt and Ullrich, 2008). The success of these initial chemotherapeutics has paved the way for researchers to discover drugs that block different functions in the Hallmarks of Cancer – Replicative Immortality. The era of chemotherapy had begun.

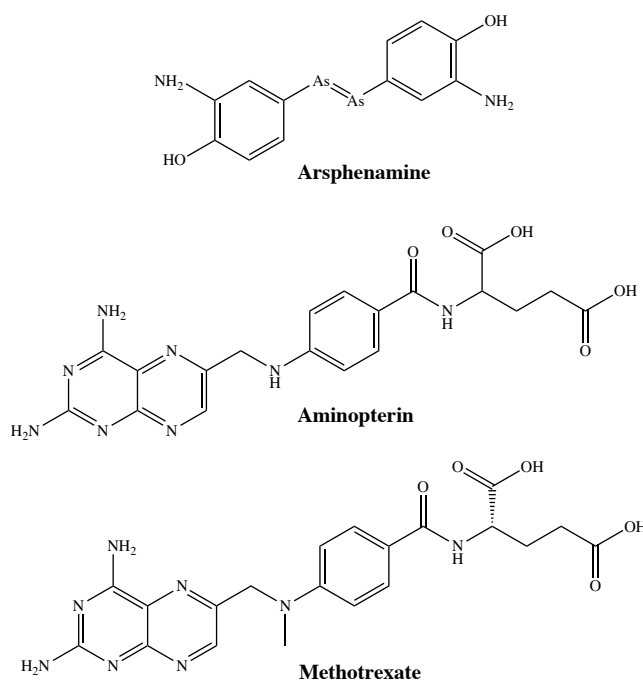


Figure 3. The chemical structures of Arsphenamine, Aminopterin and Methotrexate.

In the early 1960s, the Eli Lilly Company introduced vinca alkaloids from *Vinca rosea*, vincristine (**Figure 4**), for the treatment of various cancers such as acute leukaemia; procarbazine (**Figure 4**) for the treatment of Hodgkin's disease was also introduced by Brunner and Young (DeVita and Chu, 2008; Johnson, *et al.*, 1963; DeVita, 1970). During this time, all human cancer chemotherapy was with single agents. It was the end of 1960s when the concept of combination chemotherapy was introduced by DeVita and his colleagues. The treatment of acute lymphocytic leukaemia in children using VAMP (vincristine, amethopterin, 6-mecaptopurine, and prednisone), increased the remission rate from 25 to 60%, with 50% of the remissions being long enough to be considered as cures. Non-Hodgkin lymphoma was treated with the concept of mitochondrial outer membrane permeabilization (MOMP) program, combining nitrogen mustard with vincristine, methotrexate and prednisone and MOPP (Mustargen, Oncovin, Procarbazine and Prednisone), with approximately 80% of cases resulting in complete remissions (DeVita and Chu, 2008). Following the success of combinational therapy came the era of adjuvant chemotherapy and targeted therapy. However, despite the great advances in the field of chemotherapy, there are, however limitations due to a lack of specificity in delivery, as most chemotherapeutic agents target healthy and cancerous cells alike (Carey *et al.*, 1988; Zwicke *et al.*, 2012; McCarron *et al.*, 2018). Targeted drug delivery was one of the aims of this study and will be discussed in more detail below.

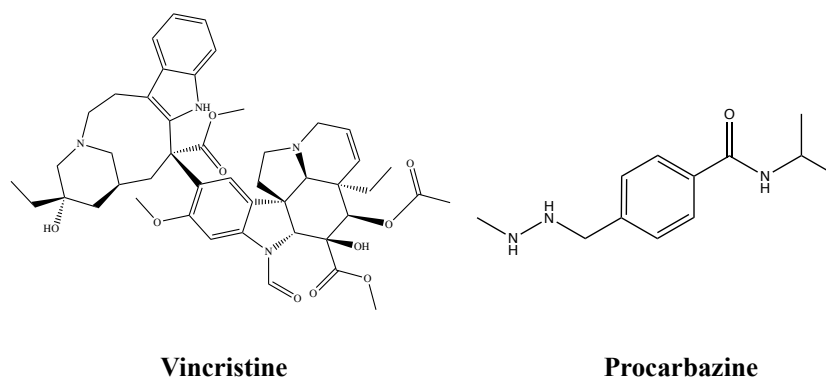


Figure 4. The chemical structures of vincristine and procarbazine.

1.2.1 Novel Chemotherapeutic Drugs

As mentioned above, chemotherapy has been widely used for cancer treatment, however, it is often accompanied with serious side effects. Hence, it is highly desirable to develop new anticancer drugs with improved tumour selectivity, safety and efficacy. Current studies have focused on natural plant-based bioactive compounds which is considered to be an unparalleled source to design novel and effective chemotherapeutic agents (Gill *et al.*, 2016; Shanmugam *et al.*, 2012). Plant bioactives are a good source of anticancer drugs because of the potential for reduced toxicity and increased activity (Shin *et al.*, 2018). It has been published that 25% of clinically used drugs are plant-derived (Schmidt, *et al.*, 2007); and more than 60% of drugs with anti-cancer activity originated from plants (Gordaliza, 2007). Such natural products have shown efficacy as anti-inflammatory, anti-depressant, anti-microbial as well as anti-cancer agents (Fridlender *et al.*, 2015).

Numerous research studies have been published over the decades for the suitability and effectiveness of a range of bioactive compounds against cancer (Muniraj *et al.*, 2019). The various anticancer activities include anti-proliferative, pro-apoptotic, anti-metastatic, anti-angiogenic effects, as well as autophagy regulation, induced apoptosis, reversal of multidrug resistance, immunity balance, and enhanced chemotherapy both *in vitro* and *in vivo* (Luo *et al.*, 2019; George and Abrahamse, 2019). Chemotherapeutic agents from plants can be categorized into four main classes of compounds: vinca alkaloids, epipodophyllotoxins, taxanes, and camptothecins (shown in **Figure 5**; Mann, 2002; Mazumder, *et al.*, 2013).

Vinca alkaloids are the first plant-derived agents to advance into clinical trials, vinblastine and vincristine isolated from *Catharanthus roseus* G. Don. (Apocynaceae). They are still effectively used in the treatment of several types of cancers, such as testicular, breast and bladder (Dias, *et al.*, 2012; Mazumder, *et al.*, 2013). Taxanes are considered as one of the most important classes of cancer chemotherapeutic drugs in clinical use. Paclitaxel and Docetaxel are the two most clinically effective drugs of this class. Paclitaxel is used in the treatment of breast, ovarian, and non-small cell lung cancer (NSCLC), while docetaxel is primarily used for breast cancer and NSCLC treatment (Cragg and Pezzuto, 2015). Camptothecin is a DNA topoisomerase I inhibitor which is involved in the cleavage and re-assembly of DNA (Mazumder, *et al.*, 2013). Lastly, podophyllotoxin was initially used for skin cancer and warts, however, it failed clinical trials due to lack of efficacy and unacceptable toxicity (Cragg and Pezzuto, 2015). Hence, this study focuses on the development of a plant bioactive which will be discussed more in detail below.

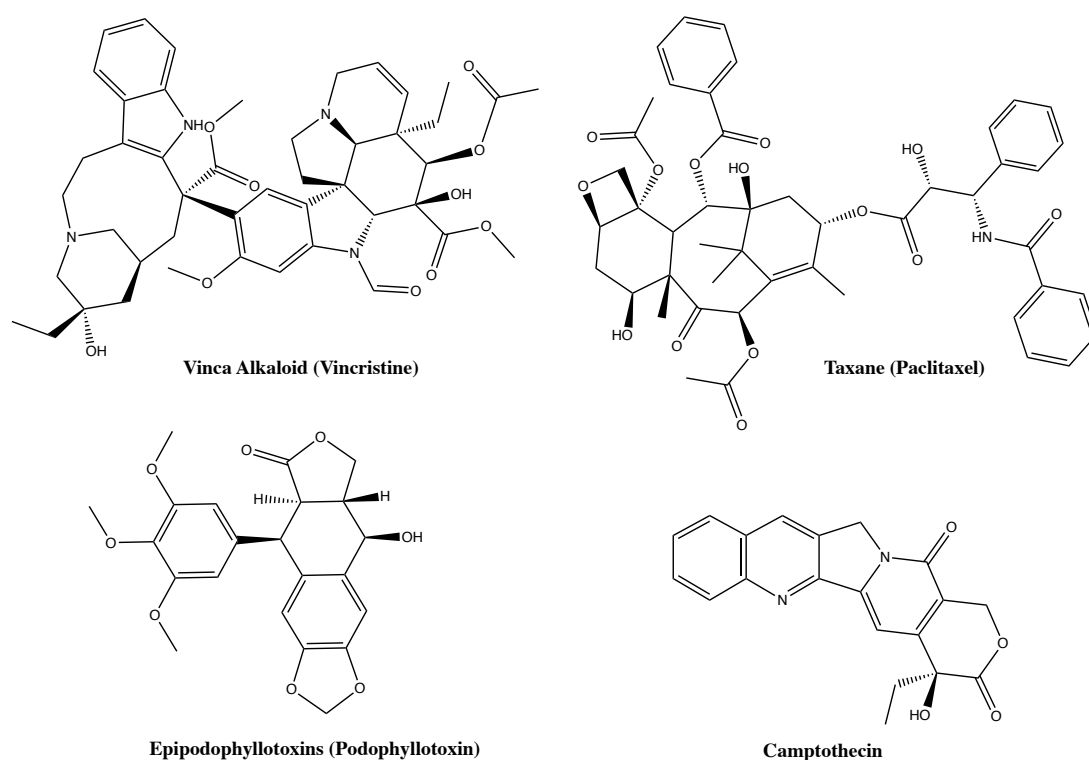


Figure 5. Plant derived anti-cancer agents: Four main classes of natural products.

1.3 Glioblastoma Multiforme (GBM)

Glial tumours or gliomas are the commonly occurring tumours of the CNS, accounting for almost 30% of all primary brain tumours, and 80% of all malignant ones, and are responsible for the majority of deaths from primary brain tumours (Gould, 2018; Hanif, *et al.*, 2017). Gliomas have been classified based on their presumed cell origin: astrocytic tumours, ependymomas, oligodendrogliomas, and mixed gliomas (Hanif *et al.*, 2017). Tumours derived from astrocytomas, are the most common subtype (about 67%) of all malignant brain cancers, and was defined as diffused infiltrated tumours, which includes differentiated neoplastic astrocytes (NCRI, 2015; Hanif *et al.*, 2017). This glioma comprises of two subgroups: (1) diffuse infiltrating glioma – more prevalent; and (2) non-diffuse gliomas – less prevalent (Khani *et al.*, 2019). Gliomas have been classified by WHO into four histological grades of increasing malignancies into grade I to IV: grade I gliomas include mild lesions that are characterised by low proliferative potential, while grades II to IV are highly invasive and malignant (**Table 1**; Louis *et al.*, 2016; Rahman *et al.*, 2022).

Table 1. The classification of astrocytic tumours by WHO (Louis *et al.*, 2016).

WHO Grade	WHO Description
Grade I	Pilocytic astrocytoma
Grade II	Diffuse astrocytoma
Grade III	Anaplastic astrocytoma
Grade IV	Glioblastoma

Glioblastoma (GBM), sometimes called glioblastoma multiforme, was classified as highly malignant grade IV astrocytoma, and is biologically considered to be the most aggressive, invasive and undifferentiated type of brain tumour (Dong *et al.*, 2015; Litak *et al.*, 2019). The large portion of GBM tumour cells reproduce and divide at any given time. It is infiltrative and can invade nearby regions of the brain, but exceedingly rare to spread outside of the brain (Taylor, *et al.*, 2019). It accounts for approximately 57% of gliomas and 48% of primary brain tumours (Philips *et al.*, 2018; Taylor, *et al.*, 2019; Tan *et al.*, 2020). Unfortunately, patients diagnosed with GBM have only 2 years survival post diagnosis; and only 2% of patients diagnosed and admitted for medical treatment survive for 3 years. Patients with no treatment can only survive for less than 3 months (Scott *et al.*, 2011).

1.3.1 Primary and Secondary Glioblastoma

Glioblastoma comprises distinct disease entities which evolve through different genetic pathways, affect patients at different ages, and likely differ in prognosis and response to therapies (Peiffer and Kleihues, 2006; Ohgaki and Kleihues, 2012). The terms “primary GBM” and “secondary GBM” were first defined by the German neuropathologist Hans-Joachim Scherer (1906-1945) in 1940, where he distinguished the two types on the basis of their mode of evolution. The current (5th edition; 2016 CNS WHO) update breaks the century-old principle of diagnosis based entirely on microscopy by incorporating molecular parameters into the classification of CNS tumour entities (Louis *et al.*, 2016).

GBM is now divided into three different subgroups based on isocitrate dehydrogenase 1 (IDH1) and IDH2 mutation status: (1) IDH-wildtype, (2) IDH-mutant, and (3) NOS (not otherwise specified) (Philips *et al.*, 2018). IDH1 and IDH2 are key enzymes involved in epigenetic regulation, cellular metabolism, redox states, and DNA repair (Philips *et al.*, 2018). These different types correspond to distinct disease entities with different genetic pathways, age groups, and prognosis (Kleihues and Ohgaki, 1999; Ohgaki and Kleihues, 2013; Louis *et al.*, 2016; Tamimi and Juweid, 2017). The vast majority of cases (~90%), primary or *de novo* IDH-wildtype, have no clinical or histological evidence of a less malignant precursor lesion (Ohgaki and Kleihues, 2013; Louis *et al.*, 2016). The remaining 10% of the cases are secondary or IDH-mutant, progress from low-grade diffuse astrocytoma or anaplastic astrocytoma, have a lesser degree of necrosis and are preferentially located in the frontal lobe, and carry a significantly better prognosis (Taylor *et al.*, 2019).

Histologically, primary and secondary GBMs are largely indistinguishable, but they develop from different genetic precursors and show different genetic alterations that permit differentiation (Ohgaki and Kleihues, 2012; Seifert *et al.*, 2015). With respect to prevalence, primary GBM predominates in patients over 55 years of age (mean age = 64 years), whereas secondary GBM preferentially arises in younger patients (mean age = 45 years) (Louis *et al.*, 2016). Therefore, the survival expectancy for patients diagnosed with primary GBM, after application of current concomitant and adjuvant therapies, reaches up to only 15 months. Whereas patients diagnosed with secondary GBM are statistically reported to have higher survival expectancy, twice longer than primary GBM (Ohgaki and Kleihues, 2012).

Hallmark alterations of primary GBM include epidermal growth factor receptor (EGFR) gene mutation and amplification, over expression of mouse double minute 2 (MDM2), deletion of p16 and loss of heterozygosity (LOH) of chromosome 10q holding phosphatase and tensin homolog (PTEN), and telomerase reverse transcriptase (TERT) promoter mutation (Hanif *et al.*, 2017). The characteristic features of secondary GBMs include over expression of p53, platelet-derived growth factor A, and platelet-derived growth factor receptor alpha (PDGFA/PDGFRa), Retinoblastoma (RB) protein and LOH of 19q (Montemurro, 2019). Mutations in IDH1 and IDH2 are present in 70 - 80% of low-grade glioma and secondary GBM, and is only 5 - 10% of primary GBM (Tamimi and Juweid, 2020; Ohgaki and Kleihues, 2013).

This research study mostly focused on elucidating a novel treatment for the onset of primary GBM. Thus, the reference to GBM in the remainder of this thesis refers to primary GBM, unless otherwise specified.

1.3.2 Epidemiology of Glioblastoma

Glioblastoma accounts for almost 60% of all gliomas in all age groups but the peak incidence is between 55 to 60 years, with incidence rate higher in men compared to women - 11,170 males and 9,330 females (Hanif *et al.*, 2017; Johnson *et al.*, 2017). Diagnosed patients have poor prognosis with about one-year survival rate of 37.2% post diagnosis, and a five-year survival rate of approximately 5% (Philips *et al.*, 2018; Hanif *et al.*, 2017). The median survival timeline of GBM is approximately 14 to 15 months from diagnosis (Sasmita *et al.*, 2017) and attributes to the highest years of life lost (~20

years) for any primary adult tumour due to its relatively early onset and poor prognosis (Rouse *et al.*, 2016).

CBTRUS 2022 reported that GBM is responsible for 14.3% of all tumours and 49.1% of primary malignant CNS tumours in the United States (Figure 6; Ostrom *et al.*, 2021). Europe has the highest incidence and mortality compared to other continents, and accounts for approximately 65% of all primary brain tumours with a low five-year survival rate of 10% (Kiskova, *et al.*, 2020). Whereas in Ireland, GBM and other high-grade astrocytic tumours have the poorest survival with a five-year survival rate of only 4% (NCRI, 2016).

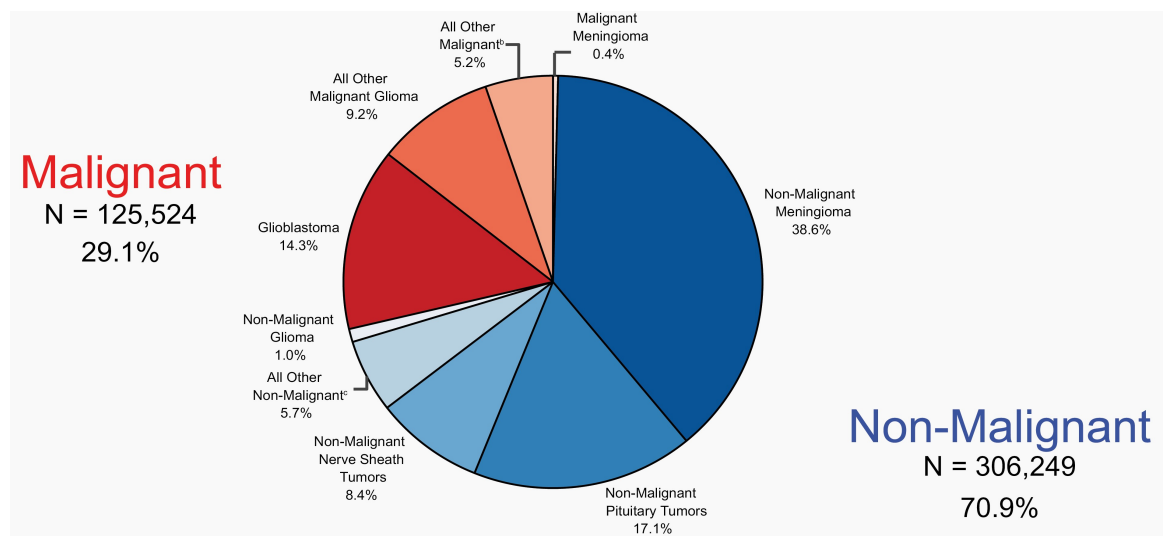


Figure 6. Distribution of Primary Brain and Other CNS Tumours by Behaviours (Five-Year Total of 431,773; Annual Average Cases of 86,355), CBTRUS Statistical Report: US Cancer Statistics - NPCR and SEER, 2014–2018 (Ostrom *et al.*, 2021).

1.3.3 Glioblastoma Core Signalling Pathways (Gliomagenesis)

Gliomagenesis is a multicomponent process involving several genetic mutations affecting numerous molecular pathways. As a result of genome profiling and the Cancer Genome Atlas project (Parsons, *et al.*, 2008), more than 600 genes were sequenced from >200 human tumour samples, which revealed the complicated genetic profile of GBM and established a set of three core signalling pathways that are commonly dysregulated – the activation of the receptor tyrosine kinase (RTK)/RAS/phosphoinositol-3-kinase (PI3K) pathway, inhibition of p53, and RB signalling pathways (Davis, 2016; Taylor, *et al.*, 2019). The majority of GBM have alterations on those pathways, which leads to uncontrolled cell proliferation, enhanced cell survival and escape of cell-cycle checkpoints, senescence and apoptosis, as well as cell invasion and angiogenesis (Davis, 2016; Pearson and Regad, 2017; Taylor *et al.*, 2019). It is also worth noting that mutations in GBM may not affect one single pathway but may be the result of alterations in several pathways (Pearson and Regad, 2017). This results in additional complexity in developing GBM therapies.

RTK/RAS/PI3K Signalling Pathway

The RTK/RAS/PI3K signalling pathway was found to be altered in 90% of GBM patients and has been the most extensively studied pathway in malignant gliomas to date (Pearson and Regad, 2017; Mandel and Kesari, 2016). The disruption of this pathway is also considered to play an important role in the tumorigenesis and progression of GBM (Zhou, *et al.*, 2020). RTKs are cell-surface receptors that bind growth factors. It is activated through two major downstream pathways, Ras/MAPK/ERK and Ras/PI3K/AKT (Regad, 2015; Pearson and Regad, 2017). The alterations in this pathway are mainly mediated by

mutations on EGFR – the most common; and PDGFR – the second most amplified RTK (Mandel and Kesari, 2016). The overexpression of EGFR was the most attractive therapeutics found to be overexpressed in 57.4% of GBM cases, and has gained much interest as a primary driver of tumour proliferation and survival. In addition, 50% of GBM tumours with EGFR amplification, mutates to EGFR variant (EGFRvIII), which corresponds to the loss of exons 2-7 resulting to constitutive activation and enhanced RAS/PI3K signalling. PI3K mutations and deletions/mutation, PTEN, were commonly found and reported to be mutually exclusive with GBM and presents one way or the other. The strong association between RTK/RAS/PI3K pathways and tumorigenesis reaffirms these genomic alterations (Kohsaka and Tanaka, 2013; Ware and Zhu, 2018; Mansouri, *et al.*, 2017). Deregulation of this pathway affects several hallmarks of cancer, such as sustaining proliferative signalling, evading growth suppressors, activating invasion and resisting cell death (Venkatesan, *et al.*, 2016).

p53 Tumour Suppressor Pathway

The p53 pathway was found to be altered in 85% of GBM cases and also functions in cell cycle control, DNA damage response, cell death, and differentiation (Ware and Zhu, 2018). p53 is the most frequently mutated gene in human cancer and is critical to cancer prevention (Pearson and Regad, 2017). It is activated by various stresses, such as replicative or oxidative stress, and anti-tumour therapy by increasing p53 stability. When activated, p53 acts as transcriptional regulator of its downstream genes (Ham, *et al.*, 2019). However, this pathway has a negative feedback loops. When p53 induces transcription of MDM2, a proto-oncogene, it leads to degradation of p53 which in turn prevents DNA repair. Deregulated p53 pathway components have been implicated in

GBM cell invasion, migration, proliferation, evasion of apoptosis, and cancer cell stemness (Zhang, *et al.*, 2018).

RB1/p16INK4a Tumour Suppressor Pathway

The RB signalling pathway was found to be affected in 79% of GBM cases. It is a tumour suppressor protein that is dysfunctional in several cancer types (Mandel and Kesari, 2016; Ware and Zhu, 2018). This pathway also plays a critical role in inhibiting cell cycle progression in the G1/S phase by binding and inhibiting transcription factors of the E2 factor (E2f) family (Mandel and Kesari, 2016; Vleeschouwer, 2017). The deregulation of this pathway leads to the sustainment of proliferative signalling, often through deletion or mutation of RB1 and cyclin D, and amplification of CDK4 and CDK6 (Venkatesan, *et al.*, 2016; Butowski, 2018).

1.3.4 Current Therapeutic Strategies in Glioblastoma

Despite recent advances in molecular biology and current combination strategies, GBM still remains the most challenging CNS cancer to treat with an incredibly low survival rate (15 months median survival) (Hanif *et al.*, 2017). Main challenges of GBM therapy is due to the location of the disease, its complex heterogeneity, and aggressive infiltrative growth (Kesari, 2011; Jena *et al.*, 2019). Maximal tumour resection, followed by radiotherapy and treatment with chemotherapeutic agents (either alone or in combination, referred to as ‘Stupp Protocol’) has been the standard of care for patients with newly diagnosed GBM and good performance status since 2005 (Stupp *et al.*, 2005; Hanif *et al.*, 2017; Lakomy *et al.*, 2020). However, recurrence within a few months remains inevitable

(Alifieris and Trafalis, 2015). Moreover, even combination treatment strategies have often proved to be ineffective as residual cells have the tendency to become radio and chemo resistant, with a 90% relapse rate (Kiskova *et al.*, 2020; Hanif *et al.*, 2017).

Currently, there is no standard of care for the treatment of recurrent GBM and treatment is based on new onset of recurrence, time of diagnosis, the performance status and age of the patient (Alifieris and Trafalis, 2015; Aparicio-Blanco *et al.*, 2020). In addition, treatment of brain tumours is particularly difficult due to the presence of protective CNS barriers such as blood-brain barrier (BBB), which will be discussed further in the next section. Thus, many anticancer drugs do not readily cross the BBB, limiting options for GBM treatment (Mannas *et al.*, 2014; Taylor *et al.*, 2019; Tan *et al.*, 2020). As a result, prognosis of GBM patients is bleak and remains an incurable disease with a median survival rate of 14 – 15 months, and ~6.2 months after recurrence (Aparicio-Blanco *et al.*, 2020).

1.3.4.1 Surgery

Surgical resection is considered as the principal component of standard care for patients with GBM (Hanif *et al.*, 2017). The majority of cases are treated by surgery because it relieves pressure (caused by the brain tumour) by debulking of the tumour and extends survival by approximately 15 months (Paolillo *et al.*, 2018). GBMs that are newly diagnosed have better survival by complete surgical resection in comparison to biopsy or subtotal resection. However, most tumour reoccurs within 8 - 10 months of initial resection (Mallick, *et al.*, 2016; Sacko *et al.*, 2021). In addition, extensive and complete surgical resection is difficult in GBM because these tumours are frequently invasive and

are often in eloquent areas of the brain. (Wilson, *et al.*, 2014; Davis, 2016). Even with advances in surgical resection, the prognosis for patients with GBM remains poor, with a median survival of 14 - 15 months (Thakkar, *et al.*, 2014; Sacko *et al.*, 2021). Hence, resection surgery is coupled to a course of drug and/or radiotherapy.

1.3.4.2 Radiotherapy

Radiotherapy has long been the standard adjuvant approach in GBM, and remains the primary treatment modality in unresectable GBM (Barani and Larson, 2014; Tan *et al.*, 2020). It was also shown to improve life expectancy of GBM patients. The stereotactic radiosurgery and brachytherapy were found to be effective treatments against relapsed GBM, but has vague roles in newly diagnosed GBM (Hanif *et al.*, 2017). In addition, radiotherapy doses depend on the tumour type and conditions of patients (Anjum *et al.*, 2017). However, due to the invasive nature of GBM, radiotherapy has risks and limitations, such as radiation necrosis, radio-resistance of some tumours, and radiation-induced permanent neuronal damage (Hanif *et al.*, 2017; Tan *et al.*, 2020)

1.3.4.3 Chemotherapy

The current gold standard GBM treatment is temozolomide (TMZ; **Figure 7**), an EMA- and FDA-approved DNA alkylating agent that has an excellent penetration in CNS, due to its small size (194 Da), stability at acidic pH, and lipophilicity. (Hanif *et al.*, 2017). TMZ was also the major advanced treatment that significantly improved GBM patient survival. It was approved for use following phase I, II and III trials in 1999 (Friedman *et al.*, 2000), and has increased patient median survival rate from 12 to 14 months (Wang *et*

et al., 2019). The dosage of TMZ delivered ranges from 150 – 200 mg/m² for 1-5 days, every 28 days for six cycles (Friedman *et al.*, 2000; Alifieris and Trafalis, 2015; Tan *et al.*, 2020). However, there are limitations, as prolonged TMZ treatment leads to resistance and poor response to subsequent treatments. Higher doses of TMZ are associated with greater toxicity and deterioration in function, and quality of life (Wang *et al.*, 2019; Bjorland *et al.*, 2021; Byrne *et al.*, 2021).

The implementation of the Stupp protocol in 2005 as an adjunct therapy, that is radiation therapy given as 60 Gy in 2 Gy fractions with concomitant TMZ, followed by six courses of TMZ monotherapy improved the overall survival of GBM patients (Stupp *et al.*, 2005; Bjorland *et al.*, 2021). This combination therapy was considered more effective (two-year survival rate of 26.4%) compared to radiotherapy alone (10.4%). However, over 50% of patients do not respond to TMZ treatment due to overexpression of O6-methylguanine methyltransferase (MGMT), a DNA repair enzyme, which decreases the rate of DNA repair in GBM cells, involving critical regulator of p53 tumour suppressor (Ganipineni, *et al.*, 2018; Lakomy *et al.*, 2020; Kiskova, *et al.*, 2020). Methylation of the MGMT promoter (found in 30 – 50% of GBM cases) silences the MGMT gene, which then reduces ability of tumour cells to repair the damage that has been induced by TMZ (Lapointe *et al.*, 2018; Aparicio-Blanco *et al.*, 2020). Moreover, TMZ presents numerous side effects due to off-target DNA damage that prevents dose escalation, and tumour recurrence invariably occurs (Hegi *et al.*, 2008; Lee 2016; Lakomy *et al.*, 2020).

Several chemotherapeutic alkylating agents other than TMZ, carmustine (BCNU) and lomustine (CCNU) (**Figure 7**), can induce cross-linking between DNA strands and causes damage in cells which then inhibits cell cycle progression leading to cell death (Aparicio-

Blanco *et al.*, 2020). These compounds have also shown some advantage and have been clinically used in the treatment of GBM, which were used as a second-line treatment after TMZ (Hanif *et al.*, 2017). However, BCNU and CCNU are harshly cytotoxic and present continuous suppression of bone marrow, and toxicity to kidney and liver, resulting to lung related disease (Anjum *et al.*, 2017). Hence, treatment with these drugs resulted in early development of resistance which further limit their benefits (Hanif *et al.*, 2017; Lakomy *et al.*, 2020).

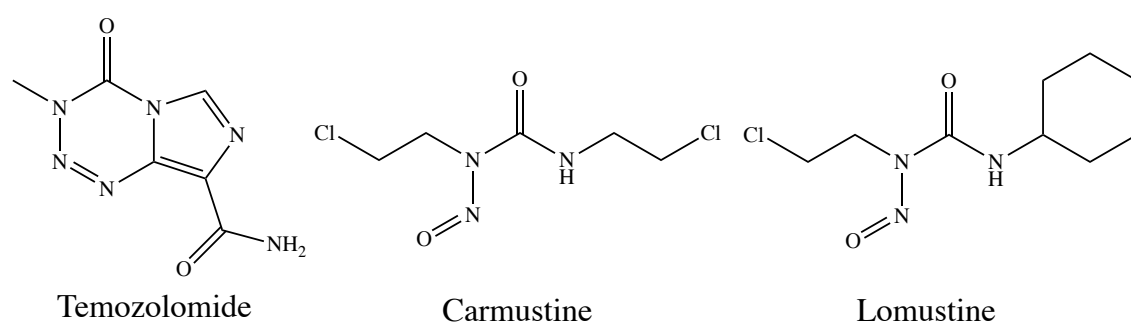


Figure 7. Structures of different chemotherapeutic alkylating agents for GBM treatment.

1.4 Drug Delivery Barriers in Brain Cancer

As mentioned in (section 1.3.4) treatment of brain tumours, especially GBM, is hampered by various barriers preventing drug from reaching the tumour sites (Karim *et al.*, 2016). There are two main barriers for the treatment of brain cancer: the BBB as mentioned above, and the blood-brain tumour barrier (BBTB) (Figure 8; Wei *et al.*, 2014; Taylor *et al.*, 2019). Overcoming these barriers will provide a means for selectively targeting tumours for drug delivery, and may offer new hopes for patients with GBM (Fakhoury, 2015).

The brain is protected by the BBB, a highly selective semi-permeable barrier, which presents different defence mechanisms to block the passage of toxic agents to the brain (Jena, *et al.*, 2019). The BBB comprises of endothelial cells of capillaries, astrocytes surrounding the capillary, microglia and pericytes embedded in the capillary basal lamina, which together play a role in the differentiation and maintenance of BBB (Dohgu *et al.*, 2005). The tight junctions in BBB are hydrophilic channels between two adjacent endothelial cells, preventing paracellular transport of ~98% of small molecules and nearly all large molecule (>400 Da) drugs from entering the CNS (Ohgaki and Kleihues, 2013; Taylor *et al.*, 2019). Therefore, therapeutic drugs must possess characteristics that enable passage across BBB (Jena *et al.*, 2019). The ability of a molecule to cross the BBB are based on physiochemical properties, including molecular weight, lipophilicity and charge (Taylor *et al.*, 2019).

When tumours develop, the brain endothelium can be modified to a different extent resulting in a BBTB (Guo *et al.*, 2017). It is located between brain tumour tissues and micro vessels formed by endothelial cells, which limits paracellular delivery of most hydrophilic molecules to tumour tissues. The BBTB becomes the main obstacle in drug delivery when brain tumours deteriorate which causes BBB angiogenesis and gradual impairment (Wei *et al.*, 2014).

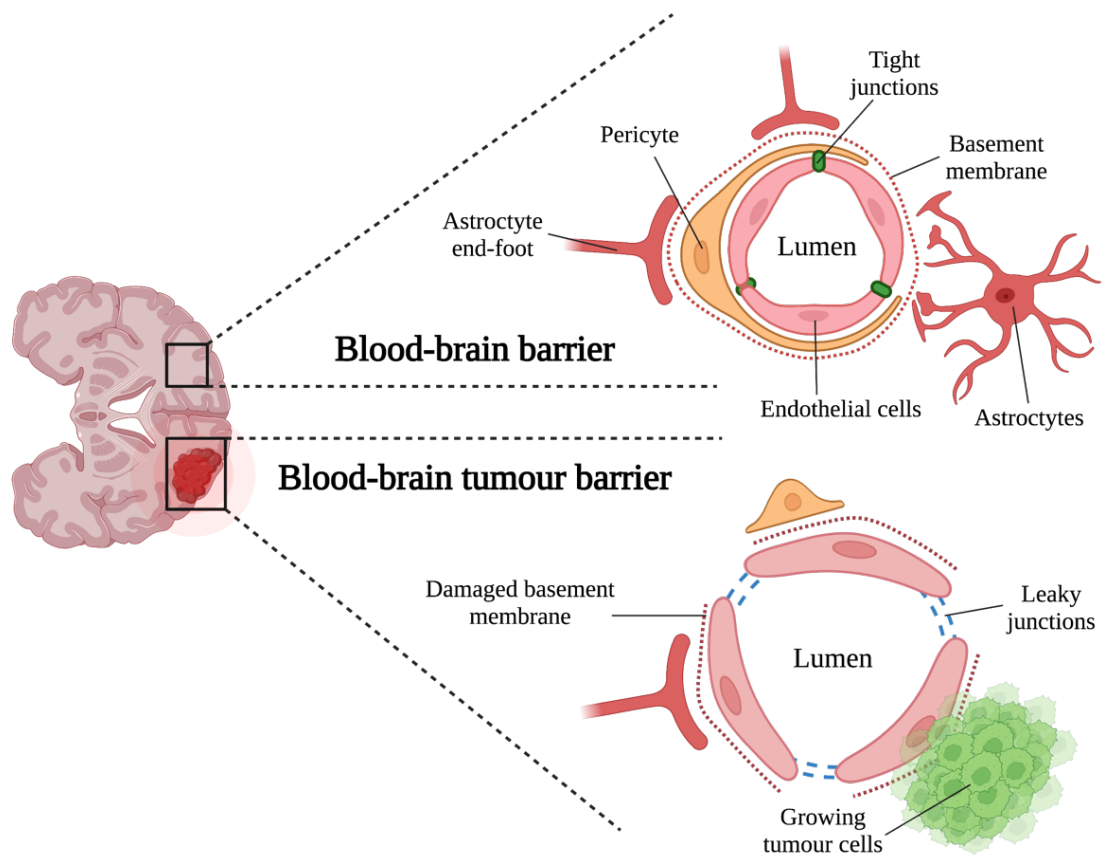


Figure 8. Schematic representation of the healthy blood-brain barrier (BBB) and blood-brain tumour barrier (BBTB) (modified from Raucher, Dragojevic and Ryu, 2018). Image created with BioRender.com.

Hence, drug delivery can account to hindrance to the development of effective therapies for GBM. Although the BBTB is impaired to some extent within the tumour core, GBM infiltrative areas responsible for recurrence are mostly associate with an intact BBTB which prevents chemotherapeutic drugs from reaching the tumour site (Aldape *et al.*, 2019; Alexander and Cloughesy, 2017; Sarkaria *et al.*, 2018; Aparicio-Blanco *et al.*, 2020)

1.4.1 Drug Delivery for Brain Cancer

As discussed above, brain cancer treatment is hindered by barriers, such as the BBB. To overcome the inability of effective drug delivery to the brain due to its tight junction, metabolic and immunological barrier, active targeting strategies were adopted. Active targeting systems are mainly divided into absorptive-mediated transcytosis (AMT), transporter-mediated transcytosis (TMT), and receptor-mediated endocytosis (RME) (Pardridge, 2007; Wei, *et al.*, 2014).

AMT is non-specific and delivers drugs across the BBB by cationic proteins or cell-penetrating peptides. It provides both the potential for binding and uptake of cationic molecules to the luminal surface of endothelial cells, and then for exocytosis at the abluminal surface (Hervé, *et al.*, 2008). TMT takes advantage of the different transport system in the cerebral endothelium (i.e., glucose transporter, GLUT, that facilitates transport of glucose from the blood to the brain). It is substrate-selective, hence only drugs that closely mimic the endogenous substrate will be taken up and transported into the brain (De Boer and Gaillard, 2007). RME is considered one of the most effective strategies for brain targeted drug delivery. This is due to its high specificity, selectivity and affinity, although the ligand may have an effect on the homeostasis and a possible competition of natural ligand to the drug ligand, reducing targeting efficiency (Zhang and Liu, 2015). Some of the receptors overexpressed in the brain tumour include transferrin receptor, integrin receptor and folate receptor (Wu and Pardridge, 1999; Wei *et al.*, 2014). In this study, RME was the chosen drug delivery strategy and will be discussed further in detail. A summary of the different strategies for drug delivery into the brain can be seen in **Figure 9**.

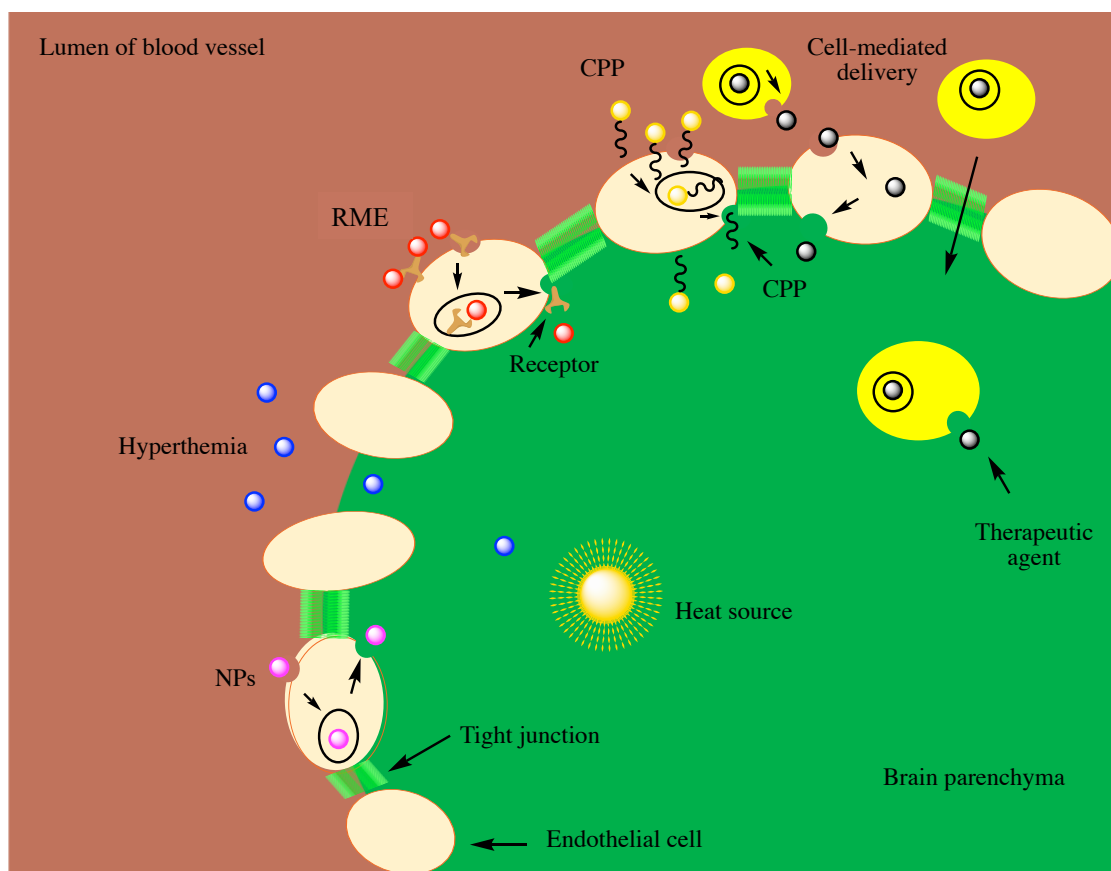


Figure 9. A schematic of several strategies for brain cancer drug delivery of therapeutic agents. Cell-penetrating peptides (CPP); nanoparticles (NPs); receptor-mediated endocytosis (RME) (adapted from Zhang *et al.*, 2015)

1.4.2 Targeted Therapy/Targeted Drug Delivery

Since Paul Ehrlich created the concept of “magic bullet” to describe targeted therapy, where drug selectively targets diseased cells but are not toxic to healthy cells, a plethora for cancer treatment has been channelled to this direction (DeVita and Chu, 2008; Strebhardt and Ulrich, 2008). The era of targeted therapy began with the FDA approval of Rituximab (1997), as the first targeted therapy for cancer, and it was also the first

monoclonal antibody available for cancer treatment (Scott, 1998; Chabner and Roberts, 2005). Targeted therapy aims to target genes or proteins that have become essential for the cancer cell's survival but are not essential for the survival of other cells in the body. It involves developing drugs that block specific biological transduction pathways or cancer proteins that are involved in tumour growth and progression, for example, molecular targets (receptors, growth factors, kinase cascades or molecules related with apoptosis and angiogenesis) that are present in normal cells, but are overexpressed in cancer cells (Raschi *et al.*, 2010; Gerber, 2008; Herrero and Medarde, 2015).

There are two strategies involved in the development of tumour-targeted therapies. The first strategy involves pursuing agents that selectively block novel pathways or proteins that emerge or become overexpressed in malignant cells (Xia and Low, 2010). Examples of this include Imatinib, a BCR-ABL tyrosine kinase inhibitor, which arises solely from chromosomal translocation during tumorigenesis (Galmarini, *et al.*, 2012); and Bevacizumab, a monoclonal antibody that suppresses neoangiogenesis required to nourish tumours for proliferation (Gerber, 2008). The second strategy is the use of a ligand that specifically bind to a receptor that is overexpressed primarily on the cellular target. This ligand can be exploited to carry a tumour-specific drug when linked to a chemotherapeutic drug, avoiding unwanted damage to receptor negative tissues when released (Zwicke *et al.*, 2012). Ligands that have been exploited for this approach to tumour targeting include monoclonal antibodies and low molecular weight receptor-binding molecules such as peptide hormones, receptor antagonists, oligosaccharides, oligopeptides, and vitamins (vitamin B, vitamin B12, biotin and riboflavin) (Xia and Low, 2010; Gupta *et al.*, 2008; Bareford and Swann, 2007). Moreover, it has long been recognised that folate receptors (FRs) are excellent targets to this end (Zwicke *et al.*,

2012; McCarron *et al.*, 2018). Hence, was chosen as the target in this study and will be discussed later in more detail.

Ligand targeted therapies offer a plethora of advantages over the first strategy – (1) Most potent drug is linked reversibly to a targeting ligand and can be targeted to a tumour tissue specific to pathological cell type; (2) It is generally preferred for the delivery of membrane-impermeable drugs as it enables attached cargo to enter target cells *via* RME; (3) Overexpression of receptors on cancer cells is more common than enzymes. Thus, ligand-targeted therapies have more development potential than functionality-targeted therapies (Low and Kularatne, 2009; Leamon *et al.*, 2002; Thomas, *et al.*, 2009; Xia and Low; 2010; McCarron *et al.*, 2018).

Despite the advantages of ligand-targeted therapies, they also possess several disadvantages – (1) Drugs must be effective at low concentrations because most endocytic pathways transport relatively few molecules into a cell; (2) Delivery to target cells does not guarantee therapeutic efficacy and it also must be released within the cell. Thus, drugs must contain chemical moieties or a cleavable linker (with -SH, -COOH, -OH, or -NH₂) that can facilitate release; (3) An efficient drug release mechanism must be designed into the conjugate (Thomas, *et al.*, 2009; Ojima, 2008, Xia and Low, 2010).

A typical structure of a receptor-targeted drug delivery system (shown in **Figure 10**) is based on the direct coupling of an anti-tumour drug to a ligand capable of detecting or overexpress in cancer cell *via* a linker that can enhance the pharmacokinetics and pharmacodynamics of the anti-tumour drug and/or can cleave allowing release of the latter (Leamon and Reddy, 2004; Yu, *et al.*, 2010).

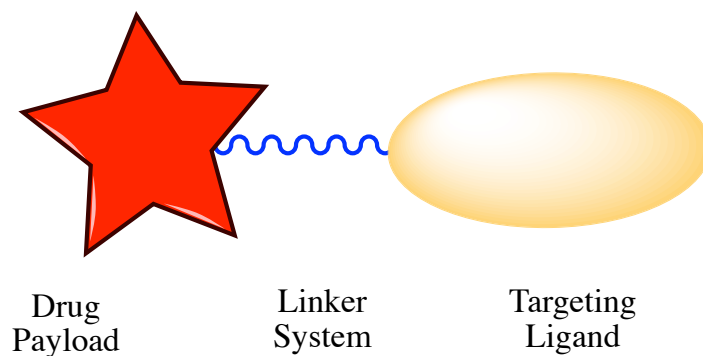


Figure 10. Typical structure of receptor-directed drug delivery system (modified from Leamon and Reddy, 2004). Image created using ChemDraw Professional 16.0.

1.4.2.1 Folate Targeted Drug Delivery

Folate targeting started soon after Bart Kamen and his group at the University of Texas Southwestern Medical Centre reported that folates enter cells *via* a receptor-mediated endocytotic process (Kamen and Capdevila, 1986). They proposed that uptake may occur by (1) binding to a surface folate receptor, (2) internalization by endocytosis, and (3) release from the receptor in the acidic endosome (Kamen and Capdevila, 1986). In the early 1990's, Leamon and Low reported that the physiological process that mediates folate-targeted drug delivery is identical to that of the free folic acid vitamin (Leamon and Low, 1991; Leamon and Low, 1993). These discoveries opened an avenue to the development of folate-targeted drug delivery. Furthermore, Leamon and Low stated that macromolecules can be non-destructively delivered into cells *via* folate receptor-mediated endocytosis if the macromolecules are covalently conjugated to folic acid prior to addition to cells expressing the folate receptor (Leamon and Low, 1991; Leamon and Low, 1993; Leamon and Reddy, 2004). The exploitation of FR-mediated drug delivery was often referred to as a “molecular Trojan horse” approach whereby folate conjugates

are shuttled inside a targeted FR positive (FR+ve) cells in a stealth-like manner (Leamon and Reddy, 2004).

There are two main strategies designed for FR targeted drug delivery in overexpressing tumour cells, (1) monoclonal antibody (mAb) coupling of the desired drug against FR (Kue *et al.*, 2016), an example of which is farletuzumab (Morphotek, USA), which has a mechanism of action distinct from that of drug conjugates (Armstrong *et al.*, 2013); and (2) folic acid conjugation which shows high affinity to FR and thus good targeting properties (Kue *et al.*, 2016; Ceborska, 2017). An example of which is the chemotherapeutic agent vintafolide, which is composed of folic acid and the vinca alkaloid desacetylvinblastine hydrazide (DAVLBH, Endocyte Inc., USA) (Lutz, 2015; Edelman *et al.*, 2012). The development of vintafolide was halted in Phase III clinical trial due to poor efficacy on the pre-specified outcome of progression free survival (Lutz, 2015; Vergote, *et al.*, 2015).

Initial studies on folate targeting drug delivery were conducted with radiolabelled and fluorescent proteins covalently attached to folic acid. To date, a variety of folate-linked molecules and complexes have been designed to enable selective drug delivery to FR+ve conjugates (Gazzano *et al.*, 2017; McCarron *et al.*, 2018). These include radiopharmaceutical agents (Leamon *et al.*, 2002), MRI contrast agents (Konda *et al.*, 2000), low molecular weight chemotherapeutic agents (Gazzano *et al.*, 2017; Liu *et al.*, 2001), antisense oligonucleotides and ribozymes (Zhao and Lee, 2004), proteins and protein toxins (Leamon and Low, 1993), immunotherapeutic agents, micelles (Sahoo *et al.*, 2013), liposomes with entrapped drugs (Chaudhury, 2015), drug-loaded nanoparticles

(Sahoo *et al.*, 2013) and plasmids (Reddy and Low, 2000) which have been successfully delivered to FR-expressing cancer cells (Leamon and Reddy, 2004).

Numerous cancer cell lines overexpress FR because of their fast growth and cell division. FR is highly expressed in epithelial, ovarian, cervical, breast, lung, kidney, colorectal, and brain tumours (Parker *et al.*, 2005; Garin-Chesa *et al.*, 1993). Sarcomas, lymphomas, and cancers of the pancreas, testicles, bladder, prostate, and liver often do not show elevated levels of FRs (Parker *et al.*, 2005). When expressed in normal tissue, FRs are restricted to only a few sites including lung, kidney, placenta, and choroid plexus in the brain. In these tissues, the receptors are limited to the apical surface of polarized epithelia and therefore are not in contact with circulating folates or intravenously administered folic acid conjugates (Gonen and Assaraf, 2012; Muller, 2012).

FRs have been identified as molecular markers for targeted delivery due to their higher expression in cancer cells than in healthy cells (Sudimack and Lee, 2000; Yoo and Park, 2004). Folate has been used as a ligand associated with different carriers and chemotherapeutic drugs for drug delivery system in cancer treatment, and is the ligand used in this research.

1.5 Folic Acid as a Targeting Ligand

Folic acid is a non-immunogenic water-soluble B9 vitamin, for which the molecular structure is composed of three covalently linked components: a pteridine ring, *para*-aminobenzoic acid (PABA), and a glutamic acid moiety (**Figure 11**). The glutamate tail

consists of an α and γ carboxylic acid groups which have markedly different pK_a values which result in different reactivities (Poe, 1977; McCarron *et al.*, 2018; Guo *et al.*, 2017). A study by Leamon *et al.* (1999) determined that macromolecules attached to folic acid by either or both of the α and γ glutamyl linkages could associate with FR bearing cells at virtually identical levels (Geersing *et al.*, 2019). However, others have shown that conjugates at the γ moiety can bind FR in orders of magnitude better when compared to the α regioisomer (Geersing *et al.*, 2019; Trindade *et al.*, 2014).

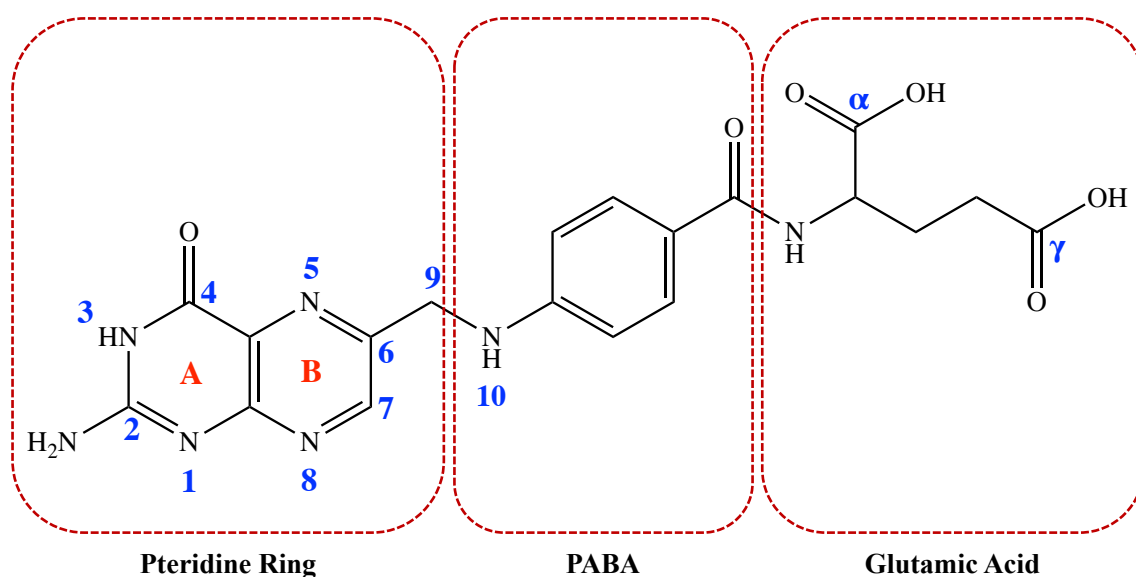


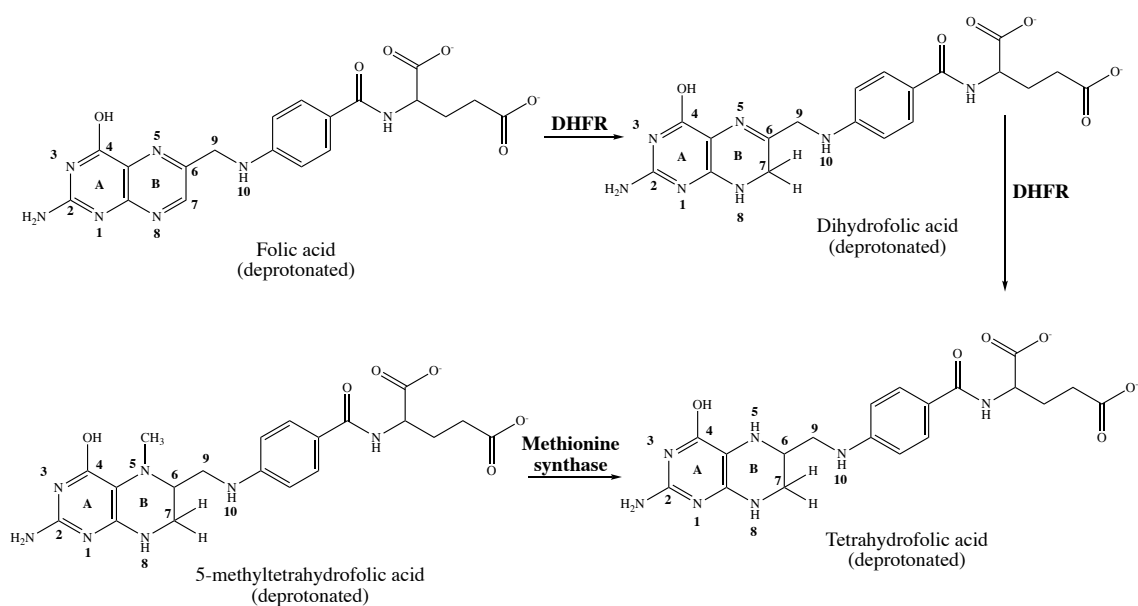
Figure 11. The chemical structure of folic acid highlighting the three core components: pteridine ring, para-aminobenzoic acid (PABA), and the glutamate moiety. The α and γ COOH functionalization are indicated.

The terms ‘folate’ and folic acid are often used interchangeably but it should be noted that folic acid (**Figure 11**) is a pharmacological agent and does not exist in nature (Marchetti *et al.*, 2014). ‘Folate’ is the generic term used to refer to the various members of the B9 vitamin family present in foods (i.e., 5-methyltetrahydrofolate) (Scaglione and

Panzavolta, 2014). In this study, folate and folic acid will be referred to interchangeably, unless otherwise stated.

Folic acid is used in cell culture media and vitamin supplements due to its chemical stability, but within the cell, folic acid is first converted into dihydrofolate (DHF) and then to tetrahydrofolate (THF) by the enzyme dihydrofolate reductase (DHFR) (**Scheme 1**) (Zhao *et al.*, 2009). Folic acid is not found in human cells and can only be derived entirely from dietary sources, such as 5-methyltetrahydrofolic acid (5-methylTHF) which is the major folate derived from dietary sources and the dominant folate found in the blood of humans and rodents (Blom and Smulders, 2011). Folate plays an essential role in critical biosynthetic processes in mammalian cells. These one-carbon donors are required for the *de novo* synthesis of purines and thymidine, which in turn are required for DNA and RNA synthesis, methylation, and repair (Zwicke *et al.*, 2012). Folate is also required for the vitamin B12-dependent synthesis of methionine, converted to S-adenosylmethionine, which orchestrates various methylation reactions within the DNA, histones and lipids (Zhao *et al.*, 2009; Desmoulin *et al.*, 2012; McCarron *et al.*, 2018).

Deficiencies in folate (<400 µg) or aberrations in its metabolism may pose a problem during pregnancy when embryonic cells are differentiating and proliferating constantly, that could lead to neural tube defects (Crider *et al.*, 2012). Proliferating tumour cells harbour increased folate requirements characterized by enhanced nutrient uptake and metabolic pathways to support the biosynthesis of macromolecules needed for cell growth and division (Visentin *et al.*, 2012; Gonen and Assaraf, 2012). This renders the FR an ideal target for targeted delivery.



Scheme 1. Folic acid is reduced to dihydrofolic acid (DHF), which is in turn reduced to tetrahydrofolic acid (THF) in reactions mediated by dihydrofolate reductase (DHFR). 5-Methyltetrahydrofolic acid (5-methylTHF) is the major folate found in blood (modified from Zhao *et al.*, 2009).

Folic acid is considered one of the optimal targeting ligands used for targeted drug delivery of therapeutic agents to cancer tissues (Low *et al.*, 2008). This is due to its small size (441 Da), availability, stability over a broad range of temperature and pH values, cost efficiency, non-immunogenicity, simple conjugation chemistry and more importantly its high affinity to FRs which are overexpressed by many cancerous cells (Muller and Schibli, 2011; Salazar and Ratnam, 2007; Fernandez *et al.*, 2018).

Due to the hydrophilic nature of folate at physiological pH, which hinders passive diffusion through biological membranes, the cell uptake of folate is mediated by three major transporters (Low and Kularatne, 2009), including: (1) the ubiquitously expressed in normal tissues, reduced folate carrier (RFC/SLC19A1), which is the primary pathway for reduced folate uptake into various tissues under physiological pH and shows a very high affinity for reduced folates, but very low transportation capacity of folic acid

(Matherly and Goldman, 2003; Zhao *et al.*, 1997); (2) the FR which is a glycosylphosphatidylinositol (GPI)-associated receptor and mediates endocytosis of folates and reduced folic acid derivatives after binding them with high affinity at neutral pH (Gonen and Assaraf, 2012; Guo *et al.*, 2017); and (3) the proton-coupled folate transporter (PCFT/SLC46A1) that has an optimal activity at pH 5.5 and is responsible for the uptake of folates into enterocytes in the small intestine (Qui *et al.*, 2006).

1.5.1 The Folate Receptor

The folate receptor belongs to family of glycoproteins (38-40 kDa), with high binding affinity towards folic acid (Parker *et al.*, 2005; Quici *et al.*, 2015). The human FRs can be divided into four isoforms (α , β , γ , and δ), encoded by the *FOLR* multigene family (*FOLR1-4*), which are differentially expressed in individual tissues. FR α and FR β are anchored to the GPI-membrane proteins; whereas FR γ is found only in hematopoietic cells and lacks the GPI component, making it freely soluble (Elnakat and Ratnam, 2006; Low and Kularatne, 2009); lastly the FR δ has been identified but is hard to detect in human tissues and was only found on regulatory T-cells (Spiegelstein *et al.*, 2000; Tian *et al.*, 2012).

FRs show high binding affinity for folic acid – $K_D \sim 0.1$ nM (FR α), $K_D \sim 1$ nM (FR β), and $K_D \sim 0.4$ nM (FR γ), and display divergent patterns of tissue expression (Parker *et al.*, 2005; Kumar *et al.*, 2019). However, it is important to note that FR γ is a secreted protein and therefore is not involved in cellular uptake (Gonen and Asaraf, 2012; Tian *et al.*, 2012). Furthermore, most of the studies in literature have been focused on FR α and FR β ,

as these isoforms share high amino acid sequence identity (~70%) and are distinguishable by different affinities for folic acid and stereoisomers of reduced folates (Lynn *et al.*, 2015). It is important to note that although RFC are also ubiquitously expressed, their affinity (K_D) is in the μM range, making FRs having $>10^3$ -fold higher affinity for folate, enabling *in vivo* targeting *via* folate conjugation with no concerns of any potential interference from the much weaker RFC binding (Kennedy *et al.*, 2003; Holm *et al.*, 1991). In other words, distribution of FR-targeted agents is unlikely to be affected by the presence of RFC in non-target tissues.

Both the FR α and FR β shows limited expression on healthy tissues. FR α is confined to the luminal surface of polarized epithelia and, therefore is in contact with circulating folates or intravenously administered FA conjugates (Elnakat and Ratnam, 2006; Gonen and Assaraf, 2012; Assaraf *et al.*, 2014). The FR β is expressed on activated myeloid cells (primarily macrophages and monocytes) that participate in inflammatory and autoimmune diseases (Xia *et al.*, 2009; Jager *et al.*, 2012; Gonen and Assaraf, 2012). In addition, FR β isoform has been detected in tumour-associated macrophages of many cancers, including liver, kidney, lung, skin, blood, and soft tissue (Shen *et al.*, 2015; Sun *et al.*, 2014).

Notwithstanding the expression level of FR β in some cancers, the FR α isoform is the most widely expressed of all the FR isoforms, and exhibits higher binding affinity to FA and 5-methylTHF ($K_D \sim 10^{10}$ M) than FR β (Della-Longa and Arcovito, 2013; Chen *et al.*, 2013). Therefore, it is more efficient in folate uptake and has the most potential for targeted drug delivery. Most healthy cells use the RFC for folate uptake and thus expression and distribution of FR α in healthy tissue is largely restricted to cells crucial

for embryonic development, choroid plexus of the brain, lung, and kidneys, where folate are filtered through the glomeruli and subsequently reabsorbed in the proximal tubule cells *via* FR binding (Betzel *et al.*, 2013; Muller, 2012).

Numerous studies have shown that FR α is overexpressed on the vast majority of cancer tissues, including ovarian, lung, kidney, brain, endometrial, colorectal, pancreatic, gastric, prostate, testicular, bladder, head and neck, and breast cancers (Christoph *et al.*, 2013; Elnakat and Ratnam, 2006; Nunez *et al.*, 2012; Weitman *et al.*, 1992; Stallivieri *et al.*, 2017). There are evidence suggesting FR expression increases with advancing stage (Siu *et al.*, 2012; Kalli *et al.*, 2008) and overexpression of FR α is a negative prognostic factor for breast, colorectal, ovarian, and endometrial cancer (Hartmann *et al.*, 2007; Teng *et al.*, 2012). The low expression of FR α in normal cells, but overexpression in many types of cancer cells, utilized FR α as a tumour cell marker and a target for drug delivery of therapeutic agents.

In 2013, Chen *et al.*, successfully elucidated the crystal structure of human FR α in complex with folic acid at 2.80 Å resolution (**Figure 12**). They reported that human FR α has an overall globular structure stabilised by eight disulphide bonds. It was reported that the folate pteroyl ring binds deep within the receptor pocket, leaving the glutamate moiety exposed outside the pocket entrance, allowing it to be conjugated to drugs without unfavourably affecting FR α binding (Chen *et al.*, 2013).

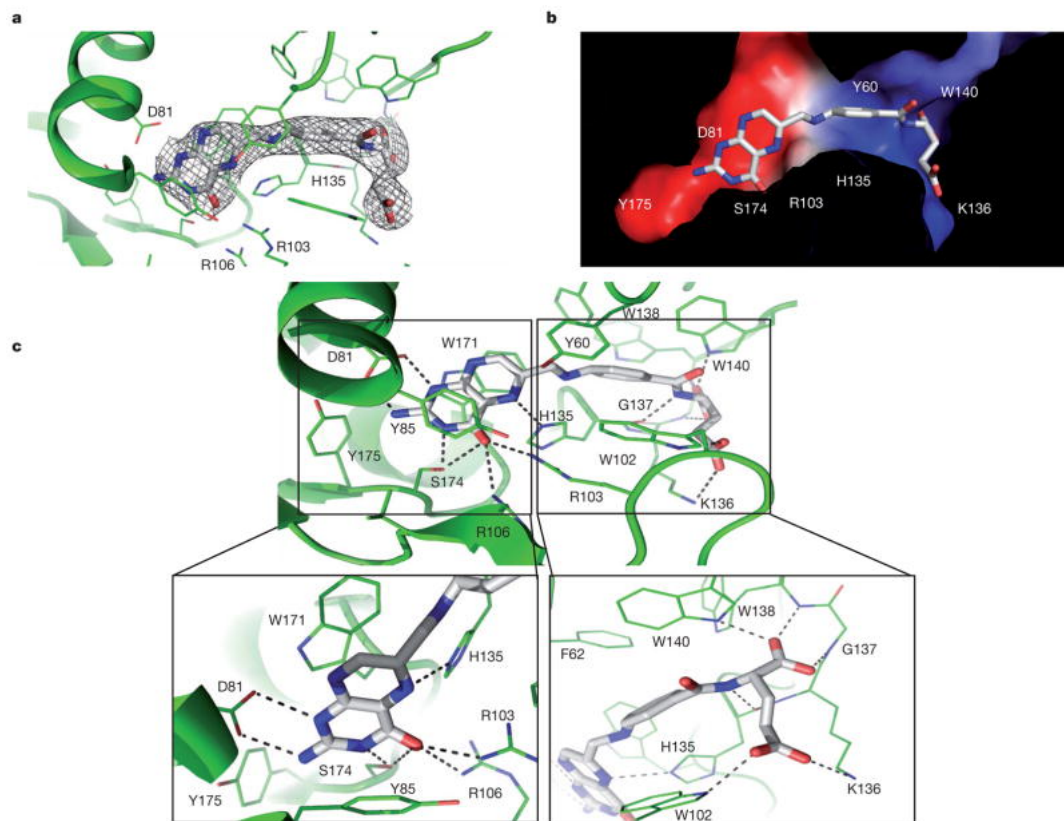


Figure 12. The 3D interaction map of folic acid bound to FR α (PDB ID: 4LRH) found by Chen and his colleagues (image adapted from Chen *et al.*, 2013).

In addition, there are various benefits in using folic acid to target FR α , such as cost efficient, non-immunogenic, high stability and tissue permeability, low molecular weight, and can be easily conjugated to diverse types of organic molecules, antibodies and nanoparticles (Chen *et al.*, 2013; Fernandez *et al.*, 2018). Thus, this study will focus on targeting FR α expressing cancer cells to target folate receptor.

1.5.2 The Mechanism of Folate Uptake *via* the Folate Receptor

The precise pathway(s) involved in the uptake of folic acid *via* FR is still poorly understood and are widely discussed in the literature. But, researchers have proven that entry of folic acid is governed by RME (Kim *et al.*, 2008; Gupta *et al.*, 2017). Endocytosis is the physiological process by which both dietary folate and folate-drug conjugates enter FR expressing cells (Leamon and Jackman, 2008; Lynn *et al.*, 2015).

The folate portion of the conjugate acts as the tumour-targeting ligand and will strongly bind to FR α on a cancer cell, resulting in subsequent internalisation of the folate-drug conjugate (shown in **Figure 13**). Once the construct is sequestered within the early endosome, the action of the proton pumps (co-localized in the endosome membrane) drops pH to ~ 5 . The acidification presumably protonates numerous carboxyl moieties on the FR protein, altering the FRs conformation (Vlahov and Leamon, 2012; Vlahov *et al.*, 2006). The late endosome then fuses with the lysosome and intracellular thiols such as glutathione (GSH), which can degrade the conjugate by cleaving a self-immolative linker, enabling release of the cytotoxic drug. This lethal payload can subsequently diffuse out of the endosome into the cytosol where it induces cell death. The FRs are then recycled back to the surface of the cell to engage in further rounds of drug internalisation (Vlahov and Leamon, 2012).

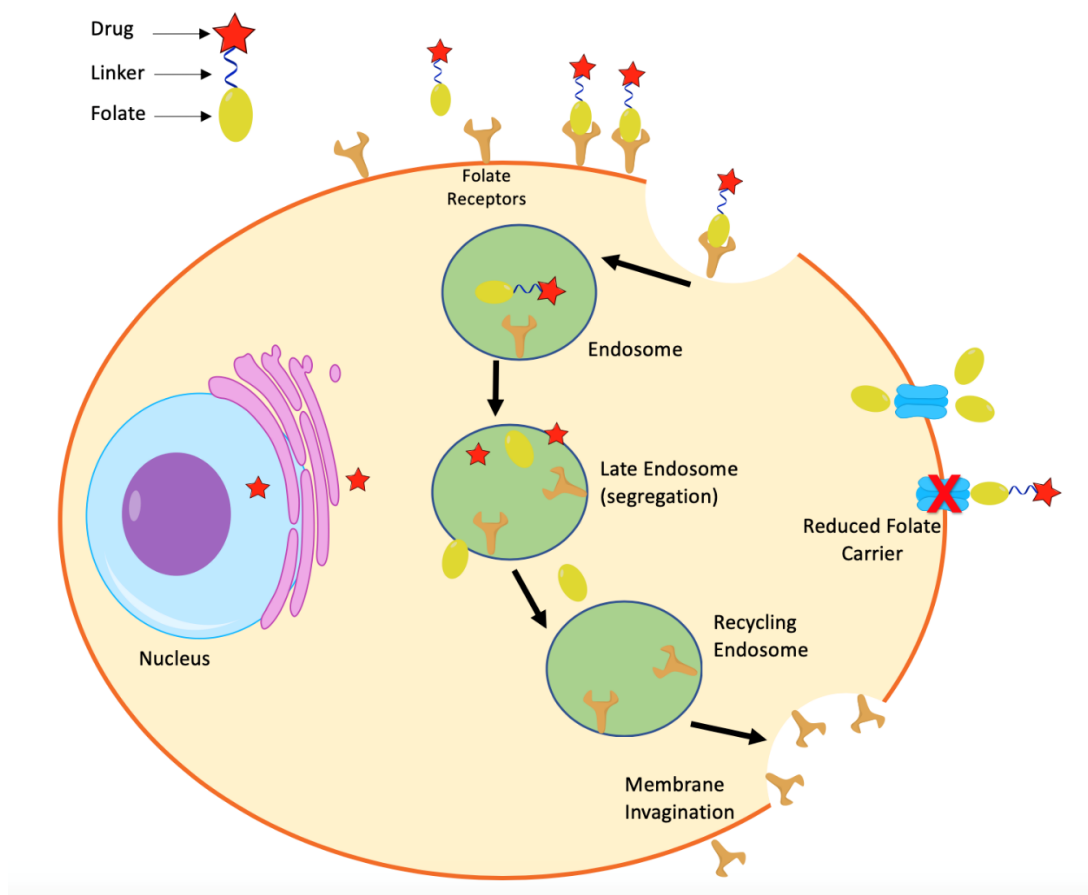


Figure 13. Uptake of folate-drug conjugates. The folate-drug conjugate is taken up by cells by binding of folate to the folate receptor. Invagination of the plasma membrane results in receptor mediated endocytosis. The acidic pH (~5) results in dissociation of the drug cargo and the folate receptor is recycled to the cell surface once more (modified from Hilgenbrink and Low, 2005). Image created using ChemDraw Professional 16.0.

Receptor-mediated endocytosis facilitates the entry of the drug moiety offers an advantageous uptake system than that of untargeted drug moieties (Gupta *et al.*, 2017). The availability of unoccupied receptors on the cell surface is dependent on the recycling rate of empty receptors from the endosome, and due to its rapid recycling rate (8-12 hours), the FR has the potential to maximise drug capture and internalisation (Vlahov and Leamon, 2012). The ability to attach chemotherapeutic agents to ligands that seek out FR α -expressing cancer cells, confers excellent selectivity to the construct while preserving drug potency (Fernandez *et al.*, 2018).

1.6 Ursolic Acid

As mentioned in **1.2.1 Novel Chemotherapeutic Drugs**, development of plant-based bioactive compounds has attracted great attention in designing novel and effective chemotherapeutic agents. This is due to the various anticancer activities it possesses both *in vitro* and *in vivo* (George and Abrahamse, 2019; Luo *et al.*, 2019). The bioactive compound used in this study, ursolic acid (UA; 3 β -hydroxy-urs-12-en-28-oic-acid) shown in **Figure 14**, is a lipophilic pentacyclic triterpenoid, that belongs to the ursane type which are widely distributed in natural environment and may occur as a free acid or aglycone of saponins (Lei *et al.*, 2014; Shanmugam *et al.*, 2013).

UA has a molecular formula C₃₀H₄₈O₃, a molecular weight of 456.70032 g/mol, a melting point of 283-285 °C, and is a white crystalline powder, with fine hair-like spikes (Chen *et al.*, 2018; Feng and Su, 2019; Navin and Mi Kim, 2016). It is a secondary plant metabolite usually present in apple (*Malus domestica*) fruit peel, oregano (*Origanum vulgare*) leaves, marjoram (*Origanum majorana*) leaves, rosemary (*Rosemary officinalis*) leaves, sage (*Salvia officinalis*) leaves, lavender (*Lavandula angustifolia*) leaves, eucalyptus (*Eucalyptus*) leaves and bark, thyme (*Thymus vulgaris*), sage and flowers, coffee (*Coffea arabica*) leaves, hawthorn (*Crataegus* spp.) leaves and flowers, and the waxy coating of many edible fruits (Shanmugam *et al.*, 2012; Kashyap *et al.*, 2016; inci). UA is highly insoluble in water, but soluble in organic solvents such as dimethyl sulfoxide (DMSO), dimethylformamide (DMF), and slightly soluble in methanol, ethanol, and diethyl ether.

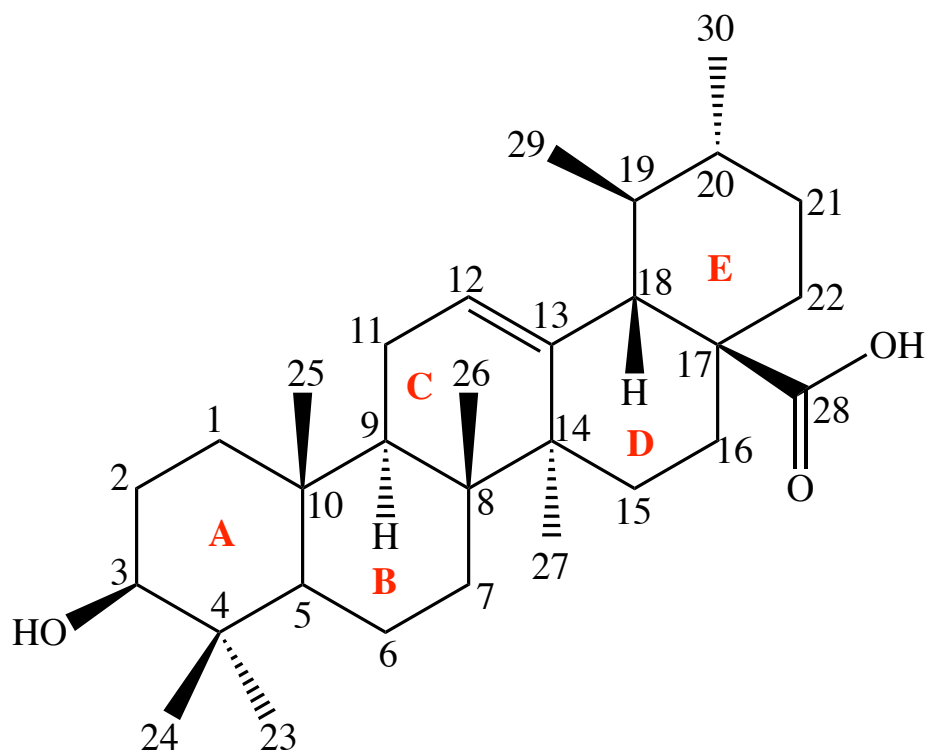


Figure 14. The chemical structure of ursolic acid. Numbers indicate the different carbons present and letters indicate the different rings.

UA and its derivatives exhibit extensive pharmacological and biological activities, including hepatoprotective, antioxidant (Wojciak-Kosior *et al.*, 2011), anti-inflammatory (Kim *et al.*, 2015), antiviral, antidiabetic (Jang *et al.*, 2009), antimicrobial (Shao *et al.*, 2020) and cytotoxic activities (Gu *et al.*, 2017; Chen *et al.*, 2018; Sun *et al.*, 2020; Shao *et al.*, 2020). In addition, UA has the ability to decrease reactive oxygen species (ROS) toxicity (Wang *et al.*, 2021) and increase the activity of antioxidant enzymes (Kim *et al.*, 2016). It was also associated with suppression of the nuclear factor-kB (NF-kB) pathway, inhibiting the expression of cyclooxygenase-2 (COX-2) and nitric oxide synthase (Feng and Su, 2019). However, its most prominent function is on the anti-cancer space as it can influence many different cancer pathways, which are discussed further below.

1.6.1 UA on the Hallmarks of Cancer

Recently, UA has been attracting increasing attention due to its broad anti-tumour effects and minimal toxicity. Even though the concrete mechanisms are poorly understood, an increasing number of studies are emerging using UA both *in vitro* and *in vivo* which affects multiple cancer hallmarks (Chen *et al.*, 2018; Sun *et al.*, 2020). It can influence many different cancer pathways, including cancer cell proliferation, modulated apoptosis (Meng *et al.*, 2015; Sun *et al.*, 2020), can regulate cancer cell metabolism, prevent angiogenesis, inhibit tumorigenesis, promote autophagy, enhance cell differentiation, and protect healthy tissues from the oxidative and inflammatory stimulation leading to metastasis, through different mechanisms and signalling pathways (Shanmugam *et al.*, 2013; Chen *et al.*, 2018; Lernoux *et al.*, 2018; Ghante *et al.*, 2019; Khwaza, Oyedeji and Aderibigbe, 2020).

UA has shown anticancer properties in gall bladder carcinoma (Weng *et al.*, 2014), colorectal cancer (Abdali *et al.*, 2020), prostate cancer (Gai *et al.*, 2016), bladder cancer, hepatocellular carcinomas (Liu *et al.*, 2014), cervical cancer (Guo *et al.*, 2019), lung cancer (Liu *et al.*, 2013), skin carcinomas, gastric cancer (Xu *et al.*, 2017), pancreatic cancer (Li *et al.*, 2012; Bergamin *et al.*, 2017), breast cancer (Iqbal *et al.*, 2018; Chan *et al.*, 2019), and gliomas (Bergamin *et al.*, 2017;). Moreover, there were many studies indicating that UA has strong killing effect on multidrug-resistant cell lines such as human colon cancer (SW480, SW620), acute myelocytic leukaemia (HL60, HL60/ADR), chronic myelogenous leukaemia (K562, K562/ADR), and breast (MCF-7) cancer cells (Wang *et al.*, 2021) (Shan *et al.*, 2011).

Molecular targets of UA reported for the treatment of cancer include its effect on p53 pathways (Prasad *et al.*, 2019; Wang *et al.*, 2019) and Ras signalling (Kim *et al.*, 2019); and transcription pathways like NF-kB (Jiang *et al.*, 2018), Tumour Necrosis Factor-Related Apoptosis-Inducing Ligand (TRAIL) (Shin and Park, 2013), and signal transducer and activator of transcription 3 (STAT 3) (Wang *et al.*, 2013; Liu *et al.*, 2017; Khwaza, Oyedeji and Aderibigbe, 2020). In addition, several inflammatory signalling pathways (summarised in **Figure 15**) including NF-kB, STAT3, serine/threonine protein kinase B (AKT), and COX-2 have been associated with different stages of cancer progression and have been reported to regulate tumour proliferation, survival, invasion, metastasis, and angiogenesis (Shanmugam *et al.*, 2013; Khwaza, Oyedeji and Aderibigbe, 2020).

A study by Kim *et al* (2016) showed that UA induced apoptosis by activating caspase-3 in HepG2 cell line. Another study showed the UA suppressed breast cancer growth by decreasing cancer cell proliferating, inducing apoptosis and autophagy, and lessening inflammatory reactions by PI3K/Akt signalling pathways (Luo *et al.*, 2017). It also reportedly suppressed the epidermal growth factor receptor/mitogen-activated protein kinase (EGFR/MAPK) pathway which induced apoptosis and inhibited cell proliferation (Shan *et al.*, 2009). UA was also shown to induce apoptosis and factor-mediated killing in ADR-resistant human hepatoma cells (Yang *et al.*, 2010); and overcome apoptosis resistance in prostate cancer mediated by Bcl-2 (Zhang *et al.*, 2010). An *in vitro* study of bladder cancer demonstrated UA to induce ER stress in T24 cells and to activate Jun N-terminal kinase (JNK) signalling pathway and induce apoptosis and inhibit cancer cell proliferation and tumour angiogenesis (Shao *et al.*, 2020). Glioma (U-251 MG) cells also

exhibit an inhibition of proliferation and initiation of apoptosis by activating caspase-3 in a dose-dependent manner (Navin and Mi Kim, 2016).

According to the study by Kanjoormana *et al* (2010), the expression of E-selectin, CD-31 and I-CAM was downregulated by UA which inhibits the PI3K/Akt pathway, and vascular endothelial growth factor (VEGF) expression. Lin *et al* (2011) has reported that UA inactivates STAT3, as well as AKT pathways responsible for tumour proliferation, invasion, and angiogenesis. They used UA to treat human liver cancer (Hep3B, Huh7 and HA22T) cells, and found that expression of HIF-1, VEGF, and IL-8 significantly reduced in a dose-dependent manner. The anti-metastatic property of UA was tested on a prostate cancer mouse model. UA was found to downregulate the expression of CXCR4, subsequently reducing the expression of CXCL12-induced metastasis. UA can also inhibit cell proliferation by blocking cell cycle progression in the G1 phase which in turn downregulate the expression of cyclin D1, D2, E and their activating partners CDK2, 4, 6, along with induction of p21/WAF1 (Zou *et al.*, 2019).

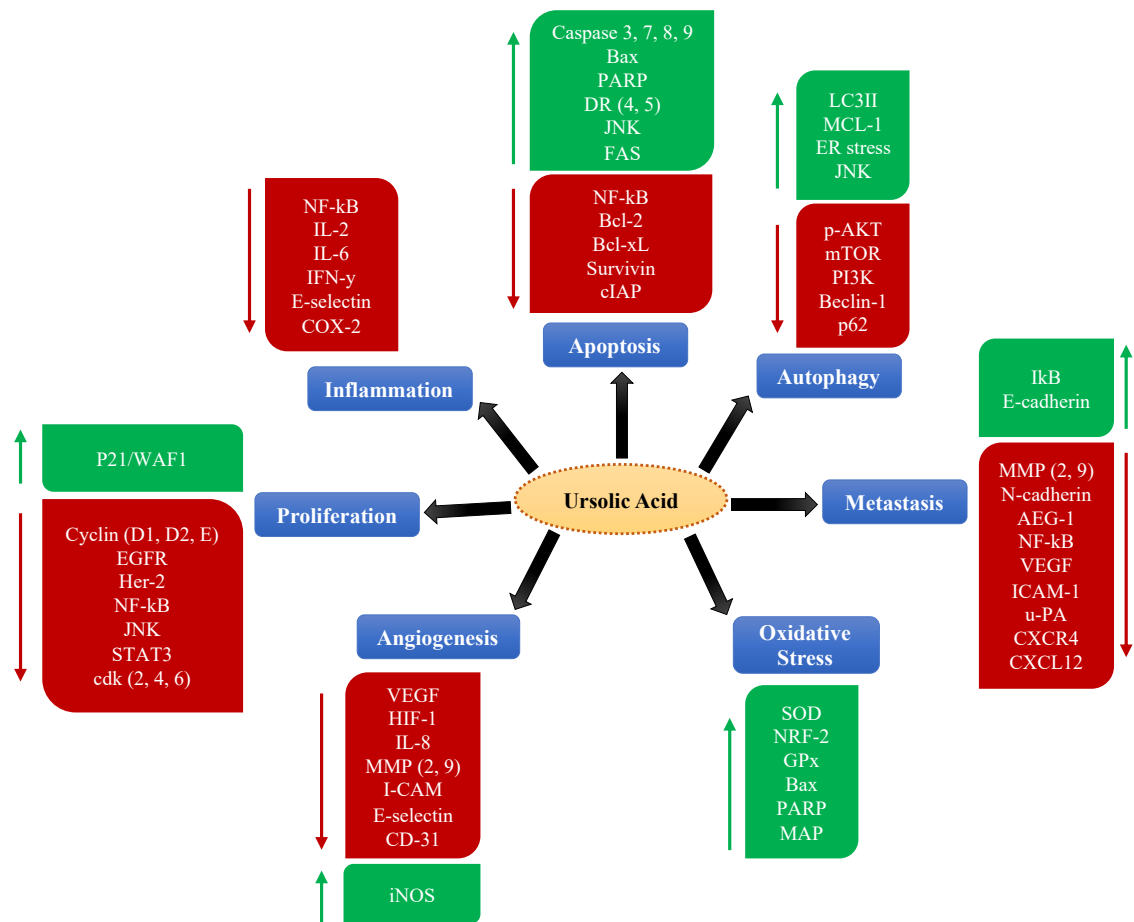


Figure 15. The current knowledge of the molecular mechanism of action of UA in cancer cells. Red - downregulated; green – upregulated (Modified from Iqbal *et al.*, 2018).

Studies of UA have also shown great potential as a new chemotherapeutic drug for GBM treatment as it can pass through the BBB *in vivo* (using a xenograft model) (Chen *et al.*, 2011). UA has been studied in different GBM cells (DBTRG-05 MG and U-87 MG) and was found to inhibit proliferation, induce apoptosis, thus promoting autophagy (Lu *et al.*, 2014). In addition, UA was also found to downregulate O₆-methylguanine-DNA methyltransferase *in vitro* and *in vivo*, decreasing cell invasion, and attenuating TMZ resistance in human GBM cells (xenograft model) (Zhu *et al.*, 2016). Bergamin *et al* (2017) used the orthotopic glioma model and found that UA decreased glioma cell

numbers and induced apoptotic death. Their results also showed that UA slightly reduced glioma tumour size but did not decrease malignant features.

Our recently published study has also demonstrated that UA exhibited a significant anti-cancer activity in U-251 MG GBM cells by activating cytotoxicity, inhibiting mobility and partially activating autophagy (by activation of the JNK-dependent pathway) over conventional chemotherapeutic agents used to treat GBM. In addition, a sub-toxic concentration of UA (~12 μ M) inhibited cell migration that was independent of the JNK pathway (Conway *et al.*, 2020). This study prompted the hypothesis of chemically modifying UA to enhance its activity and increase the molecular target selectivity and uptake in cancer cells, specifically in GBM cells.

1.6.2 Pharmacokinetic Study of Ursolic Acid

Despite the potential of UA to effectively inhibit a series of cancer cell growth, indicating its great potential as a promising chemotherapeutic agent, its poor water solubility and permeability greatly hindered its clinical applications (Shao *et al.*, 2020). In terms of toxicity, UA exhibited low toxicity as revealed in *in vivo* toxicity analysis in Kunming mice (0.2 mL/10 g). However, the biopharmaceutical classification system (BCS) classified UA as a class IV drug with limited pharmacological effect due to its low aqueous solubility (<5.64 μ g/mL) (Lin *et al.*, 2012; Yu *et al.*, 2020) and difficulty permeating membranes ($P_{app} = 2.8 \times 10^{-6}$ cm/s in the apical-to-basolateral direction at 20 μ M) in Caco-2 cell monolayers (Qiang *et al.*, 2011). This type of drug usually has slow dissolution and limited penetration through gastrointestinal mucosa, hence oral

bioavailability was low. UA is mainly absorbed by intestinal tract through passive diffusion, with a very fast absorption rate. Another study with the Caco-2 cell model showed that uptake concentration ranged from 10 – 40 $\mu\text{mol/L}$; and was more active at 4 °C (Jinhua, 2019; Yu *et al.*, 2020). Furthermore, Caco-2 cell model suggested that UA was the substrate for P-gp and easily pumped out in the gut, resulting to insufficient drug concentration in blood (Huayi, 2009; Qiang *et al.*, 2011).

Liao *et al* (2005) developed and validated a rapid, sensitive, and accurate liquid chromatography-mass spectrometry (LC-MS) method to determine UA in rat plasma. They found that there was only about 0.6% of ingested UA recovered in rat plasma after oral administration (Liao *et al.*, 2005). Distribution of UA has also been studied in animal models and showed that concentrations of UA in the liver, kidneys, and heart increased gradually with the observation time. These results suggest that UA distribution may be related to blood flow and perfusion rate (Chen *et al.*, 2011). Studies of UA have revealed that it was rapidly eliminated by gut wall/liver metabolism, ultimately resulting in low bioavailability of UA (Chen *et al.*, 2011; Liao *et al.*, 2005; Shao *et al.*, 2020).

There was also a study in human plasma levels of UA which was primarily assessed using LC-MS/MS. Hirsch *et al* (2014) showed that a single oral dose of UA had very low bioavailability. They used a 100 mg dose in fourteen subjects and showed that only 4 out of 14 subjects had detectable levels of UA. However, when dose was increased to 1000 mg, 9 of 14 subjects had detectable levels of UA. Their study suggested that poor absorption and rapid metabolism might have contributed to low levels of UA detected in these subjects (Hirsh *et al.*, 2014; Nguyen *et al.*, 2021).

There are also UA nano systems that are in clinical trials. In 2011, UA nano-liposomes (UA NLs) was evaluated in human pharmacokinetic study by Tianjin Medicinal University Cancer Institute, China. The clinical data showed that UA NL achieved a mean C_{\max} of 3404.6 ± 748.8 ng/ml. (Xia, *et al.*, 2011). Wang *et al* (2013) evaluated the toxicity in a single-dose pharmacokinetics of UA NLs and showed a maximum tolerated dose of 98 mg/m^2 and dose-limiting toxicity was hepatotoxicity and diarrhoea. A further study by Zhu *et al* (2013) evaluated a single- and multi-dose pharmacokinetic study and revealed that UA NLs exhibited a relatively linear pharmacokinetic behaviour at dose levels between 37 and 98 mg/m^2 . A more recent clinical study by Qian *et al* (2015) revealed that 60% of the subjects achieved satisfactory therapeutic effect after two treatment cycles (dose of 56 , 74 and 98 mg/m^2 UA for 14 d consecutively over a 21 d treatment).

These results in clinical phases I trials confirmed that UA NLs could show high tolerance and low toxicity in healthy volunteers. However, more extensive studies is needed in patients with different solid tumour.

1.6.3 Molecular Targets of UA

UA was found to influence many different cancer pathways such as inhibiting cell proliferation, induce apoptosis and exert anti-angiogenic effects (Kim *et al.*, 2015; Shao, *et al.*, 2020). However, the target protein for UA has remained unknown, hence cellular mechanism has been elusive. Below are the molecular studies of UA with potential protein targets published in the literature.

Vaccinia-Related Kinase (VRK1)

A study by Kim *et al* (2015) identified a target protein for UA and its cell-killing mechanism. An *in vitro* study in lung carcinoma derived cancer cell model (A549) showed that UA inhibited VRK1-mediated phosphorylation in a concentration and time-dependent manner (EC_{50} 39 μ M). (Kim *et al.*, 2015). The study by Kim *et al* (2015) (**Figure 16**) predicted that UA has a strong binding affinity with VRK1 ($K_D=731$ nM). They found that UA is mainly located in the vicinity of the catalytic domain that is involved in ATP binding and predicted that UA fits into the vicinity of the P-loop, catalytic site and C-terminal lobe of VRK1 kinase domain (Kim *et al.*, 2015

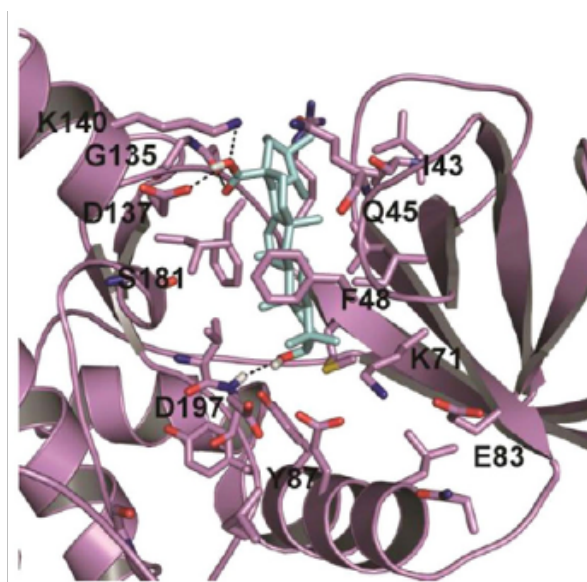


Figure 16. The 3D interaction map UA bound to VRK1 (PDB ID: 6AC9) showing residues essential for ligand binding (Image obtained from Kim *et al.*, 2015).

Akt1 and MDM2

Another study by Frolova *et al* (2019) looked at the Akt1 and Mouse double minute 2 homolog (MDM2) as targets for UA. Akt1 – a protein that inhibits apoptosis, is localised mostly on the inner membranes, while MDM2 is located in the nucleoli. Experimental results using MCF-7 breast cancer cell line, they obtained in tracing the dynamics of penetration and distribution of Fluorescein isothiocyanate (FITC)-labelled UA, showed

that when UA enters the cell, it initially localises in the inner membranes. This in turn induced apoptosis, followed by breaching of the mitochondrial membrane and the integrity of the cell nucleus. However, docking studies (**Figure 17**) they performed did not specify the different interactions involved. The conclusion they made was a potential interaction with Akt1, and in contrast UA and MDM2 lacks interactions (Frolova *et al.*, 2019).

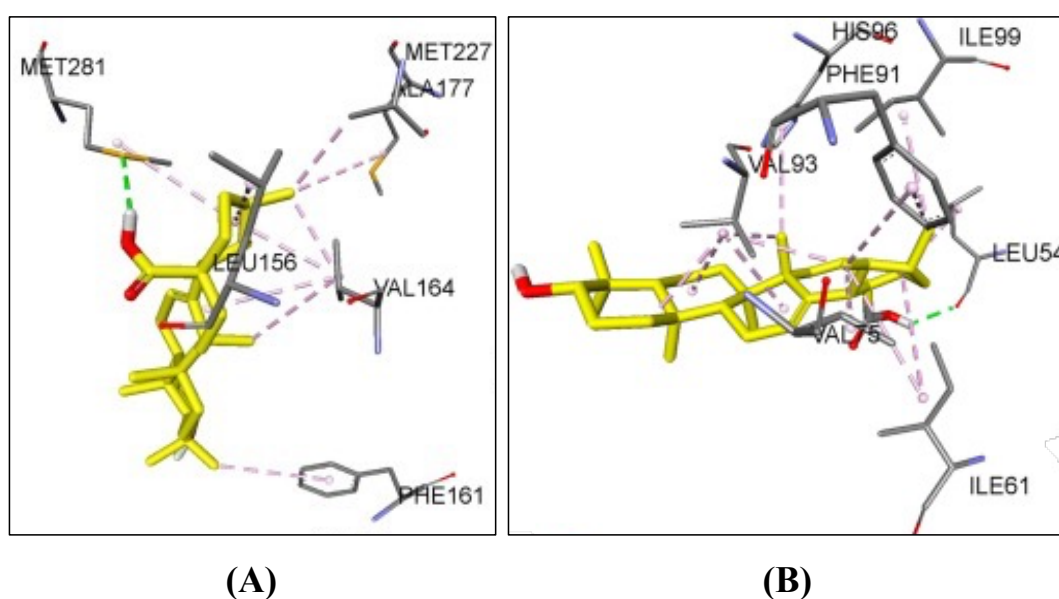


Figure 17.The 3D interaction map of UA bound to (A) Akt1/protein kinase B (PDB ID: 3OCB) and (B) MDM2/E₃ ubiquitin-protein ligase (PDB ID: 4HG7) (Image obtained from Frolova *et al.*, 2019)

PLK1 and CCNB1

Recent findings by Zhang *et al* (2021) have found that UA may also affect the expression of Polo-like kinase 1 (PLK1) and Cyclin B1 (CCNB1) by mediating p53 signalling pathway in triple negative breast cancer. They explored potential interaction of UA to 15 targets that they narrowed down according to different targets of triple negative breast cancer by topological analysis and molecular docking. Their results showed that PLK1

(PDB ID: 2RKU) and CCNB1 (PDB ID: 6GU3) exhibited the highest scores (Zhang *et al.*, 2021). There was no further data on the different interactions and important binding sites in the paper.

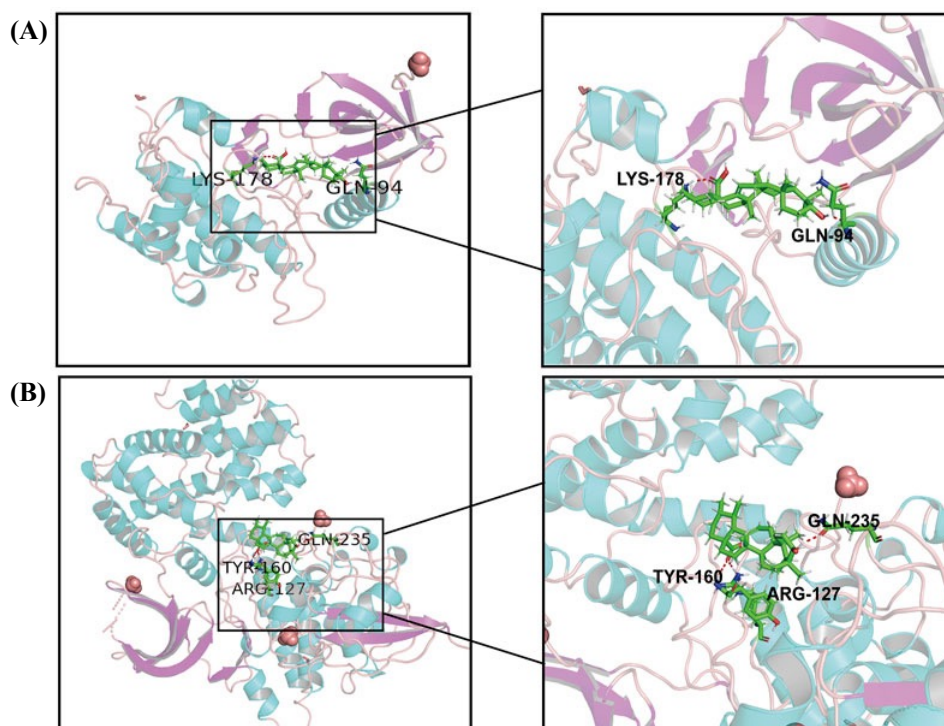


Figure 18. The 3D interaction map of UA bound to (A) PLK1 (PDB ID: 2RKU) and (B) CCNB1 (PDB ID: 6GU3) The green structure represents the small molecule compound, and the red structure represents the binding site of the compound to the hub proteins. (Image obtained from Zhang *et al.*, 2021)

Results suggest that UA may have a multi-target pathway. Since only the study of Kim *et al.* (2015) had more detail on the protein and different interaction, our research was mainly focused on VRK1 as a proposed target.

1.6.4 Modifications to UA and their impact on Cytotoxicity

Despite the significant safety and potential efficacy of UA in cancer treatment, its low solubility, rapid metabolism and poor bioavailability currently detract from its therapeutic potential, thus restricting its further clinical application. Therefore, researchers have modified UA to enhance its solubility and bioavailability (Chen *et al.*, 2018; Khwaza, Oyedeji and Aderibigbe, 2020). Modifications of UA published in the literature are at the ring A and C2/C3 positions, C3, C3/C28, C17 and C28 (see **Figure 14**). Some of the modifications are shown below and others are summarized in **Table 2**.

The modification of ring A was studied by Tu *et al* (2009) where they synthesised ring opening conjugates of UA (**Scheme 2**) against NTUB1 cells (human bladder cancer cell line). They found that inhibitory effect of compound **A** (**Figure 19**) weakened the cytotoxic activity of UA ($29.44 \pm 1.90 \mu\text{M}$), whereas compound **B** (**Figure 19**) indicated a potent cytotoxic activity. Their results showed that the dimethyl ester at C3 further enhanced inhibitory effect on the cell growth. Compound **B** was further tested and they found that it mediates the generation of ROS in NTUB1 cells inducing G2/M and G1 cell cycle arrest, and apoptosis.

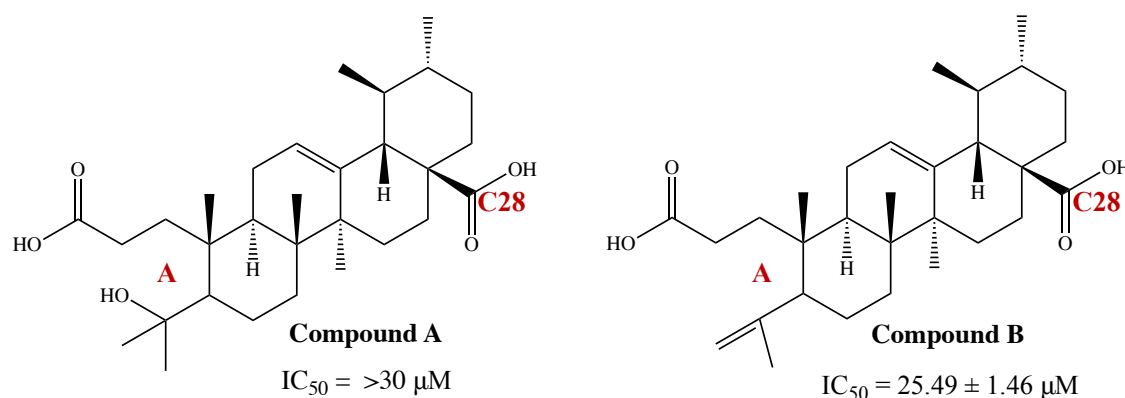
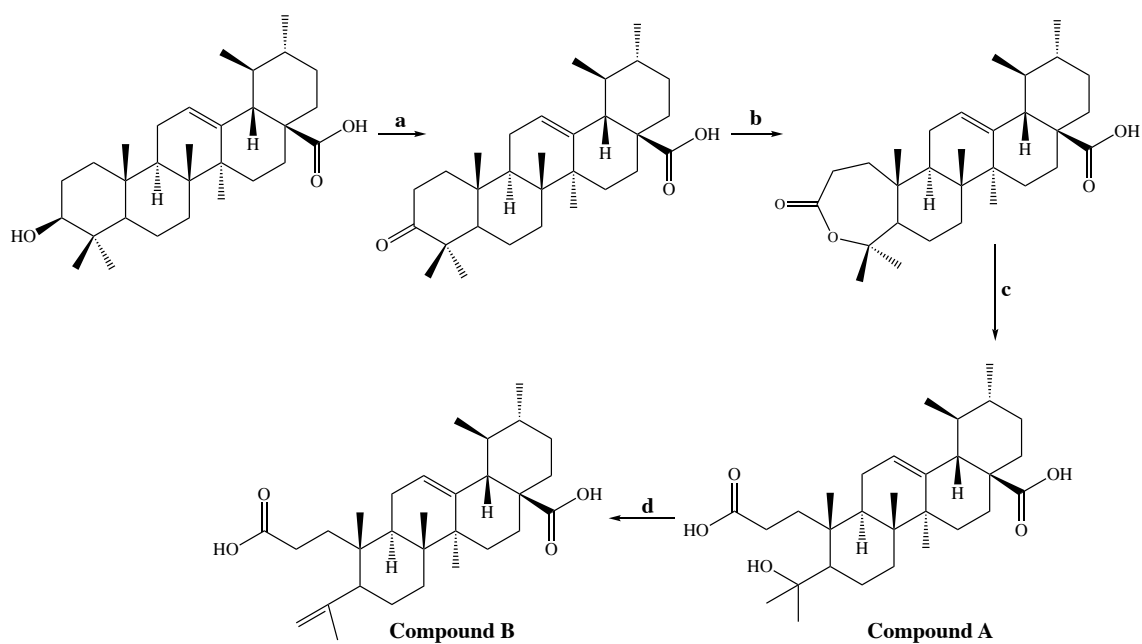
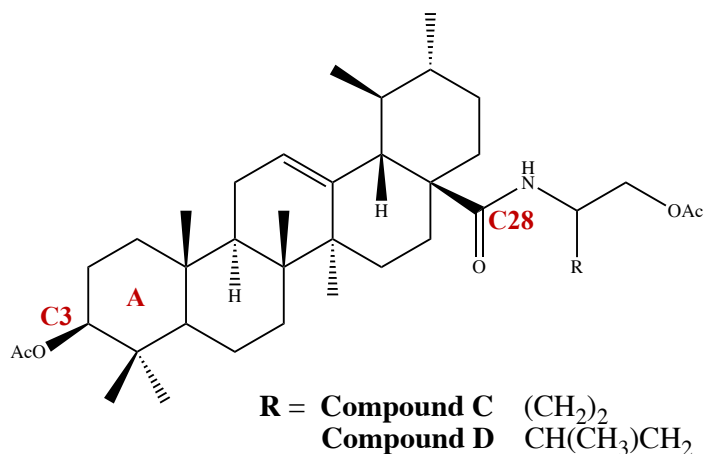


Figure 19. UA derivatives modifying ring A by Tu *et al* (2009).



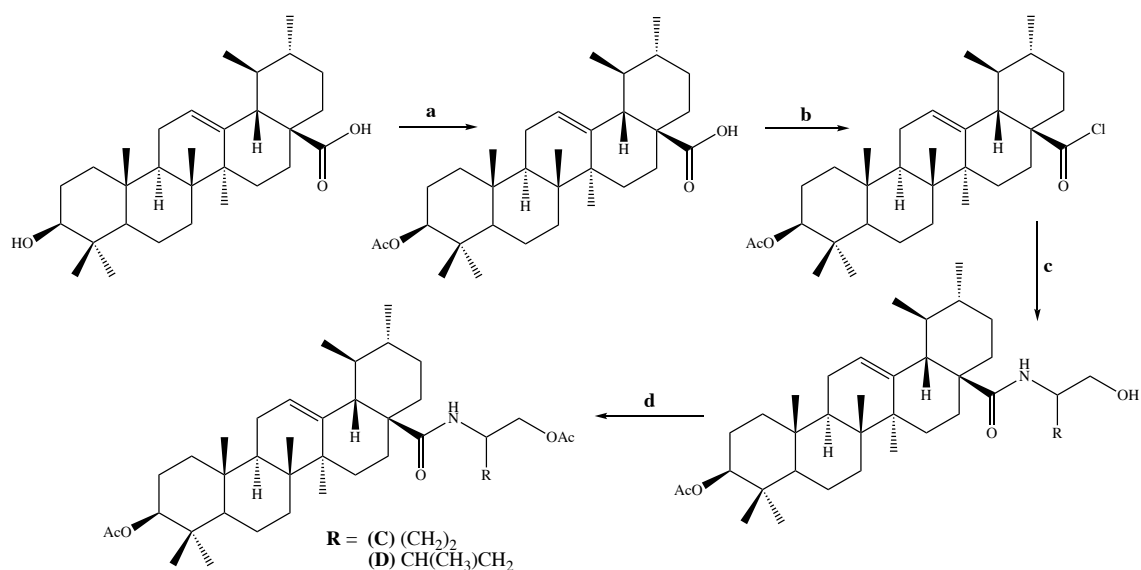
Scheme 2. Schematic diagram of the ring A modification of UA. Reagents and conditions: (a) CrO_3 , H_2SO_4 , DMF; (b) m-CPBA, CHCl_3 ; (c) KOH, MeOH; (d) H_2SO_4 , MeOH (Tu *et al.*, 2009). * CrO_3 – chromium trioxide, m-CPBA – meta-Chloroperoxybenzoic acid.

The study by Meng *et al* (2009) explored the benefit of modifying C3 and C28 with derivatives featured with UA-amino acid conjugates or amino alcohol moieties (**Scheme 3**) against HeLa (cervical cancer cell line) and SKOV-3 (ovarian cancer cell line) (UA IC_{50} is $>10 \mu\text{M}$ for both cell lines). The preliminary structural activity relationship (SAR) studies suggested that acetylation at C3 and coupling an amino acid methyl ester or amino alcohol acetate at C28 improves anti-cancer activity (**Figure 20**).



C $\text{IC}_{50} = 1.13 \pm 0.09$ (HeLa); 6.09 ± 0.92 (SKOV3)
D $\text{IC}_{50} = 2.62 \pm 1.25$ (HeLa); 2.24 ± 0.56 (SKOV3)

Figure 20. UA derivatives modifying C3 and C28 of Meng *et al* (2009).



Scheme 3. Schematic diagram of C3 and C28 modification of UA. Reagents and conditions: (a) and (d) $(\text{CH}_3\text{CO})_2\text{O}$, DMAP, THF, RT; (b) $(\text{COCl})_2$, CH_2Cl_2 , RT; (c) $\text{NH}_2\text{-ROH}$, Et_3N , RT (Meng *et al.*, 2009). * $(\text{CH}_3\text{CO})_2\text{O}$ – acetic anhydride, DMAP- 4-dimethylaminopyridine, THF – tetrahydrofuran, $(\text{COCl})_2$ – oxalyl chloride.

Ma *et al* (2005) extracted UA from apple peels (*Malus pumila* Mill) and tested its cytotoxicity against HL-60 (human leukaemia), BGC-823 (human gastric), Bel-7402 (human hepatoma) and HeLa (cervical) cancer cell lines (UA IC₅₀ are 72.0, 53.7, 45.0 and 49.4 μM, respectively). Structural modifications at C3 and C28 (**Scheme 4**) were performed to enhance cytotoxicity of UA against the four cell lines. As observed in **Figure 21**, the C3 3-oxo derivative (**E**) showed more potent cytotoxicity than UA, whereas the cytotoxicity of hydroxyimino derivative (**F**) is comparable to UA. Compounds with β-oriented (G) hydrogen bond forming group at C3 exhibit more potent cytotoxicity than its α-counterpart (**H**).

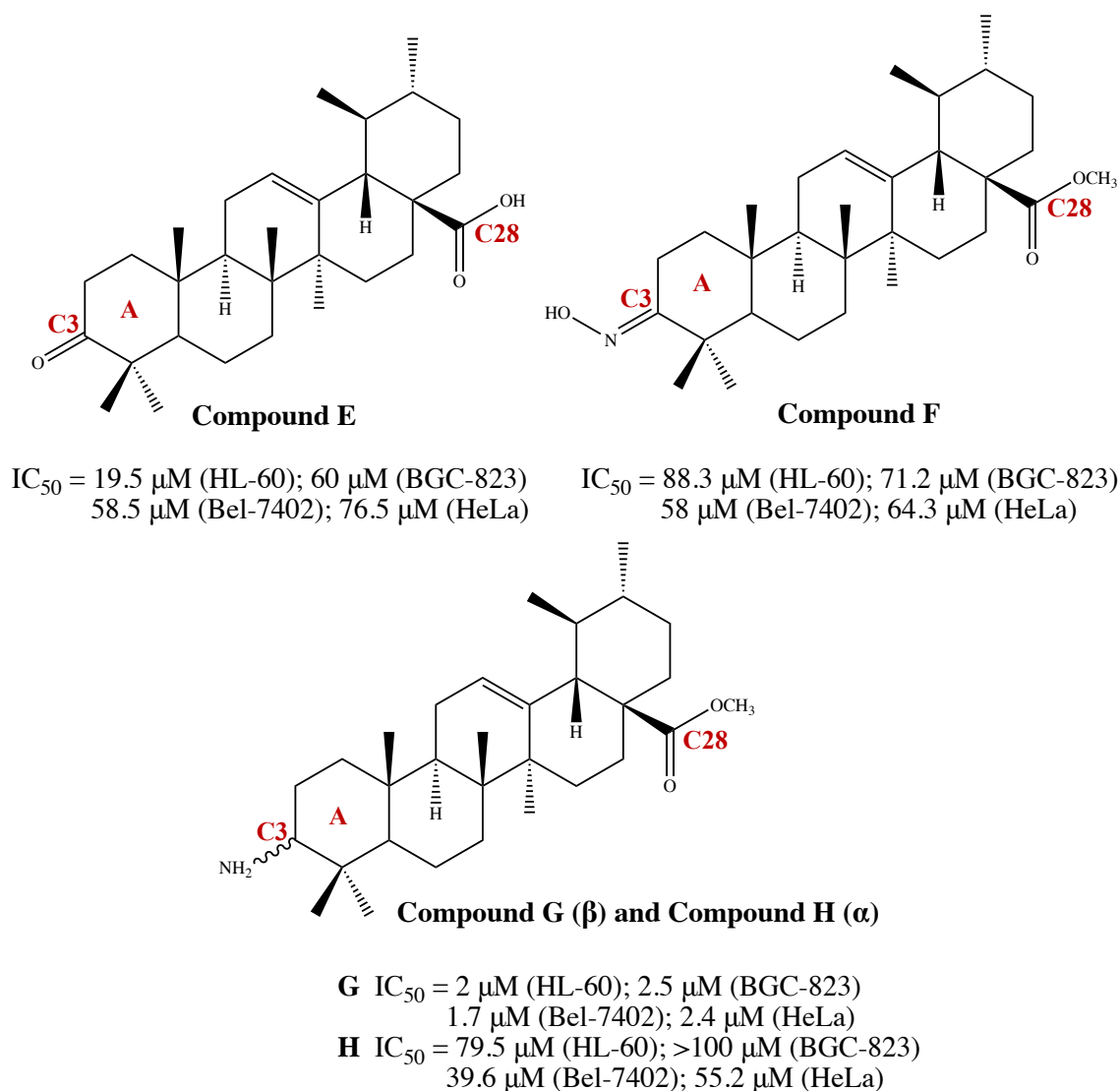
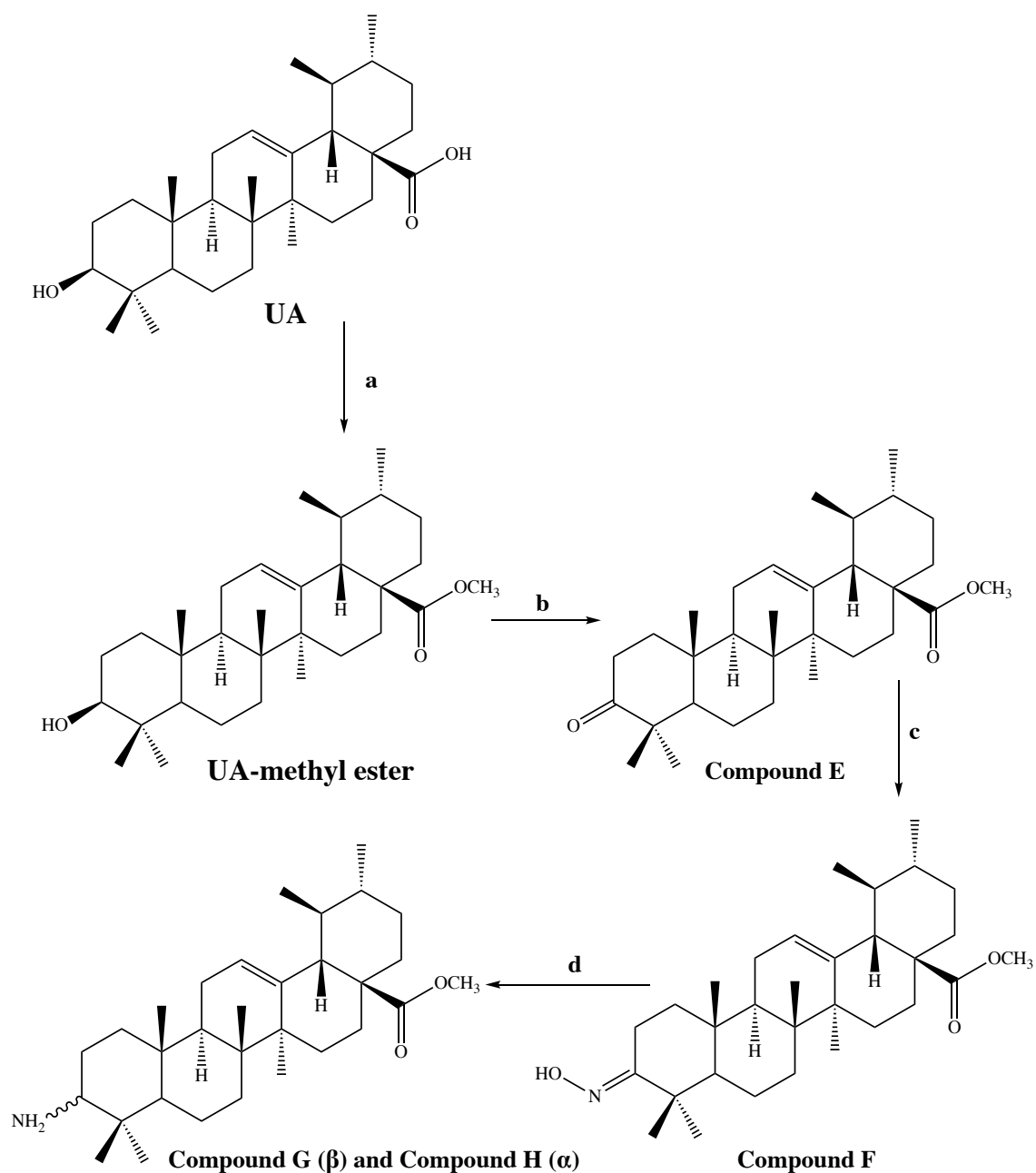


Figure 21. UA derivatives modifying C3 and C28 of Ma *et al* (2005).



Scheme 4. Schematic diagram of the modification at C3 and C28 (compounds **E – H**). Reagents and conditions: (a) CH_2N_2 , Et_2O , 20°C ; (b) PCC; (c) NH_2OH ; (d) NaBH_3CN , TiCl_3 (Ma *et al.*, 2005) *PCC – pyridinium chlorochromate, NH_2OH – hydroxylamine, NaBH_3CN – sodium cyanoborohydride, TiCl_3 – titanium (III) chloride.

Table 2. Some published UA modifications and anti-cancer activities. Cell lines used below are A549, H460 and H322 (human lung); HCT-116 (colorectal); MCF-7, FR-2, SUM149PT, HCC1937 and Bcap-37 (breast); THP-1 (human monocytic), MGC803 (gastric); LKB1 and HepG2 (liver); T24 (urinary bladder); U87, GBM02 and GBM95 (GBM); and HT-29 (colon) cancer cell lines.

Modification	Derivative	Experimental Models	IC ₅₀ (μM)	Activity (<i>in vivo/in vitro</i>)	Reference
C3	Benzylidine	A549 HCT-116 MCF-7 THP-1 FR-2	0.55 ≤0.1 5.5 0.9 0.8	<i>In vitro</i> : induce apoptosis, cell cycle arrest in the G1 phase, caused accumulation of cytochrome c in the cytosol and increased the expression levels of caspase-9 and caspase-3 proteins.	Dar <i>et al.</i> , 2016
C3 and C28	Piperazine FZU3010	SUM149PT HCC1937	4-6	<i>In vitro</i> : impede cell progression by inducing apoptosis and cell cycle arrest at S and G0/G1 phase	Li <i>et al.</i> , 2017
C28	acyl piperazine	MGC803 Bcap-37	2.5 9.24	<i>In vitro</i> : lower anti-proliferative effects and induce apoptosis	Liu <i>et al.</i> , 2012
Ring A and C3	Cleaved ring A and secondary amine in C3	H460 H322 LKB1+/+	2.6 3.3 4.4	<i>In vitro</i> : induced apoptosis <i>via</i> activation of caspase-7 and 8 <i>via</i> decrease of Bcl-2. Induction of autophagy detected with increased levels of Beclin-1 and and decreased levels of mTOR and p62	Mendes <i>et al.</i> , 2016
C3 and C28	Piperazine-thioureas	MGC-803 HCT-116 T24 HepG2 A549	9.82 18.97 13.64 5.40 11.06	<i>In vitro</i> : blocked cell cycle at G1 phase and induced apoptosis through mitochondrial pathway. Arrest cell cycle progression at the S phase and increase the activity of caspase-3 to inhibit cell growth	Hua <i>et al.</i> , 2015

Modification	Derivative	Experimental Models	IC ₅₀ (μM)	Activity (in vivo/in vitro)	Reference
C3 and C28	Acetyl at C3 and alkylamino at C28	HepG2 BGC-823 SH-SY5Y HeLa Kunming mice	20.25 ± 1.52 15.52 ± 0.56 13.24 ± 0.89 10.87 ± 3.21	<i>In vitro</i> : inhibit cell growth by apoptosis, arrest cell cycle progression at S phase of HepG2 cells, and increase activity of caspase-3 <i>In vivo</i> : anti-tumour activity in H22 xenograft Kunming mice	Shao <i>et al.</i> , 2011
C3 and C28	Triazole	U87 GBM02 GBM95	27.1 30.6 28.7	<i>In vitro</i> : high cytotoxic potential in GBM cells	Da Silva <i>et al.</i> , 2018
C28	Amino alkyl	HeLa	>20	<i>In vitro</i> : suppressed adhesion, invasion and migration <i>In vivo</i> : prevent cancer metastasis	Wang <i>et al.</i> , 2014
C3 and C28	Acetyl at C3 and esterification at C28	HT-29 HepG2 BGC-823 xenograft nude mice	18.43 ± 1.83 27.46 ± 1.78 15.66 ± 1.38	<i>In vitro</i> : induce apoptosis via mitochondrial signalling pathway, upregulate caspase-3, downregulate Survivin and Bcl-2 <i>In vivo</i> : anti-cancer mechanism; inhibition of tumour growth greater than Taxol for gastric cancer	Bai <i>et al.</i> , 2011
C3	NO-donating	HepG2	3.2	<i>In vitro</i> : significant cytotoxic activity <i>In vivo</i> : induce cell apoptosis	Chen <i>et al.</i> , 2011

PROJECT RATIONALE

Project Rationale

GBM is considered to be the most biologically aggressive type of brain tumour accounting for approximately 48% of all malignant primary brain tumours. GBM patients diagnosed have poor prognosis with a low five-year survival rate of <10% (Ostrom, *et al.*, 2019), highlighting the need for novel and more effective treatment for these tumours.

Targeted-drug delivery is a highly desirable goal for the treatment of GBM tumours, offering the potential to address challenges in overcoming the various barriers that prevent effective levels of drugs from reaching and reducing tumours. Receptor-mediated endocytosis (RME) is considered one of the most effective strategies for brain targeted drug delivery. The folate receptor (FR) is over-expressed in the brain and in a range of cancer cells including GBM, offering a potential target for suitably modified anticancer drugs.

In recent studies, ursolic acid (UA) has been shown, both *in vitro* and *in vivo*, to demonstrate anti-inflammatory, anti-proliferative and anti-migratory properties, suppress tumour growth, and enhance efficacy and sensitivity of chemotherapeutics against many common cancers including breast, ovarian, skin, and colorectal cancers (Navin and Mi Kim, 2016). Our previous research has demonstrated that UA induces JNK dependent cytotoxicity and JNK independent anti-migration in GBM cells and activates features associated with autophagy. We found that UA demonstrates significant advantages in anti-cancer activity in GBM by activating cytotoxicity, inhibiting mobility and partially activating autophagy when compared to conventional chemotherapeutic agents used to treat GBM (i.e. TMZ) (Conway *et al.*, 2021). Notwithstanding UA's potent anti-cancer

activities, effective targeted delivery strategies for UA have proven difficult to achieve to date, with low natural bioavailability and lack of known selective uptake mechanisms.

The carboxylic acid functional group (C-28; **Figure 14**) of UA was targeted for this study due to accumulating evidences indicating that UA modified on C-28 could improve anti-cancer activities of UA (Liu *et al.*, 2008; Liu *et al.*, 2012; Bai *et al.*, 2012). Folic acid, which binds to FR with high affinity, was used for folate-targeted drug delivery for GBM due to evidences that FR is highly expressed in the brain.

The current project seeks to deliver novel FUA/UA derivatives, and study their biological profiles against different cancer cells, specifically GBM.

Research Questions

1. Treatment for GBM has remained poor to date with a low five-year survival rate of <10%. Despite advancement in treatment modalities in recent years, the disease remains largely incurable. Can we develop novel compounds as potential treatment for these tumours?
2. Carboxylic acid functional group of UA was found to be robust in improving cytotoxicity. Can we conjugate FA and/or diamines to C-28 of UA to generate novel UA derivatives?
3. UA displays potent anti-cancer activities but bioavailability and delivery to brain tumours is expected to be problematic due to its poor solubility. Can we enhance the bioactivity of UA against GBM without interfering with anti-migratory or cytotoxic activities?

4. Targeted delivery of UA has proven difficult to date, with low natural bioavailability and lack of known selective uptake mechanisms. Folic acid displays high affinity to FRs, and due to the low expression in normal tissues, FR can be exploited to target cancer cells. Can the folate receptor be targeted to enhance the chemotherapeutic potential of ursolic acid *via* improvement in selectivity and bioactivity against GBM and other cancer cells, without interfering with anti-migratory or cytotoxic activities?
5. We recently found that UA exhibited significant anti-cancer activity in GBM cells. Could these novel UA derivatives retain/enhance the inherent cytotoxicity, anti-migratory and anti-proliferative effects of UA in a panel of cancer cell lines, specifically in U-251 MG GBM cells? In addition, can we investigate the apparent cell death mechanisms involved in U-251 MG cells?
6. FR is targeted for this study, and a docking study showed that folic acid binds to FOLR1 with high affinity. In addition, a study has identified that UA has a strong binding affinity towards VRK1, which is responsible for modulating DNA repair mechanism. Could we develop a computational docking model for novel UA derivatives and investigate possible molecular interactions with FOLR1 and VRK1 protein, and investigate if activities of folic acid and UA, respectively, are retained/improved?

Aims and Objectives

The aims of the current research project were:

- (i) To generate novel folate-ursolic acid (FUA) conjugated compounds which comprise a folate receptor binding moiety linked to UA with the linkers intended to enhance and/or release UA following uptake by cells *via* the folate receptor.
- (ii) To generate novel UA derivatives which comprise of different linkers intended to enhance solubility, bioavailability and bioactivity of UA.
- (iii) To explore the structural activity relationship (SAR) of UA and novel UA derivatives that were designed to improve its activity and bioavailability (predicted ADMET profile), and utilise molecular docking studies against proposed targets – FOLR1 and/or VRK1, with an in-depth analysis of predicted interactions.
- (iv) To assess and quantify the FR-targeting capabilities and biological profiles of the FUA's against relevant FR+ve and FR-ve cancer cell lines.
- (v) To study the biological profiles of novel UA derivatives in 2D and 3D cell culture models.
- (vi) To investigate the cell-death mechanism(s), anti-migratory and anti-proliferative properties, of novel UA derivatives.

To achieve these aims the main objectives of the project were:

- (i) To generate and fully characterise three novel FUA derivatives and six novel UA derivatives. To achieve this, three different types of linkers have been chosen as the moieties to bridge the folate and the ursolic acid components of the conjugates: (1) an ethylenediamine linker intended to simply reduce steric hindrance; (2) a diamine containing a disulphide bond which can be cleaved within the cell to release UA; and (3) a diamine containing an ethereal oxygen chain to improve water solubility.
- (ii) To assess the cytotoxic activity of the three novel FUA derivatives in a range of confirmed FR+ve and FR-ve cancer cell lines.
- (iii) To assess the cytotoxic activity of the six novel UA derivatives in a range of cancer cell lines.
- (iv) To elucidate, where possible, aspects of the mechanism of action of the active compounds in GBM cellular systems.
- (v) To perform an *in silico* study of novel UA derivatives and examine their proposed interactions with target proteins.

CHAPTER 2

RESULTS & DISCUSSION 1

“The Synthesis and Characterisation of Novel UA Derivatives.”

2.0 The Synthesis of Novel UA and FUA Derivatives

Research Question:

Can we conjugate folic acid *via* a diamine linker(s) to C-28 of UA to generate novel UA derivatives?

Aims and Objectives:

To generate and fully characterise novel UA/FUA derivatives with linkers intended to enhance and/or release UA following uptake by cells *via* the folate receptor.

In this study, folic acid was reversibly conjugated to UA *via* four-step synthesis using carbodiimide chemistry and/or *N*-guanidinium salt. Three different types of linkers have been chosen as the moieties to bridge the folate and the UA components of the conjugates: (1) an ethylenediamine linker intended to simply reduce steric hindrance; (2) a diamine containing a disulphide bond which can be cleaved within the cell to release UA; and (3) a diamine containing an ethereal oxygen chain to improve water solubility.

It was reported in the literature that only the carboxylic acid group γ -conjugate of folic acid can retain affinity toward the receptor. Hence, the γ carboxylic acid group of FA was targeted for this study. Similarly, the carboxylic acid functional group (C-28) of UA was targeted for the synthesis due to evidences suggesting that modifications at C-28 can enhance activity of UA.

All novel UA and FUA derivatives were characterized using Fourier Transform Infrared Spectroscopy (FTIR), Hydrogen-Nuclear Magnetic Resonance ($^1\text{H-NMR}$), Carbon-13-Nuclear Magnetic Resonance ($^{13}\text{C-NMR}$), and Mass spectroscopy (MS).

2.1 The comparison of UA Hunan and UA Sigma

UA Hunan (referred to as UA for the entire study) was purchased from Hunan, China and was compared to a reference (UA Sigma purchased from Sigma-Aldrich (Merck), Ireland with >90% purity) to confirm its chemical and biological properties.

2.1.1 Chemical comparison of UA Hunan and UA Sigma

Chemical properties were compared by FTIR, NMR and RP-HPLC analysis. Purity of UA Hunan was further confirmed using mass spectroscopy and elemental analysis. UA Hunan was isolated from the leaves of *Rosemary officinalis* as an off-white crystalline powder with $\geq 98\%$ purity (certificate of analysis provided in **A.1**). The molecular formula was determined to be $C_{30}H_{47}O_3$ based on LC-MS (ESI) revealing a molecular ion peak at m/z 455.3531[M-H]⁻ (calculated for $C_{30}H_{48}O_3$, 455.3533). Based on the molecular formula, the degrees of unsaturation were found to be seven, indicating that the isolated compound is probably a pentacyclic triterpenoid metabolite.

Further confirmation was provided by ¹³CNMR (**Table 3**) revealing the presence of 30 carbon resonances distinguished into seven methyl groups, nine methylene moieties, seven methine carbons in addition to two carbon resonances at 76.84 and 124.59 ppm representing one oxygenated aliphatic (C3) and one olefinic (C12), respectively, together with seven quaternary carbons. The appearance of peaks at 124.59 and 138.23 ppm indicate the presence of a double bond (C12 and C13). The most downfield signal at 178.35 ppm represents the carboxylic acid function (C28) (**Figure 14**). The purity was confirmed by elemental analysis and was found to be C, 78.72; H, 10.75 (calculated: C, 78.90; H, 10.59). From results obtained (**A.2**), UA Hunan has sufficient purity to be used in this study.

Table 3. Key ¹HNMR and ¹³CNMR resonances for UA Hunan and UA Sigma.

Position	Chemical Shift (ppm)			
	UA Hunan		UA Sigma	
	¹ HNMR	¹³ CNMR	¹ HNMR	¹³ CNMR
C1		38.24		38.21
C2		27.56		27.52
C3	4.32 (d, 1H)	76.84	4.31 (d, 1H)	76.81
C4		38.41		38.35
C5		54.79		54.76
C6		17.07		16.99
C7		32.72		32.68
C8		39.52		39.52
C9		46.85		46.80
C10		36.55		36.51
C11		23.31		23.25
C12	5.12 (t, 1H)	124.59	5.12 (t, 1H)	124.55
C13		138.23		138.18
C14		41.67		41.63
C15		28.29		28.24
C16		23.83		23.79
C17		47.03		46.99
C18	2.10 (d, 1H)	52.39	2.10 (d, 1H)	52.36
C19		38.53		38.48
C20		38.46		38.41
C21		30.21		30.16
C22		36.35		36.29
C23		22.88		22.82
C24		21.13		21.05
C25		15.27		15.20
C26		16.95		16.90
C27		27.02		26.97
C28	11.99 (s, 1H)	178.35	11.99 (s, 1H)	178.24
C29		16.14		16.05
C30		18.02		17.97

2.1.2 Biological comparison of UA Hunan and UA Sigma

UA Hunan and UA Sigma were biologically compared using human glioblastoma (U-251 MG) and human colorectal (SW480) cell lines. The conditions for cytotoxicity studies were performed as identical as possible. To elucidate cell cytotoxicity, alamarBlue cell viability assay (7.8.3) was performed 48 hours post incubation, in triplicates. The results obtained showed that there is no significant difference ($P > 0.05$) in the IC_{50} values between the two compounds. A slightly lower cytotoxicity was obtained from UA Hunan in both cell lines. The IC_{50} obtained using U-251 MG cells are 17.68 and 20.65 μM , respectively; and in SW480 cells are 14.69 and 16.46 μM , respectively (Figure 22; Table 4).

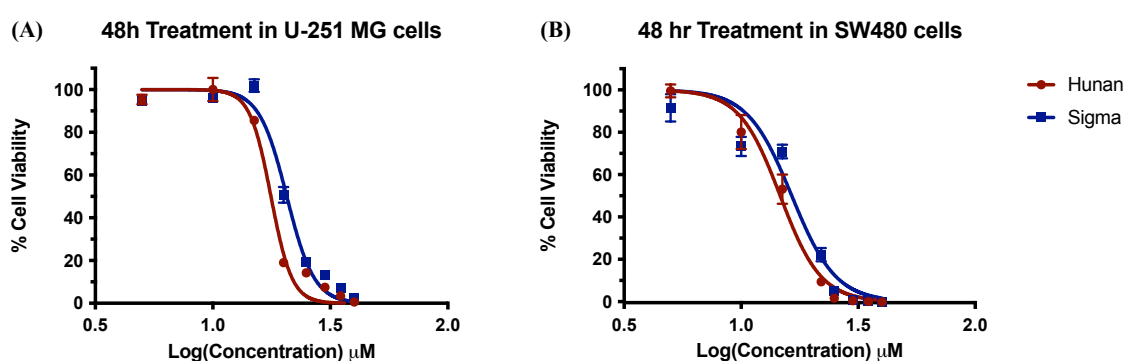


Figure 22. Cytotoxicity of UA Hunan vs UA Sigma on (A) U-251 MG and (B) SW480 cell lines after 48 hours treatment. An initial concentration of 100 μM in culture medium was added to cells and serially diluted to different concentrations (100 μM to 3.125 μM). Cell viability was measured using AlamarBlue assay. Data shown were normalised to the untreated control and are shown as the % mean \pm SEM. Statistical analysis was carried out using non-linear regression analysis and Two-way ANOVA with Bonferroni post-tests, ($n = 3$) ($P > 0.05$).

Table 4. Cytotoxicity evaluation summary of two different UA origins obtained from natural sources.

Compound	IC ₅₀ (μM)		95% Confidence Intervals (IC ₅₀)		Statistical significance
	U-251 MG	SW480	U-251 MG	SW480	
UA Hunan (Hunan Dalore)	17.68	14.69	17.07 to 18.32	13.86 to 15.56	P > 0.05
UA Sigma (Sigma-Aldrich)	20.65	16.46	19.95 to 21.37	15.17 to 17.86	P > 0.05

This study showed that extracted UA - UA Hunan and UA Sigma are chemically and biologically similar. Hence, UA Hunan can be used in subsequent studies.

2.2 The Synthesis of Novel Folate-Ursolic Acid (FUA) Conjugates

The synthesis of three novel folate-ursolic acid (FUA) conjugates is the fundamental objective for this component of the project. All three novel FUA compounds contain a linker intended to enhance and/or release UA following uptake by cells (**Figure 23**). To achieve this, three different types of linkers were chosen: (1) the first contains an ethylenediamine linker intended to simply reduce steric hindrance; (2) the second possesses a disulphide bond which can be cleaved within the cell to release UA; and (3) the third contains an ethereal oxygen chain to improve water solubility. A brief summary of the synthetic steps undertaken are listed in **Table 5** and the synthetic route to novel FUA conjugates is shown in **Scheme 5**. Initial approach to generating FUAs is shown in **Scheme 6**.

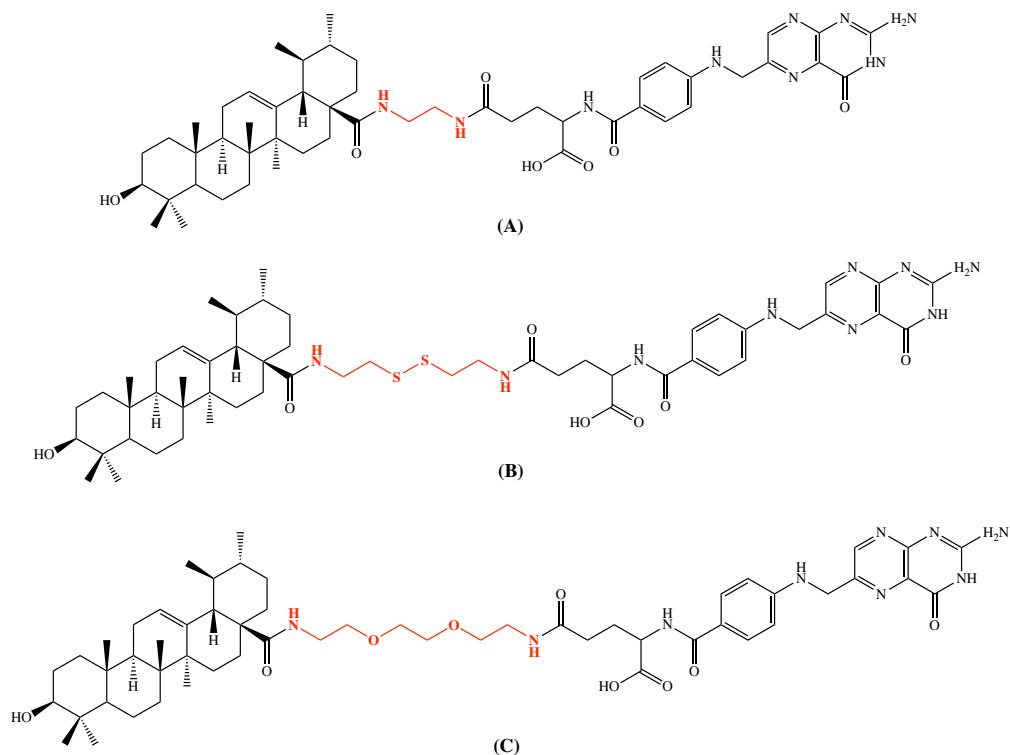
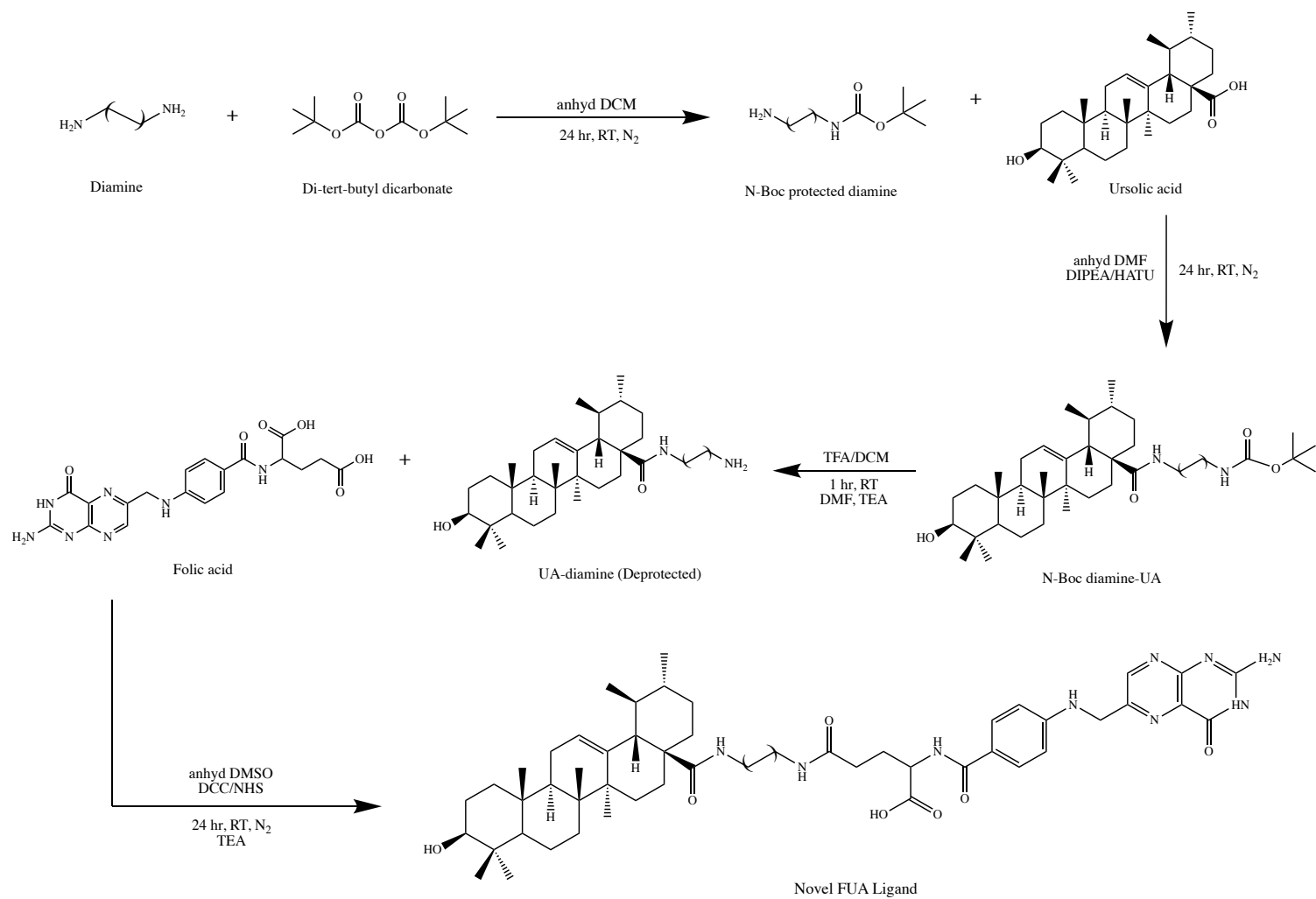


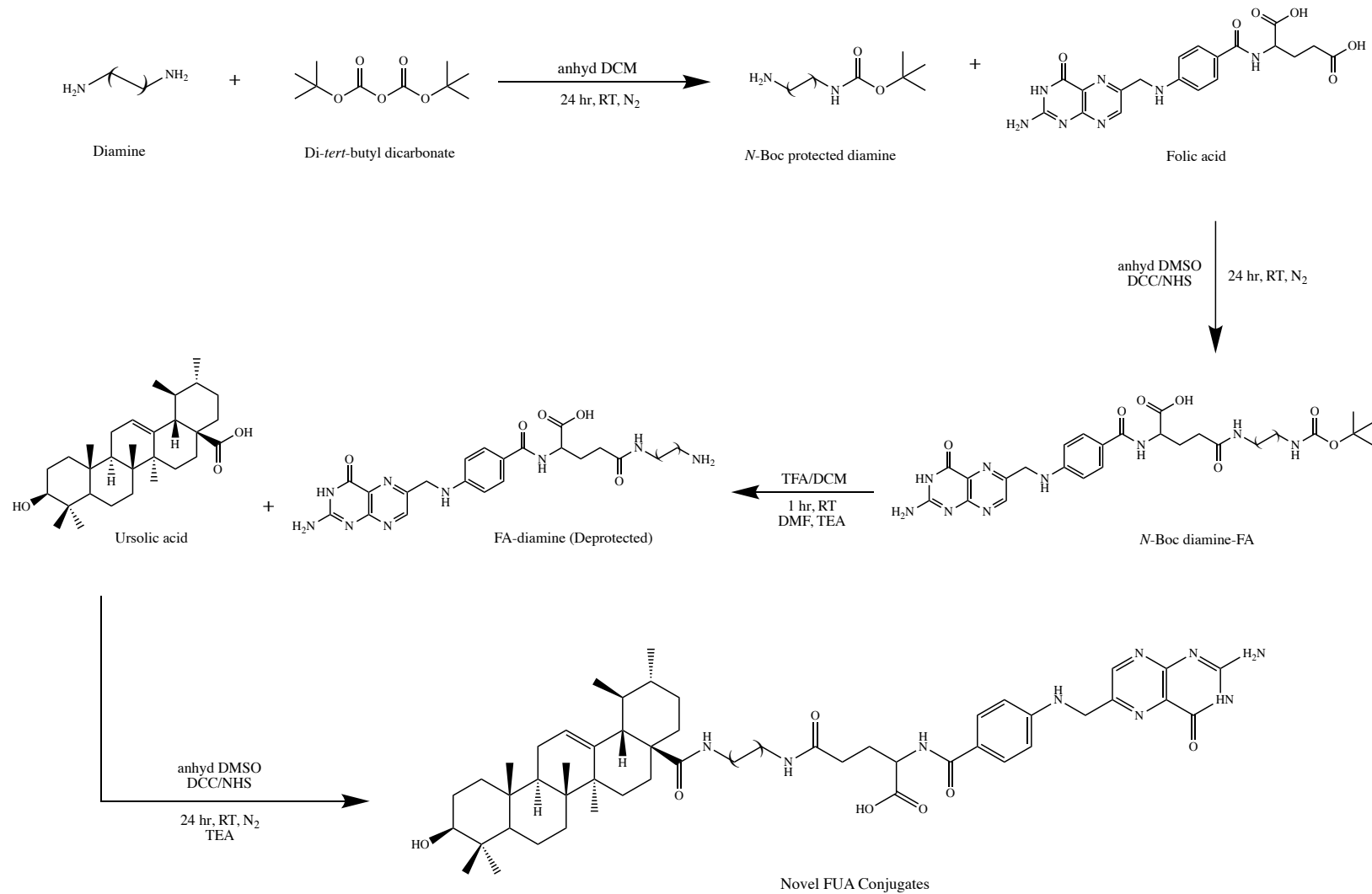
Figure 23. The structures of the novel FUA compounds (functionalised linkers highlighted in red). (A) ethylenediamine linker (B) disulphide linker (C) ethereal oxygen linker.

Table 5. A summary of the synthetic steps undertaken for the synthesis of novel FUA derivatives.

Step	Synthetic Steps	Section
Step 1	<i>N</i> -Boc protection of three diamine functional linkers	2.2.1
Step 2a	Conjugation of <i>N</i> -Boc ethylenediamine (<i>N</i> -Boc-EDA) to FA	2.2.2
Step 2b	Deprotection of <i>N</i> -Boc-EDA-FA conjugate	2.2.3
Step 2c	Conjugation of UA to FA-EDA	2.2.4
Step 3a	Conjugation of <i>N</i> -Boc diamine linkers to UA	2.3.1
Step 3b	Deprotection of <i>N</i> -Boc diamine-UA conjugate	2.3.2
Step 3c	Conjugation of FA with the diamine-UA to form the folate-ursolic acid (FUA) compounds	2.3.3



Scheme 5. A schematic of the synthesis of the novel FUA derivatives (based on similar synthetic procedures from the literature). The synthesis of novel FUA compounds B and C were conjugated using a similar approach.



Scheme 6. A schematic of the initial approach carried out to synthesise novel FUA derivatives. The first attempt was to conjugate FA to UA.

2.2.1 The *N*-Boc Protection of Diamine Functional Linkers (Step 1)

Di-*tert*-butyl dicarbonate (Boc_2O) is one of the most commonly used protecting group for amines in organic synthesis (Ragnarsson and Grehn, 2013; Cheraiet *et al.*, 2012). The general route for *N*-Boc protection of diamines is shown in **Scheme 7**. The diamines ethylenediamine and 2, 2'-(ethylenedioxy)bis(ethylamine) were *N*-Boc-protected in a similar manner, following methods previously published (Trindade *et al.*, 2014; Hart *et al.*, 2015) to produce compounds **1** and **3**, respectively (**Figure 24**). A ten-fold excess of the diamine was slowly reacted with Boc_2O to produce the mono-Boc product. Products were obtained, as colourless viscous oils with enough purity and yield (> 50%) to be used in subsequent reactions. The *N*-Boc protection reaction with cystamine (compound **2**; **Figure 24**) produced a pale yellow viscous oil at a lower yield (< 40%). The lower yield is due to significantly more work-up compared to that required for compounds **1** and **3**. Published data are quite similar, with yields of 37 – 45% obtained (Baek *et al.*, 2015; Li *et al.*, 2015; Shirazi *et al.*, 2011).

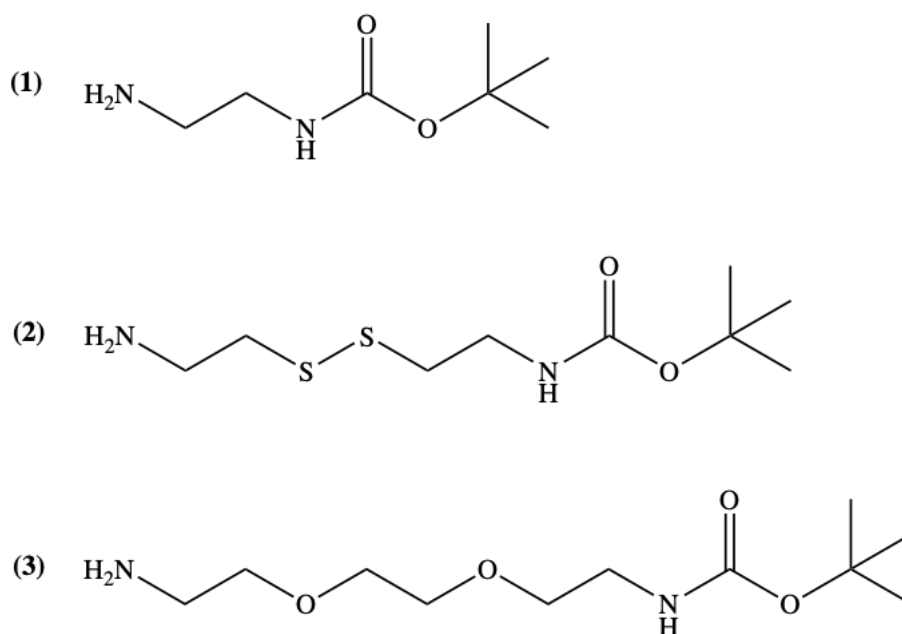
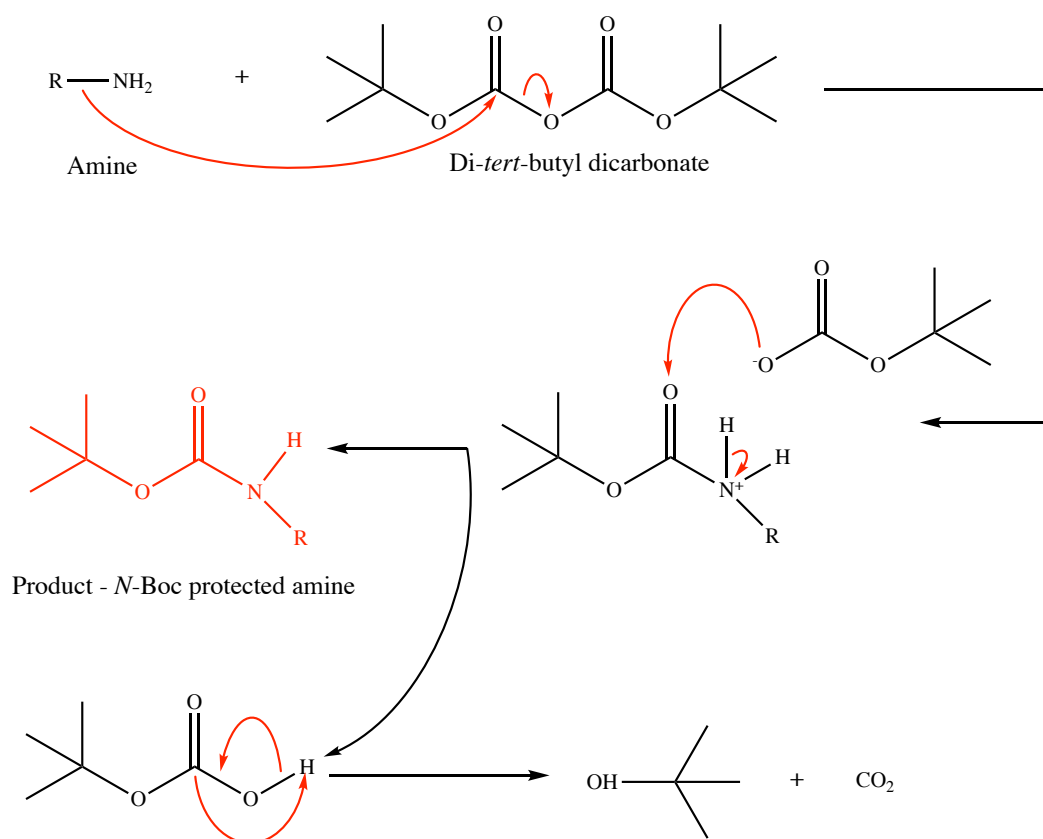


Figure 24. *N*-Boc protected diamines **1-3**.



By-products: *tert*-butyl hydrogen carbonate breaks down to give *tert*-butanol (water soluble) and carbon dioxide (gas)

Scheme 7. The *N*-Boc protection of diamines where R = (CH₂)₂NH₂, (CH₂)₂SS(CH₂)₂NH₂ and (CH₂)₂O(CH₂)₂O(CH₂)₂NH₂ (Common Organic Chemistry, 2020).

N-Boc diamines **1** – **3** were characterised primarily by NMR (¹HNMR and ¹³CNMR) and mass spectroscopy. In the ¹HNMR spectra, the shielded Boc group, consisting of three methyl branches, was found in the furthest upfield in all spectra, appearing from 1.35 – 1.42 ppm (**Table 6**). In the ¹HNMR spectra of compounds **1** and **3** (**A.4** and **A.6**), the NH₂ peak can be observed as a singlet at 1.14 ppm and 1.79 ppm, respectively. However, the unprotected NH₂ peak of compound **2** (**A.5**) appears to merge with the Boc group, representing the singlet peak at 1.42 ppm, increasing integration from nine to eleven. In all *N*-Boc protected diamines, the NH group is observed as a singlet at 5.19, 5.00 and 5.19 ppm, respectively. The remaining peaks are associated with the aliphatic CH₂ groups.

Similar results have been published in the literature (Trindade *et al.*, 2014; Hart *et al.*, 2015; Li *et al.*, 2015).

Table 6. ^1H NMR resonances for *N*-Boc protected diamines **1** – **3**. The integration and peak splitting are shown in brackets.

Compound	Chemical Shifts (ppm)			
	NH	CH ₂ groups	Boc group	NH ₂
1	5.19 (s, 1H)	3.08 (dd, 2H) 2.70 (t, 2H)	1.35 (s, 9H)	1.14 (s, 2H)
2	5.00 (s, 1H)	3.43 (dd, 2H) 2.99 (t, 2H) 2.82 – 2.66 (m, 4H)	1.42 (s, 11H)*	* Peak hidden under Boc at 1.42 ppm
3	5.19 (s, 1H)	3.58 (s, 4H) 3.49 (dt, 4H) 3.28 (dd, 2H) 2.84 (t, 2H)	1.40 (s, 9H)	1.79 (s, 2H)

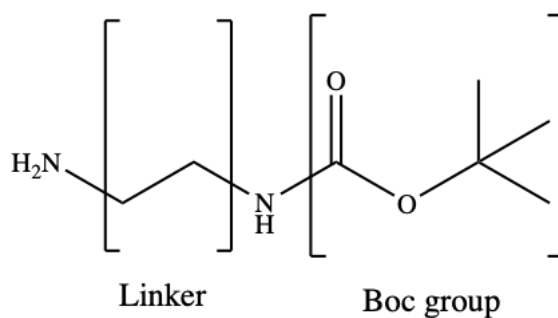


Figure 25. The aliphatic CH₂ group (linker) and Boc group of diamine linker for ^{13}C NMR interpretation.

In the ^{13}C NMR spectra, the carbonyl peak is the furthest upfield in all spectra, appearing from 155.86 – 156.27 ppm. While the shielded Boc group, consisting of three methyl branches, is observed at the nearest upfield in all spectra, appearing at 28.38 – 28.49 ppm (**Table 7**). The remaining peaks are associated with the aliphatic CH_2 groups (linker) (**Figure 25**; **Table 7**).

Table 7. ^{13}C NMR resonances for *N*-Boc protected diamines **1** – **3**.

Compound	Chemical Shifts (ppm)	
	CH_2 groups (linker)	Boc group
1	43.39, 41.85	156.27, 79.02, 28.38
2	42.54, 40.65, 39.33, 38.44	155.86, 79.61, 28.49
3	73.42, 70.28, 70.25, 41.74, 40.38	156.10, 79.21, 28.48

Mass spectroscopy was performed on compounds **1** – **3** in addition to NMR spectroscopy (**Table 8**). Results for all three compounds were expected and complement structures determined through NMR analysis.

Table 8. Mass spectroscopy results of *N*-Boc protected diamines **1** – **3**.

Compound	Chemical Formula	$[\text{M}+\text{H}]^+$ Calculated	$[\text{M}+\text{H}]^+$ Found
1	$\text{C}_7\text{H}_{17}\text{N}_2\text{O}_2$	161.1285	161.1289
2	$\text{C}_9\text{H}_{21}\text{N}_2\text{O}_2\text{S}_2$	253.1039	253.1039
3	$\text{C}_{11}\text{H}_{25}\text{N}_2\text{O}_4$	249.1809	249.1813

2.2.2 Conjugation of *N*-Boc-Ethylenediamine with Folate (Step 2a)

In the first instance the approach to generating the novel folate-ursolic acid (FUA) compounds (**Figure 26**) was initiated with attempted conjugation of the *N*-Boc ethylenediamine with folate (**Scheme 6**) with a view to subsequently conjugating the de-protected product with ursolic acid.

The approach for the folate-diamine conjugation used is based on the method described by Trindade *et al.*, 2014 (**Scheme 8**). This involves the generation of an activated-folate ester *via* *N*-hydroxysuccinimide (NHS) and the coupling agent, *N,N'*-dicyclohexylcarbodiimide (DCC). The newly formed activated ester cleanly reacts with amines under mild conditions allowing for simple amide formation. The by-product of the DCC mediated coupling, dicyclohexylurea (DCU) is highly insoluble in all organic solvents, allowing for easy removal *via* filtration.

In the same paper, Trindade *et al.*, 2014 reported that only γ conjugates have medicinal relevance as it has higher affinity towards the FR in comparison to α -conjugates. The glutamate residue of the FR structure is stabilized by six hydrogen bonds, four of which involves α -carboxylic acid. Therefore, it is evident that only γ -conjugates can retain affinity toward the receptor, although this is a controversial subject in the literature (Trindade *et al.*, 2014; McCarron *et al.*, 2018). Previous studies published using carbodiimide chemistry have proven that γ conjugates are inherently obtained as the major product (from 55 to 90% selectivity) (Aronov *et al.*, 2003; Santos *et al.*, 2017; Figliola *et al.*, 2019; Bertuzzi *et al.*, 2020). Furthermore, the markedly different pK_a

values of the carboxylate groups contribute to their different reactivities (Bertuzzi *et al.*, 2020).

The reaction of the *N*-Boc ethylenediamine with folate was carried out by activating the γ carboxylic group of folic acid using DCC and NHS under nitrogen for 24 hours in the absence of light. After which time, a precipitate, DCU by-product was removed *via* filtration. Compound **1** was then added with triethylamine (TEA) as a base and reacted overnight. A fine, yellow powder (Yield: 1.35 g; 92.25%) was obtained after adding 20% acetone in diethyl ether.

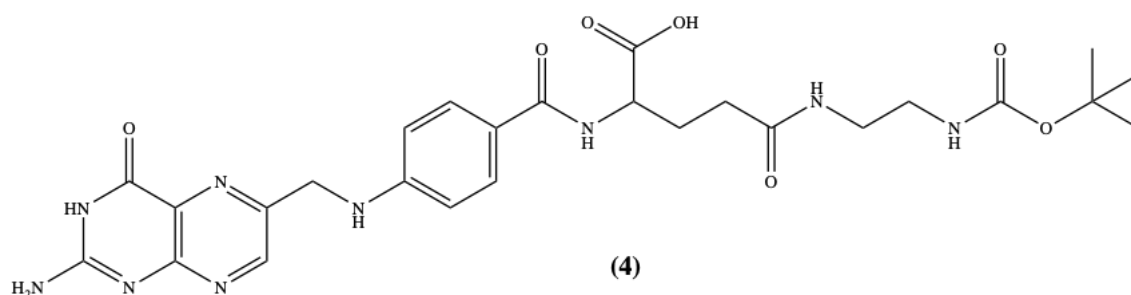
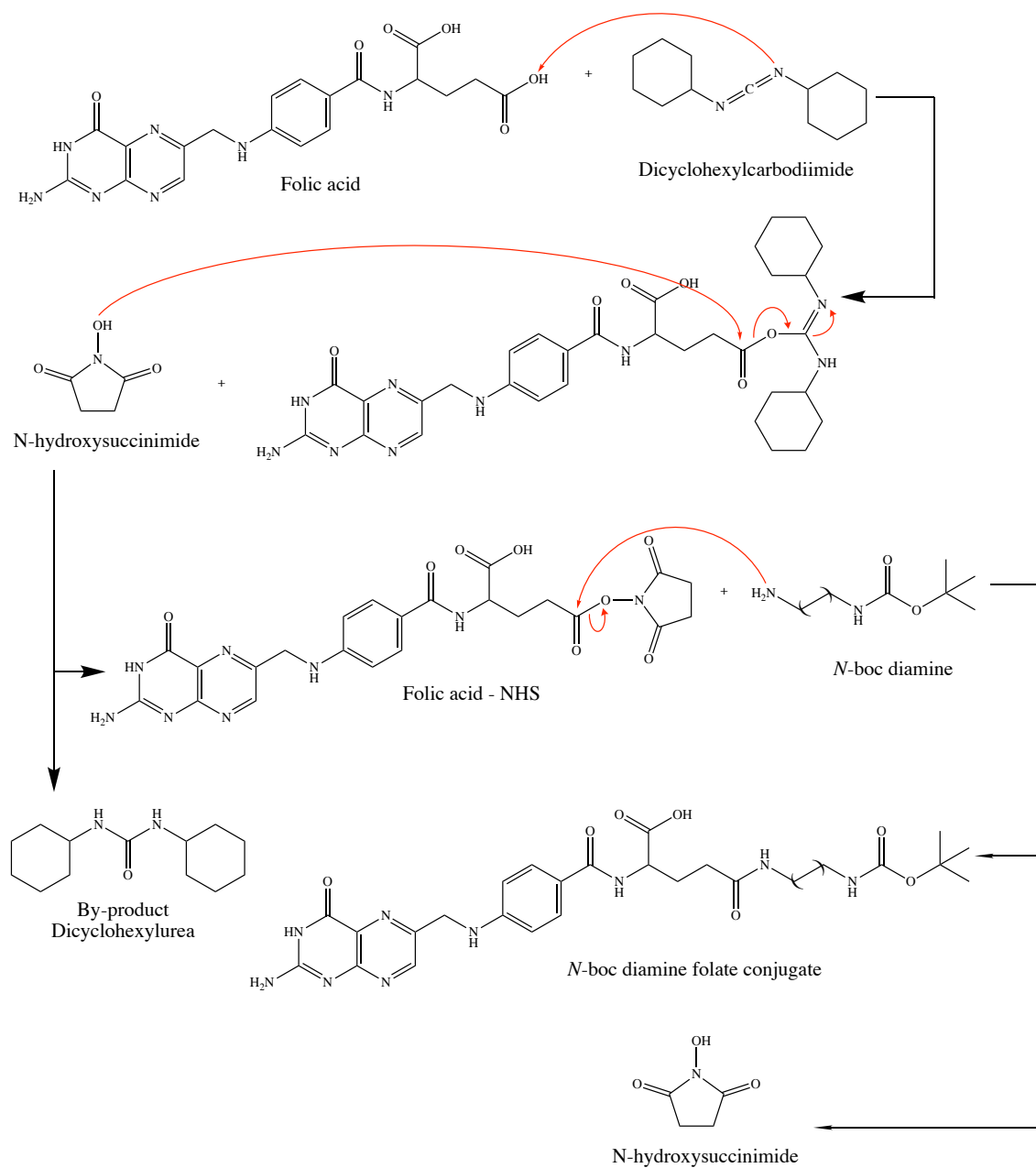


Figure 26. The proposed structure of *N*-Boc ethylenediamine-folate conjugate **4**.



Scheme 8. The conjugation of N-Boc protected diamines to folic acid (Trindade *et al.*, 2014).

The primary method used to interpret the structure of folate-ethylenediamine conjugate product **4** was NMR spectroscopy (^1H NMR and ^{13}C NMR). However, characterisation did prove difficult due to the poor solubility of compounds (hot DMF and hot DMSO only); and the presence of broad solvent peaks in the NMR spectra.

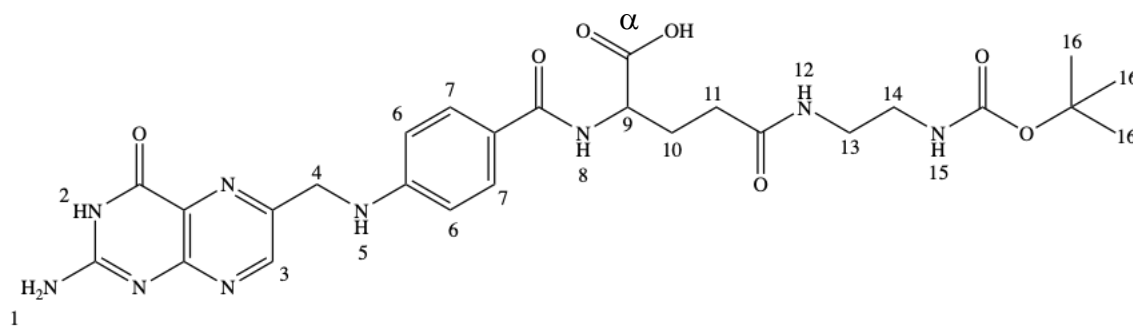


Figure 27. *N*-Boc-ethylenediamine folate conjugate **4** illustrating numbering scheme for ^1H NMR analysis.

In order to determine if conjugation was successful, ^1H NMR spectrum was analysed to identify peaks associated with folic acid and the Boc protection group. In the spectra (**A.7**), the α carboxylic acid group appeared at 11.58 ppm, confirming conjugation to only one carboxylic acid group of folic acid. The peaks related to methylene groups (**Figure 27**: H13 and H14) of the diamine linkers were observed overlapping at 3.01 ppm. Peaks corresponding to aromatic CH groups (H3, H6 and H7) appeared at 8.63, 7.84 and 6.94 ppm, respectively; NH groups (H2, H5 and H8) appeared at 6.63, 6.76 , 8.02 ppm, respectively and NH groups (H12 and H15) overlapped at 7.67 ppm. The peaks corresponding to the hydrogen bound to a carbonyl carbon (H9) was observed at 4.28 ppm, while its neighbouring peak at 4.49 ppm was identified as a CH_2 (H4). Two aliphatic methylene groups (H10 and H11) appeared at 2.04 and 1.92 ppm, respectively. Finally,

the large peak at 1.34 ppm relates to the Boc protection group (H16) and NH₂ group (H1) overlapping, giving an integration of 11H.

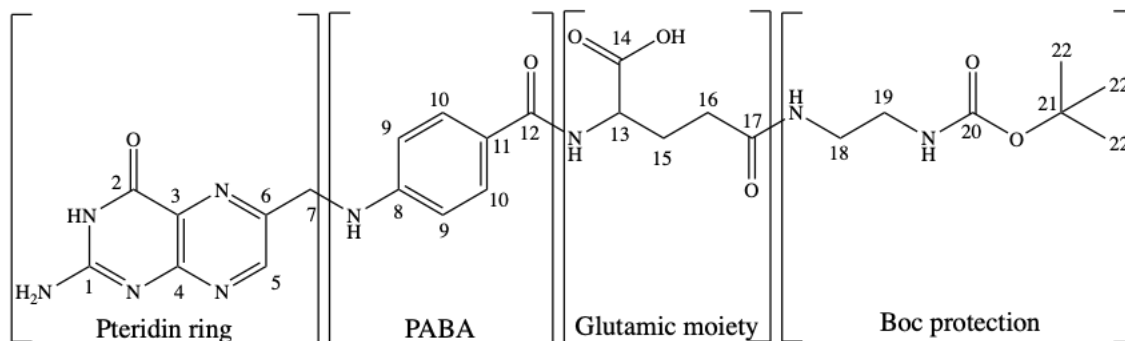


Figure 28. *N*-Boc-ethylenediamine folate conjugate illustrating numbering scheme for ¹³C NMR analysis.

In ¹³C NMR spectrum (A.7), the carbons in the pteridine ring (**Figure 28**: C1 – C7) appeared at 155.65, 153.96, 127.98, 150.97, 150.73, 148.67 and 40.43 ppm, respectively. Peaks corresponding to carbons in PABA (C8 – C12) appeared at 148.61, 77.71, 121.41, 111.18 and 166.25 ppm, respectively. The peaks related to the glutamic moiety (C13 – C17) appeared at 45.93, 171.90, 25.28, 27.54 and 171.97 ppm. Lastly, the Boc protection group (C18 – C21) appeared at 38.82, 32.05, 129.16 and 53.8 ppm, respectively; and the large peak at 28.24 ppm corresponds to C22.

2.2.3 Deprotection of *N*-Boc-Ethylenediamine-Folate (Step 2b)

N-Boc ethylenediamine-folate conjugate **4** was deprotected to produce conjugate **5** (**Figure 29**). This involved the deprotonation of the Boc group with trifluoroacetic acid (TFA) which results in the loss of the *tert*-butyl cation (this will either be deprotonated to

form isobutylene gas, or it will polymerize to form isobutylene oligomers). The remaining carbamic acid is quickly decarboxylated to produce a free amine. In the presence of excess TFA, the product may be present as a TFA salt which can be neutralised with a base such as triethylamine to give the free amine as a stable product (**Scheme 9**; Commonorganicchemistry, 2020). The product was obtained as a yellow powder with a yield of 0.38 g (92.94 %).

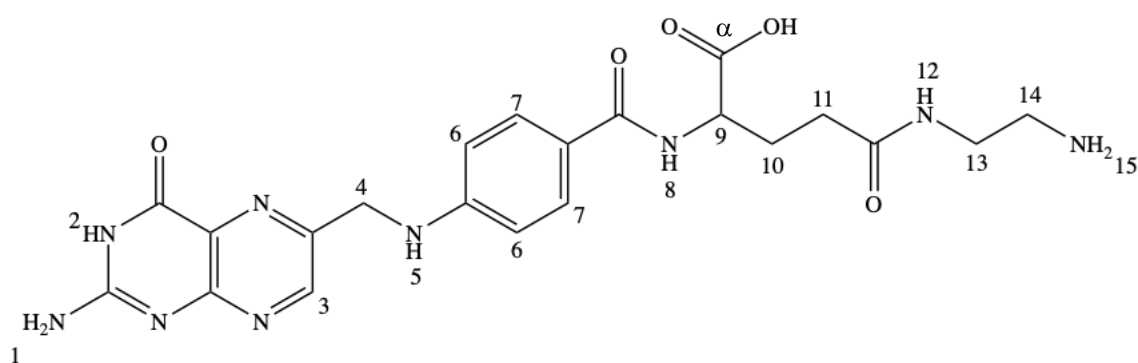
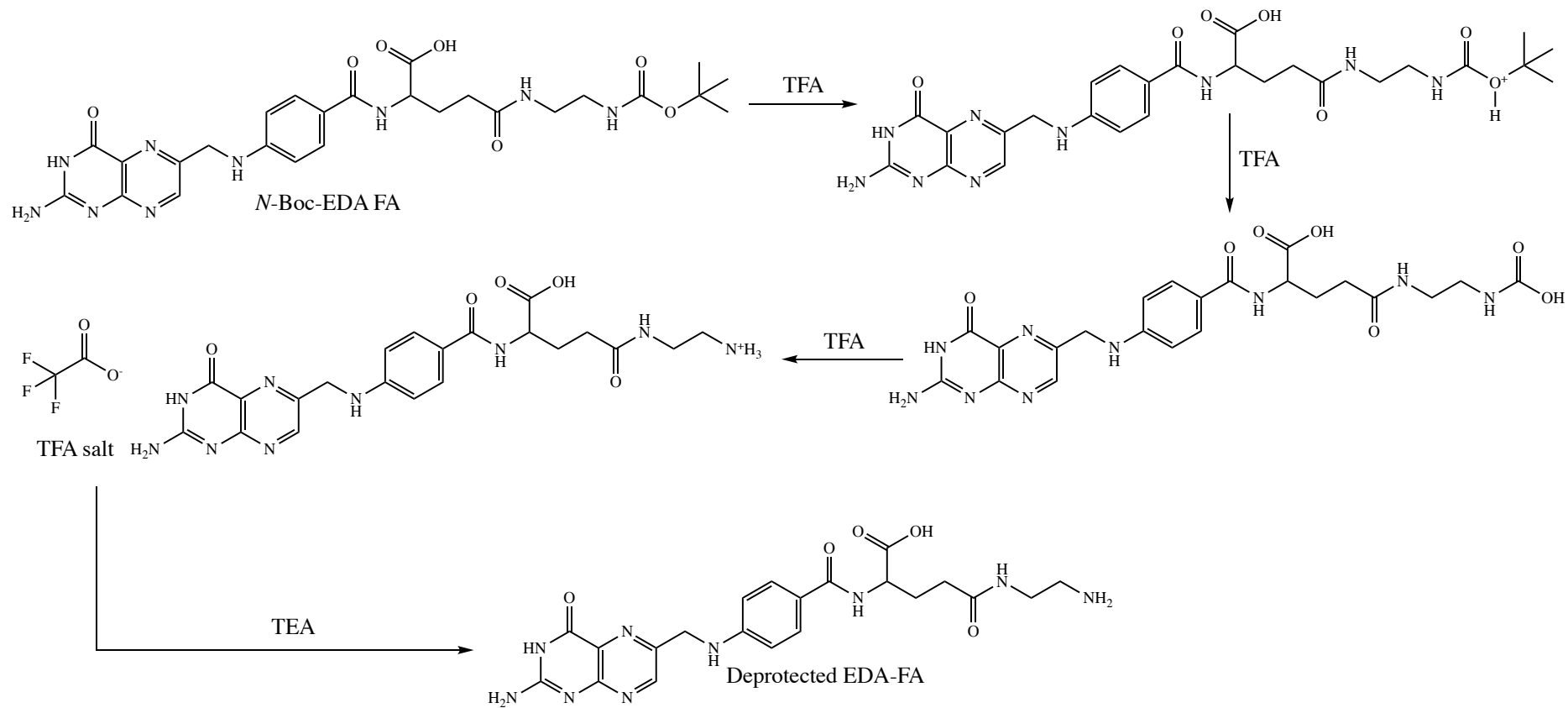


Figure 29. Folate ethylenediamine conjugate **5** illustrating the numbering scheme for ^1H NMR analysis.

Analysis of ^1H NMR indicates the successful cleavage of the *N*-Boc protection group which is normally present as a singlet at 1.34 ppm. The spectra of α carboxylic acid group appeared at 11.68 ppm. The peaks related to methylene groups (H13 and H14) of the diamine linkers were observed overlapping at 2.85 ppm. Peaks corresponding to aromatic CH groups (H3, H6 and H7) appeared at 8.63, 8.04 and 7.67 ppm, respectively; NH groups (H2, H5 and H8) appeared at 6.65, 7.03, 8.16 ppm, respectively and NH groups (H12 and H15) appeared overlapping at 7.81 ppm. The peaks corresponding to the hydrogen bound to a carbonyl carbon (H9) was observed at 4.49 ppm, while its neighbouring peak at 4.32 ppm was identified as a CH_2 (H4). Two aliphatic methylene groups (H10 and H11) appeared at 2.12 ppm and H1 NH_2 group appeared at 1.85 ppm.



Scheme 9. The Boc deprotection of *N*-Boc ethylenediamine folate.

2.2.4 Attempted conjugation of Ursolic acid with Folate-Ethylenediamine (Step 2c)

A range of attempts were made to conjugate UA to folate-ethylenediamine (**Table 9**). The main problem encountered was the activation of the carboxylic acid group (C28; **Figure 14**) of UA. The successful activation of carboxylic acid group of folic acid (**2.2.2**) was successfully performed using coupling reagents DCC and NHS. The same method described in **Scheme 7** was tried for UA carboxylic acid activation, however, by-product DCU was not observed after 24 hr reaction. The activation *via* the DCC/NHS was tried again by increasing reaction time to 48 hr under nitrogen. After which time, a DCU precipitate was observed and easily removed *via* filtration. Compound **5** was then added with TEA and reacted overnight. A fine, yellow product (Compound **6**) (Yield: 0.038 g; 20.61%) was obtained using a dialysis method and freeze drying (**Figure 30**; **7.4.3 - Experimental Section**).

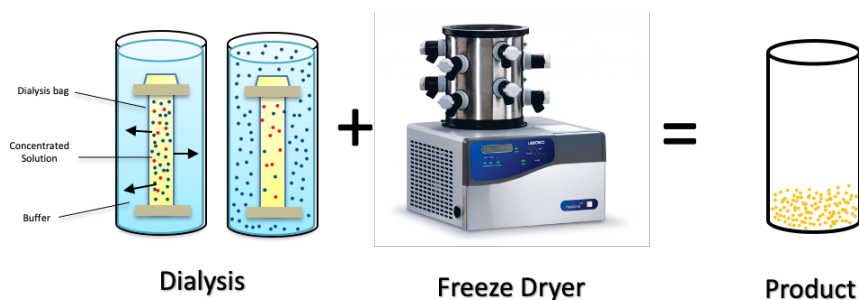


Figure 30. The dialysis method used to obtain compound **6**.

The ^1H NMR spectrum obtained for compound **6** (Figure 31) shows some of the characteristic peaks of folic acid ($\sim 6.5 - 8$ ppm) and UA ($\sim 0.5 - 2$ ppm), but did not integrate as expected. Firstly, the α carboxylic acid group disappeared at ~ 12 ppm. Peaks corresponding to aromatic CH groups appeared at 8.63, 7.88 and 6.61, respectively. The amide bond linking pteridine moiety to PABA, and PABA to glutamate moiety of folic acid appeared at 7.62 and 6.94 ppm, respectively; the NH at the pteridine ring which is expected to be around the same peak was not found. Two aliphatic methylene groups at the glutamate tail of folic acid appeared at around 1.82 ppm. The peak related to the olefinic H of UA was observed at 5.63 ppm whilst the peak at 4.44 – 4.53 ppm was identified as the OH group in C3. The structural aliphatic near OH (C3) appeared at around 4.31 – 4.25 ppm. Peaks corresponding to the seven terminal CH_3 methyl groups (C23 – 27, C29 and C30), structural aliphatic CH_2 groups (C1, C2, C6, C7, C11, C15, C16, C21 and C22) and CH groups (C5, C19 and C20) appeared overlapping at the most upfield region 0.67 – 1.64 ppm.

The peaks corresponding to the hydrogen bound to a carbonyl, the CH_2 , NH_2 groups and peaks of ethylenediamine linker, were not observed. This indicates that there was no amide bond formed linking the two compounds. This was proven when tested for mass spectroscopy (found m/z 762.6641; calculated 950.5404) and elemental analysis (found C, 36.33; H, 4.80; N, 7.39; calculated C, 66.42; H, 7.76; N, 13.67). A review of the literature exposed a frequently encountered problem with steric hindrance at the carbon 28-COOH (Zacchigna *et al.*, 2014; Bekker *et al.*, 2013; Huang *et al.*, 2016).

Table 9 summarises all of the other unsuccessful attempts to conjugate the folate-ethylenediamine to ursolic acid. As this general approach to the formation of the linked folate-ursolic acid (FUA) compounds was not successful it was decided to reconsider how best to approach the synthesis of the FUA's.

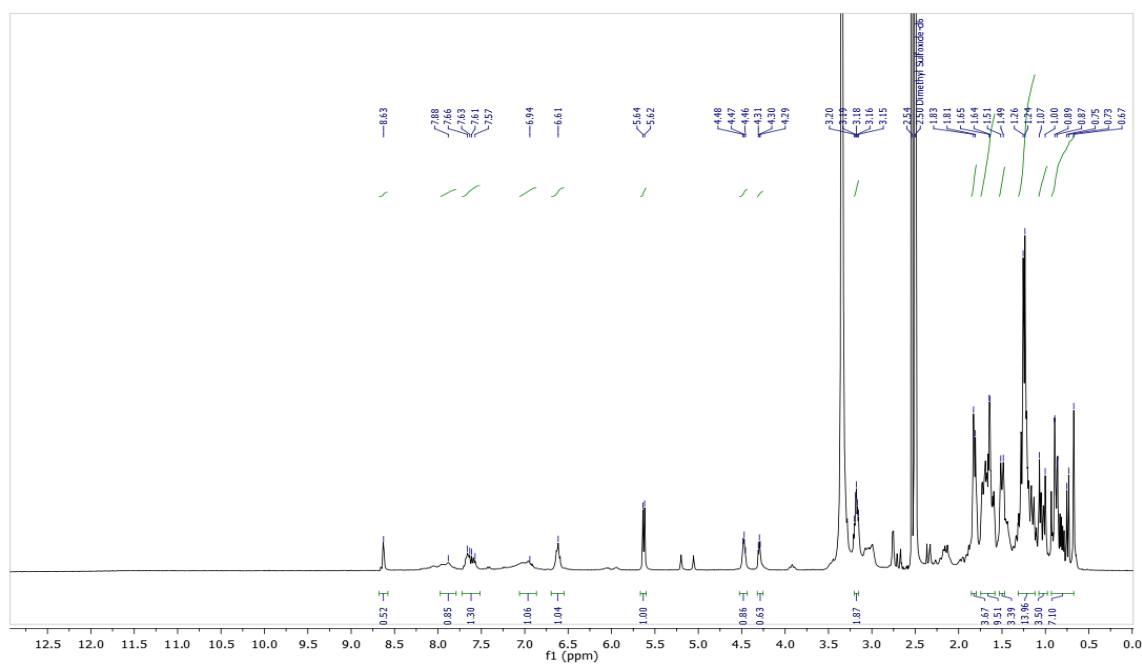


Figure 31. The ¹H NMR spectrum obtained for compound 6.

Table 9. Summary of other failed attempts to conjugate ursolic acid with the folate-ethylenediamine (**6**).

Coupling reagents and solvents	Reaction time	Solvent to precipitate product	Comment
DCC/NHS (anhydrous DMSO)	48 h, N ₂	30% acetone/diethyl ether	IR spectrum same as DCU by-product
DCC/NHS (anhydrous DMF)	24 h, N ₂	-	No DCU by-product precipitate after 24 h
DCC/NHS (methanol)	24 h, N ₂	-	No DCU by-product precipitate after 24 h
DCC/NHS (anhydrous DMSO)	48 h, N ₂	Ethyl acetate	No product precipitate
DCC/NHS (anhydrous DMSO)	48 h, N ₂	Distilled water	No product precipitate
DCC/NHS (anhydrous DMSO)	48 h, N ₂	Methanol	No product precipitate
DCC/NHS (anhydrous DMSO)	48 h, N ₂	Chloroform	No product precipitate
DCC/NHS (anhydrous DMSO)	48 h, N ₂	Brine	Sticky white powder precipitate

2.3 An alternative approach to the synthesis of the Folate-Ursolic Acid (FUA) compounds

Due to activation difficulties associated with the sterically hindered carboxylic acid functional group (COOH; C-28; **Figure 14**) of UA and the resultant failure in conjugating it with the folate-ethylenediamine, the approach to synthesising the folate-ursolic acid (FUA) compounds was reconsidered, i.e. the reverse reaction, involving the coupling UA to the diamine linkers and then to the folate.

2.3.1 Conjugation of *N*-Boc diamines with Ursolic Acid (Step 3a)

The carboxylic acid functional group (COOH; C-28; **Figure 14**) of UA was targeted for this study due to accumulating evidences indicating that UA modified at C-28 could improve anti-cancer activities (Liu *et al.*, 2008; Liu *et al.*, 2012; Bai *et al.*, 2012). Given the problematic solubility of the folate-ethylenediamine conjugate **4** and subsequent failure to conjugate to UA, it was decided to approach the generation of the FUA conjugates differently. The conjugation of *N*-Boc protected diamine(s) **1 – 3** with UA was undertaken with a view to generating compounds **7 – 9** (**Figure 32**).

The activation of the carboxylic acid group of folic acid (**2.2.2**) was successfully performed using coupling reagents DCC and NHS. The same method described in **Scheme 10** was tried for UA carboxylic acid activation, however, by-product DCU was not observed after 24 hours reaction. The activation *via* the DCC/NHS was tried again by increasing a reaction time of 48 hours under nitrogen. After which time, a DCU precipitate was observed and easily removed *via* filtration. However, all attempts to activate UA *via* the DCC/NHS method described in **Scheme 10** were unsuccessful,

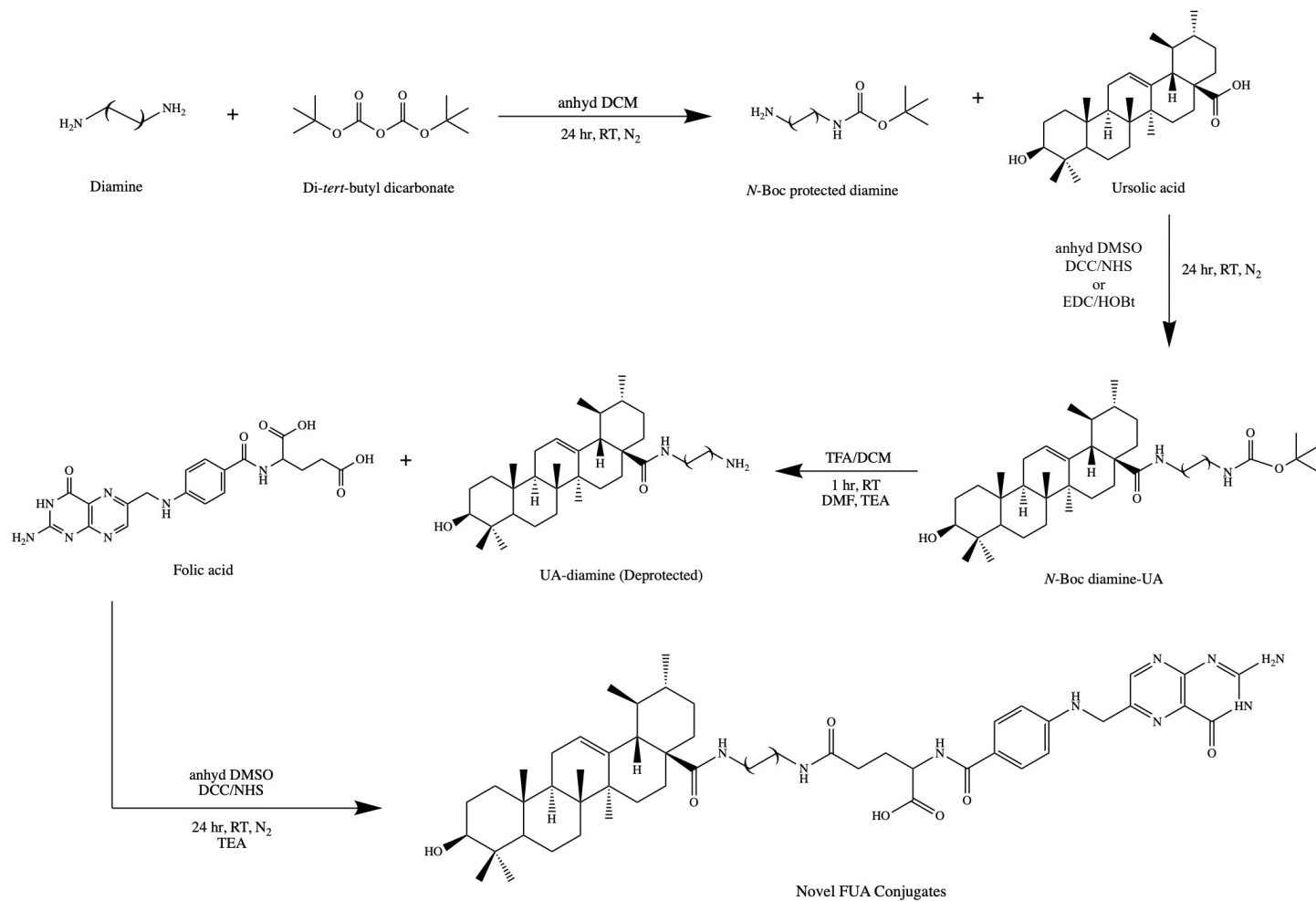
producing a similar IR spectrum to by-product DCU but strangely, the NMR spectra showed characteristic peaks of UA. This could be due to tiny amounts of UA present in the sample.

To try resolve this issue, NHS was replaced with a fast acting nucleophile hydroxybenzotriazole (HOBt). HOBt is known to reduce undesirable formation of the unreactive N-acylurea, by reacting faster than competing acyl transfers and generating an active intermediate capable of coupling with the amine (Valeur and Bradley, 2009; Montalbetti and Falque, 2005). The protocol was adjusted further by replacing the coupling agent DCC with 1-ethyl-3-(3-dimethylaminopropyl)carbodiimide (EDC) and ensuring its addition was performed at 0 °C. Attempts using this method were successful in producing the desired product, however, NMR spectra showed the presence of a lot of impurities, necessitating the employment of a different coupling strategy.

UA carboxylic acid activation using carbodiimide chemistry was not feasible. A review of the literature exposed a frequently encountered problem with steric hindrance at the carbon 28-COOH (Zacchigna *et al.*, 2014; Bekker *et al.*, 2013; Huang *et al.*, 2016). Further research led to the method described by Liu *et al.* in 2018 to overcome this inherent problem at the carbon 28 site. This approach uses *N*-guanidinium salt, 1-[Bis(dimethylamino)methylene]-1H-1,2,3-triazolo[4,5-b]pyridinium 3-oxide hexafluorophosphate (HATU), a reagent used in peptide coupling chemistry to generate an active ester from a carboxylic acid (**Scheme 11**). HATU has been proven to be very efficient in difficult sterically hindered couplings (Montalbetti and Falque, 2005). It is commonly used along with Hunig's base *N,N*-diisopropylethylamine (DIPEA) to deprotonate carboxylates and form unstable *O*-acyl(tetramethyl) (OAt) isouronium salts.

(Commonorganicchemistry, 2020). The OAt anion attacks the isorinium salt, affording the OAt-active ester and liberating tetramethylurea by-product which is miscible in water and many organic solvents (Albericio and El-Faham, 2018; Carpino *et al.*, 2000; Yang, 2016).

This method (**Scheme 5**) was chosen to explore the conjugation of *N*-Boc diamines **1 – 3** (**Figure 32**) with ursolic acid. DIPEA was added to UA in anhydrous DMF in an ice bath for ~10 min. HATU was then added followed by *N*-Boc diamines and stirred overnight under N₂. Liu's method on isolating the crude product was to extract with ethyl acetate, wash with sodium bicarbonate, 1N HCl and brine, dry with Na₂SO₄ and concentrate in *vacuo*. However, extracting with ethyl acetate did not work as DMF and ethyl acetate are miscible. UA is not water soluble, hence, crude product was isolated by precipitation with distilled water. The three products were isolated as colourless powders with better purity and higher yields than the carbodiimide chemistry reported – compound **7**: 1.23 g (98.79 %); compound **8**: 1.40 g (97.90 %); compound **9**: 1.20 g (87.59 %). It is worth noting that compound **8** containing ethereal oxygen linker, slightly improves water solubility of UA and challenges were faced in isolating the product, which could also resulted to slightly lower yield. It was successfully isolated using ice cold distilled water.



Scheme 10. A schematic of the initial approach to conjugating UA to FUA to generate novel FUA conjugates. This attempt uses carbodiimide chemistry with two most common coupling reagents – DCC/NHS and EDC/HOBt.

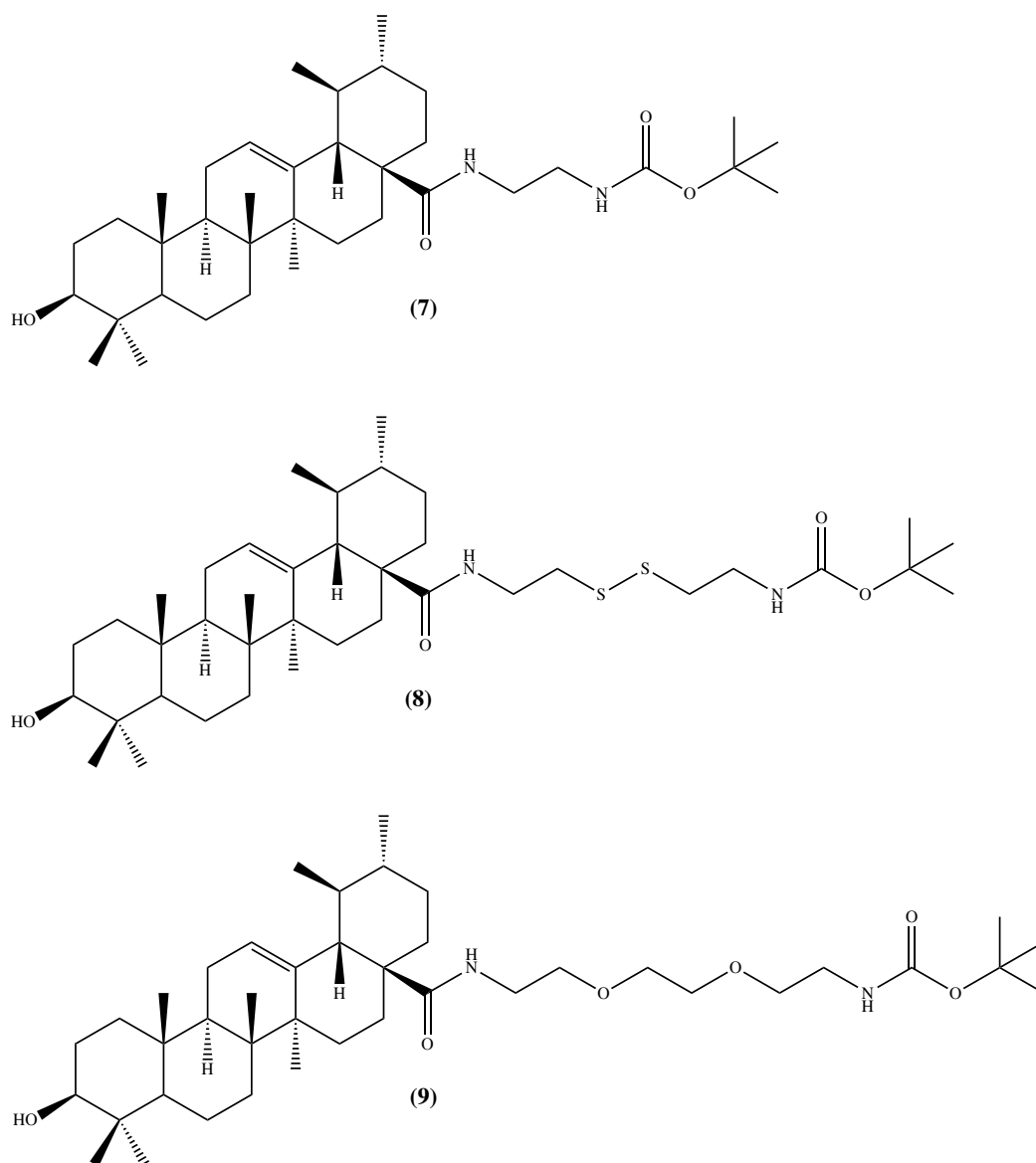
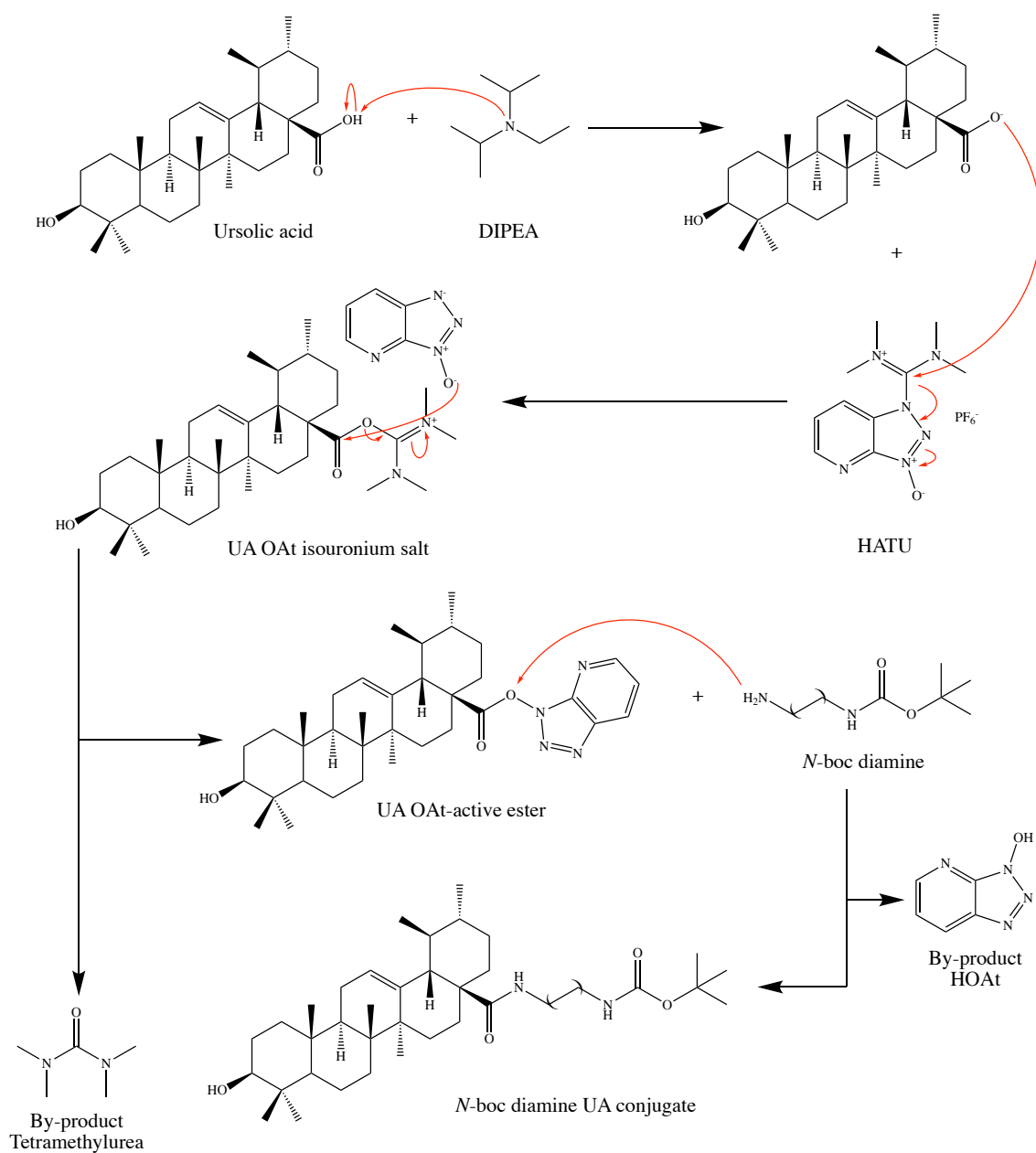


Figure 32. The proposed structures of *N*-Boc diamine-UA conjugates 7 – 9.



Scheme 11. The conjugation of N-Boc protected diamines to ursolic acid (Liu *et al.*, 2018).

The primary methods used to interpret the structure of UA-diamine conjugates **7 – 9** were NMR spectroscopy (^1H NMR and ^{13}C NMR) and mass spectroscopy.

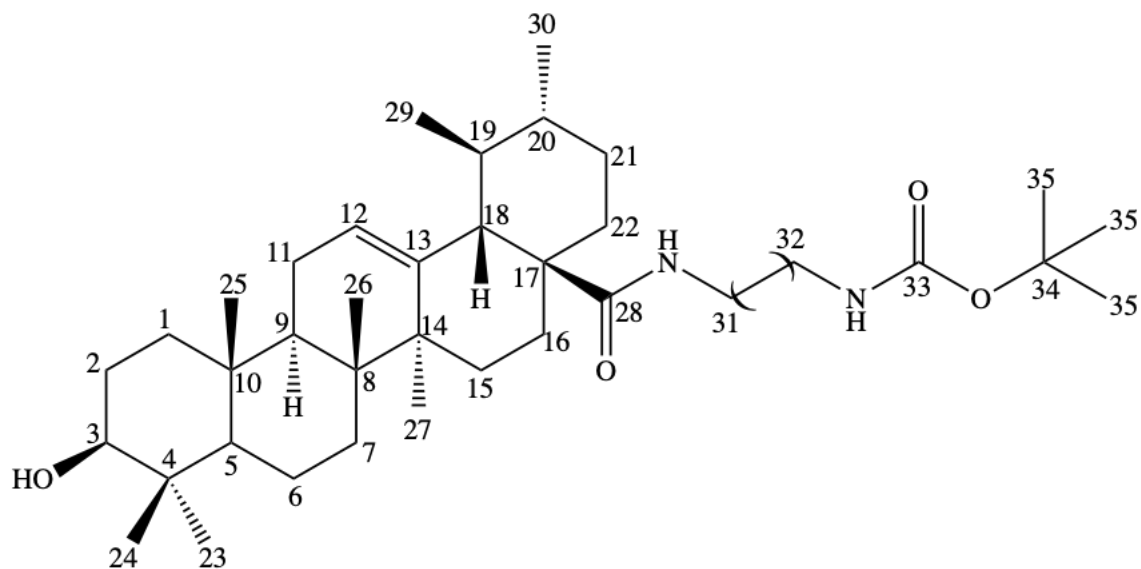


Figure 33. *N*-Boc diamine UA conjugates illustrating numbering scheme for ^1H NMR and ^{13}C NMR analysis.

In order to determine if conjugation was successful, ^1H NMR spectra were analysed to identify peaks associated with UA and the Boc protection group (**Table 10**). In the spectra (**A.11 – A.13**), the disappearance of the peak at ~ 12 ppm, carboxylic acid group (C28; **Figure 33**), and the appearance of NH groups of the diamine linkers (near C31 and C32; **Figure 33**) observed between 6.74 ppm – 7.35 ppm, are indicative of amide bond formation. The peak related to the olefinic H in C12 was observed at 5.20 ppm whilst the peak at 4.30 ppm was identified as the OH group in C3. Two aliphatic methylene groups of diamine linkers (C31 and C32) and structural aliphatic near OH (C3) appeared overlapping at 2.87 – 3.47 ppm. Peaks corresponding to the seven terminal CH_3 methyl groups (C23 – 27, C29 and C30) appeared overlapping at 0.66 – 0.97 ppm. The structural

aliphatic CH₂ groups (C1, C2, C6, C7, C11, C15, C16, C21 and C22) and CH groups (C5, C19 and C20) appeared overlapping at 1.02 – 2.76 ppm. Finally, the large peak at 1.40 ppm relates to the Boc protection group (C35).

Table 10. Key ¹HNMR resonances for *N*-Boc diamine-UA **7** – **9**. The integration and peak splitting are shown in brackets.

Position	Compounds		
	Chemical Shifts (ppm)		
	7	8	9
C3 - OH	4.30 (d, 1H)	4.29 (d, 1H)	4.30 (d, 1H)
Olefinic (C12)	5.21 (d, 1H)	5.19 (s, 1H)	5.20 (s, 1H)
Diamine NH (linker)	7.14 (s, 1H)	7.35 (t, 1H)	7.09 (t, 1H)
	6.74 (t, 1H)	6.99 (t, 1H)	6.75 (t, 1H)
Diamine CH ₂ (linker)	3.11 – 2.89 (m, 4H)	3.19 (d, 2H)	3.47 (d, 4H)
		2.95 (dd, 3H)	3.34 (s, 3H)
		2.75 – 2.69 (m, 4H)	3.21 – 2.95 (m, 6H)
Boc group	1.37 (s, 9H)	1.37 (s, 11H)	1.37 (s, 9H)

In the ¹³CNMR, the presence of the characteristic peaks of UA, linker(s) and boc group are evident (**Table 11**). The most downfield signal at ~176.40 ppm indicates the carbon at C28. The seven methyl groups (C23 – 27, C29 and C30; Figure 25) appeared between 15.23 ppm – 22.90 ppm. Peaks corresponding to the nine methylene moieties (C1, C2,

C6, C7, C11, C15, C16, C21 and C22) appeared between 23.34 ppm – 38.26 ppm, while the methine carbons (C5, C9, C18, C19 and C20) appeared between 38.26 ppm – 54.80 ppm. The quaternary carbons (C4, C8, C10, C14 and C17) showed between 36.51 ppm – 46.65 ppm. Two olefinic (C12 and C13) appeared at 124.75 ppm and 138.37 ppm, respectively and the oxygenated aliphatic (C3) appeared at 76.84 ppm. The peak related to diamine linker was observed between 37.00 ppm – 69.59 ppm. Lastly the boc protection group C33 appeared at ~155.58 ppm while C34 showed at ~77.78 and the peak at ~28.24 ppm represents C35.

Table 11. Key ^{13}C NMR resonances for *N*-Boc diamine-UA 7 – 9.

Position	Compounds		
	Chemical Shifts (ppm)		
	7	8	9
C28 – C=O	176.49	176.41	176.39
C3 - OH	76.85	76.84	76.84
Olefinic (C12, C13)	138.39, 124.70	138.25, 124.75	138.37, 124.75
CH ₂ groups (linker)	40.19, 38.26	39.19, 38.76, 37.44, 37.19	69.59, 69.20, 68.93, 41.62, 38.84, 37.00
Boc group	155.83, 77.74, 28.26	155.50, 77.78, 28.24	155.58, 77.59, 28.23

Mass spectra were also recorded for compound **7 – 9** in addition to NMR spectroscopy. Results were as expected and complement structural data determined through NMR analysis (**Table 12**).

Table 12. Mass spectroscopy result of *N*-Boc diamine UA **7 – 9**.

Compounds	Chemical Formula	[M+H]⁺ Calculated	[M+H]⁺ Found
7	C ₃₇ H ₆₂ N ₂ NaO ₄	621.4602	621.4595
8	C ₃₉ H ₆₆ N ₂ NaO ₄ S ₂	713.4356	713.4359
9	C ₄₁ H ₇₀ N ₂ NaO ₆	709.5126	709.5135

2.3.2 The Deprotection of *N*-Boc Diamine UA conjugates (Step 3b)

The deprotection of *N*-Boc diamine-UA conjugates was adapted from Trindade *et al.*, 2014 and Liu *et al.*, 2018. This involved the deprotonation of the Boc group with trifluoroacetic acid (TFA), resulting in the loss of the *tert*-butyl cation (this will either be deprotonated to form isobutylene gas, or it will polymerize to form isobutylene oligomers). The remaining carbamic acid is quickly decarboxylated to produce a free amine. In the presence of excess TFA, the product may be present as a TFA salt which can be neutralised with a base such as triethylamine to give the free amine as a stable product (**Scheme 12**; Commonorganicchemistry, 2020).

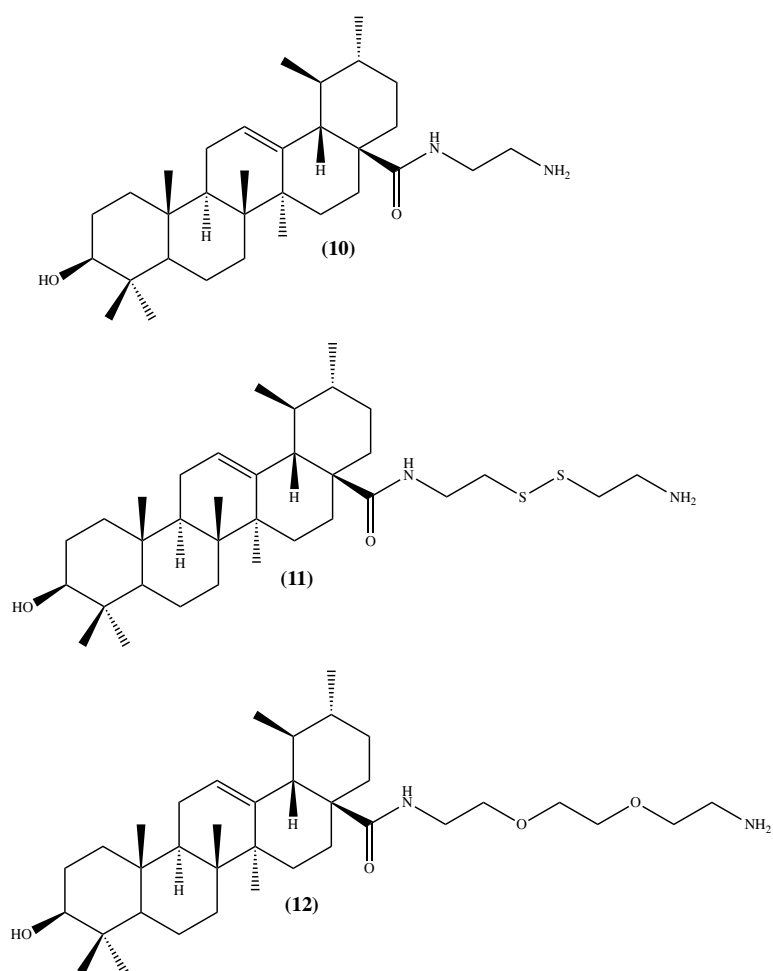
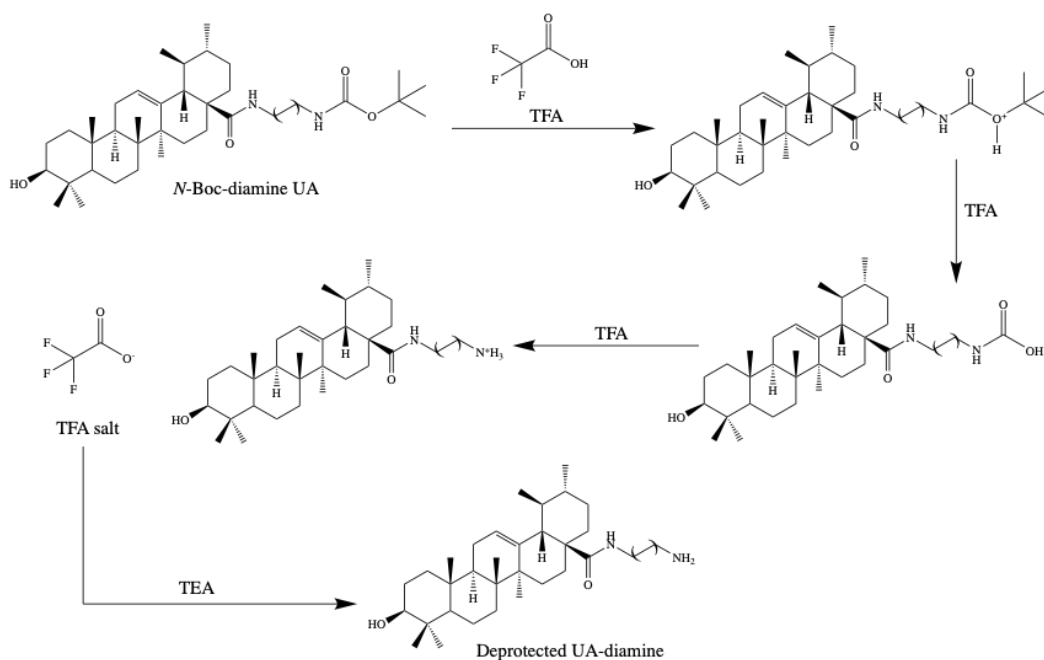


Figure 34. The proposed structures of deprotected *N*-Boc diamine-UA conjugates **10** – **12**.



Scheme 12. The Boc deprotection of UA-diamine.

The three *N*-Boc-Diamine-UA conjugates (**7 - 9**) have been deprotected to produce compounds **10**, **11** and **12** as colourless powders with yields 0.45 g (89.29%), 0.48 g (81.56%) and 0.38 g (64.41%), respectively (**Figure 34**). Similar to compound **8**, difficulty in isolating compound **11** was faced. It was successfully isolated using ice cold distilled water.

Analysis of ^1H NMR (**A.14 – A.16**; **Table 13**) indicates the successful cleavage of the *N*-Boc protection group which is normally present as a singlet at 1.40 ppm. The secondary amide NH of the diamine linkers (near C31 and C32; **Figure 35**) was observed between 7.11 ppm – 7.37 ppm and the amine NH_2 appeared overlapping with structural aliphatic CH_2 and CH groups at \sim 1.60 ppm. The peak related to the olefinic H in C12 was observed at 5.20 ppm whilst the peak at 4.30 ppm was identified as the OH group in C3. Two aliphatic methylene groups of diamine linkers (C31 and C32) and structural aliphatic near OH (C3) appeared overlapping at 2.66 – 3.04 ppm. Peaks corresponding to the seven

terminal CH₃ methyl groups (C23 – 27, C29 and C30) appeared overlapping at 0.68 – 0.97 ppm. The structural aliphatic CH₂ groups (C1, C2, C6, C7, C11, C15, C16, C21 and C22) and CH groups (C5, C19 and C20) appeared overlapping at 1.03 – 1.64 ppm.

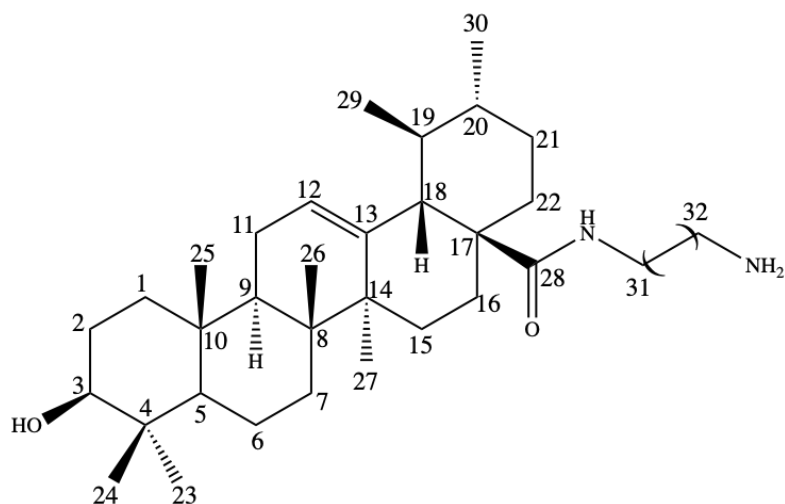


Figure 35. The deprotected *N*-Boc diamine UA conjugates illustrating numbering scheme for ¹HNMR analysis.

Table 13. Key ¹HNMR resonances for deprotected *N*-Boc diamine-UA **10** – **12**. The integration and peak splitting are shown in brackets.

Position	Compounds		
	Chemical Shifts (ppm)		
	10	11	12
C3 - OH	4.31 (s, 1H)	4.30 (d, <i>J</i> = 4.9 Hz, 1H)	4.31 (s, 1H)
Olefinic (C12)	5.20 (s, 1H)	5.19 (t, <i>J</i> = 3.1 Hz, 1H)	5.20 (s, 1H)
Diamine NH	7.12 (t, <i>J</i> = 5.5 Hz, 1H)	7.37 (t, <i>J</i> = 5.5 Hz, 1H)	7.11 (t, <i>J</i> = 5.1 Hz, 1H)
Diamine CH ₂	3.04 – 2.84 (m, 4H)	2.86 – 2.66 (m, 8H)	3.23 – 3.05 (m, 4H) 3.04 – 2.65 (m, 8H)

Mass spectroscopy was also recorded for compound **10** – **12** in addition to NMR spectroscopy. Results were as expected and complement structural data determined through NMR analysis (**Table 14**).

Table 14. Mass spectroscopy result of deprotected *N*-Boc diamine UA **10** – **12**.

Compounds	Chemical Formula	[M+H] ⁺ Calculated	[M+H] ⁺ Found
10	C ₃₂ H ₅₅ N ₂ O ₂	499.4258	499.4258
11	C ₃₄ H ₅₉ N ₂ O ₂ S ₂	591.4012	591.4015
12	C ₃₆ H ₆₃ N ₂ O ₄	587.4782	587.4789

2.3.3 The conjugation of Ursolic Acid diamine with Folic Acid (Step3c)

Folate was conjugated to the three UA-diamines using carbodiimide chemistry (coupling reagents DCC/NHS). It was tried and proven that FA γ conjugates are inherently obtained as the major product using carbodiimide chemistry and thus this approach was adopted for this conjugation. The approach for the UA-diamine-FA conjugation used is based on the method described by Trindade *et al.*, 2014 (**Scheme 5**). This involves the generation of an activated-folate ester *via* NHS and the coupling agent DCC. The newly formed activated ester cleanly reacts with amines under mild conditions allowing for simple amide formation. The by-product of the DCC mediated coupling, DCU is highly insoluble in all organic solvents, allowing for easy removal *via* filtration. Results obtained has enough yield for subsequent reactions/tests – compound **13**: 0.12 g (64.10 %); compound **14**: 0.24 g (80 %); compound **15**: 0.20 g (66.6 %).

The primary methods used to interpret the structure of UA-diamine-FA conjugates **13** - **15** were NMR spectroscopy (^1H NMR and ^{13}C NMR) and mass spectroscopy.

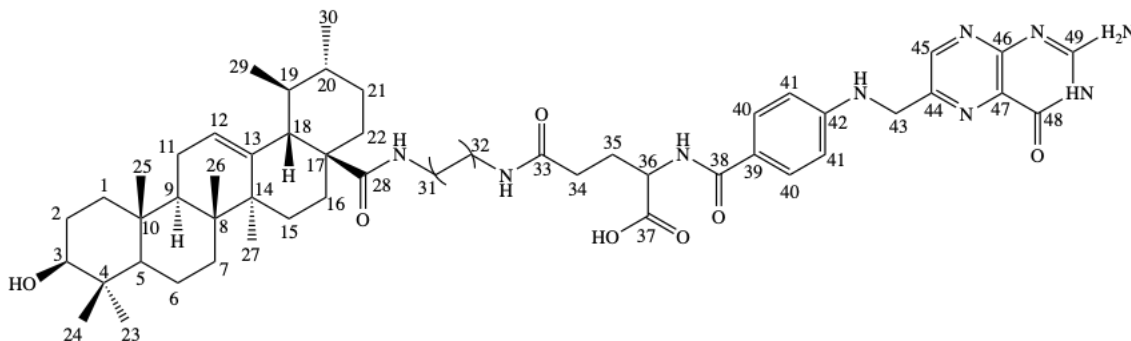


Figure 36. General structure of the FUA conjugates **13** - **15** illustrating numbering scheme for ^1H NMR analysis.

In order to determine if conjugation was successful, ^1H NMR and ^{13}C NMR (**Figure 36** and **A.17** – **A.19**) spectra of compounds **13** – **15** were analysed to identify peaks associated with FA as well as the characteristic peaks associated with UA-diamine moiety. In the ^1H NMR spectra, the downfield region are the characteristic peaks of FA, whereas the upfield region corresponds to characteristic peaks of UA. The α carboxylic acid group appeared at ~ 11 ppm, indicating conjugation to only one carboxylic acid group of FA. Peaks corresponding to aromatic CH groups (C45, C40 and C41) appeared overlapping at around 6.62 – 8.04 ppm and NH groups (C48, C42-43 and C36-38) overlapped at 7.16 – 8.63 ppm. The peaks corresponding to the hydrogen bound to a carbonyl carbon (C36) was observed at 4.47 ppm, while its neighbouring peak at 4.28 ppm was identified as a CH_2 (C43). Two aliphatic methylene groups (C34 and C35) appeared at around 1.83 – 2.01 ppm while the NH_2 group (C49) appeared at ~ 6.95 ppm. The peaks related to the methylene groups of the linker (C31 and C32) were observed

overlapping at around 2.60 – 3.02 ppm and NH groups (C31 and C32) overlapped at 6.93 – 7.67 ppm.

The peak related to the olefinic H in C12 was observed at 5.18 ppm whilst the peak at 4.47 ppm was identified as the OH group in C3. The structural aliphatic near OH (C3) appeared at around 3 ppm. Peaks corresponding to the seven terminal CH₃ methyl groups (C23 – 27, C29 and C30), structural aliphatic CH₂ groups (C1, C2, C6, C7, C11, C15, C16, C21 and C22) and CH groups (C5, C19 and C20) appeared overlapping at the most upfield region 0.66 – 1.73 ppm.

Mass spectroscopy was also recorded for compound **13** - **15** in addition to NMR spectroscopy. Results were as expected and complement structural data determined through NMR analysis (**Table 15**).

Table 15. Mass spectroscopy result of FUA compound **13** – **15**.

Compounds	Chemical Formula	[M+H] ⁺ Calculated	[M+H] ⁺ Found
13	C ₅₁ H ₇₀ N ₉ O ₇	920.5404	920.5381
14	C ₅₃ H ₇₅ N ₉ NaO ₇ S ₂	1014.5304	1014.5276
15	C ₅₅ H ₇₉ N ₉ NaO ₉	1032.5893	1032.5913

2.4 Summary

UA Hunan (purchased from Hunan Dalore Ltd., Hunan, China) was compared to a reference, UA Sigma (purchased from Sigma-Aldrich, Arklow, Ireland), to confirm its chemical and biological properties. Results obtained indicate that both were chemically and biologically similar.

The pure *N*-Boc protected diamines (compounds **1 – 3**) were successfully obtained in good yield, and characterised using NMR (¹HNMR and ¹³CNMR) and mass spectroscopy. All attempts to conjugate deprotected *N*-Boc ethylenediamine folate (compound **4**) to UA using carbodiimide chemistry (DCC/NHS and EDC/HOBt) were unsuccessful, yielding only the un-characterised compound **6**. This is believed to be due to the activation difficulties associated with the sterically hindered carboxylic acid functional group (COOH; C-28) of UA. Hence, this approach to generating the FUA's was abandoned and an alternative approach was undertaken, i.e. the reverse reaction, involving the coupling UA to the diamine linkers and then to the folate.

Using a modified method from the literature UA was successfully conjugated to the *N*-Boc diamines to form the *N*-Boc diamine-UA compounds **7 – 9** using HATU and DIPEA with superior yield (> 87 %) and purity. Compounds **7 – 9** were easily deprotected producing the UA-diamines compounds **10 – 12** in high yield (> 60 %) and purity.

Finally, folic acid was successfully conjugated to the UA-diamine (compounds **10 – 12**) producing the FUA compounds **13 – 15** in good yields (64.10 %, 80 % and 66.6 %, respectively).

CHAPTER 3

RESULTS & DISCUSSION 2

“The SAR and Biological Assessment of Novel FUA Derivatives.”

3.0 The Activity of Novel FUA Derivatives

Research Questions:

- Can the folate receptor be targeted to enhance the chemotherapeutic potential of UA *via* improvement in bioavailability, selectivity and bioactivity against high expressing folate receptor cancer cells, without interfering with the cytotoxic activities of UA?
- Could we develop a computational docking model for UA and novel FUA derivatives and investigate possible molecular interactions with FOLR1 and VRK1 proteins?

Aims and Objectives:

- To assess and quantify the FR-targeting capabilities and biological profiles of the FUA's against relevant FR+ve and FR-ve cancer cell lines.
- To explore the structure activity relationship (SAR) of UA *vs* novel FUA derivatives that were designed to improve its activity and bioavailability (predicted ADMET profile), and utilise molecular docking studies against proposed targets – FOLR1 and/or VRK1, with an in-depth analysis of predicted interactions.

This study was focused on the computational, pharmacodynamics and experimental evaluation of the fully synthesised and characterised novel FUA derivatives (**13 – 15**).

3.1 The *in silico* studies of Novel FUA Derivatives

The *in silico* ADME (absorption, distribution, metabolism, and excretion)-related physicochemical properties of novel FUA derivatives in comparison to UA, were predicted by the Swiss ADME online web server (www.swissadme.ch/). Lipinski *et al* (1997) proposed the “Rule-of-Five”, which is used to examine a compound’s oral bioavailability. This includes: molecular weight (MW) ≤ 500 Da, hydrophobic/hydrophilic partition coefficient $\text{Log } P_{o/w} \leq 5$ (SwissADME uses $\text{MLOGP} \leq 4.15$), number of hydrogen bond donors (HBDs) ≤ 5 , and number of hydrogen bond acceptors (HBAs) ≤ 10 . Under the rule-of-five, a violation of two or more rules depicts a molecule as not orally bioavailable. The drug-likeness analysis of UA and novel FUA derivatives are listed in **Table 16**.

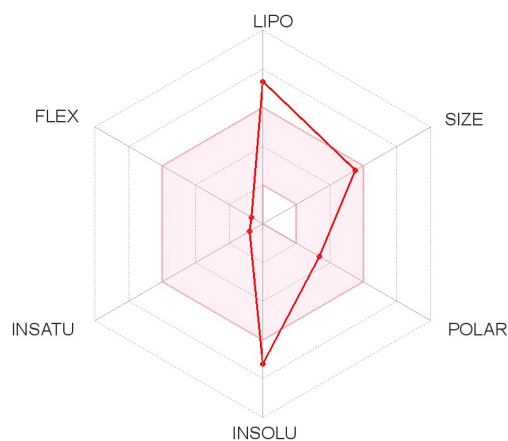
Table 16. Predicted physicochemical and pharmacokinetic properties, and drug-likeness accepted values of novel FUA derivatives (**13 – 15**). Colours are represented as: within the predicted range (green), slightly above the predicted range (orange), and out of predicted range (red). *MW in Da

Molecule	Physicochemical Properties						Lipophilicity			Solubility Log S (ESOL)	Pharmacokinetics			Bioavailability Score	Synthetic Accessibility
	MW	HBD	HBA	No. of rotatable bonds	Fraction Csp3	TPSA	XLOGP3	MLOGP	Consensus Log P		GI absorption	BBB permeant	P-gp Substrate		
UA	456.7	2	3	1	0.9	57.53	7.34	5.82	5.93	-7.23	Low	No	No	0.85	6.21
Comp 13	922.17	8	10	16	0.65	254.41	5.54	2.91	4.72	-8.17	Low	No	Yes	0.11	8.42
Comp 14	1014.35	8	10	20	0.66	305.01	6.23	3.22	5.62	-8.9	Low	No	Yes	0.11	8.92
Comp 15	1010.27	8	12	22	0.67	272.87	5.25	2.07	4.91	-8.12	Low	No	Yes	0.11	9.12

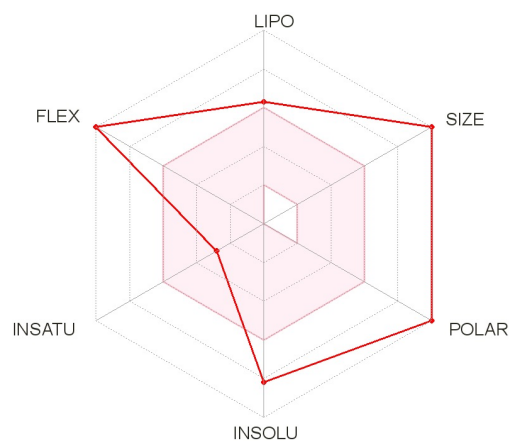
3.1.1 SwissADME Bioavailability Radar

One of the features of SwissADME is the ‘bioavailability radar’ that provides a drug-likeness plot which encloses a coloured zone, representing the ideal physicochemical properties and graphically indicates which properties fall outside this zone (Daina *et al.*, 2017; Bojarska *et al.*, 2020). It is presented in the form of a hexagon with each of the vertices following six properties: lipophilicity (XLOGP between -0.7 to +0.5), size (MW between 150 and 500 g/mol), polarity (TPSA between 20 and 140 Å²), solubility (log *S* not higher than 6), saturation (fraction of carbons in sp³ hybridization not less than 0.25), and flexibility (no more than 9 rotatable bonds) (Daina *et al.*, 2017; Nojarska *et al.*, 2020).

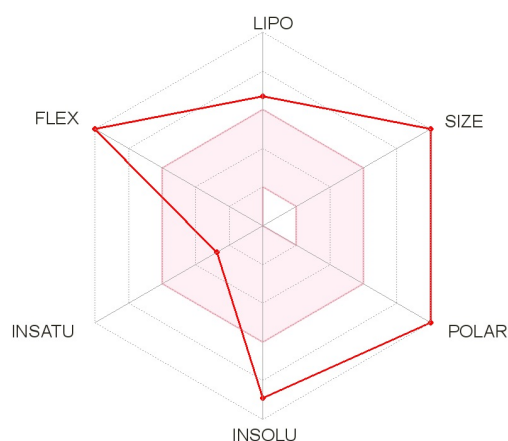
The ‘bioavailability radars’ of the UA and novel FUA derivatives (**13** – **15**) can be analysed intuitively (**Figure 37**). Drug-likeness of properties are represented by the red distorted hexagon within the pink-shaded region. It was found that UA is slightly outside the pink area on the solubility (-7.23) and lipophilicity side. This is in agreement with what was published in the literature (Khwaza, Oyedeji and Aderibigbe, 2020; Shao *et al.*, 2020) as UA is highly lipophilic in nature and it has low aqueous solubility (<5.64 µg/mL) (Lin *et al.*, 2012). However, all three novel FUA derivatives are off-target in almost all the properties except insaturation. It is noteworthy that lipophilicity (XLOGP3) of novel FUA derivatives (**13** – **15**) improved slightly in comparison to UA. The results obtained for MLOGP and consensus Log P (**Table 16**) confirms the result in the bioavailability radar (**Figure 37**).



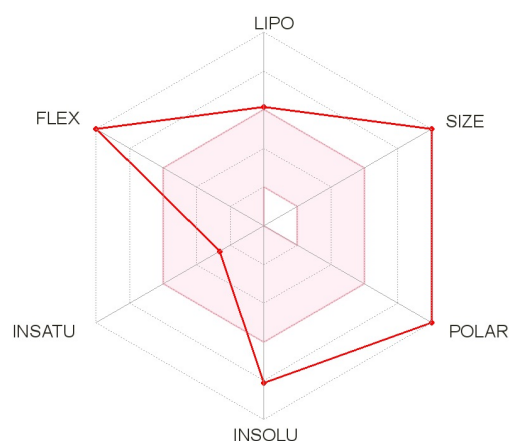
Ursolic Acid



Compound 13



Compound 14



Compound 15

Figure 37. The bioavailability radar (pink area exhibits optimal range of particular property) of UA and novel FUA derivatives (**13 – 15**) evaluated using SwissADME. Lipophilicity (LIPO): XLOGP3 between -0.7 and +5.0; molecular weight (SIZE): MW between 150 and 500 g/mol; polarity (POLAR) TPSA between 20 Å² and 130 Å²; Solubility (INSOLU): log *S* not higher than 6; Saturation (INSATU): fraction of carbons in sp³ hybridization between 0.25 and 1; and flexibility (FLEX): no more than 9 rotatable bonds.

3.1.2 Physicochemical Properties of Novel FUA Derivatives

Low molecular weight compounds can pass through the cell membrane more easily, and thus are favoured for oral absorption (Lipinski, 2004). Whereas compounds with MW > 500 g/mol are not absorbed *via* passive diffusion (Ibrahim *et al.*, 2021). From the results obtained, all three novel FUA derivatives (**13 – 15**) were found to have MW > 500 g/mol.

The lipophilicity is the hydrophobic/hydrophilic solvent partition coefficients of a particular molecule in two immiscible solvents (Lipinski *et al.*, 2001). Lipophilicity plays a critical role in absorption, as well as facilitating drug interactions with their biological targets. This is due to its hydrophilic and lipophilic qualities, n-octanol was thought to mimic features of phospholipid membrane (Gleeson *et al.*, 2011; Liu *et al.*, 2011). SwissADME gives five predicted lipophilicity models: XLOGP3, WLOGP, MLOGP, SILICOS-IT and iLOGP; with consensus Log P_{o/w} as the arithmetic mean of the values predicted by the five proposed methods (Daina *et al.*, 2017). In this study, we used XLOGP3 which is the predicted value in the ‘bioavailability radar’, the MLOGP which was used in Lipinski’s rule-of-five, and the consensus Log P which is the average of all predicted lipophilicity. Lipinski’s rule-of-five recommended that Log P_{o/w} should be ≤ 5 (MLOGP ≤ 4.15 as per SwissADME). Three novel FUA derivatives (**13 – 15**) predicted for MLOGP have value of ≤ 4.15 and consensus Log P value of < 5, except compound **14**, which had a Log P value of 5.62. On the other hand, UA was predicted to have >5 lipophilicity value. Hence, the novel FUA derivatives have predicted improved oral absorption qualities.

The water solubility for this study was predicted by ESOL – estimating aqueous solubility directly from molecular structure, followed by MW. The log *S* scale value ranges between -10 (insoluble), -6 (poorly soluble), -4 (soluble), -2 (very soluble) and 0 (highly soluble) (Delaney, 2004). All novel FUA derivatives were predicted to be less soluble than UA.

3.1.3 BBB penetration, Bioavailability and Synthetic Accessibility of Novel FUA Derivatives

The Abbott bioavailability (F) score is a prediction of a compound to have at least 10% oral bioavailability in rat or measurable Caco-2 permeability (Martin, 2005). To have a good biological activity, a drug should have sufficient lipophilic characteristic for it to cross the cell membrane. This semi-quantitative rule-based score does not just depend on the total charge, TPSA, nor violation of Lipinski's rule. Instead, bioavailability of compounds depends on their predominant charge at biological pH. The bioavailability is 85% if TPSA is $\leq 75 \text{ \AA}^2$; 56% if TPSA is between 75 and 150 \AA^2 , 11% if TPSA is $\geq 150 \text{ \AA}^2$. On the other hand, bioavailability is 55% if the neutral, zwitterionic, or cationic compounds passes the rule-of-five, and 17% if it fails (Martin, 2005; Suhud *et al.*, 2019). UA was found to have a bioavailability score of 0.85, which means it has 85% probability of rat bioavailability. Results obtained for all novel FUA derivatives were 0.11 (11%) as predicted TPSA obtained were all $\geq 150 \text{ \AA}^2$.

The topological polar surface area (TPSA) of a molecule is the sum of all polar atoms (oxygen, nitrogen, and their connected hydrogen) on the molecule's surface, calculated by adding all polar fragments (Ertl *et al.*, 2000). The goal of the TPSA is to predict drug

transport qualities such as intestinal absorption and BBB penetration (Li *et al.*, 2005). For virtual screening and ADME property prediction, TPSA has gained prominence in medicinal chemistry (Maximo da Silva *et al.*, 2015). When the quantitative value of TPSA is $< 140 \text{ \AA}^2$, it becomes a good predictor of intestinal absorption, and when it is $< 60 \text{ \AA}^2$, it indicates good BBB penetration (Maximo da Silva *et al.*, 2015). All novel FUA derivatives had TPSA values of $> 140 \text{ \AA}^2$ indicating that it does not have good intestinal absorption.

In contrast to other ADMET predictions, the BBB permeation predicted by SwissADME (BOILED-Egg model) shows that UA does not penetrate the BBB. In addition, the folic acid conjugation to ursolic acid was aimed for folate receptor mediated endocytosis, and FR α is overexpressed on a vast majority of cancer cells including brain cancer (Elnakat and Ratnam, 2006; Liu *et al.*, 2017; Elechalawar *et al.*, 2019). Which was aimed to improve novel FUA derivatives' BBB penetration. It is worth noting that SwissADME is a prediction tool and hence, further experimental investigation is needed.

P-glycoprotein (P-gp) is an active efflux transporter that expels substances out of the cells and has an important impact on the pharmacokinetic and pharmacodynamic properties of drugs. It affects the absorption, distribution, and elimination of a variety of substances (Elmeliegy *et al.*, 2020). P-gP can bind to a wide variety of substrates, which are widely distributed throughout the body. P-gp transporters are located in the small intestine, BBB capillaries, and several critical organs such as kidney and liver. Substances can enter the cell *via* active transport or passive diffusion, and they can be effluxed with the help of P-gp (Ibrahim *et al.*, 2021). Moreover, P-gp is overexpressed in some types of cancer and as a result the protein is responsible for expelling drug from the cells, and

hence, for drug resistance (Vilar *et al.*, 2019). All three novel FUA derivatives were found to be P-gp substrates, which indicates potential problems of excretion and drug resistance.

Lastly, synthetic accessibility score was predicted which ranges from 1 (very easy) to 10 (very difficult) based on 1024 fragmental contributions (FP2) modulated by size and complexity penalties trained on 12'782'590 molecules and tested on 40 external molecules ($r^2 = 0.94$) (Daina *et al.*, 2017). All three novel FUA derivatives were found to be > 8 which was higher than UA (6.21).

The *in silico* pharmacokinetic studies of novel FUA derivatives (**13 – 15**) predicted values obtained violated 3 of the Lipinski's rule-of-five. It also did not improve most of the predicted ADME-related physicochemical properties of UA, but slightly improved its lipophilicity. In addition, it was predicted to be P-gp substrates, and was predicted to have lower BBB penetration, bioavailability and synthetic accessibility than UA. Nevertheless, there are FDA approved drugs that has violated more than one of Lipinski's rule-of-five (beyond rule of five) (Doak and Kihlberg, 2017; DeGoey *et al.*, 2018; Poongavanam, Doak and Kihlberg, 2018). There are approximately 30% of approved kinase inhibitors that are beyond the rule-of-five compounds (Wu, Nielsen and Clausen, 2016; Durán-Iturbide, Díaz-Eufracio and Medina-Franco, 2020). Additionally, larger molecules offers increased selectivity due to large binding sites of proteins (Pathania and Singh, 2020). Although the *in silico* studies performed did not improve physicochemical properties of UA, it is worth investigating its molecular binding to target proteins and further determine its *in vitro* activity.

3.2 The Pharmacodynamic Studies of Novel FUA Derivatives

In this study, the synthesised three novel folate-ursolic acid (FUA) derivatives (**Figure 23**) were docked and analysed for interactions with potential protein targets - folate receptor alpha (FR α) and Vaccinia-related kinase 1 (VRK1). The three derivatives consist of three different types of linkers: (1) ethylenediamine linker (**13**); (2) disulphide bond linker (**14**); and (3) ethereal oxygen linker (**15**). The FR α structure (PDB ID: 4LRH) was used to compare the predicted binding affinity of folate and novel FUA derivatives. While the VRK1 (PDB ID: 6BU6) was used to compare the predicted binding affinity of UA and novel FUA derivatives.

3.2.1 The Molecular Docking of Novel FUA Derivatives to Folate Receptor

In 2013, Chen *et al*, successfully elucidated the crystal structure of human FR α in complex with folic acid at 2.80 Å resolution; composed of 8 chains (A-H), each 218 residues in length (**Figure 38**). They reported that FR α has an overall globular structure comprising of four long α -helices (α 1, α 2, α 3, α 6), two short α -helices (α 4, α 5), and four short β -strands (β 1- β 4) as shown in **Figure 38**. It was reported that the folate pteroate ring binds deep within the receptor pocket, leaving the glutamate moiety exposed outside the pocket entrance, allowing it to be conjugated to drugs without unfavourably affecting FR α binding (Chen *et al.*, 2013).

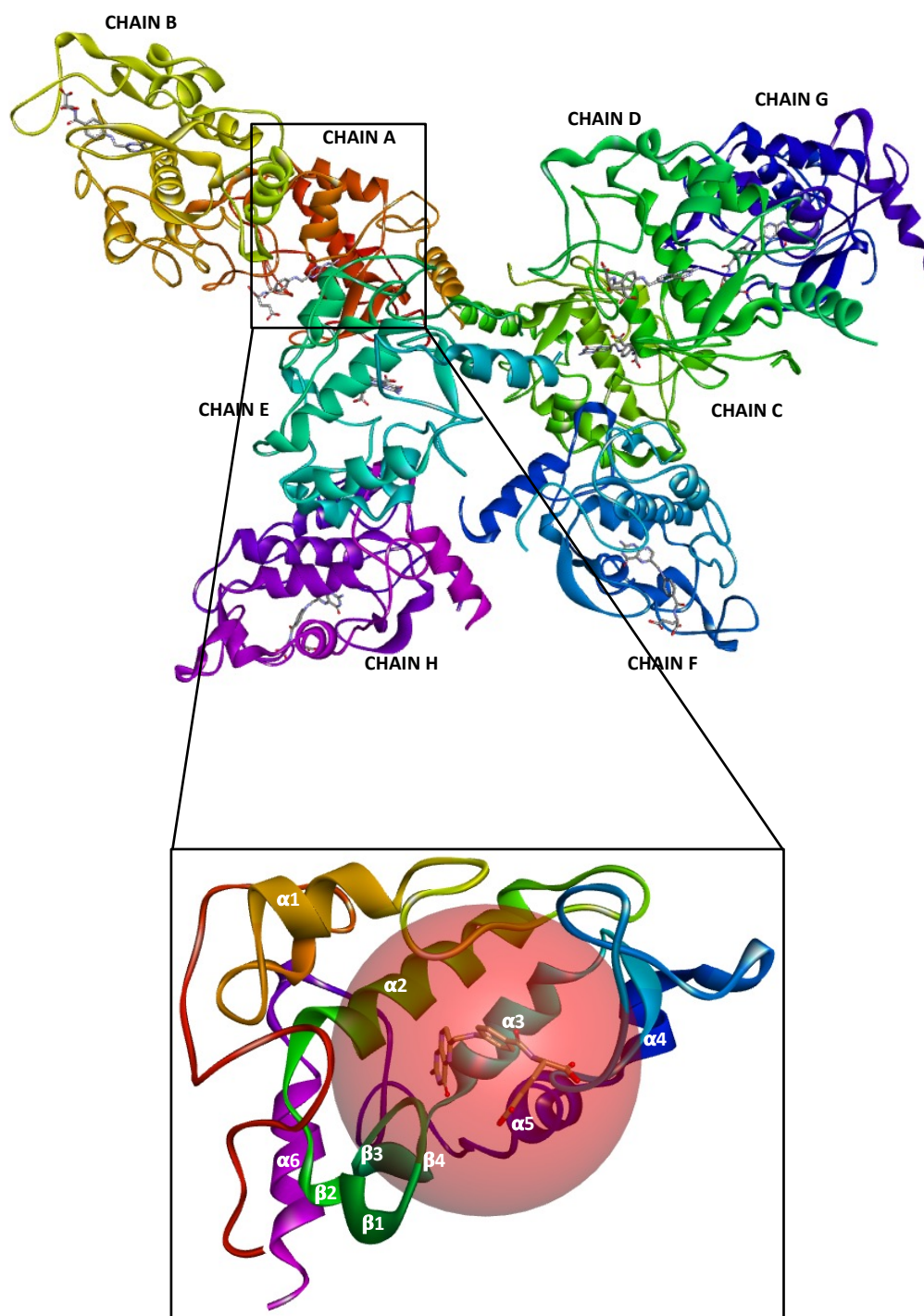


Figure 38. The 3D crystal structure of the FR α -folic acid complex (PDB code: 4LRH), denoting the chains (A-H) that were recrystallised by Chen *et al.* (2013). Chain A is zoomed in showing the co-crystallised ligand and the sphere indicating the binding pocket. Image generated in BIOVIA DS Client Visualizer 2020 and PyMOL™ v2.4.1.

3.2.1.1 Visualization and Interaction Analysis

A validation of the implemented docking protocols was conducted by examining the re-docking of the co-crystallised ligand and comparing the docked and original crystal structure poses. The re-docking of folic acid to FR α (4LRH) (**Figure 39**) (compound structure obtained from PubChem) was performed using AutoDock Vina and visualised using PyMOL v2.4.1 and Discovery Studio 2020. The deviation expressed as the root mean square deviation (RMSD) produced a value of 0.860 Å for FR α . This, low deviation and the overlay performed as seen in **Figure 39** validates the protocols employed in the docking and can be deployed in docking the designed derivatives.

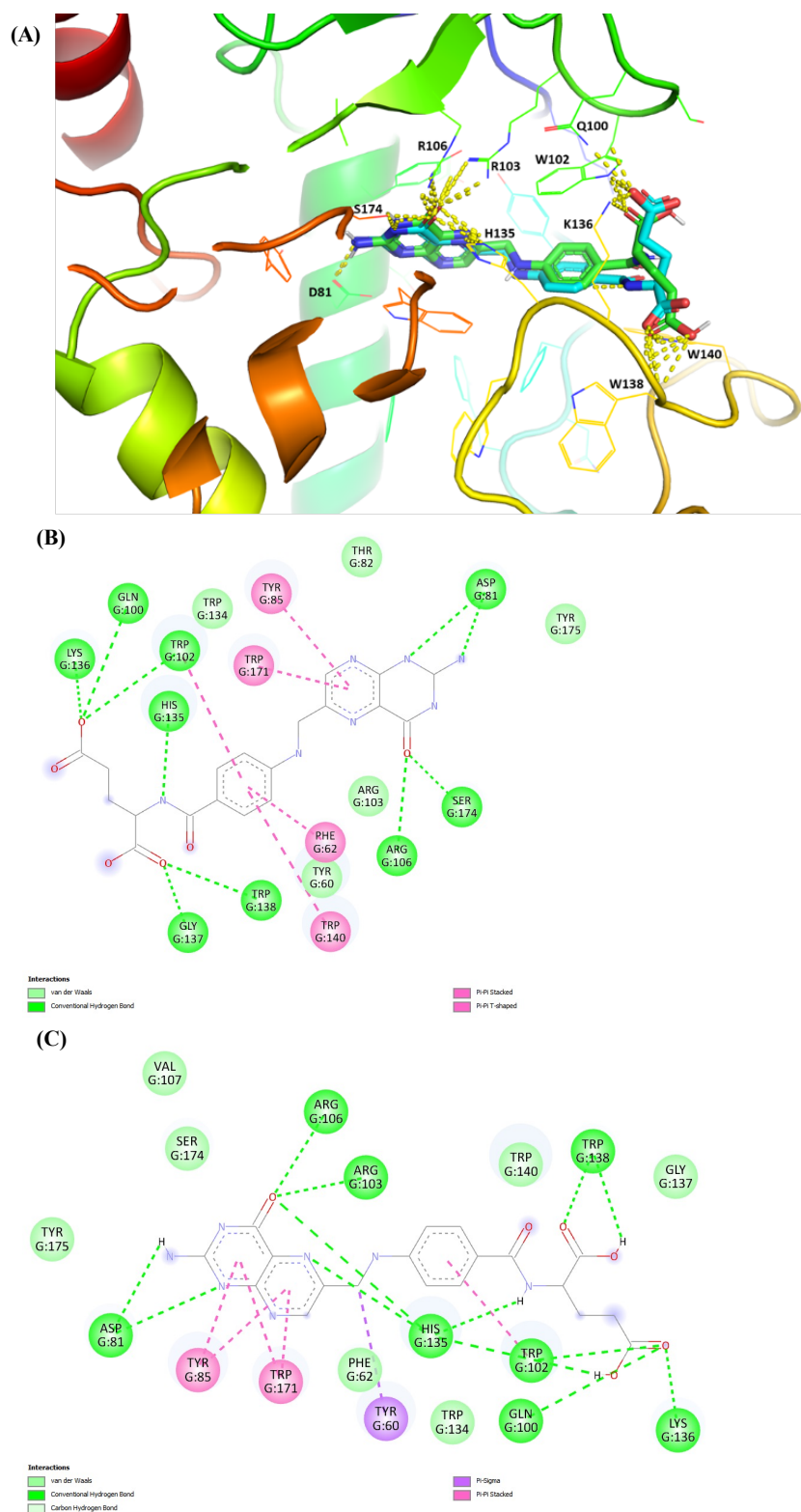


Figure 39. (A) The superimposed 3D images of folic acid - 4LRH (cyan) and docked folic acid ligand (green) showing residues essential for ligand binding. The 2D diagram of (B) folic acid – 4LRH, and (C) docked to folic acid FR α (PDB ID: 4LRH). The 3D image was visualised and rendered in PyMOL™ v2.4.1. The 2D interaction map was generated in BIOVIA DS Client visualizer 2020.

Results for folic acid bound to FR α produced 9 docking poses, with predicted binding affinity values between -11.2 to -9.4 kcal/mol, and with different orientations and configurations of the folic acid. To select a functionally relevant docking conformation, pose 1 was chosen with a binding affinity of -11.2 kcal/mol. The generated result showed that folic acid is oriented with the pteridine ring buried inside the negatively charged pocket, whereas the two negatively charged carboxyl groups of the glutamate are exposed at the positively charged entrance of the ligand-binding pocket (**Figure 40**). The interactions around the pterate (pteridine ring and PABA) moiety contain both conventional hydrogen bonds and hydrophobic interactions.

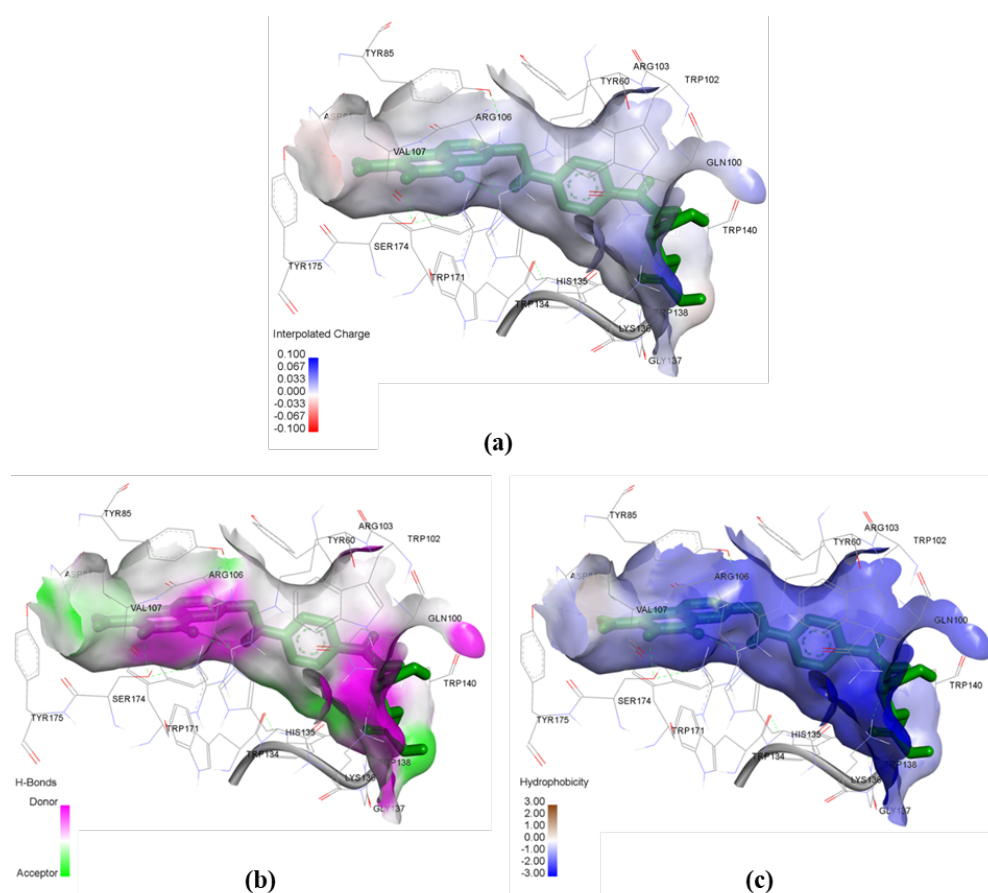


Figure 40. The folic acid docked to FR α surface showing (a) charge distribution surface (b) hydrogen bond donor/acceptor and (c) hydrophobicity (images generated are our own results analysed using BIOVIA DS Client Visualizer 2020).

In this study (**Figure 39**), we found D81 of FR α having a strong hydrogen bond with NH and an unfavourable acceptor-acceptor with N in the pteridine ring; also the R103, R106 and H135 form a hydrogen bond with the carbonyl group. A pi-pi stacking interaction was also observed in the pteridine ring between Y85 and W171, capped by Y175. The PABA ring is stabilized by the hydrophobic interaction of F62, W134 and W140, with a pi-sigma interaction with Y60; and pi-pi stacked with W102. Hydrogen bond interactions are also observed on the glutamate moiety, with Q100, W102, H135 and K136 at the γ -carboxylic acid group and W138 at the α -carboxylic group.

The crystal structure study by Chen *et al* (2013) also found that interactions around the pteroate moiety contain both hydrogen bonds and hydrophobic interactions. They found that the pteridine ring was stacked between the parallel side chains of Y85 and W171, capped by Y175; the hydrophilic pterin ring N and O atoms formed hydrogen bonds with the receptor. The pterin N1 and N2 atoms formed a strong hydrogen bond with the side chain carboxyl D81, N3 and O4 atoms with S174 hydroxyl group, and the O4 atoms formed two hydrogen bonds with the H135 side chain (Chen *et al.*, 2013).

3.2.2.2 Docking Studies of Novel FUA Derivatives (13 – 15) with FR α

The three novel FUA derivatives (**13** – **15**) were docked to FR α to determine if the folic acid still interacts with the same residues in the binding pocket and if we can retain or improve the binding affinity. All three novel FUA derivatives were docked successfully. Compound **13** produced 9 docking poses, with predicted binding affinity of -12.2 to -10.6 kcal/mol; while compound **14** produced 8 docking poses, with predicted binding affinity values between -11.0 to -8.1 kcal/mol; lastly compound **15** generated 9 docking poses, with predicted binding affinity ranging from -10.0 to -8.8 kcal/mol, with different orientations and configurations. To select a functionally relevant docking conformation, pose 1 was chosen for all three conjugates for comparison, compound **13** (**Figure 42**), compound **14** (**Figure 43**) and compound **15** (**Figure 44**), with binding affinities of -12.2 kcal/mol, -11.0 kcal/mol and -10.0 kcal/mol, respectively.

From the results obtained, it can be seen that folic acid is still oriented with the pteridine ring buried inside the binding pocket. This indicated that the UA part does not interfere with folic acid binding to FR α (**Figure 41**). Two of the conjugates, with the exception of Compound **15** have higher/similar binding affinity towards the receptor compared to folic acid alone. This indicates that additional interactions are facilitated by the conjugates.

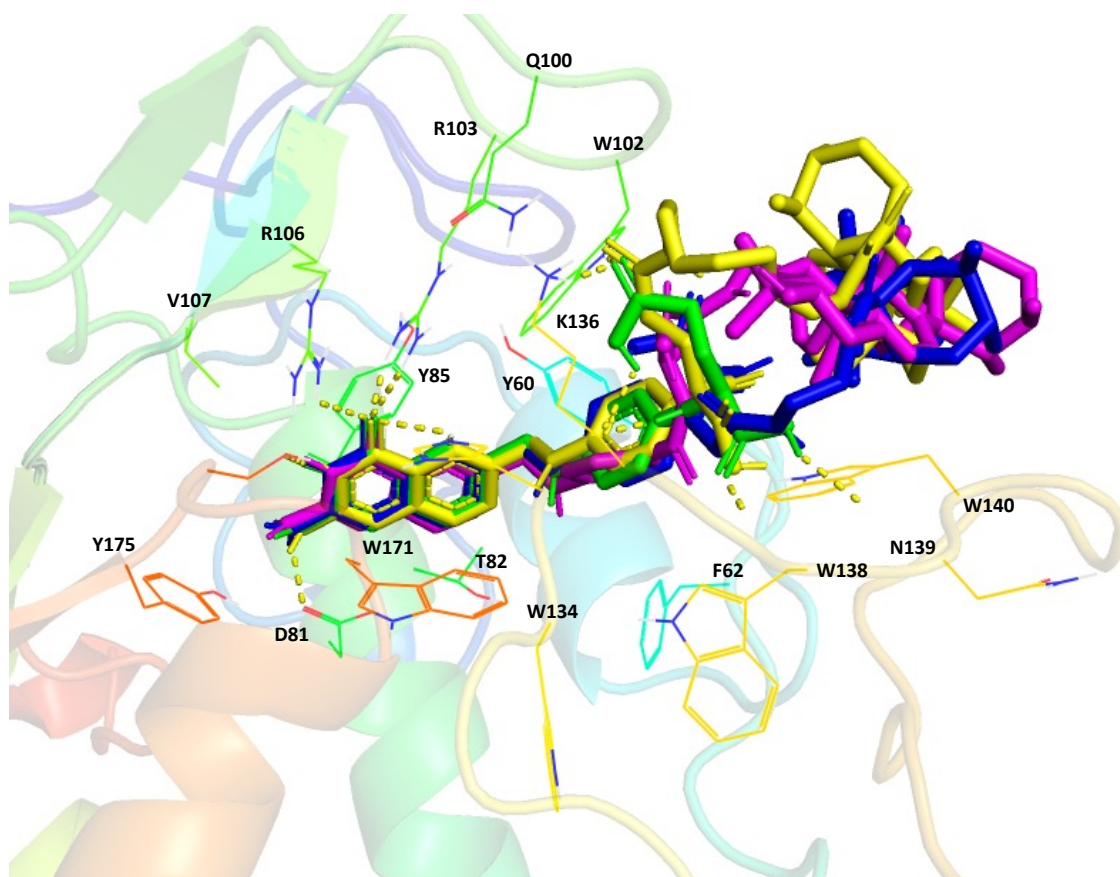


Figure 41. The 3D overlay of folic acid (green), compound **13** (blue), compound **14** (magenta) and compound **15** (yellow) docked to FR (PDB ID: 4LRH). The image was generated in PyMOL™ v2.4.1.

For compound **13** (Figure 42), we found that the pteridine N atom formed a conventional hydrogen bond with D81, and the carbonyl group also formed a series of hydrogen bonds with R106, R103 and H135. The pteridine ring still also forms a pi-pi stacking between Y85 and W171, capped by Y175. The PABA ring is π stacked with W102, and this residue also formed a hydrogen bond with α -carboxylic acid group, with H135 forming a hydrogen bond with only the hydroxyl group. The W140 residue forms a hydrophobic interaction, and the residue W138 forms a hydrogen bond with the amide linker of the γ -carboxylic acid group. The residue K136 forms a carbon hydrogen bond with the carbonyl of the γ -carboxylic acid group. Finally, UA forms an alkyl interaction with R61.

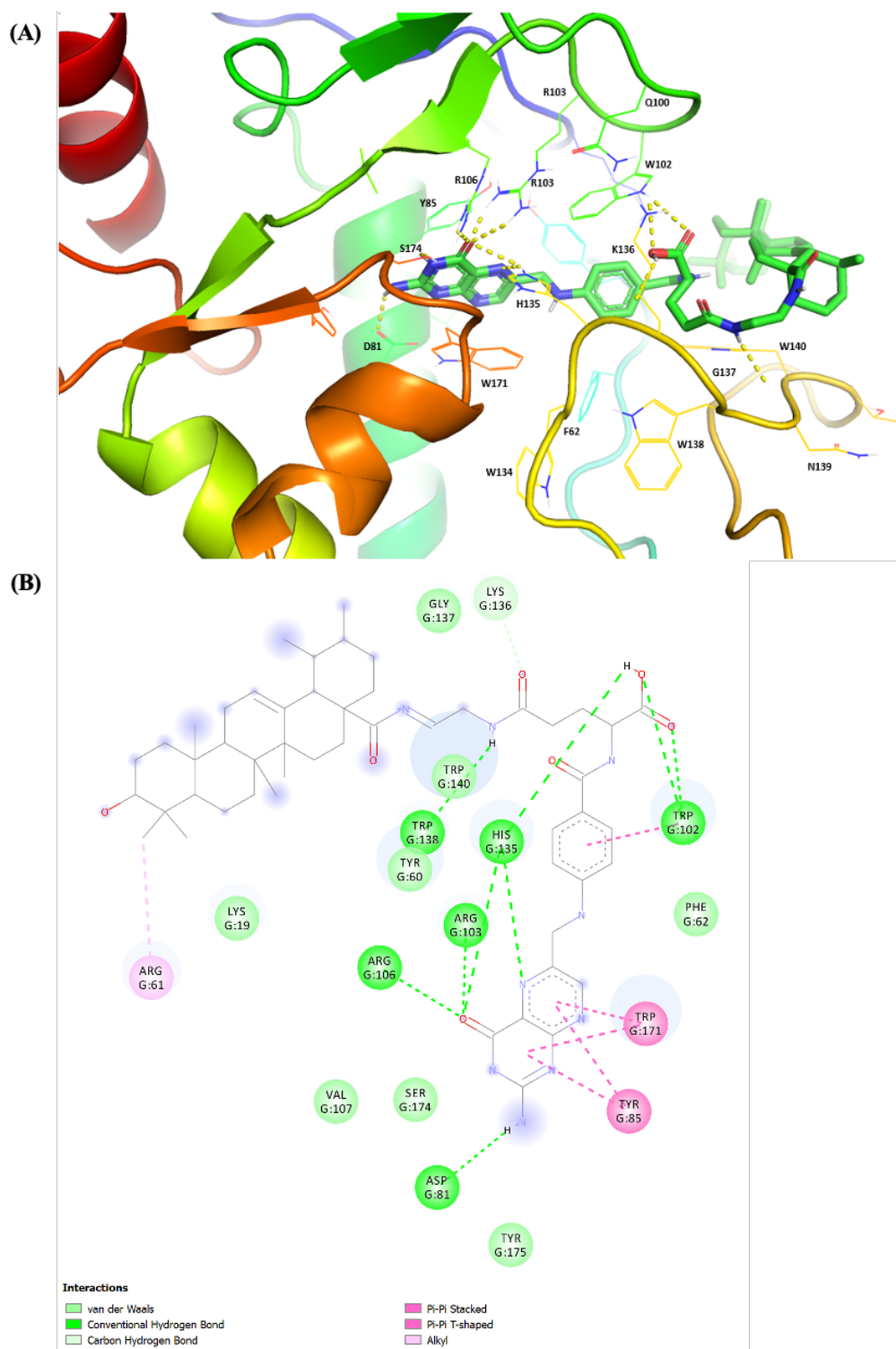


Figure 42. The (A) 3D image and (b) 2D interaction map of compound **13** docked to FR α (PDB ID: 4LRH). The 3D image was analysed and rendered in PyMOL™ v2.4.1 and the 2D interaction map was generated in BIOVIA DS Visualizer 2020.

The study of compound **14** (**Figure 43**) was similar to compound **13** where the pteridine N atom formed a conventional hydrogen bond with D81, and the carbonyl group also formed a series of hydrogen bond with R106, R103 and H135. The residue H135 formed another hydrogen bond with N atom of the second pteridine ring. The pteridine ring still also formed a pi-pi stacking between Y85 and W171, capped by Y175. The PABA ring is stacked with F62 instead of W102; the carbonyl in PABA formed a conventional hydrogen bond with the W140 residue and a carbon hydrogen bond with W138. The residue W102 formed a hydrogen bond with the carbonyl of the α -carboxylic acid group and a pi-sigma with the CH₂ near the γ -carboxylic acid group. A conventional hydrogen bond was formed by K19 with the carbonyl of γ -carboxylic acid group. UA has a pi-sigma interaction with W140.

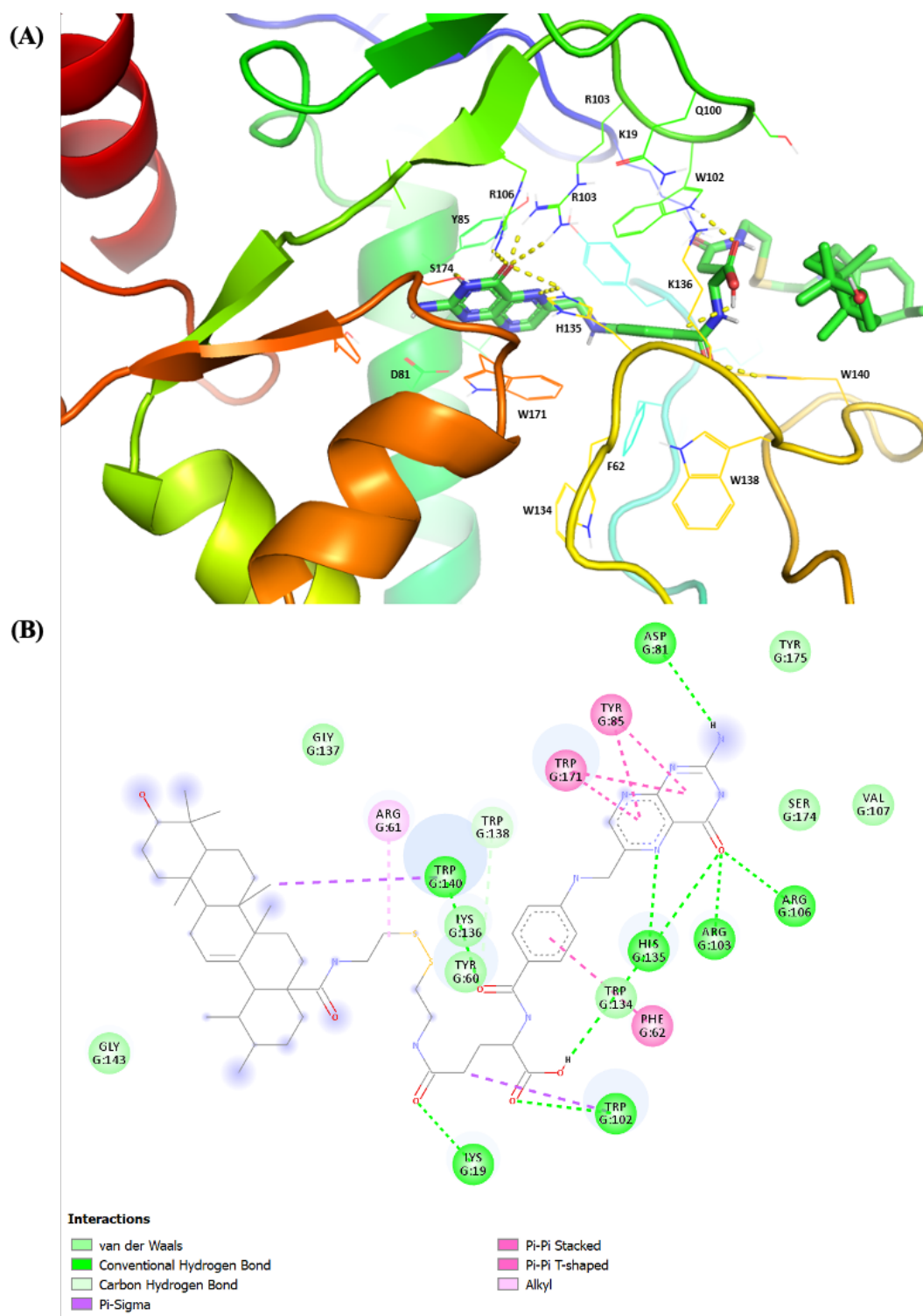


Figure 43. The (A) 3D image and (b) 2D interaction map of compound **14** docked to FR α (PDB ID: 4LRH). The 3D image was analysed and rendered in PyMOL™ v2.4.1 and the 2D interaction map was generated in BIOVIA DS Visualizer 2020.

Similarly, in compound **15** (**Figure 44**) the pteridine N atom formed a conventional hydrogen bond with D81, and the carbonyl group also formed a series of hydrogen bond with R106, R103 and H135. The residue H135 formed another hydrogen bond with N atom of the second pteridine ring. The pteridine ring also formed a pi-pi stacking between Y85 and W171. The PABA ring is stacked with W102 and Y60; and Y60 residue also formed a pi-sigma bond with the CH₂ of pteridine moiety. The residue W140 formed a hydrogen bond with the PABA moiety carbonyl. Hydrogen bond interaction was observed with residue G137 to carbonyl and W138 with hydroxyl group of the α -carboxylic acid group. The carbonyl of γ -carboxylic acid group formed a hydrogen bond with S101. UA forms an alkyl interaction with R61.

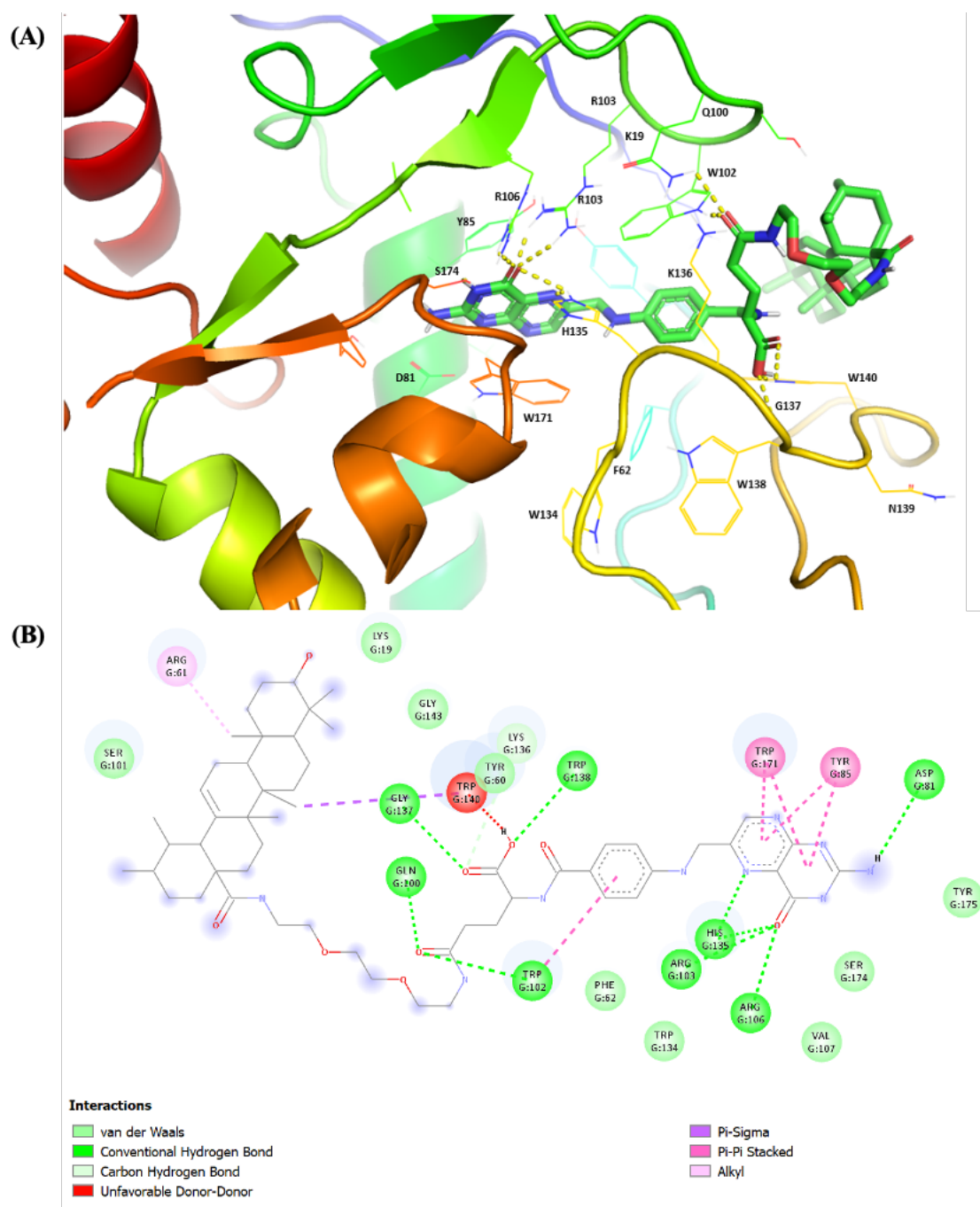


Figure 44. The (A) 3D image and (b) 2D interaction map of compound **15** docked to FRO α (PDB ID: 4LRH). The 3D image was analysed and rendered in PyMOL™ v2.4.1 and the 2D interaction map was generated in BIOVIA DS Visualizer 2020.

In summary (**Table 17**), compound **13** has better predicted binding affinity compared to folic acid, whereas compounds **14** and **15** have slightly lower. All novel FUA derivatives (**13 – 15**) bound deep into the receptor pocket, with the pteridine ring interactions the same as folic acid. The pi-sigma bond (Y60) interaction in the PABA ring was lost in all the novel FUA derivatives, but the pi-pi stacked (W102) was observed; except for compound **14** where W102 was replaced with F62. The interaction observed at the γ -carboxylic acid group of the glutamate tail of folic acid interacted with the α -carboxylic acid group in the novel FUA derivatives. Hence, it can be concluded that novel FUA derivatives (**13 – 15**) binds to FR α and may warrant a RME uptake in cells.

Table 17. Summary of the molecular docking results for FA and the novel FUA derivatives with FR α (PDB: 4LRH). HB – hydrogen bond.

Name	Predicted Binding Affinity (kcal/mol)	Interactions
FA	-11.2 to -9.4	Conventional HB (D81, Q100, W102, R103, R106, H135, K136, W138) Pi-Sigma (Y60) Pi-Pi stacked (Y85, W171) Unfavourable Acceptor-Acceptor (D81)
Compound 13	-12.2 to -10.6	Conventional HB (D81, W102, R103, R106, H135, W138) Carbon HB (K136) Pi-Pi stacked (Y85, W171) Pi-Pi T-shaped (W102) Alkyl (R61)
Compound 14	-11.0 to -8.1	Conventional HB (K19, D81, W102, R103, R106, H135, W140) Carbon HB (W138) Pi-Sigma (W102, W140) Pi-Pi stacked (Y85, W171) Pi-Pi T-shaped (F62) Alkyl (R61)
Compound 15	-10.0 to -8.8	Conventional HB (D81, Q100, W102, R103, R106, H135, G137, W138) Carbon HB (K136) Pi-Sigma (W140) Pi-Pi stacked (Y85, W171) Alkyl (R61) Unfavourable Donor-Donor (W140)

3.2.2 The Molecular Docking of Novel FUA Derivatives to VRK1

As mentioned in Introduction - 1.6.3, one of the studied molecular targets for UA is VRK1 and hence was investigated in this study. The *in silico* study by Kim *et al* (2015) (**Figure 16**) showed that UA has a strong binding affinity with VRK1 ($K_D=731$ nM). They found that UA is mainly located in the vicinity of the catalytic domain that is involved in ATP binding. They predicted that UA fits into the vicinity of the P-loop, catalytic site and C-terminal lobe of VRK1 kinase domain (Kim *et al.*, 2015). The predicted binding affinity of novel FUA derivatives (**13 – 15**) to VRK1 kinase was compared to UA to examine their interaction to the target protein.

The crystal structure of the human VRK1 bound to a bis-difluorophenol-aminopyridine inhibitor (E8V), with a 1.80 Å resolution was used for this study (Couñago *et al.*, 2017). This was selected based on the best resolution crystal structure in PDB and a review of the literature. The serine/threonine-protein kinase VRK1 crystallographic structure is composed of 4 chains (A, B, C, D; PDB 6BU6), each with 364 sequence length (**Figure 45**). In the human VRK1 protein, the N-terminal domain containing the kinase domain has altered three conserved peptide motifs that are characteristic of kinases. The C-terminal region has a low structural complexity, is highly flexible, and can have alternative folding conformations that control the kinase activity. Moreover, proteins interacting with the C-terminal region, or phosphorylating it, also modulate its kinase activity (Campillo-Marcos *et al.*, 2021). A review of the literature showed that VRK1 comprises of seven α -helices ($\alpha C - \alpha I$), one unique α -helix ($\alpha C4$), seven β -strands ($\beta 1 - \beta 7$), a P-loop, a C and N terminal (**Figure 45**). Previous VRK structures revealed that

α C4 plays a major role in stabilising the closed, active conformation of VRKs (Couñago *et al.*, 2017).

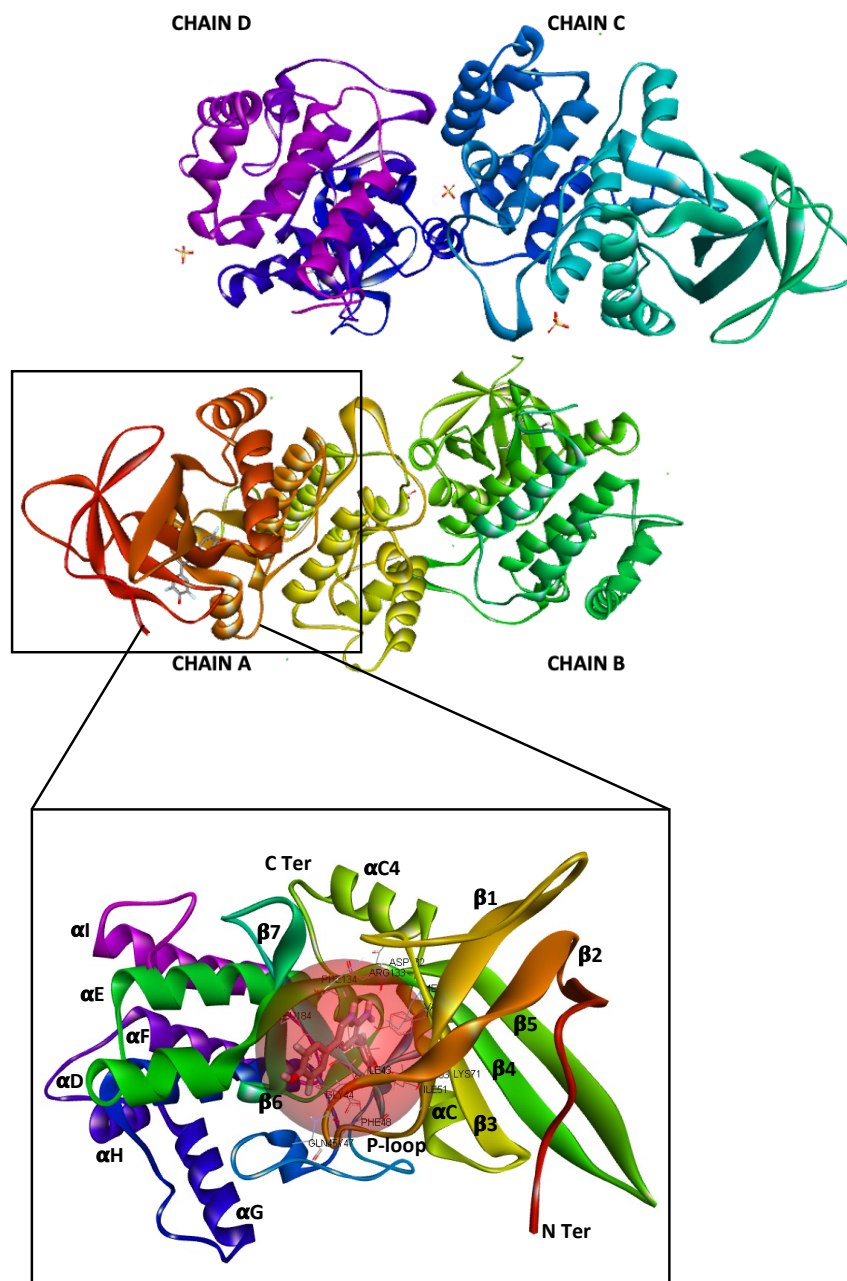


Figure 45. The 3D crystal structure of VRK1-bis-difluorophenol-aminopyridine complex (PDB: 6BU6), denoting the chains (A-D) that were recrystallised by Couñago *et al.* (2017). Chain A is zoomed in showing the co-crystallized ligand and the binding pocket. Image generated in BIOVIA DS Client Visualizer 2020 and PyMOLTM v2.4.1.

3.2.2.1 Visualization and Interaction Analysis

A validation of the docking protocols was conducted by examining the deviation of the re-docking output from the original crystal structure pose. The re-docking of 4,4'-(2-aminopyridine-3,5-diyl)bis(2,6-difluorophenol) (E8V) in VRK1 (6BU6), (**Figure 46**) (compound structure obtained from PubChem) was performed using AutoDock Vina and visualised using PyMOL v2.4.1 and Discovery Studio 2020. The deviation expressed as the RMSD produced a value of 1.443 Å for VRK1. This, low deviation and the overlay performed as seen in **Figure 46** validates the protocols employed in the docking and can be deployed in docking the designed derivatives

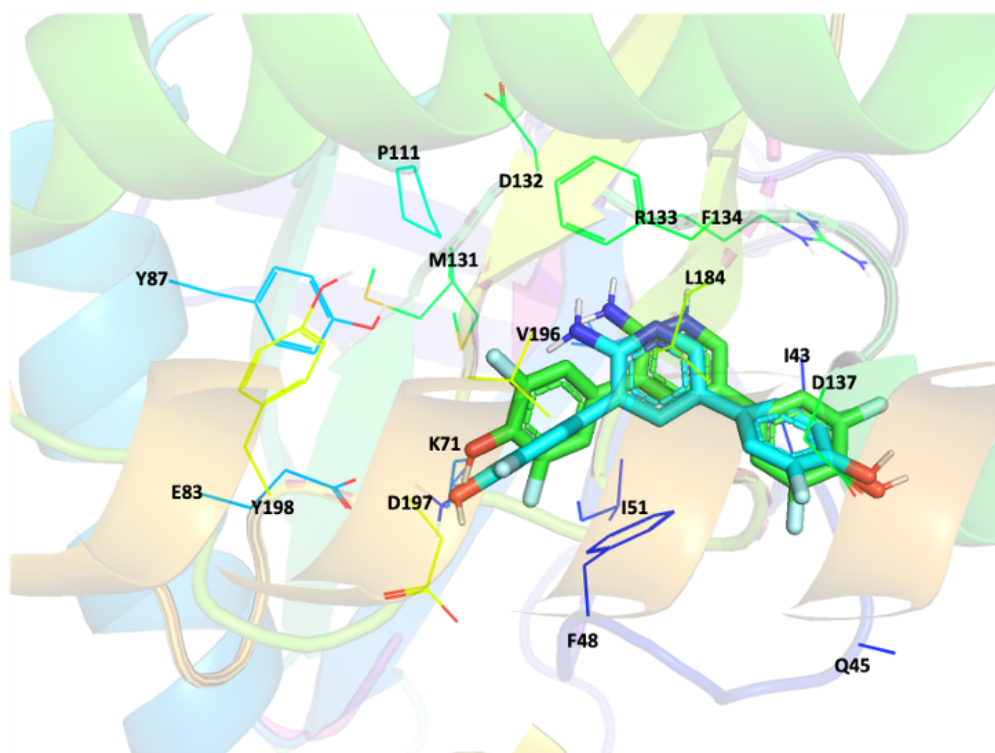


Figure 46. The superimposed 3D images of E8V - 6BU6 (green) and docked ligand (cyan) showing residues essential for ligand binding. Images were visualised and rendered in PyMOL v2.4.1.

3.2.2.2 Docking Studies of Novel FUA Derivatives (13 – 15) with VRK1

The co-crystallised inhibitor was found bound to chain A, hence this was selected for this study (Couñago *et al.*, 2017). A review of the literature showed that human VRK1 has a canonical kinase fold and possess a unique $\alpha C4$ helix near αC and $\beta 4$. It also has a large, non-catalytic C-terminal regions, containing putative regulatory autophosphorylation sites. The solution structure of VRK1 revealed that this region interacts with residues from the protein ATP-binding pocket and activation segment. Ser/Thr residues within this region are phosphorylated, which may be necessary for dissociation of the C-terminal domain from the ATP-binding pocket and activation of VRK1 (Ngow, *et al.*, 2018; Couñago *et al.*, 2017). It can be seen in **Figure 47** that UA was bound to the negatively charged binding pocket with the carboxylic acid group exposed outside.

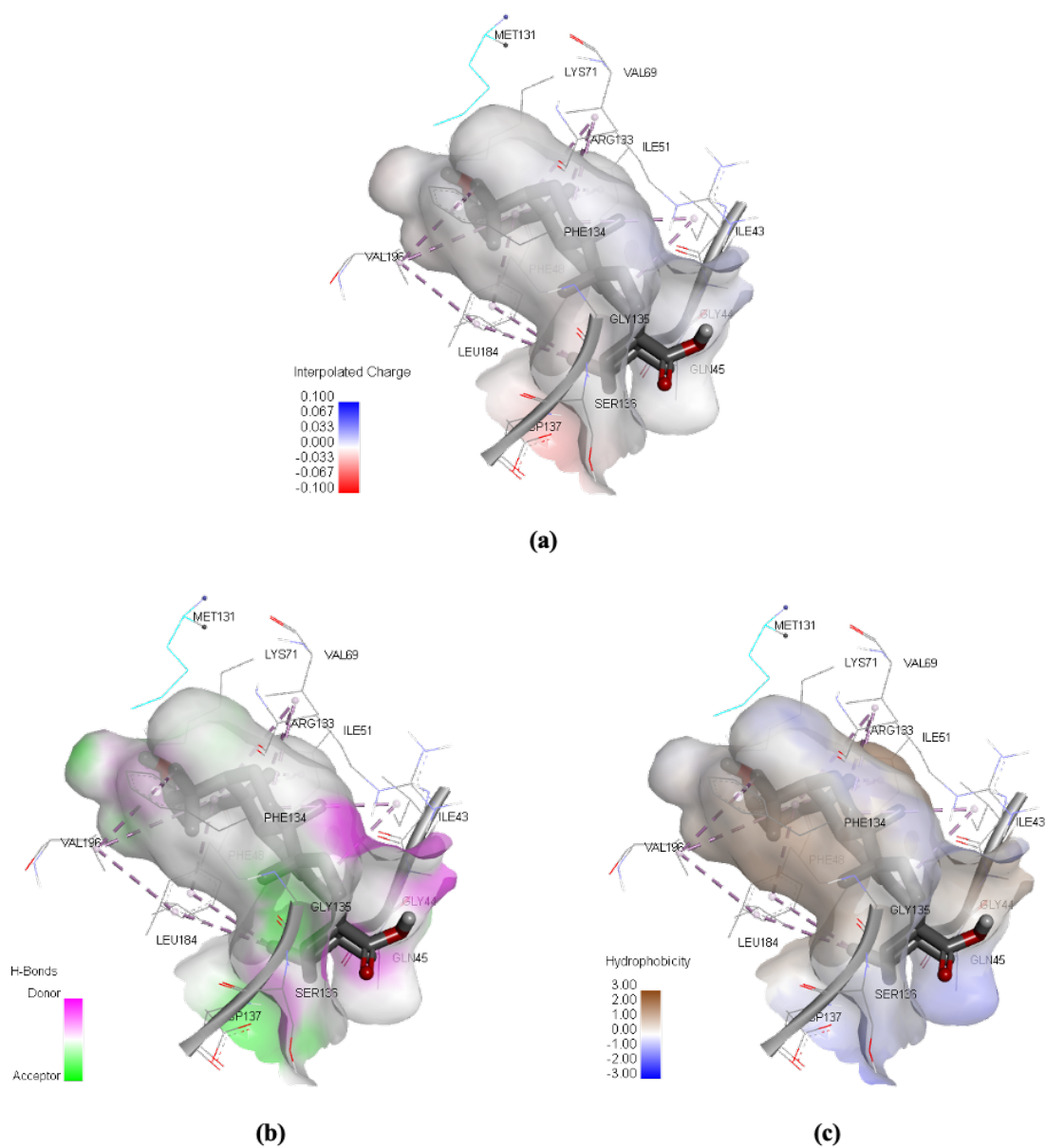


Figure 47. The UA docked to VRK1 surface showing (a) charge distribution surface (b) hydrogen bond donor/acceptor and (c) hydrophobicity. Images generated are our own results analysed using BIOVIA DS Visualizer 2020.

The study by Kim *et al* (2015) as shown in **Figure 16** showed that carboxyl group of UA was bound deeply into the binding pocket, however, the aim for this study is to have the hydroxyl group bound as the carboxyl group was the target to conjugate novel FUA derivatives. A rigid docking of UA was initially performed, however, UA was found to have different binding positions. A review of the literature indicates that key residues are important for binding - I51, K71, D132, F134, S181, L184 and D197 (Kim *et al.*, 2015; Couñago *et al.*, 2017; Ngow *et al.*, 2018; Serafim *et al.*, 2019). Hence, a flexible docking was performed instead and successfully docked UA producing 7 docking poses, with predicted binding affinity of -8.8 to -6.6 kcal/mol to the binding pocket (**Figure 49**). To select a functionally relevant docking conformation, pose 1 with a binding affinity of -8.8 kcal/mol, was chosen. The overlay of UA and E8V shows that UA is slightly outside of the binding pocket compared with E8V (**Figure 48**), but still interacts with the important residues.

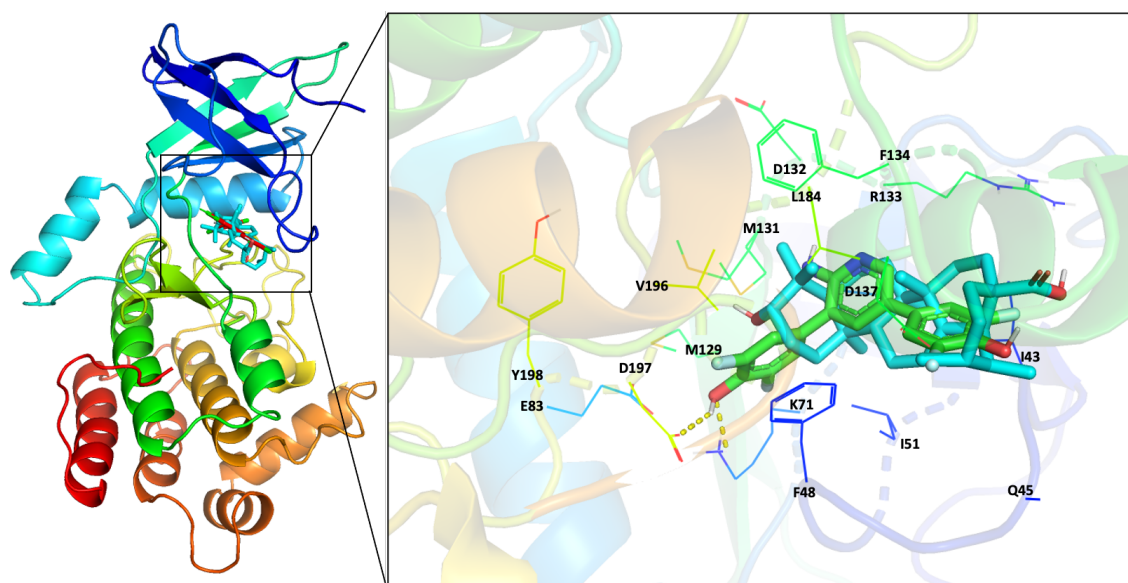


Figure 48. The superimposed 3D image of 6BU6 ligand E8V (green) and UA (cyan). Image was visualised and rendered in PyMOL™ v2.4.1.

As seen in **Figure 49**, UA docked to the binding pocket with the hydroxyl bound deep in the binding pocket and the carboxyl group exposed. The results obtained with UA bound to VRK1 (PDB ID: 6BU6) in this study shows that the hydroxyl group of UA has hydrogen bond interaction with K71 residue. Pi-alkyl interaction was also observed with I43, F48, I51, V69, F134, L184, V196 residues. A similar study by Kim *et al* (2015) with UA bound to VRK1 (PDB ID: 6AC9; **Figure 16**) by NMR titration assay shows that the carboxyl moiety of UA interacts with main chain carbonyl atoms of G135, side chain atoms of D137 and K140 residues *via* hydrogen bonding. Similarly, the hydroxyl moiety has hydrogen bonding interaction with main chain amide of D197 residue. The steroid nucleus has strong hydrophobic interactions with F48, I51, V69, K71, F134, and L184 residues that outline the VRK1 kinase domain.

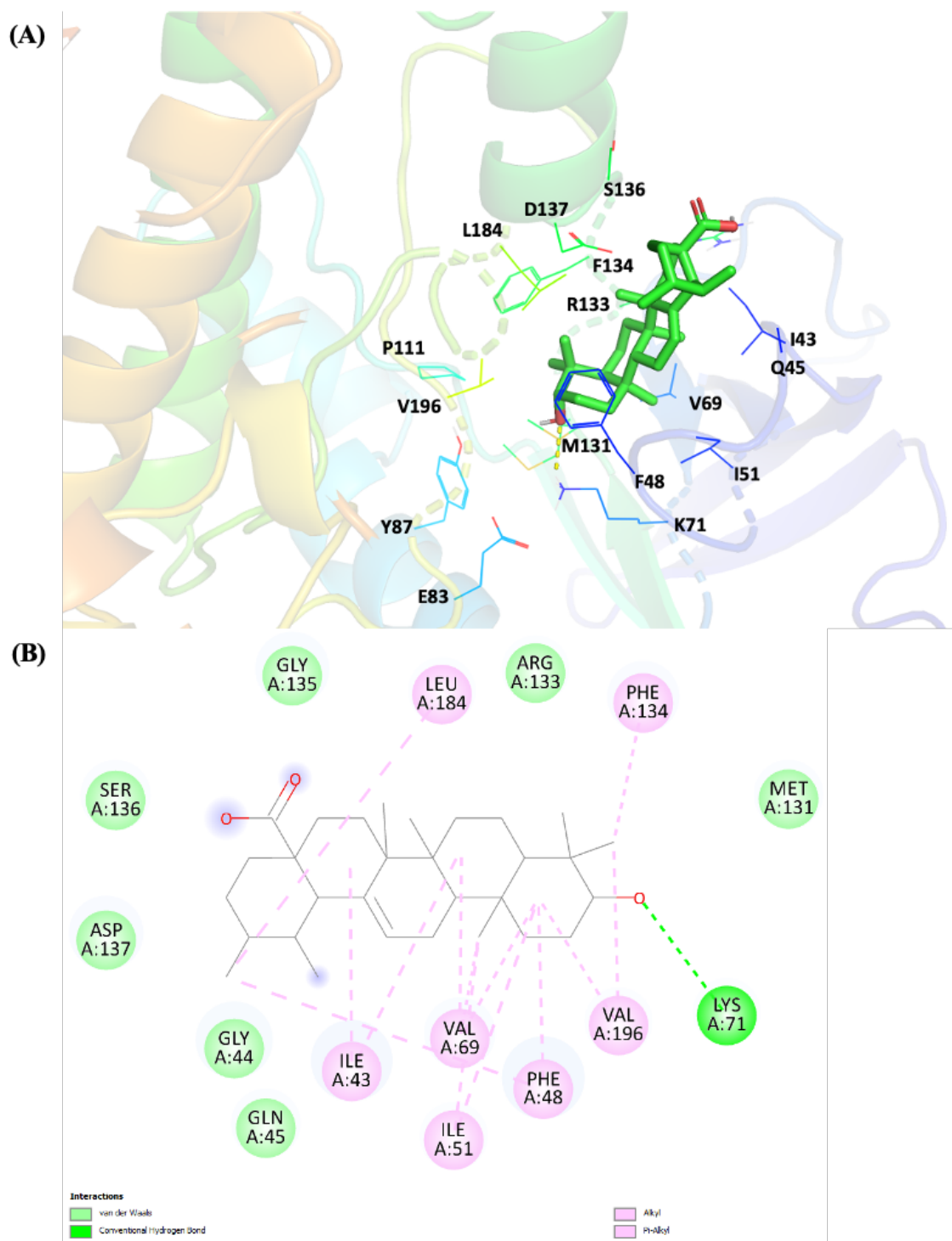


Figure 49. The (A) 3D image and (B) 2D interaction map of UA docked to VRK1 (PDB ID: 6BU6). The 3D image was analysed and rendered in PyMOL™ v2.4.1 and the 2D interaction map was generated in BIOVIA DS Visualizer 2020.

The three novel FUA derivatives (**13** – **15**) were docked to VRK1 to determine if UA interacts with the desired residues in the binding pocket and if we can retain or improve its binding affinity. All three novel FUA derivatives were docked successfully using flexible docking. Compound **13** produced 7 docking poses, with predicted binding affinity of -8.4 to -5.6 kcal/mol; while compound **14** produced 3 poses, with predicted binding affinity values between -8.8 to -5.9 kcal/mol; lastly, compound **15** generated 3 docking poses, with predicted binding affinity values between -10.2 to -7.4 kcal/mol. To select a functionally relevant docking confirmation, pose 1 was chosen for all three conjugates for comparison, compound **13** (**Figure 51**), compound **14** (**Figure 52**), and compound **15** (**Figure 53**), with binding affinities of -8.4 kcal/mol, -8.8 kcal/mol and -10.2 kcal/mol, respectively. Folic acid was also docked to VRK1 and produced 9 docking poses, with predicted binding affinity of -9.0 to -8.5 kcal/mol. The pose 1 conformation was selected for the study with a binding affinity of -9.0 kcal/mol (**A.24**). The results showed that folic acid has more interactions to VRK1 in comparison to UA.

From the results obtained (**Figure 50**), it can be seen that the UA of compound **13** (blue) was bound and oriented at the same binding pocket as UA, but has a lower binding affinity (-8.4 kcal/mol) compared to UA (-8.8 kcal/mol). In contrast, compounds **14** (magenta) and **15** (yellow) was oriented differently from UA and FA was found to interact with residues in the binding pocket, with UA exposed outside of the binding pocket. Interestingly, predicted binding affinities for compounds **14** (-8.8 kcal/mol) and **15** (-10.2 kcal/mol) were higher than compound **13**.

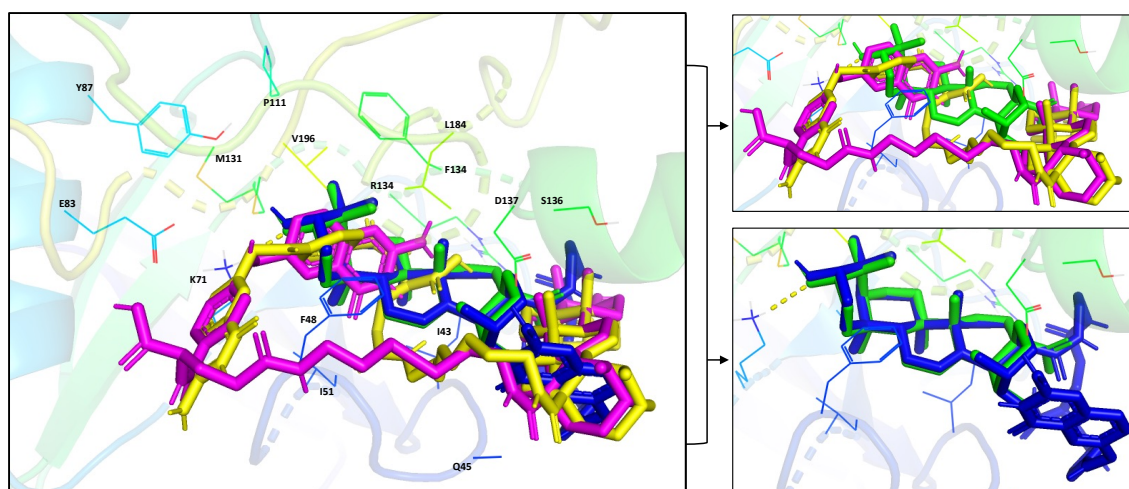


Figure 50. The 3D overlay of UA (green), compound **13** (blue), compound **14** (magenta) and compound **15** (yellow) docked to VRK1 (PDB ID: 6BU6). The image was generated in PyMOL™ v2.4.1.

For compound **13** (**Figure 51**), the hydroxyl group of UA was bound to the binding pocket and still interact with some of the residues in the binding pocket *via* alkyl interactions – I43, F48, I51, V69, K71, F134 and V196. In addition, the pteridine N atom of FA formed a conventional hydrogen bond with D137; pteridine ring had pi-anion interaction with D137 and pi-alkyl interaction with K140. A conventional hydrogen bond interaction was also observed on the carbonyl of α -carboxylic acid group (G44) and carbonyl of the γ -carboxylic acid (R133) group of FA; and a carbon hydrogen bond of E143 formed with α -carboxylic acid group.

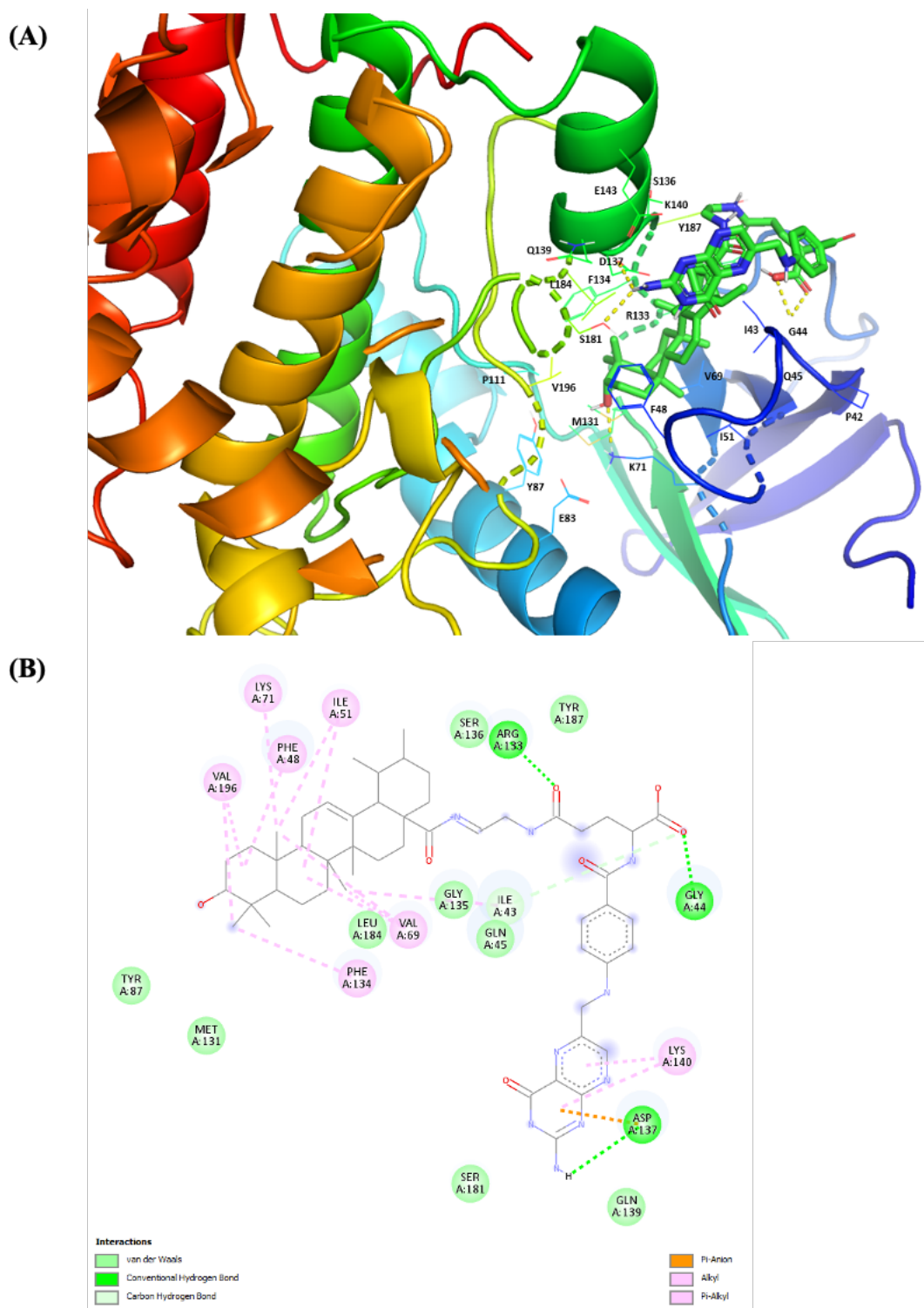


Figure 51. The (A) 3D image and (B) 2D interaction map of compound **13** docked to VRK1 (PDB ID: 6BU6). The 3D image was analysed and rendered in PyMOL™ v2.4.1 and the 2D interaction map was generated in BIOVIA DS Visualizer 2020.

The UA end of the compound **14 (Figure 52)** was found exposed outside of the binding pocket and only forms pi-alkyl interaction with I43 and K140. The disulphide linker was found to have a strong hydrogen bond interaction with G47 and pi-sulphur with F48. Most of the residues in the binding pocket formed a strong interaction with FA. The PABA formed a conventional hydrogen bond with K71 in the carbonyl and the ring formed a pi-anion with D197. The pteridine ring formed a pi-sigma interaction with L184 and pi-alkyl with I51 and V196. The findings with the bound FA (-9.0 kcal/mol) to VRK1 produced a higher binding affinity than UA (-8.8 kcal/mol). This could be one reason as to why most interaction was observed with the folic acid. There is no experimental data published in the literature of folic acid binding to VRK1.

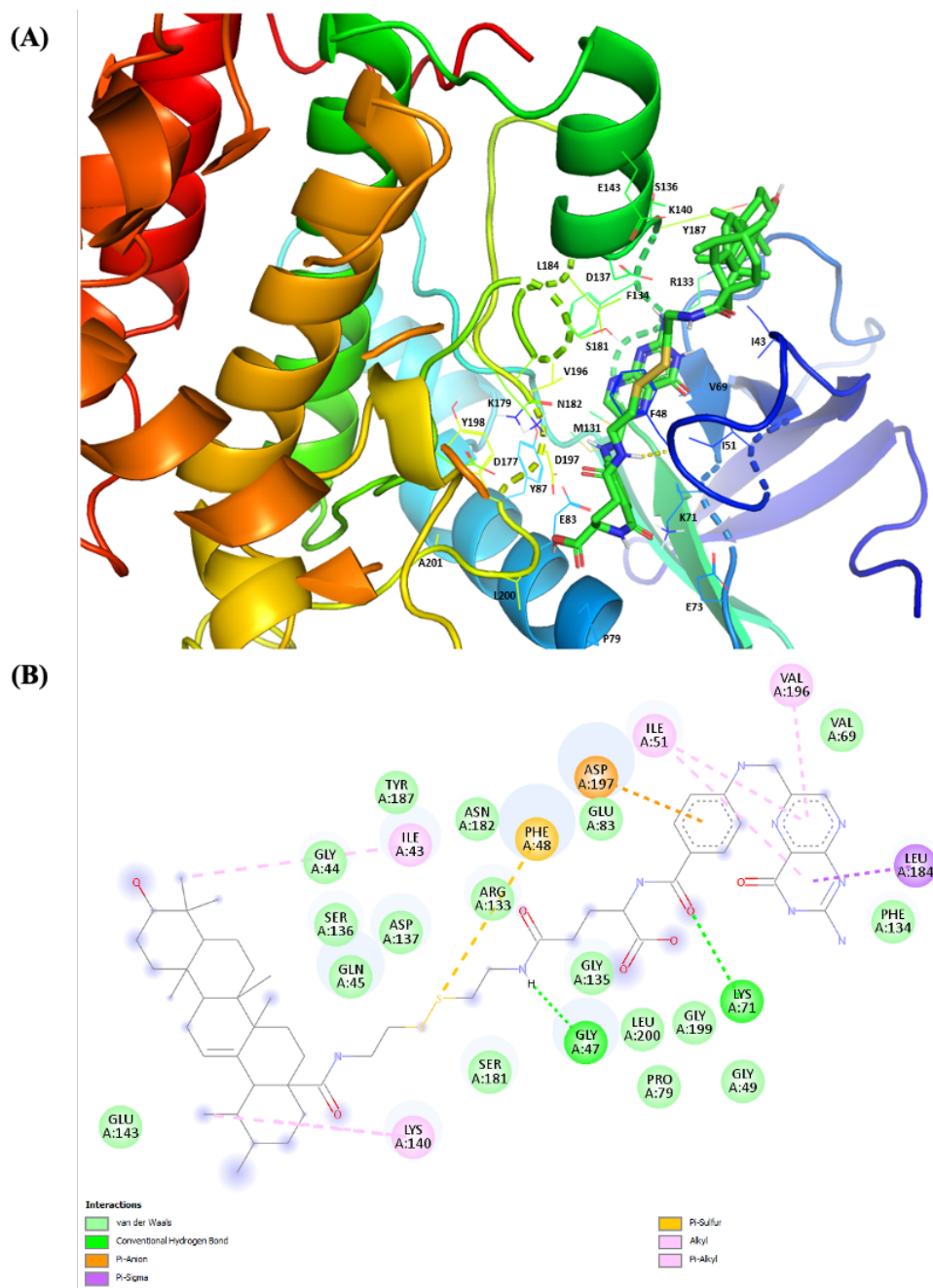


Figure 52. The (A) 3D image and (B) 2D interaction map of compound **14** docked to VRK1 (PDB ID: 6BU6). The 3D image was analysed and rendered in PyMOL™ v2.4.1 and the 2D interaction map was generated in BIOVIA DS Visualizer 2020.

Similarly, the UA end for compound **15 (Figure 53)** was found exposed outside of the binding pocket and forms a pi-alkyl interaction with I43 and K140. The ethereal oxygen linker formed a carbon hydrogen bond with D137 and conventional hydrogen bond with G47. Most interactions are observed on the FA end. The carbonyl of γ -carboxylic acid had a strong hydrogen bond interaction with F48. The PABA ring of FA formed a pi-pi stacked with F48 and pi-alkyl interaction with L184 and V196. Lastly, the pteridine ring was observed with a conventional hydrogen bond with K71, carbon hydrogen bond with E83 and pi-anion with D197.

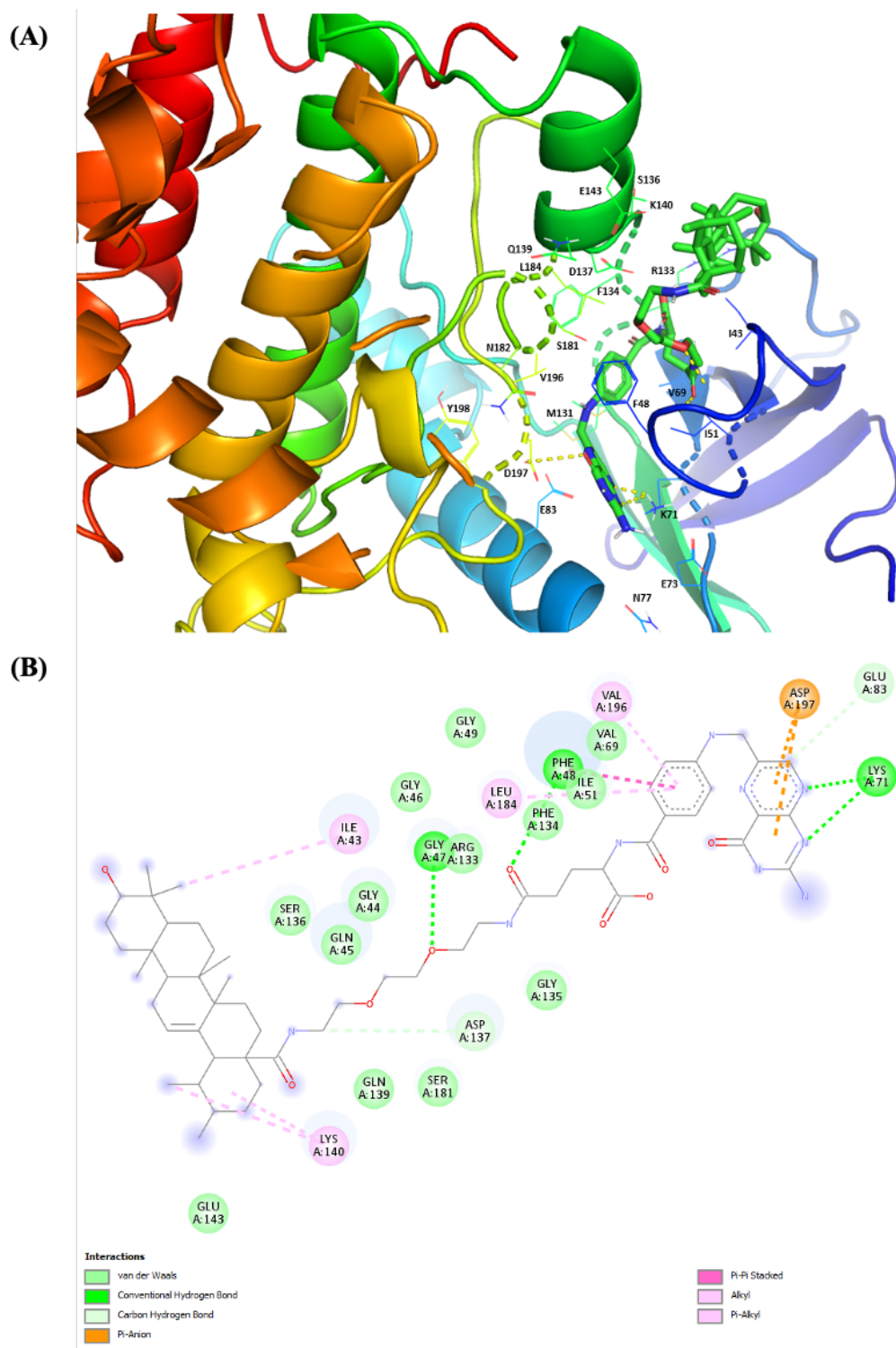


Figure 53. The (A) 3D image and (B) 2D interaction map of UA-EDEA-FA (**15**) docked to VRK1 (PDB ID: 6BU6). The 3D image was analysed and rendered in PyMOL™ v2.4.1 and the 2D interaction map was generated in BIOVIA DS Visualizer 2020.

In summary (**Table 18**), out of the three novel FUA derivatives, compound **15** produced the best predicted binding affinity, better than UA. Compound **13** was the only compound where the UA side was bound to the same binding pocket as the UA, however, predicted binding affinity was slightly lower. Compounds **14** and **15** has the same and/or improved predicted binding affinity but UA was found exposed out of the binding pocket; with most interactions observed on the folic acid end. The findings with the bound folic acid (-9.0 kcal/mol) to VRK1 produced a higher binding affinity than UA (-8.8 kcal/mol). This could be one reason as to why most interaction was observed with the folic acid end. To the best of our knowledge, there has been no studies of folic acid bound to VRK1 published in the literature.

Results obtained from the *in silico* pharmacodynamic (molecular docking) studies suggests that novel FUA derivatives have higher predicted binding affinity to FR α than in VRK1. Novel FUA derivatives binding to FR α is crucial in our study as our aim was to target cancer cells that overexpress FRs. Hence, our results provide confidence that our compounds are able to predictably bind to our target.

Table 18. Summary of the molecular docking results for ursolic acid and the novel FUA derivatives (**13 – 15**) with VRK1 (PDB: 6BU6). HB – hydrogen bond.

Name	Predicted Binding Affinity (kcal/mol)	Interactions
UA	-8.8 to -6.6	Conventional HB (K71) Pi-alkyl (I43, F48, I51, V69, F134, L184, V196)
Compound 13	-8.4 to -5.6	Conventional HB (G44, R133, D137) Carbon HB (E143) Pi-anion (D137) Pi-alkyl (I43, F48, I51, V69, K71, F134, K140, V196)
Compound 14	-8.8 to -5.9	Conventional HB (G47) Pi-anion (D197) Pi-sigma (L184) Pi-sulphur (F48) Pi-alkyl (I43, I51, K140, V196)
Compound 15	-10.2 to -7.4	Conventional HB (G47, F48, K71) Carbon HB (E83, D137) Pi-anion (D197) Pi-pi stacked (F48) Pi-alkyl (I43, K140, L184, V196)

3.3 The Chemotherapeutic Potential of Novel FUA Derivatives

Targeted drug delivery of UA has proven difficult to date, with low natural bioavailability and lack of known selective uptake mechanisms (Shao *et al.*, 2020). On the other hand, folic acid can also be conjugated to small molecules through either direct folate coupling or folate coupling *via* a spacer to create potentially FR-selective cytotoxic compounds. Although not always required, the inclusion of a spacer allows for effective unhindered binding of the folate moiety to the FR and control over the lipophilicity of the folate conjugate, which are requirements for cellular internalization of the entire molecule through endocytosis (Vlahov and Leamon, 2012; Crowley *et al.*, 2019).

Hence, the chemotherapeutic potential of the novel FUA derivatives generated in the present study, compounds **13 – 15**, were tested against a panel of common and difficult to treat cancers by coupling with folate. Our work sought to elucidate the mechanism of action of novel FUA derivatives (**13 – 15**) and determine its potential to improve delivery of UA to a range of cancer cells. In addition, the presence of folate was used in an attempt to target novel FUA derivatives (**13 – 15**) through the folate receptor.

3.3.1 Novel FUA Derivatives in Different Cell Lines (folate free medium)

A review of the literature was conducted to identify expression of the FR α in different cell models. It was found that levels of FRs differ between cell lines and current literature contradicts expression of the same cell line. For example, the breast cancer cell line MCF-7 was reported to have normal folate receptor expression (Chen *et al.*, 2009), while more recent studies reported that this cell line overexpress the receptor (Zhang *et al.*, 2015). However, some authors reported MCF-7 cell line with low folate expression (Kelley *et al.*, 2003; Al-Kattan *et al.*, 2014). The ovarian cancer cell line SKOV-3, are commonly used as a FR-overexpressing cell model. A study by Crowley *et al* (2019) detected folate expression of SKOV-3 using western blot, and they found that SKOV-3 cells express high level of FR α protein. Similarly, high folate expression was observed by Mendes *et al* (2018) in SKOV-3 cell and colorectal cancer cell line Caco-2, whereas they found that MCF-7 cell line has low folate expression. There are not many studies on the folate expression of U-251 MG cells but FR α has been shown to overexpress in gliomas (McCord *et al.*, 2021).

Studies have shown that FR levels are upregulated in low folate conditions. They proposed that these conditions stimulate the cells to upregulate its FR levels in order to maintain the necessary levels of intracellular folate (Antony *et al.*, 2004; Siwowska *et al.*, 2017). Hence, a folate free medium was used in this study for 2 – 5 days before treatment. Different cellular models were used to test the cytotoxicity of novel FUA derivatives. Cellular models chosen vary with different folate receptor expression: U-251 MG, Caco-2 and SKOV-3 (FR-overexpressing) and MCF-7 (FR-underexpressing) cells. Cells were treated with the novel FUA derivatives (**13** – **15**) for 48 and 144 hours in free folate RPMI-1640 medium and cell viability was measured using alamarBlue assay.

In a preliminary screen conducted to elucidate if novel FUA derivatives improve cytotoxicity of UA, U-251 MG, SKOV-3, MCF-7 and Caco-2 cells were treated with 3.125 – 100 μ M of compounds **13** – **15**, ursolic acid and folic acid. DMSO (20%) was used as a positive control and cells were also treated with a vehicle control with the highest concentration present in each drug, 0.5% DMSO (negative control). No significant reduction in cell viability was observed in the vehicle control. Folic acid is an essential component in cell culture media due to its role in cell development and in the conversion of homocysteine to methionine and is therefore not expected to have a cytotoxic effect on cell lines used in this study (Sawowski *et al.*, 2017). From results obtained, treatment with folic acid did not significantly affect the cell viability; however, some effects could be seen at higher concentrations (100 μ M).

Results obtained (**Figure 54**) shows that UA retained its biological and inherent cytotoxic activity across all four cell lines at both 48 and 144 hours timepoints. In U-251 MG cells, UA demonstrated a significant activity with an IC_{50} of 16.04 and 10.37 μ M after 48 and 144 hours treatment, respectively. However, all novel FUA derivatives (**13 – 15**) had very little reduction in cell viability, with only approximately 20% after 144 hours treatment. Similarly, novel FUA derivatives (**13 – 15**) in Caco-2 and MCF-7 cells only had very little to no cytotoxicity (approximately 20%) on both 48 and 144 hours treatment. Moreover, UA had a cytotoxicity in Caco-2 cells with an IC_{50} of 10.79 and 4.72 μ M after 48 and 144 hours, respectively; whereas in MCF-7 had 12.51 and 10.32 μ M, after 48 and 144 hours treatment, respectively. In SKOV-3 cell line, UA exhibited an IC_{50} of 15.82 and 6.36 μ M after 48 and 144 hours treatment, respectively.

All novel FUA derivatives (**13 – 15**) have very little to no activity after 48 hours treatment. However, after 144 hours treatment, compound **15** had 20% reduction in cell viability, whereas compound **14** exhibited an approximately 50% cell reduction giving an IC_{50} of 98.41 μ M. Compound **13** after 144 hours treatment was found to have the best results out of all the three novel FUA derivatives in the panel of cancer cell lines tested, with an approximately 60% reduction in cell viability, with an IC_{50} of 45.89 μ M in SKOV-3 cells. In spite of that, UA was still >seven-fold more cytotoxic in comparison to compound **13**. These results suggest that biological activity of UA was inhibited, which could be due to a lot of factors such as the cell culture medium, activity of folate receptor in cells, or the conjugation of the folic acid. Hence, was further investigated below.

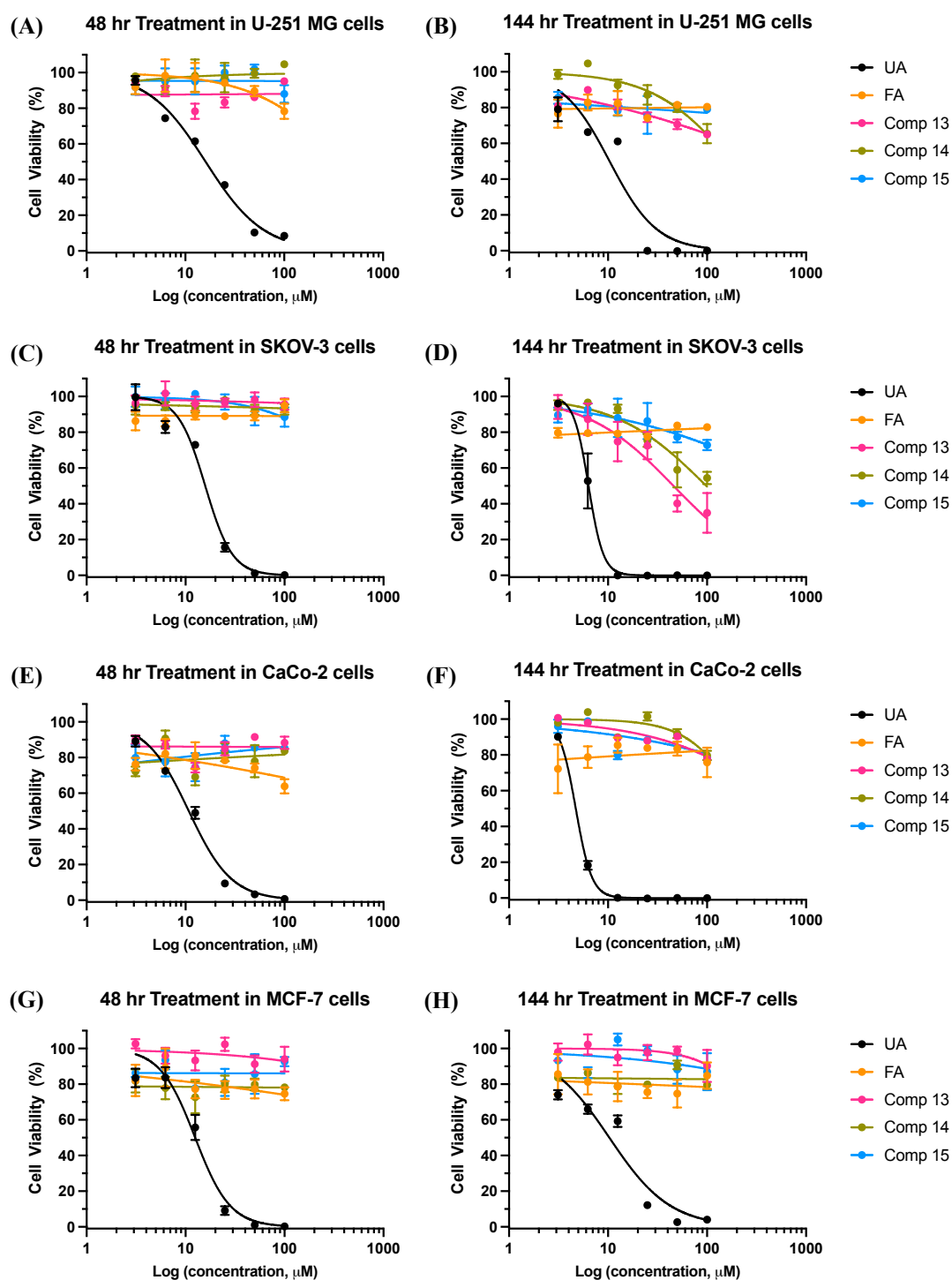


Figure 54. Cytotoxicity of novel FUA derivatives (13 – 15) in different cancer cell lines. An initial concentration of 100 μM in culture medium was added to cells and serially diluted to different concentrations (100 μM to 3.125 μM). AlamarBlue cell viability assay was then carried out following treatment for 48 and 144 hours. Data shown were normalised to the untreated control and are shown as the % mean \pm SEM. Statistical analysis was carried out using non-linear regression analysis and Two-way ANOVA with Bonferroni post-tests, ($n = 3$) ($P < 0.0001$).

3.3.2 Novel FUA Derivatives in Different Cell Lines and Media

Due to the results obtained above, low and medium folate media were used to determine whether media condition was one of the factors for the lost cytotoxicity. RPMI-1640 with 0.001 g/L of folic acid (low folate) was studied in three different cell lines – U-251 MG, SKOV-3 and MCF-7 cell lines. As seen in **Figure 55**, all novel FUA derivatives (**13 – 15**) exhibited very little to no cytotoxicity in U-251 MG and MCF-7 cell lines both after 48 and 144 hours treatment. However, a little reduction in cell viability was observed in SKOV-3 cells after 144 hours treatment. Cell viability reduction have been observed more after 48 hours treatment in low folate medium with an approximately 40%, 30% and 20% reduction for compounds **13**, **14**, **15**, respectively.

Another medium used was DMEM-high glucose with 0.004 g/L folic acid (medium folate), tested in three different cell lines – U-251 MG, human epidermal cancer cell line A431 and colorectal cancer SW480 cell lines (**Figure 56**). Results obtained in U-251 MG cells were similar to low and medium folate media used, with very little to no cytotoxicity; this was also observed in SW480 and A431 cell lines. The study conducted in different media and cell lines indicated that all novel FUA (**13 – 15**) derivatives inhibited the cytotoxicity of UA, regardless of the amount of folic acid present in media.

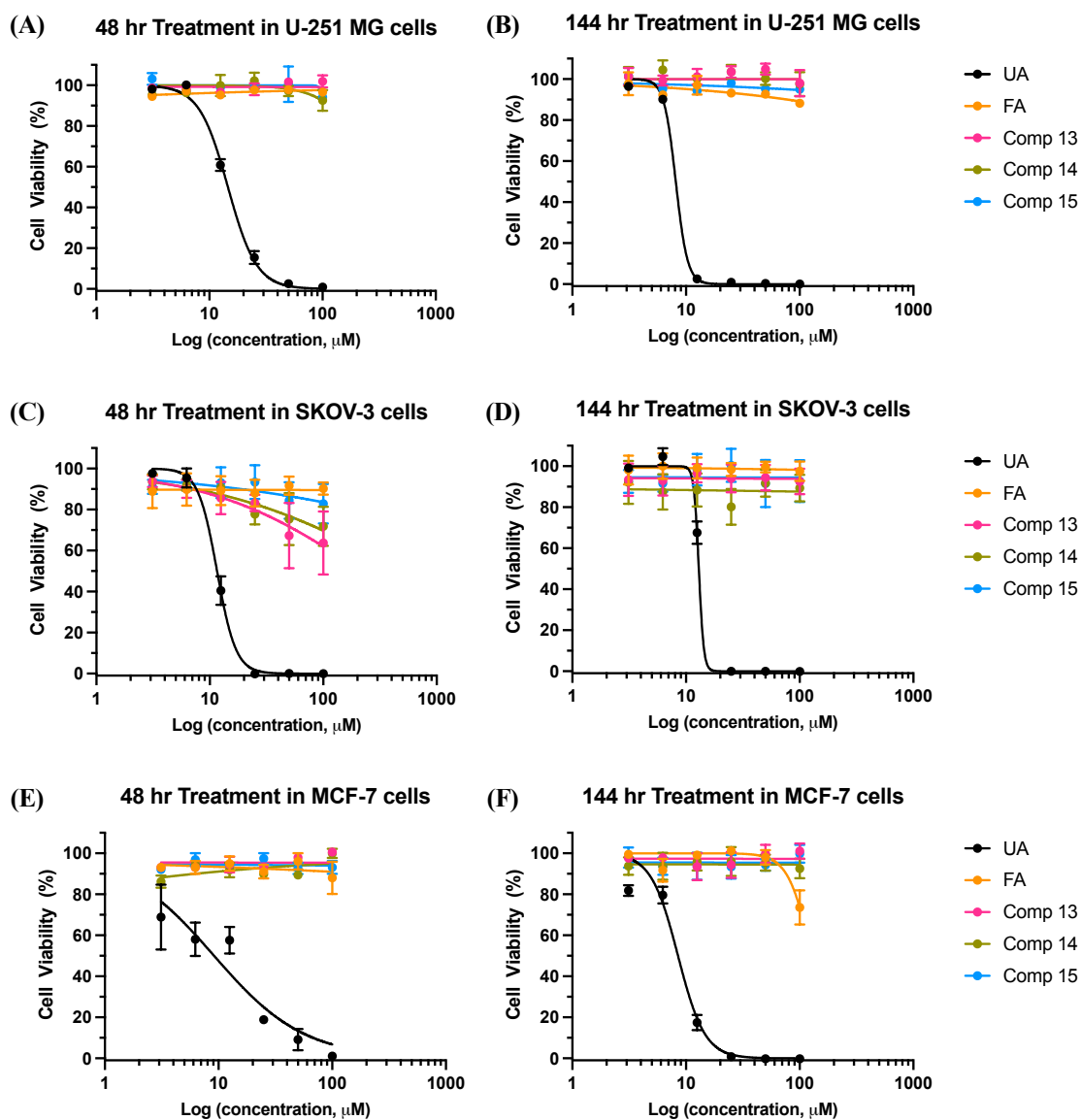


Figure 55. Cytotoxicity of novel FUA derivatives (**13 – 15**) in cancer cells (low folate medium). An initial concentration of 100 μM in culture medium was added to cells and serially diluted to different concentrations (100 μM to 3.125 μM). AlamarBlue cell viability assay was then carried out following treatment for 48 and 144 hours. Data shown were normalised to the untreated control and are shown as the % mean ± SEM. Statistical analysis was carried out using non-linear regression analysis and Two-way ANOVA with Bonferroni post-tests, (n = 3) (P < 0.0001).

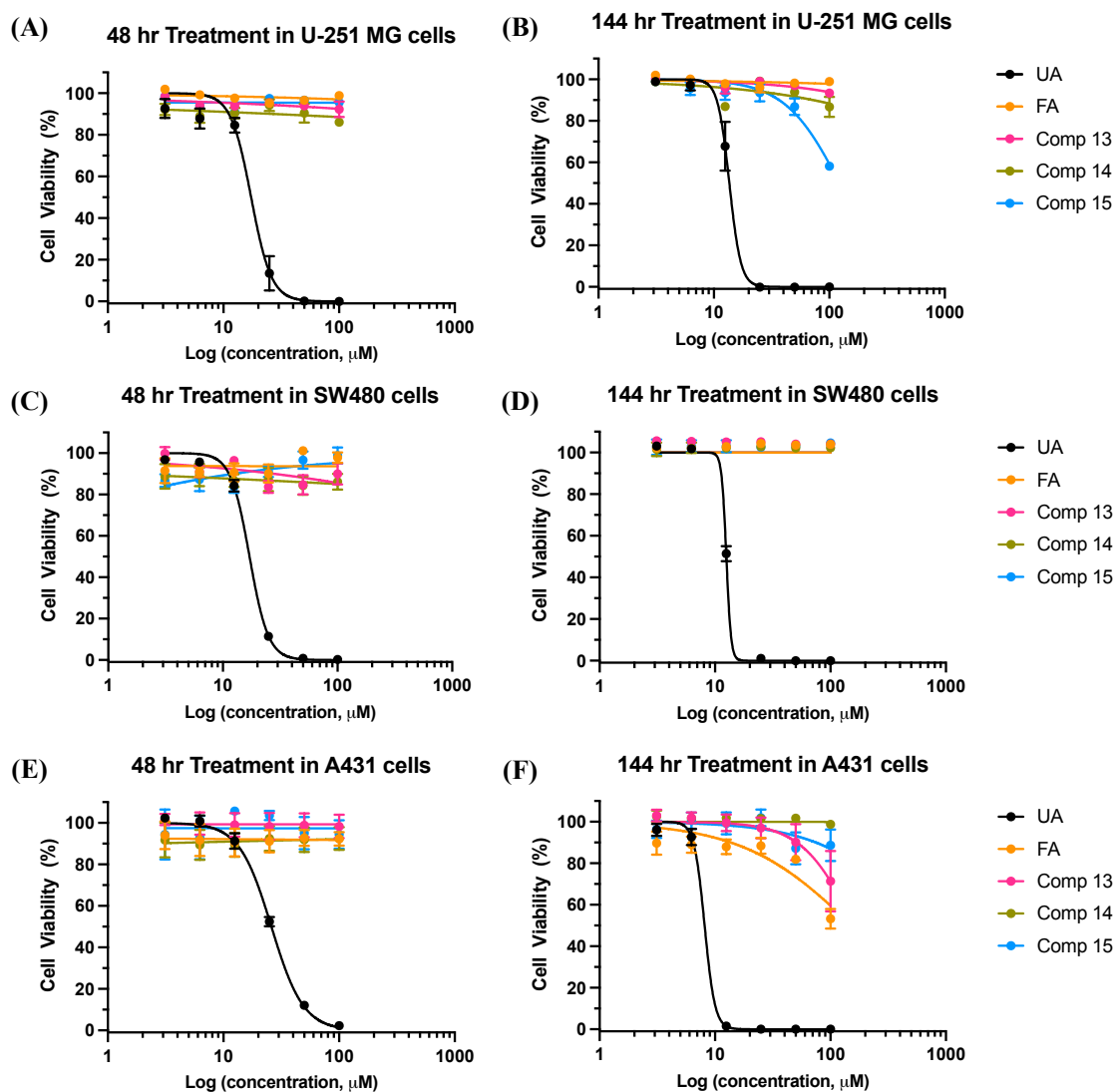


Figure 56. Cytotoxicity of novel FUA derivatives (**13** – **15**) in cancer cells (medium folate medium). An initial concentration of 100 μM in culture medium was added to cells and serially diluted to different concentrations (100 μM to 3.125 μM). AlamarBlue cell viability assay was then carried out following treatment for 48 and 144 hours. Data shown were normalised to the untreated control and are shown as the % mean \pm SEM. Statistical analysis was carried out using non-linear regression analysis and Two-way ANOVA with Bonferroni post-tests, ($n = 3$) ($P < 0.0001$).

3.3.3 Novel FUA Derivatives with Methotrexate control in elected cell lines

The folate antagonist methotrexate is a cytotoxic drug used in the treatment of various types of cancer (Nogueira *et al.*, 2018; Scaranti *et al.*, 2020). It inhibits DHFR, an enzyme involved in the biosynthetic pathway of nucleotides, hence methotrexate is highly toxic to rapidly dividing cancer cells. Methotrexate is mediated by two main transport system: the reduced folate carrier (RFC) and membrane-associated folate receptors (Nogueira *et al.*, 2018; Mazzotta *et al.*, 2020). Moreover, due to its similar structure to folate, methotrexate is effectively internalized by the cell *via* specific interactions with folate receptors on cell membranes present in carcinoma and brain tumours (Lan *et al.*, 2021). Hence, methotrexate was used as a control to determine the extent of which the folate receptor is active in different cell lines tested – U-251 MG, SKOV-3, Caco-2 and MCF-7 cell lines.

The folate-free medium was established as the optimum medium and hence was used in this study. It can be seen in **Figure 57** that methotrexate produced a concentration and time independent cytotoxicity which are more evident in Caco-2 and MCF-7 cell lines. In addition, the cytotoxicity obtained for U-251 MG and SKOV-3 cells was found to have concentration-independent but time-dependent cytotoxicity. As seen in **Figure 57** (A, B, C, D), cell viability of methotrexate was approximately 80% after 48 hours treatment, but greatly reduced to only 10% after 144 hours in U-251 MG and SKOV-3 cell lines. Whereas in Caco-2 and MCF-7 cells, methotrexate cell viability was approximately 30% at both 48 and 144 hours treatment. It can be concluded that folate receptor is active in all cell lines used in this study. Hence, the cytotoxic activity of novel FUA derivatives (**13 – 15**) was inhibited due to the conjugation of folic acid.

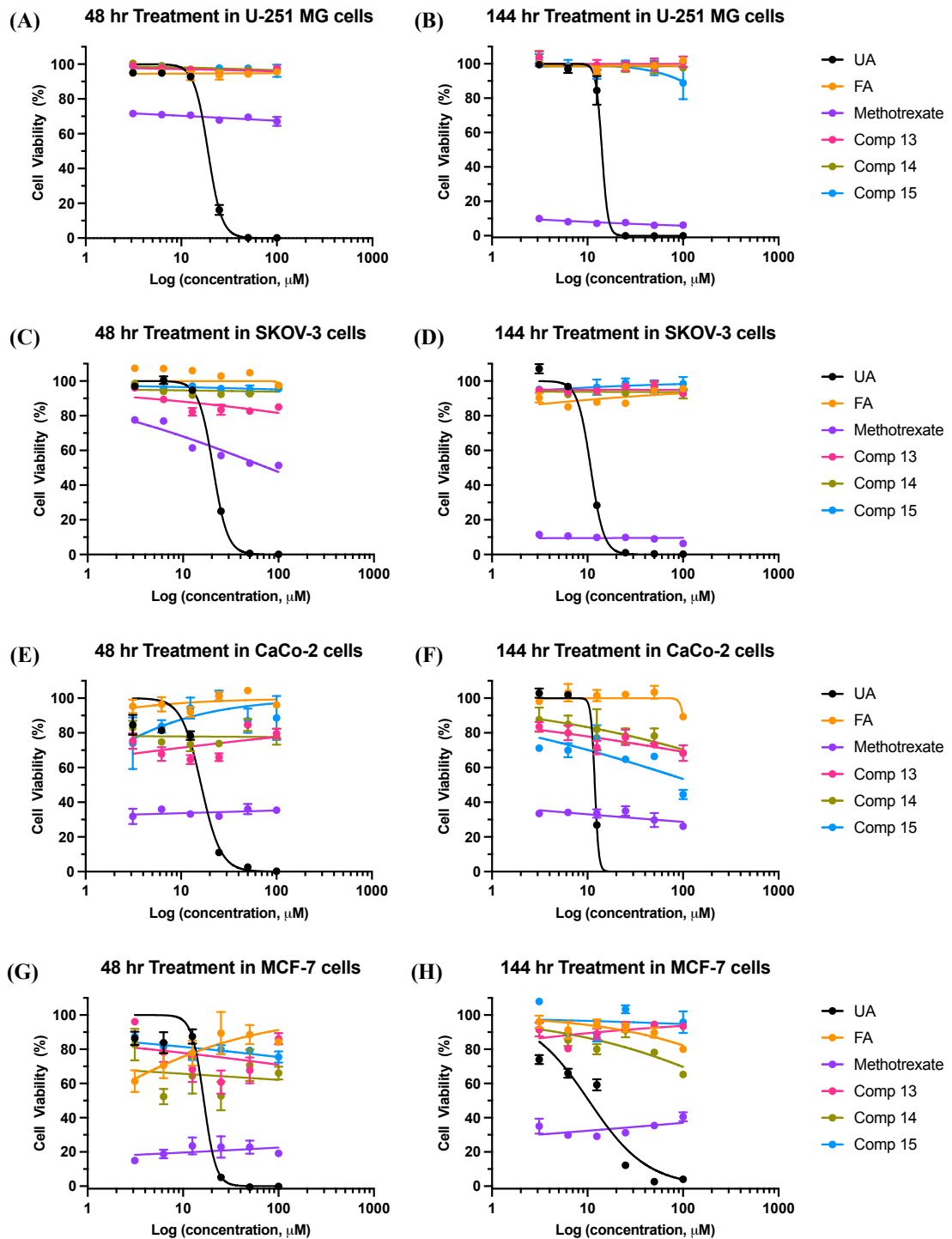


Figure 57. Methotrexate activity in different cancer cell lines. An initial concentration of 100 μM in culture medium was added to cells and serially diluted to different concentrations (100 μM to 3.125 μM). AlamarBlue cell viability assay was then carried out following treatment for 48 and 144 hours. Data shown were normalised to the untreated control and are shown as the % mean \pm SEM. Statistical analysis was carried out using non-linear regression analysis and Two-way ANOVA with Bonferroni post-tests, ($n = 3$) ($P < 0.0001$).

3.3.4 Novel FUA Derivatives Inhibit Cytotoxicity of Ursolic Acid

From results obtained, we know that activity of UA was inhibited in novel FUA derivatives. To further investigate and confirm that it was due to the conjugation of folic acid, making it a larger molecule, we examined if novel FUA derivatives block the activity of UA in U-251 MG cells. All three novel FUA derivatives were tested in U-251 MG cells to determine whether it inhibit the inherent cytotoxic activity of UA. Cells were treated with different concentrations (5 μ M to 40 μ M) of novel FUA derivatives (**13 – 15**) and co-treated with UA IC_{50} determined after 48 and 144 hours treatment, 20 and 10 μ M, respectively. Folic acid was used as a control and it can be seen from **Figure 58** (A, B) that it inhibited the activity of UA in both 48 and 144 hours timepoint. Similarly, all novel FUA derivatives (**13 – 15**) inhibited the cytotoxicity of UA in both 48 and 144 hours timepoints. Hence, it can be concluded that co-treatment of novel FUA derivatives blocks the inherent cytotoxic activity of UA.

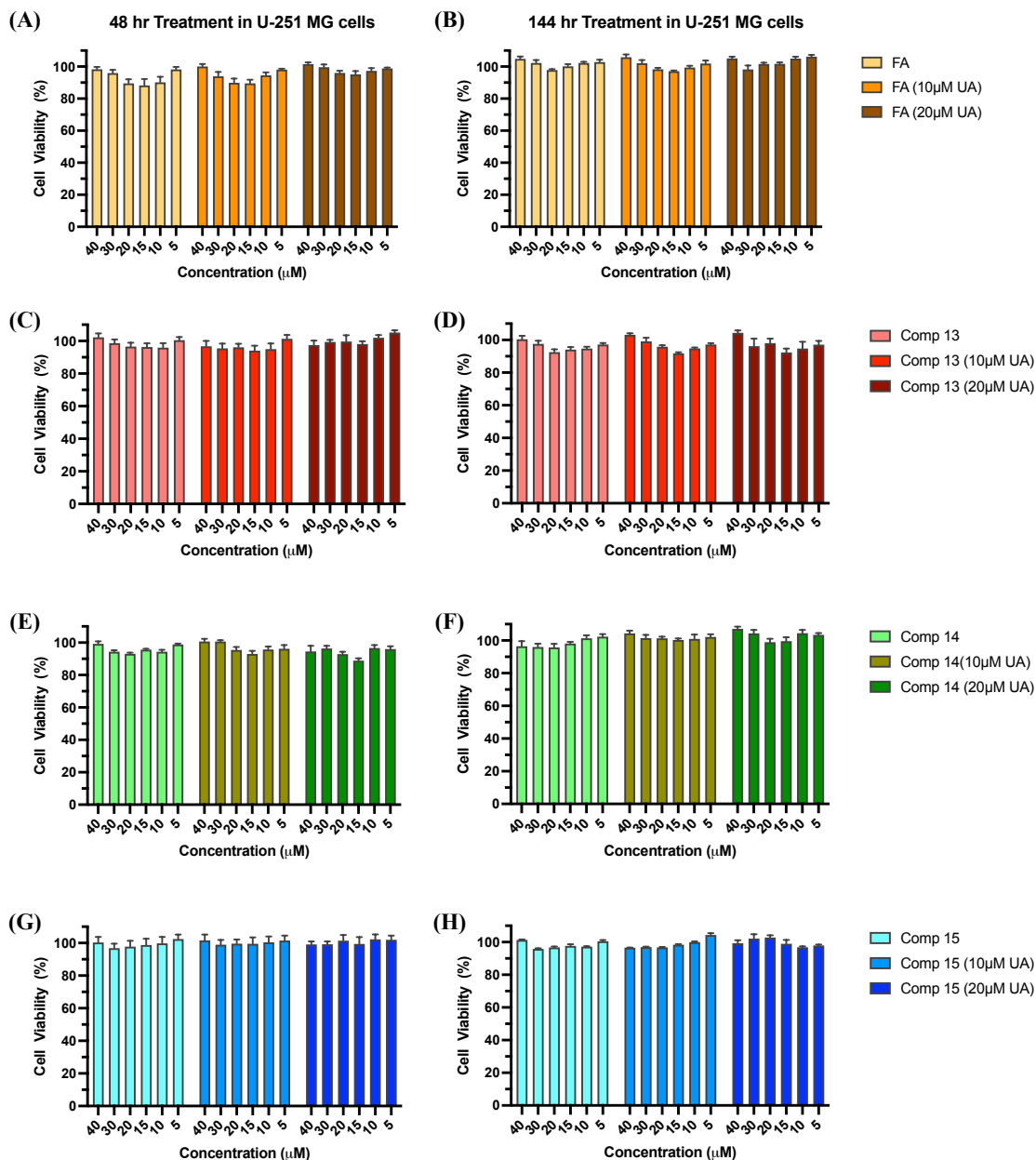


Figure 58. Inhibitory studies of novel FUA derivatives (**13 – 15**) with ursolic Acid. U-251 MG cells were treated with different concentrations of FA and novel FUA derivatives (40 μM to 5 μM) and co-treated with 10 or 20 μM UA. AlamarBlue cell viability assay was then carried out following treatment for 48 and 144 hours. Data shown were normalised to the untreated control and are shown as the % mean \pm SEM (n = 3).

3.3.5 Ultrasound assisted delivery of novel FUA derivatives

The novel FUA derivatives (**13 - 15**) are large with molecular weights > 900 g/mol, which could possibly limit cell membrane permeability. An in-house ultrasound water bath optimised by Carvalho *et al* (2022) was used for this study to assist delivery and enhance cell membrane permeability of the novel FUA derivatives (**13 – 15**). They optimised ultrasound assisted delivery using cell impermeable dye – propidium iodide, and found that optimum settings are: sweep mode, 100 % power (550 W), 25 kHz, with maintained temperature of < 35 °C for 5 and 10 minutes. They showed that ultrasound can open membrane pores for short period of time (1 minute), with very little to no damage to the cells; which can enhance drug delivery across the membrane and into the cell.

The results obtained from this study showed (**Figure 59**) that there were very little to no activity even at 100 µM concentration in all novel FUA derivatives (**13 – 15**). On the other hand, there was an approximately 20% increase in the cytotoxicity of UA control observed in combination with ultrasound (5 and 10 min) at 144 hours timepoint. With all the assays performed in investigating the lost cytotoxicity of UA in novel FUA derivatives (**13 – 15**), it can be concluded that conjugating folic acid to UA completely inhibited its activity.

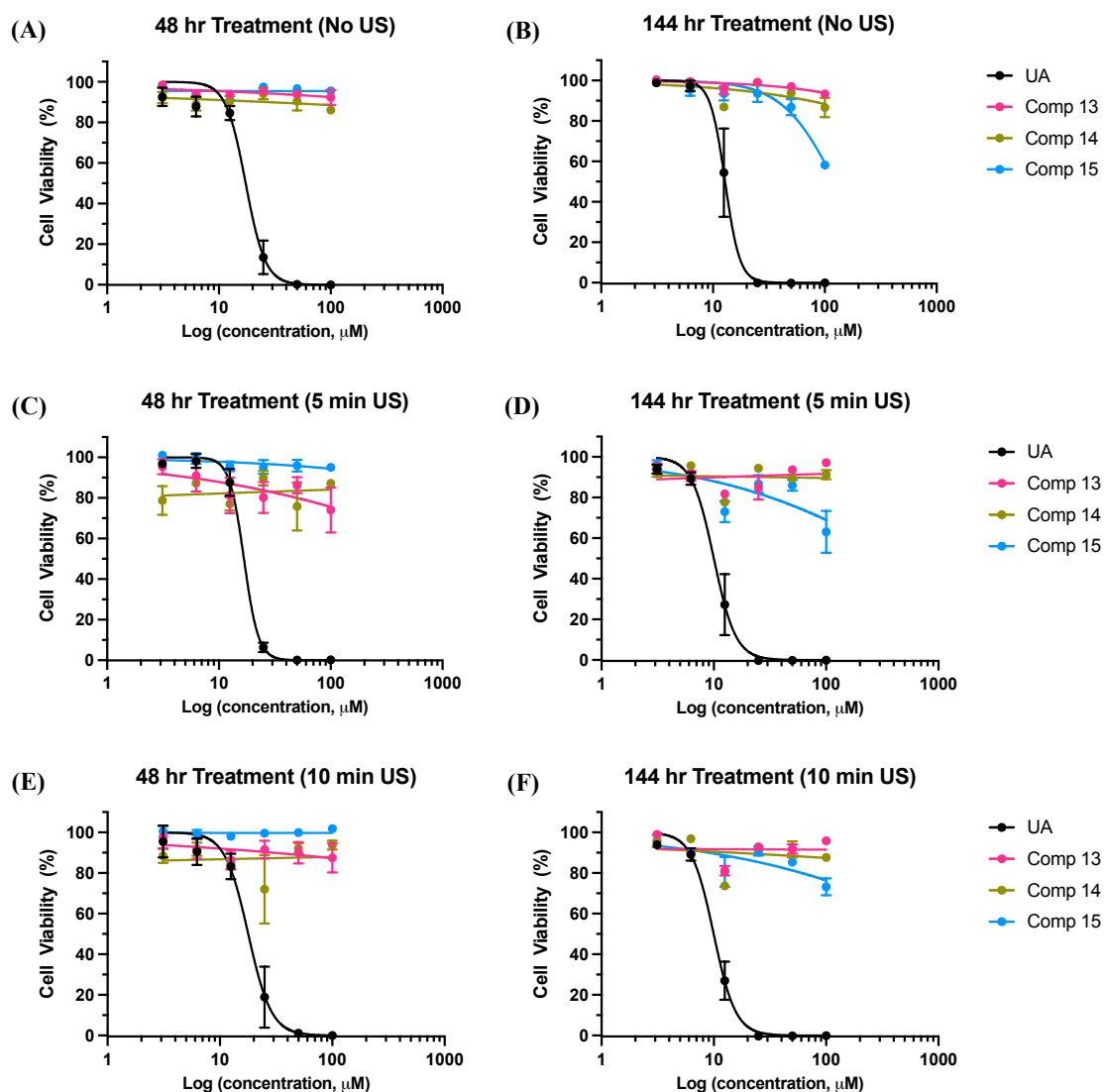


Figure 59. Ultrasound assisted delivery of novel FUA derivatives (**13 – 15**) in U-251 MG cells. An initial concentration of 100 μM in culture medium was added to cells and serially diluted to different concentrations (100 μM to 3.125 μM). Cells were then treated with water bath ultrasound at 25 kHz, and temperature was maintained at $<35^\circ\text{C}$. AlamarBlue cell viability assay was then carried out following treatment for 48 and 144 hours. Data shown were normalised to the untreated control and are shown as the % mean \pm SEM. Statistical analysis was carried out using non-linear regression analysis and Two-way ANOVA with Bonferroni post-tests, ($n = 3$) ($P < 0.0001$).

3.3.6 Increased Concentration of Novel FUA Derivatives

The loss of activity observed above prompted us to test the novel FUA derivatives (**13** – **15**) at higher concentrations in U-251 MG cells to determine passive uptake response. A stock solution of 200 mM of compounds in DMSO was used in this study and was diluted to 1000 μ M in cell culture medium as initial concentration. A 0.5% DMSO vehicle control was used and there was no deleterious effect observed.

It can be seen in **Figure 60** that all novel FUA derivatives exhibited an activity even after 24 hours treatment. The IC_{50} calculated for all novel FUA derivatives in each timepoint is summarised in the **Table 19**. All novel FUA derivatives (**13** – **15**) were found to be more cytotoxic after 144 hours treatment. It is worth noting that compound **15** which has an ethereal oxygen linker, intended to enhance water solubility, is the most cytotoxic out of all the three novel FUA derivatives.

Table 19. The IC_{50} values of novel FUA derivatives in U-251 MG cells at high concentrations.

Compounds	IC_{50} (μ M)		
	24 hr	48 hr	144 hr
Compound 13	910.50 \pm 36.97	592.60 \pm 20.00	315.50 \pm 15.97
Compound 14	753.30 \pm 50.63	548.50 \pm 33.85	327.40 \pm 17.35
Compound 15	570.30 \pm 51.24	495.50 \pm 21.53	200.20 \pm 14.80

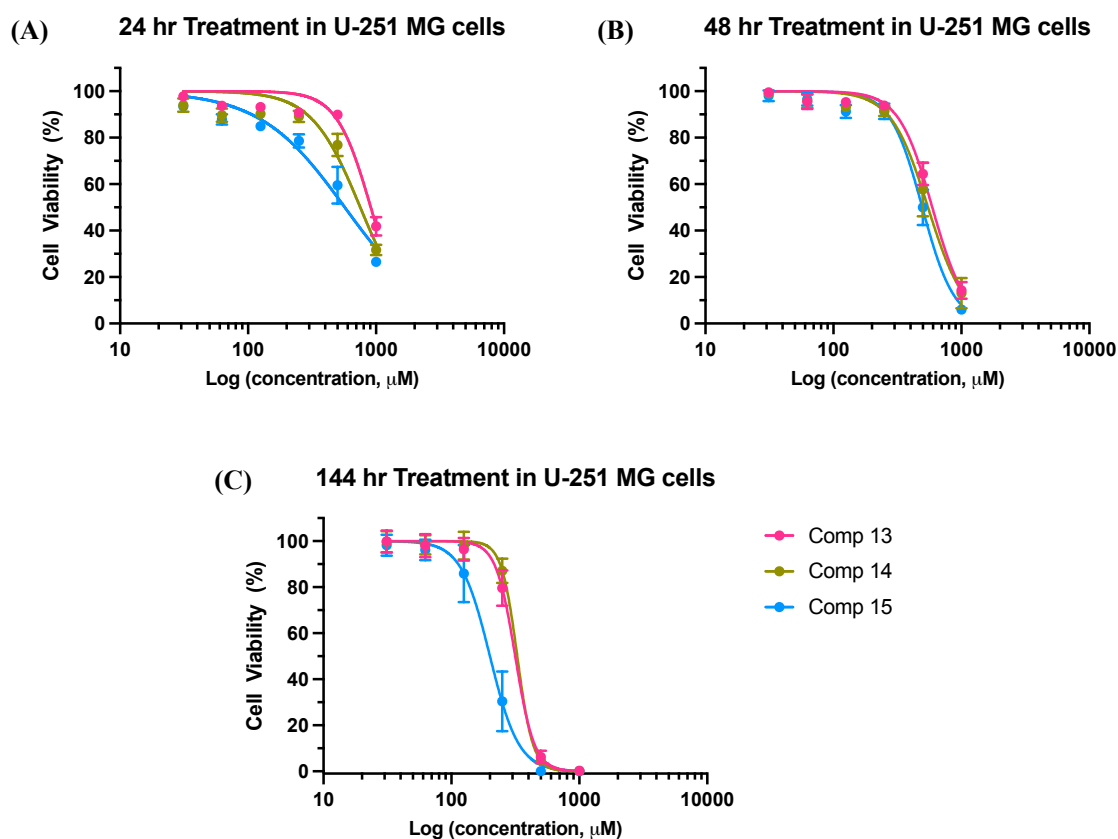


Figure 60. Cytotoxic activity of novel FUA derivatives (**13 – 15**) at higher concentrations in U-251 MG cells. An initial concentration of 1000 μM in culture medium was added to cells and serially diluted to different concentrations (1000 μM to 31.25 μM). AlamarBlue cell viability assay was then carried out following treatment for 48 and 144 hours. Data shown were normalised to the untreated control and are shown as the % mean \pm SEM. Statistical analysis was carried out using non-linear regression analysis and Two-way ANOVA with Bonferroni post-tests, ($n = 3$) (* $P < 0.0001$).

Results obtained from this study suggest that conjugation of folic acid to ursolic acid decreased its cytotoxic effect in U-251 MG cells. The IC_{50} obtained has greatly reduced to more than ten-fold.

3.4 Summary

The *in-silico* pharmacokinetic studies of novel FUA derivatives (**13 – 15**) showed that they violated three of the Lipinski's rule-of-five and physicochemical properties of UA was reduced in terms of predicted bioavailability. However, its lipophilicity slightly improved. In addition, novel FUA derivatives (**13 – 15**) were predicted to have a lower BBB penetration bioavailability and synthetic accessibility than UA, and they were also predicted to be P-gp substrates. Nevertheless, although only one novel FUA derivative bound to target protein VRK1, the molecular docking studies obtained for FR α showed that novel FUA derivatives were predicted to bind to FRs with binding pocket interactions similar to those in the crystal structure, indicating that UA does not interfere with binding. Hence, compounds can still be facilitated by RME uptake.

All attempts in testing novel FUA derivatives (**13 – 15**) using different media (free, low and medium folate) and different cell lines (U-251 MG, SKOV-3, CaCo-2, MCF-7, A431, SW480 cells) showed that cytotoxicity of UA was inhibited in all three novel UA derivatives (**13 – 15**). The methotrexate control that was used confirmed that the FR is active on all main cell lines used in this study. Hence, was not the issue for the lost cytotoxicity. Moreover, the ultrasound assisted delivery performed also did not enhance the novel FUA derivatives' uptake in cells. This prompted the test of novel FUA derivatives at higher concentrations (1000 to 31.25 μ M) to determine passive uptake response in U-251 MG cells. Results obtained has revealed that the cytotoxicity of novel FUA derivatives was decreased by more than ten-fold in comparison to UA. The lost biological activity of UA when conjugated to folic acid could be due to a lot of factors. As revealed in the pharmacokinetic studies, although it has improved lipophilicity of UA, novel FUA derivatives (**13 – 15**) violated 3 of Lipinski's rule-of-five.

CHAPTER 4

RESULTS & DISCUSSION 3

“The SAR and Biological Assessment of Novel UA Derivatives.”

4.0 The Activity of Boc and Deprotected Conjugates

The synthesis of novel FUA derivatives were composed of 4 steps and the study in **Chapter 3 – Results and Discussion 2**, has revealed that the inherent cytotoxic activity of UA was lost in all three novel FUA derivatives (**13 – 15**). Hence, to investigate the reason for the lost cytotoxicity of novel FUA derivatives (**13 – 15**), we looked at all our starting materials and intermediates. In this study, promising results were obtained from compounds in steps 2 and 3 of the synthesis from **Chapter 2 - Results and Discussion 1**. This prompted our study to explore the biological properties and activities of these intermediates in which we then called novel UA derivatives (**7 – 12; Figure 61**).

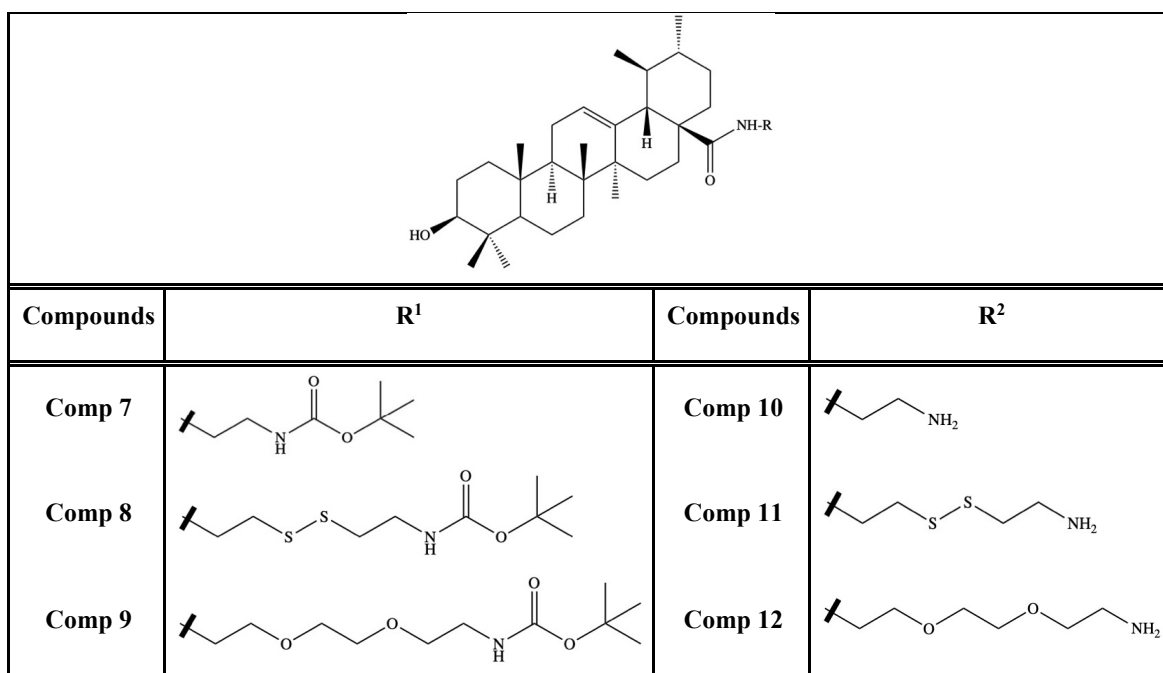


Figure 61. The structures of the novel UA derivatives (**7 – 12**) with Boc-protected (R1) and deprotected (R2) ends. All compounds structures drawn using ChemDraw Professional v16.0.

Research Questions:

- Can we determine if starting materials and/or intermediates contributed to the lost cytotoxicity of novel FUA derivatives (**13 – 15**)?
- Could these novel UA derivatives retain/enhance the inherent cytotoxic, anti-migratory and anti-proliferative effects of UA in a panel of cancer cell lines, specifically in U-251 MG GBM cells? In addition, can we investigate the apparent cell death mechanisms involved in U-251 MG cells?

Aims and Objectives:

- To assess the cytotoxic activity of all the starting materials and intermediates (novel UA derivatives) in a range of cancer cell lines.
- To explore the structural activity relationship (SAR) of UA and novel UA derivatives that were designed to improve its activity and bioavailability (predicted ADMET profile), and utilise molecular docking studies against proposed target for UA - VRK1, with an in-depth analysis of predicted interactions.
- To study the biological profiles of novel UA derivatives in 2D and 3D cell culture models.
- To investigate the cell-death mechanism(s), anti-migratory and anti-proliferative properties, of novel UA derivatives.

4.1 The activity of Boc-protected and deprotected UA-linkers

Further investigation was done due to the increased cytotoxic concentration of novel FUA derivatives in comparison to UA. The compounds generated from step 2 (*N*-Boc protected UA-diamines; **Figure 32**) and step 3 (deprotected UA-diamines; **Figure 34**) of the synthesis (**Scheme 5**) were tested to determine if it contributed to the lost cytotoxicity. These conjugates were tested in U-251 MG cells at 100 μ M to 3.125 μ M concentrations for 48 and 144 hours. The ethylenediamine linker compounds were compounds **7** and **10**, Boc-protected and deprotected, respectively. Whereas compound with disulphide linker were compounds **8** and **11**, Boc-protected and deprotected, respectively. Lastly, compounds with ethereal oxygen linker were compounds **9** and **12**, Boc-protected and deprotected, respectively. The calculated IC₅₀ cytotoxicity of each of the compounds after 48 and 144 hours in U-251 MG cells are summarised in **Table 20**. It can also be seen in **Figure 62** that most of intermediates exhibited a more than two-fold increase in cytotoxicity in comparison to UA, which is more prominent after 144 hours treatment. It is also interesting that Boc-protected compounds has delayed cytotoxicity compared to the deprotected compounds. Due to the results obtained in this study, our research has focused on the investigation of these compounds in which from this point onward were called novel UA derivatives (**7 – 12**).

Table 20. The IC₅₀ Cytotoxicity of novel UA derivatives (**13 – 15**) in U-251 MG cells.

Compound	48 hr IC₅₀ (μM)	144 hr IC₅₀ (μM)
UA	16.46 ± 0.89	12.83 ± 0.72
Comp 7	134.10 ± 79.64	6.67 ± 0.51
Comp 8	1374 ± 1703.82	117.2 ± 29.46
Comp 9	117.4 ± 58.75	8.61 ± 0.42
Comp 10	7.58 ± 0.39	5.40 ± 0.43
Comp 11	32.10 ± 3.50	14.59 ± 1.69
Comp 12	14.22 ± 1.02	7.66 ± 0.63

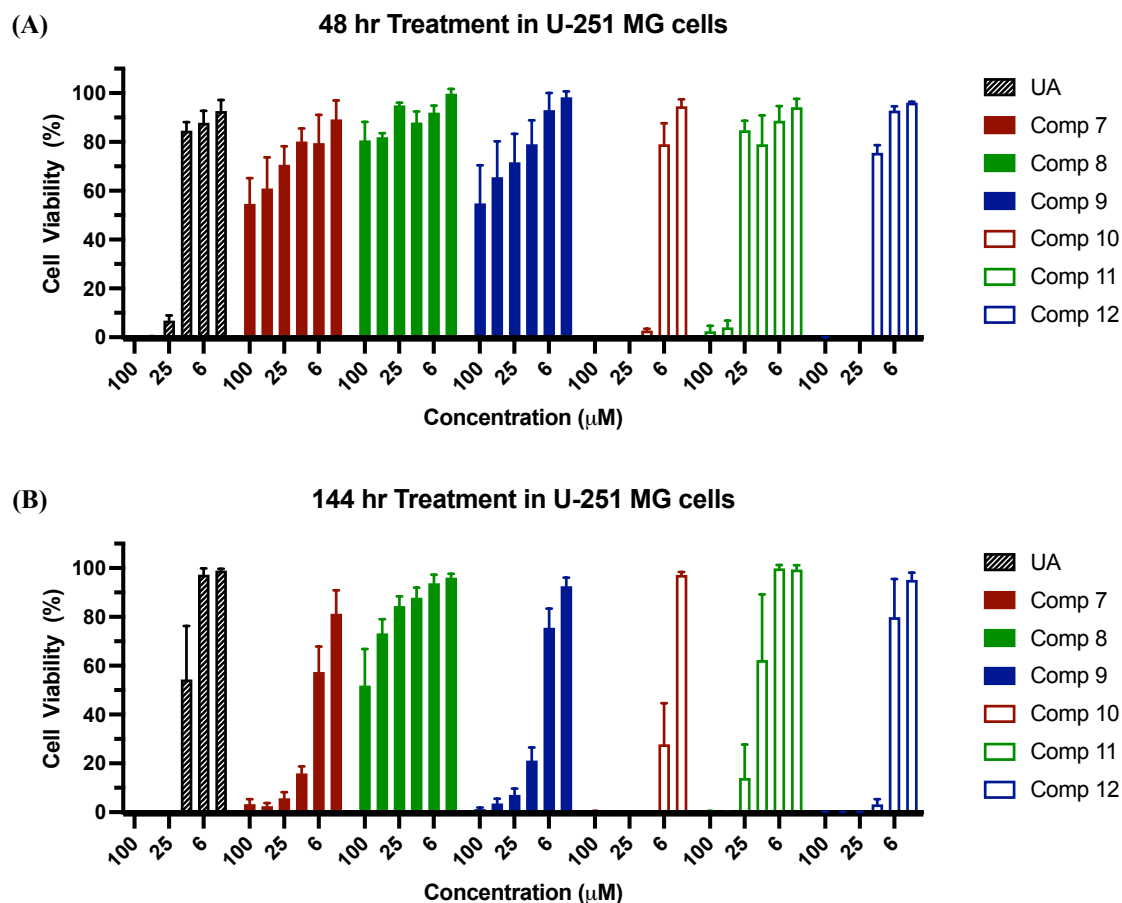


Figure 62. Cytotoxic activity of intermediates (novel UA derivatives) in U-251 MG cells. An initial concentration of 100 µM in culture medium was added to cells and serially diluted to different concentrations (100 µM to 3.125 µM). AlamarBlue cell viability assay was then carried out following treatment for 48 and 144 hours. Data shown were normalised to the untreated control and are shown as the % mean \pm SEM, (n = 3).

4.1.1 Cytotoxic Activity of Linkers

The cytotoxicity of the linkers were studied to determine if it contributed to the enhanced activity observed from the novel UA derivatives (7 – 12) in U-251 MG cells. We looked at the three different linkers that were used and the *N*-Boc protected linkers (Compound 1 – 3). It can be seen in Figure 63 that both the deprotected (A, B) and the *N*-Boc protected (C, D) at two different timepoints, 48 and 144 hours, did not exhibit any activity. Hence, shows that the linkers does not contribute to any activity observed for the novel UA derivatives (7 – 12).

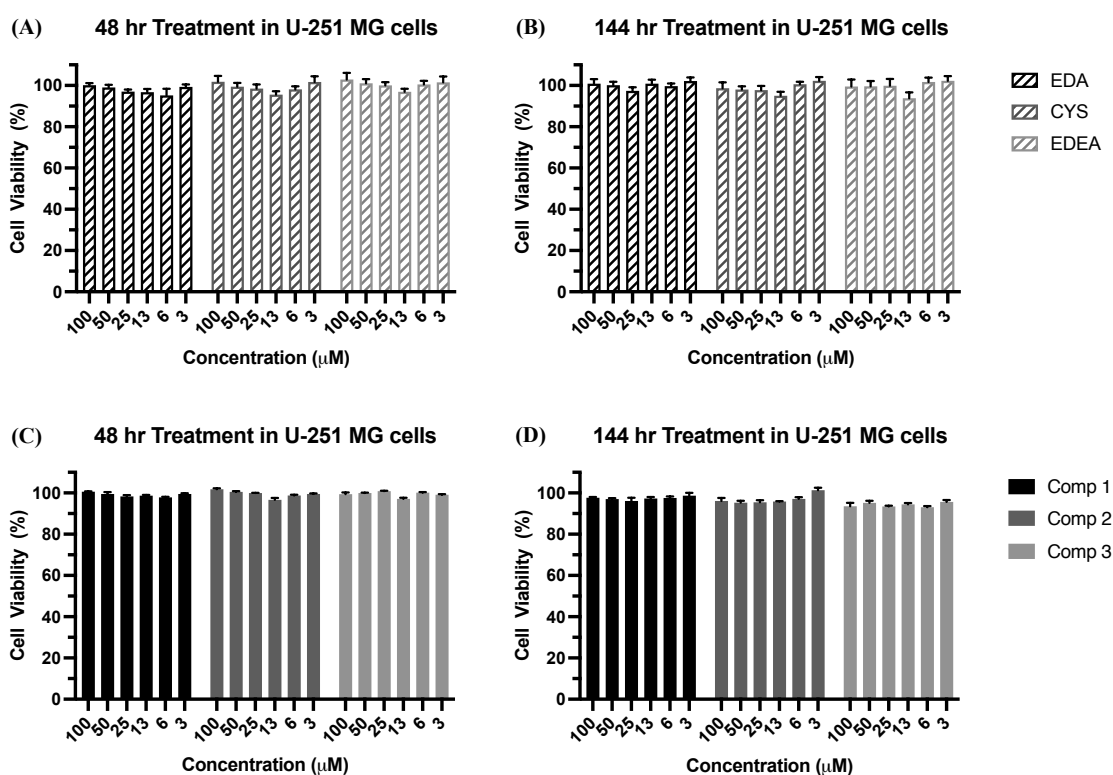


Figure 63. Cytotoxicity of Linkers. An initial concentration of 100 μ M in culture medium was added to cells and serially diluted to different concentrations (100 μ M to 3.125 μ M). AlamarBlue cell viability assay was then carried out following treatment for 48 and 144 hours. Data shown were normalised to the untreated control and are shown as the % mean \pm SEM, (n = 3).

4.2 The *in-silico* studies of Novel FUA Derivatives

The activity of intermediates observed in section 4.1 U-251 MG cells opened a new avenue for this project for novel UA derivatives as potential therapeutic agents for cancer. Similar to the *in-silico* studies conducted in section 3.1, the ADME-related physicochemical properties of novel UA derivatives (**7 – 12**) were compared to UA using SwissADME. Additionally, molecular docking studies to a known target protein of UA, VRK1, was investigated.

4.2.1 SwissADME Bioavailability Radar

The results of Lipinski's parameters, drug-likeness as well as the *in-silico* ADMET screening predicted for UA and novel derivatives of UA are depicted in **Table 21**. The SwissADME 'bioavailability radar' in **Figure 64** shows that although still slightly outside of range, deprotected compounds (**10 – 12**) slightly improve lipophilicity of UA (XLOGP3: 7.34) – compound **10** (XLOGP3: 6.15); compound **11** (XLOGP3: 6.84); compound **12** (XLOGP3: 5.86). In addition, solubility of UA (ESOL Log *S*: -7.24) was also slightly improved in the predicted values obtained from compounds **10** and **12** with ESOL Log *S* -6.54 and -6.51, respectively. However, compound **12** has higher molecular weight (586.89 g/mol) and rotatable bonds (10) in comparison to UA.

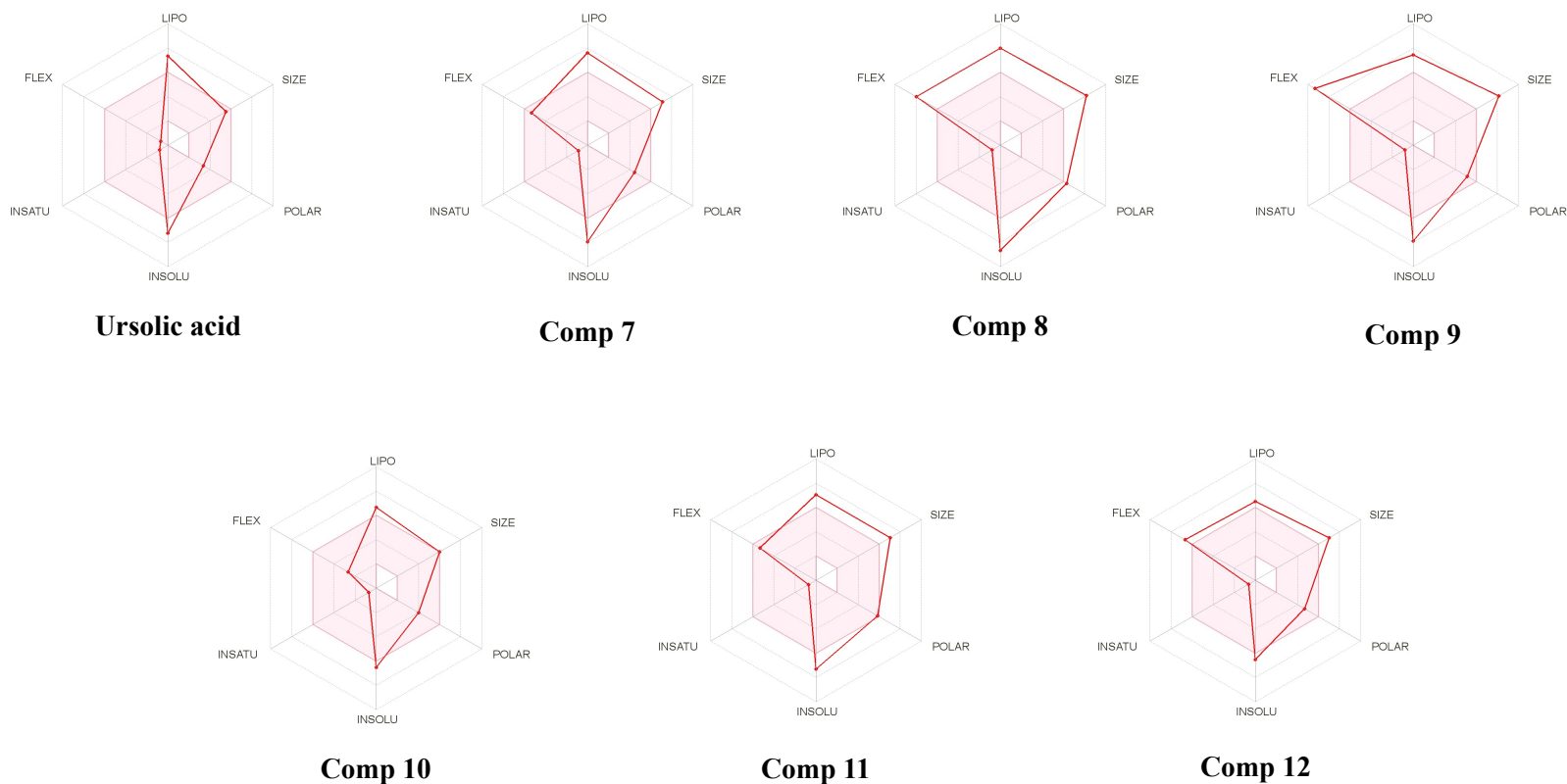


Figure 64. The bioavailability radar (pink area exhibits optimal range of particular property) of UA and novel UA derivatives (7 – 12) evaluated using SwissADME. Lipophilicity (LIPO): XLOGP3 between -0.7 and +5.0; molecular weight (SIZE): MW between 150 and 500 g/mol; polarity (POLAR) TPSA between 20 Å² and 130 Å²; Solubility (INSOLU): log *S* not higher than 6; Saturation (INSATU): fraction of carbons in sp³ hybridization between 0.25 and 1; and flexibility (FLEX): no more than 9 rotatable bonds.

Table 21. Physicochemical and pharmacokinetic properties, and drug-likeness predictions of novel UA derivatives (7 – 12). Colours are represented as: within the predicted range (green), slightly above the predicted range (orange), and out of predicted range (red). *MW in Da.

Compound	Physicochemical Properties						Lipophilicity			Solubility Log S (ESOL)	Pharmacokinetics			Bioavailability Score	Synthetic Accessibility
	MW	HBD	HBA	No. of rotatable bonds	Fraction Csp3	TPSA	XLOGP3	MLOGP	Consensus Log P		GI absorption	BBB permeant	CYP3A4		
UA	456.70	2	3	1	0.9	57.53	7.34	5.82	5.93	-7.23	Low	No	No	0.85	6.21
Comp 7	598.90	3	4	8	0.89	87.66	7.80	5.33	6.55	-7.94	Low	No	Yes	0.17	6.90
Comp 8	691.08	3	4	12	0.9	138.30	8.48	5.68	7.31	-8.68	Low	No	Yes	0.17	7.58
Comp 9	687.00	3	6	14	0.9	106.10	7.50	4.43	6.61	-7.90	Low	No	Yes	0.17	7.75
Comp 10	498.78	3	3	4	0.91	75.35	6.15	4.94	5.29	-6.54	High	No	No	0.55	6.07
Comp 11	590.97	3	3	8	0.91	126.00	6.84	5.31	6.20	-7.29	Low	No	No	0.17	6.85
Comp 12	586.89	3	5	10	0.92	93.81	5.86	4.03	5.42	-6.51	Low	No	No	0.55	6.89

4.2.2 Physicochemical Properties of Novel UA Derivatives

As mentioned in 3.1.2, Lipinski's rule states that molecules < 500 g/mol can pass through cell membrane more easily. In this study, all novel UA derivatives has MW > 500 g/mol, except compound **10** which has MW of 498.78 g/mol, slightly higher than UA (456.70 g/mol) but still within the predicted acceptable range. Out of the five predicted lipophilicity models in SwissADME, XLOGP3, MLOGP and Consensus Log *P* values were used in this study which were represented in the bioavailability radar and Lipinski's rule. The SwissADME predicted lipophilicity in accordance to Lipinski's rule-of-five recommended that MLOGP should be ≤ 4.15. All novel UA derivatives (**7 – 12**) was found to have slightly lower MLOGP values than UA (5.82) but are outside of recommended range, except compound **12** which is within the acceptable range (MLOGP 4.03) (**Table 21**). It is noteworthy that compound **12** is a deprotected compound that has an ethereal oxygen linker which aim to improve water solubility. However, the consensus Log *P* (average of all predicted lipophilicity model) obtained were all > 5, but compounds **10** and **12** slightly improved the lipophilicity compared with UA, which is also depicted in the 'bioavailability radar' (**Figure 64**). The water solubility ESOL log *S* predicted for novel UA derivatives were all > 6 (poorly soluble), but compounds **10** and **12** slightly improved solubility of UA as discussed in bioavailability radar section above.

4.2.3 BBB penetration, Bioavailability and Synthetic Accessibility of Novel UA Derivatives

Predicted TPSA values of compounds has gained prominence in medicinal chemistry, where TPSA value of $< 140 \text{ \AA}^2$ is a good predictor of intestinal absorption, and $< 60 \text{ \AA}^2$ indicates good BBB penetration (Maximo da Silva *et al.*, 2015). All novel UA derivatives (**7 – 12**) have TPSA values of $< 140 \text{ \AA}^2$ indicating good intestinal absorption. Whereas UA was found to have TPSA value of $< 60 \text{ \AA}^2$, indicating that it penetrates the BBB which is beneficial for GBM treatment. This confirms the study by Chen *et al* (2011) where they found UA present in plasma and tissue samples of Sprague-Dawley rats at 0.5 ng mL^{-1} or 4.0 ng g^{-1} and reliably assayed by HPLC-MS using a sample injection technique. The UA present in brain implies that it can cross the BBB *in vivo* (Chen *et al.*, 2011).

In contrast to other predictions, the BBB permeation predicted by SwissADME using Brain Or IntestinaL EstimatedD permeation (BOILED-Egg) model shows that UA does not permeate the BBB (**Figure 65**). The ADME properties *in vivo* predicted using the Egan BOILED-Egg permeation predictive model diagram, includes passive human human intestinal absorption (HIA) and BBB permeation. BOILED-Egg method is proposed as an accurate predictive model which computes the lipophilicity and polarity of small molecules (Daine and Zoete, 2016; Daina *et al.*, 2017; Bojarska *et al.*, 2020). The BBB is a microvascular endothelial layer of cells surrounding the CNS. It is a structural and chemical barrier preventing various medicines from entering the brain (Bojarska *et al.*, 2020). The predicted result obtained showed that BBB permeability test performed on UA and novel UA derivatives (**7 – 12**) demonstrated lack of BBB permeability. Nevertheless, prediction of HIA was high for compound **10** (in the white

region) (**Figure 65**). UA and the rest of the novel UA derivatives (**7 - 9; 11 - 12**) were predicted to have low HIA. Compound **8** was predicted to be out of range and hence cannot be seen in the BOILED-Egg diagram. Similarly, novel FUA derivatives (**13 – 15**) were also out of range and hence were not reported in Chapter 3.

The BOILED-Egg diagram prediction was based on lipophilicity and apparent polarity of compounds. Results obtained for novel FUA derivatives and compound **8** were outside of the range suggested by SwissADME. It is worth noting that both compartments of the BOILED-Egg are not mutually exclusive and the outside grey region are molecules with properties implying predicted low absorption and limited brain penetration (Daina, Michielin and Zoete, 2017). As mentioned previously, UA was classified as a class IV drug by BSC due to its low solubility, difficulty permeating membranes and limited HIA penetration (Jinhua, 2019; Yu *et al.*, 2020). This correlates as to why UA is in the grey region of the BOILED-Egg. In addition, studies have shown that UA was absorbed in intestinal tract by passive diffusion, with very fast absorption rate. In spite of that, studies of UA have shown that some traces were still detected in human plasma (Nguyen *et al.*, 2021) and brain (Chen *et al.*, 2011). Results obtained from this study warrants an investigation on the activity of novel UA derivatives in cancer cells.

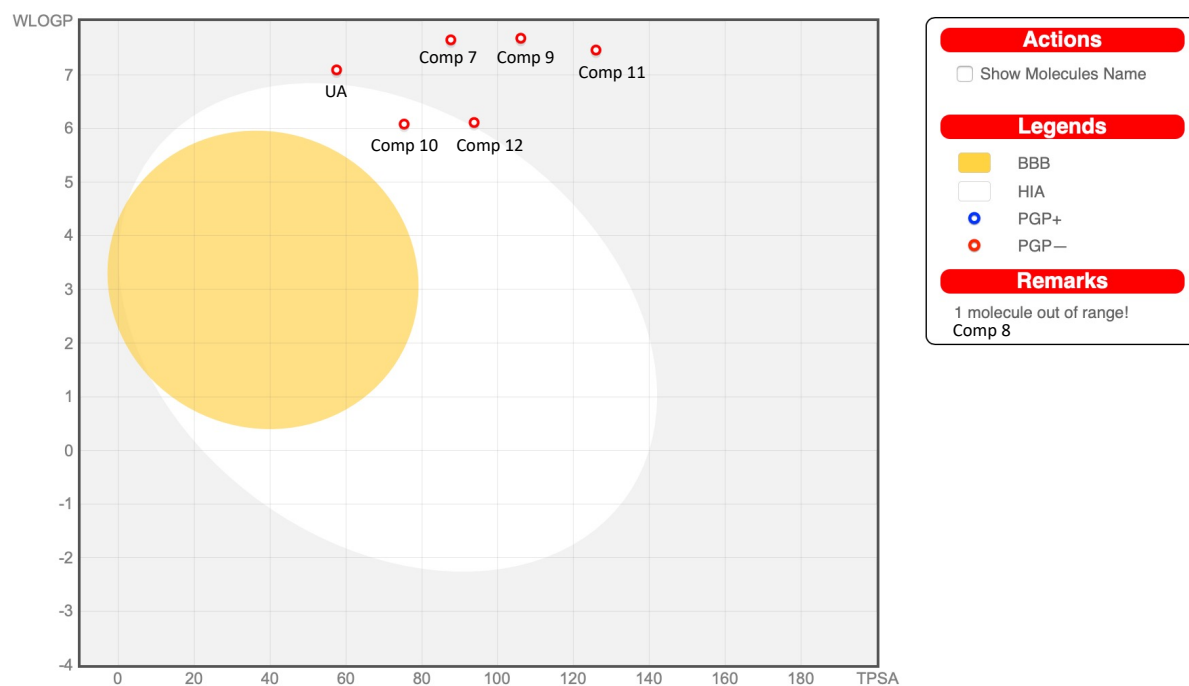


Figure 65. The predicted BOILED-Egg diagram of UA and novel UA derivatives (7 – 12) obtained from SwissADME tool for the evaluation of passive human gastrointestinal absorption (HIA), brain penetration (BBB) and P-glycoprotein (P-gp) activity in presence of the molecule. Note that in the remarks, 1 molecule is out of range – compound 8.

Cytochrome P450 enzymes found in the gut and liver metabolise the majority of drugs through oxidation. It can either be induced or inhibited by various drug substances, resulting in drug interaction, leading to toxicity or reduction in therapeutic effect (Durán-Iturbide *et al.*, 2020; Beck *et al.*, 2021). Consequently, the interaction (induction or inhibition) of compounds with any of CYP isoenzymes could lead either to fast metabolism (when induced) or bioaccumulation of drugs (when inhibited) in the body (Ji *et al.*, 2020). CYP3A4 is the most widely expressed and clinically significant cytochrome responsible for 30.2% biotransformation of xenobiotics that undergo hepatic clearance (Durán-Iturbide *et al.*, 2020). CYP3A4 has been studied to metabolise 60% of drugs currently on the market and a number of anti-cancer drugs (Kawahara *et al.*, 2021). All

the Boc-protected novel UA derivatives (**7 – 9**) were predicted to be an inhibitor of CYP3A4 (**Table 21**). As a result, Boc-protected compounds activity can either be amplified or weaken if modified by CYP3A4.

In relation to this, the Abbott bioavailability score for UA as mentioned in section **3.1.3** is 0.85, indicating 85% probability of rat bioavailability. However, due to having predicted two violations of Lipinski's rule-of-five, compounds **7, 8, 9** and **11** were found to be 0.17 (17%). On the other hand, compounds **10** and **12** were predicted to have a value of 0.55 which implies the compliance of Lipinski's rule-of-five with a 55% probability of rat bioavailability. In addition, synthetic accessibility score was predicted which ranges from 1 (very easy) to 10 (very difficult). All novel UA derivatives (**7 – 9; 11 – 12**) were predicted to be < 7 (moderately difficult), with compound **10** (6.07) having a slightly better synthetic accessibility than UA (6.21) (**Table 21**).

The obtained predicted values of *in silico* pharmacokinetic studies of novel UA derivatives (**7 – 9; 11**) violated two (MW and MLOGP) of the Lipinski's rule-of-five, except for compounds **10** (MLOGP) and **12** (MW) which only violated one. Both compounds **10** and **12** also improved most of the ADME-related physicochemical properties of UA, most especially its lipophilicity and solubility. All novel UA derivatives were not predicted to cross the BBB, but compound **10** was predicted to have high HIA and has slightly better synthetic accessibility than UA.

4.3 The Pharmacodynamic Studies of Novel FUA Derivatives

In this study, the synthesised six novel UA derivatives (**7 – 12**; **Figure 61**) were docked and analysed for interactions to VRK1. The six derivatives consist of three different types of linkers and divided into two groups – Boc-protected and deprotected compounds. The VRK1 (PDB ID: 6BU6) was used to compare the predicted binding affinity of UA and novel UA derivatives (**7 – 12**).

4.3.1 The Molecular Docking of Novel UA Derivatives in VRK1

The visualisation and interaction analysis for UA with VRK1 was explained in section **3.2.2** The Molecular Docking of Novel FUA Derivatives in VRK1. A flexible docking was performed and successfully docked UA to the binding pocket (**Figure 49**) with the hydroxyl bound deep into the binding pocket and forms a strong hydrogen bond interaction with K71 and the carboxyl group exposed. UA was also found to have van der Waals interaction with M131 (hydroxyl); R133 (ring B); G44, Q, Q45 and D137 (ring E); G135 and S136 (carboxylic acid). In addition, alkyl and pi-alkyl interactions were observed at ring A (F48, I51, V69, F134, V196), ring B (I43, I51, V69), ring D (I43) and ring E (F48, L184). The predicted binding affinity obtained for UA was -8.8 to -6.6 kcal/mol as discussed in section **3.2.2.2**.

The six novel UA derivatives (**7 – 12**) were docked to VRK1 to determine if we can retain or improve the binding affinity of UA. All six novel UA derivatives (**7 – 12**) were docked

successfully using flexible docking. Number of docking poses and predicted binding affinities are summarised in **Table 22** below.

Table 22. Number of docking poses and predicted binding affinity of novel UA derivatives (7 – 12).

Compounds	Docking Poses	Predicted Binding Affinity (kcal/mol)
UA	7	-8.8 to -6.6
Compound 7	9	-7.5 to -4.8
Compound 8	8	-7.2 to -5.3
Compound 9	9	-6.3 to -4.8
Compound 10	9	-6.9 to -5.0
Compound 11	9	-6.5 to -4.4
Compound 12	8	-6.8 to -4.4

To select a functionally relevant docking confirmation, pose 1 was chosen for all six compounds for comparison, compound **7** (**Figure 67**), compound **10** (**Figure 68**), compound **8** (**Figure 69**), compound **11** (**Figure 70**), compound **9** (**Figure 71**), and compound **12** (**Figure 72**) with binding affinities of -7.5 kcal/mol, -6.9 kcal/mol, -7.2 kcal/mol, -6.5 kcal/mol, -6.3 kcal/mol, and -6.8 kcal/mol, respectively. It can be seen that boc-protected compounds, compounds **7** and **8** have the highest predicted binding affinity

out of all the six novel UA derivatives, followed by the deprotected compounds, compounds **10** and **12**. From the results obtained, it can be seen that all novel UA derivatives are bound slightly out of the binding pocket in comparison to UA (**Figure 66**). Hence, has lower predicted binding affinity and lost some of the interactions with residues important for binding. However, compound **9** was found oriented in a different position, with the linker end oriented near the binding pocket. As a result, it produced the lowest predicted binding affinity.

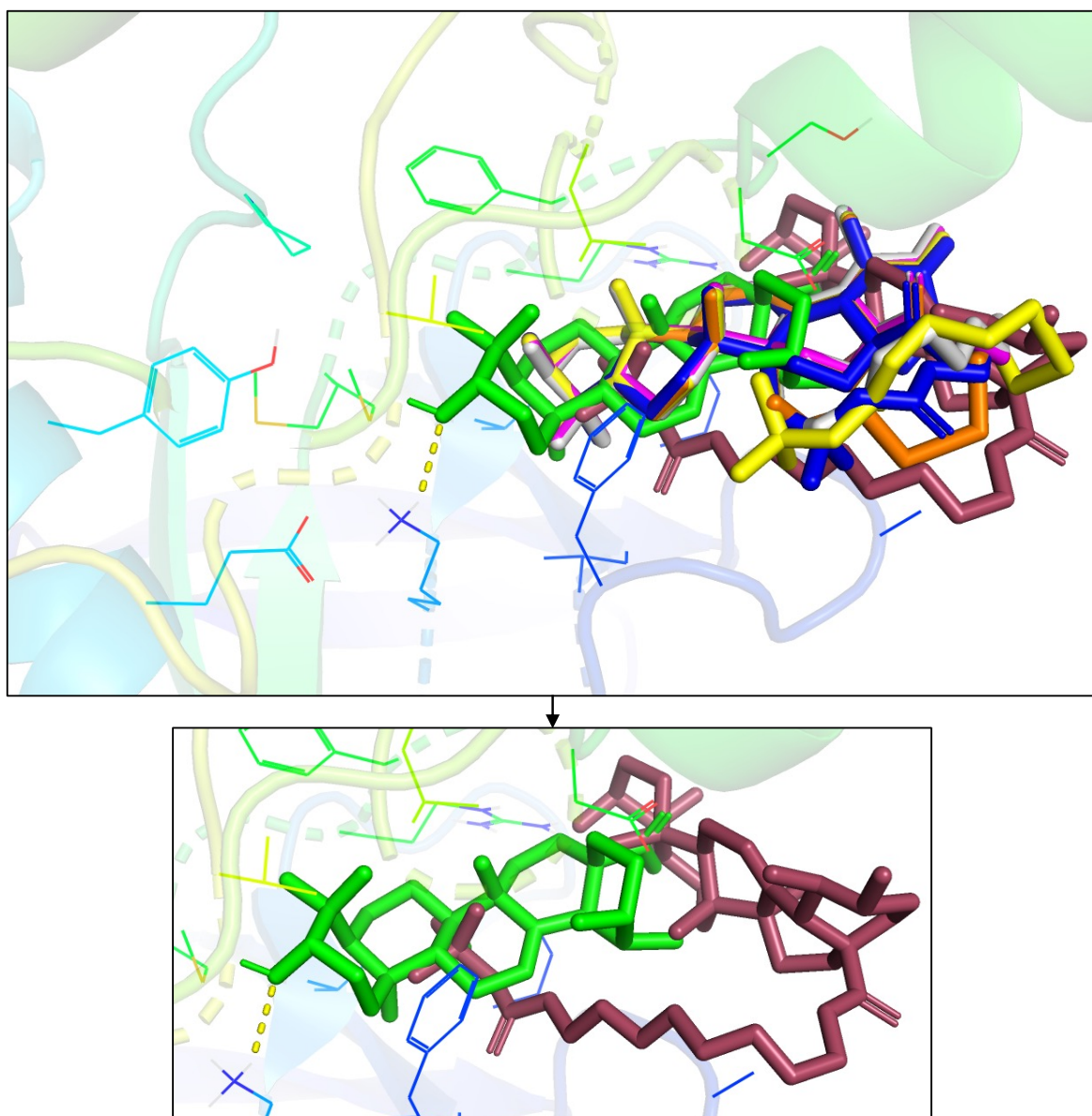


Figure 66. The 3D overlay of UA (green), compound 7 (blue), compound 10 (magenta), compound 8 (yellow), compound 11 (orange), compound 9 (raspberry) and compound 12 (grey) docked to VRK1 (PDB ID: 6BU6). The image was generated in PyMOL™ v2.4.1.

For the compounds with ethylenediamine linker, compounds **7** (**Figure 67**) and **10** (**Figure 68**), both lost the conventional hydrogen bond interaction with K71 residue, which is known to be one of the important residues for binding (Kim *et al.*, 2015; Couñago *et al.*, 2017; Ngow *et al.*, 2018; Serafim *et al.*, 2019). Alkyl and pi-alkyl interactions were observed with ring A of UA in both compounds with I43, F48, I51 and V69 which was also observed in UA. Hence, both compounds still interact with some of the important residues in the binding pocket. In addition, compound **10** also has alkyl and pi-alkyl interaction with F48 in ring B and L184 with the methyl group in between ring B and C. Furthermore, compound **10** had alkyl and pi-alkyl interaction with R133. The van der Waals interaction around the UA was the same for both compounds **7** and **10**; interaction with G47 and S181 observed in the boc-protected end of compound **7**.

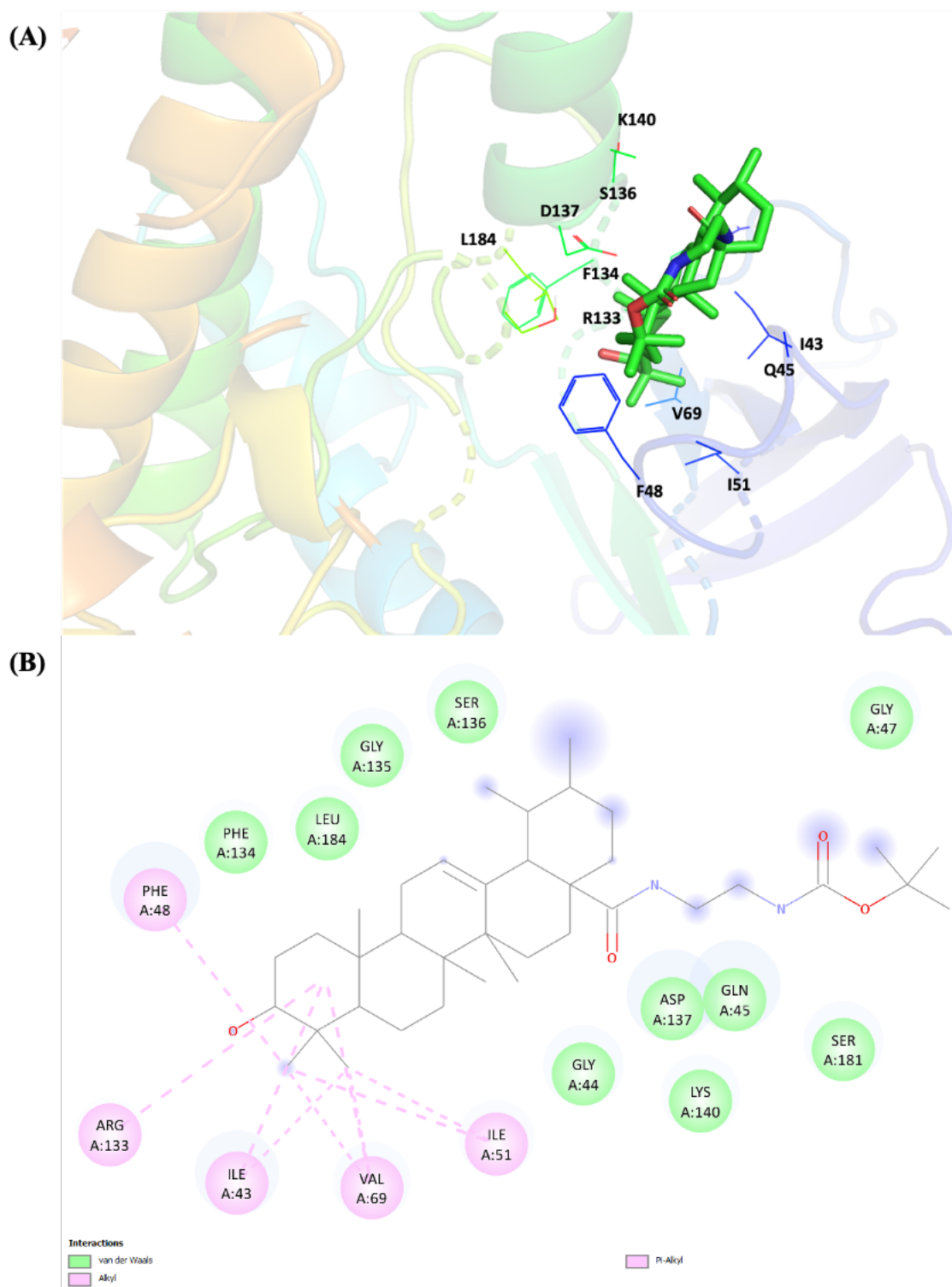


Figure 67. The (A) 3D image and (B) 2D interaction map of compound **7** docked to VRK1 (PDB ID: 6BU6). The 3D image was analysed and rendered in PyMOL™ v2.4.1 and the 2D interaction map was generated in BIOVIA DS Visualizer 2020.

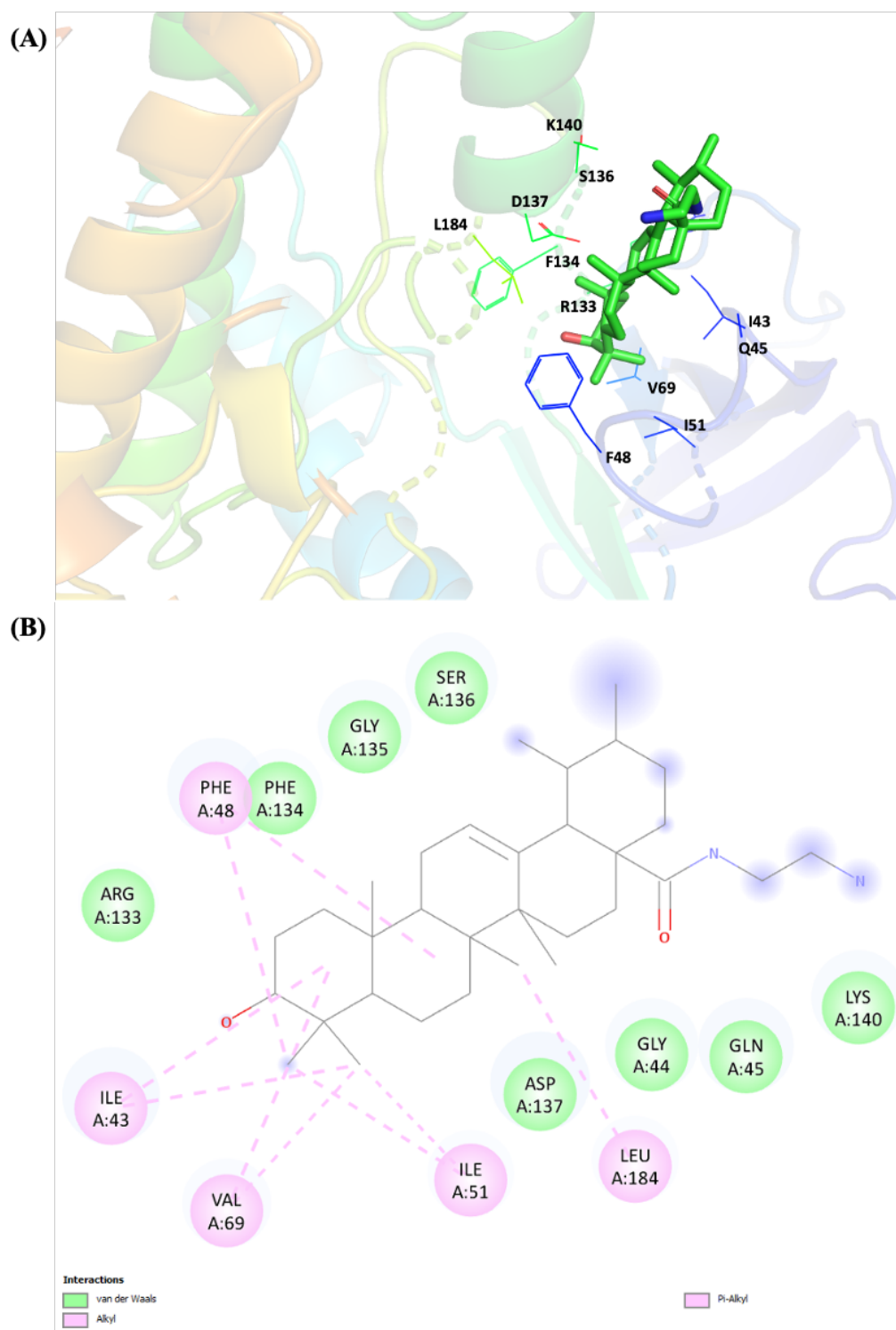


Figure 68. The (A) 3D image and (B) 2D interaction map of compound **10** docked to VRK1 (PDB ID: 6BU6). The 3D image was analysed and rendered in PyMOL™ v2.4.1 and the 2D interaction map was generated in BIOVIA DS Visualizer 2020.

Similarly, compounds with disulphide linker, compounds **8** (Figure 69) and **11** (Figure 70), both lost the conventional hydrogen bond interaction with K71 residue. However, the amine end of the deprotected compound **11**, formed a conventional hydrogen bond interaction with S181. The alkyl and pi-alkyl interactions observed at the ring A for both compounds with I43, F48, I51 and V69, confirms the interactions to some of the important residues in the binding pocket. Additionally, alkyl and pi-alkyl interactions with K140 were also found in the linker for both compounds; the boc-protected end of compound **8** interacted with F48, and ring A of compound **11** with R133. The van der Waals interaction observed was the same for both compounds **8** and **11**. Similar to compound **7**, the boc-protected end of compound **8** also had van der Waals interaction with G47 and S181.

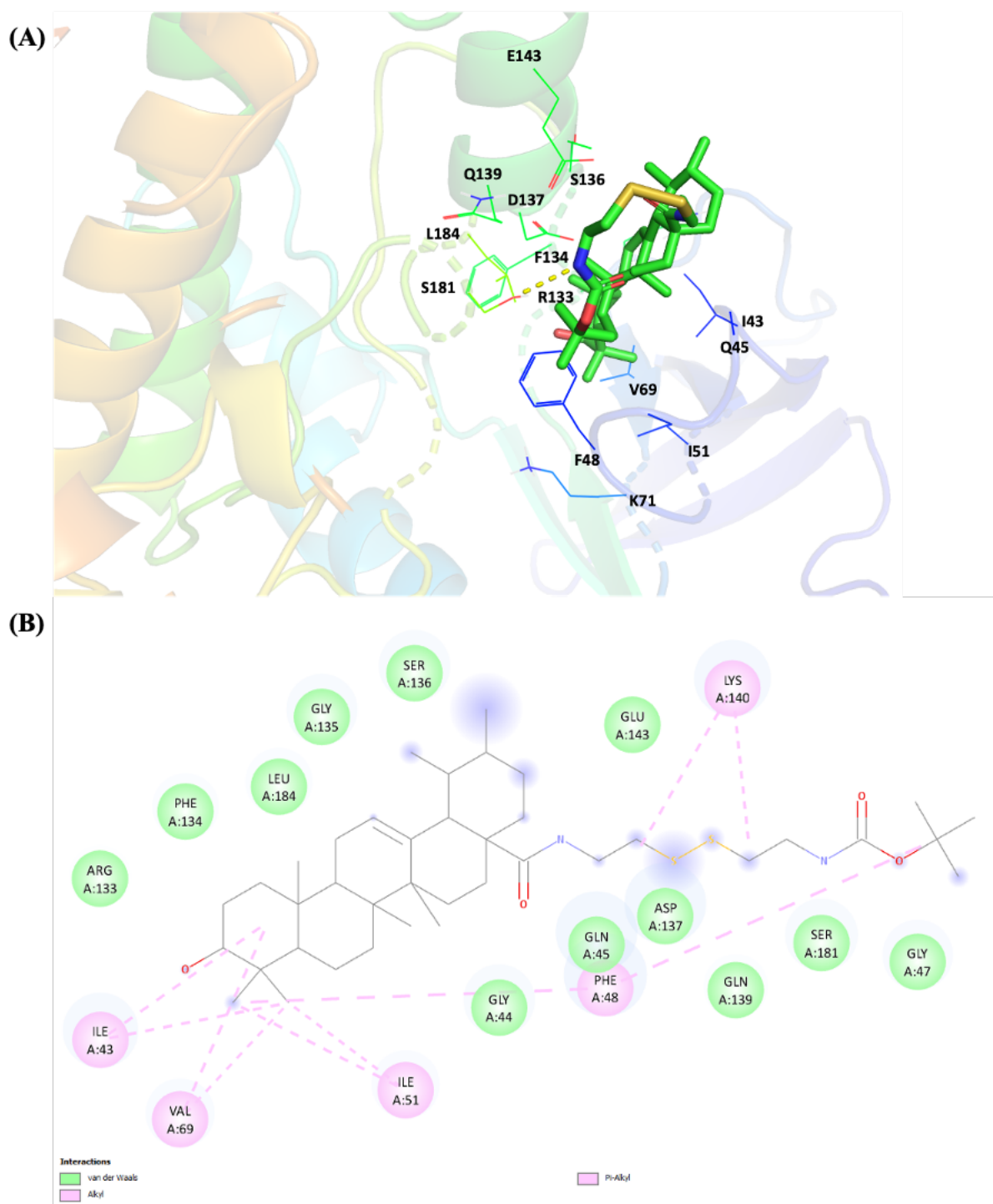


Figure 69. The (A) 3D image and (B) 2D interaction map of compound **8** docked to VRK1 (PDB ID: 6BU6). The 3D image was analysed and rendered in PyMOL™ v2.4.1 and the 2D interaction map was generated in BIOVIA DS Visualizer 2020.

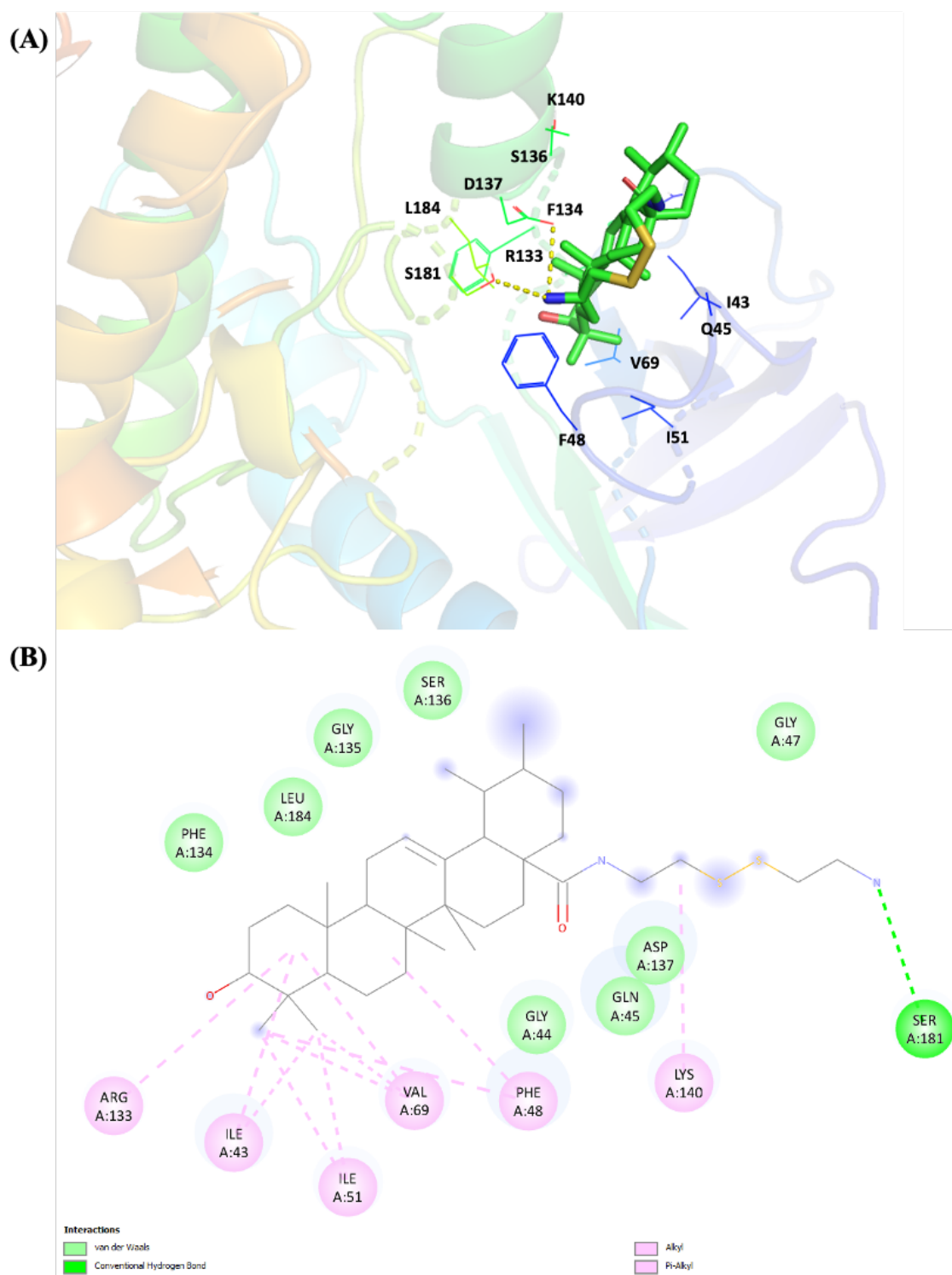


Figure 70. The (A) 3D image and (B) 2D interaction map of compound **11** docked to VRK1 (PDB ID: 6BU6). The 3D image was analysed and rendered in PyMOL™ v2.4.1 and the 2D interaction map was generated in BIOVIA DS Visualizer 2020.

Comparably, compounds with ethereal oxygen linker, compounds **9** (**Figure 71**) and **12** (**Figure 72**), lost the conventional hydrogen bond interaction with K71 residue. Compound **9** was predicted to have completely different interaction from all the novel UA derivatives as the UA side was found oriented at a different site, with the linker end bound just outside of the binding pocket with conventional hydrogen bond interaction with G47. Moreover, a carbon hydrogen bond interaction at the linker was observed with Q45 and two alkyl interactions were found with I43 and K140. Furthermore, two residues (G135 and S136) for compound **9** had the same van der Waals interaction observed as the other novel UA derivatives.

On the other hand, ring A of compound **12** has interaction comparable to other novel UA derivatives - alkyl and pi-alkyl interactions with I43, F48, I51 and V69. This confirms interaction with some of the important residues in the binding pocket. Similar to compound **9**, conventional hydrogen bond was also observed at the linker but with S181. The van der Waals interaction observed was the same as compounds **7**, **8**, **10** and **11**.

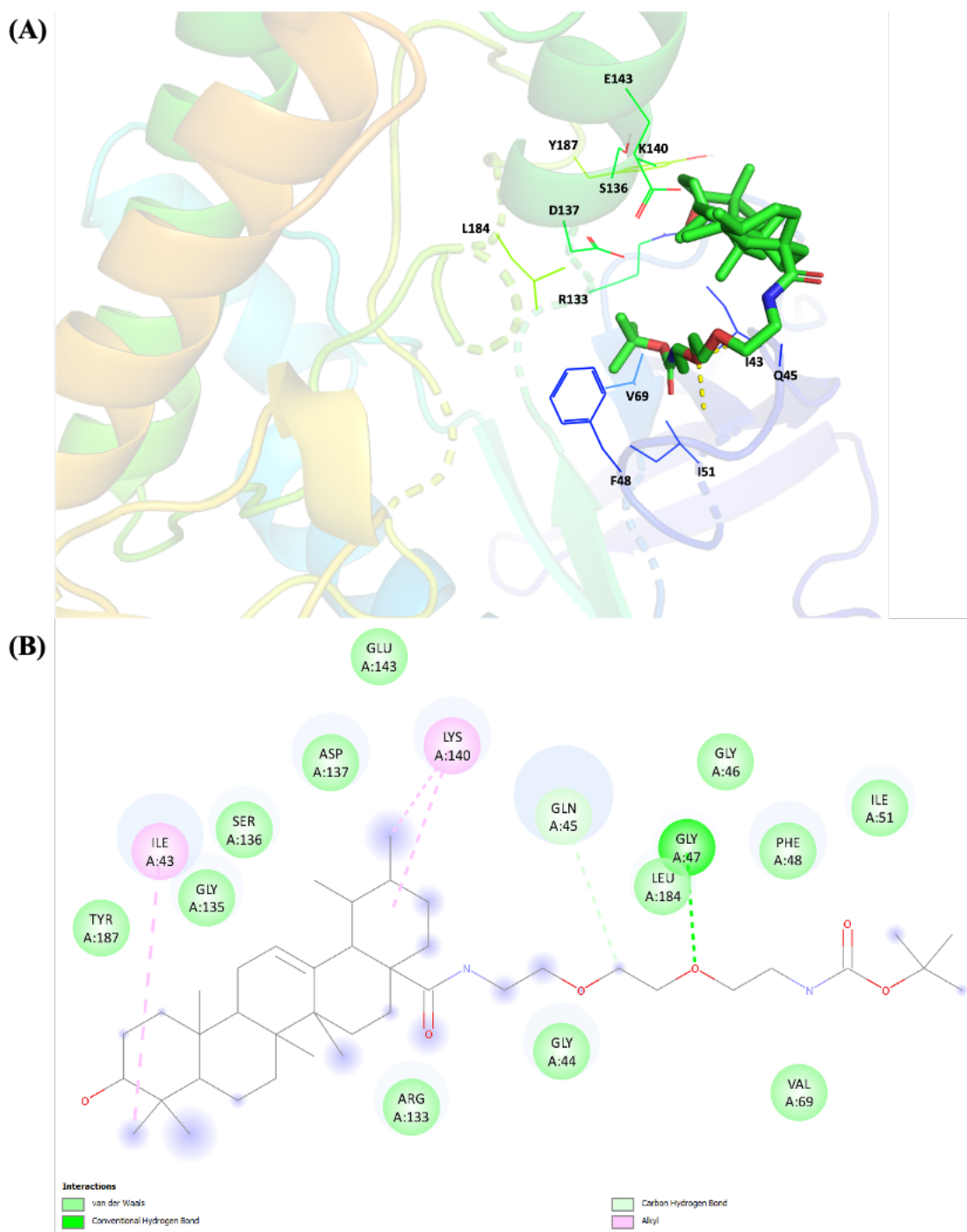


Figure 71. The (A) 3D image and (B) 2D interaction map of compound **9** docked to VRK1 (PDB ID: 6BU6). The 3D image was analysed and rendered in PyMOL™ v2.4.1 and the 2D interaction map was generated in BIOVIA DS Visualizer 2020.

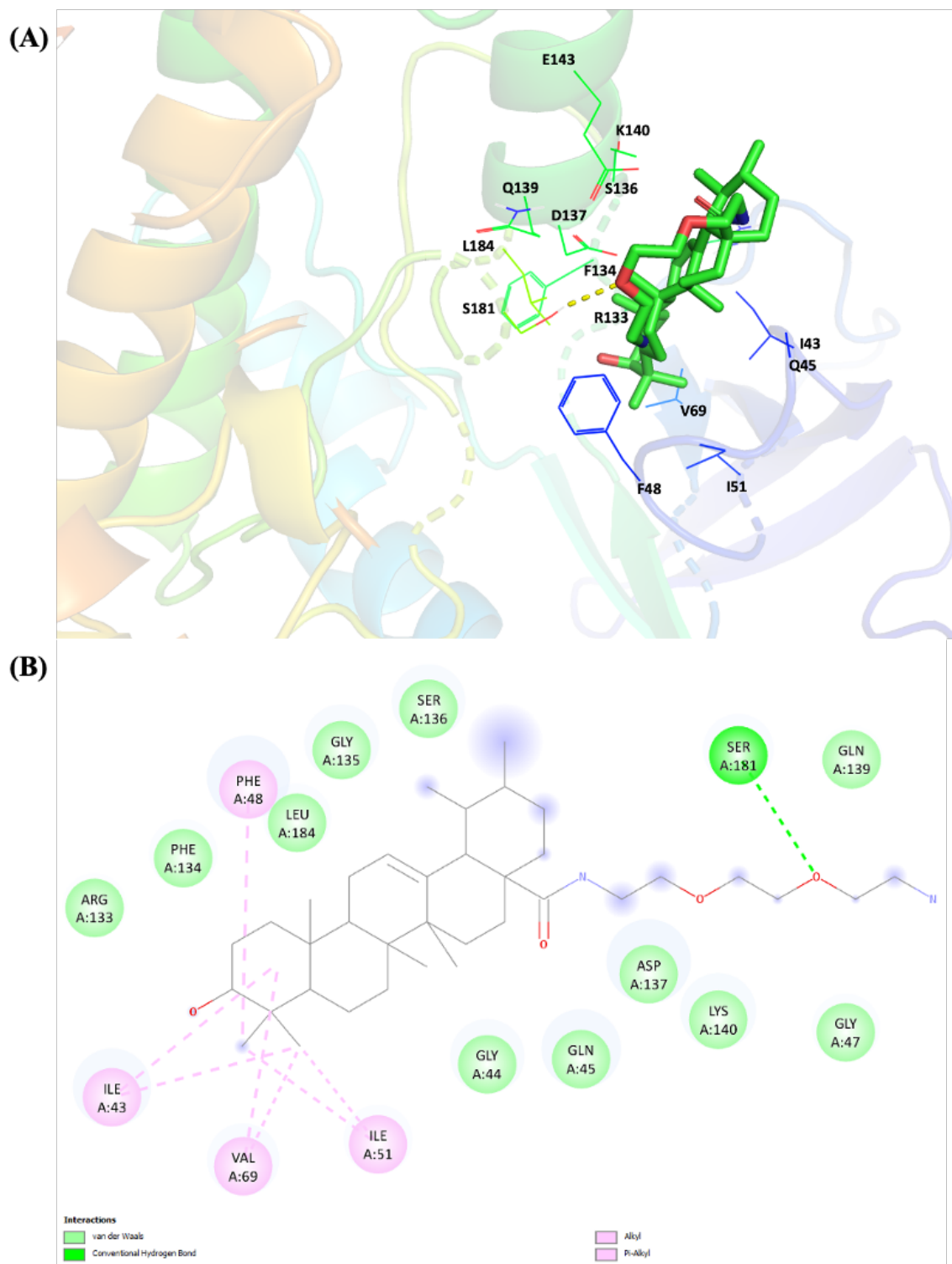


Figure 72. The (A) 3D image and (B) 2D interaction map of compound **12** docked to VRK1 (PDB ID: 6BU6). The 3D image was analysed and rendered in PyMOL™ v2.4.1 and the 2D interaction map was generated in BIOVIA DS Visualizer 2020.

In summary (**Table 23**), the six novel UA derivatives (**7 – 12**) were found bound slightly outside of the binding pocket in comparison to UA, except compound **9** which was found bound at a different binding site and resulted with the lowest predicted binding affinity. Nevertheless, all the other novel UA derivatives (**7 – 12**) still interacted with some of the important residues at the ring A of UA. Out of the six novel UA derivatives, Boc-protected compounds **7** and **8** produced the best predicted binding affinity, but lower than UA. This study suggest that UA may not be directly bind to VRK1 or as mentioned previously, may have multi-target pathway.

Table 23. Summary of the molecular docking results for UA and the novel UA derivatives (**7 – 12**) with VRK1 (PDB: 6BU6). HB – hydrogen bond.

Name	Predicted Binding Affinity (kcal/mol)	Interactions
UA	-8.8 to -6.6	van der Waals (G44, Q45, M131, R133, G135, S136, D137) Conventional HB (K71) Alkyl and pi-alkyl (I43, F48, I51, V69, F134, L184, V196)
Compound 7	-7.5 to -4.8	van der Waals (G44, Q45, G47, F134, G135, S136, D137, K140, S181, L184) Alkyl and pi-alkyl (I43, F48, I51, V69, R133)
Compound 8	-7.2 to -5.3	van der Waals (G44, Q45, G47, R133, F134, G135, S136, D137, Q139, E143, S181, L184) Alkyl and pi-alkyl (I43, F48, I51, V69, K140)
Compound 9	-6.3 to -4.8	van der Waals (G44, G46, F48, I51, V69, R133, G135, S136, D137, E143, L184, Y187) Conventional HB (G47) Carbon HB (Q45) Alkyl (I43, K140)
Compound 10	-6.9 to -5.0	van der Waals (G44, Q45, R133, F134, G135, S136, D137, K140) Alkyl and pi-alkyl (I43, F48, I51, V69, L184)
Compound 11	-6.5 to -4.4	van der Waals (G44, Q45, G47, F134, G135, S136, D137, L184) Conventional HB (S181) Alkyl and pi-alkyl (I43, F48, I51, V69, R133, K140)
Compound 12	-6.8 to -4.4	van der Waals (G44, Q45, G47, R133, F134, G135, S136, D137, Q139, K140, L184) Conventional HB (S181) Alkyl and pi-alkyl (I43, F48, I51, V69)

4.4 Cytotoxicity of Novel UA Derivatives

4.4.1 Cell Viability of Novel UA Derivatives in Different Cancer cell lines

The cytotoxic activity of UA and novel UA derivatives were determined using alamarBlue™ cell viability assay in a panel of cancer cell lines - human brain glioblastoma cancer cell line U-251 MG, human ovarian cancer cell line SKOV-3, human epidermal cell line A431, human breast cancer cell line MCF-7, and human colorectal cell line Caco-2. The normal cell line used was a normal human embryonic kidney cell line (HEK-293).

The calculated IC₅₀ cytotoxicity values are compiled in **Table 24**, and the heatmap of the IC₅₀ values can be depicted in **Figure 74**. The cytotoxic activity of the novel UA derivatives was significantly improved in comparison to UA as seen in the cytotoxicity dose-response curve (**Figure 73**). It can be seen in both **Figure 74** and **Table 24**, that Boc-protected compounds **7** and **9**, and deprotected compounds **10** and **12** harboured prominent cytotoxicity, which are more apparent after 144 hours treatment. However, Boc-protected compounds **7** and **9** did not exhibit cytotoxic activity after 48 hours, whereas deprotected analogues displayed more than two-fold increase in cytotoxicity in comparison to UA in U-251 MG and A431 cell lines. Interestingly, after 144 hours treatment, the IC₅₀ of Boc-protected compounds **7** and **9** has no significant difference ($p \leq 0.0001$) (**Figure 73**) to the deprotected analogues compounds **10** and **12**.

On the other hand, compounds with disulphide linkers, compounds **8** and **11**, has shown very low to no cytotoxicity. Disulphide bonds are known to cleave within the cell at acidic environment or in the presence of cytoplasmic thiol co-factor, such as (reduced) glutathione (GSH) (Lee *et al.*, 2013). The disulphide cleavage of compounds **8** and **11** resulted with a thiol (SH) end instead of Boc or amine (NH₂) end, which could be the reason for the lost cytotoxicity.

Hence, it can be concluded that the amino group end at C-28 is important for the cytotoxicity. A similar study conducted by Kahnt *et al.*, 2018 has shown that ethylenediamine derived carboxamide derivatives at C-28 has improved cytotoxicity of UA. The delayed cytotoxicity observed in U-251 MG and A431 cell lines lead us to investigate the cause of the delayed cytotoxicity of Boc-protected compounds. This study focuses more on the treatment for GBM and hence U-251 MG cell line was used for subsequent studies.

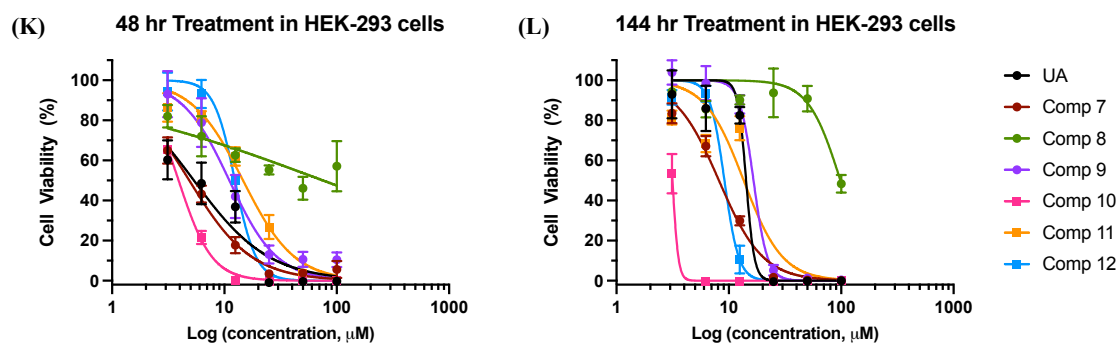


Figure 73. Cytotoxicity of novel UA derivatives (7 – 12) in different cancer cells (A, B) U-251 MG, (C, D) SKOV-3, (E, F) A431 (G, H) MCF-7, (I, J) Caco-2 and normal cell (K, J) HEK-293 cell lines. An initial concentration of 100 μM in culture medium was added to cells and serially diluted to different concentrations (100 μM to 3.125 μM). AlamarBlue cell viability assay was then carried out following treatment for 48 and 144 hours. Data shown were normalised to the untreated control and are shown as the % mean \pm SEM. Statistical analysis was carried out using non-linear regression analysis and Two-way ANOVA with Bonferroni post-tests, ($n = 3$) (* $P < 0.0001$).

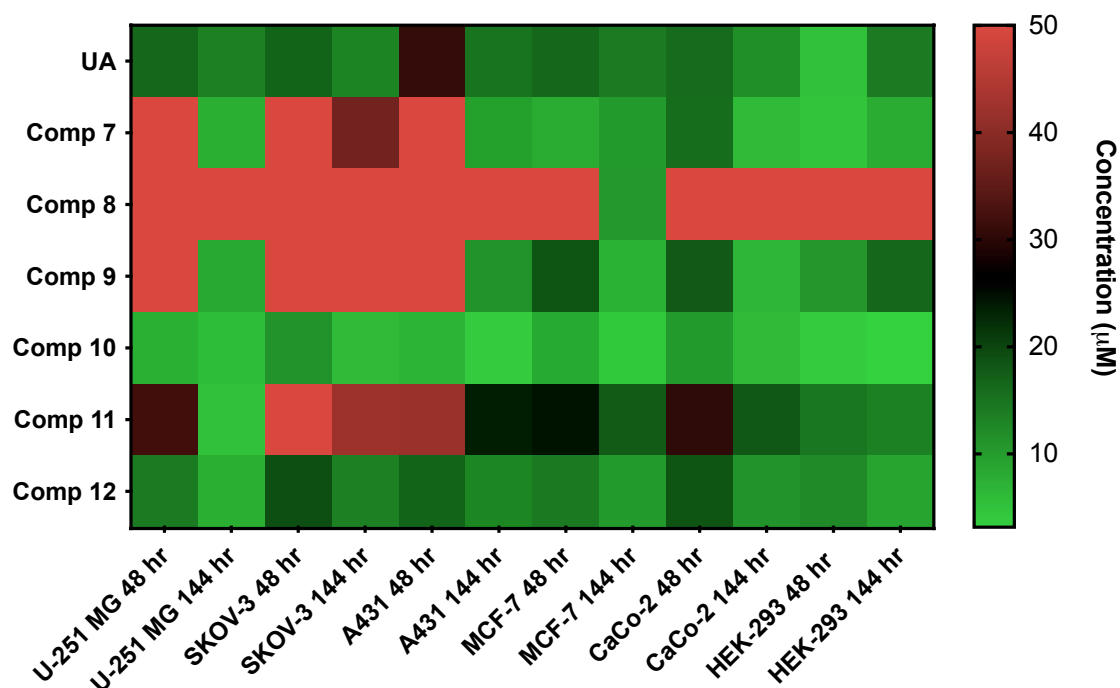


Figure 74. Heatmap of the IC₅₀ of novel UA derivatives in different cell lines. The colours indicate the IC₅₀ values of the UA and novel UA derivatives (7 – 12) from 0 – 50 μM; green being the most cytotoxic and red as the least cytotoxic. An initial concentration of 100 μM in culture medium was added to cells and serially diluted to different concentrations (100 μM to 3.125 μM). AlamarBlue cell viability assay was then carried out following treatment for 48 and 144 hours. Data shown were normalised to the untreated control and are shown as the % mean ± SEM (standard error of the mean). Statistical analysis was carried out using non-linear regression analysis (n = 3) and mean IC₅₀ values in μM are plotted in a heatmap.

Table 24. IC₅₀ of novel UA derivatives (7 – 12) on different cancer cell lines and normal cell line. The colours are in comparison to UA cytotoxicity of UA – green (enhanced), orange (slightly decreased, <5) and red (decreased, >5).

Compound	IC ₅₀ (μM)											
	U-251 MG		SKOV-3		A431		MCF-7		Caco-2		HEK-293	
	48 hr	144 hr	48 hr	144 hr	48 hr	144 hr	48 hr	144 hr	48 hr	144 hr	48 hr	144 hr
UA	<u>16.46</u>	<u>12.82</u>	<u>16.93</u>	<u>13.24</u>	<u>31.01</u>	<u>15.2</u>	<u>16.52</u>	<u>14.37</u>	<u>16.23</u>	<u>11.93</u>	<u>5.35</u>	<u>14.25</u>
Comp 7	>50	6.67	>50	37.4	>50	9.77	8.1	10.4	15.84	6.36	4.87	8.17
Comp 8	>50	>50	>50	>50	>50	>50	>50	10.74	>50	>50	>50	>50
Comp 9	>50	8.61	>50	>50	>50	11.32	18.77	7.4	18.13	6.82	11.07	16.59
Comp 10	7.58	5.40	11.3	6.19	7.09	3.84	8.37	4.27	10.3	6.29	3.91	3.15
Comp 11	32.10	14.60	>50	42.32	41.79	23.87	24.71	17.79	30.55	18.22	14.66	13.56
Comp 12	14.22	7.66	19.22	13.75	16.87	13.08	14.52	10.35	18.69	11.42	12.42	9.14

4.4.2 Novel UA Derivatives Induced Cell Membrane Damage

Propidium iodide (PI) was used to validate if novel UA derivatives induce cell death and cytotoxicity in U-251 MG cells. PI is a DNA staining dye and it is widely used to determine cell viability by flow cytometry. It binds to the DNA when the cell membrane is damaged, giving higher fluorescence to dead cells. U-251 MG cells were treated with a median concentration of compounds at both 48 and 144 hours treatment as per dose response curve (**Figure 73**) or IC_{50} (**Table 24**) obtained, which is 10 μ M. **Figure 75** shows flow cytometry analysis of PI-stained cells after treatment with different novel UA derivatives and the bar graph showing percentage cell viability.

Similar to the cytotoxicity studies obtained using AlamarBlue cell viability assay, a rapid increase in membrane permeability was observed in deprotected compounds **10** and **12**, with cell viability of only 43.23% and 67.92%, respectively, after 48 hours (**Figure 76**); a population of early apoptotic cells (**Figure 75 (A)**) were also observed. It is noteworthy that compounds **10** and **12** are significantly different from UA control ($P \leq 0.0001$). In addition, after 144 hours, significant cell death was observed in compounds **10** and **12** with 9.90% and 17.03% cell viability. Whereas UA and Boc-protected compounds **7** and **9**, also exhibited cytotoxicity and showed early apoptosis (**Figure 75 (B)**) with 83.85%, 72.82% and 61.55% cell viability, respectively. Compounds **9** ($P \leq 0.01$), **10** ($P \leq 0.0001$), and **12** ($P \leq 0.0001$), were significantly different from UA cell viability after 144 hours treatment (**Figure 76**). These results confirm the AlamarBlue cell viability assay findings. It is worth noting that compound **10** inhibited activity of UA by approximately 50 and 70% after 48 and 144 hours, respectively. Whereas compound **12** inhibited activity of UA by approximately 20 and 60% after 48 and 144 hours, respectively.

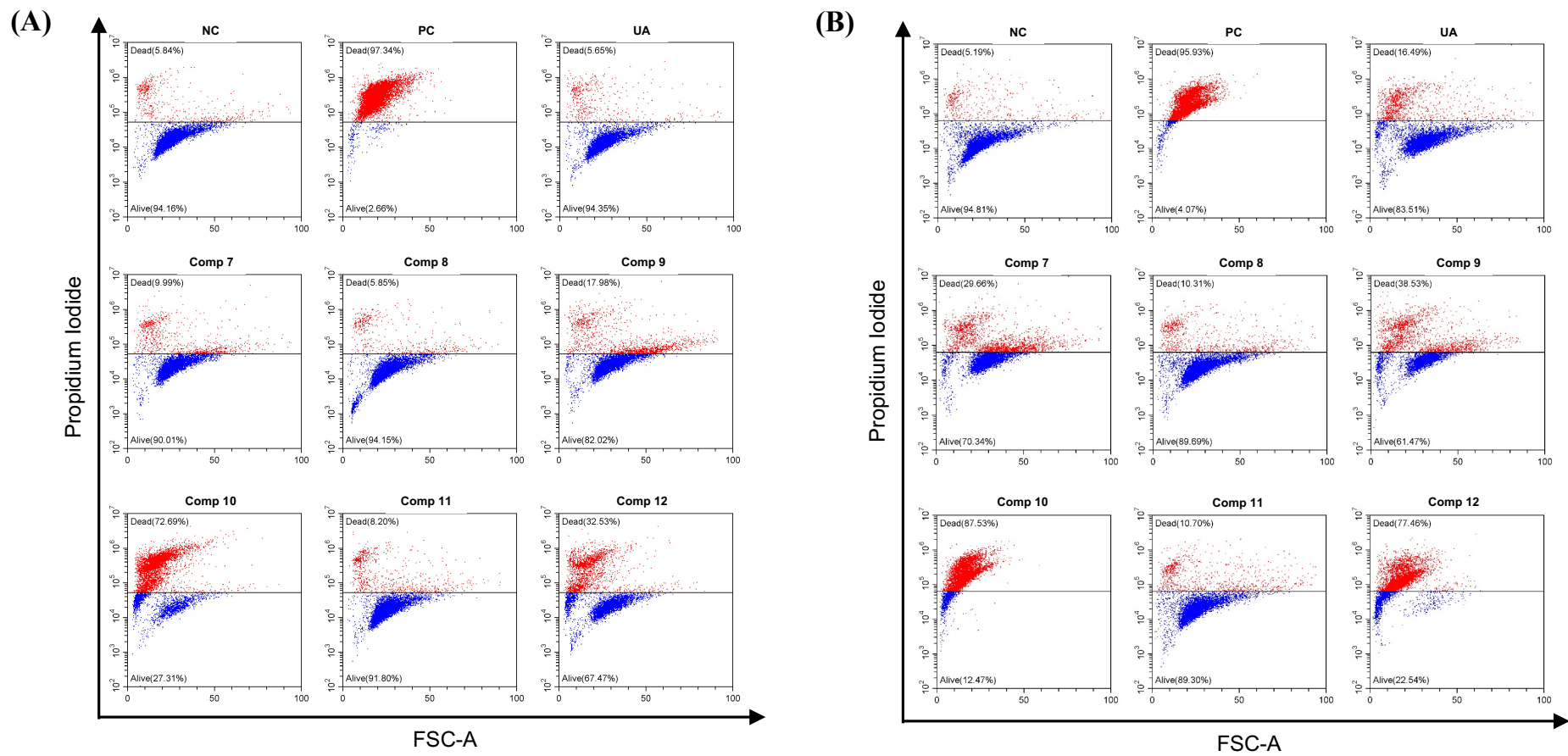


Figure 75. Dot plot of novel UA derivatives stained with propidium iodide after (A) 48 hours and (B) 144 hours. Cells were stained with 0.5 $\mu\text{g/ml}$ propidium iodide for 5 mins and analysed by flow cytometry using CytExpert software. NC – negative control; PC – positive control.

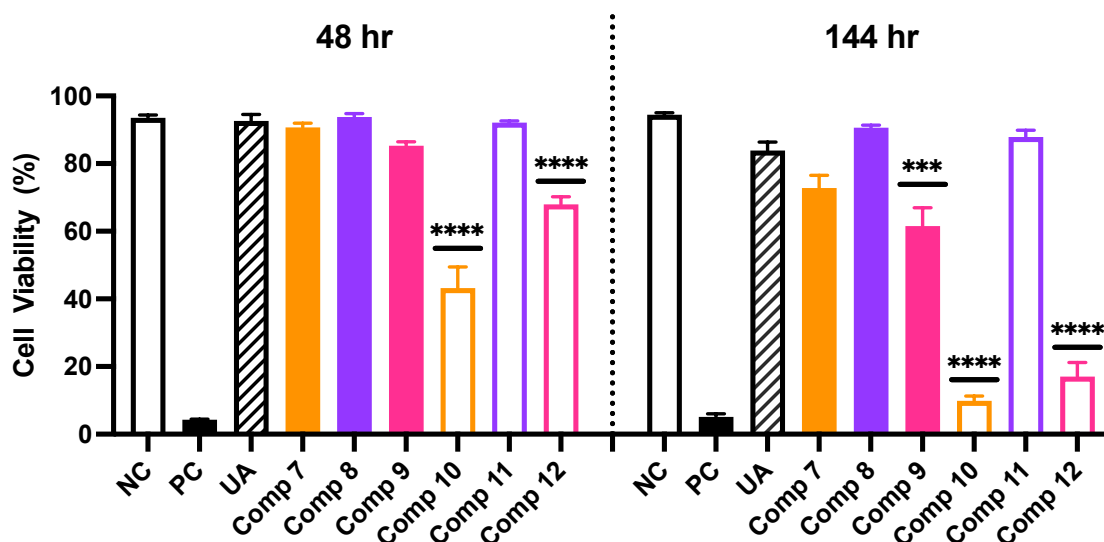


Figure 76. Cell membrane damage of novel UA derivatives using PI. U-251 MG cells were treated with 10 μ M of UA or novel UA derivatives (7 – 12) or 0.05% DMSO (NC - negative control) or 20% DMSO (positive control) for 48 and 144 hours. Cells were stained with 0.5 μ g/ml propidium iodide for 5 mins and analysed by flow cytometry. Bar graph of the % cell viability of compounds plotted using Graphpad Prism 9. Statistical analysis of novel UA derivatives *vs* UA was carried out using One-Way ANOVA with Bonferroni post-test (***) $P \leq 0.001$, ****) $P \leq 0.0001$).

4.4.3 Novel UA Derivatives Induced Mitochondrial Membrane Depolarisation

Mitochondrial membrane potential ($\Delta\Psi_m$) is an important factor of mitochondrial function and can be an indicator of early intrinsic apoptosis. Collapse of the $\Delta\Psi_m$ results in the release of cytochrome C into the cytosol, thus leading to cell death (Salido *et al*, 2007). The effect of novel UA derivatives (**7** – **12**), using 10 μ M concentration treatment, in membrane potential of U-251 MG cells were investigated using JC-1 probe and analysed using flow cytometry. Depolarisation of the mitochondria causes an increase in the green fluorescence and concomitant decrease in the red fluorescence using flow cytometry. As shown in **Figure 78**, loss in $\Delta\Psi_m$ was observed following treatment with deprotected compounds **10** and **12** after 48 hours with only 17.21% ($P \leq 0.0001$) and 67.60% ($P \leq 0.05$) cell viability, respectively; and significantly different from UA. After 144 hours, similar to PI results, Boc-protected compounds **7** and **9**, had approximately 50% loss in $\Delta\Psi_m$. Results obtained correlates to the AlamarBlue and PI obtained, and indicated that depolarisation of mitochondria is a feature of cell death induced by UA and novel UA derivatives. Our data also confirms that compounds **8** and **11** with disulphide linker decreased activity of UA; Boc-protected compounds **7** and **9** have delayed cytotoxicity, and compound **12** slightly improve activity of UA. Promising result was observed in compound **10**, inhibiting activity of UA by approximately 60 and 50% after 48 and 144 hours, respectively.

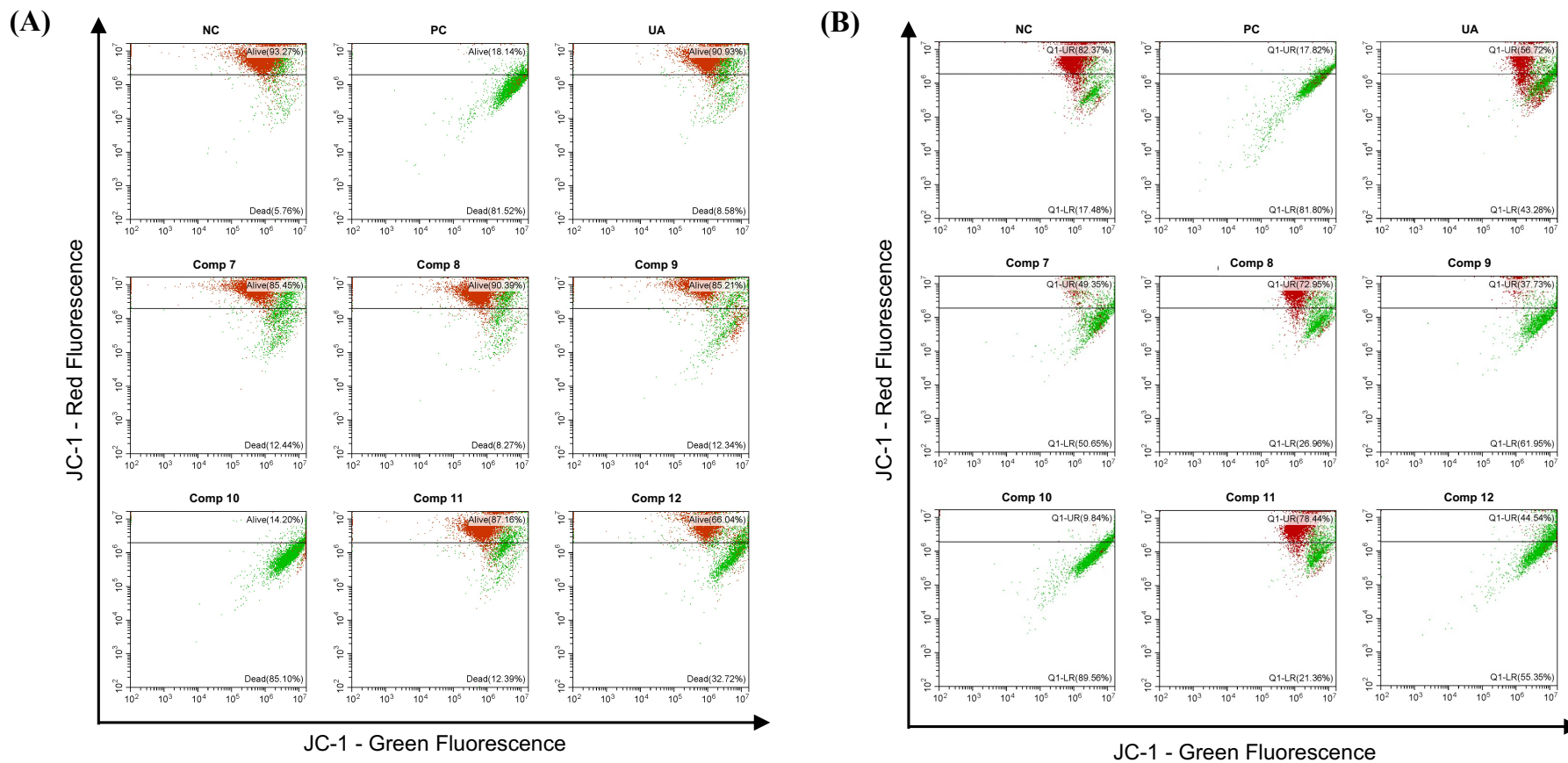


Figure 77. Dot plot of novel UA derivatives stained with JC-1 after (A) 48 hours and (B) 144 hours. Cells were loaded with 2.5 $\mu\text{g/ml}$ JC-1 dye for 5 mins and analysed by flow cytometry using CytExpert software. Active mitochondria exhibit brighter red fluorescence signal compared to mitochondria with lower membrane potential which fluoresce green. NC – negative control; PC – positive control.

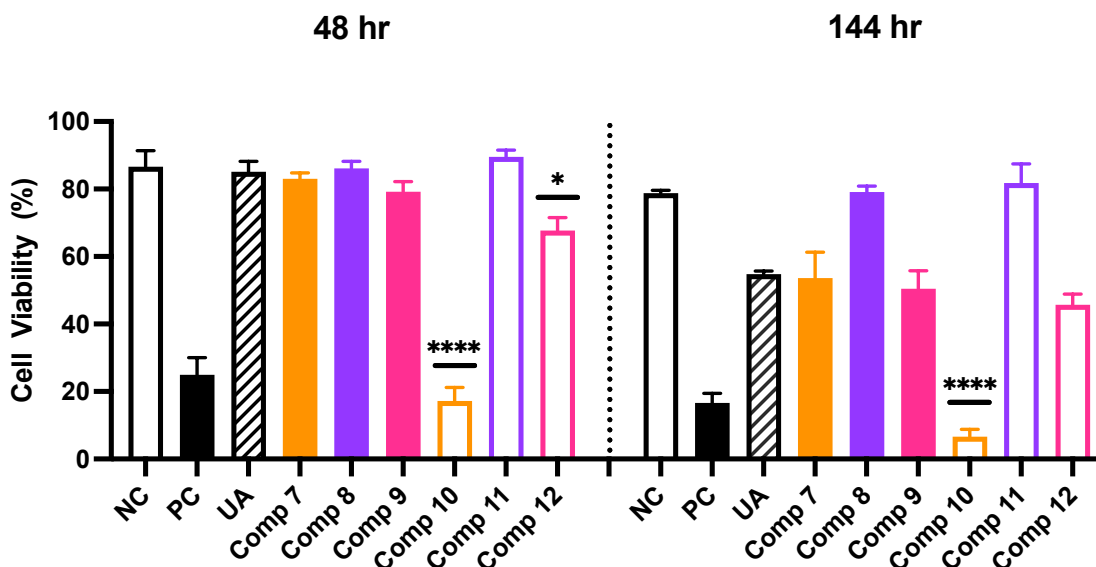


Figure 78. Mitochondrial membrane depolarisation. U-251 MG cells were treated with 10 μ M of UA or novel UA derivatives (7 – 12) or 0.05% DMSO (NC – negative control) or 0.1% H₂O₂ (positive control) for 48 and 144 hours. Cells were loaded with 2.5 μ g/ml JC-1 dye for 5 mins and analysed by flow cytometry. Bar graph of the % cell viability of compounds plotted using Graphpad Prism 9. Statistical analysis of novel UA derivatives vs UA was carried out using One-Way ANOVA with Bonferroni post-test (*P \leq 0.05, ****P \leq 0.0001).

4.5 Stability of novel UA derivatives

To investigate the cause of delayed cytotoxicity of Boc-protected compounds, stability of novel UA derivatives were tested. Compounds with ethylenediamine linker, compounds 7 and 10 were tested as representative of Boc-protected and deprotected compounds, respectively.

4.5.1 Stability in Cell Culture Medium

On the basis of the results of cytotoxicity assays, it was observed that *N*-Boc protected compounds did not exhibit much activity after 48 hours treatment which are more evident in U-251 MG and A431 cell lines. However, after 144 hours treatment, there was no significant difference ($P < 0.0001$) observed between the IC_{50} values of Boc-protected and deprotected compounds. Therefore, we investigated the stability of compound **7** in comparison to compound **10** as representative compounds, to determine whether degradation of the Boc-protected compounds into deprotected forms was causing the delayed cytotoxicity kinetics for Boc-protected compounds. Compounds were incubated in cell culture medium at 37 °C for 144 hours before adding to cells. Results obtained (Figure 79) showed that Boc-protected compound **7** exhibited the same results observed above, with no cytotoxicity after 48 hours treatment; cytotoxic activity obtained after 144 hours treatment. Hence, stability was concluded as not the reason for the delayed cytotoxicity kinetics observed for Boc-protected compounds.

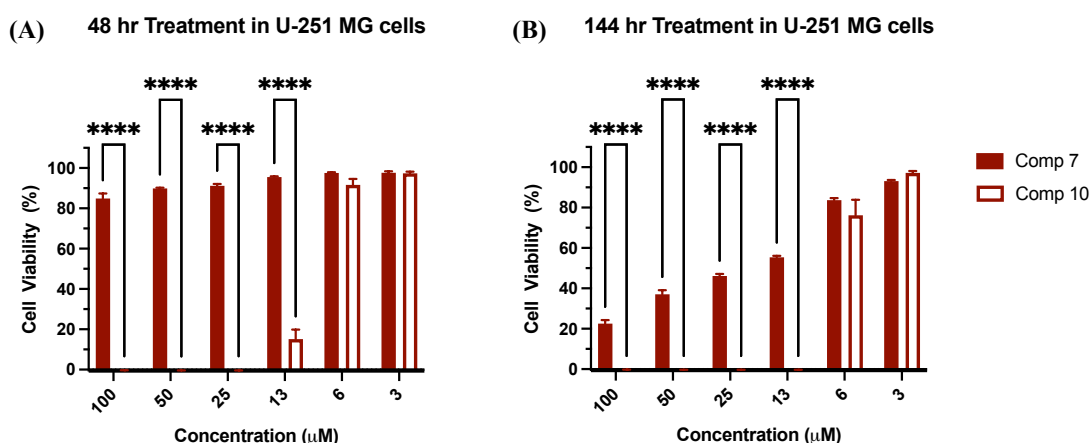


Figure 79. Stability of Boc-protected compound in cell culture medium. Compounds **7** and **10** were investigated by incubating 100 µM of the compounds in culture medium and incubated at 37 °C for 144 hours. After which time, was added to cells and serially diluted

to 3.125 μ M. AlamarBlue cell viability assay was carried out following treatment for 48 hours (A) and 144 hours (B). Data shown were normalised to the untreated control and are shown as the % mean \pm SEM. Statistical analysis was carried out using Two-way ANOVA with Bonferroni post-test, (n = 3) (****P \leq 0.0001).

4.5.2 Investigation of Possible Enzymatic Activity of *N*-Boc Protected Compounds

After investigating the stability of the compounds, we next looked at cellular or extracellular enzymatic activity for causing the delayed activity of Boc-protected compound **7**. Glioblastoma and other cancer cells express high levels of amidase enzymes which may be capable of utilising Boc-protected compounds as substrates. Protein from approximately 1 million U-251 MG cells were extracted by freeze-thawing using PBS with 1% protease cocktail inhibitor to prepare a solution of cellular enzymes. Freeze-thawed extracts were incubated with the compounds for 1 hour at 37 °C or on ice, and then added to cells. It is expected that compound **7** would exhibit activity after 48 hours treatment if cell-based enzymatic processes were involved. However, as seen in **Figure 80** (A, B) activity was only observed after 144 hours for compound **7**, whereas the control compound **10** exhibited activity both after 48 and 144 hours. These results indicates that cell-based enzymatic processes was not likely involved in the delayed cytotoxicity kinetics observed in *N*-Boc protected compounds.

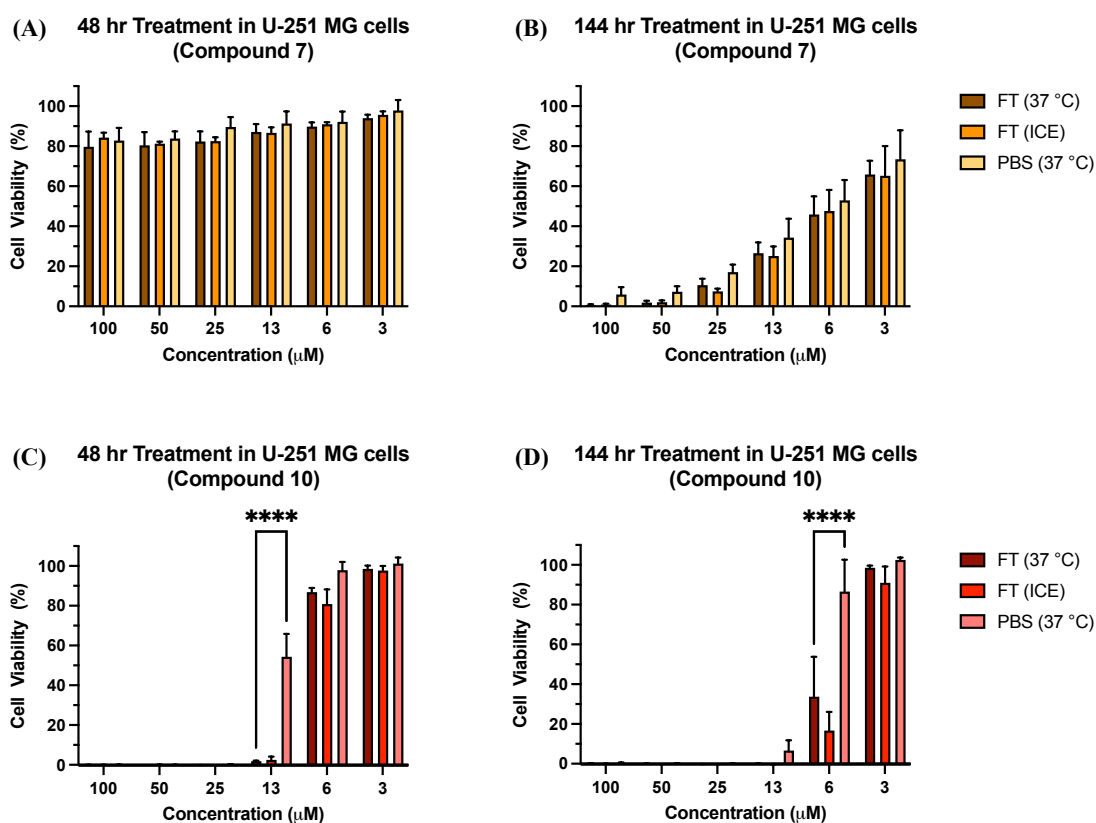


Figure 80. Enzymatic activity of *N*-Boc protected compounds. U-251 MG cells were extracted by freeze-thawing (FT). Then, compounds were added to the FT cells and pre-incubated at 37 °C or ice for 1 hour; negative control with compounds in PBS was pre-incubated at 37 °C for 1 hour. AlamarBlue cell viability assay was carried out following treatment for 48 hr and 6 days. Data shown were normalised to the untreated control and are shown as the % mean \pm SEM. Statistical analysis was carried out using Two-way ANOVA with Bonferroni post-tests, ($n = 3$) (**** $P \leq 0.0001$).

Results obtained suggests that Boc-protected compounds **7** and **10** are stable in cell culture medium even at longer timepoints. Hence, degradation of the compound is not likely the cause of delayed cytotoxicity, nor cell-based enzymatic activity. The apparent delayed cytotoxicity of Boc-protected compounds **7** and **10** observed so far in this study prompted the exploration of its activity.

4.6 Collective Cell Migration in Novel UA Derivatives

One of the most important hallmarks of GBM is an invasive behaviour and ability to migrate into surrounding healthy brain tissue. An important feature of a potential novel therapeutic for the treatment of GBM is its ability to inhibit migration (Li *et al.*, 2016). A recent study showed that UA treatment at sub-toxic concentration induced JNK independent cell migration suppression in U-251 MG cells (Conway *et al.*, 2021). The wound healing assay is a standard *in vitro* technique used for collective cell migration in 2D cell culture (Jonkman *et al.*, 2014). The collective cell migration (scratch assay) allows for preliminary investigation if novel UA derivatives (**7 – 12**) retain the inherent ability of UA to halt U-251 MG cell migration as observed by Conway *et al* (2021). Hence, UA was used as a positive control in this study. Cells were treated with each compound, at no observable adverse effect level (NOAEL) concentration (**A.25**); so that it would not initiate cytotoxic response but potentially inhibit migratory response.

This study was performed in triplicate until the control wound almost fully closed – 7-hour period. Cell monolayer at approximately 90% confluency was scratched with a 200 μ L sterile pipette tip (variability of scratch size between samples was minimised by keeping the same orientation and movement of pipette tip in generating the scratch). The images were taken using an Optika XDS-2 trinocular inverse microscope equipped with a microscope Camera ISH500. The relative wound area analysis was conducted using Fiji software (Schindelin *et al.*, 2012). The total wound area was calculated by measuring the gap width (w) and the gap length (l) using Fiji “set scale” and “measure” options. Then a simple linear regression was done in Graphpad Prism 9.0 to obtain equation of the line, of which was used to plot relative rate of closure (Jonkman *et al.*, 2014).

There are plethora of techniques in the literature, but for this study we used wound healing analysis protocol and calculated rate of closure using a formula, developed by Jonkman *et al* (2014). The rate of gap closure measures the speed of the collective motion of the cells and can be quantitatively measured by plotting the gap area as a function of time as seen in **Figure 81** (B). Jonkman *et al* (2014) demonstrated that from the slope of the line obtained, collective cell migration rate ($V_{migration}$) in $\mu\text{m/hr}$ can be calculated and is equal to dA/dT , where A is the gap (w) times the length (l) of the gap. Assuming that the gap is much longer than the field-of-view so that cells do not migrate in from the edges, then the length is constant, so $dA/dT = l \times dw/dt$. Also, the width of the gap closes in twice the rate of migration, so $dw/dt = 2 \times V_{migration}$. This gives the cell migration (wound gap closure) rate as:

$$V_{migration} = \frac{|slope|}{2 \times l}$$

The $V_{migration}$ ($\mu\text{m/hr}$) calculated for UA and novel UA derivatives (**7 – 12**), and statistical difference are summarised in **Table 25** below. Using linear regression analysis, we identified the slopes for UA and all novel UA derivatives (**7 – 12**) as significantly different ($P \leq 0.0001$). **Figure 81** (A) shows the transformation process when using Fiji to calculate the area of the scratch. It can be seen in **Figure 81** (B) that over the course of 7 hours, untreated cells have migrated into the area of the scratch, therefore significantly reducing the size of the scratch ($P \leq 0.05$). The rate of closure by linear regression analysis in **Figure 81** (C) shows that UA and novel UA derivatives (**7 – 12**) are significantly different from the negative control ($P \leq 0.0001$). Thus, indicating that the rate of migration has

slowed down as a result of exposure to NOAEL concentrations of compounds obtained after 48 hours treatment, therefore preventing scratch closure. All novel UA derivatives (**7 – 12**) has no significant difference to UA control ($P > 0.05$). Hence, indicating that all six novel UA derivatives (**7 – 12**) retain the ability of UA to halt migration of U-251 MG GBM cells (Conway *et al.*, 2022). It is interesting that the disulphide linkers, compounds **8** and **11**, was found least cytotoxic than UA but retain its ability to halt migration.

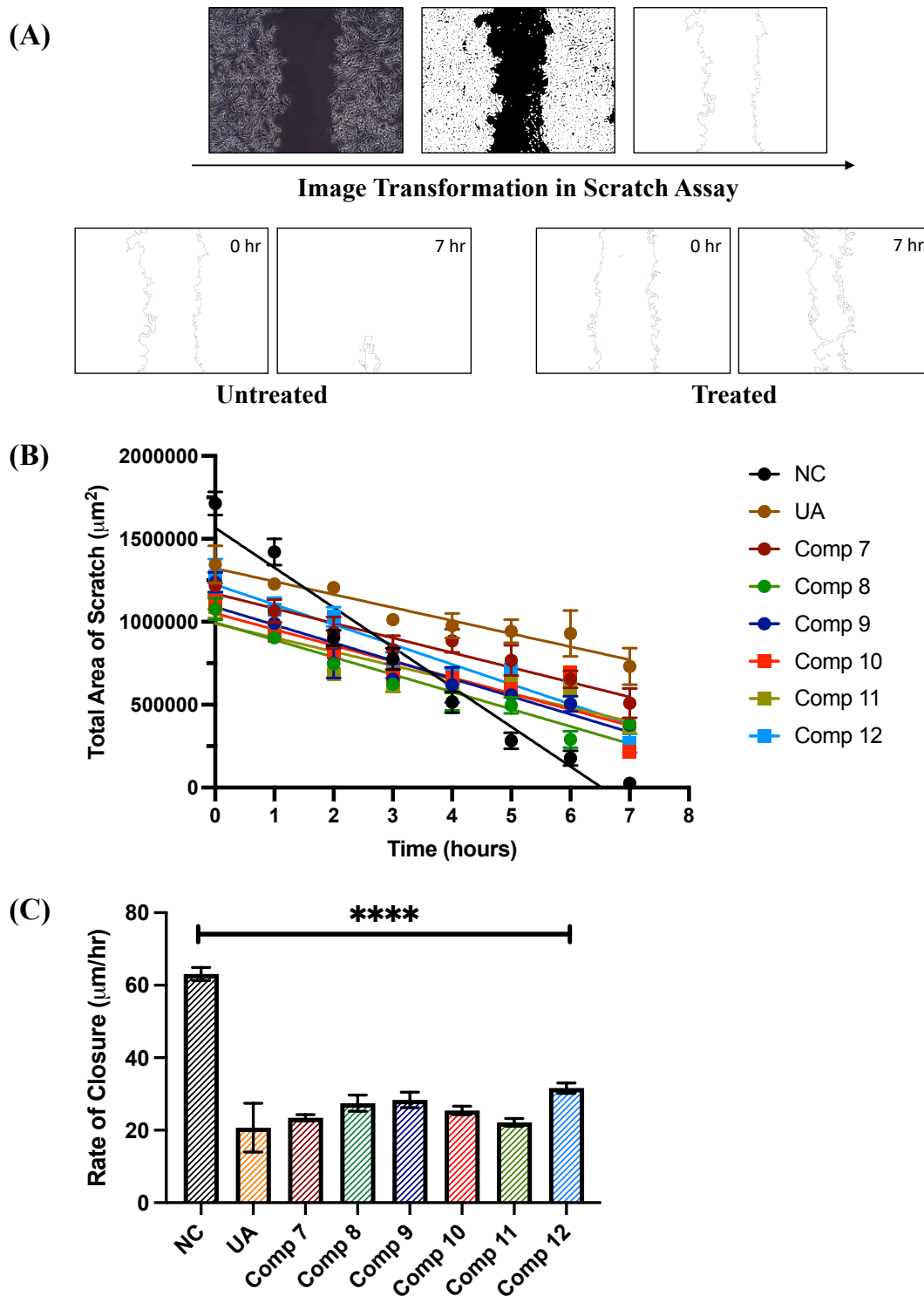


Figure 81. Collective Cell Migration of novel UA derivatives (7–12) in U-251 MG cells. Scratch assay was performed and cells were treated with sub-toxic concentration of each compounds. (A) Demonstrates the transformation process using Fiji software to analyse % size of scratch over time. (B) Scratch area analysis recorded every hour for 7 hours using 10X zoom using the Tucsen camera (ISH500) mounted Optika XDS-2 trinocular inverse microscope. Fiji software was used to analyse and calculate total scratch area.

Statistical analysis was carried out using simple linear regression. (C) Rate of closure was calculated using the slope of the line and statistical analysis was carried out using One-Way ANOVA with Bonferroni's post-test (****P ≤ 0.0001). All statistical analysis was performed using Graphpad Prism 9.0. Data are shown as the mean ± S.E.M. of three independent experiments (n = 3).

Table 25. The calculated rate of gap closure with statistical difference (Bonferroni's post-test) analysis for UA and novel UA derivatives (**7 - 12**). NC – negative control; NS – not significant.

Compound	NOAEL Concentration	$V_{migration}$ (μm/hr)	Statistical Difference (NC)	Statistical Difference (UA)
NC	0.1% DMSO	63.12%	N/A	p < 0.0001
UA	7 μM	20.72%	p < 0.0001	N/A
Compound 7	13 μM	23.41%	p < 0.0001	NS
Compound 8	13 μM	27.46%	p < 0.0001	NS
Compound 9	6 μM	28.39%	p < 0.0001	NS
Compound 10	6 μM	25.43%	p < 0.0001	NS
Compound 11	13 μM	22.17%	p < 0.0001	NS
Compound 12	6 μM	31.61%	p < 0.0001	NS

4.7 Effect of Novel UA Derivatives to Cell Membrane Damage

VRK1 is one of the most abundant nuclear kinases, which is independent of the type of DNA damage. The VRK1 protein has several roles in DDR, that protects both DNA and cells. The early activation of p53 in VRK1 can either function as a sensor or initiator of the corresponding type of responses (Lazo, 2017; Campillo-Marcos *et al.*, 2021). The early response to DNA damage requires phosphorylation of H2AX in Ser139 (γ H2AX), *in vitro* and *in vivo*. (Campillo-Marcos and Lazo, 2018). The phosphorylation of γ H2AX is independent of the cell cycle phase, and occurs in proliferating as well as arrested and non-dividing cells (Campillo-Marcos *et al.*, 2021). The VRK1 kinase activity increases by 10-fold after independently inducing DNA damage, which includes pyrimidine dimers caused by UV irradiation, transcription and replication blocks caused by hydroxyurea treatment, or double-stranded DNA breaks induced by either doxorubicin or ionizing radiation (Campillo-Marcos and Lazo, 2018; Campillo-Marcos *et al.*, 2021). This makes VRK1 an ideal kinase for the early sensor and rectification mechanism of the DNA damage cascade (Compillo-Marco & Lazo, 2018).

As discussed above in 3.2.2, Kim *et al* (2015) found that UA inhibits the DNA damage defence activity of VRK1 in lung cancer cells *in vitro* (A549). In addition, they showed that UA has synergistic effects with DNA damaging drugs and trigger more severe cell death in *in vivo* xenograft mouse model (Kim *et al.*, 2015). The *in silico* study obtained in 3.2.2 has revealed that compounds 7 and 8 produced the best predicted binding affinity out of all the six novel UA derivatives. However, predicted binding affinity scores obtained were lower than UA. To determine and/or confirm this, chemotherapeutic agent TMZ and ionizing radiation UV-Vis, were used as surrogate for radioactivity to

investigate the effect of novel UA derivatives (**7 – 12**) to cell membrane damage and synergistic activity to current treatment employed for GBM. The chemotherapeutic agent, TMZ that can cross the BBB, is converted to an alkylating methyldiazonium cation and then methylates the guanine residues in the DNA molecule. This then results in the formation of O6- and N7-methylguanine, which inhibits DNA repair mechanisms therefore results to DNA damage such as DNA double strand breaks (Kiskova, *et al.*, 2020). NOAEL concentrations of compounds (**A.25**), TMZ and UV-Vis were used for this study to determine any synergistic effect.

4.7.1 Cytotoxicity Curve of TMZ

Cytotoxicity curve was established for TMZ. Cells were treated with a vehicle control present in drug - 0.5% DMSO. No significant reduction in cell viability was observed in vehicle control and was used as negative control for this study. As demonstrated in **Figure 82** below, cell viability was only reduced to 20% at 250 μM after 48 hours, giving an IC_{50} of 300.10 μM . A longer exposure time was carried out, 144 hours timepoint, and IC_{50} was calculated as 13.06 μM . The NOAEL concentration used in this study was 15 μM of TMZ which was also determined as sub-toxic concentration by Conway *et al.* (2016).

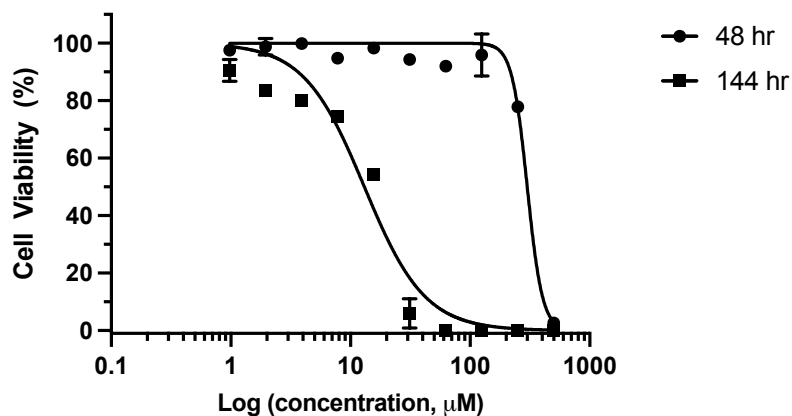


Figure 82. TMZ Dose Response Curve in U-251 MG cells. U-251 MG cells were exposed to TMZ at varying concentrations (0 – 500 μM). Cells were also treated with a vehicle control of 0.5% DMSO. After 48 and 144 hours, cells were analysed using AlamarBlue cell viability assay. Data shown was normalised to the untreated control and are shown as the % mean \pm S.E.M (n=3). Statistical analysis was carried out using non-linear regression using Prism 9 statistical software.

4.7.2 Cytotoxicity Curve of UV-Vis

Cytotoxicity curve was also established for UV-Vis to determine NOAEL in U-251 MG cells. Cells were seeded at a density of 1×10^4 cells (48 hours) or 2.5×10^3 (144 hours) exposure time period and was allowed to adhere overnight. After which time, was exposed to UV-Vis at varying times and incubated for 48 and 144 hours. As seen in **Figure 83** (A) below, cell viability was only reduced to 45% after 240 seconds UV-Vis exposure at 48-hour timepoint. A longer incubation period, 144 hours in **Figure 83** (B), showed that cells exposed for 60 seconds killed >95% of the cells and hence was used as positive control; whereas 10 and 15 seconds were determined as NOAEL with cell viability of 94 and 85%, respectively.

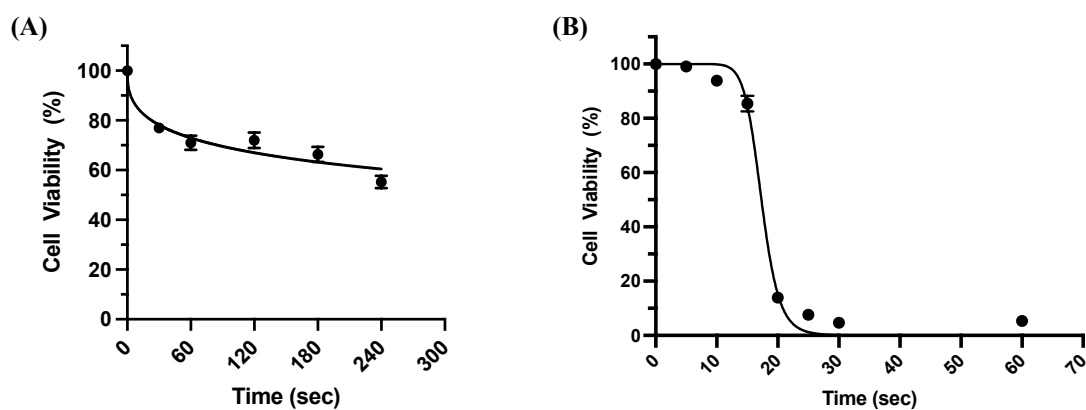


Figure 83. UV-Vis Dose Response Curve in U-251 MG cells. U-251 MG cells were exposed to UV light at different timepoints. Cells were then incubated for (A) 48 hours and (B) 144 hours, and analysed by AlamarBlue. Data shown was normalised to the untreated control and are shown as the % mean \pm S.E.M (n=3). Statistical analysis was carried out using non-linear regression.

4.7.3 Synergistic Effect of TMZ and Novel UA Derivatives

The activity of no TMZ and with 15 μ M TMZ in **Figure 84 (A)** confirms that NOAEL was observed. There was no synergistic effect observed between low doses of UA and TMZ. However, Two-Way ANOVA with Bonferroni's post-test demonstrated a significant difference ($P \leq 0.0001$) at higher doses (15 and 20 μ M) of UA after 144 hours treatment (**Figure 84 (C)**). The result obtained seem to imply protective effect of UA to U-251 MG cells when co-treated with TMZ.

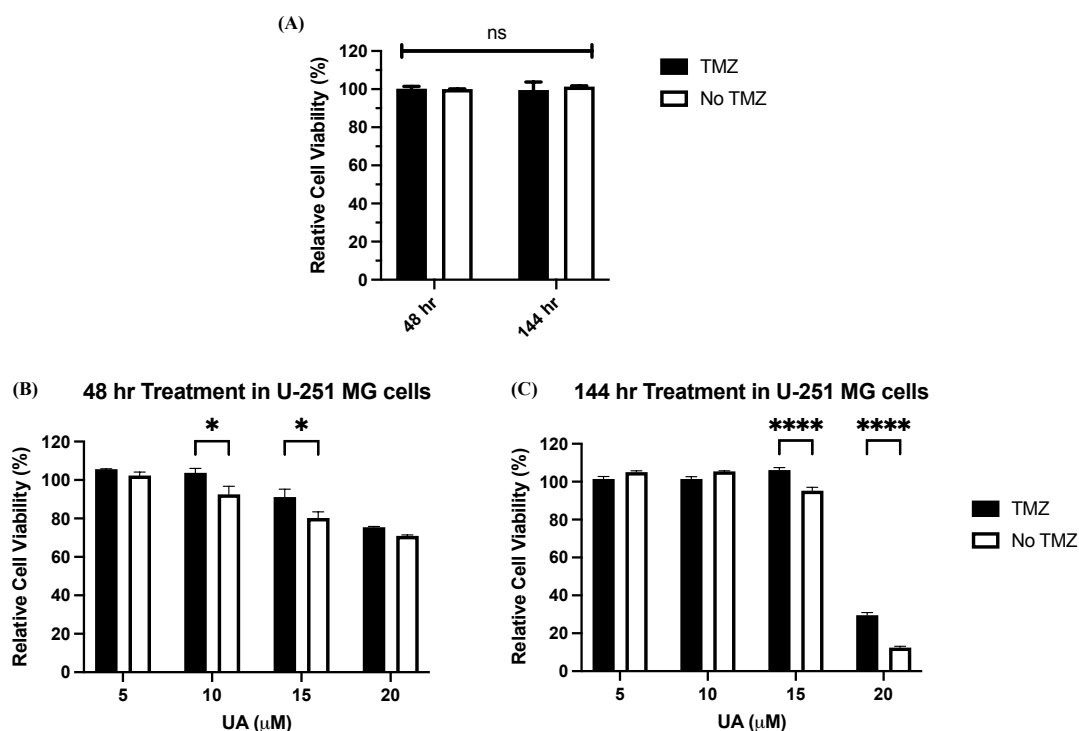


Figure 84. Synergistic activity of UA and low dose of TMZ. (A) U-251 MG cells treated with and without 15 μM TMZ as controls. (B) U-251 MG cells pre-treated with 5-20 μM UA for 1 hour, after which 15 μM TMZ was added to the wells. Cells were incubated for 48 and 144 hours, and analysed by AlamarBlue. Data shown was normalised to the untreated control and are shown as the % mean ± S.E.M (n=3). Statistical analysis was carried out using Two-Way ANOVA with Bonferroni post-test (ns, not significant $P > 0.05$) (* $P \leq 0.05$, **** $P \leq 0.0001$).

All novel UA derivatives (**7** – **12**) did not exhibit any synergistic effect with TMZ. The Boc-protected compounds **7** and **9** (**Figure 85 (A) and 81 (E)**) exhibited significant difference at low concentrations after 48 hours, 10 μM ($P \leq 0.05$) and 5 μM ($P \leq 0.001$), respectively. Furthermore, out of the three deprotected compounds, only compound **12** has significant difference at 15 μM ($P \leq 0.0001$) after 144 hours timepoint (**Figure 86**). All results obtained are indicating that co-treatment with TMZ alleviate the compounds' cytotoxicity.

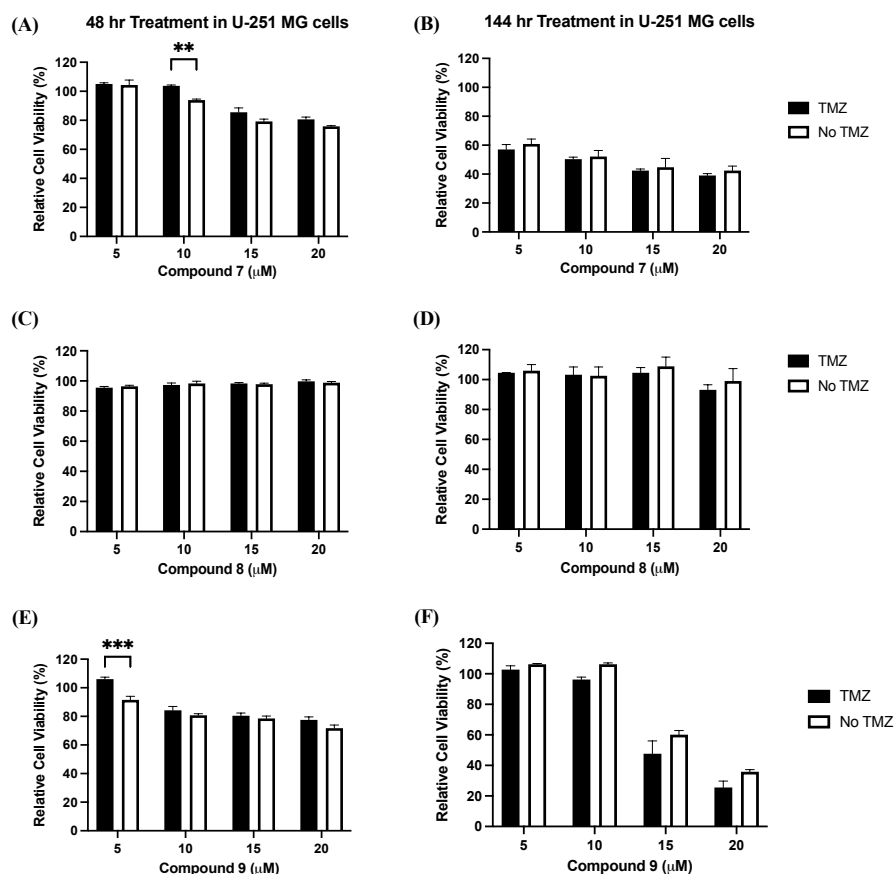


Figure 85. Synergistic activity of Boc-protected compounds (7 – 9) and low dose of TMZ. U-251 MG cells were pre-treated with 5-20 μM (A, B) compound 7; (C, D) compound 8; (E, F) compound 9 for 1 hour, after which 15 μM TMZ was added to the wells. Cells were incubated for 48 and 144 hours, and analysed by AlamarBlue. Data shown was normalised to the untreated control and are shown as the % mean ± S.E.M (n=3). Statistical analysis was carried out using Two-Way ANOVA with Bonferroni post-test (**P ≤ 0.01, ***P ≤ 0.001).

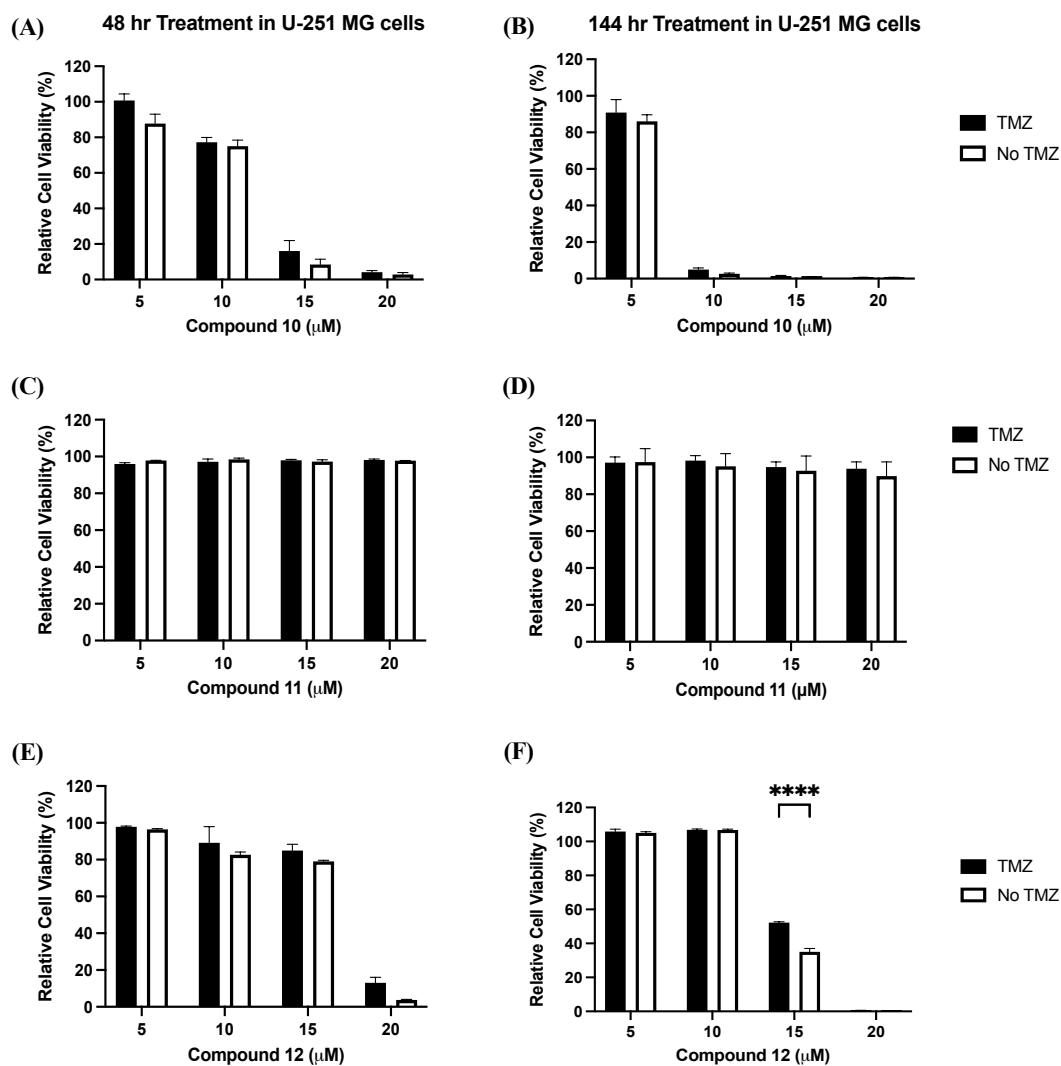


Figure 86. Synergistic activity of deprotected compounds (**10** – **12**) and low dose of TMZ. U-251 MG cells were pre-treated with 5-20 μM (A, B) compound **10**; (C, D) compound **11**; (E, F) compound **12** for 1 hour, after which 15 μM TMZ was added to the wells. Cells were incubated for 48 and 144 hours, and analysed by AlamarBlue. Data shown was normalised to the untreated control and are shown as the % mean ± S.E.M (n=3). Statistical analysis was carried out using Two-Way ANOVA with Bonferroni post-test (****P ≤ 0.0001).

4.7.4 Synergistic Effect of UV-Vis and Novel UA Derivatives

The NOAEL of UV-Vis obtained in **Figure 83** for 144 hours treatment was 10 and 15 seconds and hence was used in this study. The cells were pre-treated with 144 hours NOAEL concentration of compounds for 1 hour. After which time, cells were exposed to UV light for 10 or 15 seconds. One-Way ANOVA with Bonferroni's post-test was carried out to determine significant difference between compounds with and without UV exposure. As seen in **Figure 87 (A)**, there is no significant difference observed between the negative control and 10 seconds UV exposure, confirming NOAEL. A significant difference was observed with 10 seconds control and compound **7** with UV ($P \leq 0.05$); a significant difference in compound **7** was also observed with and without UV ($P \leq 0.05$). The synergistic effect observed between compound **7** and 10 seconds UV exposure, indicates that compound **7** may cause cell membrane damage to U-251 MG cells. However, this was not observed when co-treated with TMZ.

On the other hand, the exposure to UV light for 15 seconds (**Figure 87 (B)**) was statistically different from the negative control ($P \leq 0.0001$), with cells exposed to 15 seconds UV only having ~9% cell viability. Interestingly, significant difference was observed from the 15 seconds control with compounds **8**, **9** and **11** ($P \leq 0.0001$), and compounds **10** and **12** ($P \leq 0.05$). Results obtained seem to be suggesting protective effect of compounds after exposure to UV for 15 seconds.

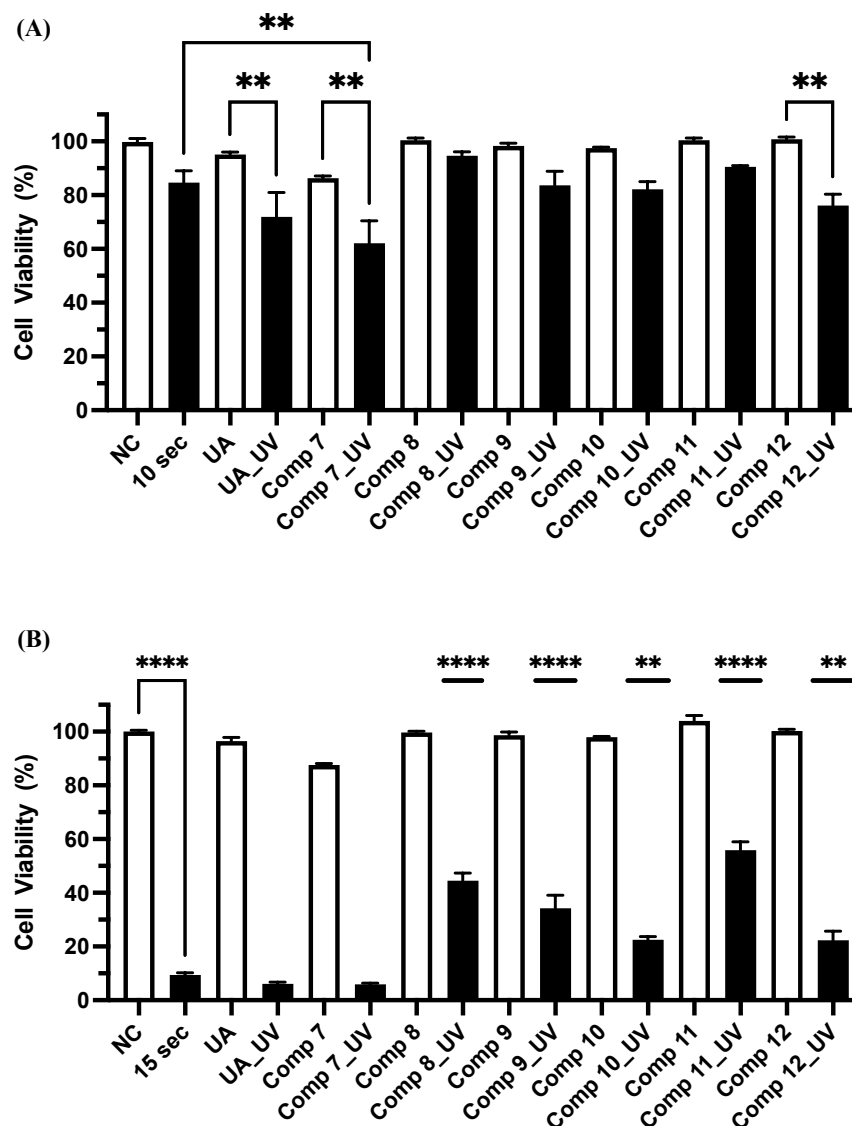


Figure 87. Combination of Compounds and low dose of UV-Vis. U-251 MG cells were pre-treated with NOAEL concentrations of compounds for 1 hour. After which was exposed to UV for 10 (A) and 15 (B) seconds. Cells were then incubated for 144 hours and analysed by AlamarBlue. Data shown was normalised to the untreated control (NC) and 1 minute UV treatment (PC) and are shown as the % mean \pm S.E.M (n=3). Statistical analysis was carried out using One-Way ANOVA with Bonferroni post-test (** $P \leq 0.01$, **** $P \leq 0.0001$). Significant difference indicated for (B) is with the NC.

The results obtained from both TMZ and UV-Vis to observe any effect of novel UA derivatives (7 – 12) to cell membrane damage implies that compounds may have a protective effect when exposed to radioactivity.

4.8 Cell Proliferation of Novel UA Derivatives

Studies of UA have shown that it could inhibit proliferation in a range of cancer cells. Wang *et al.* (2011) found that UA inhibited proliferation of gastric cancer cell line BGC-803 in a dose- and time-dependent manners. Tumour growth of hepatocellular cancer cell H22 xenografts treated with UA (20–60 $\mu\text{mol/L}$) was also inhibited at approximately 50%. Proliferation was also inhibited in colorectal cell lines HCT-116 and SW-480 cells after treating with 30 and 20 μM of UA, respectively (Yang *et al.*, 2021). In GBM models, low concentrations of UA and natural esters of UA have been shown to inhibit the proliferation of U-87 and SF-295 cells (Bonaccorsi *et al.*, 2008; Kondo *et al.*, 2011). A study by Wang *et al.* (2012) showed that treatment of UA of up to 40 μM inhibit proliferation which was caused by apoptosis. Hence, to investigate if inherent cell proliferation of UA can be retained or improved, cell proliferation in U-251 MG cells treated with novel UA derivatives (7 – 12) were determined.

4.8.1 Determining cell count using haemocytometer

Measuring cell proliferation can be performed by a number of different methods, each with varying levels of sensitivity, reproducibility and compatibility with high-throughput formatting. Initial method used in this study to determine if novel UA derivatives (7 – 12) inhibit proliferation was the conventional haemocytometer counting chamber (Morten *et al.*, 2016). The seeding density for 96 hours cell proliferation was first determined by seeding U-251 MG cells into 96-well plate at different densities - 1.5×10^3 , 3×10^3 and 5×10^3 cells/well. After each timepoint, cells were captured using Optika XDS-2 trinocular inverse microscope equipped with a microscope Camera ISH500, and then counted using haemocytometer.

Pearson's correlation obtained was not statistically significant for 1.5×10^3 cells/ml, but significant for 3×10^3 ($P \leq 0.05$) and 5×10^3 ($P \leq 0.01$) cells/well. As seen in **Figure 88** (B) cells has linear growth when seeded at 5×10^3 cells/well, however, the image in **Figure 88** (A) shows that cells become confluent after 72 hours. Hence, a median seeding density of 3×10^3 cells/well was used in this study.

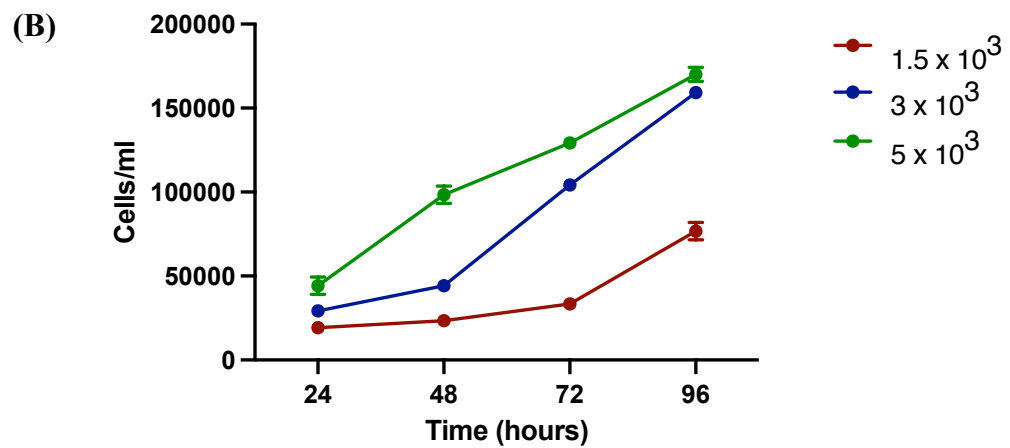
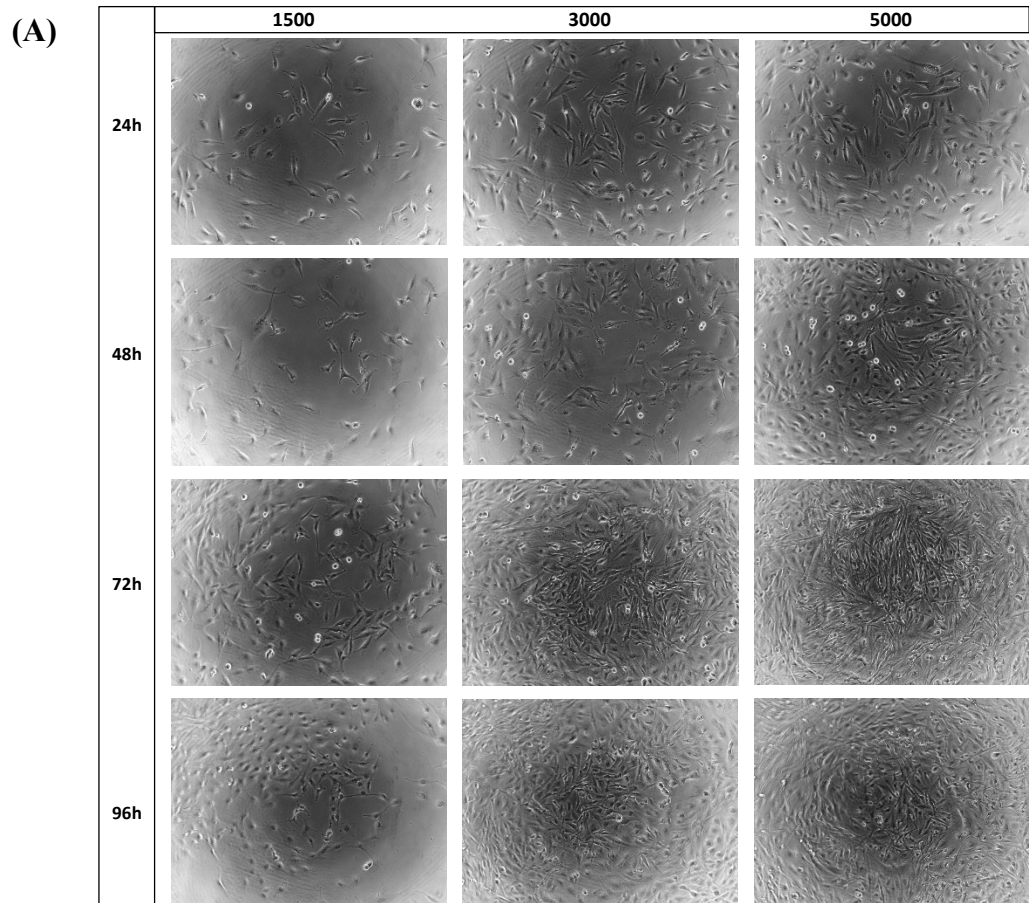


Figure 88. Cell proliferation seeding density. Cell Proliferation Measurement after 96 hours using haemocytometer in cells/ml. U-251 MG cells were seeded in a 96-well plate with 1.5×10^3 , 3×10^3 and 5×10^3 cells/well (100 μ l final volume), and incubated for 24, 48, 72 and 96 hours. Cells were dislodged and counted using a haemocytometer, for each timepoint. Concentration per ml was calculated and plotted in Graphpad Prism 9. Data are shown as the mean \pm S.E.M. of three independent experiments (n=3).

The proliferation of six novel UA derivatives (**7 – 12**) and UA at NOAEL concentration (144 hours; **A.25**), and a vehicle control of 0.1% DMSO were investigated in U-251 MG cells over the course of 96 hours. The Pearson's correlation data obtained showed that the vehicle control (0.1% DMSO) and UA were statistically significant ($P \leq 0.05$). Whereas novel UA derivatives (**7 – 12**) were not statistically significant ($P > 0.05$). This means that the cells treated with novel UA derivatives does not proliferate in a linear way. As shown in **Figure 89**, compounds **7, 9, 10** and **12** stopped proliferating and cells started to die after 72 hours treatment. Similarly, compounds **8** and **11** started to halt proliferation after 92 hours treatment.

It can be seen in **Figure 89** that both vehicle control (0.1% DMSO) and UA proliferated in the course of 96 hours, but UA proliferated slower. The control was found significantly different from UA ($P \leq 0.01$) after 24, 48 and 96 hours treatment. This confirms that UA inhibit proliferation of U-251 MG cells even at NOAEL concentration. There was no significant difference ($P > 0.05$) between UA and novel UA derivatives (**7 – 12**) at shorter time period (24 and 48 hours). Moreover, compounds **8** and **11** was not significantly different ($P > 0.05$) from UA even at longer timepoints (72 and 96 hours). However, compounds **7, 9, 10** and **12** were found statistically different from UA ($P \leq 0.0001$) at longer timepoint (72 and 96 hours).

After 72 hours treatment of NOAEL concentration, compound **7** inhibit the proliferation of U-251 MG cells of ~48%, while compounds **9, 10** and **12** inhibit ~35%, in comparison to UA. Promising results were observed after 96 hours were UA inhibited cell proliferation by ~18% compared to the vehicle control (0.1% DMSO). Furthermore, compounds **10** and **12** when compared to UA, inhibited ~49% and 28% cell proliferation,

respectively. Moreover, compounds **7** and **9**, inhibited cell proliferation of > 50% compared to UA.

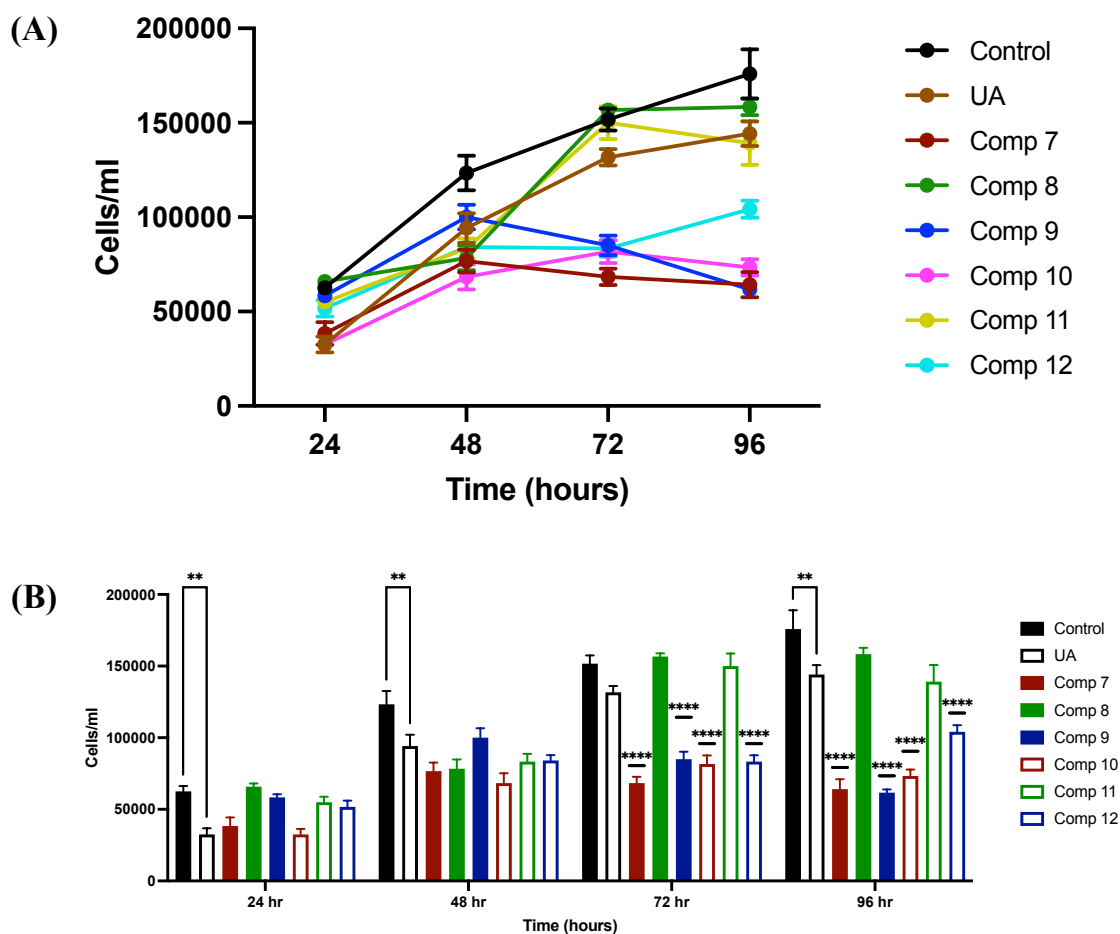


Figure 89. Cell Proliferation Measurement after 96 hours using haemocytometer in cells/ml. (A) Line graph showing growth for 96 hours and (B) Bar graph with statistical differences. U-251 MG cells were seeded in a 96-well plate with 3×10^3 cells/well (100 μ l final volume), treated with vehicle control (0.1% DMSO), NOAEL concentrations (A.25) of UA and novel UA derivatives (**7** – **12**), and incubated for 24, 48, 72 and 96 hours. Cells were dislodged and counted using a haemocytometer, for each timepoint. Concentration per ml was calculated and plotted in Graphpad Prism 9. Data are shown as the mean \pm S.E.M. of three independent experiments (n=3). Statistical analysis was carried out using Two-Way ANOVA with Bonferroni post-test (**p \leq 0.01, ****p \leq 0.0001).

4.8.2 Carboxy-luorescein succinimidyl ester (CFSE) Cell Proliferation Dye

To confirm cell proliferation results obtained using a haemocytometer, CellTrace™ CFSE Cell Proliferation kit, for flow cytometry was used to monitor distinct generations of proliferating cells. The CFSE dye fluorescently label live cells and track proliferation as the signal was diluted by cell division, and appears as different peaks on a flow cytometry histogram. To determine whether apoptosis was the cause for cells to stop proliferating, cells were also co-stained with cell impermeable dye, PI. U-251 MG cells were stained with CellTrace CFSE staining solution and adhered overnight. Then cells were treated with vehicle control (0.1% DMSO), positive control (20% DMSO), and NOAEL concentration (144 hours) of UA (**Figure 90**) and novel UA derivatives (**7 – 12; Figure 91**), and incubated for 96 hours. Cells were co-stained with PI and analysed using flow cytometry.

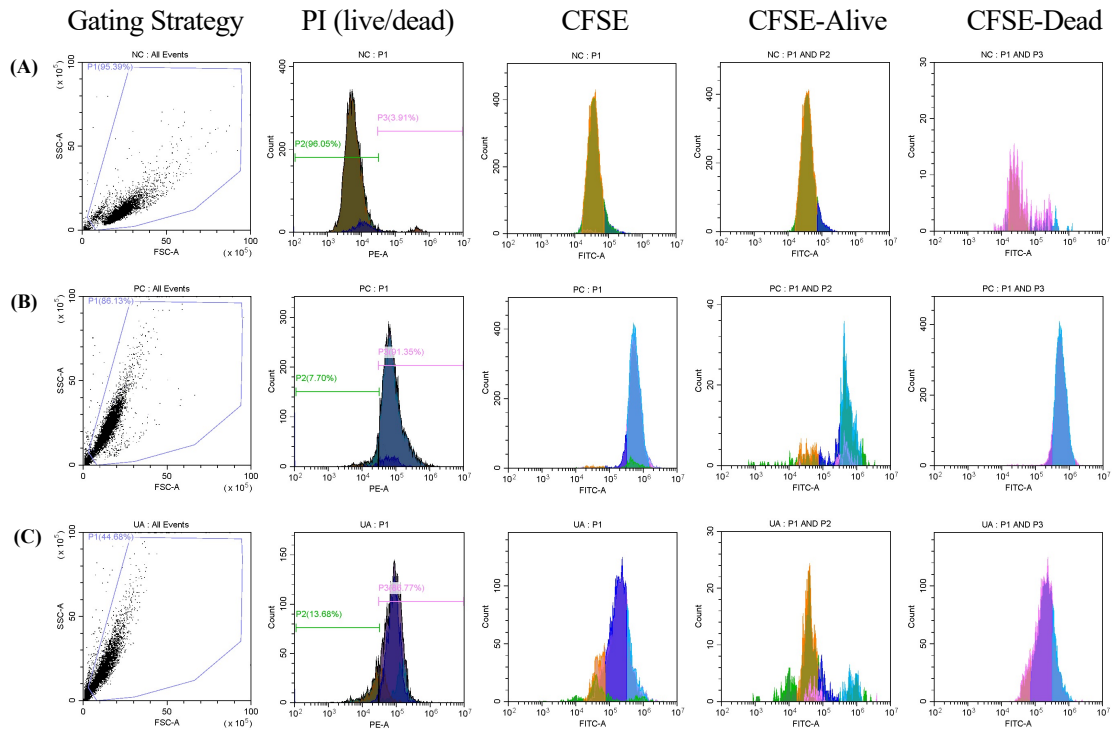


Figure 90. Histograms of CFSE proliferation of (A) vehicle control (NC; 0.1% DMSO), (B) positive control (PC; 20% DMSO), and (C) UA. Shown are the gating strategy conducted; determination of live and dead cells using PI – P2 (live cells), P3 (dead cells); cell proliferation; cell proliferation population of live cells; cell proliferation of dead cells.

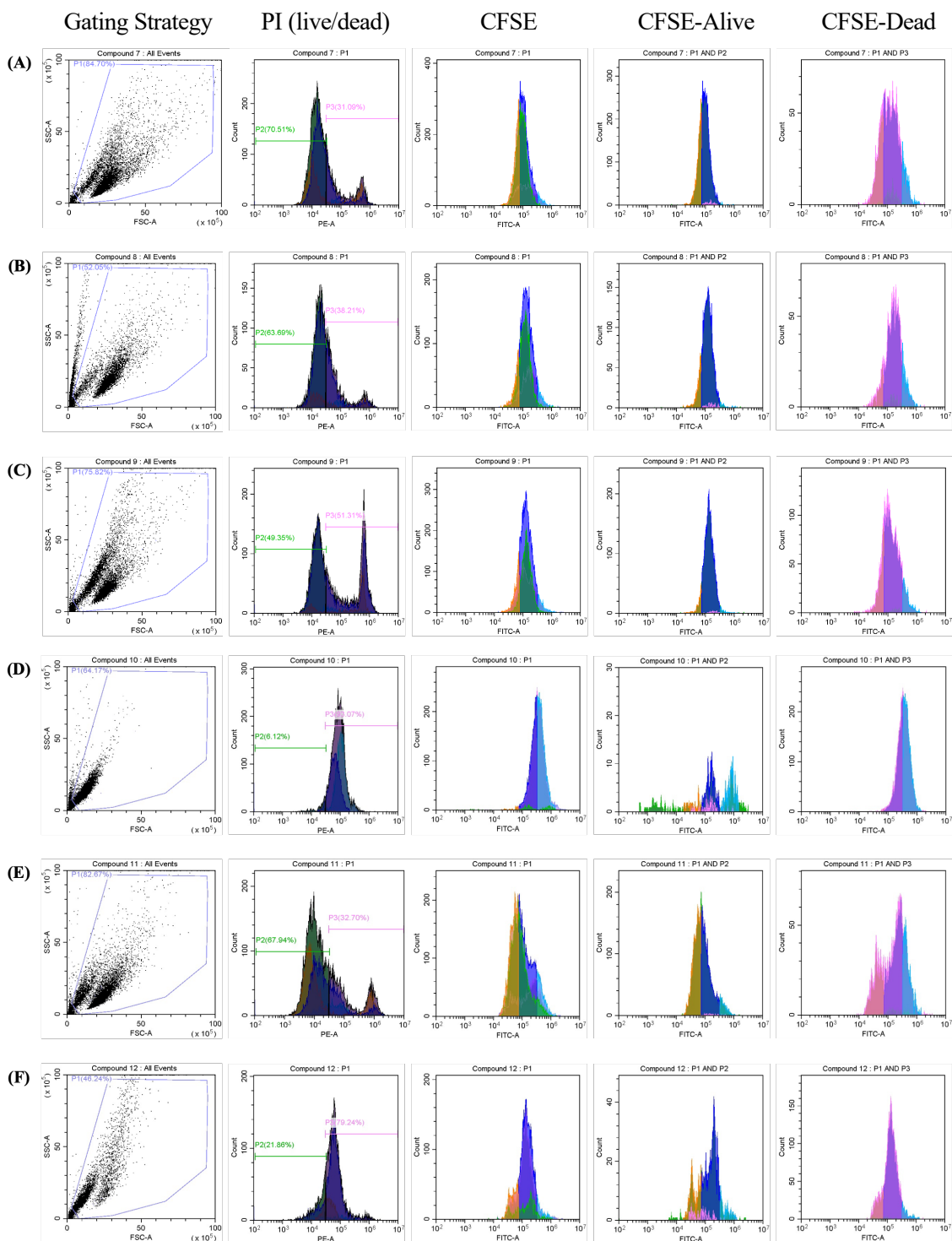


Figure 91. Histograms of CFSE proliferation of novel UA derivatives, compounds (A) 7, (B) 8, (C) 9, (D) 10, (E) 11, and (F) 12. Shown are the gating strategy conducted; determination of live and dead cells using PI – P2 (live cells), P3 (dead cells); cell proliferation; cell proliferation population of live cells; cell proliferation of dead cells.

As seen in **Figure 92**, the vehicle control (NC; 0.1% DMSO) undergone three cell divisions; a small population of apoptotic cells can also be seen. On the other hand, cells treated with the positive control (PC; 20% DMSO) died after one cell division and are PI positive. Whereas the cells treated with UA proliferated for four days but eventually died; some died after one cell division, most cells died after second cell division. Similar to the results obtained in haemocytometer, cells treated with compounds **8** and **11** started to die and become apoptotic after two cell divisions. Moreover, cells treated with compounds **7** and **9**, which inhibited > 50% cell proliferation compared to UA using haemocytometer, have undergone three cell divisions, with cells starting to die (apoptotic) after the second cell division. On the other hand, cells treated with compounds **10** and **12** have undergone two and three cell division, respectively. However, cells that survived eventually died. Results obtained from this study shows that compounds **10** and **12** retain the inherent anti-proliferative effect of UA in U-251 MG cells.

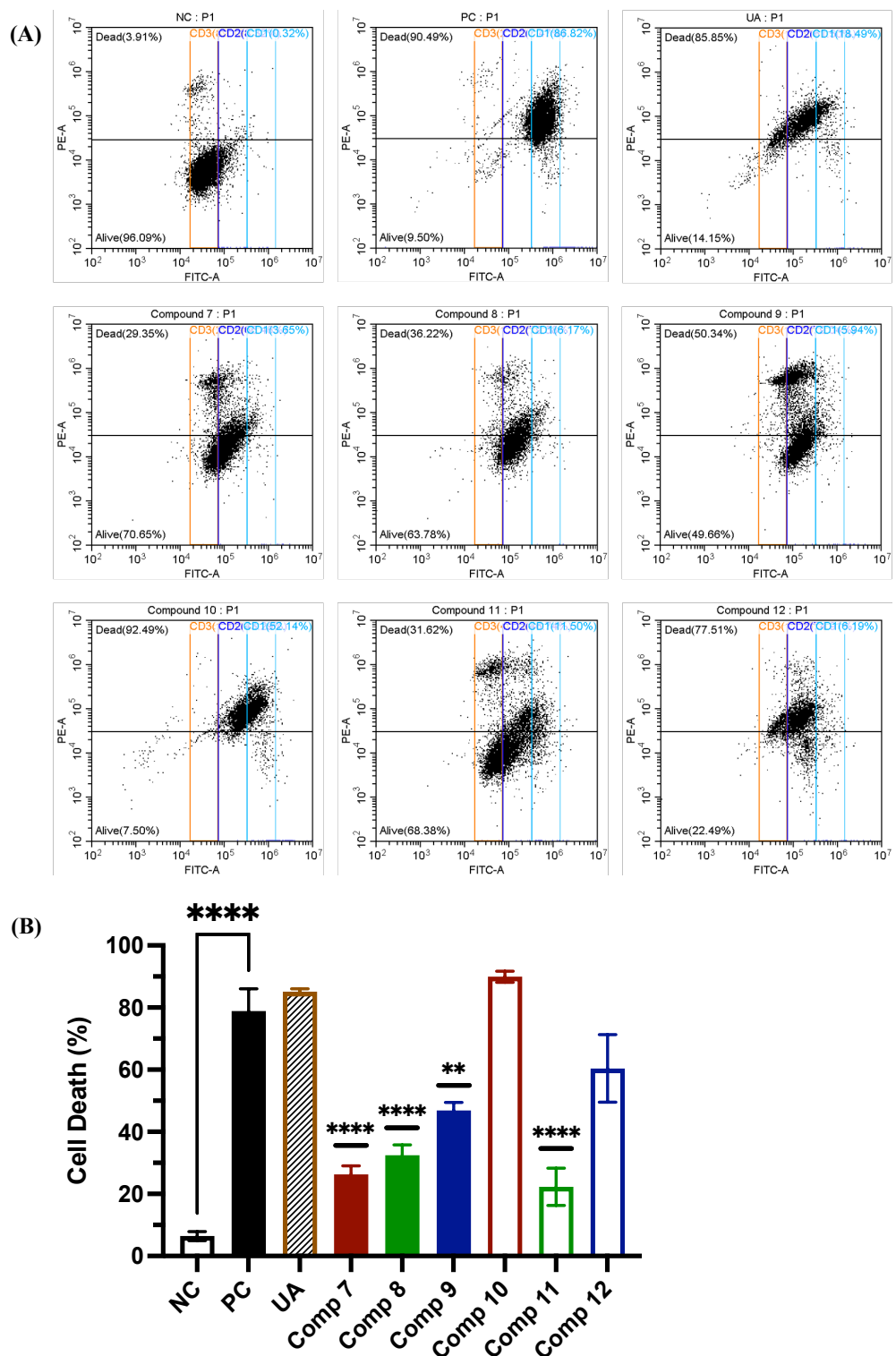


Figure 92. Cell proliferation and cell death of novel UA derivatives (7 – 12) in U-251 MG cells. (A) Dot plot of cell proliferation, co-stained with PI analysed using CytExpert software; and bar graph of the % and (B) cell death of compounds plotted using Graphpad Prism 9. Statistical analysis was carried out using One-Way ANOVA with Bonferroni post-test ($*P \leq 0.05$, $**P \leq 0.01$, $***P \leq 0.001$, $****P \leq 0.0001$). CD – cell division.

4.9 Cell Death Mechanism(s) of Novel UA Derivatives

Results obtained in this study showed that compounds **7**, **9**, **10** and **12** exhibit cytotoxic activity in a panel of cancer cell lines, especially in U-251 MG GBM cell line. The molecular mechanism involved surrounding GBM cell death in response to novel UA derivatives (**7** – **12**) were determined by exposing U-251 MG cells to a number of commonly employed inhibitors; caspase inhibitor zVAD-fmk, JNK inhibitor SP600125 and cysteine protease inhibitor E-64. The broad spectrum caspase-dependent apoptosis inhibitor, zVAD-fmk, is a cell-permeable pan-caspase inhibitor that irreversibly binds to the catalytic site of caspases (Fransolet *et al.*, 2019). Moreover, it can trigger necroptosis by inhibiting the activity of caspases 3, 7 and 8 (Li *et al.*, 2019). The JNK inhibitor, SP600125, is potent cell-permeable and reversible inhibitor which regulates both cancer cell apoptosis and survival (Wu *et al.*, 2020). Phosphorylation of JNK is inhibited in a dose-dependent manner, and is usually associated with downregulation of Beclin-1 and reduced autophagy (Lou *et al.*, 2019). Cysteine protease inhibitor, E-64, is irreversible, potent and highly selective. It irreversibly binds to an active thiol group in many cysteine proteases such as papain, and cathepsins B, H, D and L to form thioether linkage. E-64 is used in *in vivo* studies due to its specific inhibition and permeability in cells and tissues, with low toxicity (Matsumoto *et al.*, 1999; Zhang *et al.*, 2015).

These inhibitors were selected to ascertain molecular mechanisms that might be surrounding the cell death of U-251 MG cells treated with UA and the novel UA derivatives (**7** – **12**). The appropriate, non-toxic concentration of each inhibitor was obtained from previous studies by Conway *et al* (2016) and retrieved from literature search (Tiwari *et al*, 2008; Hwang *et al.*, 2009; Tuomela *et al.*, 2013; Haas *et al*, 2018)

that was based on the most recent studies which investigated the cell death inhibitory effects in U-251 MG cell line. Based on the literature information collected, working concentrations used in this study were 25 μ M of zVAD-fmk; 12.5 μ M of SP600125; and 15 μ M of E-64. To confirm activity of the inhibitors, positive controls – UV (SP600125 and zVAD-fmk) and ionomycin (E-64), were chosen as demonstrated in **Figure 93**. Dose response curve was performed for UV and ionomycin to determine IC₅₀; 12 seconds for UV and 2 μ M was used for ionomycin. It is evident from **Figure 93** that each inhibitor has significantly reduced the level of cytotoxicity induced by each compound. Vehicle control of 0.5% DMSO was used as a negative control, and 20% DMSO was employed as positive control. Cells were treated with calculated IC₅₀ for each timepoint summarised in **Table 24**. There was no deleterious effect observed from the vehicle control and working concentrations of inhibitors. Statistical significance was calculated by employing Two-Way ANOVA with Bonferroni's multiple comparison post-test (untreated control vs treatment).

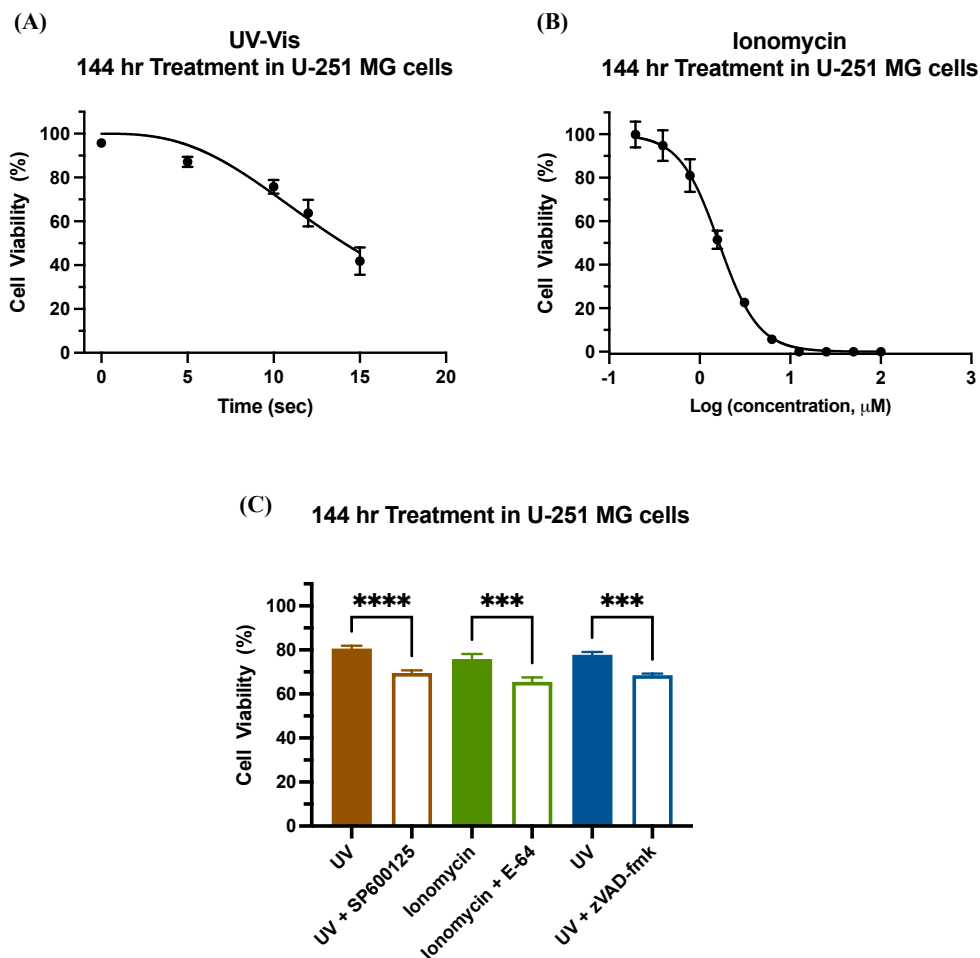


Figure 93. Optimisation of biochemical inhibitors to investigate mechanism(s) of cell death. (A) UV-Vis and (B) Ionomycin dose response curve in U-251 MG cells. (C) Cells were pre-treated with each inhibitor for 1 hour prior to addition of the positive control. After 144 hours, cells were analysed using AlamarBlue cell viability assay. Data shown was normalised to the untreated control and are shown as the % mean \pm S.E.M (n=3). Statistical analysis was carried out using One-Way ANOVA with Bonferroni post-test using Prism 9 statistical software (***P \leq 0.001, ****P \leq 0.0001).

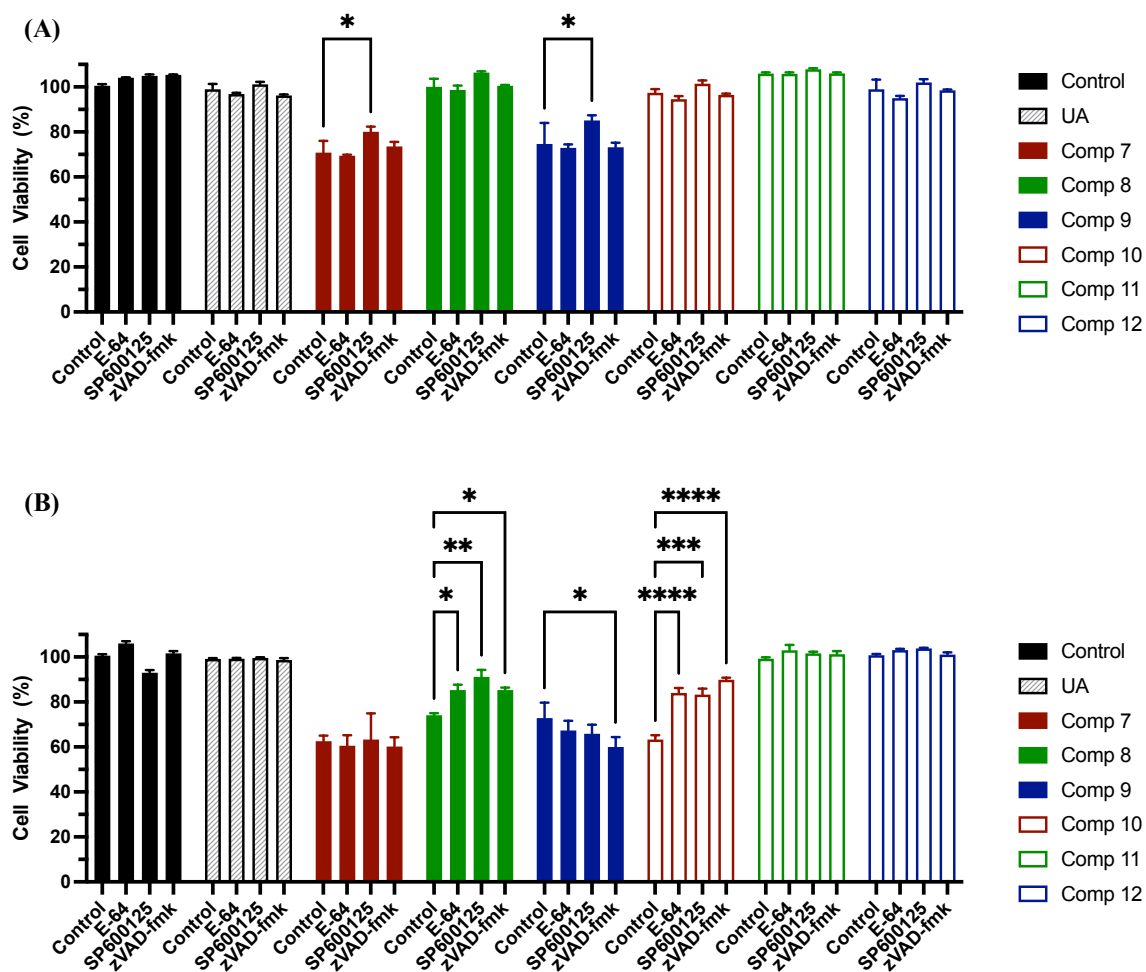


Figure 94. Inhibitor studies of novel UA derivatives (7 – 12). U-251 MG cells were pre-treated with 10 μ M E-64, 12.5 μ M SP600125 and 25 μ M zVAD-fmk for 1 hour. Cells were then treated with IC₅₀ of compounds determined for each timepoint. Then incubated for (A) 48 and (B) 144 hours, analysed by AlamarBlue. Data shown was normalised to the untreated control and are shown as the % mean \pm S.E.M (n=3). Statistical analysis was carried out using Two-Way ANOVA with Bonferroni's post-test (*P \leq 0.05, **P \leq 0.01, ***P \leq 0.001, ****P \leq 0.0001).

Results showed (**Figure 94**) that treatment with IC₅₀ of UA for 48 and 144 hours has no statistically significant ($p > 0.05$) increase in cell viability. This is in contrast to results obtained by Conway *et al.*, 2016, where they found that 20 μM of UA may induce JNK dependent cytotoxicity. However, further analysis was required for their study to confirm results they obtained. Additionally, the concentration used in this study was 14 μM and Conway *et al* (2016) did not observe increase in cell viability at 15 μM . Similarly, compounds **11** and **12** did not exhibit ($P > 0.05$) increase in cell viability both after 48 and 144 hours.

However, after 48 hours treatment, compounds **7** and **9** exhibited a statistically significant increase ($P \leq 0.05$) in cells co-treated with JNK inhibitor SP600125. This means that it could trigger JNK signalling pathway at shorter timepoint which is similar to results obtained by Conway *et al* (2021). However, there was no increase in cell viability observed in compound **7** and **9** after 144 hours.

Promising results was observed with cells treated with compounds **8** and **10** co-treated with inhibitors at longer timepoint (144 hours), which suggests that it might trigger multiple cell demise pathway. It was observed that compound **8** co-treated with E-64 ($P \leq 0.05$), SP600125 ($P \leq 0.01$) and zVAD-fmk ($P \leq 0.05$), alleviated cell viability. Similarly, compound **10** co-treatment with E-64 ($P \leq 0.0001$), SP600125 ($P \leq 0.001$) and zVAD-fmk ($P \leq 0.0001$), greatly increased cell viability. Results obtained suggests that compounds **8** and **10** might trigger a caspase-dependent, JNK-dependent and calpain-mediated cell death.

To date, there has been many studies published in understanding the molecular mechanism(s) involved in the induction of cell death following treatment with UA *in vitro*. Although reports confirmed that UA induced cytotoxic effects in different cancer cells, there have been inconsistencies on the mechanism(s) involved in cell death. Studies have suggested that apoptosis, autophagy and necrosis are the underlying mechanisms, which varies between cell lines. Very little is known on the different mechanism(s) of action of various UA derivatives in GBM models apart from it suggests that UA can induce cell death. A study by Wang *et al* (2012) reported that apoptosis in GBM cells was initiated through increased caspase-3 expression and suppression of the transforming growth factor- β 1/micro-RNA-21/ programmed-cell death protein 4(TGF- β 1 / miR-21/PDCD4) pathway. Additionally, micro-RNA-21 (miR-21), a protein involved in the regulation of apoptosis, has been shown to be up-regulated in GBM and exhibit anti-apoptotic effects through regulation PDCD4 (Chan *et al*, 2005). A more recent study have shown a different mechanism of cell death, autophagy following Ca^{2+} release from the ER lumen and activation of the AMPK-mTOR kinase signalling cascade in U-87 MG GBM cells (Shen *et al*, 2014).

Results obtained shows that compounds **8** and **10** at longer timepoint, suggests a caspase-dependent and JNK-dependent signalling pathway might have initiated apoptosis or programmed cell death. Additionally, calpain-mediated cell death/cytotoxicity may also play a role by lysosome associated membrane permeability (LMP), followed by cathepsin B and cathepsin D release from lysosomes into the cytoplasm (Liu *et al.*, 2016).

4.10 *In Vitro* Cytotoxicity Assay in 3D cell culture model

Although 2D cell culture have been widely used in the field of cancer research, 2D models are too simple and unable to mimic the complexity and interactions of the tumour microenvironment. Moreover, 2D cell culture does not reveal toxicological resistant and accurate cellular responses (Jensen and Teng, 2020; Rodrigues *et al.*, 2021). It also provides unreliable predictions on *in-vivo* drug efficiency and toxicology, which leads to a lower success rate in clinical trials. While animal testing is expensive, complex, time consuming, rising ethical concerns, inaccurate depiction of effectiveness and side effects of drugs (Li *et al.*, 2020). To overcome all the above drawbacks, 3D cell culture has attracted great interest in the field of cancer therapy. Multicellular 3D cell culture models are beneficial for bridging the gap between *in vitro* cell cultures and *in vivo* responses by closely mimicking the natural *in vivo* environment (Colombo and Cattaneo, 2021; Farhat *et al.*, 2021). It also plays a major role in understanding chemotherapeutic effects against treatment of cancer due to tumour microenvironment's role in tumour progression, metastasis, angiogenesis, cytotoxicity resistance, and immune cell modulation (Carter *et al.*, 2021; Wanigasekara *et al.*, 2022).

In our group, the *in vitro* generation of U-251 MG and A431 spheroids using low attachment plate method was optimised by Janith Wanigasekara and published in protocol.io and PLOSOne (*under review*) (Carroll *et al.*, 2021; Wanigasekara *et al.*, 2022). This method uses low-adhesion plates that are coated with hydrophilic polymer to allow cells to cluster together, forming their own extracellular matrix, rather than sticking to the plate surface. In this study, Janith Wanigasekara prepared the 3D tumour spheres which I then treated and analysed. The 2D cell culture for U-251 MG and A431 showed

that there was a delayed cytotoxicity for Boc-protected compounds (**7 – 9**). Hence, we looked at the effect of all novel UA derivatives (**7 – 12**) in U-251 MG and A431 3D cell culture models, which closely resembles human *in vivo* glioblastoma and epidermal conditions to study the novel UA derivative's effectivity towards treatment of cancer.

The calculated IC₅₀ cytotoxicity values are compiled in **Table 26**, and the heatmap of the IC₅₀ values can be depicted in **Figure 96**. The dose-response curve for each cell lines are shown in **Figure 95**. As shown in **Figure 96**, the 3D cell culture results from Boc-protected compounds (**7 – 9**) as well as compound **11**, did not show any activity both after 48 and 144 hours treatment in U-251 MG and A431 cell lines. However, deprotected compounds **10** and **12** exhibited more than a two-fold increase in IC₅₀ cytotoxicity in comparison to UA in both U-251 MG and A431 cell lines at 48 and 144 hours timepoint. In U-251 MG cells the IC₅₀ of UA, compound **10** and compound **12** were 70.01 μM, 28.36 μM and 26.38 μM after 48 hours, respectively; 33.03 μM, 14.83 μM and 7.87 μM after 144 hours, respectively. Whereas in A431 the IC₅₀ of UA, compound **10** and compound **12** obtained were 68.85 μM, 29.23 μM and 41.32 μM after 48 hours, respectively; 50 μM, 12.83 μM and 23.51 μM after 144 hours, respectively.

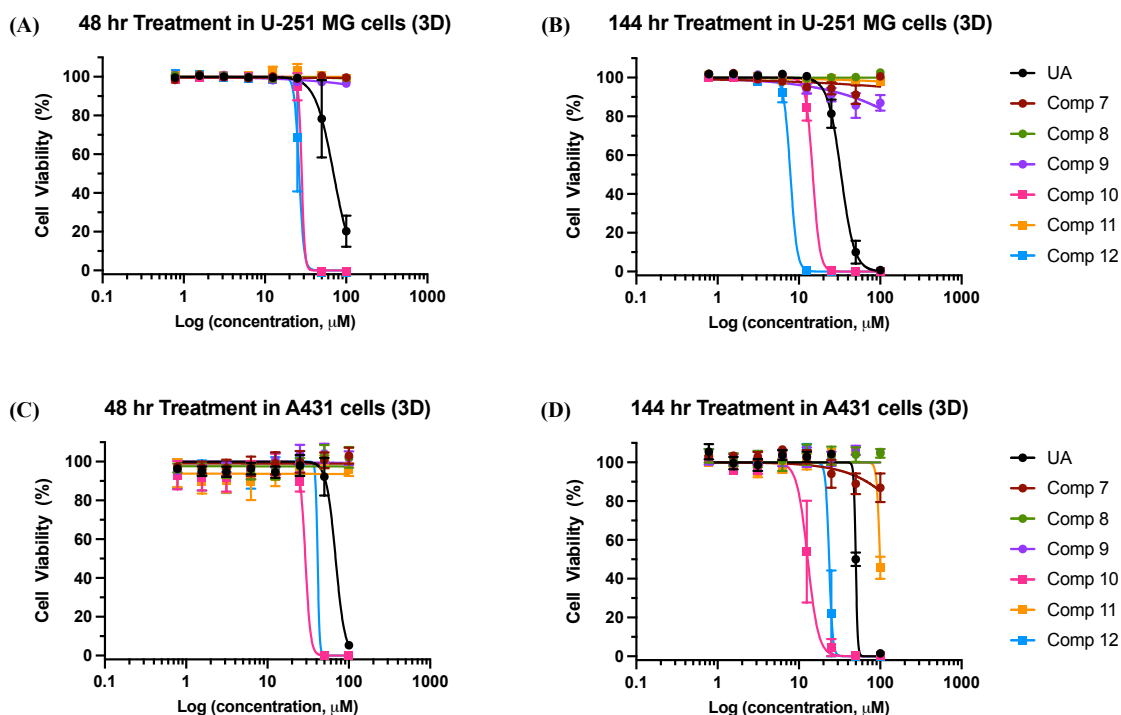


Figure 95. Cytotoxicity of novel UA derivatives in 3D cell culture. An initial concentration of 100 μM in culture medium was added to **(A, B)** U-251 MG and **(C, D)** A431 cells and serially diluted to different concentrations (100 μM to 3.125 μM). AlamarBlue cell viability assay was then carried out following treatment for 48 and 144 hours. Data shown were normalised to the untreated control and are shown as the % mean \pm SEM. Statistical analysis was carried out using non-linear regression analysis and Two-way ANOVA with Bonferroni post-tests, ($n = 3$) ($P < 0.0001$).

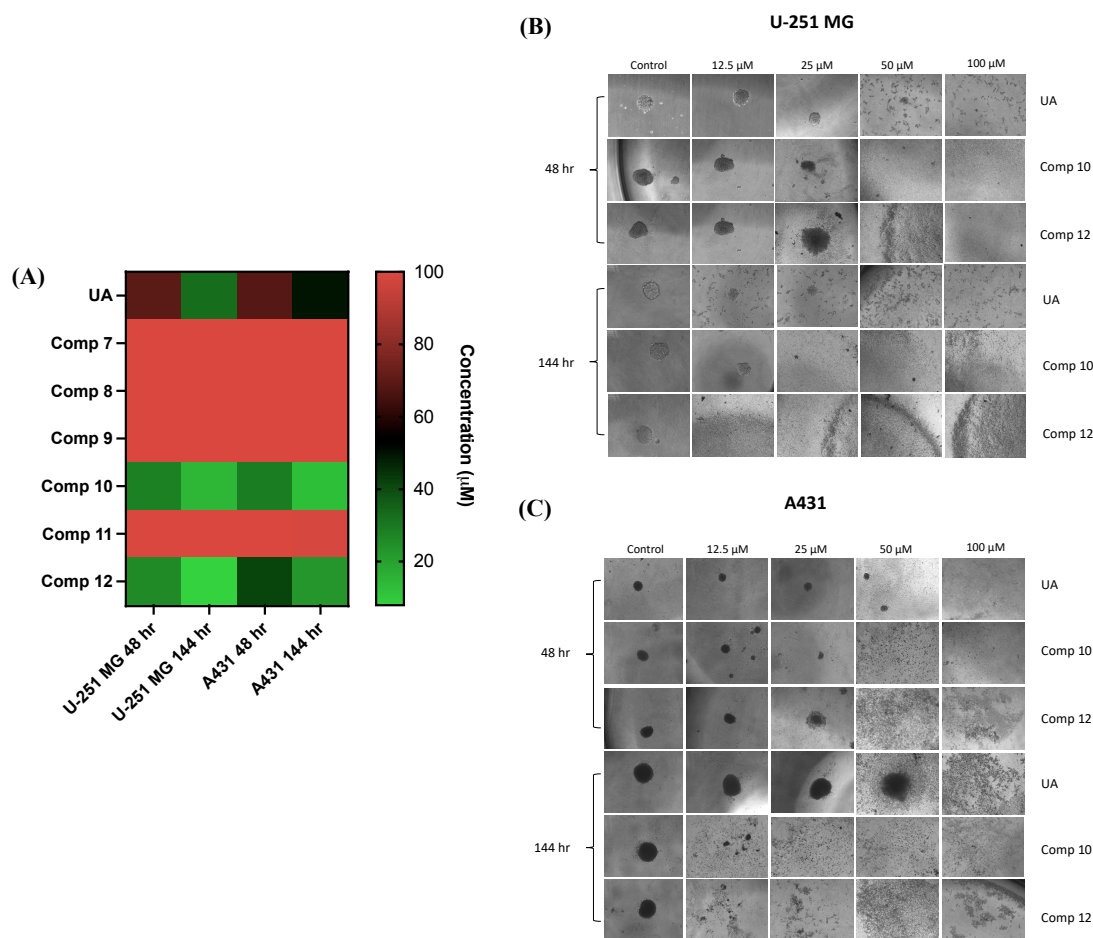


Figure 96. Novel UA derivatives in U-251 MG and A431 cells using 3D cell model. **(A)** Heatmap of the IC_{50} of Novel UA derivatives. Initial concentration of 100 μM in culture medium was added to cells and serially diluted to different concentrations, as indicated. Alamar blue cell viability assay was then carried out following treatment for 48 and 144 hours. Statistical analysis was carried out using non-linear regression analysis, ($n = 3$). Images of **(B)** U-251 MG cells and **(C)** A431 cells. Captured using Optika XDS-2 trinocular inverse microscope equipped with a microscope Camera ISH500.

Table 26. The 2D and 3D cell culture IC₅₀ of novel UA derivatives (**7 – 12**) in U-251 MG and A431 cell lines. The colours are in comparison to the cytotoxicity of UA – green (enhanced), orange (slightly decreased) and red (decreased).

Compound	IC ₅₀ (μ M) in 2D cells				IC ₅₀ (μ M) in 3D cells			
	U-251 MG		A431		U-251 MG		A431	
	48 hr	144 hr	48 hr	144 hr	48 hr	144 hr	48 hr	144 hr
UA	<u>16.46±0.89</u>	<u>12.83±0.72</u>	<u>31.01±1.60</u>	<u>15.20±5.64</u>	<u>70.01±5.08</u>	<u>33.03±1.10</u>	<u>68.85±4.71</u>	<u>50.00</u>
Comp 7	> 50	6.67±0.51	> 50	9.77±0.38	> 100	> 100	> 100	> 100
Comp 8	> 50	>50	> 50	>50	> 100	> 100	> 100	> 100
Comp 9	> 50	8.61±0.42	> 50	11.32±0.31	> 100	> 100	> 100	> 100
Comp 10	7.58±0.39	5.40±0.43	7.09±2.37	3.84±0.03	28.36	14.83±1.55	29.23±49.55	12.83±0.76
Comp 11	32.10±3.50	14.60±1.69	41.79±0.70	23.87±2248.6	> 100	> 100	> 100	99.21
Comp 12	14.22±1.02	7.66±0.63	16.87±0.69	13.08±0.58	26.38±148.76	7.87±0.60	41.32	23.51

Results obtained in this study correlates with data from 2D cell culture assay where compounds with disulphide linker (**8** and **11**), inhibited activity of UA. The Boc-protected compounds (**7** and **9**) exhibited delayed activity in 2D cell culture assay, however, no activity was observed in 3D cell culture assay. The Boc-protection of the compound may be inhibiting cell penetration to 3D tumour spheres. In contrast, the deprotected analogues (**10** and **12**) exhibited an activity with more than two-fold increase in comparison to UA which is consistent in both 2D and 3D cell culture assay.

4.11 Summary

The investigation on the increased cytotoxic activity of the novel FUA derivatives has opened a new research avenue. The intermediates (novel UA derivatives; **7 – 12**) exhibited cytotoxic activity in U-251 MG cells, and we found that the linkers on their own did not contribute to the observed cytotoxicity. Hence, it was the modification at the C-28 of UA and the conjugation of amine moiety that demonstrated the activity.

The *in silico* pharmacokinetic studies of UA, and compounds **10** and **12** predicted using SwissADME, have violated one Lipinski's rule-of-five. UA is highly lipophilic (MLOGP 5.82), and so it was greater than the lipophilicity value recommended by SwissADME (MLOGP ≤ 4.15); compound **10** also had MLOGP value of 4.94 which is slightly better than UA. On the other hand, compound **12** has improved the solubility of UA which confirms our aim as it is an ethereal oxygen linker designed to improve water solubility, however MW was slightly above 500 g/mol. Nevertheless, both compounds **10** and **12** slightly improved the physicochemical properties of UA. This was further confirmed by the BOILED-Egg diagram obtained which showed that compound **10** has high gastrointestinal absorption, and compound **12** had slightly better HIA than UA. However, all the other novel UA derivatives violated 2 Lipinski's rule-of-five and did not improve *in silico* physicochemical properties of UA. The Boc protected compounds (**7 – 9**) were also predicted to be an inhibitor of CYP3A4, wherein activity can either be amplified or weakened. In addition, all novel UA derivatives (**7 – 12**) were not predicted to cross the BBB.

The molecular docking studies performed for novel UA derivatives (**7 – 12**) was predicted to bind to some of the important residues in the binding pocket of the target protein VRK1. However, all compounds except compound **9**, was bound slightly outside of the binding pocket; compound **9** had a different orientation and was found bound to a different site but still interacted with some important residues in the binding pocket. All predicted binding affinities obtained for novel UA derivatives (**7 – 12**) were lower than UA.

The cytotoxicity assays (alamarBlue, PI and JC-1) obtained for novel UA derivatives (**7 – 12**) showed that compounds **8** and **11** inhibited the activity compared with UA, which could be due to the disulphide bond that cleaves within the cell, yielding a thiol (SH) end group instead of a Boc (methyl) or an amine. The Boc-protected compounds **7** and **9**, exhibited a delayed activity which are more apparent in U-251 MG and A431 cell lines, whereas deprotected compounds **10** and **12** exhibited an activity with more than two-fold increase in comparison to UA across all cell lines tested. The delayed cytotoxicity of Boc-protected compounds prompted the investigation of its stability. It was concluded that neither the stability in media nor a cell-based enzymatic process was the reason for the delayed cytotoxicity observed.

The preliminary investigation for the inherent ability of UA to halt U-251 MG cell migration was performed by collective cell migration (scratch assay). This study has revealed that novel UA derivatives (**7 – 12**) can inhibit cell migration of U-251 MG cells even at NOAEL concentrations. Furthermore, the inherent cell proliferative effect of UA was investigated using cell counter (haemocytometer) and CFSE dye over the course of 96 hours. Compounds **7**, **8**, **9** and **11** partially inhibited proliferation, with majority of cells started dying after two cell divisions. However, cytotoxicity was only observed after

6 days, hence it will be interesting to determine proliferative activity of these compounds at longer timepoints. On the other hand, compounds **10** and **12** inhibited proliferation which were not statistically different from UA ($P > 0.05$). The synergistic studies focusing on the cell membrane damage performed showed that novel UA derivatives (**7 – 12**) may have a protective effect when exposed to radioactivity. In addition, the initial inhibitor studies suggests that compounds **8** and **10** at longer timepoint, may trigger multiple cell demise pathway. Lastly, the 3D cell culture assay performed showed that compounds **10** and **12** enhanced the cytotoxic activity of UA by more than two-fold. All results obtained in this study warrant further investigation.

CHAPTER 5

GENERAL DISCUSSION

5.0 General Discussion

Glioblastoma is considered to be the most biologically aggressive type of brain tumour due to the localisation within the brain tissue, complex heterogeneity and aggressive infiltrative growth. Current therapeutic strategies such as maximal tumour resection, radiotherapy and treatment with TMZ (either alone or in combination, referred to as ‘Stupp protocol’) has been the standard of care for patients with GBM since its publication in 2005 (Stupp *et al.*, 2005). Even though overall survival has improved, recurrence within few months remain inevitable and combination treatment strategies have proven to be ineffective due to cells becoming radio and chemo resistant. It is evident that there is a need for the development of more novel and effective therapeutic strategies for the treatment of glioblastoma. It is essential that these targets have the ability to overcome GBM resistance, and be able to cross the BBB, taken into account its effect on patient’s quality of life due to off-target side effects.

This study was primarily designed on developing a targeted drug delivery for GBM. Wherein we examined the folate targeted drug delivery due to the overexpression of folate receptors in a range of cancer cell lines, including GBM, and low expression in normal cells. A review of the literature has revealed that folic acid (vitamin B9) has high affinity to folate receptors (specifically FR α which is overexpressed in majority of cancer cells), along with other advantages such as it is relatively small in size, readily available, stable over a broad range of temperature and pH, and simple conjugation chemistry. In addition, it has been proven that entry of folic acid is governed by RME, which is also one of the most effective drug delivery for brain cancer. This strategy confers excellent selectivity to FR α -expressing cancer cells while preserving drug potency.

Chemotherapeutic drugs have been widely used in cancer treatment, and approximately 60% anti-cancer drugs are derived from natural products (Gordaliza, 2007). The effectiveness of a range of bioactive compounds against cancer prompted our group to investigate the activity of a pentacyclic triterpenoid, UA, derived from leaves, berries and waxy coating of apples (Chen *et al.*, 2018). UA has been attracting increasing attention both *in vitro* and *in vivo* due to its broad anti-cancer activities and minimal toxicity to normal cells. It has also been shown to influence many different cancer pathways. Our recent publication demonstrated that UA exhibited anti-cancer activities over conventional chemotherapeutic agents used to treat GBM (TMZ, BCNU and Gefitinib). Additionally, UA was shown to induce cytotoxicity, inhibit migration and partially activate autophagy in U-251 MG GBM cell line (Conway *et al.*, 2021). However, its low solubility, permeability and low natural bioavailability hindered its clinical application (Shao *et al.*, 2020). Hence, in this study, we attempted to improve delivery of UA by conjugating it to folic acid for targeted drug delivery to the brain (GBM).

In this study, six novel UA derivatives (**7 – 12**) and three novel FUA derivatives (**13 – 15**) were synthesised with good yield and purity. The compounds were characterised using FTIR, NMR (¹H NMR and ¹³C NMR) and mass spectrometry. However, it is worth noting that the initial aim for this study was the conjugation of folic acid to UA – novel FUA derivatives (**13 – 15**) for targeted drug delivery. Hence, in this study, we conjugated UA and folic acid by conjugating a diamine linker to both carboxylic acid end. Three different linkers were used to improve bioactivity, solubility and bioavailability (1) the first contains an ethylenediamine linker intended to simply reduce steric hindrance; (2) the second possesses a self-immolative disulphide linker that can be cleaved within the cell to release UA; and (3) the third contains an ethereal oxygen chain to improve water

solubility. The successful synthesis of compounds **13** – **15** allowed the biological assessments in different cellular models.

Cytotoxicity studies conducted using alamarBlue cell viability assay showed that novel FUA derivatives (**13** – **15**) were only reducing ~20% cell viability at 100 μ M which were more evident after 144 hours in U-251 MG, Caco-2 and MCF-7 cell lines. Optimum result was observed in SKOV-3 cells at 144 hours treatment, with compounds **13** and **14** reducing ~50% cell viability. However, UA control was found to be >seven-fold more cytotoxic than compounds **13** and **14**. In which was then concluded that cytotoxic activity of UA was inhibited or decreased. An attempt to improve delivery of novel FUA derivatives was performed using an in-house ultrasound water bath. However, no difference was observed in combination with 5 and 10 min ultrasound treatment. It is worth noting that ultrasound assisted delivery has potential as activity of UA was enhanced by ~20% in combination with 5 and 10 min ultrasound treatment.

The lost or decreased cytotoxicity of novel FUA derivatives were investigated using different media (no, low and medium folate) in where we did not observe any improvement in the cytotoxicity. However, it is worth noting that activity was better in the media with no folic acid which is apparent in U-251 MG cells used in all three different media (**A.26**). Studies have shown that higher FR expression in cancer cells grown in folate-free medium (Yang *et al.*, 2007; Necela *et al.*, 2014; Mendes *et al.*, 2018; Crowley *et al.*, 2019). According to Antony *et al* (2004), folate deficiency results in homocysteine cellular accumulation, and due to interaction of homocysteine with protein-mRNA complex which stimulates FR expression, there are higher levels of FR in the membrane to capture folate molecules and normalise the cellular levels of folate. Hence,

folate-free medium was established as the optimum medium for the study of novel FUA derivatives (**13 – 15**). Since the folate expression of cell lines (U-251 MG, SKOV-3, Caco-2 and MCF-7) used in this study was not measured, we used methotrexate as a control to determine if FR is active in these cell lines. Results obtained have revealed that the folate receptor was active in all cell lines used. The treatment of U-251 MG cells with higher concentrations of novel FUA derivatives (**13 – 15**) has revealed that cytotoxicity of UA was greatly reduced. The most cytotoxic compound was found to be compound **15** which had an IC₅₀ of ~200 µM after 144 hr treatment, which was more than ten times the cytotoxicity of UA. It can be concluded that the conjugation of folic acid to UA significantly decreased the inherent cytotoxic activity of UA.

The ability to attach chemical warheads to ligands that seek out FR α -expressing tumours, due to its excellent selectivity while preserving drug potency, has led to the development of many small molecule-drug conjugates based on folic acid. Some of the studies published in the literature are vintafolide, folate-taxoid, and folate-camptothecin (Fernandez, Javaid and Chudasama, 2017). Vintafolide, a water-soluble conjugate, is composed of folic acid, a hydrophilic peptide spacer and self-immolative disulphide linker to deliver the drug desacetyl vinblastine monohydrate (Leamon *et al.*, 2014). It has a molecular weight of 1917 Da with a distribution time of 6 minutes indicating rapid uptake which is desirable in minimising circulation time and avoiding premature drug release (Bailly, 2014). It also rapidly cleared from the body (elimination half-life of 26 minutes) *via* kidneys and liver (Vergote and Leamon, 2015). Vintafolide has shown promise both as a single agent, as well as in combination with doxorubicin in phase II trials (ovarian and non-small cell lung carcinoma) and phase III trials for advanced stage platinum-resistant ovarian cancer. Folate-taxoid has self-immolative disulphide linker

and hydrophilic PEGylated dipeptide spacer (Seitz *et al.*, 2015). It is more cytotoxic (three-fold) in FR-positive cells than in FR-negative cells. It exhibited more than 1000-fold decrease toxicity in normal cells. Ideally, a drug should be for maximum biological activity in its unmodified forms. Release of drugs from folate conjugates depends on GSH levels in cells (Fernandez, Javaid and Chudasama, 2017). On the other hand, folate-camptothecin does not bear a disulphide linker but is cleaved by an enzyme. It has been developed to deliver enzyme to FR prior to administration of a prodrug that is converted to the active form by this enzyme (Paranjpe, Stein and Sinko, 2005). Example is penicillin-V amidase and doxorubicin prodrug (Lu *et al.*, 1999).

Similar to the vintafolide and folate-taxoid, UA-CYS-FA (**14**), consisted a self-immolative linker, whereas UA-EDA-FA (**13**) and UA-EDEA-FA (**15**) consisted a non-cleavable linkers or linkers with stable amides. Disulphide linker is susceptible to cleavage in circulation by a number of free thiol-containing substances, which might result in unwanted premature drug release (Fernandez *et al.*, 2018). Hence, linkers with no disulphide bond such as in compounds **13** and **15**, might limit off-target drug release in the circulation. The decreased cytotoxicity observed from the novel FUA derivatives suggests that incorporation of a cleavable linker did not exhibit significant difference to non-cleavable linkers. This is contrary to previous studies with vintafolide where Vlahov and Leamon (2012) evaluated that self-immolative linkers have enhanced activity in comparison to linkers with more stable amide.

The molecular docking studies performed has revealed that novel FUA derivatives (**13** – **15**), although slightly outside of the binding pocket in comparison to folic acid, were predicted to bind to FR α and interacts with the important residues in the binding pocket.

The predicted binding affinity were also similar to folic acid which indicates that the conjugation of UA does not interfere with folic acid binding to FR α . Thus, confirming published data that the pteroyl element of folate was buried inside the receptor, whereas glutamate moiety sits at the pocket entrance (Vlahov *et al.*, 2012). In addition, UA was conjugated at the γ -carboxylic acid which was known to be further away from the binding pocket as α -carboxylic acid group is known to be involved in the interaction with the FR α (Chen *et al.*, 2013). The novel FUA derivatives (**13** – **15**) binding to FR α may predictedly warrant a folate RME uptake in cells. Hence, it can be concluded that the lost or decreased cytotoxicity was not likely due to the uptake of novel FUA derivatives in cells *via* folate RME. However, the molecular docking studies with the target protein for UA, VRK1, were decreased in novel FUA derivatives (**13** – **15**). This is because the folic acid moiety was predicted to be bound to the binding pocket, interacting with the important residues. Whereas the UA moiety was predicted bound outside of the binding pocket.

The solubility of novel FUA derivatives (**13** – **15**) proved challenging and most were only partly soluble in hot DMSO. The pharmacokinetic studies performed showed that novel FUA derivatives are less soluble than UA. This highlights some of the challenges faced by medicinal chemists in developing novel compounds with therapeutic potential and their sustainability in *in vitro* testing. The lipophilicity obtained for novel FUA derivatives in the pharmacokinetic study conducted showed that it improved the lipophilicity of UA, but the polarity was higher and beyond the accepted predicted SwissADME value $> 140 \text{ \AA}^2$. In addition, molecular weight of novel FUA derivatives were twice that of UA. As a result, novel FUA derivatives were predicted to have a very low gastrointestinal absorption and BBB penetration. Typical folate-drug conjugates are

lower than 2000 Da and novel FUA derivatives (**13 – 15**) were only ~1,000 Da. Hence, the size might not be the reason for the decreased cytotoxicity but possibly water solubility, which hindered uptake and possibly warrant premature drug release. Folate-small molecule drug conjugates also consisted of a hydrophilic spacer which was not incorporated in our study (Mustafa, 2021).

Our study was then shifted to the investigation of the novel UA derivatives (**7 – 12**) due to the promising results observed. Structural modifications of UA published in the literature was focused more on C3, C12 - 13 and C28. It was found that configuration at C3 is crucial for the cytotoxicity, C12 and C13 contributes to cytotoxicity, and modification at C28 could enhance cytotoxicity with appropriate substitution (Chen *et al.*, 2015; Khwaza, Oyedeki and Aderibigbe, 2020). Hence, in this study, we focused more on the modification of C28 in an attempt to improve solubility and bioavailability of UA. A lot of studies have shown that an amine moiety at the C28 greatly improved the anti-cancer activity of UA. A study by Daneshtelab *et al* (2005) have shown that an amino alkyl group significantly improved cytotoxicity in HL-60 and Bel-7402. Another study has revealed that amide coupling with an amino alcohol acetate or amino acid methyl ester at C28 enhanced anticancer activity in HeLa cells. However, too many branched alkyl side chains at C28 amide chain could decrease anticancer effect (Meng *et al.*, 2010). Bai *et al* (2012) showed that a positively charged (amine) under physiological conditions have enhanced therapeutic potential in gastric tumour (AGS). The potent anticancer activity observed was due to the enhanced lipophilicity and aqueous solubility. This compound has a similar structure to our compound **10**. However, synthesis strategies used were different. In the study conducted by Bai *et al* (2012), carboxylic acid group of UA was activated using an oxalyl chloride to afford UA acyl chloride, which initiates an

amide bond formation under basic conditions. However, oxalyl chloride is considered a corrosive respiratory irritant and lachrymator. It also decomposes upon contact with water and produce toxic and corrosive fumes (Merck, 2022). Hence, the coupling strategy used in our study which is the use of N-guanidinium salt, HATU and base DIPEA, is more favourable.

UA is a highly lipophilic compound with low solubility and so the aim of this study was to improve its solubility and lipophilicity to enhance bioavailability. The predicted ADME-physicochemical properties obtained from SwissADME has revealed that compounds **10** and **12** improved most of the physicochemical properties of UA, most especially the solubility and lipophilicity. Compound **10** was predicted to have high gastrointestinal absorption based on the BOILED-Egg diagram. However, it was not predicted to effectively cross the BBB. Similarly, UA was not predicted to cross the BBB but it has been shown that some traces of UA were detected from the brain plasma and tissue samples of Sprague-Dawley rats (Chen *et al.*, 2011). It is worth noting that even when the BOILED-Egg diagram showed that UA does not cross the BBB, the TPSA value of UA is $< 60 \text{ \AA}^2$ which indicates it might cross the BBB. However, novel UA derivatives have $> 60 \text{ \AA}^2$ which are predicted to not cross the BBB. Nevertheless, a lot of new technologies have been currently employed to increase BBB permeability to drugs, such as focused ultrasound (Whelan, Hargaden and Knox, 2021).

The cytotoxic activity determined using cell viability assay alamarBlue, cell membrane damage dye PI and mitochondrial potential dye JC-1, have revealed that compounds with disulphide linkers **8** and **11** inhibited activity of UA. Disulphide linkers are known to cleave within the cell due in the presence of GSH, resulting to a thiol end instead of an

amine. Results obtained that a thiol end may be inhibiting the cytotoxic activity of compounds **8** and **11**. Interesting results were obtained from the Boc-protected compounds **7** and **9**, which had a delayed cytotoxicity in U-251 MG and A431 cell lines. This delayed cytotoxicity was investigated and it was concluded that neither the compounds' stability in media nor enzymatic cleavage or processes were involved *in vitro*. However, the cleavage or modification by enzymatic processes in the cells cannot be ruled out in our study and warrants further investigation. Boc-protected compounds were also predicted to be inhibitors of CYP3A4 in where activity might have amplified or weakened. The deprotected compounds **10** and **12** which were predicted to improve most of the physicochemical properties of UA, has greatly improved cytotoxic activity by more than two-fold even at shorter timepoints. This indicates that compounds **10** and **12** induced apoptosis at shorter timepoint.

Boc-protected and deprotected amine moieties at C28 of UA was also reported in the literature. Tien *et al* (2017) synthesized a series of UA derivatives bearing diamine moieties with glycolic linkage at C28 position in three different cancer cell lines (MCF-7, HeLa and A549). Their study revealed that derivatives with primary amine moieties (ethylenediamine) showed more potent antiproliferative activity compared to those with secondary (butanediamine) and tertiary (hexanediamine) amine moieties. Their Boc-protected amine intermediates displayed poor cytotoxicity against the cancer cell lines with IC₅₀ values > 100 µM after 48 hours incubation, whereas the deprotected amines exhibited cytotoxicity of < 10 µM against cancer cell lines tested. The results they obtained are similar to our study. The enhanced antitumour effect of the diamines could be explained by their capacity for forming hydrogen bonds, improved water solubility, and enhanced physicochemical properties.

This is evident in our study as the physicochemical properties of UA was enhanced with deprotected compounds **10** and **12** when compared to the Boc-protected compounds **7** and **9**. The study by Tien *et al* (2017) regarding the Boc protected compounds was only after 48 hours treatment. There are very limited studies on Boc-protected compounds as they are considered intermediates and most studies does not give much details on the biological activities. In our study, we investigated the activity of Boc-protected compounds at longer timepoint – 144 hours, where we observed delayed cytotoxic activity in U-251 MG and A431 cell lines. However, compounds **7** and **9** exhibited an enhanced/similar activity to UA at both shorter and longer timepoint in MCF-7, Caco-2 and HEK-293 cell lines. In contrast, decreased activity was observed in SKOV-3 cells. The different activity observed could be due to the different protein levels present in cancer cells. Studies have demonstrated that UA binds to several different receptor targets in cells, each with different functions and outcomes. The differing expression profile of proteins in cells can therefore lead to different outcomes when a fixed concentration of UA is used (Khwaza, Oyedeji and Aderibigbe, 2020).

Interestingly, the compounds with disulphide linker **8** and **11**, decreased the cytotoxicity of UA. However, due to the cleavage at the disulphide bridge, compounds **8** and **11** were expected to produce similar results. In our study, the Boc-protected compound **8** exhibited lower activity than deprotected compound **11**. In addition, novel FUA derivative compound **14**, was also expected to be similar to compounds **8** and **11**, resulting to a thiol end after cleavage at physiological pH. Cytotoxic activity of compounds with disulphide linker is compound **11** > **8** > **14**. This result suggests that Boc protection and folate end might have influenced the uptake of compounds into cells. Furthermore, physicochemical

properties predicted showed that between the three compounds, compound **11** has improved solubility.

As mentioned, the target protein for UA has remained elusive. However, most of the target proteins of UA published in the literature are members of the serine-threonine kinase family which are involved in DNA damage and repair (Kim *et al.*, 2015; Frolova *et al.*, 2019). Since VRK1 was more studied in detail, it was chosen for this study to determine the predicted binding of the novel UA derivatives in comparison to UA. Results obtained showed that all novel UA derivatives (**7 – 12**) have lower predicted binding affinity to VRK1 in comparison to UA. Nevertheless, with the exception of compound **9**, all novel UA derivatives were still predicted to interact with some of the important residues in the binding pocket. The cellular assay performed using DNA damaging agents, TMZ and UV-Vis, showed that low concentrations of compounds **7** and **9** inhibit the activity when co-treated with TMZ at shorter timepoint. Similarly, compound **12** cytotoxicity was alleviated when co-treated with TMZ at longer timepoint at 15 μ M concentration. Our results suggests that no synergistic effect between low doses of novel UA derivatives and TMZ. Reason for this is that U-251 MG cells are relatively resistant to TMZ and therefore has no effect on MGMT. On the other hand, co-treatment with 10 seconds UV-Vis, compound **7** indicated a synergistic activity which indicates that it may cause cell membrane damage in U-251 MG cells. On the other hand, NOAEL concentrations of compounds **8 – 12** co-treated with 15 seconds UV-Vis may be suggesting a protective effect.

DDR functions by regulating the cell cycle by triggering either the repair or cell death signalling pathways. When DNA damage is detected, cell cycle is arrested, after which,

cell attempt to repair the damage. However, if such damage is too extended, prolonged activation of DDR kinases triggers either apoptotic or necrotic death pathways (Ferri, Stagni and Barilà, 2020). Conventional therapy for GBM treatment such as ionizing radiation (UV) and TMZ exert cytotoxic function by DNA damage and cell death in tumours whereas normal cells possess several DNA repair mechanisms to combat DNA damage. However, in cancer cells, DNA repair systems are frequently altered compared to normal cells (Yoshimoto *et al.*, 2012). UV directly cause irreversible cluster DNA damage, generating single- or double-strand breaks leading to cell death (Barnes *et al.*, 2018). On the other hand TMZ has more intricate mechanism of action. It produce different DNA lesions, including N7-methylguanine, N3-methyladenine or N3-methylguanine. These damaged DNA bases then trigger the activation of several repair systems such as MGMT (Fujii, Sobol and Fuchs, 2022).

The preliminary investigation performed has revealed that all novel UA derivatives can retain anti-migratory properties of UA in U-251 MG cells even at NOAEL concentrations. In addition, the anti-proliferative effect of UA was retained by compounds **10** and **12** after 96 hours timepoint in U-251 MG cells. However, results obtained for other novel UA derivatives (**7, 8, 9, 11**) have partially inhibited proliferation after 96 hours. Compounds **7** and **9** had delayed cytotoxicity (144 hours) in U-251 MG cells, hence, further investigation on the proliferative effect at longer timepoint is suggested.

The preliminary inhibitor studies performed using caspase, calpain-cathepsin and JNK inhibitors (**Figure 97**) to determine cell death mechanism(s) involved has revealed that compounds **8** and **10** may trigger multiple cell demise pathway at a longer timepoint; no

significant difference observed with the control at shorter timepoint. Together these results point towards either a novel pathway inducing cell death, where Caspases, Calpain-Cathepsins and Stress kinase involvement is not rate limiting, or alternatively, activation of multiple cell death pathways creates redundancy where inhibition of a single pathway does not significantly alter the rate of cell death. Whereas compounds **7** and **9** indicates a JNK-dependent cell death at shorter timepoint. Hence, it can be concluded that SP600125 is the most potent inhibitor of cytotoxicity suggesting that novel UA derivatives (both in Boc protected and deprotected) induces JNK-dependent cell death. However, UA did not trigger any of the inhibitors used in this study which might be due to different mechanism of cell death.

As seen in **Table 27**, deprotected compounds **10** and **12** exhibited prominent activities in comparison to UA in all the assays performed. However, the delayed activity of Boc-protected compounds **7** and **9** are very interesting which can be used for targeted pro-drug strategy. Both Boc-protected and deprotected compounds warrant further investigation.

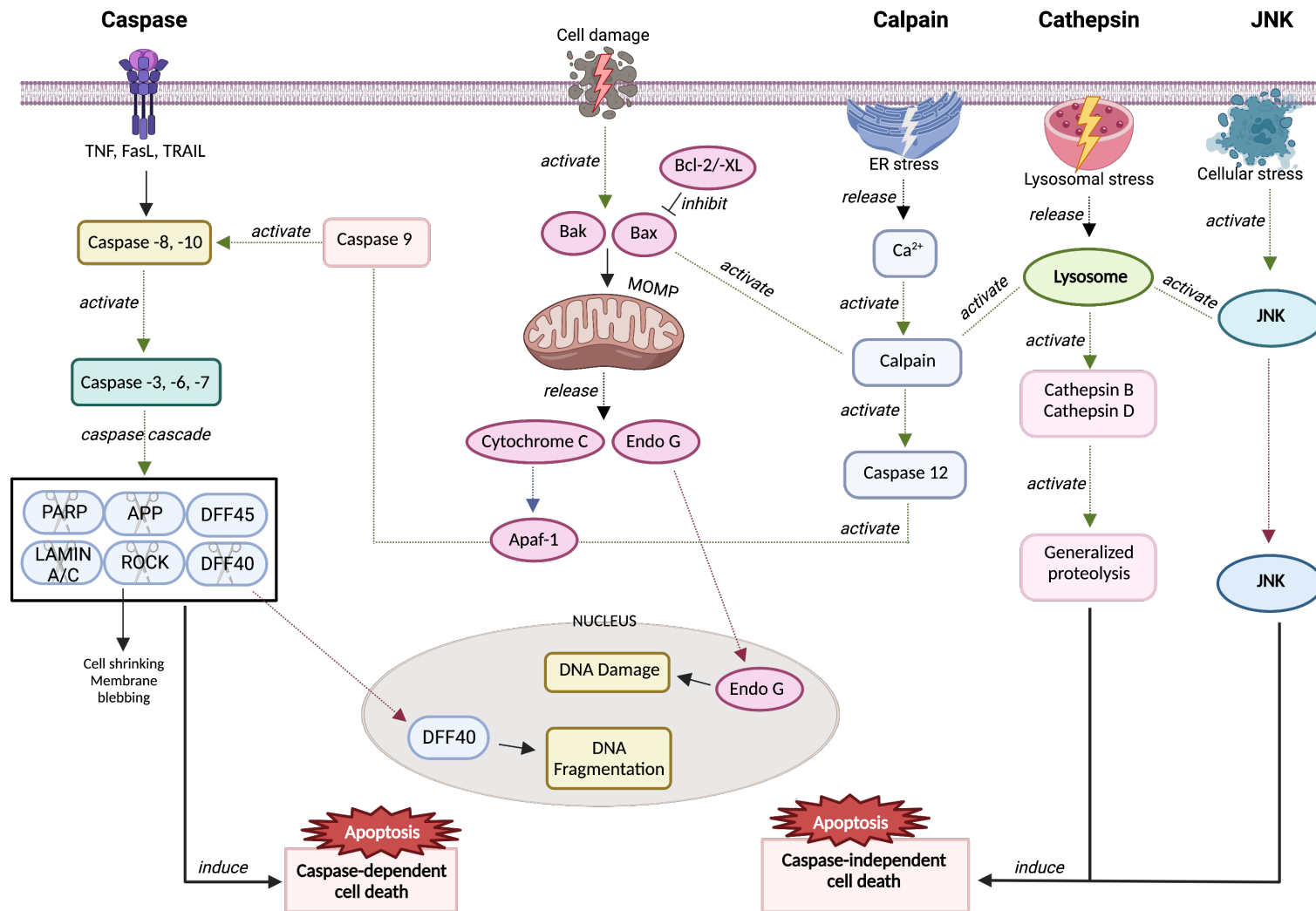


Figure 97. Suggested cell death mechanism(s) of novel UA derivatives. Image created with BioRender.com.

Table 27. Summary of different activities of UA, novel UA and FUA derivatives (7 - 15)

	Lipinski's violation	Cytotoxicity in U-251 MG cells	Cell death pathway	Cell Migration	Cell membrane damage	Cell Proliferation	Effect on U-251 MG 3D cell model
UA	1	Cytotoxic below 20 μ M (48 and 144 hr)	No activity	Inhibit migration	Protective (TMZ)	Inhibit cell proliferation	Causes disaggregation of spheroids after 144 hr (33 μ M)
Compound 7	2	Delayed cytotoxicity - below 10 μ M	JNK-dependent at shorter timepoint	Inhibit migration the same as UA	Yes	Inhibit cell proliferation	Ineffective against 3D spheroids
Compound 8	2	Not cytotoxic	JNK and caspase-dependent associated with autophagy at longer timepoint	Inhibit migration the same as UA	Protective (UV-Vis)	Inhibit cell proliferation	Ineffective against 3D spheroids
Compound 9	2	Delayed cytotoxicity - below 10 μ M	JNK-dependent at shorter timepoint	Inhibit migration the same as UA	Protective (UV-Vis)	Inhibit cell proliferation	Ineffective against 3D spheroids
Compound 10	1	Cytotoxic below 10 μ M (48 and 144 hr)	JNK and caspase-dependent associated with autophagy at longer timepoint	Inhibit migration the same as UA	Protective (UV-Vis)	Inhibit cell proliferation better than UA	Causes disaggregation of spheroids after 48 hr (28 μ M) and 144 hr (15 μ M)
Compound 11	2	Delayed cytotoxicity - below 20 μ M	No activity	Inhibit migration the same as UA	Protective (UV-Vis)	Inhibit cell proliferation	Ineffective against 3D spheroids
Compound 12	1	Cytotoxic below 15 μ M (48 hr) and 10 μ M (144 hr)	No activity	Inhibit migration the same as UA	Protective (UV-Vis)	Inhibit cell proliferation	Causes disaggregation of spheroids after 48 hr (26 μ M) and 144 hr (8 μ M)
Compound 13	3	Cytotoxicity > 100 μ M	Not tested	Not tested	Not tested	Not tested	Not tested
Compound 14	3	Cytotoxicity > 100 μ M	Not tested	Not tested	Not tested	Not tested	Not tested
Compound 15	3	Cytotoxicity > 100 μ M	Not tested	Not tested	Not tested	Not tested	Not tested

CHAPTER 6

CONCLUSION & FUTURE WORK

6.1 Conclusion and Future Work

6.1.1 Conclusion

The aim of this project was to generate novel FUA derivatives for targeted drug delivery and novel UA derivatives to enhance solubility, bioavailability and bioactivity of UA in GBM cells. The synthesis work in this thesis was complex and challenging. Novel UA and FUA derivatives were generated with good yields and purity using coupling reagent HATU and base DIPEA.

Folate has been successfully used in the past for targeted drug delivery due to its high affinity to folate receptor which are overexpressed in cancer cells and low expression in normal cells. However, in our study, novel FUA derivatives (**13** – **15**) greatly reduced cytotoxicity of UA in U-251 MG, SKOV-3, Caco-2 and MCF-7 cancer cells. UA has very low water solubility and our strategy initially involved coupling UA with folate to enhance drug bioavailability and uptake. However, novel FUA derivatives further lowered solubility, which could be the reason for the decreased cytotoxicity observed. In addition, compound **14** which is the self-immolative linker, did not exhibit any significant difference to non-cleavable linkers (compounds **13** and **15**). Hence, the hydrophobicity of novel FUA derivatives might be improved by incorporating a hydrophilic spacer or further modification to UA to enhance water solubility. It is worth noting that all novel FUA derivatives (**13** – **15**) were predicted to be bound at the same binding pocket as folic acid, which may still warrant a folate RME uptake in high folate expressing cancer cells.

It has been shown in the literature that amine moieties at C28 of UA greatly improved anti-cancer activity in different cell lines. Our study showed that even with an amine moiety, self-immolative linker compounds **8** and **11**, produced lowest activity in vitro in U-251 MG, A431, SKOV-3, Caco-2 and MCF-7 in comparison to other novel UA derivatives with non-cleavable linkers. This indicates that the loss of an amine end, resulting to a thiol end, might have contributed to the decreased cytotoxicity. It is also worth noting that compounds **8**, **11** and **14** were expected to have similar structures if cleaved within the cell. However, results U-251 MG cell line indicates that Boc protected (compound **8**) decreased cytotoxicity of deprotected (compound **8**) by more than two-fold; conjugation of folate (compound **14**) further reduced cytotoxicity of compound **8** by more than ten-fold.

Deprotected novel UA derivatives (compounds **10** and **12**) exhibited potent cytotoxic activity and with more than two-fold increase in cytotoxicity compared to UA both in across all cell lines tested in 2D and U-251 MG and A431 cell lines in 3D cell culture. This could be due to the enhanced physicochemical properties in comparison to UA. Compounds **10** and **12** were also predicted to have a better gastrointestinal absorption. In addition, these compounds also retained anti-migratory and anti-proliferative effects of UA in U-251 MG cells. Preliminary data obtained in co-treatment with DNA damaging agents TMZ and UV-Vis suggests that novel UA derivatives may have an inhibitory effect or antagonises activity of TMZ and/or UV at longer timepoint.

Boc-protected novel UA derivatives (compound **7** and **9**) exhibited an activity in MCF-7, Caco-2 and HEK-293 cells both at shorter and longer timepoint. However, decreased activity was observed in SKOV-3 cells. Interesting results were obtained from U-251 MG

and A431 cell lines where compounds **7** and **9** exhibited a delayed cytotoxicity (144 hours) which could be due to the Boc protection inhibiting uptake in cells. It is worth noting that these compounds had decreased lipophilicity and solubility resulting to lower bioavailability than UA and deprotected analogues which may have affected cytotoxicity. They were also predicted to be inhibitors of CYP3A4 and as a result Boc-protected compounds activity might have amplified or weakened. It is worth noting that these compounds retained the anti-migratory and anti-proliferative effects of UA in U-251 MG cells.

The preliminary results obtained in the cell death mechanism(s) of novel UA derivatives (**7 – 12**) suggests that a JNK-dependent cell death might play a role. The protective effect observed from co-treatment with TMZ and UV might have been due to the JNK cell death pathway.

6.2 Future Work

This study has identified exciting potential for the development of novel cytotoxic agents for GBM. While the use of folic acid as a means of targeting cells *via* the FR by chemically conjugating to UA decreased the activity, other formulation strategies can be employed. Novel UA derivatives (**7 – 12**) exhibited potent cytotoxicity but BBB permeation remains challenging. However, new technologies have now been explored to aid this. Future proposed work is detailed below and provides useful information to improve solubility, bioavailability and delivery of UA to GBM cells:

- The Boc-protected compounds exhibited very little activity after 48 hours, but exhibited potent activity with more than two-fold increase in comparison to UA at longer timepoint (144 hours). A different protecting agent may have more or less stable long-lasting protection from cell death. The delayed cytotoxicity observed from the Boc protected compounds in comparison to their deprotected analogues warrants a switch on/off pro-drug strategy. It is worth determining whether it can be enhanced with the incorporation of new technologies such as ultrasound and plasma. Another interesting study is to identify whether the Boc protection can be cleaved by physical destruction or different pH. The linkers also shed light to the use of different types of linkers with different properties for targeted and/or enhanced delivery.
- The potential of deprotected compounds **10** and **12** to exhibit more than two-fold increase in activity than UA in U-251 MG cells both in 2D and 3D cell culture models warrants further investigation. The 3D cytotoxicity of compounds **10** and **12** warrant further investigation. Other studies such as flow cytometry analysis and confocal can be used to determine similar activity of cell death mechanism, as well as migration and proliferation studies. It is also worth identifying whether they inhibit cell aggregation by affecting the extracellular matrix or cause disaggregation through cell death.
- The preliminary inhibitor studies performed are limited to programmed cell death. Other inhibitory studies which target autophagy and necrosis can be performed to determine cell death mechanism(s) involved. Further investigation can be performed to determine the exact cell death pathway involved.

- All compounds were predicted BBB impermeable but warrants further study as even UA was predicted not to cross BBB but studies have shown that some traces of UA in brain indicated BBB permeation which could also be due to residual levels in blood vessels of the brain. However, BBB penetration can be improved by incorporation of assisted delivery such as ultrasound and nanotechnology, and then to test experimentally.
- The challenge in our study is the highly hydrophobic nature of UA and the spacers. Hence, folate-targeted drug delivery can be enhanced by incorporation of a hydrophilic moiety or spacer or can be facilitated by incorporation of nanoparticles such as liposomes, dendrimers, antibodies, and proteins or further modification to increase the hydrophilicity of UA.
- The molecular docking studies performed in this study was focused more on DNA damage and repair – Vrk1. Hence, it is worth screening different molecular target for UA and novel UA derivatives.
- Studies using animal models could be considered to determine the efficacy of compounds **10** and **12** *in vivo*. Mouse or guinea pig models could be suitable for studies on absorption, metabolism, distribution, and excretion of the compounds. Given the poor solubility of both compounds, administration to animals would be challenging and oral administration would be the most suitable route of administration. Improvement in solubility is a key priority to advance the research to *in vivo* models.

CHAPTER 7

EXPERIMENTAL

7.1 Experimental Methods and Instrumentation

All chemicals and reagents were purchased from Merck-Sigma Ireland, Thermo Fisher Ireland, and Fluorochem UK, and used without further purification.

Ursolic acid was purchased from Hunan Dalore Ltd. Republic of China with >98% purity and was further purified by re-crystallisation and/or column chromatography.

Infrared (IR) spectra were obtained as KBr disks in the region 4000 – 400 cm^{-1} on a Perkin Elmer Spectrum 100 FT-IR spectrometer.

All Nuclear Magnetic Resonance (NMR) spectra were recorded in deuterated DMSO- d_6 or deuterated chloroform, on Bruker Avance 400 spectrometer (^1H at 400 MHz, ^{13}C at 101 MHz). All chemical shifts are reported in units of δ relative to deuterated DMSO- d_6 or deuterated chloroform unless otherwise stated. Peak positions are relative to trimethylsilane (TMS; 0 ppm chemical shift). Multiplicities are indicated as s (singlet), d (doublet), dd (doublet of doublet), dt (doublet of triplets), t (triplet), and m (multiplet), and coupling constants (J) are reported in hertz (Hz). All NMR spectra were processed and analysed using MestReNova NMR software.

Mass spectroscopy were carried out by Dr Gary Hessman, School of Chemistry, Trinity College Dublin, Ireland. Mass spectral data are reported in the form of m/z (intensity relative to base = 100).

Elemental analyses were carried out by the Microanalytical Laboratory, University College Dublin, Ireland.

7.2 UA Purification

7.2.1 Recrystallisation

UA was dissolved in minimum amount of ethanol under reflux. Once fully dissolved, transferred to a flask and crystallised overnight. The product was filtered and dried.

7.2.2 Thin Layer Chromatography (TLC)

Mobile phase for UA was made as previously described (Charville *et al.*, 2011). Mobile phase consisted of petroleum ether (82%), ethyl acetate (17%) and acetone (1%). Stationary phase used was C18 silica gel coated aluminium plate. Plates were visualized using 5% H₂SO₄ in MeOH visualization reagent and heat dried.

7.2.3 Column Chromatography

UA was dissolved in methanol. Mobile phase was the same as described in TLC analysis. Silica gel used was C18 mesh number 230.

7.2.4 Reverse Phase High Performance Liquid Chromatography

RP-HPLC analysis was performed as previously described (Zacchigna *et al.*, 2009). Quantification was performed on a WatersE2695 pump 2998 HPLC and Waters 2998 Photodiode Array Detector, using a Phenomenex C18 column. Isocratic elution was carried out with a mobile phase consisting of 940 ml MeOH, 50 ml millipore H₂O and 10 ml tetrahydrofuran (THFR) adjusted to pH 5 with acetic acid. The flow rate used was 1 ml/min with a column temperature of 25 ± 5.0 °C. Samples were monitored according to their UV absorbance at 208 nm. Analysis was performed using Empower software.

7.3 N-Boc protection of diamines linkers

7.3.1 N-Boc protection of Ethylenediamine (N-Boc-EDA) (1)

Ethylenediamine (EDA) was protected as previously described (Trindade *et al.*, 2014). Ethylenediamine (9.359 ml, 140 mmol) was dissolved in anhydrous dichloromethane (DCM) (50 ml) and cooled to 0°C. A solution of di-*tert*-butyl dicarbonate (Boc₂O; 3.056 g, 14 mmol) in 50 ml anhydrous DCM was added drop-wise over a period of 2 hours under nitrogen. The solution was stirred for 24 hr at room temperature under nitrogen. The solvent was removed under reduced pressure and replaced with water (50 ml). The aqueous suspension was filtered to remove the di-Boc protected by-product and the filtrate was washed with three portions of DCM (50 ml). The combined organic layers were dried over Na₂SO₄ and evaporated to yield a viscous oil.

Yield: 2.37 g (52.78%); Appearance: Colourless viscous oil; Solubility: H₂O, MeOH, EtOH, Acetone, CHCl₃, Et₂O, EtOAc, DCM, ACN, DMF and DMSO; LC-MS (ESI) calculated for C₇H₁₇N₂O₂ 161.1285 [M+H]⁺, found 161.1289; ¹H NMR (400 MHz, CDCl₃) δ 5.19 (s, 1H), 3.08 (dd, *J* = 11.5, 5.7 Hz, 2H), 2.70 (t, *J* = 5.9 Hz, 2H), 1.35 (s, 9H), 1.14 (s, 2H). ¹³C NMR (101 MHz, CDCl₃) δ 156.27, 79.02, 43.39, 41.85, 28.38; IR: 3360, 2975, 2931, 1687, 1519, 1453, 1391, 1364, 1273, 1249, 1166, 953, 871, 779 cm⁻¹.

7.3.2 *N*-Boc protection of cystamine dihydrochloride (*N*-Boc-Cys) (2)

Cystamine bis-hydrochloride (CYS) was *N*-Boc protected as previously described (Shirazi *et al.*, 2011). To a cooled solution of cystamine bis-hydrochloride (8.107 g, 36 mmol) in methanol (200 ml), 0.726 ml (107.7 mmol) of triethylamine was added. A solution of Boc₂O (7.857 g, 36 mmol) in 100 ml methanol was added drop-wise over a period of 2 hours under nitrogen. The reaction was stirred for 24 hr at room temperature under nitrogen and the solvent was removed under reduced pressure. The white residue was dissolved in 80 ml of 1 M aqueous NaH₂PO₄, and the mixture was extracted twice with diethyl ether to remove di-Boc-cystamine. The aqueous solution was basified to pH 10 with 1 M NaOH and subsequently extracted three times with ethyl acetate (50 ml). The combined ethyl acetate phases were washed twice with distilled water (50 ml), dried with Na₂SO₄ and evaporated to yield a pale yellow, viscous oil.

Yield: 3.40 g (37.42 %); Appearance: Pale yellow viscous oil; Solubility: MeOH, EtOH, Acetone, CHCl₃, Et₂O, EtOAc, DCM, ACN, DMF and DMSO; LC-MS (ESI) calculated for C₉H₂₁N₂O₂S₂ 253.1039 [M+H]⁺, found 253.1039; ¹H NMR (400 MHz, CDCl₃) δ 5.00 (s, 1H), 3.43 (dd, *J* = 12.1, 6.0 Hz, 2H), 2.99 (t, *J* = 6.2 Hz, 2H), 2.82 – 2.66 (m, 4H), 1.42

(s, 11H). ^{13}C NMR (101 MHz, CDCl_3) δ 155.86, 79.61, 42.54, 40.65, 39.33, 38.44, 28.49; IR: 3366, 2975, 2930, 2866, 1697, 1514, 1453, 1390, 1364, 1337, 1269, 1246, 1164, 1044, 1005, 949, 918, 866, 778 cm^{-1} .

7.3.3 *N*-Boc protection of 2,2'-(ethylenedioxy)bis(ethylamine) (*N*-Boc-EDEA) (3)

2, 2'-(ethylenedioxy)bis(ethylamine) (EDEA) was protected as previously described (Hart *et al.*, 2015). 2,2-(ethylenedioxy)bis(ethylamine) (20.54 ml, 140 mmol) was dissolved in 20 ml anhydrous chloroform and cooled to 0°C. A solution of Boc_2O (3.056 g, 14 mmol) in 50 ml anhydrous chloroform was added drop-wise over a period of 2 hours under nitrogen. The reaction was stirred for 24 hr at room temperature under nitrogen. The solvent was removed under reduced pressure and the residue was dissolved in DCM (50 ml), washed with three portions of distilled water (50 ml), dried over Na_2SO_4 and evaporated to yield a colourless, viscous oil.

Yield: 2.80 g (80.46 %); Appearance: Colourless viscous oil; Solubility: H_2O , MeOH, EtOH, Acetone, CHCl_3 , Et_2O , EtOAc, DCM, ACN, DMF and DMSO; LC-MS (ESI) calculated for $\text{C}_{11}\text{H}_{25}\text{N}_2\text{O}_4$ 249.1809 $[\text{M}+\text{H}]^+$, found 249.1813; ^1H NMR (400 MHz, CDCl_3) δ 5.19 (s, 1H), 3.58 (s, 4H), 3.49 (dt, $J = 10.5, 5.2$ Hz, 4H), 3.28 (dd, $J = 10.1, 5.0$ Hz, 2H), 2.84 (t, $J = 5.2$ Hz, 2H), 1.79 (s, 2H), 1.40 (s, 9H). ^{13}C NMR (101 MHz, CDCl_3) δ 156.10, 79.21, 73.42, 70.28, 70.25, 41.74, 40.38, 28.48; IR: 3360, 2974, 2930, 2867, 1697, 1520, 1477, 1454, 1391, 1364, 1274, 1249, 1170, 1103, 1041, 1000, 968, 919, 864, 780 cm^{-1} .

7.4 The attempted conjugation of Folate-Ethylenediamine linker to UA

7.4.1 Synthesis of *N*-Boc-EDA-FA (4)

Folic acid is conjugated to *N*-Boc-EDA as previously described (Trindade *et al.*, 2014). Folic acid (1.104 g, 2.5 mmol) was dissolved in 30 ml anhydrous dimethyl sulfoxide (DMSO). After the dissolution was complete (about 30 minutes with mild heating) and was cooled to room temperature, *N*, *N'*-dicyclohexylcarbodiimide (DCC; 1.032 g; 5 mmol) and *N*-hydroxysuccinamide (NHS; 0.576 g; 5 mmol) were added successively. The reaction mixture was stirred in the absence of light for 24 hr at room temperature under nitrogen, after which time a colourless precipitate, dicyclohexylurea (DCU), was removed by vacuum filtration. To the orange filtrate, 0.697 ml (5 mmol) of triethylamine was added followed by 0.801 g (5 mmol) of compound **1** dissolved in 5 ml DMSO. The mixture was stirred overnight at room temperature, in the absence of light before a mixture of 20% acetone in diethyl ether was added (100 ml). The fine, yellow precipitate was filtered and washed thoroughly with excess acetone/diethyl ether mix (20% v/v) and dried in a 60°C oven overnight.

Yield: 1.35 g (92.25 %); Appearance: Yellow powder; Solubility: DMSO (hot), DMF (hot); Elemental Analysis (Found): C, 53.51; H, 5.70; N, 21.60; ¹H NMR (400 MHz, DMSO) δ 11.58 (s, 1H), 8.63 (s, 1H), 8.02 (d, *J* = 7.2 Hz, 1H), 7.84 (d, *J* = 24.6 Hz, 2H), 7.67 (d, *J* = 8.4 Hz, 2H), 6.94 (s, 2H), 6.76 (d, *J* = 14.9 Hz, 1H), 6.63 (d, *J* = 8.5 Hz, 1H), 4.49 (d, *J* = 5.3 Hz, 2H), 4.28 (s, 1H), 3.01 (d, *J* = 44.1 Hz, 4H), 1.92 (dd, *J* = 94.9, 26.5 Hz, 3H), 1.34 (d, *J* = 5.9 Hz, 11H). ¹³C NMR (101 MHz, DMSO) δ 171.97, 171.90, 166.25, 155.65, 153.96, 150.78, 150.73, 148.67, 148.61, 129.15, 127.98, 121.41, 111.18,

77.71, 53.08, 45.93, 40.43, 38.82, 32.05, 28.24, 27.54, 25.28; IR: 3302, 2977, 2934, 1687, 1643, 1605, 1509, 1454, 1391, 1365, 1336, 1272, 1248, 1165, 1127 cm⁻¹.

7.4.2 Synthesis of FA-EDA (deprotection) (5)

N-Boc-EDA-FA was deprotected as described (Trindade *et al.*, 2014). Compound 4 (0.5 g, 0.85 mmol) was added to cooled trifluoroacetic acid (TFA; 5 ml) and stirred at room temperature for two hours. The TFA was removed under pressure with the aid of DCM (50 ml) and the red-dark residue was dissolved in a minimal volume of dimethylformamide (DMF). The addition of 500 μ l triethylamine (TEA) resulted in precipitation of a yellow powder. A 70:30 mixture of diethyl ether and acetone was used to wash the product. The product was filtered and washed with an excess of acetone and diethyl ether and dried at 60°C oven overnight.

Yield: 0.38 g (92.94 %); Appearance: Yellow powder; Solubility: DMSO (hot), DMF; ¹H NMR (400 MHz, DMSO) δ 11.68 (s, 1H), 8.63 (s, 1H), 8.10 (dd, J = 48.8, 15.5 Hz, 2H), 7.81 (s, 2H), 7.66 (s, 1H), 7.03 (d, J = 23.2 Hz, 2H), 6.64 (d, J = 8.0 Hz, 2H), 4.49 (s, 1H), 4.32 (d, J = 1.8 Hz, 1H), 3.37 (s, 4H), 2.85 (s, 2H), 2.12 (d, J = 31.5 Hz, 2H), 1.85 (dd, J = 9.6, 3.8 Hz, 1H). ¹³C NMR (101 MHz, DMSO) δ 172.62, 172.56, 166.56, 158.65, 158.34, 153.94, 150.94, 148.56, 129.17, 127.94, 121.09, 111.20, 52.97, 45.89, 40.15, 39.94, 39.73, 39.52, 39.52, 39.31, 39.10, 38.89, 38.73, 38.60, 36.40, 31.82, 26.92; IR: 3306, 3058, 1651, 1634, 1602, 1574, 1505, 1455, 1435, 1331, 1301, 1175, 1126, 834, 720 cm⁻¹.

7.4.3 Synthesis of FA-EDA-UA (6)

UA is conjugated to EDA-FA similar as described (Trindade *et al.*, 2014). UA (0.091 g, 0.2 mmol) was dissolved in 5 ml anhydrous DMSO. After the dissolution was complete DCC (0.083 g; 0.4 mmol) and NHS (0.047 g; 0.4 mmol) were added successively. The reaction mixture was stirred for 24 hr at room temperature under nitrogen, after which time a colourless precipitate, DCU, was removed by vacuum filtration. To the clear filtrate, 56 μ l (0.4 mmol) of triethylamine was added followed by compound **5** 0.193 g (0.4 mmol) dissolved in 1 ml DMSO. The mixture was stirred overnight at room temperature in the absence of light and was dialysed using dialysis tubing (14, 000 molecular weight cut-off) in distilled water for 24 h (water changed twice). A fine, yellow powder was obtained after freeze drying for 24 h.

Yield: 0.038 g (20.61 %); Appearance: Yellow powder; Solubility: DMSO (hot), DMF; LC-MS (ESI) calculated for $C_{51}H_{70}N_9O_7$ 920.5404 [M+H]⁺, found 762.6641; ¹H NMR (400 MHz, DMSO) δ 8.63 (s, 1H), 7.88 (s, 1H), 7.62 (dd, J = 21.9, 13.2 Hz, 1H), 6.94 (s, 1H), 6.61 (s, 1H), 5.63 (d, J = 8.0 Hz, 1H), 4.53 – 4.44 (m, 1H), 4.32 – 4.25 (m, 1H), 3.20 – 3.15 (m, 2H), 1.82 (d, J = 8.7 Hz, 4H), 1.64 (d, J = 3.5 Hz, 10H), 1.50 (d, J = 11.7 Hz, 3H), 1.25 (d, J = 8.4 Hz, 14H), 1.04 (d, J = 26.5 Hz, 4H), 0.93 – 0.67 (m, 7H). IR: 3315, 2958, 2843, 1789, 1745, 1644, 1605, 1543, 1502, 1450, 1389, 1304, 1186, 1068, 986, 864 cm^{-1} .

7.5 The conjugation of UA diamine with FA

7.5.1 The attempted conjugation of *N*-Boc-EDA with UA

7.5.1.1 *N*-Boc-EDA-UA with DCC/NHS

UA was conjugated to *N*-Boc-EDA similar as described with some modification (Trindade *et al.*, 2014). UA (0.457 g, 1 mmol) was dissolved in 10 ml anhydrous DMSO. After the dissolution was complete DCC (0.413 g; 2 mmol) and NHS (0.230 g; 2 mmol) were added successively. The reaction mixture was stirred for 48 hr at room temperature under nitrogen, after which time a colourless precipitate, DCU, was removed by vacuum filtration. To the clear filtrate, 0.27 ml (2 mmol) of TEA was added followed by compound **1** 0.32 g (2 mmol) dissolved in 5 ml DMSO. The mixture was stirred overnight at room temperature under nitrogen. To the clear solution, 100 ml distilled water was added to produce a white precipitate which was isolated through filtration. The crude product was washed well with excess distilled water and dried at 60°C oven overnight.

Yield: 0.17 g (27.38 %); Appearance: Colourless powder; Solubility: MeOH, EtOH, DCM, DMSO, DMF, Acetone, CHCl₃, EtOAc; ¹H NMR (400 MHz, DMSO) δ 7.15 (s, 1H), 6.75 (t, J = 4.9 Hz, 1H), 5.21 (s, 1H), 4.31 (d, J = 4.9 Hz, 1H), 3.12 – 2.87 (m, 5H), 2.11 (d, J = 10.7 Hz, 1H), 1.99 (s, 1H), 1.89 (dd, J = 19.5, 10.6 Hz, 3H), 1.47 (dd, J = 36.5, 10.3 Hz, 11H), 1.37 (s, 9H), 1.24 (s, 4H), 1.02 (s, 3H), 0.95 – 0.80 (m, 16H), 0.67 (d, J = 3.4 Hz, 6H). ¹³C NMR (101 MHz, DMSO) δ 176.48, 155.83, 138.40, 124.69, 77.74, 76.85, 59.81, 54.77, 51.96, 47.05, 46.59, 41.60, 39.52, 38.54, 38.41, 38.25, 37.10, 36.52, 32.66, 30.39, 28.27, 27.37, 27.02, 23.54, 23.34, 22.91, 21.17, 20.82, 17.99, 17.21, 16.75, 16.13, 15.26, 14.13. IR: 3389, 2956, 2864, 1654, 1586, 1534, 1428, 1321, 1252, 1089, 905, 654 cm⁻¹.

7.5.1.2 *N*-Boc-EDA-UA with EDC/HOBt

UA was conjugated to *N*-Boc-EDA similar as described with some modification (Pu *et al.*, 2009). UA (0.457 g, 1 mmol) was dissolved in 10 ml anhydrous DMF and hydroxybenzotriazole (HOBt; 0.270 g; 2 mmol) were added. The suspension was cooled to 0°C and 1-Ethyl-3-(3-dimethylaminopropyl)carbodiimide (EDC; 0.383 g; 2 mmol) was added and stirred for 20 min. The final addition of *N*-Boc-EDA (0.320g; 2 mmol) in 10 ml DMF was performed at room temperature. The reaction was left to stir for 24 hr at room temperature. To the clear solution, 100 ml distilled water was added to produce a white precipitate which was isolated through filtration. The crude product was washed well with brine and excess distilled water and dried at 60°C oven overnight.

Yield: 0.34 g (54.75 %); Appearance: Colourless powder; Solubility: MeOH, EtOH, DCM, DMSO, DMF, Acetone, CHCl₃, EtOAc; ¹H NMR (400 MHz, DMSO) δ 7.15 (t, J = 4.1 Hz, 1H), 6.75 (t, J = 4.9 Hz, 1H), 5.21 (t, J = 3.2 Hz, 1H), 4.31 (d, J = 5.2 Hz, 1H), 4.02 (q, J = 7.1 Hz, 1H), 3.11 – 2.89 (m, 5H), 2.11 (d, J = 10.8 Hz, 1H), 1.99 (s, 1H), 1.88 (dt, J = 22.0, 10.5 Hz, 3H), 1.80 – 1.39 (m, 11H), 1.37 (s, 9H), 1.30 – 1.23 (m, 4H), 1.17 (s, 1H), 1.02 (s, 3H), 0.94 – 0.81 (m, 16H), 0.67 (d, J = 3.4 Hz, 6H). ¹³C NMR (101 MHz, DMSO) δ 176.47, 170.40, 167.03, 155.83, 138.39, 131.74, 128.71, 124.69, 77.73, 76.85, 59.81, 54.77, 51.96, 47.05, 46.59, 41.60, 40.19, 39.98, 39.52, 38.77, 38.54, 38.41, 38.26, 38.10, 37.10, 36.52, 32.67, 30.40, 29.82, 28.41, 28.27, 27.37, 27.02, 23.55, 23.34, 22.90, 22.46, 21.17, 20.81, 18.00, 17.21, 16.75, 16.12, 15.26, 14.13, 13.96, 10.85. IR: 3357, 2966, 2926, 2870, 1693, 1637, 1518, 1454, 1388, 1378, 1365, 1275, 1169, 1106, 1093, 1045, 1029, 997, 974, 849, 781, 663, 558 cm⁻¹.

7.5.2 The conjugation of *N*-Boc protected diamine linkers with UA

UA was conjugated to *N*-Boc-diamine as previously described (Liu *et al.*, 2018) but product isolation was modified. Extraction by ethyl acetate was not successful due to DMF being miscible to ethyl acetate. Instead, filtration using a glass filter (porosity 5) was carried out. Purification by flash chromatography was also not conducted. To a solution of UA (0.913 g, 2 mmol) dissolved in anhydrous DMF (10 ml) was added *N,N*-Diisopropylethylamine (DIPEA) (1.714 ml, 10 mmol) and the reaction mixture was cooled to 0°C. HATU (1.521 g, 4 mmol) was added and stirred for 10 min followed by the addition of *N*-Boc-diamine (6 mmol) dissolved in 2 ml DMF. The solution was stirred for 24 h at room temperature under nitrogen. To the orange solution, 100 ml distilled water was added to produce a white precipitate which was isolated through filtration. The crude product was washed well with excess distilled water and dried at 60°C oven overnight.

7.5.2.1 Synthesis of *N*-Boc-EDA-UA (7)

Yield: 1.23 g (98.79 %); Appearance: Colourless powder; Solubility: MeOH, EtOH, DCM, DMSO, DMF, Acetone, CHCl₃, EtOAc; LC-MS (ESI) calculated for C₃₇H₆₂N₂NaO₄ 621.4602 [M+H]⁺, found 621.4595; ¹H NMR (400 MHz, DMSO) δ 7.14 (s, 1H), 6.74 (t, J = 4.8 Hz, 1H), 5.21 (d, J = 3.2 Hz, 1H), 4.30 (d, J = 5.2 Hz, 1H), 3.11 – 2.89 (m, 4H), 2.42 (dd, J = 14.2, 7.1 Hz, 1H), 2.11 (d, J = 10.9 Hz, 1H), 1.96 – 1.80 (m, 3H), 1.77 – 1.39 (m, 11H), 1.37 (s, 9H), 1.25 (dd, J = 22.0, 12.0 Hz, 3H), 1.02 (s, 3H), 0.95 – 0.82 (m, 18H), 0.67 (d, J = 3.4 Hz, 6H). ¹³C NMR (101 MHz, DMSO) δ 176.49, 155.83, 138.39, 124.70, 77.74, 76.85, 54.77, 51.96, 47.62, 47.05, 46.59, 41.60, 40.19,

39.52, 38.77, 38.54, 38.40, 38.26, 37.10, 36.51, 32.66, 30.40, 28.26, 27.35, 27.01, 23.55, 23.33, 22.90, 21.16, 20.69, 17.99, 17.20, 16.74, 16.11, 15.25; IR: 3357, 2966, 2926, 2870, 1693, 1637, 1518, 1454, 1388, 1378, 1365, 1275, 1251, 1169, 1105, 1093, 1044, 997, 974, 849, 781, 663 cm^{-1} .

7.5.2.2 Synthesis of *N*-Boc-CYS-UA (8)

Yield: 1.40 g (97.90 %); Appearance: Off-white powder; Solubility: MeOH, EtOH, DCM, DMSO, DMF, Acetone, CHCl_3 , EtOAc; LC-MS (ESI) calculated for $\text{C}_{39}\text{H}_{66}\text{N}_2\text{NaO}_4\text{S}_2$ 713.4356 $[\text{M}+\text{H}]^+$, found 713.4359; ^1H NMR (400 MHz, DMSO) δ 7.35 (t, $J = 4.9$ Hz, 1H), 6.99 (t, $J = 5.5$ Hz, 1H), 5.19 (s, 1H), 4.29 (d, $J = 4.9$ Hz, 1H), 3.19 (d, $J = 6.4$ Hz, 2H), 2.95 (dd, $J = 27.2, 5.6$ Hz, 3H), 2.75 – 2.69 (m, 4H), 2.13 (d, $J = 10.9$ Hz, 1H), 1.97 – 1.68 (m, 5H), 1.54 (dd, $J = 47.3, 25.5$ Hz, 8H), 1.37 (s, 11H), 1.26 (dd, $J = 23.4, 10.4$ Hz, 4H), 1.02 (s, 3H), 0.89 (dt, $J = 24.1, 8.6$ Hz, 15H), 0.68 (d, $J = 7.8$ Hz, 6H). ^{13}C NMR (101 MHz, DMSO) δ 176.42, 155.50, 138.25, 124.76, 77.78, 76.84, 54.80, 52.00, 47.06, 46.63, 41.59, 39.52, 38.77, 38.48, 38.39, 38.26, 37.45, 37.19, 37.02, 36.51, 32.72, 30.42, 28.23, 27.36, 27.01, 23.53, 23.31, 22.90, 21.14, 20.63, 17.99, 17.16, 16.93, 16.10, 15.25; IR: 3357, 2968, 2925, 2869, 1694, 1638, 1514, 1454, 1387, 1364, 1272, 1251, 1166, 1044, 1029, 997, 949, 844 cm^{-1} .

7.5.2.3 Synthesis of *N*-Boc-EDEA-UA (9)

Yield: 1.20 g (87.59 %); Appearance: Colourless powder; Solubility: MeOH, EtOH, DCM, DMSO, DMF, Acetone, CHCl₃, EtOAc; LC-MS (ESI) calculated for C₄₁H₇₀N₂NaO₆ 709.5126 [M+H]⁺, found 709.5135; ¹H NMR (400 MHz, DMSO) δ 7.09 (t, J = 5.2 Hz, 1H), 6.75 (t, J = 5.3 Hz, 1H), 5.20 (s, 1H), 4.30 (d, J = 5.1 Hz, 1H), 3.47 (d, J = 4.0 Hz, 4H), 3.34 (s, 10H), 3.21 – 2.95 (m, 6H), 2.10 (d, J = 10.8 Hz, 1H), 1.95 – 1.77 (m, 3H), 1.73 – 1.39 (m, 11H), 1.37 (s, 9H), 1.30 – 1.19 (m, 3H), 1.03 (s, 3H), 0.97 – 0.81 (m, 18H), 0.68 (d, J = 9.9 Hz, 6H). ¹³C NMR (101 MHz, DMSO) δ 176.39, 155.58, 138.37, 124.75, 77.59, 76.84, 69.59, 69.20, 68.93, 54.80, 52.08, 47.06, 46.65, 41.62, 40.19, 39.52, 38.84, 38.72, 38.46, 38.40, 38.26, 37.00, 36.51, 32.68, 30.45, 28.24, 27.34, 27.02, 23.63, 23.25, 22.89, 21.16, 20.61, 17.99, 17.15, 16.74, 16.10, 15.23; IR: 3388, 2924, 2868, 1697, 1639, 1517, 1454, 1388, 1378, 1365, 1276, 1249, 1171, 1104, 1045, 1030, 997, 973 cm⁻¹.

7.5.3 The deprotection of *N*-Boc protected Diamine linkers with Ursolic Acid

N-Boc-diamine-UA was deprotected as described (Liu *et al.*, 2018). *N*-Boc-diamine-UA (0.62 g, 1 mmol) was dissolved in 5 ml DCM and cooled to 0°C. TFA (5 ml) was added dropwise at 0°C and then stirred at room temperature for one hour. The solution was removed under pressure and was washed with DCM three times (50 ml) to ensure removal of TFA. The red-dark residue was dissolved in a minimal volume of DMF and neutralised with 10 mmol TEA. To the orange solution, distilled water was added to produce a white precipitate which was isolated via filtration. The crude product was washed well with excess distilled water and dried at 60°C oven overnight.

7.5.3.1 Synthesis of UA-EDA (10)

Yield: 0.45 g (89.29 %); Appearance: Colourless powder; Solubility: MeOH, EtOH, DCM, DMSO, DMF, Acetone, CHCl₃, EtOAc; LC-MS (ESI) calculated for C₃₂H₅₅N₂O₂ 499.4258 [M+H]⁺, found 499.4258; ¹H NMR (400 MHz, DMSO) δ 7.12 (t, J = 5.3 Hz, 1H), 5.20 (s, 1H), 4.31 (s, 1H), 3.04 – 2.84 (m, 4H), 2.14 (t, J = 11.7 Hz, 1H), 1.95 – 1.80 (m, 3H), 1.77 – 1.20 (m, 18H), 1.03 (s, 3H), 0.95 – 0.81 (m, 16H), 0.68 (d, J = 8.0 Hz, 6H). ¹³C NMR (101 MHz, DMSO) δ 176.22, 138.56, 124.57, 76.84, 54.79, 52.02, 47.06, 46.62, 42.40, 41.63, 41.17, 40.19, 39.52, 38.47, 38.40, 38.25, 37.12, 36.51, 32.74, 30.46, 28.28, 27.38, 27.01, 23.57, 23.31, 22.89, 21.16, 17.98, 17.17, 16.84, 16.12, 15.24; IR: 3370, 2925, 2869, 1687, 1638, 1524, 1455, 1387, 1378, 1305, 1280, 1240, 1201, 1177, 1135, 1107, 1093, 1045, 1029, 998, 974, 949, 829, 799, 721 cm⁻¹.

7.5.3.2 Synthesis of UA-CYS (11)

Yield: 0.48 g (81.56 %); Appearance: White powder; Solubility: MeOH, EtOH, DCM, DMSO, DMF, Acetone, CHCl₃, EtOAc; LC-MS (ESI) calculated for C₃₄H₅₉N₂O₂S₂ 591.4012 [M+H]⁺, found 591.4015; ¹H NMR (400 MHz, DMSO) δ 7.37 (t, *J* = 5.5 Hz, 1H), 5.19 (t, *J* = 3.1 Hz, 1H), 4.30 (d, *J* = 4.9 Hz, 1H), 3.46 (dt, *J* = 13.3, 6.5 Hz, 1H), 2.99 (dt, *J* = 10.6, 5.1 Hz, 2H), 2.86 – 2.66 (m, 7H), 2.13 (d, *J* = 10.6 Hz, 2H), 1.98 – 1.70 (m, 6H), 1.63 – 1.32 (m, 14H), 1.25 (dd, *J* = 14.1, 7.1 Hz, 5H), 1.12 (d, *J* = 14.0 Hz, 3H), 1.03 (s, 4H), 0.97 – 0.79 (m, 18H), 0.68 (d, *J* = 7.5 Hz, 7H). ¹³C NMR (101 MHz, DMSO) δ 177.24, 138.29, 124.71, 76.80, 54.74, 51.87, 46.99, 46.68, 41.61, 41.56, 38.69, 38.53, 38.50, 38.39, 38.20, 37.57, 36.96, 36.72, 36.51, 36.34, 32.63, 30.32, 28.26, 27.35, 27.00, 23.45, 23.36, 22.86, 21.12, 17.94, 17.16, 16.83, 16.13, 15.21; IR: 3365, 2923, 2867, 1701, 1640, 1516, 1454, 1378, 1358, 1202, 1185, 1156, 1093, 1046, 1029, 998 cm⁻¹.

7.5.3.3 Synthesis of UA-EDEA (12)

Yield: 0.38 g (64.41 %); Appearance: White powder; Solubility: MeOH, EtOH, DCM, DMSO, DMF, Acetone, CHCl₃, EtOAc; LC-MS (ESI) calculated for C₃₆H₆₃N₂O₄ 587.4782 [M+H]⁺, found 587.4789; ¹H NMR (400 MHz, DMSO) δ 7.11 (t, *J* = 5.1 Hz, 1H), 5.20 (s, 1H), 4.31 (s, 1H), 3.46 (dd, *J* = 18.3, 6.7 Hz, 2H), 3.23 – 3.05 (m, 4H), 3.04 – 2.95 (m, 4H), 2.65 (s, 4H), 2.10 (d, *J* = 10.8 Hz, 1H), 1.57 (dd, *J* = 55.8, 40.2, Hz, 25H), 1.11 (d, *J* = 10.4 Hz, 3H), 1.03 (s, 4H), 0.95 – 0.80 (m, 18H), 0.68 (d, *J* = 10.5 Hz, 7H). ¹³C NMR (101 MHz, DMSO) δ 176.39, 138.39, 124.73, 91.24, 76.84, 71.22, 69.74, 69.62, 68.94, 54.79, 54.62, 52.08, 47.06, 46.65, 45.68, 44.39, 43.29, 42.09, 41.63, 39.52, 38.73, 38.55, 38.47, 38.41, 38.26, 37.80, 37.01, 36.56, 36.51, 32.68, 30.45, 28.28, 28.09, 27.34, 27.17, 27.02, 23.62, 23.26, 22.91, 21.17, 19.46, 18.34, 17.99, 17.30, 17.17, 16.74, 16.25, 16.12, 15.84, 15.25; IR: 3368, 2923, 2865, 1701, 1638, 1522, 1453, 1386, 1357, 1252, 1202, 1185, 1105, 1094, 1047, 1029, 999 cm⁻¹.

7.5.4 The conjugation of Ursolic Acid diamine with Folic Acid

Folic acid is conjugated to UA-diamine similar as described (Trindade *et al.*, 2014). Folic acid (0.088 g, 0.2 mmol) was dissolved in 6 ml anhydrous DMSO. After the dissolution was complete (about 30 minutes with mild heating) and was cooled to room temperature, DCC (0.08 g; 0.4 mmol) NHS (0.05 g; 4 mmol) were added successively. The reaction mixture was stirred in the absence of light for 24 hr at room temperature under nitrogen, after which time a colourless precipitate, dicyclohexylurea, was removed by vacuum filtration. To the orange filtrate, 56 μ l (0.4 mmol) of TEA was added followed by 0.4 mmol of UA-diamine dissolved in 1 ml DMSO. The mixture was stirred overnight at room temperature, in the absence of light under nitrogen, before a mixture of 20% acetone in diethyl ether was added (100 ml). The fine, yellow precipitate was filtered and washed thoroughly with excess acetone/diethyl ether mix (20% v/v) and dried in a 60°C oven overnight.

7.5.4.1 Synthesis of UA-EDA-FA (13)

Yield: 0.12 g (64.10 %); Appearance: Yellow powder; Solubility: DMSO (hot), DMF (hot); LC-MS (ESI) calculated for $C_{51}H_{70}N_9O_7$ 920.5404 [M+H]⁺, found 920.5381; ¹H NMR (400 MHz, DMSO) δ 11.26 (s, 1H), 8.63 (d, J = 3.8 Hz, 1H), 8.04 (s, 2H), 7.65 (t, J = 8.3 Hz, 2H), 7.39 (s, 1H), 6.93 (s, 3H), 6.63 (d, J = 8.5 Hz, 2H), 5.18 (s, 1H), 4.48 (d, J = 5.1 Hz, 2H), 4.29 (s, 2H), 2.98 (s, 2H), 2.91 – 2.60 (m, 7H), 2.19 – 2.10 (m, 2H), 1.83 (d, J = 0.5 Hz, 4H), 1.63 – 1.17 (m, 19H), 1.01 (s, 3H), 0.92 – 0.80 (m, 16H), 0.66 (d, J = 5.1 Hz, 6H). ¹³C NMR (101 MHz, DMSO) δ 176.46, 176.45, 172.11, 166.20, 153.88, 153.86, 150.79, 150.76, 148.60, 138.33, 129.13, 128.92, 127.97, 124.71, 111.23, 76.87,

54.80, 51.93, 51.91, 47.04, 46.56, 41.55, 41.53, 40.43, 38.78, 38.39, 38.23, 36.50, 32.64, 30.41, 30.39, 30.37, 28.28, 27.35, 27.34, 27.03, 23.55, 23.33, 22.87, 21.15, 21.12, 18.00, 17.18, 17.10, 16.73, 16.10, 15.23; IR: 3317, 2926, 2869, 1686, 1654, 1637, 1605, 1508, 1458, 1376, 1333, 1296, 1271, 1241, 1185, 1127, 1106, 1044, 1029, 996, 972, 949, 836, 821, 767 cm^{-1} .

7.5.4.2 Synthesis of UA-CYS-FA (14)

Yield: 0.24 g (80 %); Appearance: Yellow powder; Solubility: DMSO (hot), DMF (hot); ^1H NMR (400 MHz, DMSO) δ 11.26 (s, 1H), 8.63 (d, $J = 3.8$ Hz, 1H), 8.04 (s, 2H), 7.65 (t, $J = 8.3$ Hz, 2H), 7.39 (s, 1H), 6.93 (s, 3H), 6.63 (d, $J = 8.5$ Hz, 2H), 5.18 (s, 1H), 4.48 (d, $J = 5.1$ Hz, 2H), 4.29 (s, 2H), 2.98 (s, 2H), 2.91 – 2.60 (m, 7H), 2.19 – 2.10 (m, 2H), 1.83 (d, $J = 0.5$ Hz, 4H), 1.63 – 1.17 (m, 19H), 1.01 (s, 3H), 0.92 – 0.80 (m, 16H), 0.66 (d, $J = 5.1$ Hz, 6H). ^{13}C NMR (101 MHz, DMSO) δ 176.44, 176.36, 172.12, 172.09, 154.31, 153.86, 150.76, 148.63, 148.58, 138.30, 130.81, 129.12, 127.94, 124.67, 121.40, 111.08, 76.86, 54.82, 54.80, 51.92, 47.04, 46.56, 45.96, 45.70, 41.55, 41.53, 40.43, 40.24, 39.52, 38.79, 38.75, 38.71, 38.50, 38.39, 38.34, 38.27, 38.23, 38.20, 36.49, 32.63, 30.39, 30.37, 28.28, 27.36, 27.02, 23.56, 23.33, 22.86, 21.15, 19.38, 17.99, 17.18, 17.11, 16.75, 16.11, 15.23; IR: 3322, 2925, 2868, 1640, 1606, 1509, 1455, 1377, 1335, 1295, 1271, 1186, 1128, 1106, 1093, 1029, 997, 973, 949, 835m 822, 766 cm^{-1} .

7.5.4.3 Synthesis of UA-EDEA-FA (15)

Yield: 0.20 g (66.6 %); Appearance: Yellow powder; Solubility: DMSO (hot), DMF (hot); ^1H NMR (400 MHz, DMSO) δ 11.48 (s, 1H), 8.64 (s, 1H), 8.07–7.84 (m, 2H), 7.65 (d, $J = 7.9$ Hz, 2H), 7.13 (s, 1H), 6.96 (d, $J = 5.4$ Hz, 2H), 6.63 (d, $J = 8.5$ Hz, 2H), 5.18 (s, 1H), 4.48 (d, $J = 5.6$ Hz, 2H), 4.32 (s, 2H), 3.22 – 3.03 (m, 6H), 2.98 (d, $J = 9.7$ Hz, 2H), 2.54 (s, 1H), 2.09 (d, $J = 9.7$ Hz, 2H), 1.86 (d, $J = 24.8$ Hz, 5H), 1.74 – 1.05 (m, 24H), 1.01 (s, 4H), 0.83 (dd, $J = 22.0, 11.1$ Hz, 19H), 0.67 (d, $J = 8.4$ Hz, 8H). ^{13}C NMR (101 MHz, DMSO) δ 176.49, 176.48, 171.95, 171.92, 156.86, 154.31, 153.03, 150.81, 148.58, 138.40, 129.14, 129.11, 124.78, 124.74, 114.89, 112.94, 111.29, 111.23, 111.19, 76.89, 69.60, 68.96, 54.82, 52.08, 47.08, 46.68, 45.96, 41.65, 40.43, 39.52, 38.75, 38.55, 38.49, 38.44, 38.28, 37.04, 36.53, 32.72, 32.71, 30.47, 28.31, 27.37, 27.04, 23.66, 23.49, 23.29, 22.93, 21.20, 18.02, 17.21, 16.77, 16.16, 16.13, 15.28; IR: 3320, 2926, 2869, 1685, 1638, 1614, 1605, 1508, 1456, 1376, 1334, 1296, 1271, 1185, 1127, 1106, 1094, 1029, 996, 972, 949, 836, 821, 767 cm^{-1} .

7.6 Pharmacokinetics

Physicochemical, pharmacokinetic and drug-likeness properties were analysed by SwissADME web-based interface provided by the Molecular Modelling Group of the Swiss Institute of Bioinformatics. SwissADME (www.swissadme.ch/) web tool is a free software utilized to predict the pharmacokinetic parameters/properties of drug-like compounds from their molecular structures (Daina *et al.*, 2017). The 2D structures of the compounds were drawn with ChemDraw Professional 16.0, and imported to the SwissADME website where the ADMET properties/parameters were generated.

The physicochemical properties, lipophilicity and solubility were considered for the analysis. In addition, the BOILED-Egg model was predicted to reveal the capability of gastrointestinal (GI) absorption and permeability of the blood-brain penetration barrier. Several other parameters/properties such as Abbott bioavailability score and synthetic accessibility were evaluated.

7.7 Pharmacodynamics

7.7.1 Computational tools and software

The computational protocols were developed, and results were analysed using an in-house (Intel® Core™ i3-6100 CPU @ 3.70 GHz) Windows 10 Enterprise version 21H2. For analysis and visualisation, academic versions of PyMOL™ 2.4.1 Incentive Product – Copyright (C) Schrodinger, LLC and BIOVIA Discovery Studio Client Visualizer v.21.1.0 – Copyright (C) 2020, Dassault Systèmes were used.

7.7.2 Protein Structures

The three-dimensional structural information of target proteins used in this study were obtained from an open source directory at Research Collaboratory for Structural Bioinformatics Protein Data Bank (RCSB PDB).

The crystal structure of FR α in complex with folic acid at 2.80 Å resolution (PDB ID: 4LRH) (Chen *et al.*, 2013) was used to study and compare the binding affinity of folic acid and the three novel FUA conjugates to FR α . The crystal structure of VRK1 in complex with 4,4'-(2-aminopyridine-3,5-diyl)bis(2,6-difluorophenol) at 1.80 Å (PDB ID: 6BU6) (Couñago *et al.*, 2017) was used to study and compare the binding affinity of UA, the novel FUA conjugates and novel UA derivatives.

Prior to molecular docking, the protein structures were prepared in AutoDock Tools (ADT) (www.autodock.scripps.edu) (Morris *et al.*, 2009). The protein was read from the PDB file to remove water, add polar hydrogens and charges are applied. Specific residues in the binding pocket were selected as residues (FR α - Chen *et al.*, 2013; VRK1 – Couñago *et al.*, 2017) with flexible sidechains for VRK1 (I51, K71, D132, F134, S181, L184 and D197) and the output file were saved in as PDBQT format.

7.7.3 Ligand Structures

The 3D structures of UA, FA and 4,4'-(2-aminopyridine-3,5-diyl)bis(2,6-difluorophenol) were downloaded from PubChem and saved as SDF file. The structures of novel FUA and novel UA derivatives were drawn using ChemDraw 3D Ultra (12.0.2) and saved as SDF files. All compounds were visualized and converted to PDB file using PyMol (2.4.1). Discovery Studio version v21.1 was used to generate 3D conformations of all compounds, according to their most preferred stereoisomers and tautomers, which were then energy minimised in the Avogadro's suite with the MMFX96 force field. The energy minimised models were pre-processed in AutoDock4 tools (www.autodock.scripps.edu) (Morris *et al.*, 2009) to assign torsion angles and add polar hydrogens and the output file were saved in as PDBQT format.

7.7.4 Molecular Docking

AutoDock Vina (Trott and Olson, 2010) was used for rigid and flexible docking. AutoDock4 tools' grid setting centred on the crystal structure ligand was employed to define the binding site grid box. Docking to FR α was performed using rigid docking; docking to VRK1 was done using flexible docking using default parameters. A review of the literature indicates that key residues are important for binding and were used to define the binding pocket- I51, K71, D132, F134, S181, L184 and D197 (Kim *et al.*, 2015; Couñago *et al.*, 2017; Ngow *et al.*, 2018; Serafim *et al.*, 2019). The grid size dimensions used and the centre point of the binding pocket set at *xyz* coordinates are tabulated in **Table 28** below.

Table 28. The binding pocket centre co-ordinates obtained from ADT and the grid box dimensions.

	FRα (PDB code: 4LRH)	VRK1 (PDB code: 6BU6)
Grid size dimension	22 x 24 x 32 units	20 x 20 x 20 units
Spacing	0.375 Å per unit	0.375 Å per unit
Center_x	-13.509	29.057
Center_y	30.598	4.152
Center_z	81.247	13.838

7.8 Cell Culture

7.8.1 Cell culture conditions

The human brain glioblastoma cancer cell line (U-251 MG (formerly known as U-373 MG) (ECACC 09063001)) was obtained from Dr Michael Carty (Trinity College Dublin) and was the main cell line used in this study. The human colorectal cancer cell line (SW480) was obtained from Dr Alan Casey (FOCAS Institute). The human ovarian cancer cell line SKOV-3, human epidermal cell line A431, human breast cancer cell line MCF-7, and human colorectal cell line Caco-2 were purchased from ATCC European distributor (LGC Standards) and were obtained from Prof. Fiona Lyng (FOCAS Institute).

The human embryonic kidney cell line, HEK-293, were obtained from Darren Fayne (Trinity College Dublin).

Cells were cultured in Dulbecco's Modified Eagle's Medium-high glucose (DMEM) (Merck, Ireland) or Roswell Park Memorial Institute (RPMI-1640) or Folate-free RPMI 1640 medium (Gibco) supplemented with 10% foetal bovine serum (FBS) (Merck, Ireland) and 1% penicillin-streptomycin solution (Merck, Ireland) in TC flask T75, standard for adherent cells (Sarstedt). The cultures were maintained in a humidified incubator containing 5% (v/v) CO₂ at 37 °C. Culture medium was changed every 2–3 days until 80% confluency was reached.

Cells were routinely sub-cultured using 0.25% trypsin-EDTA solution (Merck, Ireland). Cells were spun down at 300 x g at 4 °C for 5 minutes. The supernatant was then removed as waste and the afforded pellet was re-suspended in full media. Cells were then counted using a haemocytometer (Abcam).

7.8.2 Cytotoxicity

Stock solutions of compounds were dissolved in Dimethyl Sulfoxide (DMSO) and stored at -20 °C. These stocks were subsequently used to make the working solutions in media. The highest concentration of DMSO used was 0.5%. Cells were seeded at a density of 1×10^4 cells (24 and 48 hours) and 2.5×10^3 (144 hours) exposure time period with 100 µL media per well in 96-well plates (Sarstedt). Plates were incubated overnight at 37 °C with 5% CO₂ to allow proper adherence. Existing media were removed from each well and cells were treated with compounds at varying concentrations (100 - 3.125 µM), 20% (v/v) DMSO was used as a positive control, and 0.5% (v/v) DMSO as negative control at

appropriate time point. No deleterious effects were observed from the negative control solvent.

7.8.3 Cell Viability Assay

Cell viability was measured biochemically using the alamarBlue™ assay (Invitrogen), an oxidation-reduction (redox) fluorogenic indicator of cellular metabolic reduction. The alamarBlue™ assay encompasses a fluorometric/colorimetric growth indicator based on the detection of metabolic activity. The system incorporates an oxidation-reduction indicator that both fluoresces and changes colour in response to chemical oxidation of growth medium as a result of cell death. A decrease in cell viability results in a colour change from pink (reduced, fluorescent) to blue (oxidised, non-fluorescent).

After each exposure time point (24, 48 or 144 hours), cells were washed once with sterile Phosphate-buffered saline (PBS) (Merck, Ireland). A 10% alamarBlue™ in the DMEM (no FBS and antibiotics) was added to each well and incubated at 37 °C for 2.5 hours. The cell viability was measured by fluorescence (excitation, 530 nm; emission, 590 nm) using a Varioskan™ LUX multimode microplate reader (Thermo Fisher Scientific). All experiments were performed at least three independent times with a minimum of three replicates per experiment and are presented as mean \pm S.E.M. The data (in fluorescence units from the microplate reader) for the test wells were normalised to the assay control and cell growth was calculated as a change of viability over time.

7.9 Ultrasound Treatment

An ultrasonic bath system (TI-H-5, Elma Hans Schmidbauer, Singen, Germany) was used for ultrasound generation. Settings for ultrasound used are as follows: 25 kHz generated at the bottom of the water tank, under 100 % power (550 W), using a sweep mode for different doses of ultrasound. There was no heating or cooling system used. Temperature of the water was maintained at approximately 25 – 30 °C, using a mercury-in-glass thermometer. Cells were seeded the same as 7.8.2 for 48 and 144 hours in a 96-well plate. Treatment was performed by adding 20 µL into the 96-well plate and placed in water bath for either 5 or 10 minutes. After which time, the remaining 80 µL treatment was added to have a total volume of 100 µL per well. Cell viability was assessed after 48 or 144 hours using alamarBlue cell viability assay. Cells were also treated with a vehicle control of 0.5% DMSO and with no ultrasound.

7.10 Flow Cytometry

Propidium Iodide

Viable and dead cells were recorded using PI staining. Stock solutions of PI (Merck, Ireland) were prepared at 1 mg/mL in DMSO, aliquoted out and stored in freezer (–20 °C) until required for use. U-251 MG cells were plated in 6-well plates (Sarstedt) at a density of 1×10^5 cells/ml (48 hours) or 2×10^4 cells/ml (144 hours). After 24 hr, growth medium was removed and cells were treated with 10 µM of compounds, incubated at appropriate time point. Cells were collected by trypsinization, and pelleted by centrifugation at 500 x g for 5 min. The pellet was resuspended in 0.5 ml PBS and cells

were stained with 0.5 µg/ml PI for 3 min in the absence of light. The fluorescence of PI was then measured using the Beckman Coulter CytoFLEX Flow Cytometer with a blue laser (488 nm).

JC-1 Mitochondrial Membrane Potential Assay

Dual-emission potential-sensitive fluorescence dye JC-1 was used to measure mitochondrial membrane potential of cells following treatment. Stock solutions of JC-1 dye (Biosciences, Dublin, Ireland) were prepared at 1 mg/mL in DMSO, aliquoted out and stored in freezer (−20 °C) until required for use. U-251 MG cells were seeded in 6-well plates (Sarstedt) at a density of 1×10^5 cells/ml (48 hours) or 2×10^4 cells/ml (144 hours). After 24 hours, growth medium was removed and cells were treated with 10 µM of compounds and incubated at appropriate time point. Cells were collected by trypsinization and centrifugation at 500 x g for 5 min, and stained with 2.5 µg/mL JC-1 dye. After 10 min incubation time at room temperature and absence of light, cells were washed with PBS twice. The supernatant was removed, and cells were resuspended in 0.3 ml PBS for flow cytometry (Beckman Coulter CytoFLEX) analysis. Fluorescence intensity was measured with a blue laser (488 nm) using fluorescein isothiocyanate (FITC) and phycoerythrin (PE-A) emission filters with spectral overlap compensation (52% FITC/PE-A and 10% PE-A/FITC).

7.11 Inhibitor Studies

E-64

E-64 is an epoxide which can irreversibly inhibit a wide range of cysteine peptidases, such as broad spectrum cathepsins. Cathepsins are cysteine proteases acting within the lysosomal/autophagy pathway (late autophagy). E-64 (Merck, Ireland) was reconstituted in DMSO and frozen at -20 °C at a stock concentration of 20 mM, with a working concentration of 10 µM in full cell culture media. U-251 MG cells were pre-treated with E-64 for 1 hour, then removed by pipetting and treated with IC₅₀ of compounds. Cell viability was assessed after 48 or 144 hours using alamarBlue cell viability assay. Cells were also treated with a vehicle control of 0.5% DMSO.

SP600125

SP600125 is an inhibitor of JNK which is commonly associated with apoptosis. SP600125 (Merck, Ireland) was reconstituted in DMSO and stored at -20°C at a stock concentration of 25 mM, with a working solution of 12.5 µM in full cell culture media. U-251 MG cells were pre-treated with SP600125 for 1 hour. SP600125 was then removed by pipetting and cells were treated with IC₅₀ of compounds. Cell viability was assessed after 48 or 144 hours using alamarBlue cell viability assay. Cells were also treated with a vehicle control of 0.5% DMSO.

zVAD-fmk

Commonly employed general caspase inhibitor zVAD-fmk (Merck, Ireland), was used in order to detect determine whether caspases play a role in cell death in U-251 MG cells. zVAD-fmk was reconstituted in DMSO and frozen at -20°C at a stock concertation of 10

mM, with working concentration of 25 μ M in full DMEM. Cells were pre-treated for 1 hour with zVAD-fmk, then removed from each well and treated with IC₅₀ of compounds. Cells were then analysed after 48 or 144 hours using alamarBlue cell viability assay. Cells were also treated with a 0.5% DMSO vehicle control.

7.12 Stability of Novel UA Derivatives

Stability in Cell Culture Medium

A 100 μ M of compounds in media were prepared and incubated at 37 °C for 144 hours. After which time, U-251 MG cells were treated the same as **7.8.2** for 48 and 144 hours exposure time point, and analysed using alamarBlue cell viability assay.

Enzymatic Activity

Approximately 1×10^6 U-251 MG cells were collected, centrifuged and washed with PBS. Cells were resuspended in 50 μ l of PBS with 1 % protease inhibitor cocktail and then freeze-thawed 3 times in liquid nitrogen (1 minute) and 37 °C water bath (1 minute); vortexed vigorously after each freeze-thaw cycles. Cell extracts were pre-incubated with compounds incubated at 37 °C or ice for 1 hour. The compounds in PBS was incubated at 37 °C and used as a control. After which time, U-251 MG cells were treated the same as **7.8.2** for 48 and 144 hours exposure time point, and analysed using alamarBlue cell viability assay.

7.13 Cell Membrane Damage Assay

UV-Vis

U-251 MG cells were exposed to Syngene G:BOX Chemi XRQ UV-Vis Gel doc at different times (0 to 240 sec). A dose response curve was generated after 48 and 144 hours timepoint. There was not much effect after 48 hours treatment, and thus 144 hours treatment was used in succeeding assays. A no observable adverse effect level (NOAEL) was observed after 10 and 15 seconds UV-Vis exposure, hence was used for this study to determine if there is a synergistic effect between compounds and UV-Vis. U-251 MG cells were treated with compounds at NOAEL concentrations and incubated at 37 °C with 5% CO₂ for 1 hour. After which time, cells were exposed to UV-Vis for 10 or 15 seconds. Cells exposed for 1 minute in UV-Vis were used as positive control; cells exposed for 10 or 15 seconds were used as negative control. Cell viability was assessed after 144 hours using alamarBlue cell viability assay. A control plate with no UV-Vis was also used as a control.

Temozolomide

A 20 mM stock solution of TMZ was reconstituted in DMSO and frozen at -20°C. TMZ dose response was generated after 48 and 144 hours timepoint to determine lowest observed adverse effect level (LOAEL) and was calculated as 15 µM. U-251 MG cells were pre-treated for 1 hour with 15 µM TMZ in media, then removed from each well and treated with 5-20 µM concentrations of compounds. Cells were then analysed after 48 or 144 hours using alamarBlue cell viability assay. Cells were also treated with a 0.5% DMSO vehicle control. A control plate with no TMZ was also used as a control.

7.14 Cell Proliferation Assay

Haemocytometer

To determine optimum seeding density for 96 hours proliferation assay, U-251 MG cells were seeded at a density of 1.5×10^3 , 3×10^3 and 5×10^3 cells with 100 μ L media per well in 96-well plates (Sarstedt). Optimum seeding density was determined to be 3×10^3 . Cells were treated with NOAEL concentrations of compounds and incubated for 24, 48, 72 and 96 hours. After each incubation time, images were taken at 10x zoom using Optika XDS-2 trinocular inverse microscope equipped with a microscope Camera ISH500. Cells were dislodged using 0.25% trypsin-EDTA solution (Merck, Ireland), and were spun down at 300 x g at 4 °C for 5 minutes. The supernatant was then removed as waste and the afforded pellet was re-suspended in full media. Cells were then counted using a haemocytometer (Abcam). Cell concentration per ml was calculated from average cell count.

CFSE Cell Proliferation Assay

CellTrace™ CFSE cell proliferation assay kit, for flow cytometry (Thermo Fisher, Ireland) was used for this assay. The kit was stored at -20 °C until required for use. The CellTrace™ CFSE was reconstituted in 18 μ L DMSO (stock solution), aliquoted and stored at -20 °C until use (one time use once thawed). A 1:1000 dilution of the stock solution in PBS warmed at 37 °C was used as working solution. U-251 MG cells (5×10^5) were harvested by trypsinisation and centrifuged at 300 x g for 5 minutes. Cells were resuspended in 1 ml working solution was added and mixed well to have a single suspension and incubated at 37 °C with 5% (v/v) CO₂, protected from light. Cells were gently mixed every 5 minutes. After which, 4 ml of media was added to absorb unbound dye and incubated at RT for 5 min. Cells were then centrifuged at 300 x g for 5 minutes.

Supernatant was discarded and cells were resuspended in 20 mL pre-warmed media, mixed well to a single suspension. U-251 MG cells were seeded in 6-well plates (Sarstedt) at a density of 5×10^4 cells per well. After 24 hours, growth medium was removed and cells were treated with NOAEL concentration of compounds, and further incubated for 96 hours. Cells were collected by trypsinisation and centrifugation at 500 x g for 5 minutes, and resuspended in 0.1 ml PBS for flow analysis (Beckman Coulter CytoFLEX). The Fluorescence intensity was measured with a blue laser (488 nm) using fluorescein isothiocyanate (FITC). Cells were also co-stained with 0.5 µg/ml PI for 3 minutes in the absence of light, to determine apoptotic cells. The Fluorescence intensity was measured with a blue laser (488 nm) using fluorescein isothiocyanate (FITC) and phycoerythrin (PE-A) emission filters with spectral overlap compensation (42.80% FITC/PE-A).

7.15 Collective Cell Migration Assay

U-251 MG cells were seeded at 0.9×10^6 cells per well in 6-well plates (Sarstedt, Ireland) and incubated for 24 hours. The monolayer was scratched using a 200 µl sterile pipette tip held at 45° angle. Each well was scratched both horizontally and vertically to obtain a cross point at the centre of the well, which was used as a reference point while taking snapshots of wells. The old media was discarded, and cells was gently washed with PBS solution without disturbing or dislodging the cells in the well. After washing, cells were treated with NOAEL concentrations of UA (positive control) and compounds (**A.25**). Cells treated with 0.1% DMSO served as vehicle control. Snapshots of scratched surfaces were taken at 10X zoom using Optika XDS-2 trinocular inverse microscope equipped with a microscope Camera ISH500, every hour for 7 hours. Multiple images were taken

for each time point and the average size of scratch for that time point was obtained. Image processing and relative scratch area quantification was performed using Fiji (Schindelin *et al.*, 2012) with the Wound Healing tool plugin. Three independent experiments were performed for each test compounds in triplicates. The statistical inference was analysed and performed using Graphpad Prism 9 software.

7.16 3D Cell Culture Assay

U-251 MG and A431 cells were used to generate tumour spheroids. Single cell suspension is seeded in Nunclon™ Sphera™ 96-Well low attachment plates (Thermo Fisher Scientific) in DMEM-high glucose media without sodium pyruvate supplemented with 10 % FBS and 1 % penicillin/streptomycin. The low attachment plates were centrifuged at 1250 rpm for 5 minutes for U-251 MG cells and 4000 rpm for 10 minutes for A431 cells and the plates were maintained in a humidified incubator containing 5% (v/v) CO₂ at 37 °C. Fresh media were added every third day by replenishing old media in each well without disturbing tumour spheroids (Carroll *et al.*, 2021). Tumour spheroids formation was observed within 72 and 96 hours for A431 and U-251MG, respectively. The tumour spheroid formation was visually confirmed using 10x zoom Optika XDS-2 trinocular inverse microscope equipped with a microscope Camera ISH500.

Existing media were removed from each well and cells were treated with compounds (100, 50, 25, 12.5, 6.25, and 3.125 µM concentrations), 20% (v/v) DMSO as a positive control, and 0.5% (v/v) DMSO as negative control at appropriate time point. No deleterious effects were observed from the negative control solvent. Cell viability was measured using 10% alamarBlue™ in DMEM as stated above. All experiments were

performed at least three independent times with a minimum of three replicates per experiment.

7.17 Data Analysis

Spectrophotometer data

Data retrieved from Varioskan™ LUX multimode microplate reader (Thermo Fisher Scientific) measures the fluorescence in each well of the microplate and generates readings as arbitrary fluorescent unit values. These fluorescent unit values were extrapolated for viability calculations using statistical analyses software Prism 9, GraphPad software, Inc. (USA). All experiments were performed at least three independent times with a minimum of three replicates per experiment. Cell viability was calculated, by first subtracting any background fluorescence from the alamarBlue blank reading. The mean (average) fluorescence value from each test per plate was calculated, n=3 per individual experiment of which was repeated independently three times.

7.18 Statistical Analysis

Triplicate independent tests were carried out for each data point unless indicated otherwise. Error bars of all figures are presented using standard error of the mean (S.E.M.). Prism 9, GraphPad Software, Inc. (San Diego, CA, USA) was used to carry out curve fitting and statistical analysis. Two-tailed P values were used where alpha = 0.05. The significance between data points was verified using two-way ANOVA with Bonferroni's multiple comparison post-test, as indicated in figures (*P < 0.05, **P < 0.01, ***P < 0.001, ****p < 0.0001).

PROFESSIONAL DEVELOPMENT

Publications

- Cabral, E., Mondala, JRM., Oliveira, M., Przyborska, J., Fitzpatrick, S., Rai, D., Sivagnanam, S., Garcia-Vaquero, M., O'Shea, D., Devereux, M., Tiwari, B. and Curtin, JF. (2021). Influence of molecular weight fractionation on the antimicrobial and anticancer properties of a fucoidan rich-extract from the macroalgae *Fucus vesiculosus*. *International Journal of Biological Macromolecules*, 186, pp.994-1002. doi: 10.1016/j.ijbiomac.2021.06.182.
- Cabral, E., Oliveira, M., Mondala, JRM., Curtin, JF., Tiwari, B. and Garcia-Vaquero, M. (2021). Antimicrobials from Seaweeds for Food Applications. *Marine Drugs*, 19(4), p.211. doi: 10.3390/md19040211.
- Conway, G., Zizyte, D., Mondala, JRM., He, Z., Lynam, L., Lecourt, M., Barcia, C., Howe, O. and Curtin, JF. (2021). Ursolic Acid Inhibits Collective Cell Migration and Promotes JNK-Dependent Lysosomal Associated Cell Death in Glioblastoma Multiforme Cells. *Pharmaceuticals*, 14(2), p.91. doi: 10.3390/ph14020091.
- Field, A., Tiwari, B., Curtin, JF., Mondala, JRM., and Wanigasekara, J. (2022). Ultrasound 96 Probe Device Protocol for cancer cell treatment v1. *protocols.io*,. doi: 10.17504/protocols.io.b3udqns6.
- He, Z., Charleton, C., Devine, R., Kelada, M., Walsh, J., Conway, G., Gunes, S., Mondala, JRM., Tian, F., Tiwari, B., Kinsella, GK., Malone, R., O'Shea, D., Devereux, M., Wang, W., Cullen, P., Stephens, J. and Curtin, JF. (2021). Enhanced pyrazolopyrimidinones cytotoxicity against glioblastoma cells activated by ROS-Generating cold atmospheric plasma. *European Journal of Medicinal Chemistry*, 224, p.113736. doi: 10.1016/j.ejmech.2021.113736.
- Nguyen, HP., He, Z., Tian, F., Curtin, JF., and Mondala, JRM. (2021). Gold nanoparticle synthesis v1. *protocols.io*,. doi: 10.17504/protocols.io.bshhnb36.

Structured PhD Modules

As part of the PhD experience, it is essential to develop and refine both discipline specific and employability skills. Tables 29 and 30 list modules and extracurricular activities undertaken.

Table 29. Modules completed as part of the structured PhD - ¹Discipline Specific Skills and ²Employability Skills. The required 40 credits for structured PhD has been fully completed.

Date	Module	Institution	ECTS
06 Feb 2018	PH6022: Writing in Science & Engineering ²	UL	6
11 May 2018	Applied Biomedical Imaging ¹	RCSI	2.5
01 Oct 2018	GRSO1001: Research Methods ²	TU Dublin	5
30 Nov 2018	GRSO1012: Research Integrity ²	TU Dublin	5
05 Dec2018	CRDI: Techniques & Strategies in Molecular Medicine ¹	TCD	5
28 Jan 2019	GRSO1010: Introduction to Pedagogy for Postgraduates ²	TU Dublin	5
29 Jan 2019	ENEH1004: Multivariate Analysis & Data Mining for Biomedical Applications ¹	TU Dublin	5
27 May 2019	UCD Conway Flow Cytometry Summer School ¹	UCD	5
28 Oct 2019	ENEH1006: Applied Modelling in Environment, Food & Health ¹	TU Dublin	5

Table 30. Extracurricular activities undertaken.

Extracurricular Activity	Date
Switch on STEM	Jan 2020 – May 2022
Laboratory demonstrator for Organic and Inorganic Chemistry	Sep 2018 – Mar 2020
Laboratory demonstrator for Instrumentation	Feb 2019 – Mar 2020
Tutorial for Organic and Physical Chemistry	Feb 2019 – Dec 2021
Senior laboratory demonstrator for Organic Chemistry	Sep 2021 – May 2022
Tutorial for Instrumentation	Sep 2021 – Dec 2021
FSEH Research Committee Representative	Sep 2020 – Feb 2022
Supervised Final Year Projects	Jan 2019 – May 2022
Supervised ERASMUS Projects	Jan 2020 – Dec 2020
RSC Primary and Secondary School Outreach Programme	May 2022

Conferences and Seminars Attended

Attended the 10th Annual Postgraduate Research Symposium, TU Dublin, November 22nd 2019.

Presented at the 1st Teagasc Brainstorming Session, Teagasc Ashtown, 5th March 2020.

Attended the Institute of Chemistry of Ireland Postgraduate Chemistry Research Symposium 2020 *via zoom*.

Attended the International E-conference on Cancer Science and Therapy 2020 *via zoom*, December 7-8, 2020.

Attended the 6th EFMC-YSN MedChemBioOnline, 28th January 2021 [online].

Presented at the ESHI International Women's Day 2021, TU Dublin, 7th March 2021 [online].

Presented at Dublin Chemistry Graduate Seminar 2020/21, University College Dublin,
18th June 2021 [online].

Presented at the FSEH Research Symposium, TU Dublin, 21st June 2021 [online].

Attended Medicinal Chemistry Ireland Symposium 2021, 1st July 2021 [online].

Presented at the 12th Annual Graduate Research Symposium, TU Dublin, 15th December 2021
[online].

Attended the Young Modellers' Forum 2021-22, Molecular Graphics and Modelling
Society, 11th February 2022 [online].

Presented at the FSEH Annual Research & Innovation Showcase "Sustainability in
Research: Contributing to UN SDGs", TU Dublin, 9th May 2022.

REFERENCES

- Albericio, F., & El-Faham, A. (2018). Choosing the Right Coupling Reagent for Peptides: A Twenty-Five-Year Journey. *Organic Process Research & Development*, 22(7), pp. 760–772. doi:10.1021/acs.oprd.8b00159.
- Aldape, K., Brindle, K.M., Chesler, L., Chopra, R., Gajjar, A., Gilbert, M.R., Gottardo, N., Gutmann, D.H., Hargrave, D., Holland, E.C. and Jones, D.T. (2019). Challenges to curing primary brain tumours. *Nature reviews Clinical oncology*, 16(8), pp.509-520. doi: 10.1038/s41571-019-0177-5
- Alexander, B.M. and Cloughesy, T.F. (2017). Adult glioblastoma. *Journal of Clinical Oncology*, 35(21), pp.2402-2409. doi: 10.1200/JCO.2017.73.0119.
- Alifieris, C. and Trafalis, D.T. (2015). Glioblastoma multiforme: Pathogenesis and treatment. *Pharmacology & Therapeutics*, 152, pp.63–82. doi: 10.1016/j.pharmthera.2015.05.005.
- Anjum, K., Shagufta, B.I., Abbas, S.Q., Patel, S., Khan, I., Shah, S.A.A., Akhter, N. and Hassan, S.S. ul (2017). Current status and future therapeutic perspectives of glioblastoma multiforme (GBM) therapy: A review. *Biomedicine & Pharmacotherapy*, 92, pp.681–689. doi: 10.1016/j.biopha.2017.05.125.
- Annan, K., Dickson, R., Komlaga, G., Jackson, N., & Sam, G. (2011). Acaricidal effect of an isolate from *Hoslundia opposita* vahl against *Amblyomma variegatum* (Acari: Ixodidae). *Pharmacognosy Research*, 3(3), pp. 185-188. doi:10.4103/0974-8490.85004.
- Antônio, E., Antunes, O. dos R., de Araújo, I. S., Khalil, N. M., & Mainardes, R. M. (2017). Poly(lactic acid) nanoparticles loaded with ursolic acid: Characterization and in vitro evaluation of radical scavenging activity and cytotoxicity. *Materials Science and Engineering: C*, 71, pp. 156–166. doi:10.1016/j.msec.2016.09.080.

- Aparicio-Blanco, J., Sanz-Arriazu, L., Lorenzoni, R. and Blanco-Prieto, M.J. (2020). Glioblastoma chemotherapeutic agents used in the clinical setting and in clinical trials: nanomedicine approaches to improve their efficacy. *International Journal of Pharmaceutics*, p.119283.
- Armstrong, D. K., White, A. J., Weil, S. C., Phillips, M., & Coleman, R. L. (2013). Farletuzumab (a monoclonal antibody against folate receptor alpha) in relapsed platinum-sensitive ovarian cancer. *Gynecologic Oncology*, 129(3), pp. 452–458. doi:10.1016/j.ygyno.2013.03.002.
- Aronov, O., Horowitz, A. T., Gabizon, A., & Gibson, D. (2003). Folate-Targeted PEG as a Potential Carrier for Carboplatin Analogs. Synthesis and in Vitro Studies. *Bioconjugate Chemistry*, 14(3), pp. 563–574. doi:10.1021/bc025642l.
- Assaraf, Y. G., Leamon, C. P., & Reddy, J. A. (2014). The folate receptor as a rational therapeutic target for personalized cancer treatment. *Drug Resistance Updates*, 17(4-6), pp. 89–95. doi:10.1016/j.drug.2014.10.002.
- Azvolinsky, A. (2011). Most Cited Cell Article Of All Time, “Hallmarks Of Cancer”. [Online]. Cancer Network. Available at: <<https://www.cancernetwork.com/breast-cancer/most-cited-cell-article-all-time-hallmarks-cancer-gets-update>> [Accessed 12 April 2020].
- Baek, C., Ha, T.-L., Kim, E., Jeong, S., Lee, S., Lee, S., & Kim, H.-C. (2015). Bioreducible Micelles Self-Assembled from Poly(ethylene glycol)-Cholesteryl Conjugate As a Drug Delivery Platform. *Polymers*, 7(11), pp. 2245–2258. doi:10.3390/polym7111511.
- Bai, K.-K., Chen, F.-L., Yu, Z., Zheng, Y.-Q., Li, Y.-N., & Guo, Y.-H. (2011). Synthesis of [3 β -acetoxy-urs-12-en-28-oyl]-1-monoglyceride and investigation on its anti tumor

- effects against BGC-823. *Bioorganic & Medicinal Chemistry*, 19(13), pp. 4043–4050. doi:10.1016/j.bmc.2011.05.017.
- Bai, K.-K., Yu, Z., Chen, F.-L., Li, F., Li, W.-Y., & Guo, Y.-H. (2012). Synthesis and evaluation of ursolic acid derivatives as potent cytotoxic agents. *Bioorganic & Medicinal Chemistry Letters*, 22(7), pp. 2488–2493. doi:10.1016/j.bmcl.2012.02.009.
- Baishya, R., Nayak, D. K., Kumar, D., Sinha, S., Gupta, A., Ganguly, S., & Debnath, M. C. (2016). Ursolic Acid Loaded PLGA Nanoparticles: in vitro and in vivo Evaluation to Explore Tumor Targeting Ability on B16F10 Melanoma Cell Lines. *Pharmaceutical Research*, 33(11), pp. 2691–2703. doi:10.1007/s11095-016-1994-1.
- Barani, I. J., & Larson, D. A. (2014). Radiation Therapy of Glioblastoma. *Current Understanding and Treatment of Gliomas*, pp. 49–73. doi:10.1007/978-3-319-12048-5_4.
- Barnes, J.L., Zubair, M., John, K., Poirier, M.C. and Martin, F.L. (2018). Carcinogens and DNA damage. *Biochemical Society Transactions*, [online] 46(5), pp.1213–1224. doi:10.1042/bst20180519.
- Beck, T.C., Beck, K.R., Morningstar, J., Benjamin, M.M. and Norris, R.A. (2021). Descriptors of Cytochrome Inhibitors and Useful Machine Learning Based Methods for the Design of Safer Drugs. *Pharmaceuticals*, 14(5), p.472. doi:10.3390/ph14050472
- Bekker, K. S., Chukanov, N. V., Popov, S. A., & Grigor'ev, I. A. (2013). Conjugates of Bisphosphonates with Derivatives of Ursolic, Betulonic, and Betulinic Acids. *Chemistry of Natural Compounds*, 49(3), pp. 581–582. doi:10.1007/s10600-013-0680-3.
- Bergamin, L. S., Figueiró, F., Dietrich, F., Manica, F. de M., Filippi-Chiela, E. C., Mendes, F. B., Battastini, A. M. O. (2017). Interference of ursolic acid treatment with

- glioma growth: An in vitro and in vivo study. *European Journal of Pharmacology*, 811, pp. 268–275. doi:10.1016/j.ejphar.2017.06.030.
- Bertuzzi, D. L., Perli, G., Braga, C. B., & Ornelas, C. (2020). Synthesis, Characterization, and Anticancer Activity of Folate γ - Ferrocenyl Conjugates. *New Journal of Chemistry*. doi:10.1039/c9nj04954a.
- Betzel, T., Müller, C., Groehn, V., Müller, A., Reber, J., Fischer, C. R., Ametamey, S. M. (2013). Radiosynthesis and Preclinical Evaluation of 3'-Aza-2'-[18F]fluorofolic Acid: A Novel PET Radiotracer for Folate Receptor Targeting. *Bioconjugate Chemistry*, 24(2), pp. 205–214. doi:10.1021/bc300483a.
- Bianchi, E., Doe, B., Goulding, D., & Wright, G. J. (2014). Juno is the egg Izumo receptor and is essential for mammalian fertilization. *Nature*, 508(7497), pp. 483–487. doi:10.1038/nature13203.
- Bjorland, L.S., Fluge, O., Gilje, B., Mahesparan, R. and Farbu, E. (2021). Treatment approach and survival from glioblastoma: results from a population-based retrospective cohort study from Western Norway. *BMJ Open*, 11(3), p.e043208. doi: 10.1136/ bmjopen-2020-043208.
- Blasco, M. A. (2005). Telomeres and human disease: ageing, cancer and beyond. *Nature Reviews Genetics*, 6(8), pp. 611–622. doi:10.1038/nrg1656.
- Blom, H. J., & Smulders, Y. (2011). Overview of homocysteine and folate metabolism. With special references to cardiovascular disease and neural tube defects. *Journal of Inherited Metabolic Disease*, 34(1), pp. 75–81. doi:10.1007/s10545-010-9177-4.
- Bonaccorsi, I., Altieri, F., Sciamanna, I., Oricchio, E., Grillo, C., Contartese, G. and Galati, E.M. (2008). Endogenous reverse transcriptase as a mediator of ursolic acid's anti-proliferative and differentiating effects in human cancer cell lines. *Cancer Letters*, 263(1), pp.130–139. doi:10.1016/j.canlet.2007.12.026.

- Bray, F., Ferlay, J., Soerjomataram, I., Siegel, R. L., Torre, L. A., & Jemal, A. (2018). Global Cancer Statistics 2018: GLOBOCAN Estimates of Incidence and Mortality Worldwide for 36 Cancers in 185 Countries. *CA: A Cancer Journal for Clinicians*. doi:10.3322/caac.21492.
- Bryan, T. M., Englezou, A., Dalla-Pozza, L., Dunham, M. A., & Reddel, R. R. (1997). Evidence for an alternative mechanism for maintaining telomere length in human tumors and tumor-derived cell lines. *Nature Medicine*, 3(11), pp. 1271–1274. doi:10.1038/nm1197-1271.
- Butowski, N. (2018). Novel and Prospective Molecular Targets for Therapy of Intracranial Gliomas. *Intracranial Gliomas Part III - Innovative Treatment Modalities*, pp. 66–78. doi:10.1159/000469681.
- Bynum, W. and Porter, R., 1993. *Medicine And The Five Senses*. Cambridge University Press.
- Byrne, K.F., Pal, A., Curtin, J.F., Stephens, J.C. and Kinsella, G.K. (2021). G-protein-coupled receptors as therapeutic targets for glioblastoma. *Drug Discovery Today*, 26(12), pp.2858–2870. doi: 10.1016/j.drudis.2021.07.008.
- Carey, M. P., & Burish, T. G. (1988). Etiology and treatment of the psychological side effects associated with cancer chemotherapy: A critical review and discussion. *Psychological Bulletin*, 104(3), pp. 307–325. doi:10.1037/0033-2909.104.3.307.
- Carpino, L. A., Imazumi, H., Foxman, B. M., Vela, M. J., Henklein, P., El-Faham, A., Bienert, M. (2000). Comparison of the Effects of 5- and 6-HOAt on Model Peptide Coupling Reactions Relative to the Cases for the 4- and 7-Isomers. *Organic Letters*, 2(15), pp. 2253–2256. doi:10.1021/ol006013z.

- Carroll, L.J., Tiwari, B., Curtin, J.F., and Wanigasekara, J. (2021). U-251 MG Spheroid Generation using Low Attachment Plate Method Protocol. *protocols.io*,. doi: 10.17504/protocols.io.bszmnf46.
- Ceborska, M. (2017). Folate appended cyclodextrins for drug, DNA, and siRNA delivery. *European Journal of Pharmaceutics and Biopharmaceutics*, 120, pp. 133–145. doi:10.1016/j.ejpb.2017.09.005.
- Chabner, B. A., & Roberts, T. G. (2005). Chemotherapy and the war on cancer. *Nature Reviews Cancer*, 5(1), pp. 65–72. doi:10.1038/nrc1529.
- Charville, H., Jackson, D. A., Hodges, G., Whiting, A., & Wilson, M. R. (2011). The Uncatalyzed Direct Amide Formation Reaction - Mechanism Studies and the Key Role of Carboxylic Acid H-Bonding. *European Journal of Organic Chemistry*, 30, pp. 5981–5990. doi:10.1002/ejoc.201100714
- Chaudhury, S Das. (2015). Folate receptor targeted liposomes encapsulating anti-cancer drugs. *Current Pharm. Biotechnology*, 16(4), pp. 333-343. doi:10.2174/1389201016666150118135107.
- Chen, C., Ke, J., Zhou, X. E., Yi, W., Brunzelle, J. S., Li, J., Melcher, K. (2013). Structural basis for molecular recognition of folic acid by folate receptors. *Nature*, 500(7463), pp. 486–489. doi:10.1038/nature12327.
- Chen, C., Yang, J., Chen, W., Lu, C., Chiang, J., Chiu, H., Way, T. (2018). Ursolic acid elicits intrinsic apoptotic machinery by downregulating the phosphorylation of AKT/BAD signaling in human cisplatin-resistant oral cancer CAR cells. *Oncology Reports*. doi:10.3892/or.2018.6530.
- Chen, L., Qiu, W., Tang, J., Wang, Z. F., & He, S. Y. (2011). Synthesis and bioactivity of novel nitric oxide-releasing ursolic acid derivatives. *Chinese Chemical Letters*, 22(4), pp. 413–416. doi:10.1016/j.ccllet.2010.10.036.

- Chen, Q., Luo, S., Zhang, Y., & Chen, Z. (2011). Development of a liquid chromatography–mass spectrometry method for the determination of ursolic acid in rat plasma and tissue: Application to the pharmacokinetic and tissue distribution study. *Analytical and Bioanalytical Chemistry*, 399(8), pp. 2877–2884. doi:10.1007/s00216-011-4651-x.
- Cheraïet, Z., Ouarna, S., Hessainia, S., Berredjem, M., & Aouf, N.-E. (2012). ‘N-tert-Butoxycarbonylation of Structurally Diverse Amines and Sulfamides under Water-Mediated Catalyst-Free Conditions’, *ISRN Organic Chemistry*, 2012, pp. 1–8. doi:10.5402/2012/404235.
- Christoph, D. C., Asuncion, B. R., Hassan, B., Tran, C., Maltzman, J. D., O’Shannessy, D. J., Hirsch, F. R. (2013). Significance of Folate Receptor Alpha and Thymidylate Synthase Protein Expression in Patients with Non–Small-Cell Lung Cancer Treated with Pemetrexed. *Journal of Thoracic Oncology*, 8(1), pp. 19–30. doi:10.1097/jto.0b013e31827628ff.
- Collins, I., & Workman, P. (2006). New approaches to molecular cancer therapeutics. *Nature Chemical Biology*, 2(12), pp. 689–700. doi:10.1038/nchembio840.
- Colombo, E. and Cattaneo, M.G., 2021. Multicellular 3D Models to Study Tumour-Stroma Interactions. *International Journal of Molecular Sciences*, 22(4), p.1633. doi: 10.3390/ijms22041633.
- Common Organic Chemistry. (2020). Boc Deprotection (TFA). [Online] Available at: <http://www.commonorganicchemistry.com/Rxn_Pages/Boc_Protection/Boc_Protection_TFA_Mech.htm> [Accessed 23 March 2020].
- Common Organic Chemistry. (2020). Boc Protection Mechanism. [Online] Available at: http://www.commonorganicchemistry.com/Rxn_Pages/Boc_Protection/Boc_Protection_Mech.htm. [Accessed 18 March 2020].

- Common Organic Chemistry. 2020. [Online]. Amine to Amide (HATU). Available at: <http://commonorganicchemistry.com/Rxn_Pages/Amine_to_Amide_Coupling/Amine_to_Amide_Coupling_HATU.htm> [Accessed 20 March 2020].
- Conway, G.E., Zizyte, D., Mondala, J.R.M., He, Z., Lynam, L., Lecourt, M., Barcia, C., Howe, O. and Curtin, J.F. (2021). Ursolic Acid Inhibits Collective Cell Migration and Promotes JNK-Dependent Lysosomal Associated Cell Death in Glioblastoma Multiforme Cells. *Pharmaceuticals*, 14(2), p.91. doi:10.3390/ph14020091.
- Crider, K. S., Yang, T. P., Berry, R. J., & Bailey, L. B. (2012). Folate and DNA Methylation: A Review of Molecular Mechanisms and the Evidence for Folate's Role. *Advances in Nutrition*, 3(1), pp. 21–38. doi:10.3945/an.111.000992.
- Crocetti, E., Trama, A., Stiller, C., Caldarella, A., Soffietti, R., Jaal, J., Brandes, A. (2012). Epidemiology of glial and non-glial brain tumours in Europe. *European Journal of Cancer*, 48(10), pp. 1532–1542. doi:10.1016/j.ejca.2011.12.013.
- Da Silva, V. D., de Faria, B. M., Colombo, E., Ascari, L., Freitas, G. P. A., Flores, L. S., Buarque, C. D. (2018). Design, synthesis, structural characterization and in vitro evaluation of new 1,4-disubstituted-1,2,3-triazole derivatives against glioblastoma cells. *Bioorganic Chemistry*. doi:10.1016/j.bioorg.2018.10.003.
- Dar, B. A., Lone, A. M., Shah, W. A., & Qurishi, M. A. (2016). Synthesis and screening of ursolic acid-benzylidene derivatives as potential anti-cancer agents. *European Journal of Medicinal Chemistry*, 111, pp. 26–32. doi:10.1016/j.ejmech.2016.01.026.
- Davis, M. (2016). Glioblastoma: Overview of Disease and Treatment. *Clinical Journal of Oncology Nursing*, 20(5), S2–S8. doi:10.1188/16.cjon.s1.2-8.
- De Boer, A. G., & Gaillard, P. J. (2007). Drug Targeting to the Brain. *Annual Review of Pharmacology and Toxicology*, 47(1), pp. 323–355. doi:10.1146/annurev.pharmtox.47.120505.10523.

- De Vleeschouwer S, editor. (2017). Glioblastoma [Internet]. Brisbane (AU): Codon Publications;. Available from: <https://www.ncbi.nlm.nih.gov/books/NBK469998/> doi: 10.15586/codon.glioblastoma.2017.
- DeGoey, D.A., Chen, H.-J., Cox, P.B. and Wendt, M.D. (2017). Beyond the Rule of 5: Lessons Learned from AbbVie's Drugs and Compound Collection. *Journal of Medicinal Chemistry*, 61(7), pp.2636–2651. doi:10.1021/acs.jmedchem.7b00717.
- Della-Longa, S., & Arcovito, A. (2013). Structural and functional insights on folate receptor α (FR α) by homology modeling, ligand docking and molecular dynamics. *Journal of Molecular Graphics and Modelling*, 44, pp. 197–207. doi:10.1016/j.jmgm.2013.05.012.
- Della-Longa, S., & Arcovito, A. (2013). Structural and functional insights on folate receptor α (FR α) by homology modeling, ligand docking and molecular dynamics. *Journal of Molecular Graphics and Modelling*, 44, pp. 197–207. doi:10.1016/j.jmgm.2013.05.012.
- Desmoulin, S. K., Hou, Z., Gangjee, A., & Matherly, L. H. (2012). The human proton-coupled folate transporter. *Cancer Biology & Therapy*, 13(14), pp. 1355–1373. doi:10.4161/cbt.22020.
- Devita VT, Serpick AA, Carbone PP (1970) Combination chemotherapy in the treatment of advanced Hodgkin's disease. *Ann Intern Med* **73**: pp. 881–895.
- DeVita, V. T., & Chu, E. (2008). A History of Cancer Chemotherapy. *Cancer Research*, 68(21), pp. 8643–8653. doi:10.1158/0008-5472.can-07-6611.
- Doak, B.C. and Kihlberg, J. (2016). Drug discovery beyond the rule of 5 - Opportunities and challenges. *Expert Opinion on Drug Discovery*, 12(2), pp.115–119. doi:10.1080/17460441.2017.1264385.

- Dohgu, S., Takata, F., Yamauchi, A., Nakagawa, S., Egawa, T., Naito, M., Kataoka, Y. (2005). Brain pericytes contribute to the induction and up-regulation of blood–brain barrier functions through transforming growth factor- β production. *Brain Research*, 1038(2), pp. 208–215. doi:10.1016/j.brainres.2005.01.027.
- Dong, X., Noorbakhsh, A., Hirshman, B. R., Zhou, T., Tang, J. A., Chang, D. C., Chen, C. C. (2015). Survival trends of grade I, II, and III astrocytoma patients and associated clinical practice patterns between 1999 and 2010: A SEER-based analysis. *Neuro-Oncology Practice*, npv016. doi:10.1093/nop/npv016.
- Durán-Iturbide, N.A., Díaz-Eufracio, B.I. and Medina-Franco, J.L. (2020). *In Silico* ADME/Tox Profiling of Natural Products: A Focus on BIOFACQUIM. *ACS Omega*, 5(26), pp.16076–16084. doi: 10.1021/acsomega.0c01581
- Edelman, M. J., Harb, W. A., Pal, S. E., Boccia, R. V., Kraut, M. J., Bonomi, P., Garon, E. B. (2012). Multicenter Trial of EC145 in Advanced, Folate-Receptor Positive Adenocarcinoma of the Lung. *Journal of Thoracic Oncology*, 7(10), pp. 1618–1621. doi:10.1097/jto.0b013e318267d051.
- Ehrlich, P. (1900). Croonian Lecture: On Immunity with Special Reference to Cell Life. *Proceedings of the Royal Society of London (1854-1905)*, 66(-1), pp. 424–448. doi:10.1098/rspl.1899.0121.
- Elmore S. (2007). Apoptosis: a review of programmed cell death. *Toxicologic pathology*, 35(4), pp. 495–516. Doi: 10.1080/01926230701320337.
- Elnakat, H. and Ratnam, M. (2004). Distribution, functionality and gene regulation of folate receptor isoforms: implications in targeted therapy. *Advanced Drug Delivery Reviews*, 56(8), pp. 1067–1084. doi:10.1016/j.addr.2004.01.001.
- Elnakat, H. and Ratnam, M. (2006). Role of folate receptor genes in reproduction and related cancers. *Frontiers in Bioscience*, 11(1), 5pp. 06. doi:10.2741/1815.

- Fakhoury, M. (2015). Drug delivery approaches for the treatment of glioblastoma multiforme. *Artificial Cells, Nanomedicine, and Biotechnology*, 1–9. doi:10.3109/21691401.2015.1052467.
- Falzone, L., Salomone, S., & Libra, M. (2018). Evolution of Cancer Pharmacological Treatments at the Turn of the Third Millennium. *Frontiers in Pharmacology*, 9. doi:10.3389/fphar.2018.01300.
- Farhat, J., Pandey, I. and AlWahsh, M. (2021). Transcending toward advanced 3D-cell culture modalities: a review about an emerging paradigm in translational oncology. *Cells*, 10(7), p.1657. doi: 10.3390/cells10071657.
- Feng, D., Song, Y., Shi, W., Li, X., & Ma, H. (2013). Distinguishing Folate-Receptor-Positive Cells from Folate-Receptor-Negative Cells Using a Fluorescence Off-On Nanoprobe. *Analytical Chemistry*, 85(13), pp. 6530–6535. doi:10.1021/ac401377n.
- Feng, X., & Su, X. (2019). Anticancer effect of ursolic acid via mitochondria-dependent pathways (Review). *Oncology Letters*. doi:10.3892/ol.2019.10171.
- Ferlay, J., Colombet, M., Soerjomataram, I., Dyba, T., Randi, G., Bettio, M., Bray, F. (2018). Cancer incidence and mortality patterns in Europe: Estimates for 40 countries and 25 major cancers in 2018. *European Journal of Cancer*. doi:10.1016/j.ejca.2018.07.005.
- Ferlay, J., Colombet, M., Soerjomataram, I., Parkin, D.M., Piñeros, M., Znaor, A. and Bray, F. (2021). Cancer statistics for the year 2020: an overview. *International Journal of Cancer*. doi: 10.1002/ijc.33588.
- Fernández, M., Javaid, F., & Chudasama, V. (2018). Advances in targeting the folate receptor in the treatment/imaging of cancers. *Chemical Science*, 9(4), pp. 790–810. doi:10.1039/c7sc04004k.

- Ferri, A., Stagni, V. and Barilà, D. (2020). Targeting the DNA Damage Response to Overcome Cancer Drug Resistance in Glioblastoma. *International Journal of Molecular Sciences*, 21(14), p.4910. doi:10.3390/ijms21144910.
- Figliola, C., Marchal, E., Groves, B. R., & Thompson, A. (2019). A step-wise synthetic approach is necessary to access γ -conjugates of folate: folate-conjugated prodigiosenes. *RSC Advances*, 9(25), pp. 14078–14092. doi:10.1039/c9ra01435g.
- Fransolet, M., Noël, L., Henry, L., Labied, S., Blacher, S., Nisolle, M. and Munaut, C. (2019). Evaluation of Z-VAD-FMK as an anti-apoptotic drug to prevent granulosa cell apoptosis and follicular death after human ovarian tissue transplantation. *Journal of Assisted Reproduction and Genetics*. 36, pp. 349–359. doi:10.1007/s10815-018-1353-8.
- Fridlender, M., Kapulnik, Y., & Koltai, H. (2015). Plant derived substances with anti-cancer activity: from folklore to practice. *Frontiers in Plant Science*, 6. doi:10.3389/fpls.2015.00799.
- Friedman, H., Kerby, T. and Calvert, H. (2020). Temozolomide And Treatment Of Malignant Glioma. [Online]. *Clinical Cancer Research*. Available at: <<https://clincancerres.aacrjournals.org/content/6/7/2585#sec-17>> [Accessed 30 April 2020].
- Friedman, H.S., Kerby, T. and Calvert, H. (2000). Temozolomide and Treatment of Malignant Glioma. *Clinical Cancer Research*, [online] 6(7), pp.2585–2597. Available at: <https://aacrjournals.org/clincancerres/article/6/7/2585/288264/Temozolomide-and-Treatment-of-Malignant-Glioma1#sec-17> [Accessed 22 Apr. 2022].
- Frolova, T.S., Lipeeva, A.V., Baev, D.S., Baiborodin, S.I., Orishchenko, K.E., Kochetov, A.V. and Sinitsyna, O.I. (2019). Fluorescent labeling of ursolic acid with FITC for

- investigation of its cytotoxic activity using confocal microscopy. *Bioorganic Chemistry*, 87, pp.876–887. doi:10.1016/j.bioorg.2018.11.052.
- Fujii, S., Sobol, R.W. and Fuchs, R.P. (2022). Double-strand breaks: When DNA repair events accidentally meet. *DNA Repair*, 112, p.103303. doi:10.1016/j.dnarep.2022.103303.
- Furtado, J.C, Pirson, L., Edelberg, H., M. Miranda, L., Loira-Pastoriza, C., Preat, V., André, C. (2017). Pentacyclic Triterpene Bioavailability: An Overview of In Vitro and In Vivo Studies. *Molecules*, 22(3), pp. 400. doi:10.3390/molecules22030400.
- Gai, W.-T., Yu, D.-P., Wang, X.-S. and Wang, P.-T. (2016). Anti-cancer effect of ursolic acid activates apoptosis through ROCK/PTEN mediated mitochondrial translocation of cofilin-1 in prostate cancer. *Oncology Letters*, [online] 12(4), pp.2880–2885. doi:10.3892/ol.2016.5015.
- Galmarini, D., Galmarini, C. M., & Galmarini, F. C. (2012). Cancer chemotherapy: A critical analysis of its 60 years of history. *Critical Reviews in Oncology/Hematology*, 84(2), pp. 181–199. doi:10.1016/j.critrevonc.2012.03.002.
- Ganipineni, L. P., Danhier, F., & Pr eat, V. (2018). Drug delivery challenges and future of chemotherapeutic nanomedicine for glioblastoma treatment. *Journal of Controlled Release*, 281, pp. 42–57. doi:10.1016/j.jconrel.2018.05.008.
- Gao, Y., Li, Z., Xie, X., Wang, C., You, J., Mo, F., Jia, L. (2015). Dendrimeric anticancer prodrugs for targeted delivery of ursolic acid to folate receptor-expressing cancer cells: Synthesis and biological evaluation. *European Journal of Pharmaceutical Sciences*, 70, pp. 55–63. doi:10.1016/j.ejps.2015.01.007.
- Garin-Chesa, P., Campbell, I., Saigo, P. E., Lewis, J. L., Jr, Old, L. J., & Rettig, W. J. (1993). Trophoblast and ovarian cancer antigen LK26. Sensitivity and specificity in

- immunopathology and molecular identification as a folate-binding protein. *The American Journal of Pathology*, 142(2), pp. 557–567.
- Gazzano, E., Rolando, B., Chegaev, K., Salaroglio, I. C., Kopecka, J., Pedrini, I., Riganti, C. (2018). Folate-targeted liposomal nitrooxy-doxorubicin: An effective tool against P-glycoprotein-positive and folate receptor-positive tumors. *Journal of Controlled Release*, 270, pp. 37–52. doi:10.1016/j.jconrel.2017.11.042.
- Geersing, A., de Vries, R. H., Jansen, G., Rots, M. G., & Roelfes, G. (2019). Folic acid conjugates of a bleomycin mimic for selective targeting of folate receptor positive cancer cells. *Bioorganic & Medicinal Chemistry Letters*. doi:10.1016/j.bmcl.2019.05.047.
- George, B. P., & Abrahamse, H. (2019). Increased Oxidative Stress Induced by Rubus Bioactive Compounds Induce Apoptotic Cell Death in Human Breast Cancer Cells. *Oxidative Medicine and Cellular Longevity*, 2019, pp. 1–18. doi:10.1155/2019/6797921.
- Gerber DE. (2008). Targeted therapies: a new generation of cancer treatments. *Am Fam Physician*. 77:311–9.
- Gill, B. S., Kumar, S., & Navgeet. (2016). Triterpenes in cancer: significance and their influence. *Molecular Biology Reports*, 43(9), pp. 881–896. doi:10.1007/s11033-016-4032-9.
- Gilman A (1946) The biological actions and therapeutic applications of the B-chloroethyl amines and sulfides. *Science* **103**: pp. 409–436.
- Glioblastoma under Siege: An Overview of Current Therapeutic Strategies. (2018). *Brain Sciences*, 8(1), p.15. doi: 10.3390/brainsci8010015.

- Gonen, N., & Assaraf, Y. G. (2012). Antifolates in cancer therapy: Structure, activity and mechanisms of drug resistance. *Drug Resistance Updates*, 15(4), pp. 183–210. doi:10.1016/j.drug.2012.07.002.
- Gordaliza, M. (2007). Natural products as leads to anticancer drugs. *Clinical and Translational Oncology*, 9(12), pp. 767–776. doi:10.1007/s12094-007-0138-9.
- Gould, J. (2018). Breaking down the epidemiology of brain cancer. *Nature*, 561(7724), pp. S40–S41. doi:10.1038/d41586-018-06704-7.
- Grimm, S. A., & Chamberlain, M. C. (2016). Anaplastic astrocytoma. *CNS Oncology*, 5(3), pp. 145–157. doi:10.2217/cns-2016-0002.
- Gu, W., Jin, X.-Y., Li, D.-D., Wang, S.-F., Tao, X.-B. and Chen, H. (2017). Design, synthesis and in vitro anticancer activity of novel quinoline and oxadiazole derivatives of ursolic acid. *Bioorganic & Medicinal Chemistry Letters*, 27(17), pp.4128–4132. doi:10.1016/j.bmcl.2017.07.033.
- Guo, J., Han, T., Bao, L., Li, X., Ma, J. and Tang, L. (2019). Ursolic acid promotes the apoptosis of cervical cancer cells by regulating endoplasmic reticulum stress. *Journal of Obstetrics and Gynaecology Research*, 45(4), pp.877–881. doi:10.1111/jog.13919.
- Guo, J., Schlich, M., Cryan, J. F., & O’Driscoll, C. M. (2017). Targeted Drug Delivery via Folate Receptors for the Treatment of Brain Cancer: Can the Promise Deliver? *Journal of Pharmaceutical Sciences*, 106(12), pp. 3413–3420. doi:10.1016/j.xphs.2017.08.009.
- Gupta, A., Kaur, C. D., Saraf, S., & Saraf, S. (2017). Targeting of herbal bioactives through folate receptors: a novel concept to enhance intracellular drug delivery in cancer therapy. *Journal of Receptors and Signal Transduction*, 37(3), pp. 314–323. doi:10.3109/10799893.2016.1147581.

- Gupta, Y., Kohli D.V. and Jain, S.K. (2008). Vitamin B12-mediated transport: a potential tool for tumor targeting of antineoplastic drugs and imaging agents. *Crit. Rev. The. Drug Carrier Syst.* 25, pp. 347-379. doi:10.1615/critrevtherdrugcarriersyst.v25.i4.20.
- Gutschner, T., & Diederichs, S. (2012). The hallmarks of cancer: a long non-coding RNA point of view. *RNA biology*, 9(6), 703–719. doi: 10.4161/rna.20481.
- Haas, B., Klinger, V., Keksel, C., Bonigut, V., Kiefer, D., Caspers, J., Walther, J., Wos-Maganga, M., Weickhardt, S., Röhn, G., Timmer, M., Frötschl, R. and Eckstein, N. (2018). Inhibition of the PI3K but not the MEK/ERK pathway sensitizes human glioma cells to alkylating drugs. *Cancer Cell International*. BioMed Central Ltd., 18(1). doi: 10.1186/s12935-018-0565-4.
- Ham, S. W., Jeon, H.-Y., Jin, X., Kim, E.-J., Kim, J.-K., Shin, Y. J., Kim, H. (2018). TP53 gain-of-function mutation promotes inflammation in glioblastoma. *Cell Death & Differentiation*. doi:10.1038/s41418-018-0126-3.
- Hanahan, D. (2022). Hallmarks of Cancer: New Dimensions. *Cancer Discovery*, 12(1), pp.31–46. doi: 10.1158/2159-8290.CD-21-1059.
- Hanahan, D., & Folkman, J. (1996). Patterns and Emerging Mechanisms of the Angiogenic Switch during Tumorigenesis. *Cell*, 86(3), pp. 353–364. doi:10.1016/s0092-8674(00)80108-7.
- Hanahan, D., & Weinberg, R. A. (2000). The Hallmarks of Cancer. *Cell*, 100(1), pp. 57–70. doi:10.1016/s0092-8674(00)81683-9.
- Hanahan, D., & Weinberg, R. A. (2011). Hallmarks of Cancer: The Next Generation. *Cell*, 144(5), pp. 646–674. doi:10.1016/j.cell.2011.02.013.
- Hanif, F., Muzaffar, K., Perveen, K., Malhi, S.M., Simjee, Sh.U. (2017). GBM: A Review of its Epidemiology and Pathogenesis through Clinical Presentation and Treatment.

- Asian Pacific Journal of Cancer Prevention*, 18(1), pp. 3-9. doi: 10.22034/APJCP.2017.18.1.3.
- Hart, L. R., Harries, J. L., Greenland, B. W., Colquhoun, H. M., & Hayes, W. (2015). Molecular design of a discrete chain-folding polyimide for controlled inkjet deposition of supramolecular polymers. *Polymer Chemistry*, 6(41), 7342–7352. doi:10.1039/c5py00622h.
- Hartmann, L. C., Keeney, G. L., Lingle, W. L., Christianson, T. J. H., Varghese, B., Hillman, D., Low, P. S. (2007). Folate receptor overexpression is associated with poor outcome in breast cancer. *International Journal of Cancer*, 121(5), pp. 938–942. doi:10.1002/ijc.22811.
- He, Z., Liu, K., Manaloto, E., Casey, A., Cribaro, G.P., Byrne, H.J., Tian, F., Barcia, C., Conway, G.E., Cullen, P.J., and Curtin, J.F. (2018). Cold Atmospheric Plasma Induces ATP-Dependent Endocytosis of Nanoparticles and Synergistic U373MG Cancer Cell Death. *Scientific Reports*, 8, 5298. doi:10.1038/s41598-018-23262-0.
- Hegi, M. E., Liu, L., Herman, J. G., Stupp, R., Wick, W., Weller, M., Mehta, M. P. and Gilbert, M. R. (2008). Correlation of O6-Methylguanine Methyltransferase (MGMT) Promoter Methylation With Clinical Outcomes in Glioblastoma and Clinical Strategies to Modulate MGMT Activity, *Journal of Clinical Oncology*, 26(25), pp. 4189–4199. doi: 10.1200/JCO.2007.11.5964.
- Hervé, F., Ghinea, N., & Scherrmann, J.-M. (2008). CNS Delivery Via Adsorptive Transcytosis. *The AAPS Journal*, 10(3), pp. 455–472. doi:10.1208/s12248-008-9055-2.
- Hilgenbrink, A. R., & Low, P. S. (2005). Folate Receptor-Mediated Drug Targeting: From Therapeutics to Diagnostics. *Journal of Pharmaceutical Sciences*, 94(10), pp. 2135–2146. doi:10.1002/jps.20457.

- Hill, R. A., & Connolly, J. D. (2020). Triterpenoids. *Natural Product Reports*.doi:10.1039/c9np00067d.
- Hirsh, S., Huber, L., Zhang, P., Stein, R. and Joyal, S. (2014). A single ascending dose, initial clinical pharmacokinetic and safety study of ursolic acid in healthy adult volunteers (1044.6). *The FASEB Journal*, 28(S1). doi:10.1096/fasebj.28.1_supplement.1044.6.
- Holm, J., Hansen, S. I., Høier-Madsen, M., & Bostad, L. (1991). High-affinity folate binding in human choroid plexus. Characterization of radioligand binding, immunoreactivity, molecular heterogeneity and hydrophobic domain of the binding protein. *Biochemical Journal*, 280(1), pp. 267–271. doi:10.1042/bj2800267.
- Hottinger, A. F., Stupp, R., & Homicsko, K. (2014). Standards of care and novel approaches in the management of glioblastoma multiforme. *Chinese journal of cancer*, 33(1), pp. 32–39. <https://doi.org/10.5732/cjc.013.10207>.
- Hua, S.-X., Huang, R.-Z., Ye, M.-Y., Pan, Y.-M., Yao, G.-Y., Zhang, Y., & Wang, H.-S. (2015). Design, synthesis and in vitro evaluation of novel ursolic acid derivatives as potential anticancer agents. *European Journal of Medicinal Chemistry*, 95, pp. 435–452. doi:10.1016/j.ejmech.2015.03.051.
- Huang, B., Li, X., Li, Y., Zhang, J., Zong, Z. and Zhang, H. (2021). Current Immunotherapies for Glioblastoma Multiforme. *Frontiers in Immunology*, 11. doi: 10.3389/fimmu.2020.603911
- Huang, Q., Chen, H., Ren, Y., Wang, Z., Zeng, P., Li, X., Zheng, X. (2016). Anti-hepatocellular carcinoma activity and mechanism of chemopreventive compounds: ursolic acid derivatives. *Pharmaceutical Biology*, 54(12), pp. 3189–3196. doi:10.1080/13880209.2016.1214742.
- Hwang, S. Y., Yoo, B. C., Jung, J. won, Oh, E. S., Hwang, J. S., Shin, J. A., Kim, S. Y.,

- Cha, S. H. and Han, I. O. (2009). Induction of glioma apoptosis by microglia-secreted molecules: The role of nitric oxide and cathepsin B. *Biochimica et Biophysica Acta - Molecular Cell Research*, 1793(11), pp. 1656–1668. doi: 10.1016/j.bbamcr.2009.08.011
- Ifergan, I., & Assaraf, Y. G. (2008). Chapter 4 Molecular Mechanisms of Adaptation to Folate Deficiency. *Vitamins & Hormones*, pp. 99–143. doi:10.1016/s0083-6729(08)00404-4.
- Iqbal, J., Abbasi, B.A., Ahmad, R., Mahmood, T., Kanwal, S., Ali, B., Khalil, A.T., Shah, S.A., Alam, M.M. and Badshah, H. (2018). Ursolic acid a promising candidate in the therapeutics of breast cancer: Current status and future implications. *Biomedicine & Pharmacotherapy = Biomedecine & Pharmacotherapie*, [online] 108, pp.752–756. doi:10.1016/j.biopha.2018.09.096.
- Irish Cancer Society (2022). *Cancer statistics*. [online] Irish Cancer Society. Available at: <https://www.cancer.ie/cancer-information-and-support/cancer-information/about-cancer/cancer-statistics> [Accessed 19 April 2022].
- Irish Cancer Society. (2020). Cancer Statistics. [Online] Available at: <<https://www.cancer.ie/cancer-information-and-support/cancer-information/about-cancer/cancer-statistics>> [Accessed 30 March 2020].
- Jager, N. A., Teteloshvili, N., Zeebregts, C. J., Westra, J., & Bijl, M. (2012). Macrophage folate receptor- β (FR- β) expression in auto-immune inflammatory rheumatic diseases: A forthcoming marker for cardiovascular risk? *Autoimmunity Reviews*, 11(9), pp. 621–626. doi:10.1016/j.autrev.2011.11.002.
- Jang, S.-M., Yee, S.-T., Choi, J., Choi, M.-S., Do, G.-M., Jeon, S.-M., Yeo, J., Kim, M.-J., Seo, K.-I. and Lee, M.-K. (2009). Ursolic acid enhances the cellular immune system and pancreatic β -cell function in streptozotocin-induced diabetic mice fed a high-fat

- diet. *International Immunopharmacology*, 9(1), pp.113–119.
doi:10.1016/j.intimp.2008.10.013.
- Jena, L., McErlean, E., & McCarthy, H. (2019). Delivery across the blood-brain barrier: nanomedicine for glioblastoma multiforme. *Drug Delivery and Translational Research*. doi:10.1007/s13346-019-00679-2.
- Jensen, C. and Teng, Y., 2020. Is it time to start transitioning from 2D to 3D cell culture?. *Frontiers in molecular biosciences*, 7, p.33. doi: 10.3389/fmolb.2020.00033.
- Ji, D., Xu, M., Udenigwe, C.C. and Agyei, D. (2020). Physicochemical characterisation, molecular docking, and drug-likeness evaluation of hypotensive peptides encrypted in flaxseed proteome. *Current Research in Food Science*, 3, pp.41–50. doi:10.1016/j.crfs.2020.03.001
- Jiang, K., Chi, T., Li, T., Zheng, G., Fan, L., Liu, Y., Shao, J. (2017). A smart pH-responsive nano-carrier as a drug delivery system for the targeted delivery of ursolic acid: suppresses cancer growth and metastasis by modulating P53/MMP-9/PTEN/CD44 mediated multiple signaling pathways. *Nanoscale*, 9(27), pp. 9428–9439. doi:10.1039/c7nr01677h.
- Jiang, W., Huang, R.-Z., Zhang, J., Guo, T., Zhang, M.-T., Huang, X.-C., Zhang, B., Liao, Z.-X., Sun, J. and Wang, H.-S. (2018). Discovery of antitumor ursolic acid long-chain diamine derivatives as potent inhibitors of NF- κ B. *Bioorganic Chemistry*, 79, pp.265–276. doi:10.1016/j.bioorg.2018.05.005.
- Jin, H., Pi, J., Yang, F., Jiang, J., Wang, X., Bai, H., Chen, Z. W. (2016). Folate-Chitosan Nanoparticles Loaded with Ursolic Acid Confer Anti-Breast Cancer Activities in vitro and in vivo. *Scientific Reports*, 6(1).doi:10.1038/srep30782.
- Jin, H., Pi, J., Yang, F., Jiang, J., Wang, X., Bai, H., Shao, M., Huang, L., Zhu, H., Yang, P., Li, L., Li, T., Cai, J. and Chen, Z.W. (2016). Folate-Chitosan Nanoparticles Loaded

- with Ursolic Acid Confer Anti-Breast Cancer Activities in vitro and in vivo. *Scientific Reports*, 6(1). doi:10.1038/srep30782.
- Jin, H., Pi, J., Yang, F., Wu, C., Cheng, X., Bai, H., Chen, Z. W. (2016). Ursolic acid-loaded chitosan nanoparticles induce potent anti-angiogenesis in tumor. *Applied Microbiology and Biotechnology*, 100(15), pp. 6643–6652. doi:10.1007/s00253-016-7360-8.
- Johnson IS, Armstrong JG, Gorman M, Burnett JPJ (1963) The Vinca Alkaloids: A New Class of Oncolytic Agents. *Cancer Res* **23**: pp. 1390–1427.
- Johnson, K. J., Schwartzbaum, J., Kruchko, C., Scheurer, M. E., Lau, C. C., Woehrer, A., Hainfellner, J. A. and Wiemels, J. (2017) ‘Brain tumor epidemiology in the era of precision medicine: The 2017 Brain Tumor Epidemiology Consortium meeting report’, *Clinical Neuropathology*, 36(11), pp. 255–263. doi: 10.5414/NP301066.
- Jonkman, J.E.N., Cathcart, J.A., Xu, F., Bartolini, M.E., Amon, J.E., Stevens, K.M. and Colarusso, P. (2014). An introduction to the wound healing assay using live-cell microscopy. *Cell Adhesion & Migration*, 8(5), pp.440–451. doi:10.4161/cam.36224.
- Kahnt, M., Fischer (née Heller), L., Al-Harrasi, A. and Csuk, R. (2018). Ethylenediamine Derived Carboxamides of Betulinic and Ursolic Acid as Potential Cytotoxic Agents. *Molecules*, 23(10), p.2558. doi:10.3390/molecules23102558.
- Kalli, K. R., Oberg, A. L., Keeney, G. L., Christianson, T. J. H., Low, P. S., Knutson, K. L., & Hartmann, L. C. (2008). Folate receptor alpha as a tumor target in epithelial ovarian cancer. *Gynecologic Oncology*, 108(3), pp. 619–626. doi:10.1016/j.ygyno.2007.11.020.
- Kamen, B. A., & Capdevila, A. (1986). Receptor-mediated folate accumulation is regulated by the cellular folate content. *Proceedings of the National Academy of Sciences*, 83(16), pp. 5983–5987. doi:10.1073/pnas.83.16.5983.

- Karim, R., Palazzo, C., Evrard, B., & Piel, G. (2016). Nanocarriers for the treatment of glioblastoma multiforme: Current state-of-the-art. *Journal of Controlled Release*, 227, pp. 23–37. doi:10.1016/j.jconrel.2016.02.026.
- Kashyap, D., Tuli, H. S., & Sharma, A. K. (2016). Ursolic acid (UA): A metabolite with promising therapeutic potential. *Life Sciences*, 146, pp. 201–213. doi:10.1016/j.lfs.2016.01.017.
- Kawahara, B., Faull, K.F., Janzen, C. and Mascharak, P.K. (2021). Carbon Monoxide Inhibits Cytochrome P450 Enzymes CYP3A4/2C8 in Human Breast Cancer Cells, Increasing Sensitivity to Paclitaxel. *Journal of Medicinal Chemistry*, 64(12), pp.8437–8446. doi:10.1021/acs.jmedchem.1c00404
- Kennedy, M. D., Jallad K.N., Lu J., Low P.S., Ben-Amotz D. (2003). Evaluation of folate conjugate uptake and transport by the choroid plexus of mice. *Pharmaceutical Research*, 20(5), pp. 714–719. doi:10.1023/a:1023421232689.
- Kesari, S. (2011). Understanding Glioblastoma Tumor Biology: The Potential to Improve Current Diagnosis and Treatments. *Seminars in Oncology*, 38, S2–S10. doi:10.1053/j.seminoncol.2011.09.005.
- Khwaza, V., Oyediji, O.O. and Aderibigbe, B.A. (2020). Ursolic Acid-Based Derivatives as Potential Anti-Cancer Agents: An Update. *International Journal of Molecular Sciences*, 21(16), p.5920. doi:10.3390/ijms21165920.
- Kim, J.-H., Kim, Y.H., Song, G.-Y., Kim, D.-E., Jeong, Y.-J., Liu, K.-H., Chung, Y.-H. and Oh, S. (2014). Ursolic acid and its natural derivative corosolic acid suppress the proliferation of APC-mutated colon cancer cells through promotion of β -catenin degradation. *Food and Chemical Toxicology*, 67, pp.87–95. doi:10.1016/j.fct.2014.02.019.

- Kim, M.-H., Kim, J.N., Han, S.N. and Kim, H.-K. (2015). Ursolic acid isolated from guava leaves inhibits inflammatory mediators and reactive oxygen species in LPS-stimulated macrophages. *Immunopharmacology and Immunotoxicology*, 37(3), pp.228–235. doi:10.3109/08923973.2015.1021355.
- Kim, S., Ryu, H., Lee, J., Harikishore, A., Jung, H., Kim, Y.S., Lyu, H., Oh, E., Baek, N., Choi, K., Yoon, H.S., and Kim, K. (2015). Ursolic acid exerts anti-cancer activity by suppressing vaccinia-related kinase 1-mediated damage repair in lung cancer cells. *Scientific Reports*, 5, 14570. doi:10.1038/srep14570.
- Kim, S.H., Kim, J.K., Lim, S.J., Park, J.S., Lee, M.K., Kim, C.K. (2008). Folate-tethered emulsion for the target delivery of retinoids to cancer cells. *European Journal of Pharmaceutics and Biopharmaceutics*, 68(3), pp. 618–625. doi:10.1016/j.ejpb.2007.08.010.
- Kiskova, Kubatka, Büsselberg, & Kassayova. (2020). The Plant-Derived Compound Resveratrol in Brain Cancer: A Review. *Biomolecules*, 10(1), pp. 161. doi:10.3390/biom10010161.
- Kohsaka, S., & Tanaka, S. (2013). Chemotherapeutic Agent for Glioma. Clinical Management and Evolving Novel Therapeutic Strategies for Patients with Brain Tumors. doi:10.5772/54353.
- Kondo, M., MacKinnon, S.L., Craft, C.C., Matchett, M.D., Hurta, R.A.R. and Neto, C.C. (2011). Ursolic acid and its esters: occurrence in cranberries and other *Vaccinium* fruit and effects on matrix metalloproteinase activity in DU145 prostate tumor cells. *Journal of the Science of Food and Agriculture*, 91(5), pp.789–796. doi:10.1002/jsfa.4330.

- Kue, C. S., Kamkaew, A., Burgess, K., Kiew, L. V., Chung, L. Y., & Lee, H. B. (2016). Small Molecules for Active Targeting in Cancer. *Medicinal Research Reviews*, 36(3), pp. 494–575. doi:10.1002/med.21387.
- Kumar, P., Huo, P., & Liu, B. (2019). Formulation Strategies for Folate-Targeted Liposomes and Their Biomedical Applications. *Pharmaceutics*, 11(8), pp. 381. doi:10.3390/pharmaceutics11080381.
- Labib, R. M., Ebada, S. S., Youssef, F. S., Ashour, M. L., & Ross, S. A. (2016). Ursolic Acid, a Natural Pentacyclic Triterpene from *Ochrosia elliptica* and Its Role in The Management of Certain Neglected Tropical Diseases. *Pharmacognosy magazine*, 12(48), pp. 319–325. doi: 10.4103/0973-1296.192207.
- Lakomy, R., Kazda, T., Selingerova, I., Poprach, A., Pospisil, P., Belanova, R., Fadrus, P., Vybihal, V., Smrcka, M., Jancalek, R., Hynkova, L., Muckova, K., Hendrych, M., Sana, J., Slaby, O. and Slampa, P. (2020). Real-World Evidence in Glioblastoma: Stupp’s Regimen After a Decade. *Frontiers in Oncology*, 10, p.840. doi: 10.3389/fonc.2020.00840.
- Lapointe, S., Perry, A. and Butowski, N.A. (2018). Primary brain tumours in adults. *The Lancet*, 392(10145), pp.432-446. doi: 10.1016/S0140-6736(18)30990-5.
- Lara J Carroll, Brijesh Tiwari, James F Curtin, Janith Wanigasekara 2021. U-251MG Spheroid generation using low attachment plate method protocol. protocols.io doi: 10.17504/protocols.io.bszmnf46.
- Leamon, C. P. and Reddy, J.A. (2004). Folate-targeted chemotherapy. *Advanced Drug Delivery Reviews*, 56(8), pp. 1127–1141. doi:10.1016/j.addr.2004.01.008.
- Leamon, C. P., & Jackman, A. L. (2008). Chapter 7 Exploitation of the Folate Receptor in the Management of Cancer and Inflammatory Disease. *Vitamins & Hormones*, pp. 203–233. doi:10.1016/s0083-6729(08)00407-x.

- Leamon, C. P., & Low, P. S. (1991). Delivery of macromolecules into living cells: a method that exploits folate receptor endocytosis. *Proceedings of the National Academy of Sciences*, 88(13), pp. 5572–5576. doi:10.1073/pnas.88.13.5572 .
- Leamon, C. P., & Low, P. S. (1993). Membrane folate-binding proteins are responsible for folate-protein conjugate endocytosis into cultured cells. *Biochemical Journal*, 291(3), pp. 855–860. doi:10.1042/bj2910855.
- Leamon, C. P., Deprince, R. B., & Hendren, R. W. (1999). Folate-mediated Drug Delivery: Effect of Alternative Conjugation Chemistry. *Journal of Drug Targeting*, 7(3), pp. 157–169. doi:10.3109/10611869909085499.
- Leamon, C. P., Parker, M. A., Vlahov, I. R., Xu, L.-C., Reddy, J. A., Vetzal, M., & Douglas, N. (2002). Synthesis and Biological Evaluation of EC20: A New Folate-Derived, ^{99m}Tc-Based Radiopharmaceutical. *Bioconjugate Chemistry*, 13(6), pp. 1200–1210. doi:10.1021/bc0200430.
- Ledermann, J. A., Canevari, S., & Thigpen, T. (2015). Targeting the folate receptor: diagnostic and therapeutic approaches to personalize cancer treatments. *Annals of Oncology*, 26(10), pp. 2034–2043. doi:10.1093/annonc/mdv250.
- Lee, S. Y. (2016). Temozolomide resistance in glioblastoma multiforme, *Genes & Diseases*. Elsevier, 3(3), pp. 198–210. doi: 10.1016/J.GENDIS.2016.04.007.
- Lei, P., Zhang, W., & Men, X. (2014). Review on anti-tumor effect of triterpene acid compounds. *Journal of Cancer Research and Therapeutics*, 10(5), pp. 14. doi:10.4103/0973-1482.139746.
- Lernoux, M., Schnekenburger, M., Dicato, M., & Diederich, M. (2018). Anti-cancer effects of naturally derived compounds targeting histone deacetylase 6-related pathways. *Pharmacological Research*, 129, pp. 337–356. doi:10.1016/j.phrs.2017.11.004.

- Li, H., Jiang, H., Zhao, M., Fu, Y., & Sun, X. (2015). Intracellular redox potential-responsive micelles based on polyethylenimine-cystamine-poly(ϵ -caprolactone) block copolymer for enhanced miR-34a delivery. *Polymer Chemistry*, 6(11), pp. 1952–1960. doi:10.1039/c4py01623h.
- Li, J., Liang, X. and Yang, X. (2012). Ursolic acid inhibits growth and induces apoptosis in gemcitabine-resistant human pancreatic cancer via the JNK and PI3K/Akt/NF- κ B pathways. *Oncology Reports*, [online] 28(2), pp.501–510. doi:10.3892/or.2012.1827.
- Li, R., Li, Y., Hu, X., Lian, H., Wang, L. and Fu, H. (2016). Transcription factor TCF3 controls the cell proliferation and migration in glioblastoma multiforme cell lines. *Biochemistry and Cell Biology*, pp. 1–28. doi: 10.1139/bcb-2015-0162.
- Li, S., Zhang, Z. and Han, L., (2020). 3D spheroids propel tumor characterization. *Trends in Cancer*, 6(8), pp.622-624. doi: 10.1016/j.trecan.2020.05.002.
- Li, T., Chen, X., Liu, Y., Fan, L., Lin, L., Xu, Y., Shao, J. (2017). pH-Sensitive mesoporous silica nanoparticles anticancer prodrugs for sustained release of ursolic acid and the enhanced anti-cancer efficacy for hepatocellular carcinoma cancer. *European Journal of Pharmaceutical Sciences*, 96, pp. 456–463. doi:10.1016/j.ejps.2016.10.019.
- Li, W., Zhang, H., Nie, M., Wang, W., Liu, Z., Chen, C., Ma, K. (2017). A novel synthetic ursolic acid derivative inhibits growth and induces apoptosis in breast cancer cell lines. *Oncology Letters*. doi:10.3892/ol.2017.7578.
- Li, X., Yao, X., Zhu, Y., Zhang, H., Wang, H., Ma, Q., Yan, F., Yang, Y., Zhang, J., Shi, H., Ning, Z., Dai, J., Li, Z., Li, C., Su, F., Xue, Y., Meng, X., Dong, G. and Xiong, H. (2019). The Caspase Inhibitor Z-VAD-FMK Alleviates Endotoxic Shock via Inducing Macrophages Necroptosis and Promoting MDSCs-Mediated Inhibition of

- Macrophages Activation. *Frontiers in Immunology*, 10. doi:10.3389/fimmu.2019.01824.
- Li, Z.-H., Guan, Y.-L., Liu, Q., Wang, Y., Cui, R., & Wang, Y.-J. (2019). Astrocytoma progression scoring system based on the WHO 2016 criteria. *Scientific Reports*, 9(1). doi:10.1038/s41598-018-36471-4.
- Liang, J., Lv, X., Lu, C., Ye, X., Chen, X., Fu, J., Zhao, Y. (2020). Prognostic factors of patients with Gliomas – an analysis on 335 patients with Glioblastoma and other forms of Gliomas. *BMC Cancer*, 20(35). doi:10.1186/s12885-019-6511-6.
- Litak, J., Mazurek, M., Grochowski, C., Kamieniak, P. and Roliński, J. (2019). PD-L1/PD-1 Axis in Glioblastoma Multiforme. *International Journal of Molecular Sciences*, 20(21), p.5347. doi: 10.3390/ijms20215347.
- Liu, D., Yan-qui, M., Juan, Z., Li-gong, C. (2008). Synthesis and Anti-tumor Activity of Novel Amide Derivatives of Ursolic Acid. *Chemical Research in Chinese Universities*, 24(1), pp. 42–46. doi:10.1016/s1005-9040(08)60010-0.
- Liu, J., Kolar, C., Lawson, T. A., & Gmeiner, W. H. (2001). Targeted Drug Delivery to Chemoresistant Cells: Folic Acid Derivatization of FdUMP[10] Enhances Cytotoxicity toward 5-FU-Resistant Human Colorectal Tumor Cells. *The Journal of Organic Chemistry*, 66(17), pp. 5655–5663. doi:10.1021/jo005757n.
- Liu, K., Guo, L., Miao, L., Bao, W., Yang, J., Li, X., Xi, T. and Zhao, W. (2013). Ursolic acid inhibits epithelial–mesenchymal transition by suppressing the expression of astrocyte-elevated gene-1 in human nonsmall cell lung cancer A549 cells. *Anti-Cancer Drugs*, 24(5), pp.494–503. doi:10.1097/cad.0b013e328360093b.
- Liu, L., Zhang, J., Li, M., Zhang, X., Zhang, J., Li, Z., Wang, L., Wu, J. and Luo, C. (2014). Inhibition of HepG2 cell proliferation by ursolic acid and polysaccharides via

- the downregulation of cyclooxygenase-2. *Molecular Medicine Reports*, 9(6), pp.2505–2511. doi:10.3892/mmr.2014.2059.
- Liu, M.-C., Yang, S.-J., Jin, L.-H., Hu, D.-Y., Xue, W., Song, B.-A., & Yang, S. (2012). Synthesis and cytotoxicity of novel ursolic acid derivatives containing an acyl piperazine moiety. *European Journal of Medicinal Chemistry*, 58, pp. 128–135. doi:10.1016/j.ejmech.2012.08.048.
- Liu, T., Ma, H., Shi, W., Duan, J., Wang, Y., Zhang, C., Li, C., Lin, J., Li, S., Lv, J. and Lin, L. (2017). Inhibition of STAT3 signaling pathway by ursolic acid suppresses growth of hepatocellular carcinoma. *International Journal of Oncology*, 51(2), pp.555–562. doi:10.3892/ijo.2017.4035.
- Liu, X., Li, B., Zhang, Z., Wei, Y., Xu, Z., Qin, S., & Yang, C. (2018). Synthesis and Discovery Novel Anti-Cancer Stem Cells Compounds Derived from the Natural Triterpenoic Acids. *Journal of Medicinal Chemistry*. 61, pp. 10814-10833. doi:10.1021/acs.jmedchem.8b01445.
- Liu, Y., & Lu, W. (2012). Recent advances in brain tumor-targeted nano-drug delivery systems. *Expert Opinion on Drug Delivery*, 9(6), pp. 671–686. doi:10.1517/17425247.2012.682726.
- Lou, L., Hu, D., Chen, S., Wang, S., Xu, Y., Huang, Y., Shi, Y. and Zhang, H. (2019). Protective role of JNK inhibitor SP600125 in sepsis-induced acute lung injury. *International Journal of Clinical and Experimental Pathology*, 12(2), p.528.
- Louis, D. N., Ohgaki, H., Wiestler, O. D., Cavenee, W. K., Burger, P. C., Jouvett, A., Kleihues, P. (2007). The 2007 WHO Classification of Tumours of the Central Nervous System. *Acta Neuropathologica*, 114(2), pp. 97–109. doi:10.1007/s00401-007-0243-4.

- Louis, D. N., Perry, A., Reifenberger, G., von Deimling, A., Figarella-Branger, D., Cavenee, W. K., Ellison, D. W. (2016). The 2016 World Health Organization Classification of Tumors of the Central Nervous System: a summary. *Acta Neuropathologica*, 131(6), pp. 803–820. doi:10.1007/s00401-016-1545-1.
- Low, P. S., & Kularatne, S. A. (2009). Folate-targeted therapeutic and imaging agents for cancer. *Current Opinion in Chemical Biology*, 13(3), pp. 256–262. doi:10.1016/j.cbpa.2009.03.022.
- Low, P. S., & Kularatne, S. A. (2009). Folate-targeted therapeutic and imaging agents for cancer. *Current Opinion in Chemical Biology*, 13(3), pp. 256–262. doi:10.1016/j.cbpa.2009.03.022.
- Low, P. S., Henne, W. A., & Doorneweerd, D. D. (2008). Discovery and Development of Folic-Acid-Based Receptor Targeting for Imaging and Therapy of Cancer and Inflammatory Diseases. *Accounts of Chemical Research*, 41(1), pp. 120–129. doi:10.1021/ar7000815.
- Lu, C.-C., Huang, B.-R., Liao, P.-J., & Yen, G.-C. (2014). Ursolic acid triggers nonprogrammed death (necrosis) in human glioblastoma multiforme DBTRG-05MG cells through MPT pore opening and ATP decline. *Molecular Nutrition & Food Research*, 58(11), pp. 2146–2156. doi:10.1002/mnfr.201400051.
- Luo, H., Vong, C. T., Chen, H., Gao, Y., Lyu, P., Qiu, L., Zhao, M., Liu, Q., Cheng, Z., Zou, J., Yao, P., Gao, C., Wei, J., Ung, C., Wang, S., Zhong, Z., & Wang, Y. (2019). Naturally occurring anti-cancer compounds: shining from Chinese herbal medicine. *Chinese medicine*, 14, pp. 48. <https://doi.org/10.1186/s13020-019-0270-9>.
- Luo, J., Hu, Y.-L. and Wang, H. (2017). Ursolic acid inhibits breast cancer growth by inhibiting proliferation, inducing autophagy and apoptosis, and suppressing inflammatory responses via the PI3K/AKT and NF- κ B signaling pathways in

- vitro. *Experimental and Therapeutic Medicine*, 14(4), pp.3623–3631. doi:10.3892/etm.2017.4965.
- Lutz, R. (2015). Targeting the folate receptor for the treatment of ovarian cancer. *Translational Cancer Research*, 4(1), pp. 118-126. doi:10.21037/3838.
- Lynn, R. C., Poussin, M., Kalota, A., Feng, Y., Low, P. S., Dimitrov, D. S., & Powell, D. J. (2015). Targeting of folate receptor on acute myeloid leukemia blasts with chimeric antigen receptor-expressing T cells. *Blood*, 125(22), pp. 3466–3476. doi:10.1182/blood-2014-11-612721.
- Ma, C.-M., Cai, S.-Q., Cui, J.-R., Wang, R.-Q., Tu, P.-F., Hattori, M., & Daneshtalab, M. (2005). The cytotoxic activity of ursolic acid derivatives. *European Journal of Medicinal Chemistry*, 40(6), pp. 582–589. doi:10.1016/j.ejmech.2005.01.001.
- Madhusudhan, A., Reddy, G. B., Venkatesham, M., Veerabhadram, G., Kumar, D. A., Natarajan, S., Yang, M. Y., Hu, A., & Singh, S. S. (2014). Efficient pH dependent drug delivery to target cancer cells by gold nanoparticles capped with carboxymethyl chitosan. *International journal of molecular sciences*, 15(5), 8216–8234. doi:10.3390/ijms15058216
- Mandel, J., & Kesari, S. (2016). Targeting Aberrant Signaling Pathways. *Malignant Brain Tumors*, pp. 133–150. doi:10.1007/978-3-319-49864-5_9.
- Mansoori, G. A., Brandenburg, K. S., & Shakeri-Zadeh, A. (2010). A Comparative Study of Two Folate-Conjugated Gold Nanoparticles for Cancer Nanotechnology Applications. *Cancers*, 2(4), pp. 1911–1928. doi:10.3390/cancers2041911.
- Mansouri A, Karamchandani J, Das S. Molecular Genetics of Secondary Glioblastoma. In: De Vleeschouwer S, editor. (2017). Glioblastoma [Internet]. Brisbane (AU): Codon Publications; Chapter 2. Available from:

<https://www.ncbi.nlm.nih.gov/books/NBK469981/> doi:

10.15586/codon.glioblastoma.2017.ch2.

- Marchetti, C., Giorgini, M., De Medici, C., Palaia, I., Iadarola, R., Vertechy, L., Tomao, F. (2014). Targeted drug delivery via folate receptors in recurrent ovarian cancer: a review. *OncoTargets and Therapy*, 1223.doi:10.2147/ott.s40947.
- Matherly, L. H., & Goldman, I. D. (2003). Membrane Transport of Folates. *Vitamins & Hormones*, pp. 403–456. doi:10.1016/s0083-6729(03)01012-4.
- Matsumoto, K., Mizoue, K., Kitamura, K., Tse, W. C., Huber, C. P. and Ishida, T. (1999). Structural basis of inhibition of cysteine proteases by E-64 and its derivatives. *Biopolymers - Peptide Science Section*. John Wiley & Sons Inc, 51(1), pp. 99–107. doi: 10.1002/(SICI)1097-0282(1999)51:1<99::AID-BIP11>3.0.CO;2-R.
- McCarron, P.M., Crowley, A., O’Shea, D., McCann, M., Hunt, M., Devereux, M. (2018). Targeting the Folate Receptor: Improving Efficacy in Inorganic Medicinal Chemistry. *Current Medicinal Chemistry*, 25(23), pp. 2675-2708. doi:10.2174/0929867325666180209143715.
- Mendes, V. I. S., Bartholomeusz, G. A., Ayres, M., Gandhi, V., & Salvador, J. A. R. (2016). Synthesis and cytotoxic activity of novel A-ring cleaved ursolic acid derivatives in human non-small cell lung cancer cells. *European Journal of Medicinal Chemistry*, 123, pp. 317–331.doi:10.1016/j.ejmech.2016.07.045.
- Meng, Y.-Q., Liu, D., Cai, L.-L., Chen, H., Cao, B., & Wang, Y.-Z. (2009). The synthesis of ursolic acid derivatives with cytotoxic activity and the investigation of their preliminary mechanism of action. *Bioorganic & Medicinal Chemistry*, 17(2), pp. 848–854. doi:10.1016/j.bmc.2008.11.036.
- Meng, Y., Lin, Z.-M., Ge, N., Zhang, D.-L., Huang, J., & Kong, F. (2015). Ursolic Acid Induces Apoptosis of Prostate Cancer Cells via the PI3K/Akt/mTOR Pathway. *The*

- American Journal of Chinese Medicine*, 43(07), pp. 1471–1486. doi:10.1142/s0192415x15500834.
- Miranda, A., Blanco-Prieto, M. J., Sousa, J., Pais, A., & Vitorino, C. (2017). Breaching barriers in glioblastoma. Part II: Targeted drug delivery and lipid nanoparticles. *International Journal of Pharmaceutics*, 531(1), pp. 389–410. doi:10.1016/j.ijpharm.2017.07.049.
- Montalbetti, C. A. G. N., and Falque, V. (2005). Amide bond formation and peptide coupling. *Tetrahedron*, 61(46), pp. 10827–10852. doi:10.1016/j.tet.2005.08.031.
- Montemurro, N. (2019). Glioblastoma Multiforme and Genetic Mutations: The Issue Is Not Over Yet. An Overview of the Current Literature. *Journal of Neurological Surgery Part A: Central European Neurosurgery*. doi:10.1055/s-0039-1688911.
- Morten, B.C., Scott, R.J. and Avery-Kiejda, K.A. (2016). Comparison of Three Different Methods for Determining Cell Proliferation in Breast Cancer Cell Lines. *Journal of Visualized Experiments : JoVE*, [online] (115). Available at: <https://www.ncbi.nlm.nih.gov/pmc/articles/PMC5091975/>. doi:10.3791/54350.
- Mukherjee, S., 2011. *The Emperor Of All Maladies*. London: Fourth estate.
- Muller, C. (2012). Folate Based Radiopharmaceuticals for Imaging and Therapy of Cancer and Inflammation. *Current Pharmaceutical Design*, 18(8), pp. 1058–1083. doi:10.2174/138161212799315777.
- Muller, C., & Schibli, R. (2011). Folic Acid Conjugates for Nuclear Imaging of Folate Receptor-Positive Cancer. *Journal of Nuclear Medicine*, 52(1), pp. 1–4. doi:10.2967/jnumed.110.076018.
- Muniraj, N., Siddharth, S., & Sharma, D. (2019). Bioactive Compounds: Multi-Targeting Silver Bullets for Preventing and Treating Breast Cancer. *Cancers*, 11(10), pp. 1563. doi:10.3390/cancers11101563.

- Mustafa, Y.F. (2021). Chemotherapeutic Applications of Folate Prodrugs: A Review. *NeuroQuantology*, 19(8), pp.99–112. doi:10.14704/nq.2021.19.8.nq21120.
- National Cancer Registry Ireland (2022). *Statistical reports | National Cancer Registry Ireland*. [online] Available at: <https://www.ncri.ie/publications/statistical-reports> [Accessed 19 April 2022].
- National Cancer Registry Ireland (NCRI). (2019). Annual Report of the National Cancer Registry Ireland 2019. [Online] Available at: https://www.ncri.ie/sites/ncri/files/pubs/NCRI_Annual%20Report2019_03102019.pdf [Accessed 30 March 2020].
- National Cancer Registry Ireland. (2016). Trends In Brain Cancer In Ireland: Our Latest Report Published | National Cancer Registry Ireland. [Online] Available at: <https://www.ncri.ie/news/article/trends-brain-cancer-ireland-our-latest-report-published> [Accessed 2 April 2020].
- Navin, R., & Mi Kim, S. (2016). Therapeutic Interventions Using Ursolic Acid for Cancer Treatment. *Medicinal Chemistry*, 06(05).doi:10.4172/2161-0444.1000367.
- Nguyen, H.N., Ullevig, S.L., Short, J.D., Wang, L., Ahn, Y.J. and Asmis, R. (2021). Ursolic Acid and Related Analogues: Triterpenoids with Broad Health Benefits. *Antioxidants*, 10(8), p.1161. doi:10.3390/antiox10081161.
- Nunez, M. I., Behrens, C., Woods, D. M., Lin, H., Suraokar, M., Kadara, H., Wistuba, MD, I. I. (2012). High Expression of Folate Receptor Alpha in Lung Cancer Correlates with Adenocarcinoma Histology and Mutation. *Journal of Thoracic Oncology*, 7(5), pp. 833–840.doi:10.1097/jto.0b013e31824de09c.
- Oaks, B. M., Dodd, K. W., Meinhold, C. L., Jiao, L., Church, T. R., & Stolzenberg-Solomon, R. Z. (2010). Folate intake, post-folic acid grain fortification, and pancreatic cancer risk in the Prostate, Lung, Colorectal, and Ovarian Cancer Screening Trial. *The*

- American Journal of Clinical Nutrition*, 91(2), pp. 449–455. doi:10.3945/ajcn.2009.28433.
- Ohgaki, H., & Kleihues, P. (2007). Genetic Pathways to Primary and Secondary Glioblastoma. *The American Journal of Pathology*, 170(5), pp. 1445–1453. doi:10.2353/ajpath.2007.070011.
- Ohgaki, H., & Kleihues, P. (2012). The Definition of Primary and Secondary Glioblastoma. *Clinical Cancer Research*, 19(4), pp. 764–772. doi:10.1158/1078-0432.ccr-12-3002.
- Ohka, F., Natsume, A., & Wakabayashi, T. (2012). Current Trends in Targeted Therapies for Glioblastoma Multiforme. *Neurology Research International*, 2012, pp. 1–13. doi:10.1155/2012/878425.
- Ojima, I. (2008). Guided molecular missiles for tumor-targeting chemotherapy; case studies using the second-generation taxoids as warheads. *Acc. Chem. Res.* 41, pp. 108–119.
- Ostrom, Q. T., Cioffi, G., Gittleman, H., Patil, N., Waite, K., Kruchko, C., & Barnholtz-Sloan, J. S. (2019). CBTRUS Statistical Report: Primary Brain and Other Central Nervous System Tumors Diagnosed in the United States in 2012–2016. *Neuro-Oncology*, 21(Supplement_5), v1–v100. doi:10.1093/neuonc/noz150.
- Ostrom, Q.T., Cioffi, G., Waite, K., Kruchko, C. and Barnholtz-Sloan, J.S. (2021). CBTRUS Statistical Report: Primary Brain and Other Central Nervous System Tumors Diagnosed in the United States in 2014–2018. *Neuro-Oncology*, 23(Supplement_3), pp.iii1–iii105. doi: 10.1093/neuonc/noab200.
- Ozdemir-Kaynak, E., Qutub, A. A., & Yesil-Celiktas, O. (2018). Advances in Glioblastoma Multiforme Treatment: New Models for Nanoparticle Therapy. *Frontiers in Physiology*, 9. doi:10.3389/fphys.2018.00170.

- Pardridge, W. M. (2007). Drug Targeting to the Brain. *Pharmaceutical Research*, 24(9), pp. 1733–1744. doi:10.1007/s11095-007-9324-2.
- Parker, N., Turk, M. J., Westrick, E., Lewis, J. D., Low, P. S., & Leamon, C. P. (2005). Folate receptor expression in carcinomas and normal tissues determined by a quantitative radioligand binding assay. *Analytical Biochemistry*, 338(2), pp. 284–293. doi:10.1016/j.ab.2004.12.026.
- Patel, A. P. (2018) ‘39 - High-Grade Gliomas’, in Ellenbogen, R. G. et al. (eds) *Principles of Neurological Surgery (Fourth Edition)*. Fourth Edition. Philadelphia: Content Repository Only!, pp. 580-585.e2. doi: 10.1016/B978-0-323-43140-8.00039-1.
- Patel, A. P., Fisher, J. L., Nichols, E., Abd-Allah, F., Abdela, J., Abdelalim, A., Alam, T. (2019). Global, regional, and national burden of brain and other CNS cancer, 1990–2016: a systematic analysis for the Global Burden of Disease Study 2016. *The Lancet Neurology*. doi:10.1016/s1474-4422(18)30468-x.
- Pathania, S. and Singh, P.K. (2020). Analyzing FDA-approved drugs for compliance of pharmacokinetic principles: should there be a critical screening parameter in drug designing protocols? *Expert Opinion on Drug Metabolism & Toxicology*, 17(4), pp.351–354. doi:10.1080/17425255.2021.1865309.
- Pearson, J. R. D., & Regad, T. (2017). Targeting cellular pathways in glioblastoma multiforme. *Signal Transduction and Targeted Therapy*, 2, 17040. doi:10.1038/sigtrans.2017.40.
- Pérez-Herrero, E., & Fernández-Medarde, A. (2015). Advanced targeted therapies in cancer: Drug nanocarriers, the future of chemotherapy. *European Journal of Pharmaceutics and Biopharmaceutics*, 93, pp. 52–79. doi:10.1016/j.ejpb.2015.03.018.

- Philips, A., Henshaw, D. L., Lamburn, G., & O'Carroll, M. J. (2018). Brain Tumours: Rise in Glioblastoma Multiforme Incidence in England 1995–2015 Suggests an Adverse Environmental or Lifestyle Factor. *Journal of Environmental and Public Health*, 2018, pp. 1–10. doi:10.1155/2018/7910754.
- Poe, M. (1977). Acidic dissociation-constants of folic-acid, dihydrofolic acid, and methotrexate. *Journal of Biological Chemistry*, 252(11), pp. 3724-3728.
- Poongavanam, V., Doak, B.C. and Kihlberg, J. (2018). Opportunities and guidelines for discovery of orally absorbed drugs in beyond rule of 5 space. *Current Opinion in Chemical Biology*, 44, pp.23–29. doi:10.1016/j.cbpa.2018.05.010.
- Prasad, S., Yadav, V.R., Kannappan, R. and Aggarwal, B.B. (2011). Ursolic Acid, a Pentacyclin Triterpene, Potentiates TRAIL-induced Apoptosis through p53-independent Up-regulation of Death Receptors. *Journal of Biological Chemistry*, 286(7), pp.5546–5557. doi:10.1074/jbc.m110.183699.
- Pu, Y. J., Vaid, R. K., Boini, S. K., Towsley, R. W., Doecke, C. W., & Mitchell, D. (2009). A Practical Method for Functionalized Peptide or Amide Bond Formation in Aqueous–Ethanol Media with EDC as Activator. *Organic Process Research & Development*, 13(2), pp. 310–314. doi:10.1021/op800240d.
- Qiang, Z., Ye, Z., Hauck, C., Murphy, P.A., McCoy, J.-A., Widrlechner, M.P., Reddy, M.B. and Hendrich, S. (2011). Permeability of rosmarinic acid in *Prunella vulgaris* and ursolic acid in *Salvia officinalis* extracts across Caco-2 cell monolayers. *Journal of Ethnopharmacology*, 137(3), pp.1107–1112. doi:10.1016/j.jep.2011.07.037.
- Qiu, A., Jansen, M., Sakaris, A., Min, S. H., Chattopadhyay, S., Tsai, E., Goldman, I. D. (2006). Identification of an Intestinal Folate Transporter and the Molecular Basis for Hereditary Folate Malabsorption. *Cell*, 127(5), pp. 917–928. doi:10.1016/j.cell.2006.09.041.

- Quici, S., Casoni, A., Foschi, F., Armelao, L., Bottaro, G., Seraglia, R., Rosato, A. (2015). Folic Acid-Conjugated Europium Complexes as Luminescent Probes for Selective Targeting of Cancer Cells. *Journal of Medicinal Chemistry*, 58(4), pp. 2003–2014. doi:10.1021/jm501945w.
- Ragnarsson, U. and Grehn, L. (2013) ‘Dual protection of amino functions involving Boc’, *RSC Adv.* The Royal Society of Chemistry, 3(41), pp. 18691–18697. doi:10.1039/C3RA42956C.
- Raschi, E., Vasina, V., Ursino, M. G., Boriani, G., Martoni, A., & De Ponti, F. (2010). Anticancer drugs and cardiotoxicity: Insights and perspectives in the era of targeted therapy. *Pharmacology & Therapeutics*, 125(2), pp. 196–218. doi:10.1016/j.pharmthera.2009.10.002.
- Raucher, D., Dragojevic, S. and Ryu, J. (2018). Macromolecular Drug Carriers for Targeted Glioblastoma Therapy: Preclinical Studies, Challenges, and Future Perspectives. *Frontiers in Oncology*, 8. doi: 10.3389/fonc.2018.00624.
- Reddy, J. A., & Low, P. S. (2000). Enhanced folate receptor mediated gene therapy using a novel pH-sensitive lipid formulation. *Journal of Controlled Release*, 64(1-3), pp. 27–37. doi:10.1016/s0168-3659(99)00135-2.
- Rodrigues, J., Heinrich, M.A., Teixeira, L.M. and Prakash, J. (2021). 3D In Vitro Model (R)evolution: Unveiling Tumor–Stroma Interactions. *Trends in Cancer*, 7(3), pp.249–264. doi: 10.1016/j.trecan.2020.10.009.
- Rouse, C., Gittleman, H., Ostrom, Q. T., Kruchko, C., & Barnholtz-Sloan, J. S. (2015). Years of potential life lost for brain and CNS tumors relative to other cancers in adults in the United States, 2010. *Neuro-Oncology*, 18(1), pp. 70–77. doi:10.1093/neuonc/nov249.

- S.D Konda, M Aref, M Brechbiel, E.C Wiener. (2000). Development of a tumor-targeting MR contrast agent using the high-affinity folate receptor. *Investigative Radiology*, 35(1), pp. 50-57. doi: 10.1097/00004424-200001000-00006.
- S.D. Weitman, R.H. Lark, L.R. Coney, D.W. Fort, V. Frasca, V.R. Zurawski Jr., B.A. Kamen. (1992). Distribution of the folate receptor GP38 in normal and malignant cell lines and tissues. *Cancer Res.*, 52(12), pp. 3396-3401.
- Sacko, O., Benouaich-Amiel, A., Brandicourt, P., Niaré, M., Charni, S., Cavandoli, C., Brauge, D., Catalaa, I., Brenner, A., Moyal, E.-J. and Roux, F.-E. (2021). The impact of surgery on the survival of patients with recurrent glioblastoma. *Asian Journal of Neurosurgery*, 16(1), p.1. doi: 10.4103/ajns.AJNS_180_20.
- Sahoo, B., Devi, K. S. P., Banerjee, R., Maiti, T. K., Pramanik, P., & Dhara, D. (2013). Thermal and pH Responsive Polymer-Tethered Multifunctional Magnetic Nanoparticles for Targeted Delivery of Anticancer Drug. *ACS Applied Materials & Interfaces*, 5(9), pp. 3884–3893. doi:10.1021/am400572b.
- Salazar, M. D., & Ratnam, M. (2007). The folate receptor: What does it promise in tissue-targeted therapeutics?. *Cancer and Metastasis Reviews*, 26(1), pp. 141–152. doi:10.1007/s10555-007-9048-0.
- Santos, F. M. F., Matos, A. I., Ventura, A. E., Gonçalves, J., Veiros, L. F., Florindo, H. F., & Gois, P. M. P. (2017). Modular Assembly of Reversible Multivalent Cancer-Cell-Targeting Drug Conjugates. *Angewandte Chemie International Edition*, 56(32), pp. 9346–9350. doi:10.1002/anie.201703492.
- Sarkaria, J.N., Hu, L.S., Parney, I.F., Pafundi, D.H., Brinkmann, D.H., Laack, N.N., Giannini, C., Burns, T.C., Kizilbash, S.H., Laramy, J.K. and Swanson, K.R. (2018). Is the blood–brain barrier really disrupted in all glioblastomas? A critical assessment of

- existing clinical data. *Neuro-oncology*, 20(2), pp.184-191. doi: 10.1093/neuonc/nox175.
- Sasmita, A. O., Wong, Y. P., & Ling, A. P. K. (2017). Biomarkers and therapeutic advances in glioblastoma multiforme. *Asia-Pacific Journal of Clinical Oncology*, 14(1), pp. 40–51. doi:10.1111/ajco.12756.
- Scaglione, F., & Panzavolta, G. (2014). Folate, folic acid and 5-methyltetrahydrofolate are not the same thing. *Xenobiotica*, 44(5), pp. 480–488. doi:10.3109/00498254.2013.845705.
- Scherer, H.J. (1940). Cerebral Astrocytomas and Their Derivatives. *Am J Cancer* **40**: pp. 159–198, doi:10.1158/ajc.1940.159.
- Schindelin, J., Arganda-Carreras, I., Frise, E., Kaynig, V., Longair, M., Pietzsch, T., Preibisch, S., Rueden, C., Saalfeld, S., Schmid, B., Tinevez, J.-Y., White, D.J., Hartenstein, V., Eliceiri, K., Tomancak, P. and Cardona, A. (2012). Fiji: an open-source platform for biological-image analysis. *Nature methods*, 9(7), pp.676–682. doi: 10.1038/nmeth.2019.
- Schmidt, B. M., Ribnicky, D. M., Lipsky, P. E., & Raskin, I. (2007). Revisiting the ancient concept of botanical therapeutics. *Nature Chemical Biology*, 3(7), pp. 360–366. doi:10.1038/nchembio0707-360.
- Scott, S. D. (1998). Rituximab: A New Therapeutic Monoclonal Antibody for Non-Hodgkin's Lymphoma. *Cancer Practice*, 6(3), pp. 195–197. doi:10.1046/j.1523-5394.1998.006003195.x.
- Sega, E. I., & Low, P. S. (2008). Tumor detection using folate receptor-targeted imaging agents. *Cancer and Metastasis Reviews*, 27(4), pp. 655–664. doi:10.1007/s10555-008-9155-6.

- Seifert, M., Garbe, M., Friedrich, B., Mittelbronn, M., & Klink, B. (2015). Comparative transcriptomics reveals similarities and differences between astrocytoma grades. *BMC Cancer*, 15(1). doi:10.1186/s12885-015-1939-9.
- Shanmugam, M. K., Dai, X., Kumar, A. P., Tan, B. K. H., Sethi, G., & Bishayee, A. (2013). Ursolic acid in cancer prevention and treatment: Molecular targets, pharmacokinetics and clinical studies. *Biochemical Pharmacology*, 85(11), pp. 1579–1587. doi:10.1016/j.bcp.2013.03.006.
- Shanmugam, M. K., Nguyen, A. H., Kumar, A. P., Tan, B. K. H., & Sethi, G. (2012). Targeted inhibition of tumor proliferation, survival, and metastasis by pentacyclic triterpenoids: Potential role in prevention and therapy of cancer. *Cancer Letters*, 320(2), pp. 158–170. doi:10.1016/j.canlet.2012.02.037.
- Shao, J.-W., Dai, Y.-C., Xue, J.-P., Wang, J.-C., Lin, F.-P., & Guo, Y.-H. (2011). In vitro and in vivo anticancer activity evaluation of ursolic acid derivatives. *European Journal of Medicinal Chemistry*, 46(7), pp. 2652–2661. doi:10.1016/j.ejmech.2011.03.050.
- Shao, J., Fang, Y., Zhao, R., Chen, F., Yang, M., Jiang, J., Jia, L. (2020). Evolution from small molecule to nano-drug delivery systems - An emerging approach for cancer therapy of ursolic acid. *Asian Journal of Pharmaceutical Sciences*. doi:10.1016/j.ajps.2020.03.001.
- Shen, J., Putt, K. S., Visscher, D. W., Murphy, L., Cohen, C., Singhal, S., Sandusky, G., Feng, Y., Dimitrov, D. S., & Low, P. S. (2015). Assessment of folate receptor- β expression in human neoplastic tissues. *Oncotarget*, 6(16), pp. 14700–14709. doi:10.18632/oncotarget.3739.
- Shen, Z., Li, B., Liu, Y., Zheng, G., Guo, Y., Zhao, R., Shao, J. (2018). A self-assembly nanodrug delivery system based on amphiphilic low generations of PAMAM dendrimers-ursolic acid conjugate modified by lactobionic acid for HCC targeting

- therapy. *Nanomedicine: Nanotechnology, Biology and Medicine*, 14(2), pp. 227–236. doi:10.1016/j.nano.2017.10.007.
- Shin, S.-A., Moon, S. Y., Kim, W.-Y., Paek, S.-M., Park, H. H., & Lee, C. S. (2018). Structure-Based Classification and Anti-Cancer Effects of Plant Metabolites. *International Journal of Molecular Sciences*, 19(9), pp. 2651. doi:10.3390/ijms19092651.
- Shin, S.W. and Park, J.-W. (2013). Ursolic acid sensitizes prostate cancer cells to TRAIL-mediated apoptosis. *Biochimica et Biophysica Acta (BBA) - Molecular Cell Research*, 1833(3), pp.723–730. doi:10.1016/j.bbamcr.2012.12.005.
- Shirazi, R. S., Ewert, K. K., Leal, C., Majzoub, R. N., Bouxsein, N. F., & Safinya, C. R. (2011). Synthesis and characterization of degradable multivalent cationic lipids with disulfide-bond spacers for gene delivery. *Biochimica et Biophysica Acta (BBA) - Biomembranes*, 1808(9), pp. 2156–2166. doi:10.1016/j.bbamem.2011.04.020.
- Siegel, R. L., Miller, K. D., & Jemal, A. (2020). Cancer statistics, 2020. *CA: A Cancer Journal for Clinicians*. doi:10.3322/caac.21590.
- Silantyeve, Falzone, Libra, Gurina, Kardashova, Nikolouzakis, Tsatsakis. (2019). Current and Future Trends on Diagnosis and Prognosis of Glioblastoma: From Molecular Biology to Proteomics. *Cells*, 8(8), pp. 863. doi:10.3390/cells8080863.
- Siu, M. K. Y., Kong, D. S. H., Chan, H. Y., Wong, E. S. Y., Ip, P. P. C., Jiang, L., Cheung, A. N. Y. (2012). Paradoxical Impact of Two Folate Receptors, FR α and RFC, in Ovarian Cancer: Effect on Cell Proliferation, Invasion and Clinical Outcome. *PLoS ONE*, 7(11), e47201. doi:10.1371/journal.pone.0047201.
- Son, H.-S., Kwon, H.Y., Sohn, E.J., Lee, J.-H., Woo, H.-J., Yun, M., Kim, S.-H. and Kim, Y.-C. (2013). Activation of AMP-activated Protein Kinase and Phosphorylation of Glycogen Synthase Kinase3 β Mediate Ursolic Acid Induced Apoptosis in HepG2

- Liver Cancer Cells. *Phytotherapy Research*, 27(11), pp.1714–1722. doi:10.1002/ptr.4925.
- Spiegelstein, O., Eudy, J. D., & Finnell, R. H. (2000). Identification of two putative novel folate receptor genes in humans and mouse. *Gene*, 258(1-2), pp. 117–125. doi:10.1016/s0378-1119(00)00418-2.
- Stallivieri, A., Colombeau, L., Jetpisbayeva, G., Moussaron, A., Myrzakhmetov, B., Arnoux, P., Frochet, C. (2017). Folic acid conjugates with photosensitizers for cancer targeting in photodynamic therapy: Synthesis and photophysical properties. *Bioorganic & Medicinal Chemistry*, 25(1), pp. 1–10. doi:10.1016/j.bmc.2016.10.004.
- Strebhardt, K., & Ullrich, A. (2008). Paul Ehrlich's magic bullet concept: 100 years of progress. *Nature Reviews Cancer*, 8(6), pp. 473–480. doi:10.1038/nrc2394.
- Stupp R, Wong ET, Kanner AA, Steinberg D, Engelhard H, Heidecke V, Gutin PH. (2012). NovoTTF-100A versus physician's choice chemotherapy in recurrent glioblastoma: A randomized phase III trial of a novel treatment modality. *European Journal of Cancer*, 48:2192–2202. doi: 10.1016/j.ecja.2012.04.011.
- Stupp, R., Mason, W.P., van den Bent, M.J., Weller, M., Fisher, B., Taphoorn, M.J.B., Belanger, K., Brandes, A.A., Marosi, C., Bogdahn, U., Curschmann, J., Janzer, R.C., Ludwin, S.K., Gorlia, T., Allgeier, A., Lacombe, D., Cairncross, J.G., Eisenhauer, E. and Mirimanoff, R.O. (2005). Radiotherapy plus Concomitant and Adjuvant Temozolomide for Glioblastoma. *New England Journal of Medicine*, 352(10), pp.987–996. doi: 10.1056/NEJMoa043330.
- Sudimack, J., & Lee, R. J. (2000). Targeted drug delivery via the folate receptor. *Advanced Drug Delivery Reviews*, 41(2), pp. 147–162. doi:10.1016/s0169-409x(99)00062-9.

- Sun, J. Y., Shen, J., Thibodeaux, J., Huang, G., Wang, Y., Gao, J., Sumer, B. D. (2014). In vivo optical imaging of folate receptor- β in head and neck squamous cell carcinoma. *The Laryngoscope*, 124(8), E312–E319. doi:10.1002/lary.24606.
- Sun, Q., He, M., Zhang, M., Zeng, S., Chen, L., Zhou, L. and Xu, H. (2020). Ursolic acid: A systematic review of its pharmacology, toxicity and rethink on its pharmacokinetics based on PK-PD model. *Fitoterapia*, [online] 147, p.104735. doi:10.1016/j.fitote.2020.104735.
- Sung, H., Ferlay, J., Siegel, R.L., Laversanne, M., Soerjomataram, I., Jemal, A. and Bray, F. (2021). Global Cancer Statistics 2020: GLOBOCAN Estimates of Incidence and Mortality Worldwide for 36 Cancers in 185 Countries. *CA: A Cancer Journal for Clinicians*, 71(3), pp.209–249. doi: 10.3322/caac.21660.
- Surveillance, Epidemiology, and End Results. (2017). Cancer Statistics Review, 1975–2014. [Online]. *National Cancer Institute*. Available at: <https://seer.cancer.gov/csr/1975_2014> [Accessed 30 March 2020].
- Talmadge, J. E., & Fidler, I. J. (2010). AACR centennial series: the biology of cancer metastasis: historical perspective. *Cancer research*, 70(14), pp. 5649–5669. Doi:10.1158/0008-5472.CAN-10-1040.
- Tamimi, A.F. and Juweid, M. (2017). Epidemiology and Outcome of Glioblastoma. In: De Vleeschouwer S, editor. Brisbane (AU): *Codon Publications*; Chapter 8. doi: 10.15586/codon.glioblastoma.2017.ch8.
- Tan, A.C., Ashley, D.M., López, G.Y., Malinzak, M., Friedman, H.S. and Khasraw, M. (2020). Management of glioblastoma: State of the art and future directions. *CA: A Cancer Journal for Clinicians*, 70(4), pp.299–312. doi:10.3322/caac.21613.

- Taylor, O. G., Brzozowski, J. S., & Skelding, K. A. (2019). Glioblastoma Multiforme: An Overview of Emerging Therapeutic Targets. *Frontiers in Oncology*, 9. doi:10.3389/fonc.2019.00963.
- Teng, L., Xie, J., Teng, L., & Lee, R. J. (2012). Clinical translation of folate receptor-targeted therapeutics. *Expert Opinion on Drug Delivery*, 9(8), pp. 901–908. doi:10.1517/17425247.2012.694863.
- Thakkar, J. P., Dolecek, T. A., Horbinski, C., Ostrom, Q. T., Lightner, D. D., Barnholtz-Sloan, J. S., & Villano, J. L. (2014). Epidemiologic and molecular prognostic review of glioblastoma. *Cancer epidemiology, biomarkers & prevention : a publication of the American Association for Cancer Research, cosponsored by the American Society of Preventive Oncology*, 23(10), pp. 1985–1996. <https://doi.org/10.1158/1055-9965.EPI-14-0275>.
- Thomas, M.; Kularatne, S. A.; Qi, L.; Kleindl, P.; Leamon, C. P.; Hansen, M. J.; Low, P. S. (2009). Ligand-targeted delivery of small interfering RNAs to malignant cells and tissues. *Ann. N.Y. Acad. Sci.* 1175, pp. 32–39.
- Tian, Y., Wu, G., Xing, J.-C., Tang, J., Zhang, Y., Huang, Z.-M., Ni, B. (2012). A novel splice variant of folate receptor 4 predominantly expressed in regulatory T cells. *BMC Immunology*, 13(1), pp. 30. doi:10.1186/1471-2172-13-30.
- Tiwari, M., Kumar Bajpai, V., Sahasrabudhe, A. A., Kumar, A., Sinha, A., Behari, S. and Madhav Godbole, M. (2008). Inhibition of N-(4-hydroxyphenyl)retinamide-induced autophagy at a lower dose enhances cell death in malignant glioma cells. *Carcinogenesis*, 29(3), pp. 600–609. doi: 10.1093/carcin/bgm264.
- Trindade, A. F., Frade, R. F. M., Maçôas, E. M. S., Graça, C., Rodrigues, C. A. B., Martinho, J. M. G., & Afonso, C. A. M. (2014). “Click and go”: simple and fast folic

- acid conjugation. *Org. Biomol. Chem.*, 12(20), pp. 3181–3190. doi:10.1039/c4ob00150h.
- Tu, H.-Y., Huang, A.-M., Wei, B.-L., Gan, K.-H., Hour, T.-C., Yang, S.-C., ... Lin, C.-N. (2009). Ursolic acid derivatives induce cell cycle arrest and apoptosis in NTUB1 cells associated with reactive oxygen species. *Bioorganic & Medicinal Chemistry*, 17(20), pp. 7265–7274. doi:10.1016/j.bmc.2009.08.046.
- Tuomela, J., Sandholm, J., Kauppila, J. H., Lehenkari, P., Harris, K. W. and Selander, K. S. (2013). Chloroquine has tumor-inhibitory and tumor-promoting effects in triple-negative breast cancer. *Oncology Letters*, 6(6), pp. 1665–1672. doi:10.3892/ol.2013.1602.
- Valdés-Rives, S. A., Casique-Aguirre, D., Germán-Castelán, L., Velasco-Velázquez, M. A., & González-Arenas, A. (2017). Apoptotic Signaling Pathways in Glioblastoma and Therapeutic Implications. *BioMed Research International*, 2017, pp. 1–12. doi:10.1155/2017/7403747.
- Valeur, E., and Bradley, M. (2009). Amide bond formation: beyond the myth of coupling reagents. *Chem. Soc. Rev.*, 38(2), pp. 606–631. doi:10.1039/b701677h.
- Venkatesan, S., Lamfers, M. L., Dirven, C. M., & Leenstra, S. (2016). Genetic biomarkers of drug response for small-molecule therapeutics targeting the RTK/Ras/PI3K, p53 or Rb pathway in glioblastoma. *CNS Oncology*, 5(2), pp. 77–90. doi:10.2217/cns-2015-0005.
- Vergote, I., & Leamon, C. P. (2015). Vintafolide: a novel targeted therapy for the treatment of folate receptor expressing tumors. *Therapeutic Advances in Medical Oncology*, 7(4), pp. 206–218. doi:10.1177/1758834015584763.
- Visentin, M., Zhao, R., & Goldman, I. D. (2012). The Antifolates. *Hematology/Oncology Clinics of North America*, 26(3), pp. 629–648. doi:10.1016/j.hoc.2012.02.002.

- Vlahov, I. R., & Leamon, C. P. (2012). Engineering Folate–Drug Conjugates to Target Cancer: From Chemistry to Clinic. *Bioconjugate Chemistry*, 23(7), pp. 1357–1369. doi:10.1021/bc2005522.
- Vlahov, I. R., Santhapuram, H. K. R., Kleindl, P. J., Howard, S. J., Stanford, K. M., & Leamon, C. P. (2006). Design and regioselective synthesis of a new generation of targeted chemotherapeutics. Part 1: EC145, a folic acid conjugate of desacetylvinblastine monohydrazone. *Bioorganic & Medicinal Chemistry Letters*, 16(19), pp. 5093–5096. doi:10.1016/j.bmcl.2006.07.030.
- Wang, B., Hai, J., Wang, Q., Li, T., & Yang, Z. (2011). Coupling of Luminescent Terbium Complexes to Fe₃O₄ Nanoparticles for Imaging Applications. *Angewandte Chemie International Edition*, 50(13), pp. 3063–3066. doi:10.1002/anie.201006195.
- Wang, C.-Y., Lin, C.-S., Hua, C.-H., Jou, Y.-J., Liao, C.-R., Chang, Y.-S., Wan, L., Huang, S.-H., Hour, M.-J. and Lin, C.-W. (2019). *Cis-3-O-p*-hydroxycinnamoyl Ursolic Acid Induced ROS-Dependent p53-Mediated Mitochondrial Apoptosis in Oral Cancer Cells. *Biomolecules & Therapeutics*, 27(1), pp.54–62. doi:10.4062/biomolther.2017.237.
- Wang, D., Wang, C., Wang, L. and Chen, Y. (2019). A comprehensive review in improving delivery of small-molecule chemotherapeutic agents overcoming the blood-brain/brain tumor barriers for glioblastoma treatment. *Drug Delivery*, 26(1), pp.551–565. doi: 10.1080/10717544.2019.1616235.
- Wang, J., Jiang, Z., Xiang, L., Li, Y., Ou, M., Yang, X., Jia, L. (2014). Synergism of ursolic acid derivative US597 with 2-deoxy-D-glucose to preferentially induce tumor cell death by dual-targeting of apoptosis and glycolysis. *Scientific Reports*, 4(1). doi:10.1038/srep05006.

- Wang, J., Li, Y., Wang, X. and Jiang, C. (2012). Ursolic Acid Inhibits Proliferation and Induces Apoptosis in Human Glioblastoma Cell Lines U251 by Suppressing TGF- β 1/miR-21/PDCD4 Pathway. *Basic & Clinical Pharmacology & Toxicology*, p.n/a-n/a. doi:10.1111/j.1742-7843.2012.00870.x.
- Wang, S., Meng, X., & Dong, Y. (2017). Ursolic acid nanoparticles inhibit cervical cancer growth in vitro and in vivo via apoptosis induction. *International Journal of Oncology*, 50(4), pp. 1330–1340. doi:10.3892/ijo.2017.3890.
- Wang, S., Meng, Y., Li, C., Qian, M., & Huang, R. (2015). Receptor-Mediated Drug Delivery Systems Targeting to Glioma. *Nanomaterials*, 6(1), pp. 3. doi:10.3390/nano6010003.
- Wang, W.-Y., Wu, W.-Y., Li, A-Liang., Liu, Q.-S., Sun, Y. and Gu, W. (2021). Synthesis, anticancer evaluation and mechanism studies of novel indolequinone derivatives of ursolic acid. *Bioorganic Chemistry*, 109, p.104705. doi:10.1016/j.bioorg.2021.104705.
- Wang, X., Zhang, F., Yang, L., Mei, Y., Long, H., Zhang, X., Zhang, J., Qimuge-Suyila and Su, X. (2011). Ursolic Acid Inhibits Proliferation and Induces Apoptosis of Cancer Cells In Vitro and In Vivo. *Journal of Biomedicine and Biotechnology*, 2011, pp.1–8. doi:10.1155/2011/419343.
- Wanigasekara, J., Barcia, C., Cullen, P.J., Tiwari, B. and Curtin, J.F. (2022). Plasma induced reactive oxygen species-dependent cytotoxicity in glioblastoma 3D tumourspheres. *Plasma Processes and Polymers*, 19(4), p.2100157. doi: 10.1002/ppap.202100157.
- Ware, T.M.B., and Zhu, H.J. (2018). Glioblastoma treatment: Where to now? *Integr Cancer Sci Therap.* 5: DOI: 10.15761/ICST.1000280.

- Weitman, S.D., Lark, R.H., Coney, L.R., Fort, D.W., Frasca, V., Zurawski Jr., V.R., Kamen, B.A. (1992). Distribution of the folate receptor GP38 in normal and malignant cell lines and tissues. *Cancer Res.*, 52(12), pp. 3396-3401.
- Weng, H., Tan, Z.-J., Hu, Y.-P., Shu, Y.-J., Bao, R.-F., Jiang, L., Wu, X.-S., Li, M.-L., Ding, Q., Wang, X., Xiang, S., Li, H.-F., Cao, Y., Tao, F. and Liu, Y.-B. (2014). Ursolic acid induces cell cycle arrest and apoptosis of gallbladder carcinoma cells. *Cancer Cell International*, 14(1). doi:10.1186/s12935-014-0096-6.
- Wibowo, A. S., Singh, M., Reeder, K. M., Carter, J. J., Kovach, A. R., Meng, W., Dann, C. E. (2013). Structures of human folate receptors reveal biological trafficking states and diversity in folate and antifolate recognition. *Proceedings of the National Academy of Sciences*, 110(38), pp. 15180–15188. doi:10.1073/pnas.1308827110.
- Wohlfart S, Khalansky AS, Gelperina S, Begley D, Kreuter J. (2011). Kinetics of transport of doxorubicin bound to nanoparticles across the blood-brain barrier. *J Control Release*. 154(1): pp. 103–107. doi: 10.1016/j.jconrel.2011.05.010.
- Wójciak-Kosior, M., Paduch, R., Matysik-Woźniak, A., Niedziela, P. and Donica, H. (2012). The effect of ursolic and oleanolic acids on human skin fibroblast cells. *Folia Histochemica et Cytobiologica*, 49(4), pp.664–669. doi:10.5603/fhc.2011.0050.
- World Health Organisation (WHO). (2018). WHO_Cancer. [Online] Available at: <<https://www.who.int/news-room/fact-sheets/detail/cancer>> [Accessed 30 March 2020].
- World Health Organization: WHO (2019). *Cancer*. [online] Who.int. Available at: https://www.who.int/health-topics/cancer#tab=tab_1 [Accessed 19 April 2022].
- Wu SK, Chu PC, Chai WY, Kang ST, Tsai CH, Fan CH, et al. (2016). Characterization of different microbubbles in assisting focused ultrasound-induced blood-brain barrier opening. *Sci Rep*. 2017(7), pp. 1–11.

- Wu, D., & Pardridge, W. M. (1999). Blood-brain barrier transport of reduced folic acid. *Pharmaceutical Research*, 16(3), pp. 415–419. doi:10.1023/a:1018829920158.
- Wu, P., Nielsen, T.E. and Clausen, M.H. (2016). Small-molecule kinase inhibitors: an analysis of FDA-approved drugs. *Drug Discovery Today*, 21(1), pp.5–10. doi:10.1016/j.drudis.2015.07.008.
- Wu, Q., Wu, W., Jacevic, V., Franca, T.C.C., Wang, X. and Kuca, K. (2020). Selective inhibitors for JNK signalling: a potential targeted therapy in cancer. *Journal of Enzyme Inhibition and Medicinal Chemistry*, 35(1), pp.574–583. doi:10.1080/14756366.2020.1720013
- Xia, W., & Low, P. S. (2010). Folate-Targeted Therapies for Cancer. *Journal of Medicinal Chemistry*, 53(19), pp. 6811–6824. doi:10.1021/jm100509v.
- Xia, W., Hilgenbrink, A. R., Matteson, E. L., Lockwood, M. B., Cheng, J.-X., & Low, P. S. (2009). A functional folate receptor is induced during macrophage activation and can be used to target drugs to activated macrophages. *Blood*, 113(2), pp. 438–446. doi:10.1182/blood-2008-04-150789.
- Xu, X., Zhu, G.-Q., Zhang, K., Zhou, Y.-C., Li, X.-L., Xu, W., Zhang, H., Shao, Y., Zhang, Z.-Y. and Sun, W.-H. (2017). Cyclooxygenase-2 mediated synergistic effect of ursolic acid in combination with paclitaxel against human gastric carcinoma. *Oncotarget*, [online] 8(54), pp.92770–92777. doi:10.18632/oncotarget.21576.
- Yang, G., Yang, T., Zhang, W., Lu, M., Ma, X., & Xiang, G. (2014). In Vitro and in Vivo Antitumor Effects of Folate-Targeted Ursolic Acid Stealth Liposome. *Journal of Agricultural and Food Chemistry*, 62(10), pp. 2207–2215. doi:10.1021/jf405675g.

- Yang, M., Hu, C., Cao, Y., Liang, W., Yang, X. and Xiao, T. (2021). Ursolic Acid Regulates Cell Cycle and Proliferation in Colon Adenocarcinoma by Suppressing Cyclin B1. *Frontiers in Pharmacology*, 11. doi:10.3389/fphar.2020.622212.
- Yang, Y. (2016). Side Reactions Upon Amino Acid/Peptide Carboxyl Activation. *Side Reactions in Peptide Synthesis*, pp. 95–118. doi:10.1016/b978-0-12-801009-9.00005-7.
- Yoo, H. S., & Park, T. G. (2004). Folate-receptor-targeted delivery of doxorubicin nano-aggregates stabilized by doxorubicin–PEG–folate conjugate. *Journal of Controlled Release*, 100(2), pp. 247–256. doi:10.1016/j.jconrel.2004.08.017.
- Yoshimoto, K., Mizoguchi, M., Hata, N., Murata, H., Hatae, R., Amano, T., Nakamizo, A. and Sasaki, T. (2012). Complex DNA repair pathways as possible therapeutic targets to overcome temozolomide resistance in glioblastoma. *Frontiers in Oncology*, 2. doi:10.3389/fonc.2012.00186.
- Yu, B., Tai, H. C., Xue, W., Lee, L. J. & Lee, R. J. (2010). Receptor-targeted nanocarriers for therapeutic delivery to cancer. *Molecular Membrane Biology*. 27, pp. 286–298.
- Zacchigna, M., Cateni, F., Drioli, S., Procida, G., & Altieri, T. (2014). PEG-Ursolic Acid Conjugate: Synthesis and In Vitro Release Studies. *Scientia pharmaceutica*, 82(2), pp. 411–421. doi:10.3797/scipharm.1309-17.
- Yu, B., Tai, H. C., Xue, W., Lee, L. J. & Lee, R. J. (2010). Receptor-targeted nanocarriers for therapeutic delivery to cancer. *Molecular Membrane Biology*. 27, pp. 286–298.
- Zacchigna, M., Cateni, F., Faudale, M., Sosa, S., & Della Loggia, R. (2009). Rapid HPLC Analysis for Quantitative Determination of the Two Isomeric Triterpenic Acids, Oleanolic acid and Ursolic acid, in *Plantago Major*. *Scientia Pharmaceutica*, 77(1), pp. 79–86. doi:10.3797/scipharm.0809-08.

- Zhang, F., Xu, C., & Liu, C. (2015). Drug delivery strategies to enhance the permeability of the blood–brain barrier for treatment of glioma. *Drug Design, Development and Therapy*, 2089.doi:10.2147/dddt.s79592.
- Zhang, H., Li, X., Ding, J., Xu, H., Dai, X., Hou, Z., Sun, W. (2013). Delivery of ursolic acid (UA) in polymeric nanoparticles effectively promotes the apoptosis of gastric cancer cells through enhanced inhibition of cyclooxygenase 2 (COX-2). *International Journal of Pharmaceutics*, 441(1-2), pp. 261–268.doi:10.1016/j.ijpharm.2012.11.034.
- Zhang, Y., Dube, C., Gibert, M., Cruickshanks, N., Wang, B., Coughlan, M., Abounader, R. (2018). The p53 Pathway in Glioblastoma. *Cancers*, 10(9), pp. 297. doi:10.3390/cancers10090297.
- Zhang, Y., Ma, X., Li, H., Zhuang, J., Feng, F., Liu, L., Liu, C. and Sun, C. (2021). Identifying the Effect of Ursolic Acid Against Triple-Negative Breast Cancer: Coupling Network Pharmacology With Experiments Verification. *Frontiers in Pharmacology*, 12. doi:10.3389/fphar.2021.685773.
- Zhang, Z., Huang, Z., Dai, H., Wei, L., Sun, S. and Gao, F. (2015). Therapeutic Efficacy of E-64-d, a Selective Calpain Inhibitor, in Experimental Acute Spinal Cord Injury. *BioMed Research International*. Hindawi Publishing Corporation, 2015. doi: 10.1155/2015/134242.
- Zhao, R., Min, S. H., Wang, Y., Campanella, E., Low, P. S., & Goldman, I. D. (2009). A Role for the Proton-coupled Folate Transporter (PCFT-SLC46A1) in Folate Receptor-mediated Endocytosis. *Journal of Biological Chemistry*, 284(7), pp. 4267–4274.doi:10.1074/jbc.m807665200.
- Zhao, R., Seither, R., Brigle, K. E., Sharina, I. G., Wang, P. J., & Goldman, I. D. (1997). Impact of Overexpression of the Reduced Folate Carrier (RFC1), an Anion

- Exchanger, on Concentrative Transport in Murine L1210 Leukemia Cells. *Journal of Biological Chemistry*, 272(34), pp. 21207–21212. doi:10.1074/jbc.272.34.21207.
- Zhao, T., Liu, Y., Gao, Z., Gao, D., Li, N., Bian, Y., Liu, Z. (2015). Self-assembly and cytotoxicity study of PEG-modified ursolic acid liposomes. *Materials Science and Engineering: C*, 53, pp. 196–203. doi:10.1016/j.msec.2015.04.022.
- Zhao, X. (2004). Tumor-selective targeted delivery of genes and antisense oligodeoxyribonucleotides via the folate receptor. *Advanced Drug Delivery Reviews*, 56(8), pp. 1193–1204. doi:10.1016/j.addr.2004.01.005.
- Zhou, M., Zhang, R.-H., Wang, M., Xu, G.-B., & Liao, S.-G. (2017). Prodrugs of triterpenoids and their derivatives. *European Journal of Medicinal Chemistry*, 131, pp. 222–236. doi:10.1016/j.ejmech.2017.03.005.
- Zhou, Y., Wu, W., Bi, H., Yang, D., & Zhang, C. (2020). Glioblastoma precision therapy: From the bench to the clinic. *Cancer Letters*. doi:10.1016/j.canlet.2020.01.027.
- Zhu, Z., Du, S., Ding, F., Guo, S., Ying, G., & Yan, Z. (2016). Ursolic acid attenuates temozolomide resistance in glioblastoma cells by downregulating O(6)-methylguanine-DNA methyltransferase (MGMT) expression. *American journal of translational research*, 8(7), pp. 3299–3308.
- Zwicke, G. L., Ali Mansoori, G., & Jeffery, C. J. (2012). Utilizing the folate receptor for active targeting of cancer nanotherapeutics. *Nano Reviews*, 3(1), 18496. doi:10.3402/nano.v3i0.18496.

APPENDICES

A.1 COA of UA Hunan



Hunan Delore Natural Products Co., Ltd.

湖南德诺健康产业有限公司

Tel: +86-0731-8275 5556 Fax: +86-731-8275 5557 www.delore.cn

Office: Room 303, Depu Parkview Green, Kingsha Economic Development Zone, Changsha, Hunan, 410100, China

Factory: Shangrenli Industrial Zone, Shuangpai County, Yongzhou, Hunan Province, 425200, China

Certificate of Analysis

产品名称 Product Name	Rosemary Extract	规格 Specification	Ursolic acid 98%
拉丁名称 Latin Name	Rosmarinus officinalis	生产日期 Manufacturing Date	2018.07.25
生产批号 Batch No.	UA20180730	失效日期 Expiration Date	2020.07.25
生产批量 Batch Quantity	100KG	检验日期 Examination Date	2018.07.30
提取部位 Used Part	Leaf	提取溶剂 Extract Solvent	Water&Ethanol

项目 Item	标准 Specification	结果 Result	测试方法 Test Method
含量 Assay	Ursolic acid ≥98%	98.25%	Ch.P.C.Rule 23-HPLC
外观 Appearance	Off-white Powder	Conforms	Visual
气味 Odor	Characteristic	Conforms	Organoleptic
粒度 Particle Size	95% passes 80 mesh	Conforms	Ch.P.C.Rule 52
干燥失重 Loss on Drying	≤5.00%	0.86%	5g / 105C / 4hrs
溶解性 Solubility	Water&Ethanol	Conforms	1g/100ml Water&Ethanol
灰分 Ash	≤5%	0.62%	2g / 525C / 4hrs
重金属 Heavy Metals	≤10ppm	Conforms	Ch.P.C.Rule 21-AAS
砷 Arsenic (As)	≤2ppm	Conforms	Ch.P.C.Rule 21-AAS
铅 Lead (Pb)	≤2ppm	Conforms	Ch.P.C.Rule 21-AAS
汞 Mercury (Hg)	≤0.1ppm	Conforms	Ch.P.C.Rule 21-AAS
镉 Cadmium (Cd)	≤2ppm	Conforms	Ch.P.C.Rule 21-AAS
菌落总数 Total Plate Count	≤5000cfu/g	Conforms	Ch.P.C.Rule 80
酵母菌及霉菌 Yeast&Mold	≤500cfu/g	Conforms	Ch.P.C.Rule 80
大肠杆菌 E.Coli	阴性 Negative	Negative	Ch.P.C.Rule 80
沙门氏菌 Salmonella	阴性 Negative	Negative	Ch.P.C.Rule 80

储存 Storage: Cold, Drying, Avoid the Sunlight

保质期 Shelf life: Two Years

包装 Packing: Pack in paper-drums and two plastic-bags inside. Net Weight: 25kg/drums.

检测者 Test by 蒋智博

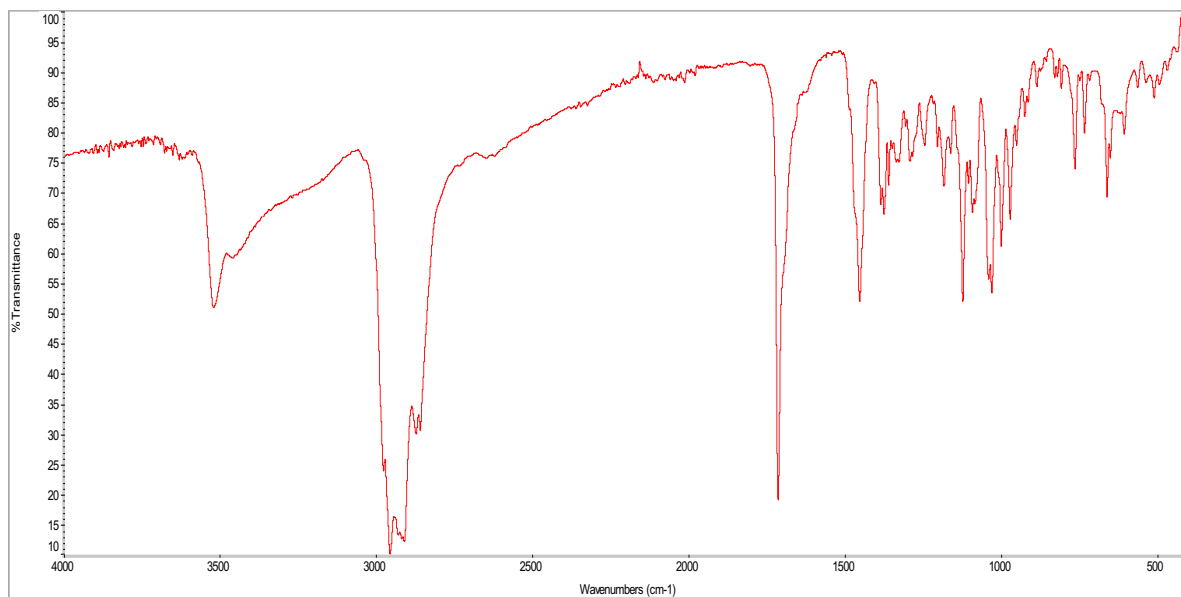
复合者 Approved by 吴俊



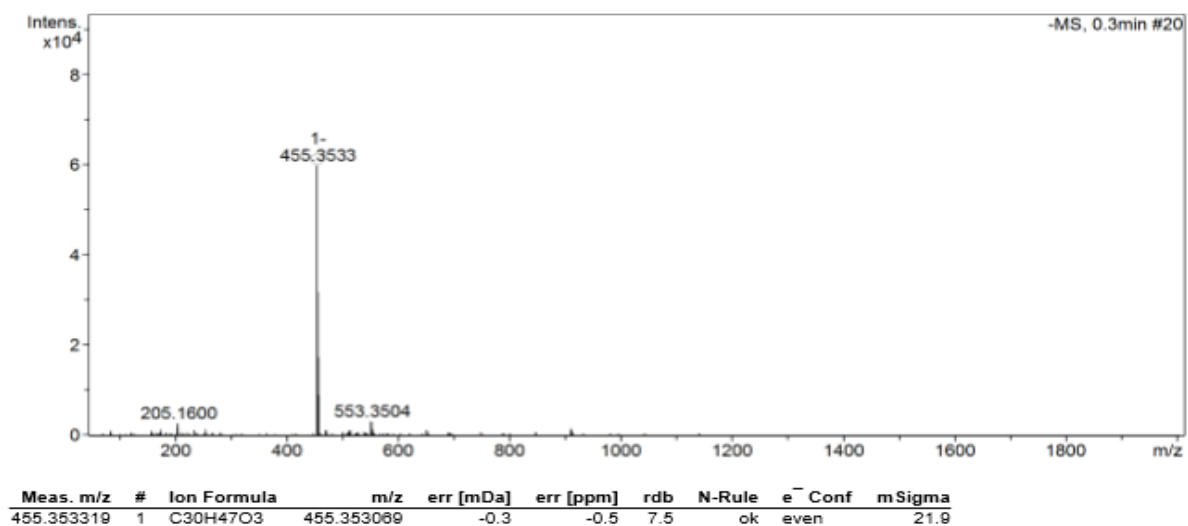
For Nature, From Nature

A.2 UA Hunan

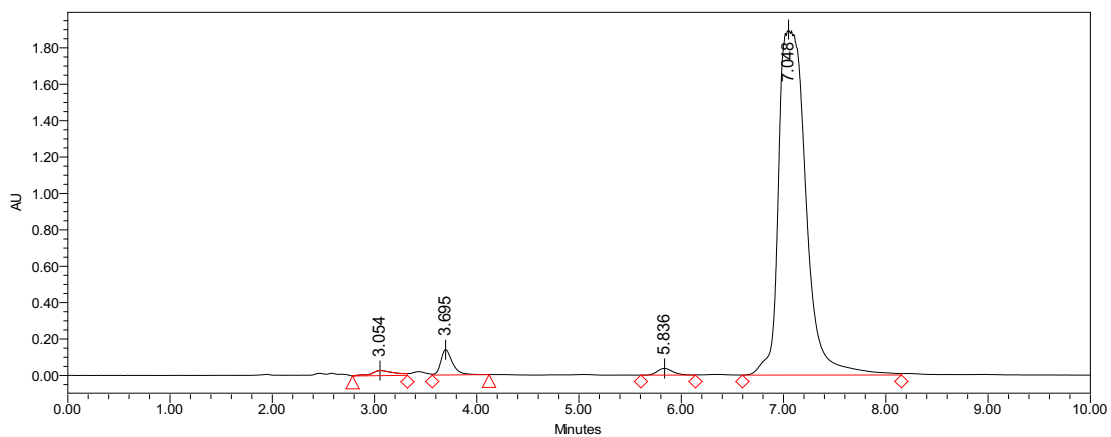
IR Spectrum



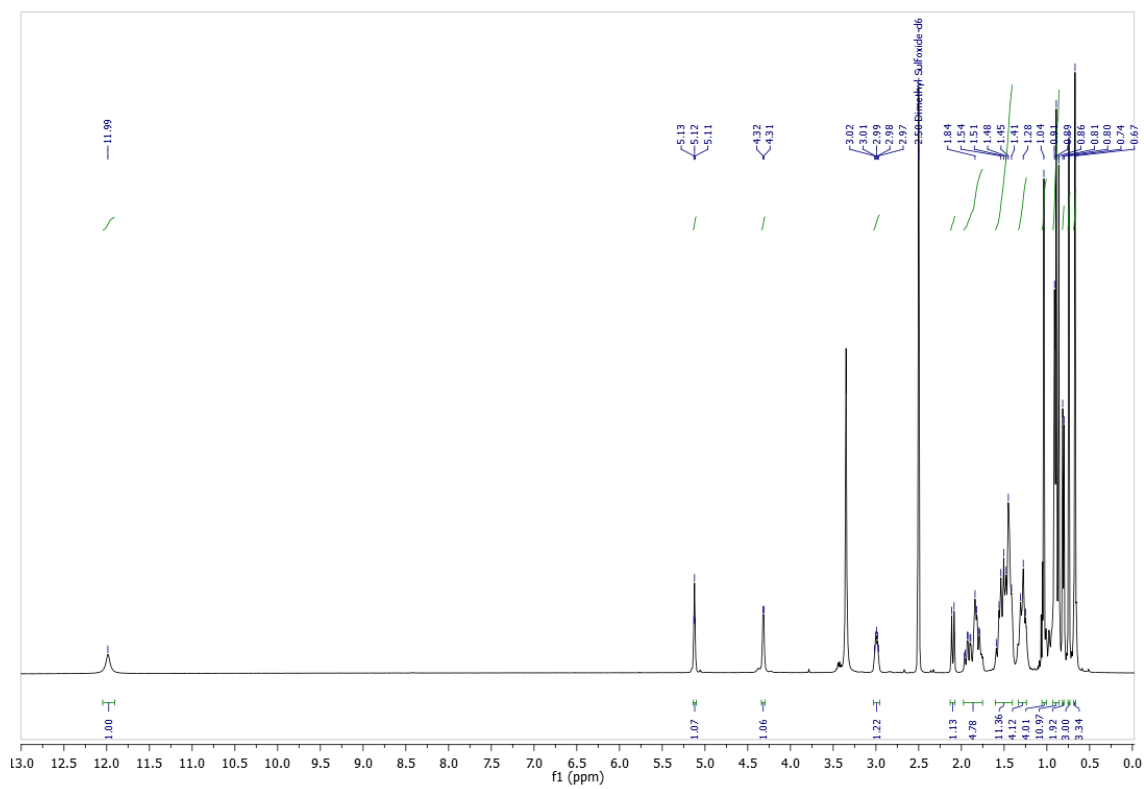
Mass Spectrum



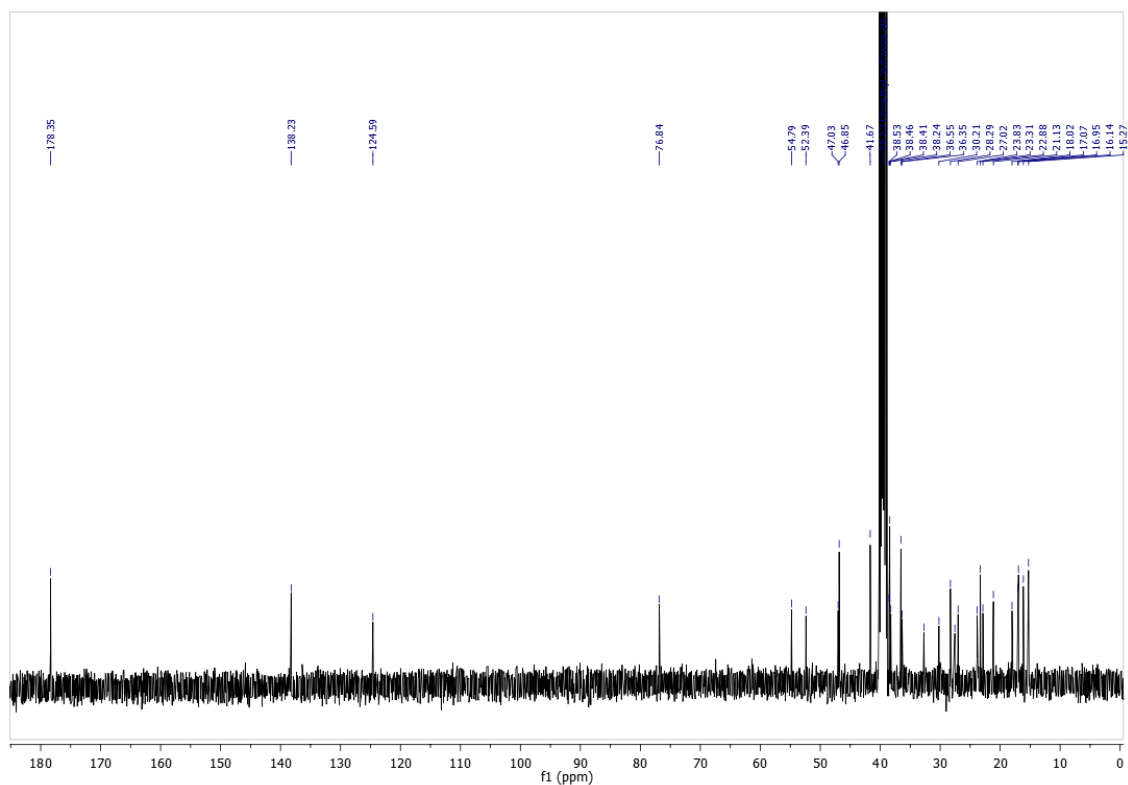
RP-HPLC



¹H NMR Spectrum (DMSO)



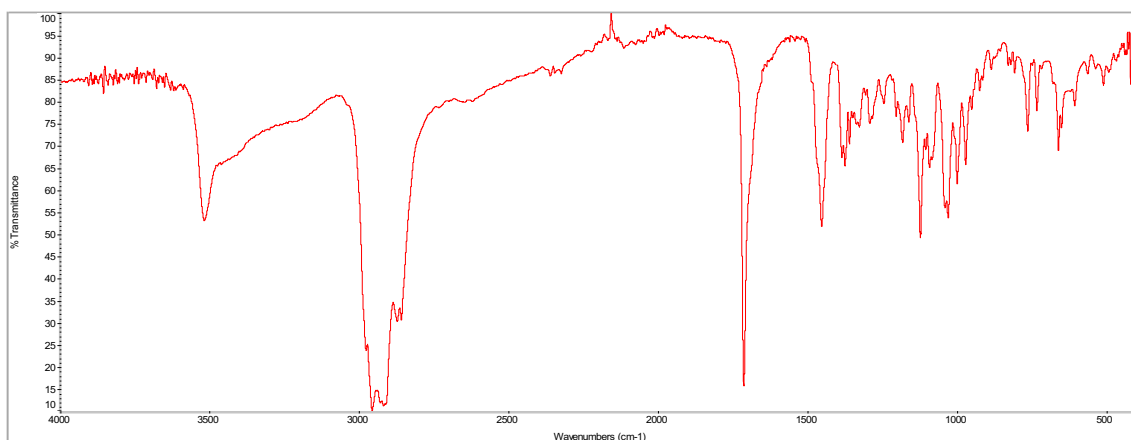
^{13}C NMR Spectrum (DMSO)



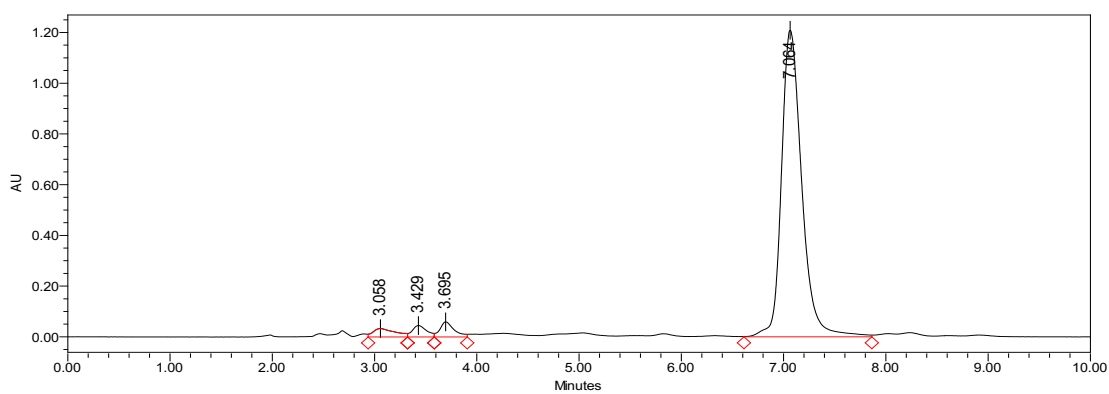
UA Hunan: LC-MS (ESI) calculated for $\text{C}_{30}\text{H}_{47}\text{O}_3$ 455.3533 $[\text{M}-\text{H}]^-$, found 455.3531; Elemental Analysis (Found) C, 78.72; H, 10.75; Elemental Analysis (Calculated): C, 78.90; H, 10.59; ^1H NMR (400 MHz, DMSO) δ 11.99 (s, 1H), 5.12 (t, $J = 3.2$ Hz, 1H), 4.32 (d, $J = 4.8$ Hz, 1H), 2.99 (dt, $J = 9.4, 4.5$ Hz, 1H), 2.10 (d, $J = 11.2$ Hz, 1H), 1.98 – 1.75 (m, 5H), 1.60 – 1.40 (m, 11H), 1.28 (t, $J = 12.0$ Hz, 4H), 1.04 (s, 4H), 0.93 – 0.86 (m, 11H), 0.81 (s, 2H), 0.74 (s, 3H), 0.67 (s, 3H). ^{13}C NMR (101 MHz, DMSO) δ 178.35, 138.23, 124.59, 76.84, 54.79, 52.39, 47.03, 46.85, 41.67, 39.52, 38.53, 38.46, 38.41, 38.24, 36.55, 36.35, 32.72, 30.21, 28.29, 27.56, 27.02, 23.83, 23.31, 22.88, 21.13, 18.02, 17.07, 16.95, 16.14, 15.27; IR: 3519, 2955, 2909, 2872, 2858, 1713, 1452, 1385, 1375, 1359, 1327, 1292, 1244, 1203, 1183, 1162, 1122, 1105, 1092, 1029, 999, 971, 951, 763, 733, 661, 651, 606 cm^{-1} .

A.3 UA Sigma

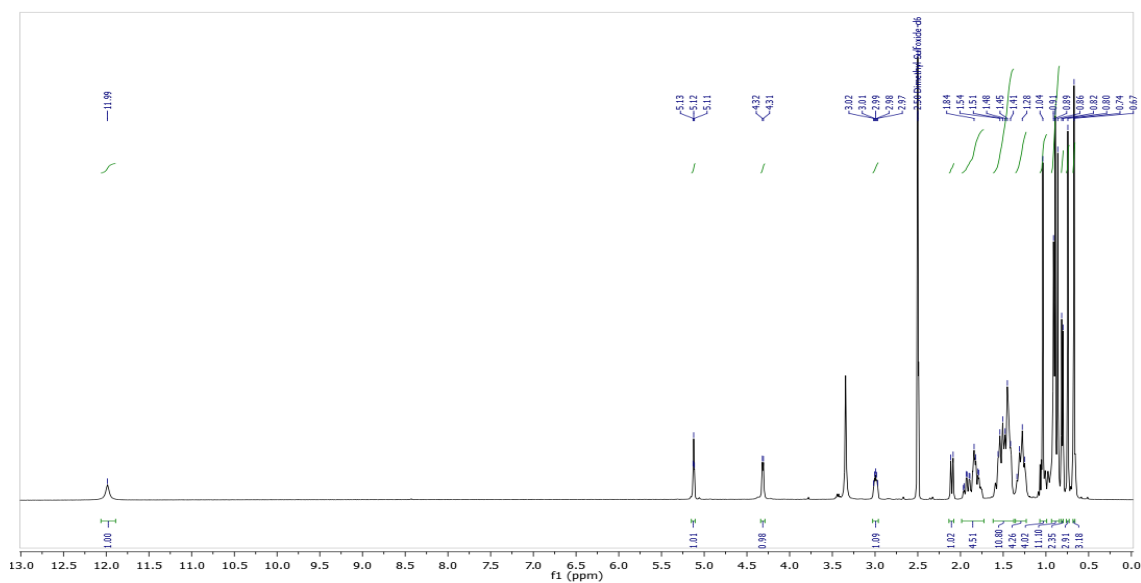
IR Spectrum



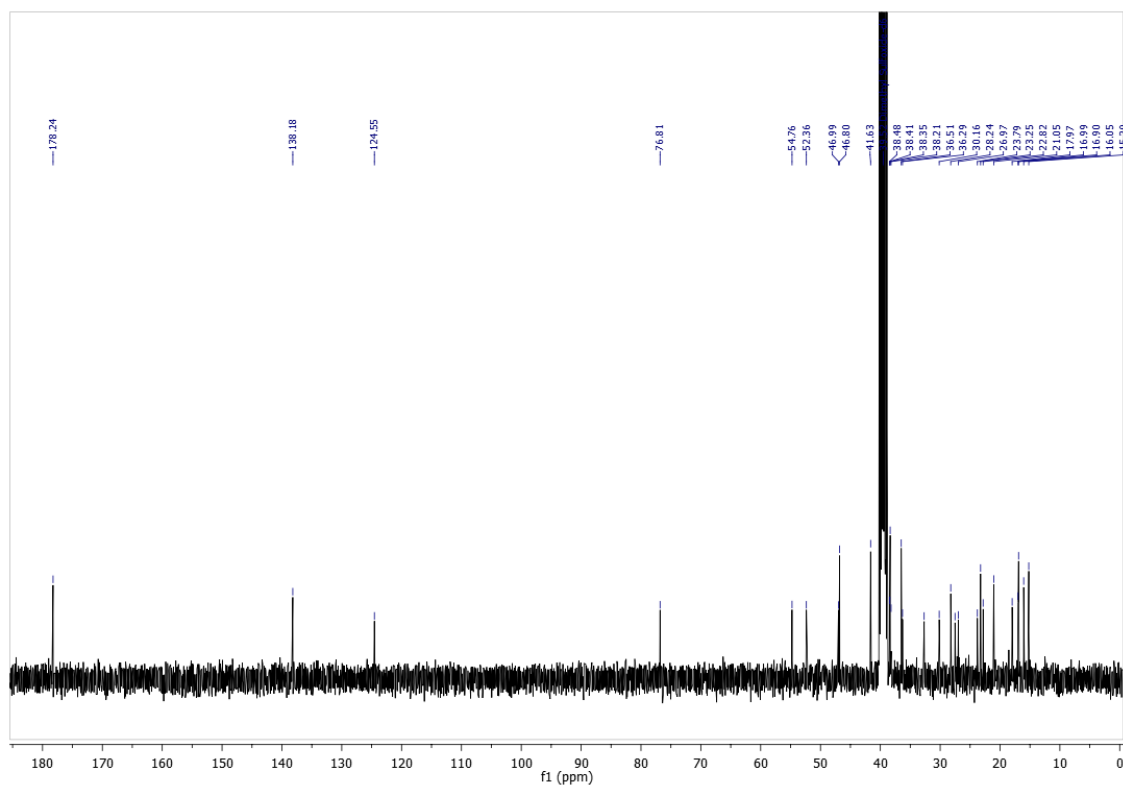
RP-HPLC



¹H NMR Spectrum (DMSO)



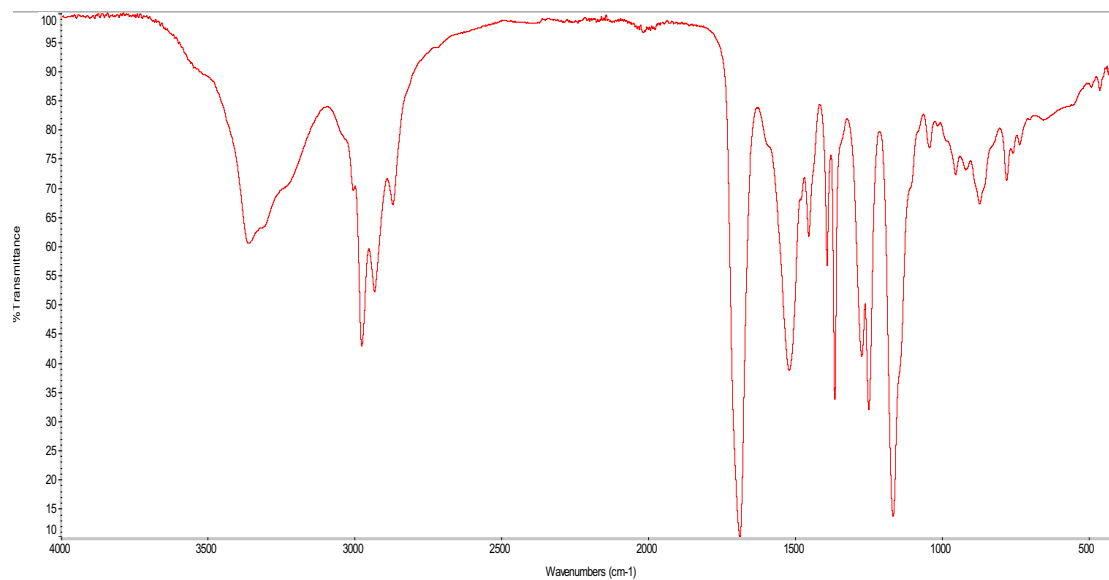
¹³C NMR Spectrum (DMSO)



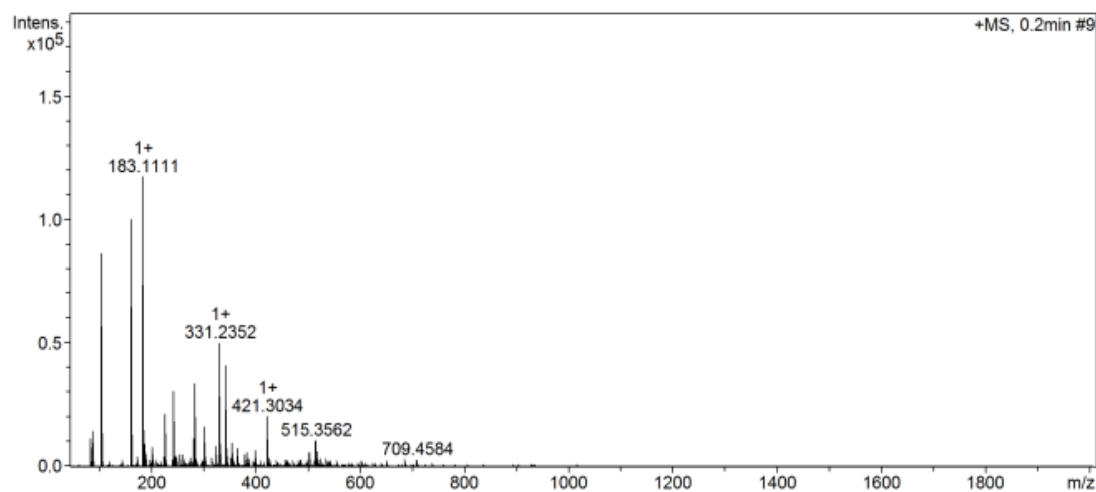
UA Sigma: Elemental Analysis (Found) C, 78.72; H, 10.75; Elemental Analysis (Calculated): C, 78.90; H, 10.59; ¹H NMR (400 MHz, DMSO) δ 11.99 (s, 1H), 5.12 (t, J = 3.3 Hz, 1H), 4.31 (d, J = 4.8 Hz, 1H), 3.03 – 2.96 (m, 1H), 2.10 (d, J = 11.3 Hz, 1H), 1.99 – 1.73 (m, 5H), 1.49 (dt, J = 25.6, 11.7 Hz, 11H), 1.29 (dd, J = 24.5, 11.2 Hz, 4H), 1.04 (s, 4H), 0.93 – 0.84 (m, 11H), 0.81 (d, J = 6.4 Hz, 2H), 0.74 (s, 3H), 0.67 (s, 3H). ¹³C NMR (101 MHz, DMSO) δ 178.24, 138.18, 124.55, 76.81, 54.76, 52.36, 46.99, 46.80, 41.63, 39.52, 38.48, 38.41, 38.35, 38.21, 36.51, 36.29, 32.68, 30.16, 28.24, 27.52, 26.97, 23.79, 23.25, 22.82, 21.05, 17.97, 16.99, 16.90, 16.05, 15.20; IR: 3517, 2956, 2917, 2872, 2858, 1713, 1452, 1385, 1375, 1359, 1327, 1291, 1244, 1204, 1182, 1162, 1122, 1105, 1092, 1030, 1000, 971, 951, 763, 733, 661, 651, 607 cm⁻¹.

A.4 N-Boc Ethylenediamine (1)

IR Spectrum

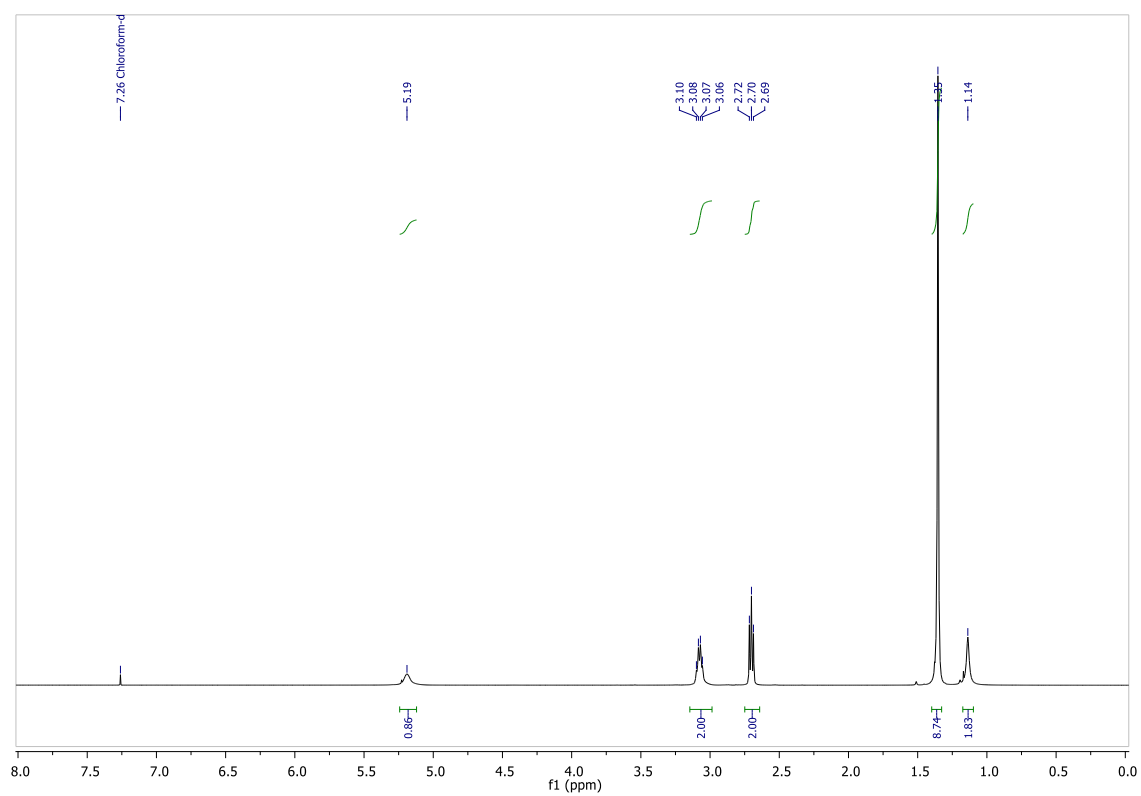


Mass Spectrum

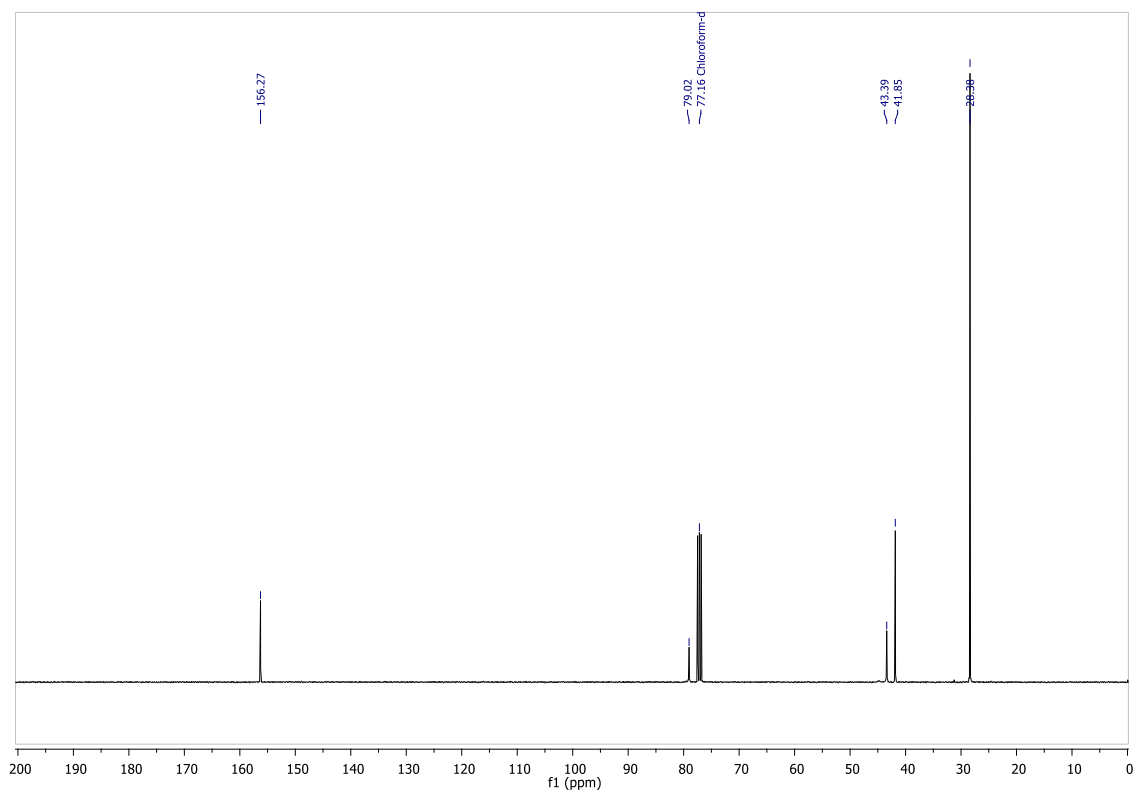


Meas. m/z	#	Ion Formula	m/z	err [mDa]	err [ppm]	rdb	N-Rule	e ⁻ Conf	mSigma
161.128882	1	C7H17N2O2	161.128454	0.4	2.7	0.5	ok	even	5.3
183.111143	1	C7H16N2NaO2	183.110398	-0.7	-4.1	0.5	ok	even	5.5

^1H NMR Spectrum (CDCl_3)

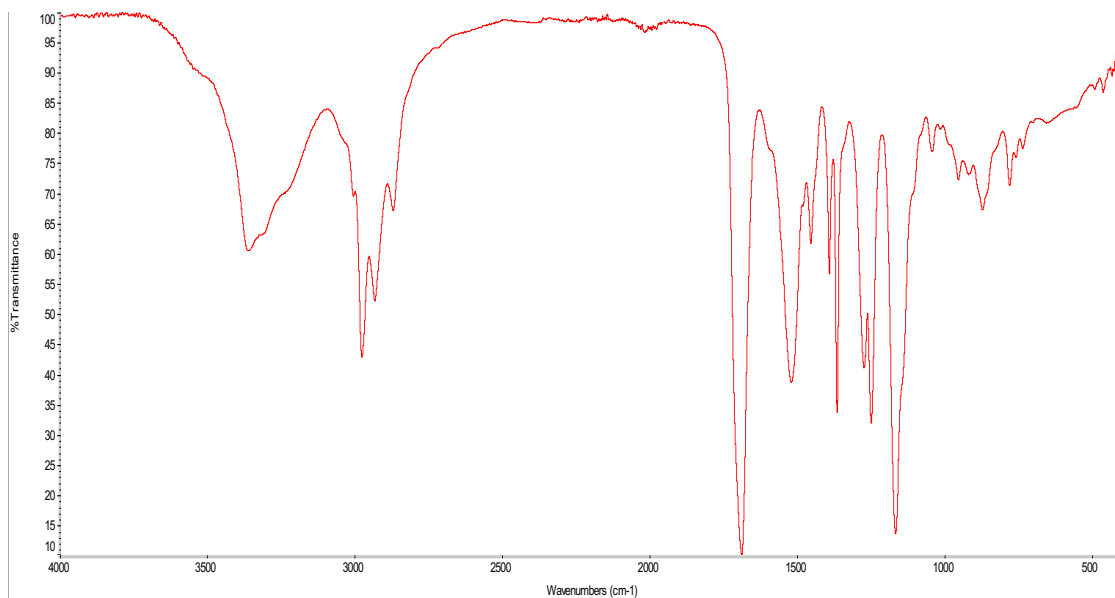


^{13}C NMR Spectrum (CDCl_3)

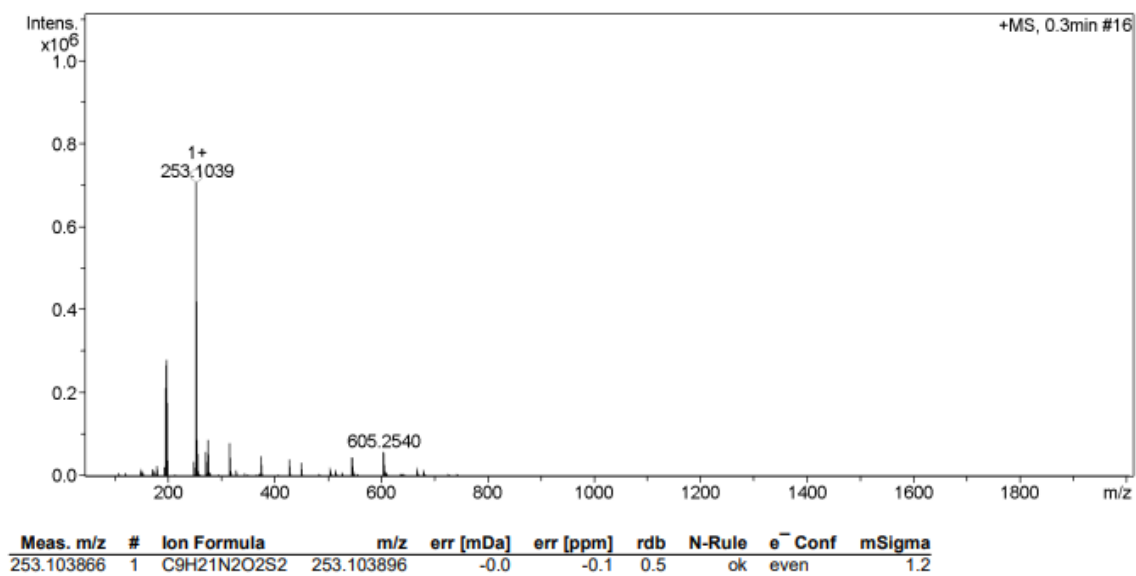


A.4 *N*-Boc cystamine dihydrochloride (2)

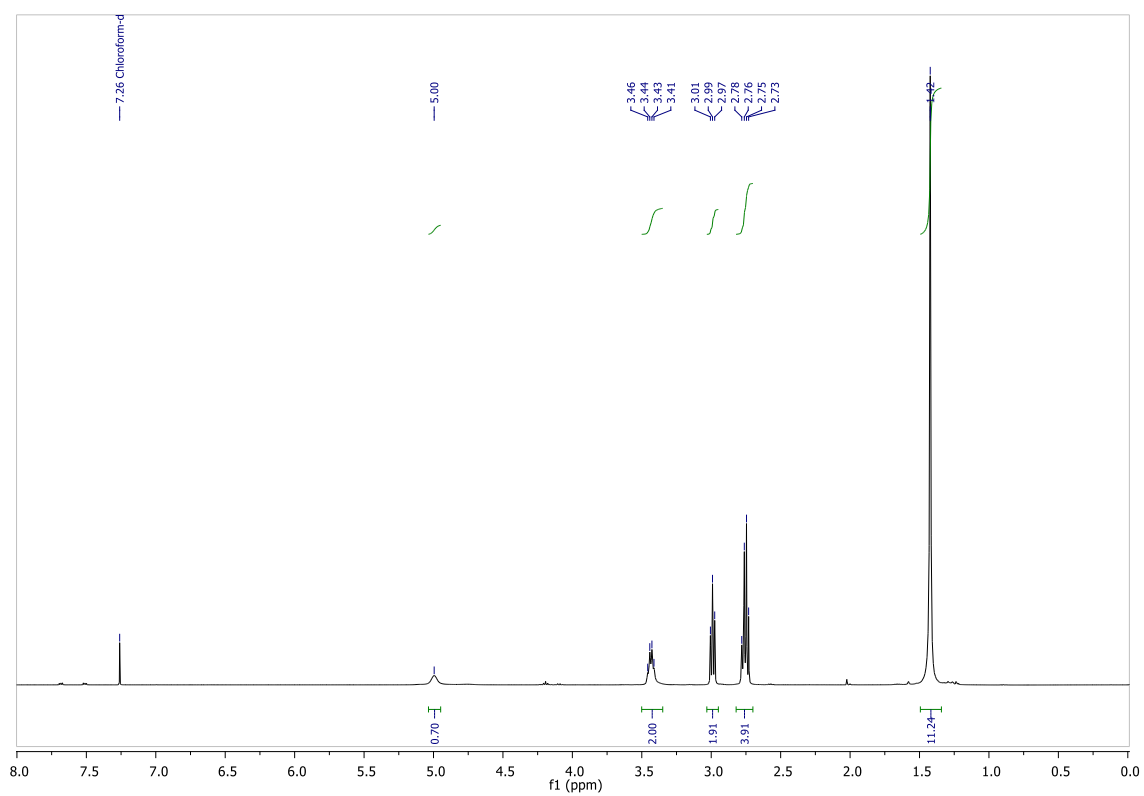
IR Spectrum



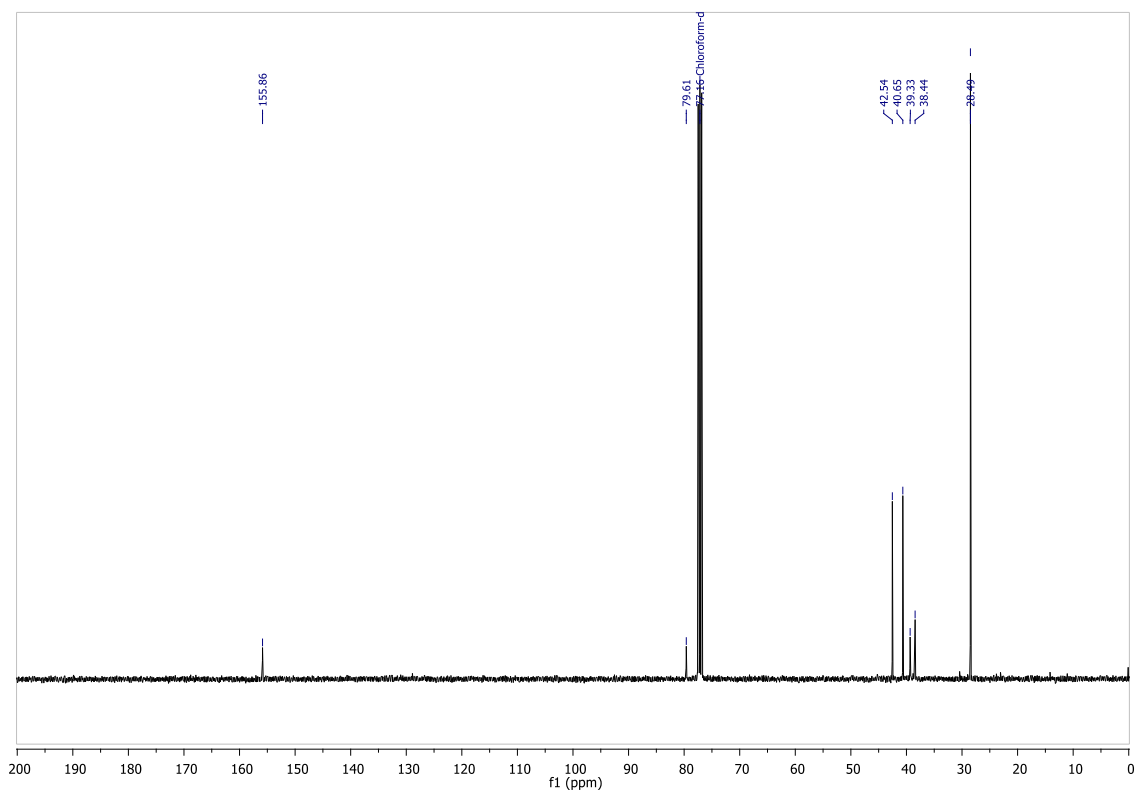
Mass Spectrum



^1H NMR Spectrum (CDCl_3)

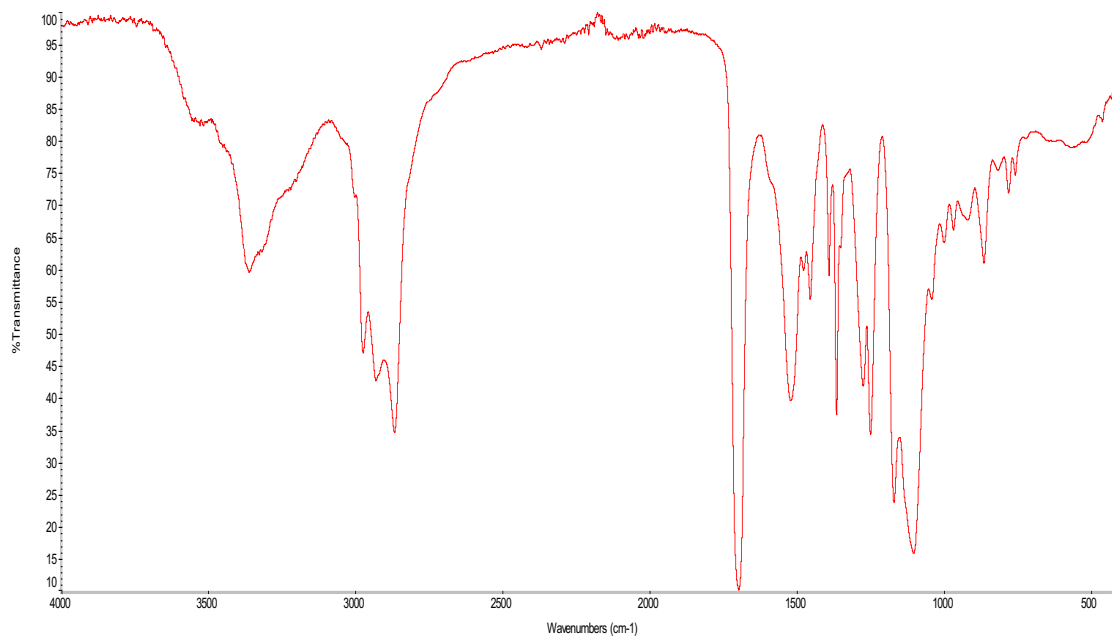


^{13}C NMR Spectrum (CDCl_3)

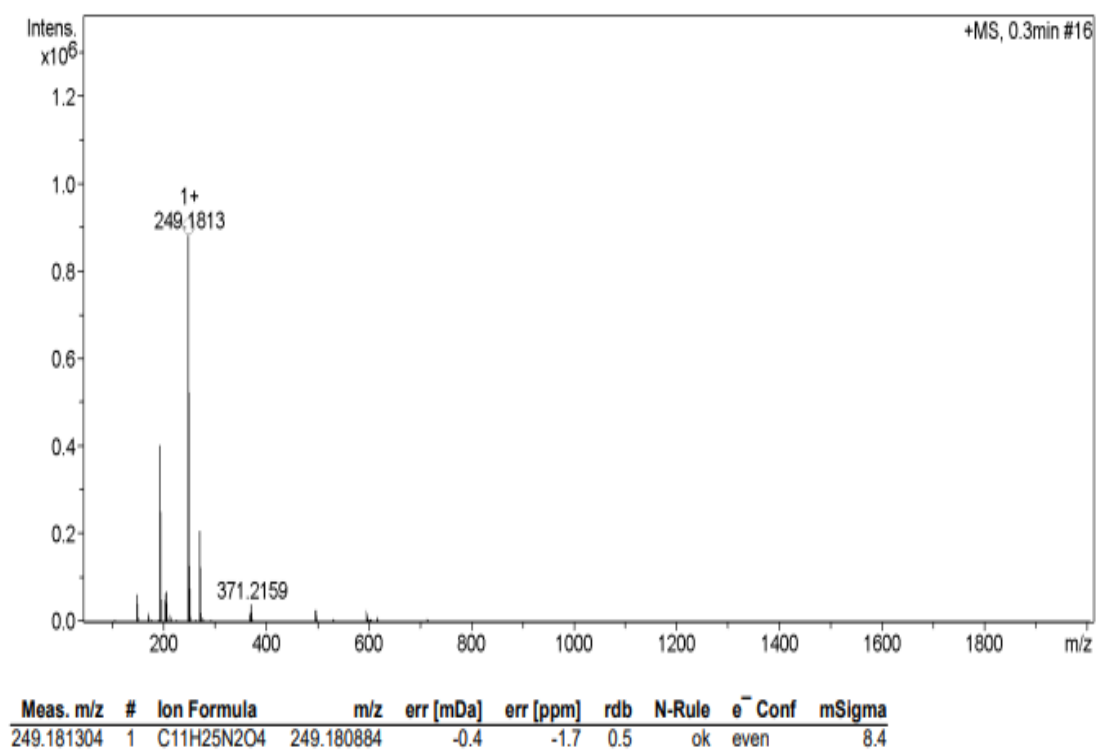


A.5 *N*-Boc 2,2'-(ethylenedioxy)bis(ethylamine) (3)

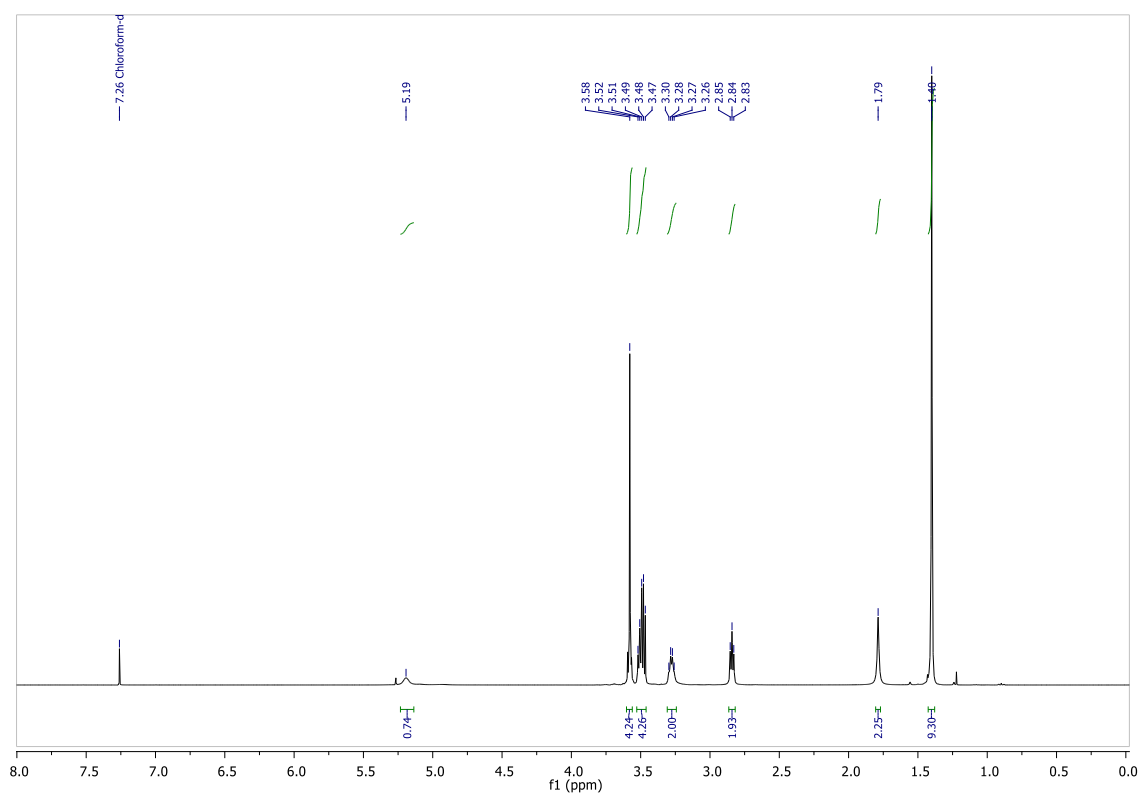
IR Spectrum



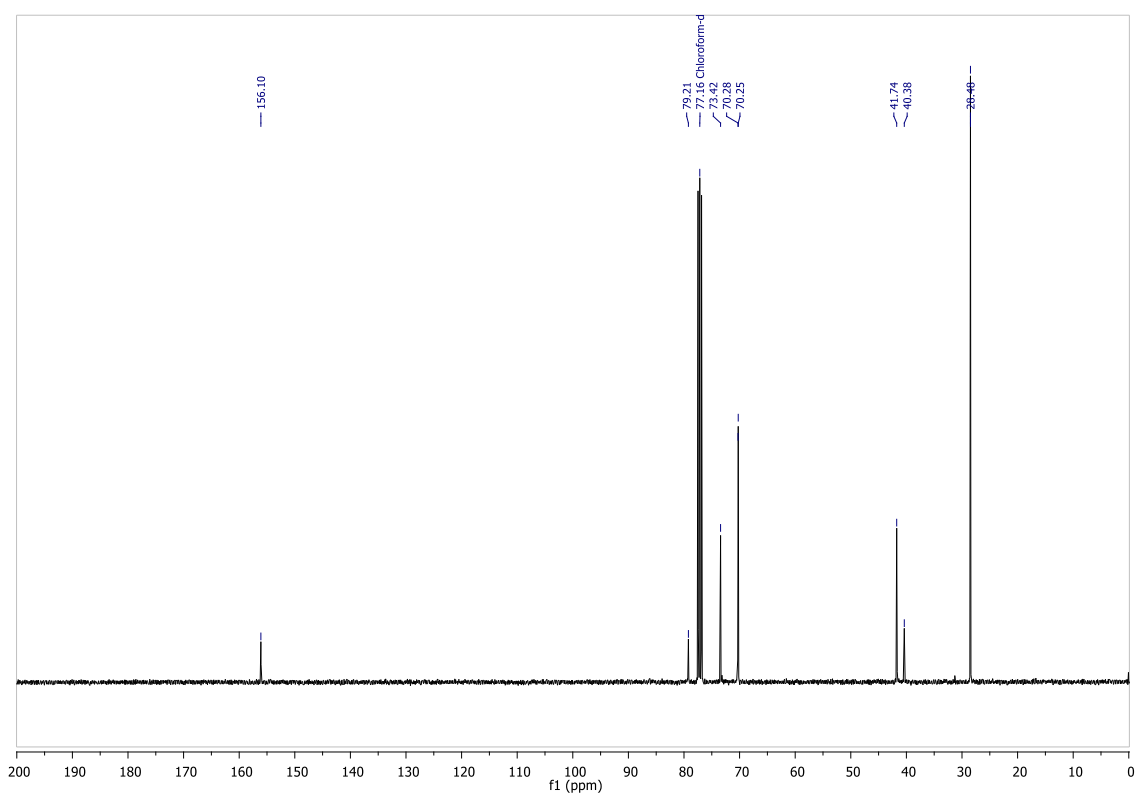
Mass Spectrum



^1H NMR Spectrum (CDCl_3)

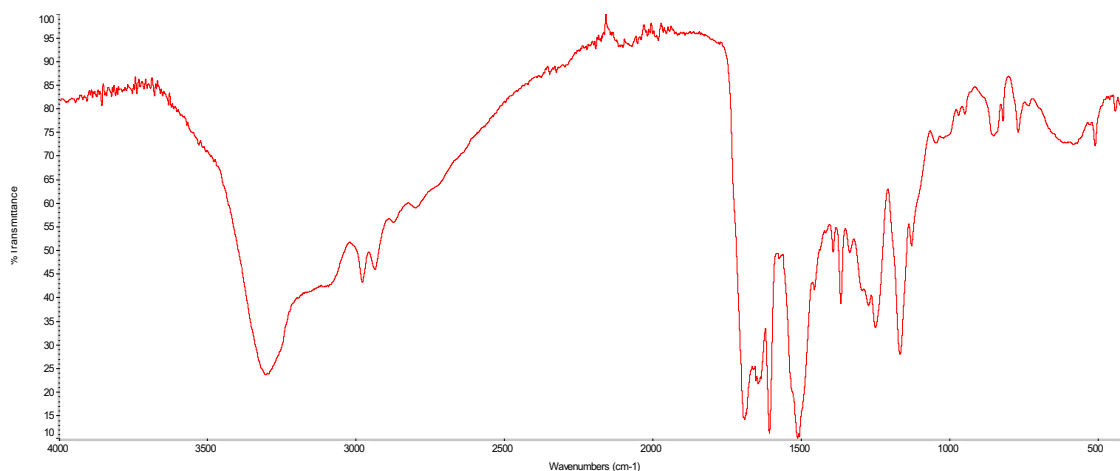


^{13}C NMR Spectrum (CDCl_3)

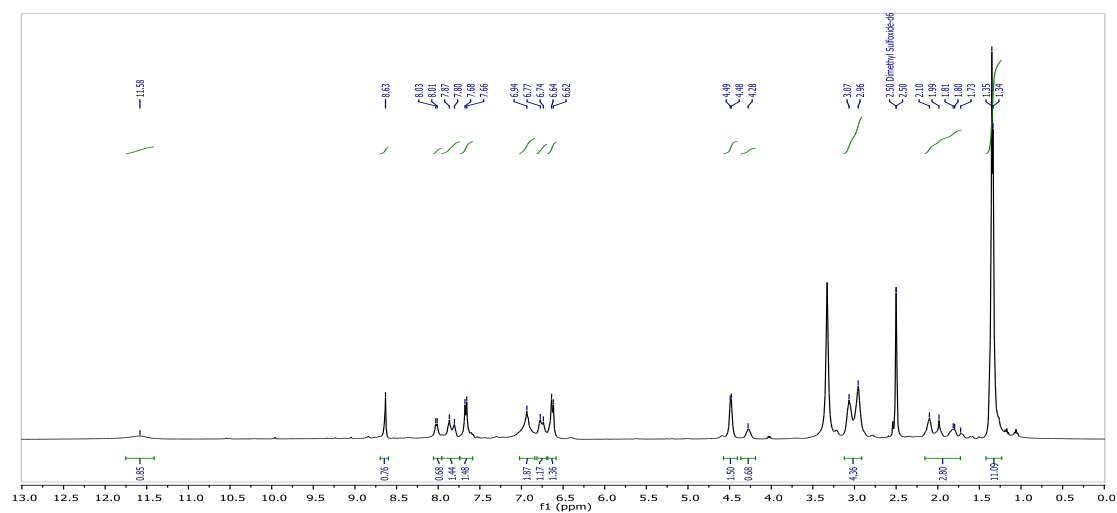


A.6 *N*-Boc-ethylenediamine-folate (4)

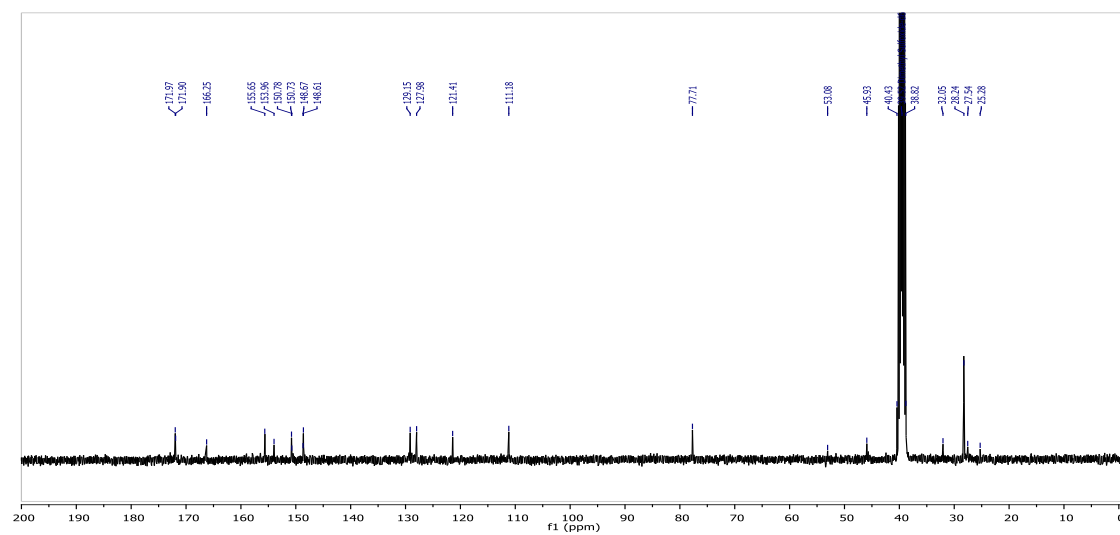
IR Spectrum



¹H NMR Spectrum (DMSO)

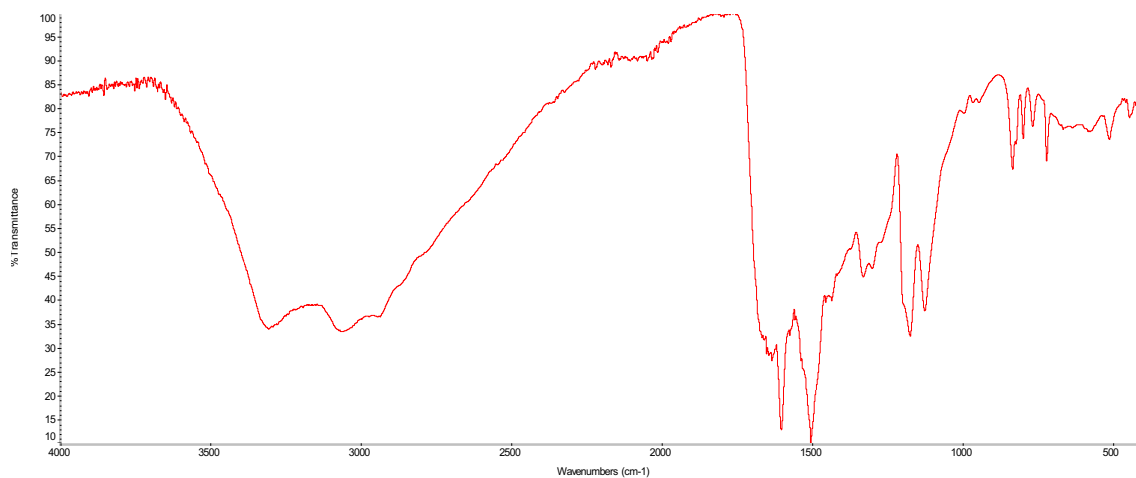


¹³C NMR Spectrum (DMSO)

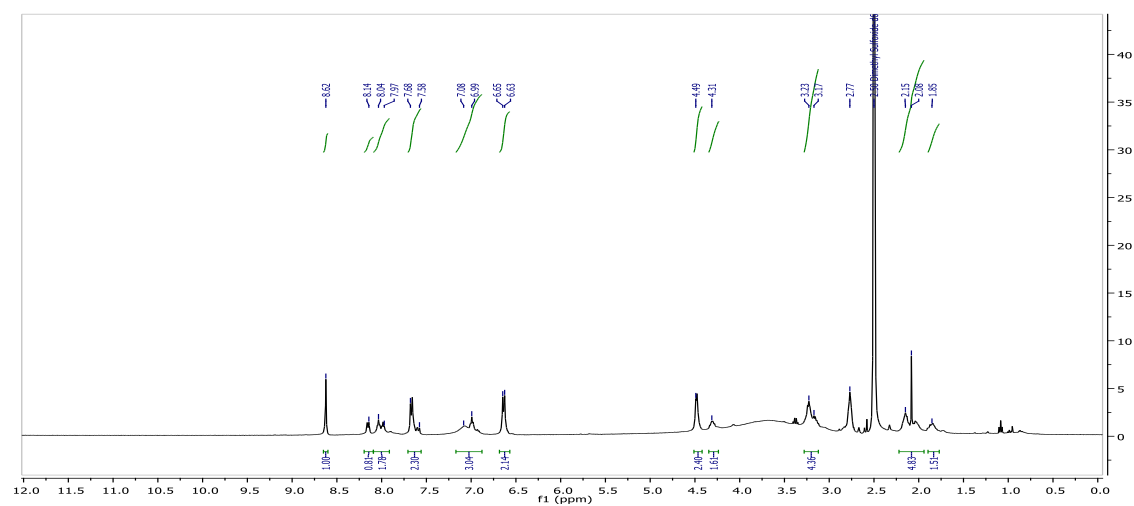


A.7 Folate-Ethylenediamine (5)

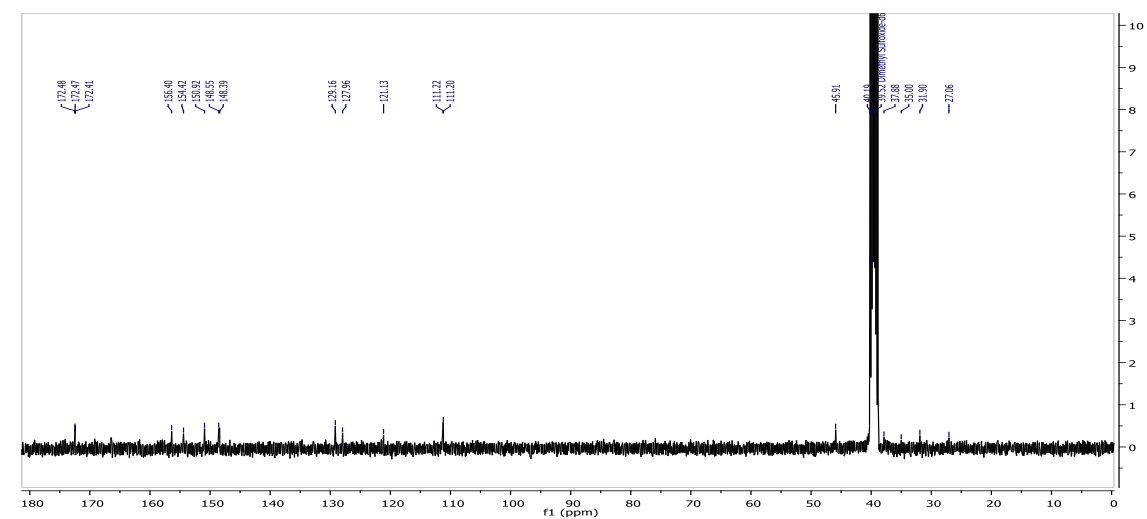
IR Spectrum



¹H NMR Spectrum (DMSO)

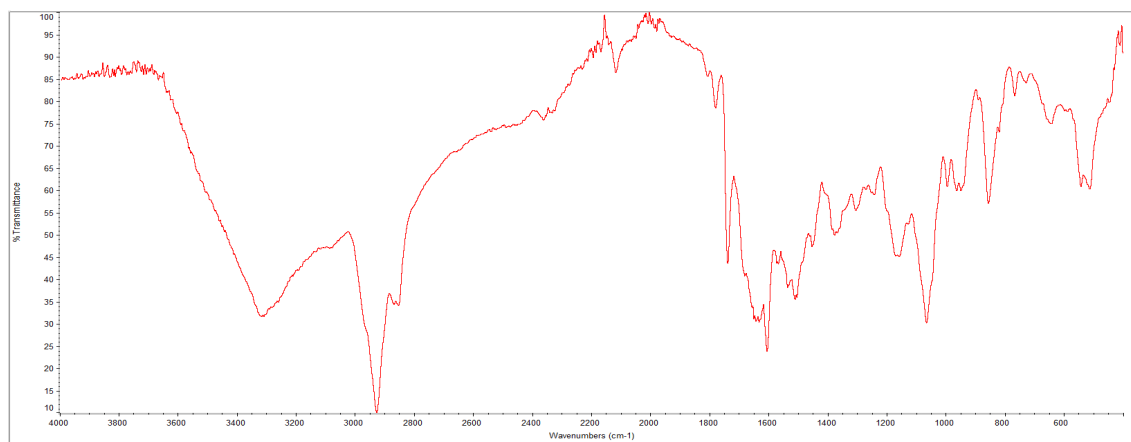


¹³C NMR Spectrum (DMSO)

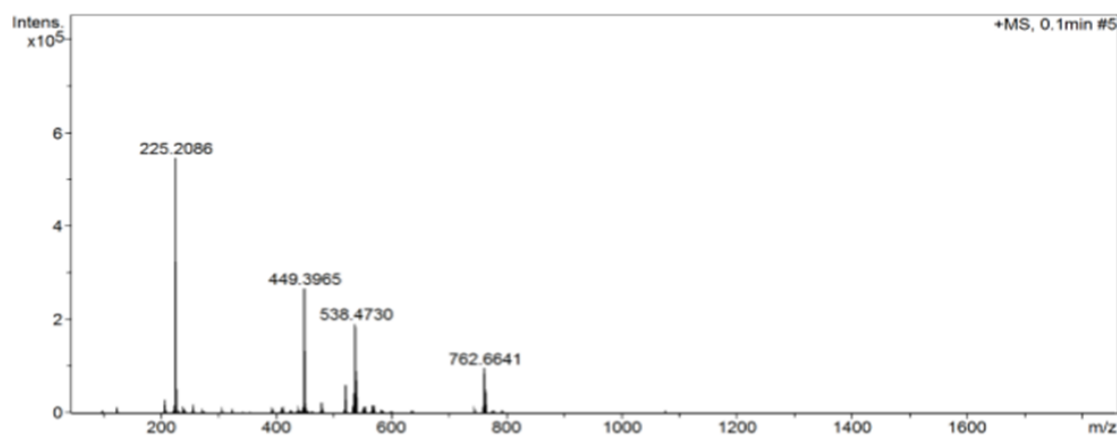


A.8 Folate-Ethylenediamine-UA (6)

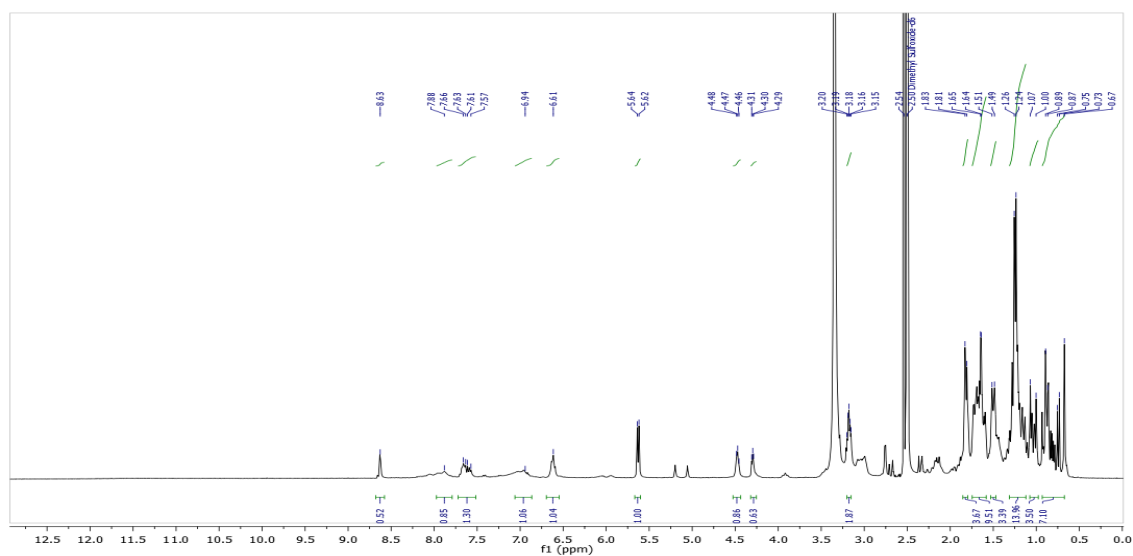
IR Spectrum



Mass Spectrum

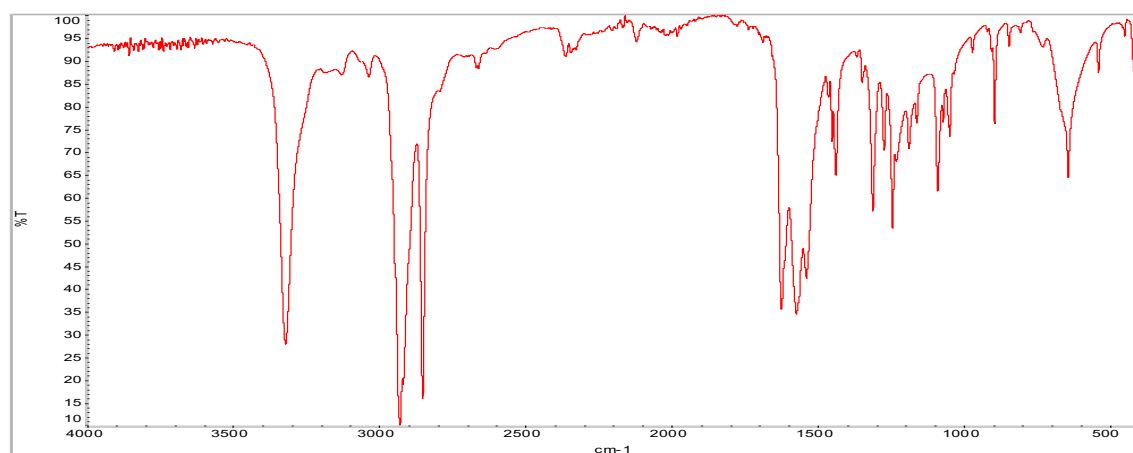


¹H NMR Spectrum (DMSO)

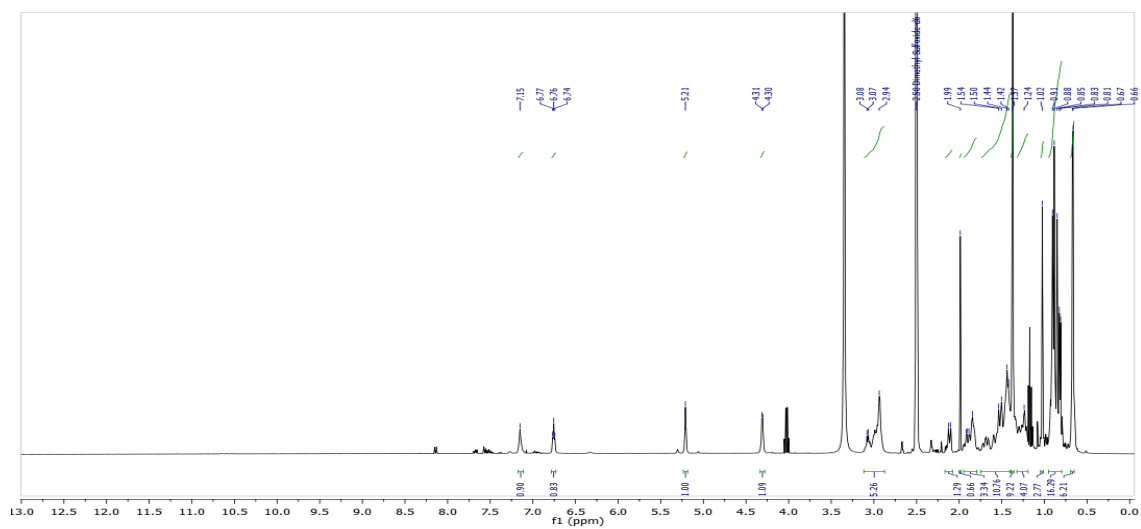


A.9 *N*-Boc-ethylenediamine-Ursolic Acid (DCC/NHS)

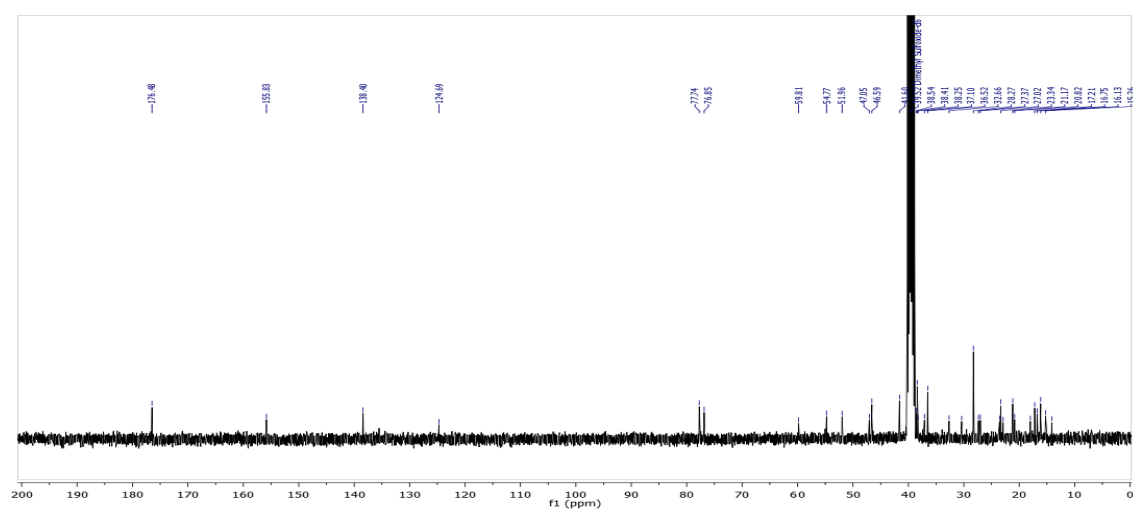
IR Spectrum



¹H NMR Spectrum (DMSO)



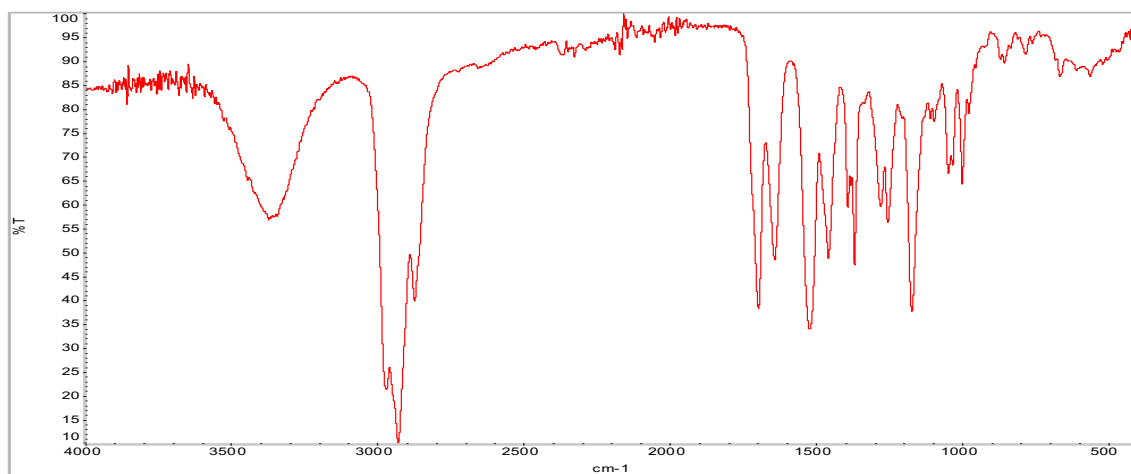
¹³C NMR Spectrum (DMSO)



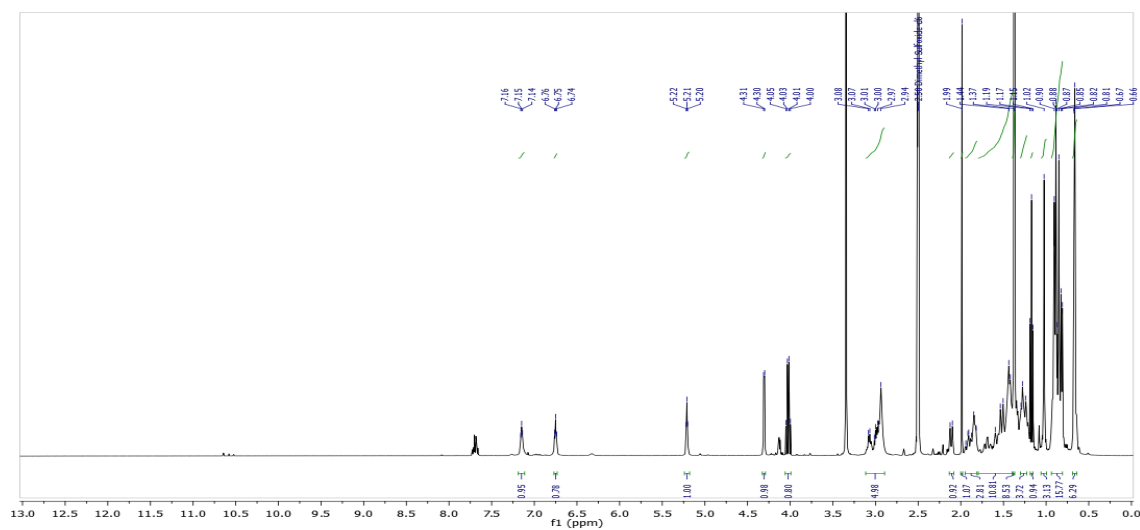
A.10

***N*-Boc-ethylenediamine-Ursolic Acid (EDC/HOBt)**

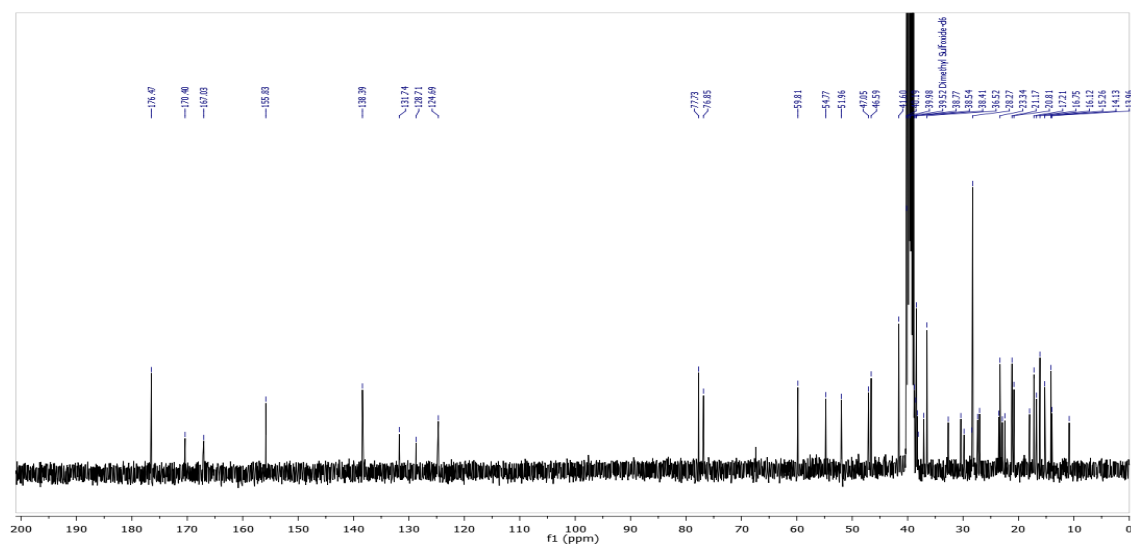
IR Spectrum



¹H NMR Spectrum (DMSO)

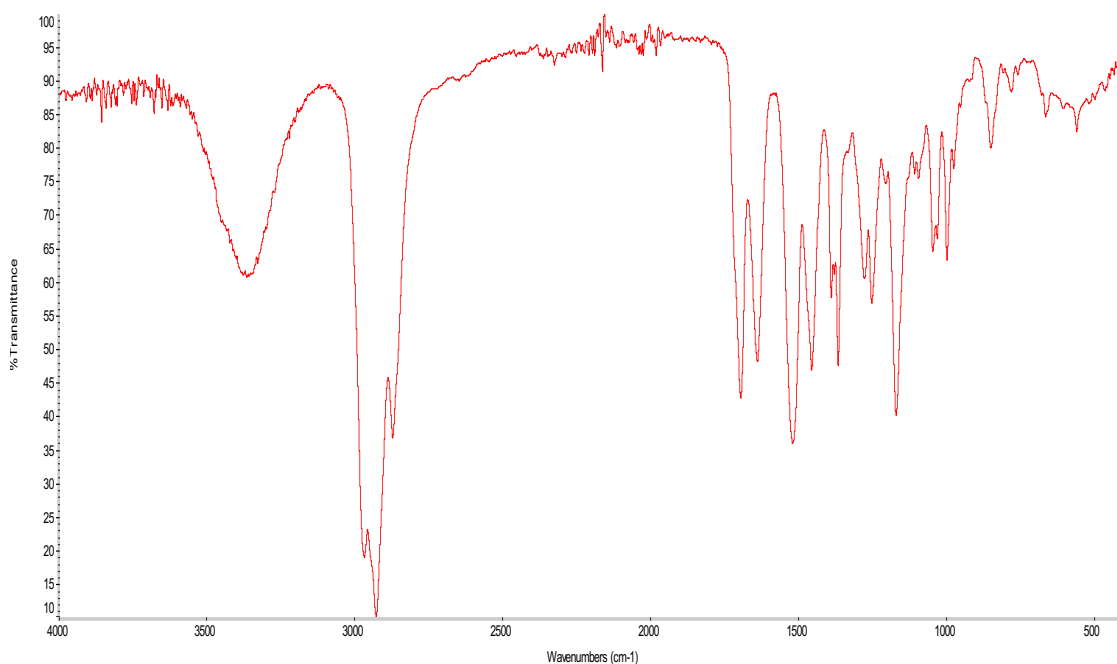


¹³C NMR Spectrum (DMSO)

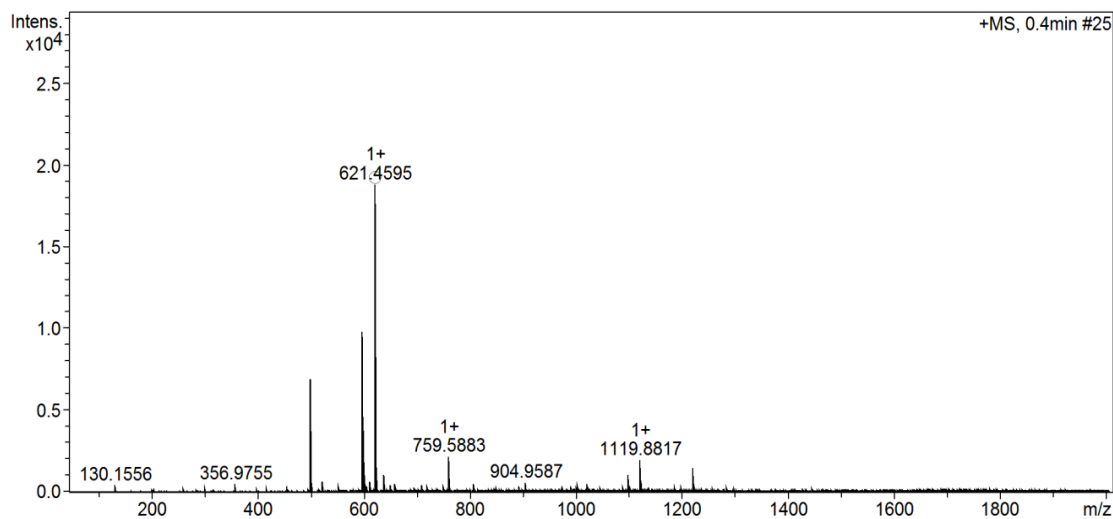


A.11 ***N*-Boc-ethylenediamine-Ursolic Acid (7)**

IR Spectrum

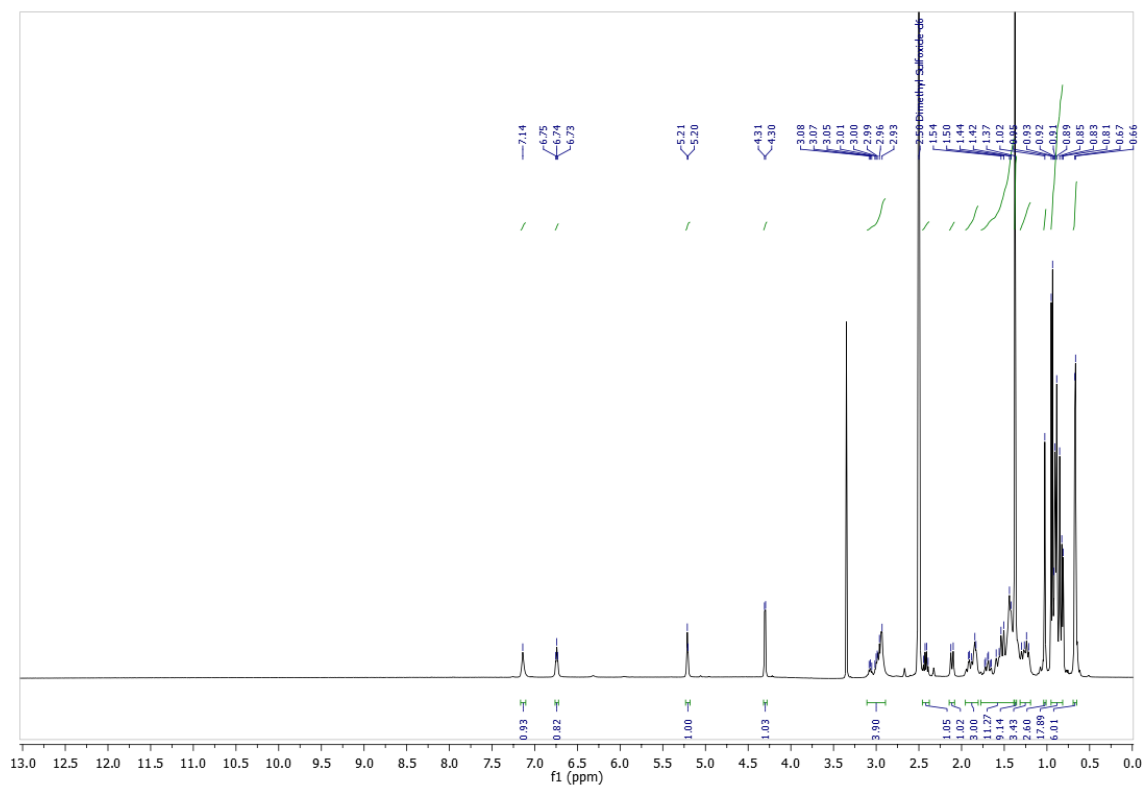


Mass Spectrum

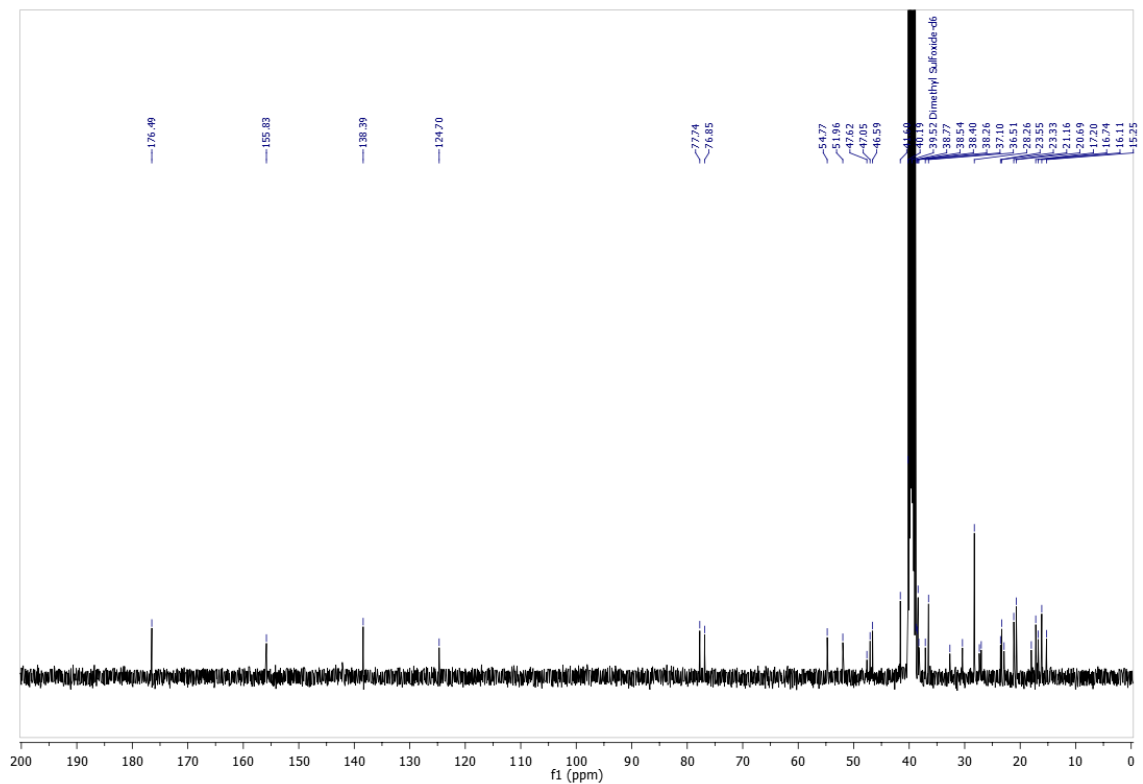


Meas. m/z	#	Ion Formula	m/z	err [mDa]	err [ppm]	rdb	N-Rule	e ⁻ Conf	mSigma
621.459493	1	C ₃₇ H ₆₂ N ₂ NaO ₄	621.460179	0.7	1.1	7.5	ok	even	3.4

¹H NMR Spectrum (DMSO)

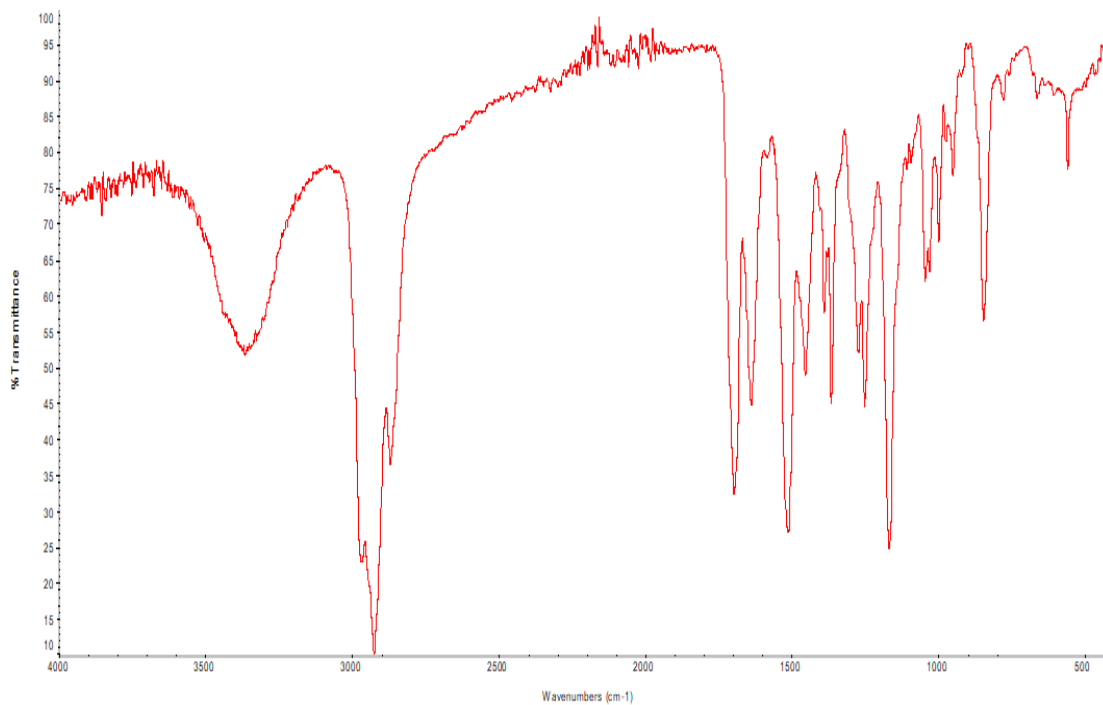


¹³C NMR Spectrum (DMSO)

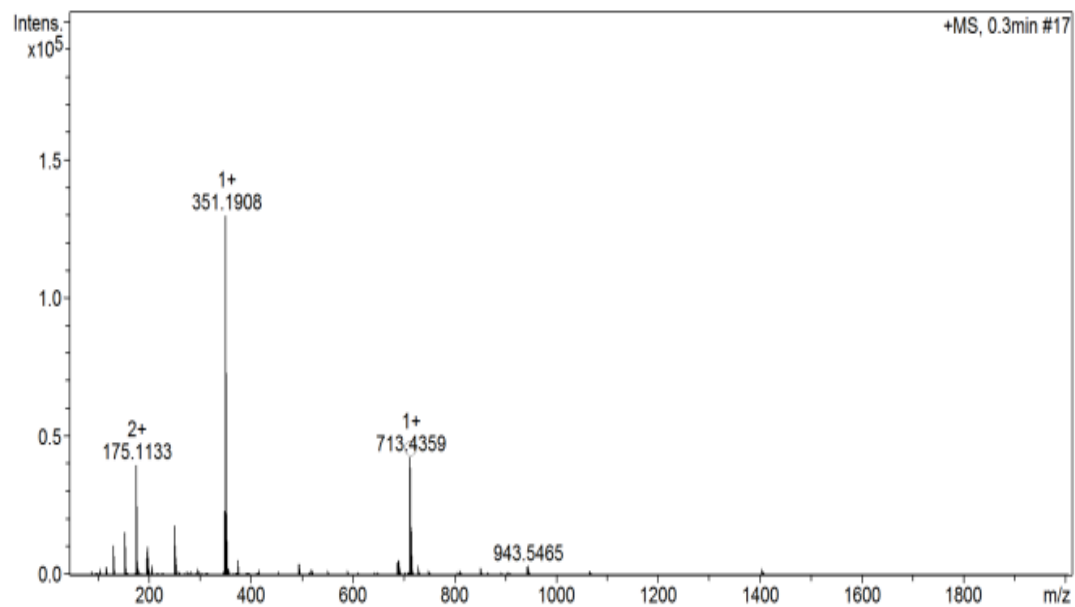


A.12 *N*-Boc-cystamine dihydrochloride-Ursolic Acid (8)

IR Spectrum

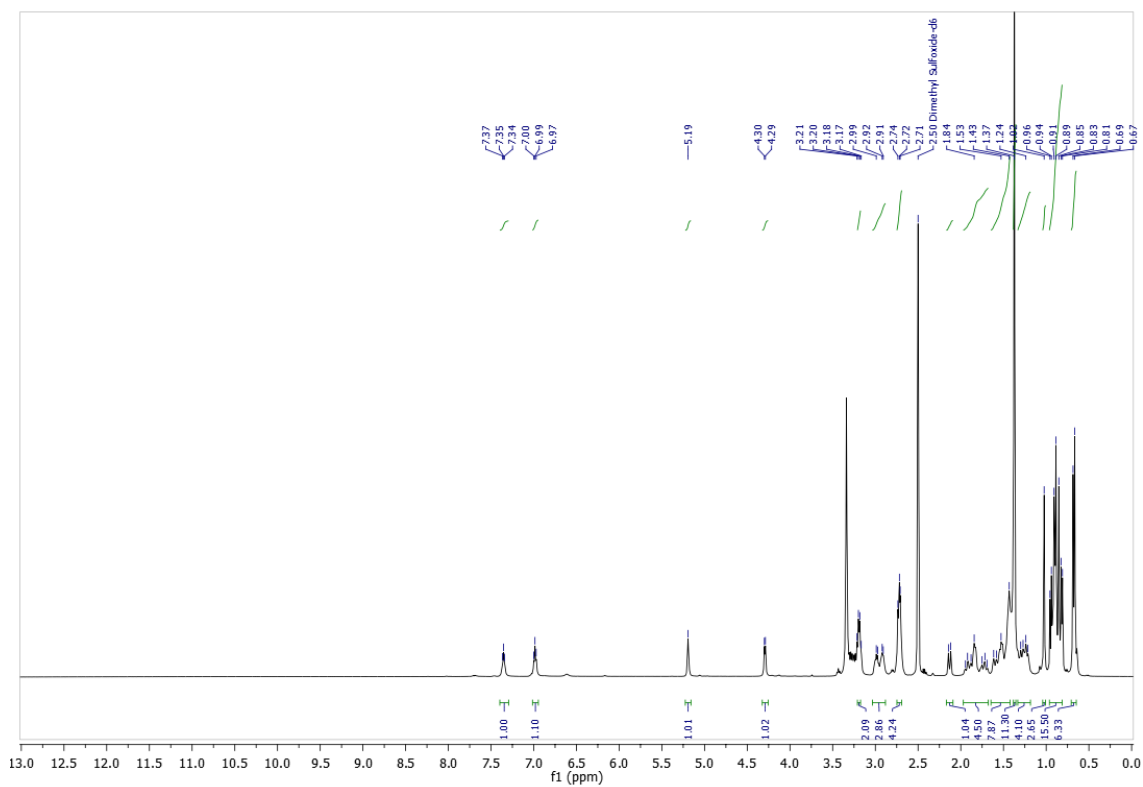


Mass Spectrum

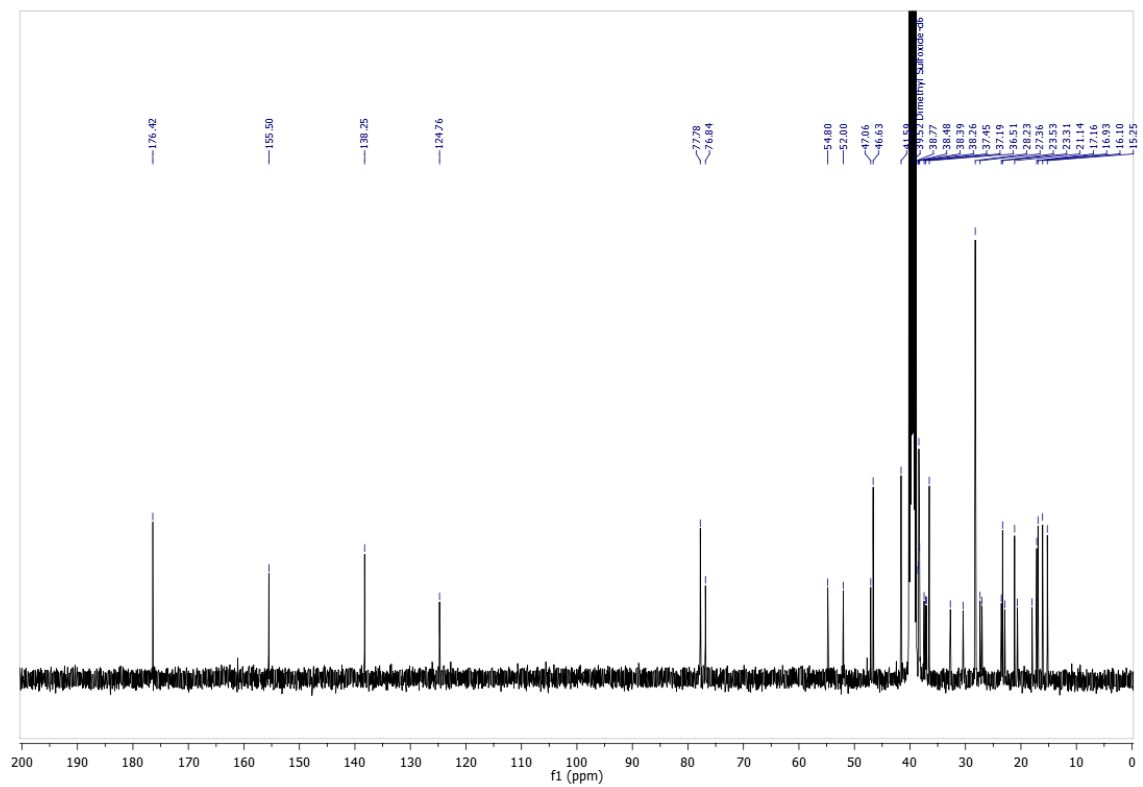


Meas. m/z	#	Ion Formula	m/z	err [mDa]	err [ppm]	rdb	N-Rule	e ⁻ Conf	mSigma
713.435876	1	C ₃₉ H ₆₆ N ₂ NaO ₄ S ₂	713.435621	-0.3	-0.4	7.5	ok	even	25.2

¹H NMR Spectrum (DMSO)

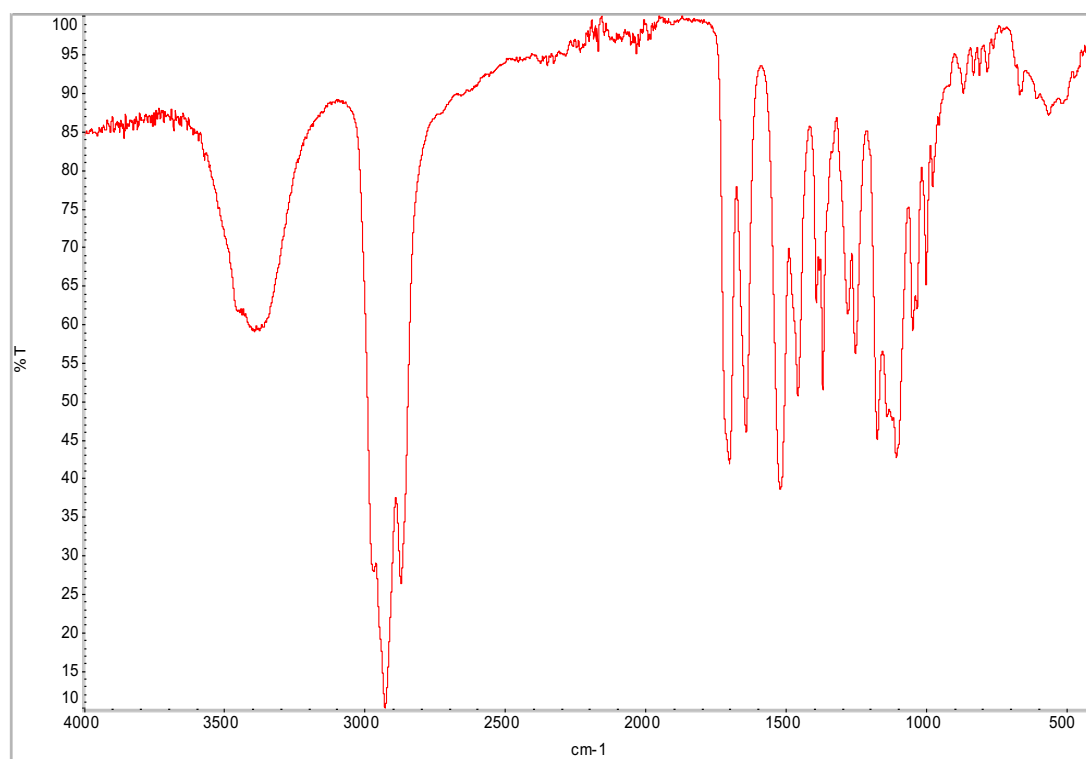


¹³C NMR Spectrum (DMSO)

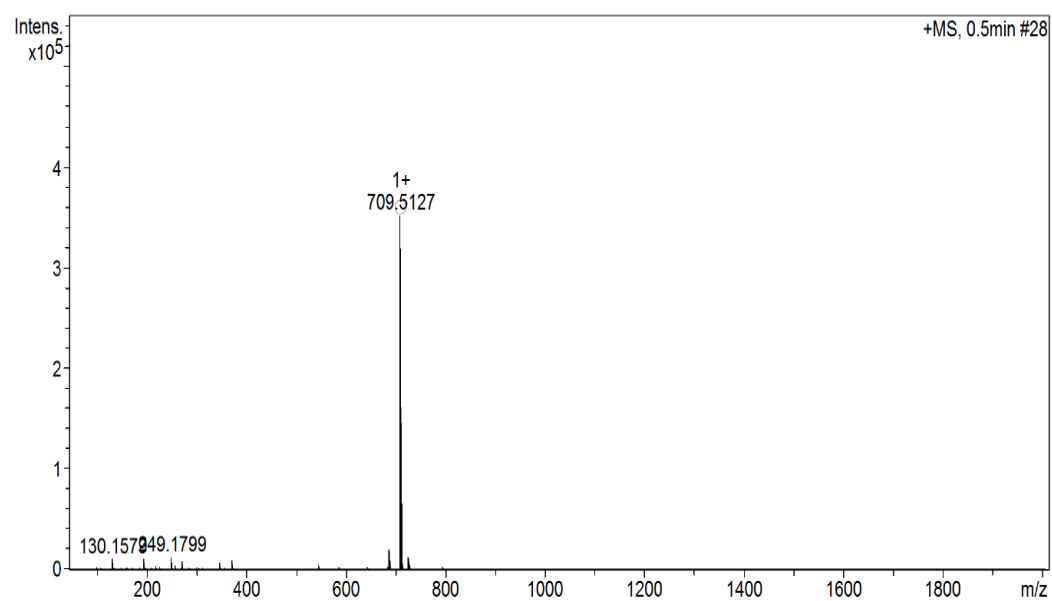


A.13 *N*-Boc-2,2'-(ethylenedioxy)bis(ethylamine)-Ursolic Acid (9)

IR Spectrum

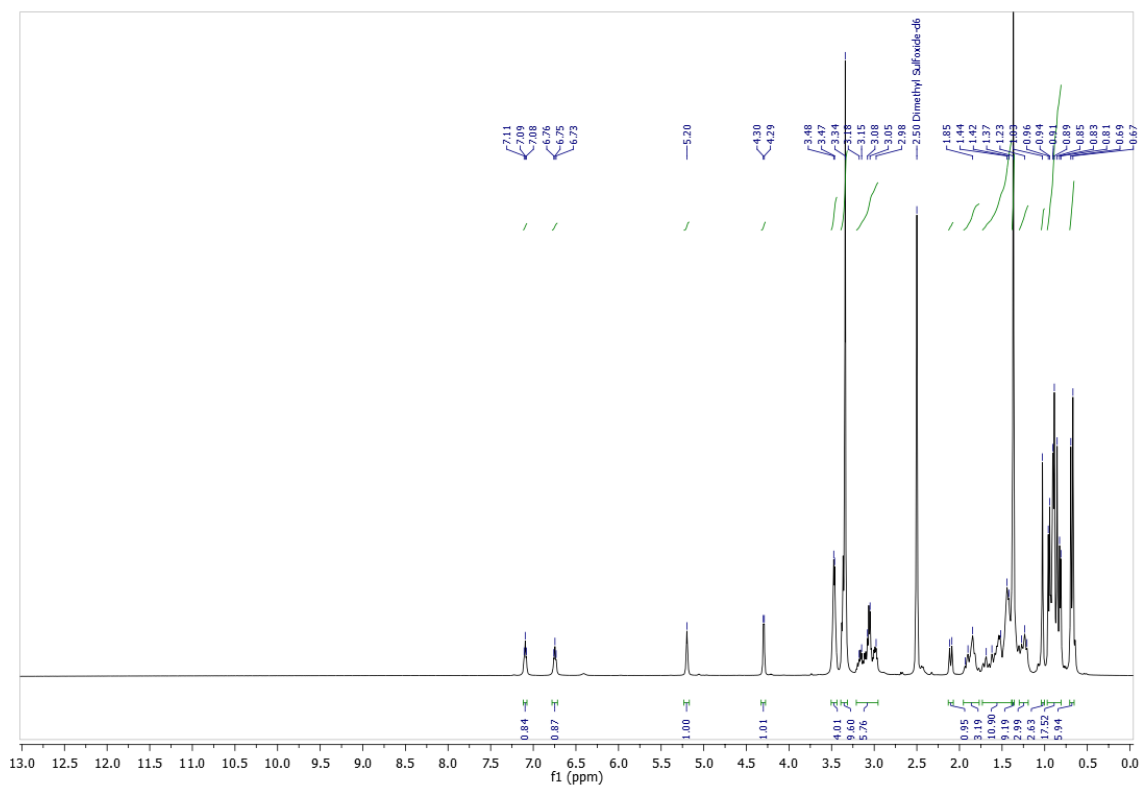


Mass Spectrum

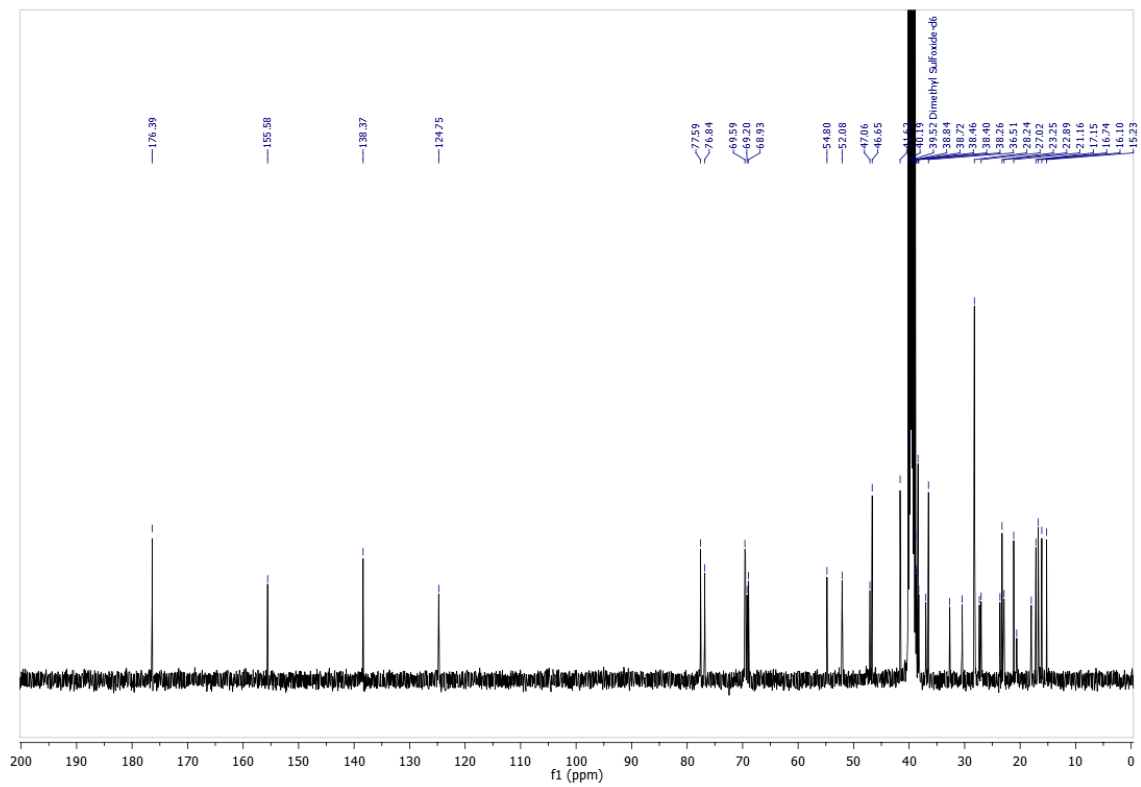


Meas. m/z	#	Ion Formula	m/z	err [mDa]	err [ppm]	rdb	N-Rule	e ⁻ Conf	mSigma
709.512682	1	C ₄₁ H ₇₀ N ₂ NaO ₆	709.512609	0.1	0.1	7.5	ok	even	3.9

¹H NMR Spectrum (DMSO)

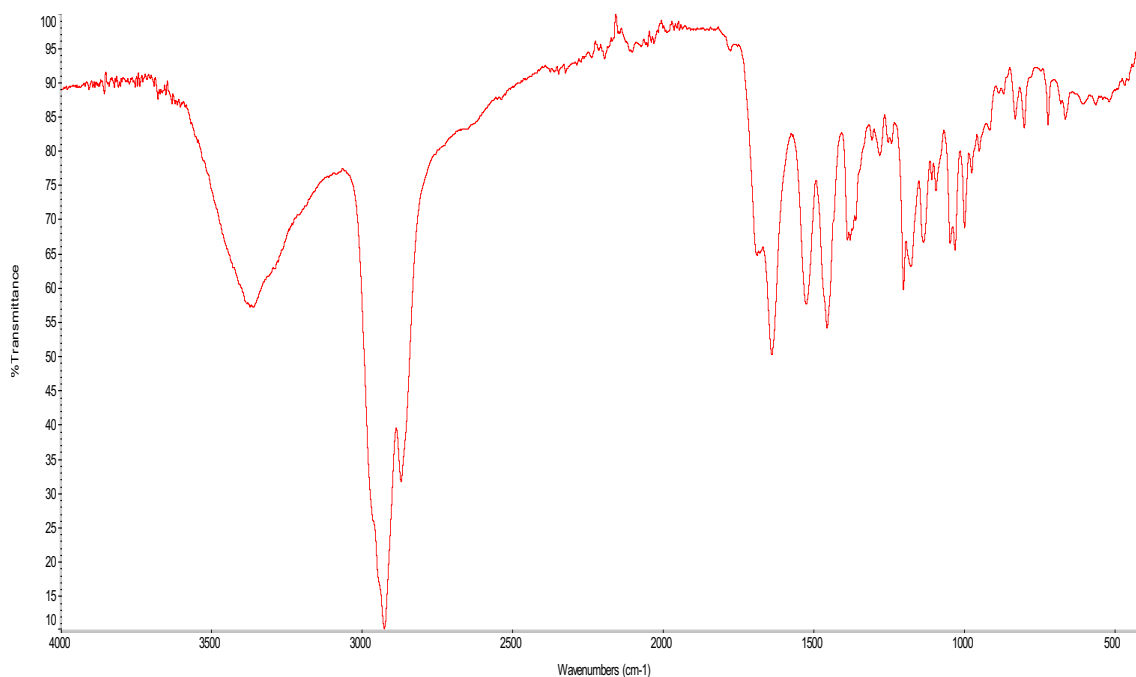


¹³C NMR Spectrum (DMSO)

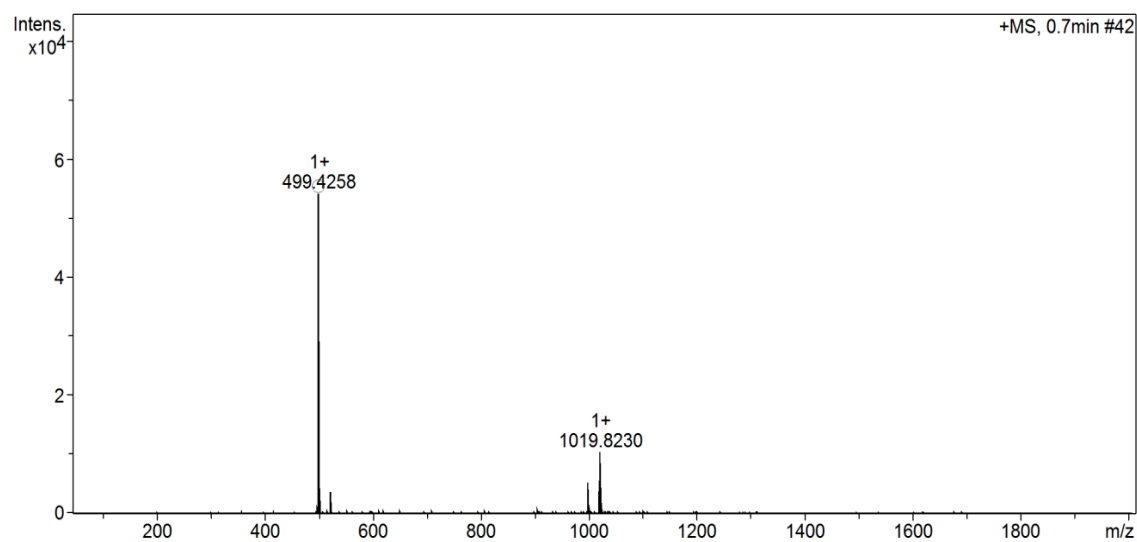


A.14 UA-Ethylenediamine (10)

IR Spectrum

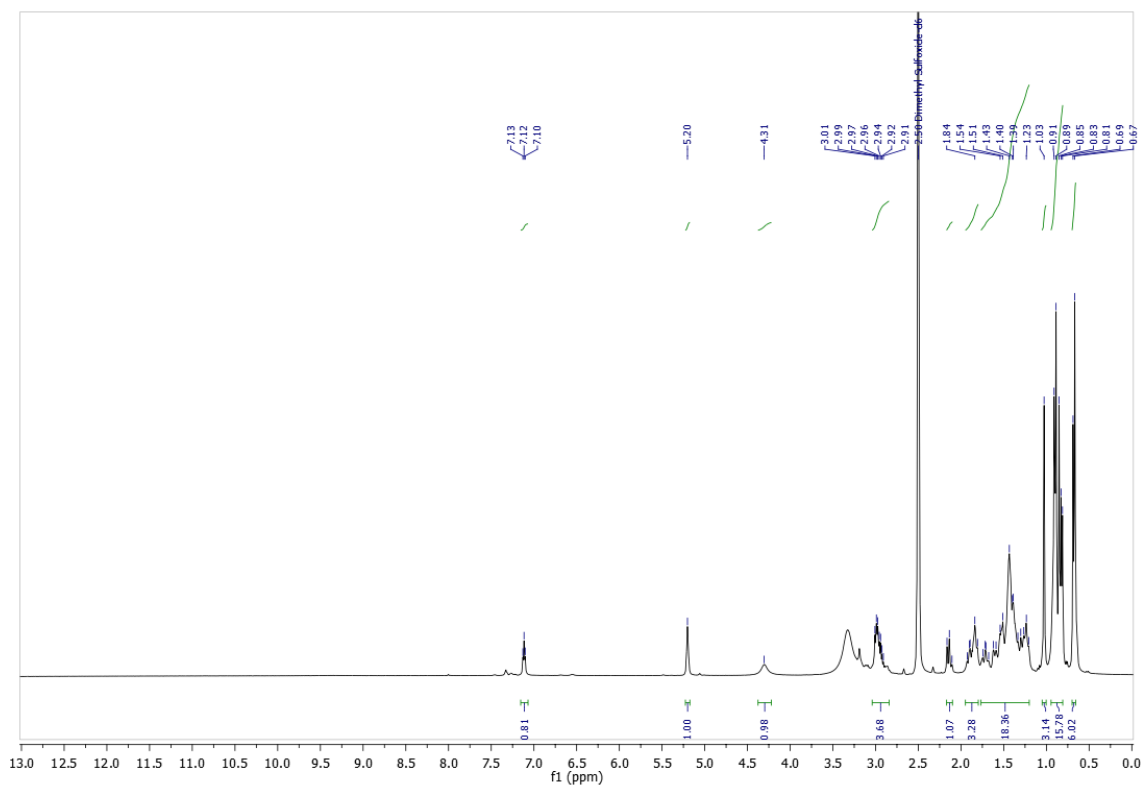


Mass Spectrum

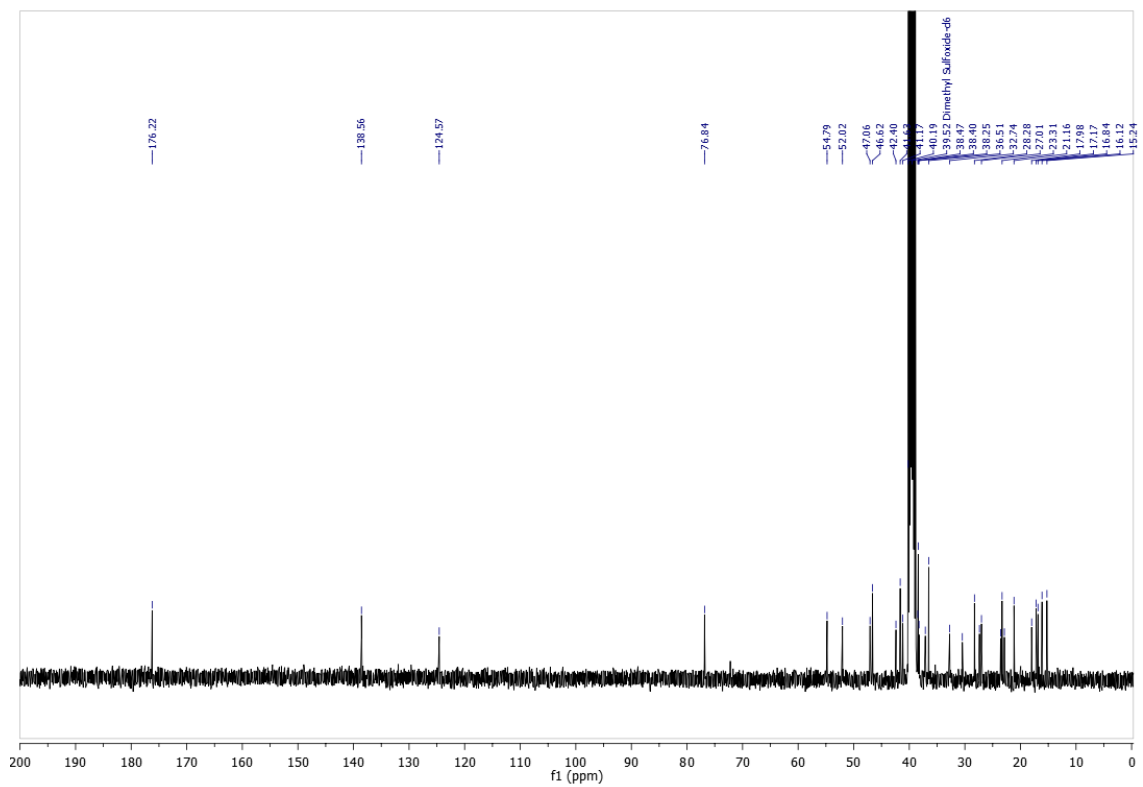


Meas. m/z	#	Ion Formula	m/z	err [mDa]	err [ppm]	rdb	N-Rule	e ⁻ Conf	mSigma
499.425819	1	C32H55N2O2	499.425805	-0.0	-0.0	6.5	ok	even	18.8

¹H NMR Spectrum (DMSO)

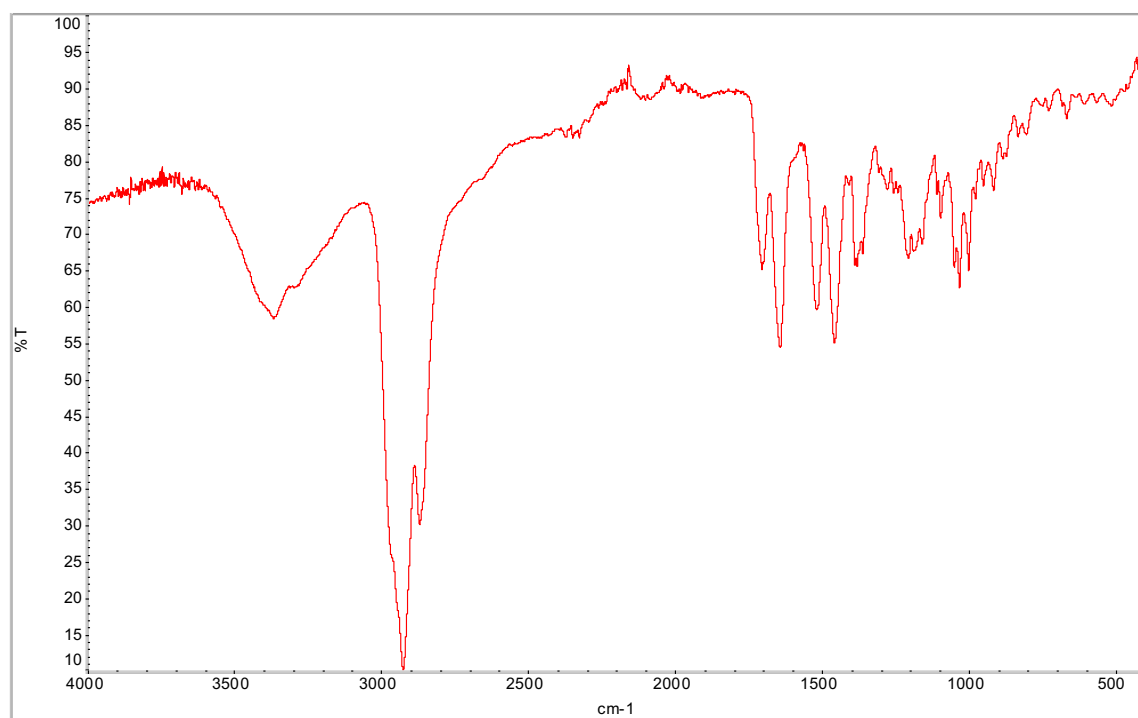


¹³C NMR Spectrum (DMSO)

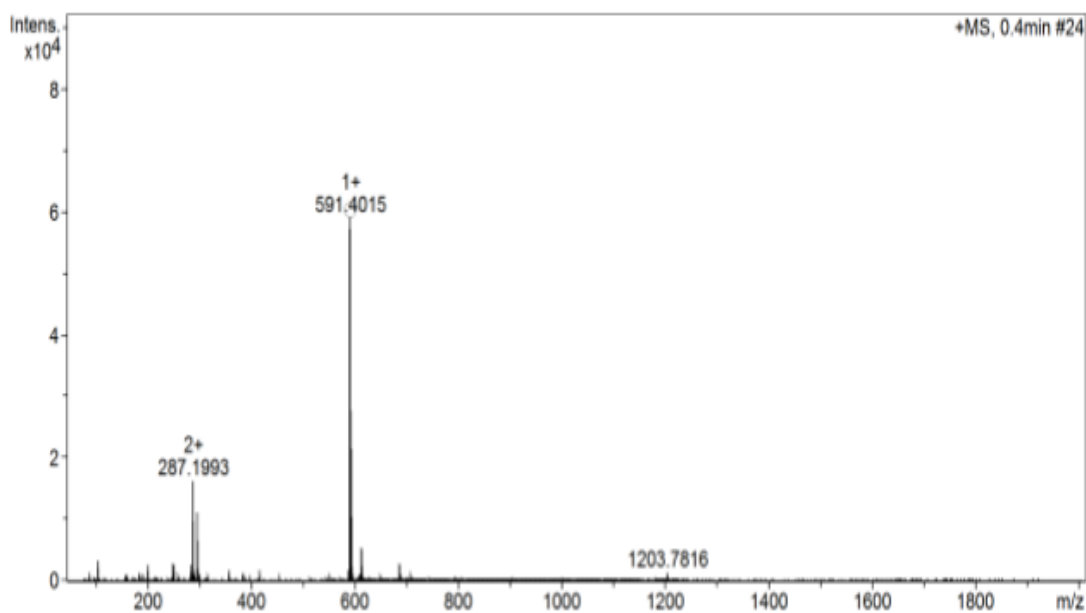


A.15 UA-Cystamine dihydrochloride (11)

IR Spectrum

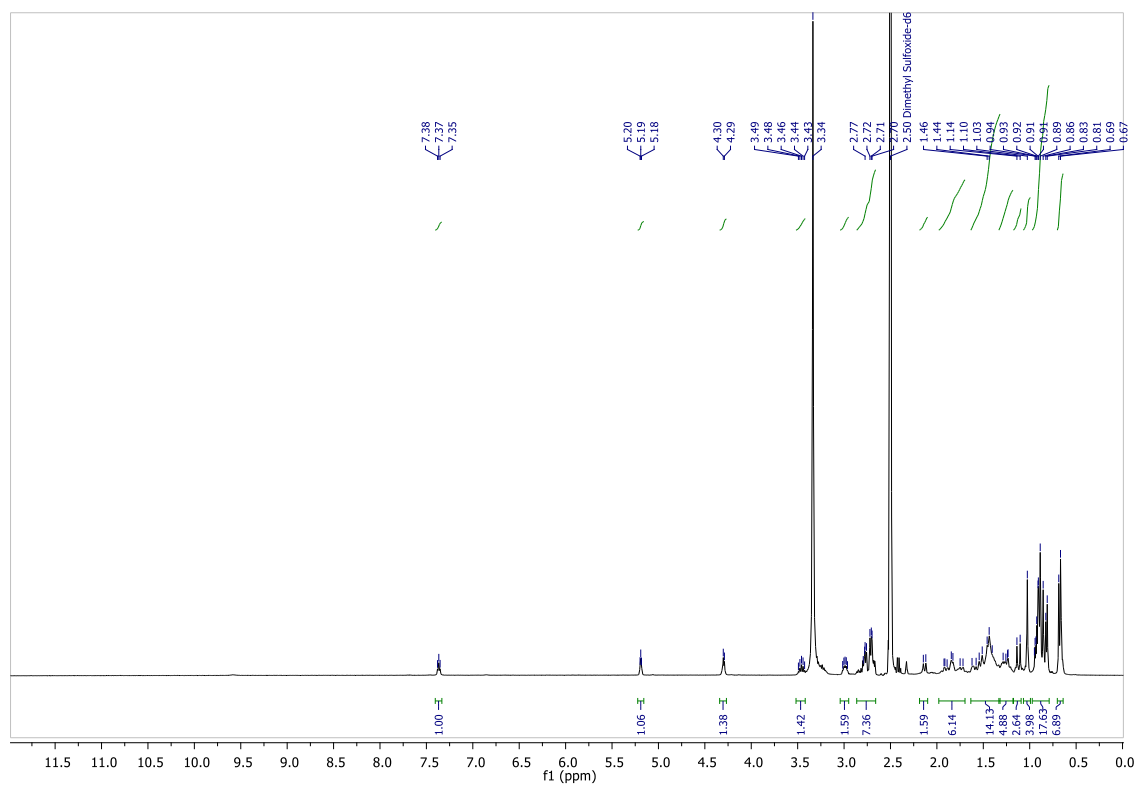


Mass Spectrum

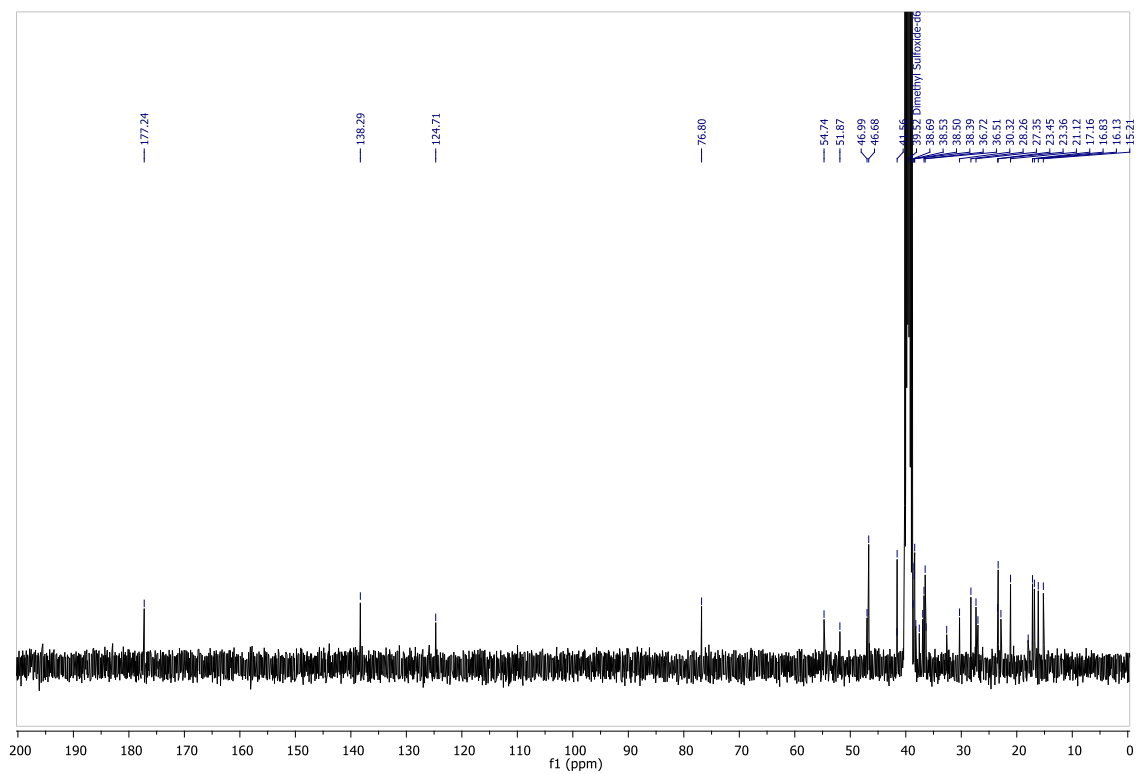


Meas. m/z	#	Ion Formula	m/z	err [mDa]	err [ppm]	rdb	N-Rule	e ⁻ Conf	mSigma
591.401455	1	C ₃₄ H ₅₉ N ₂ O ₂ S ₂	591.401248	-0.2	-0.4	6.5	ok	even	16.5

¹H NMR Spectrum (DMSO)

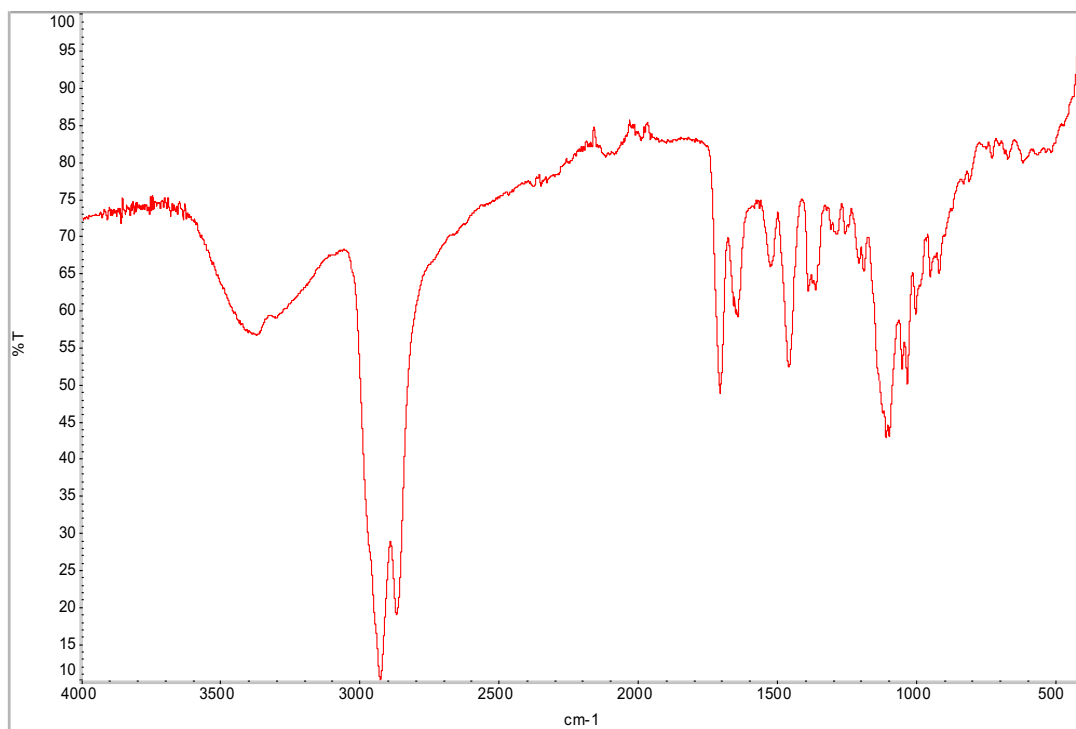


¹³C NMR Spectrum (DMSO)

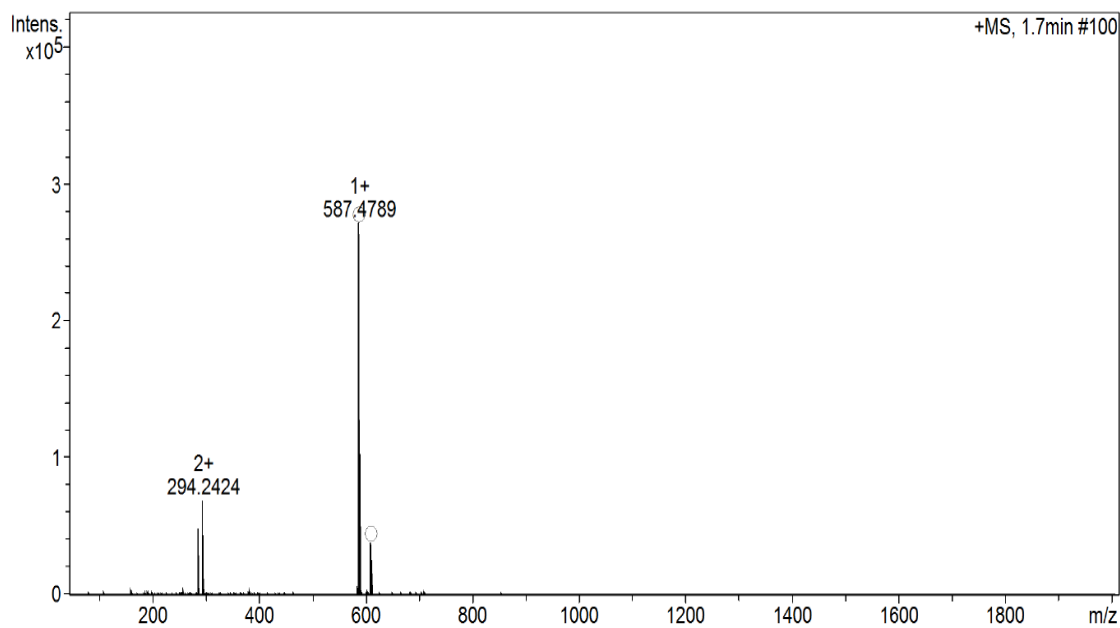


A.16 UA-N-Boc-2,2'-(ethylenedioxy)bis(ethylamine) (12)

IR Spectrum

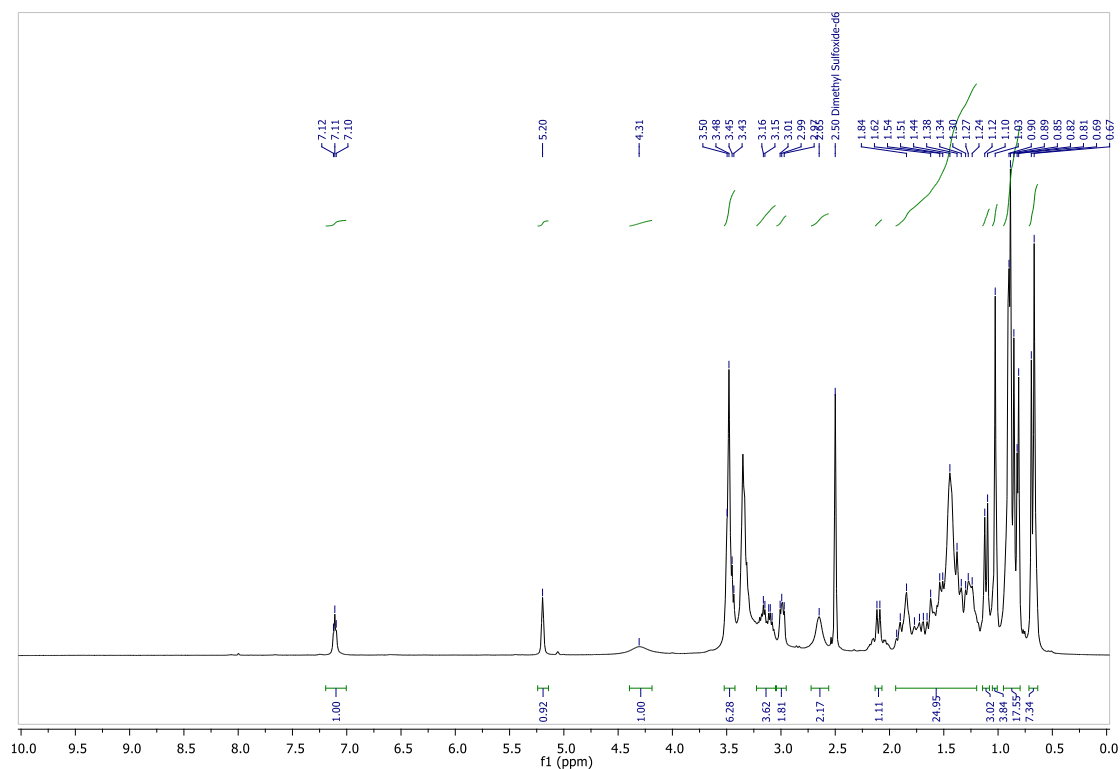


Mass Spectrum

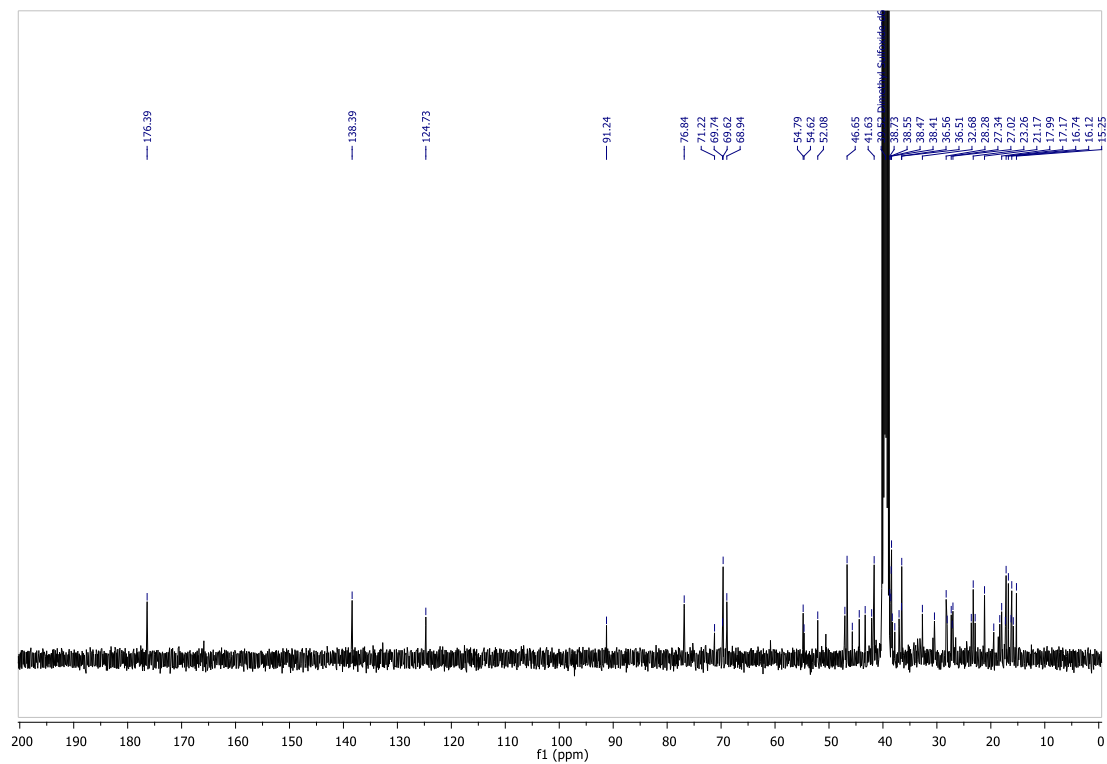


Meas. m/z	#	Ion Formula	m/z	err [mDa]	err [ppm]	rdb	N-Rule	e ⁻ Conf	mSigma
587.478935	1	C ₃₆ H ₆₃ N ₂ O ₄	587.478235	-0.7	-1.2	6.5	ok	even	9.5
609.459548	1	C ₃₆ H ₆₂ N ₂ NaO ₄	609.460179	0.6	1.0	6.5	ok	even	9.9

¹H NMR Spectrum (DMSO)

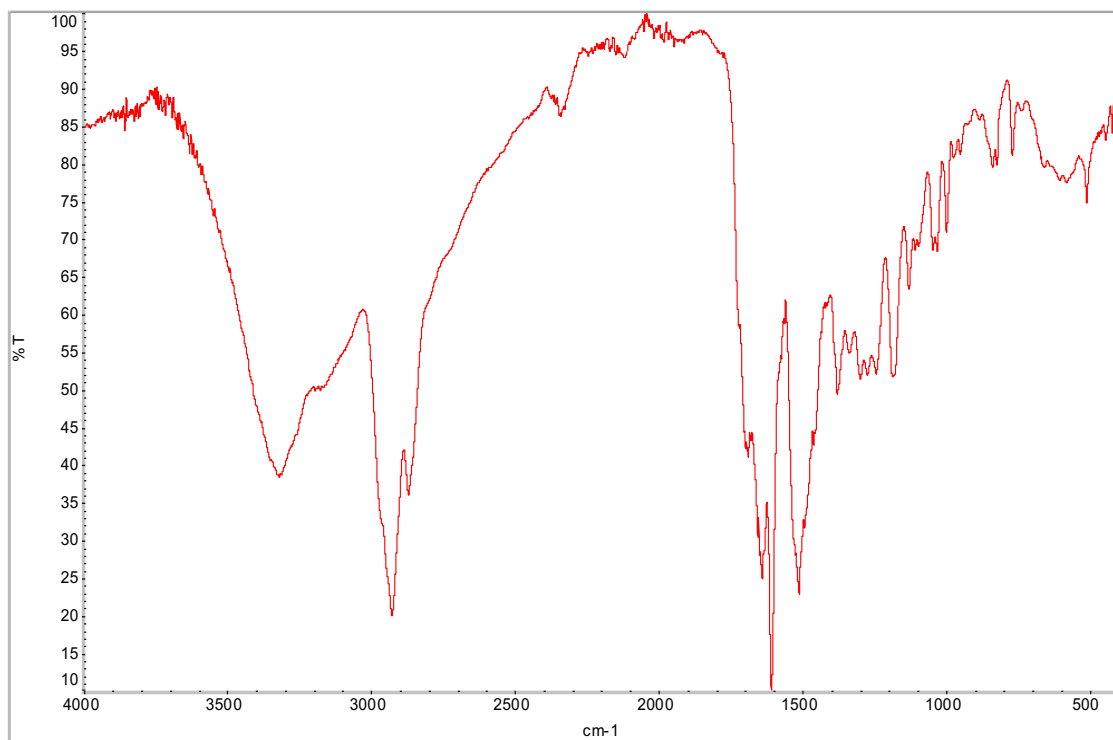


¹³C NMR Spectrum (DMSO)

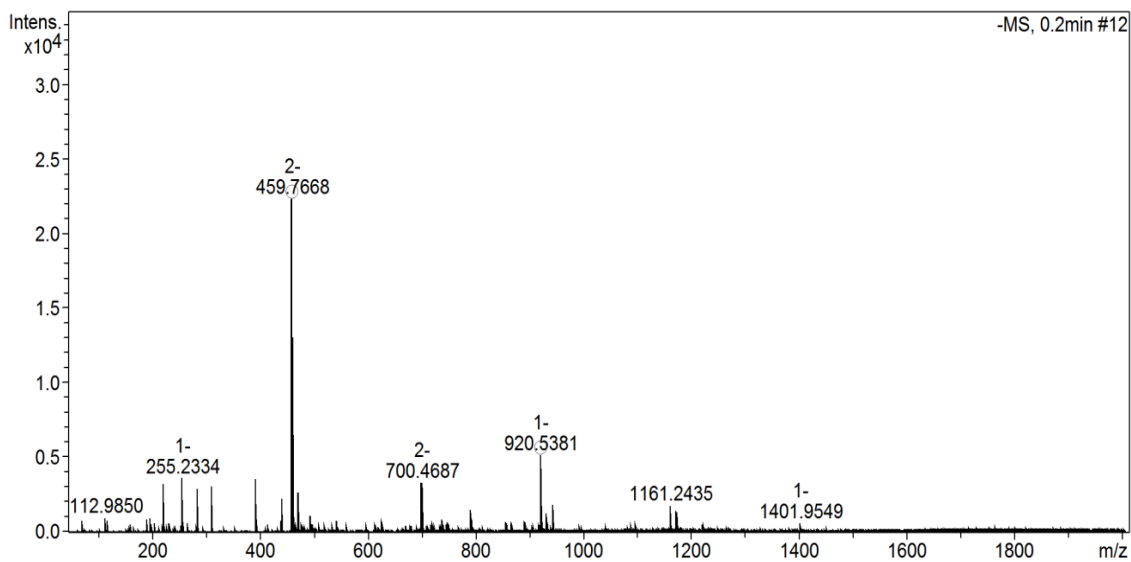


A.17 Ursolic Acid-Ethylenediamine-Folate (13)

IR Spectrum

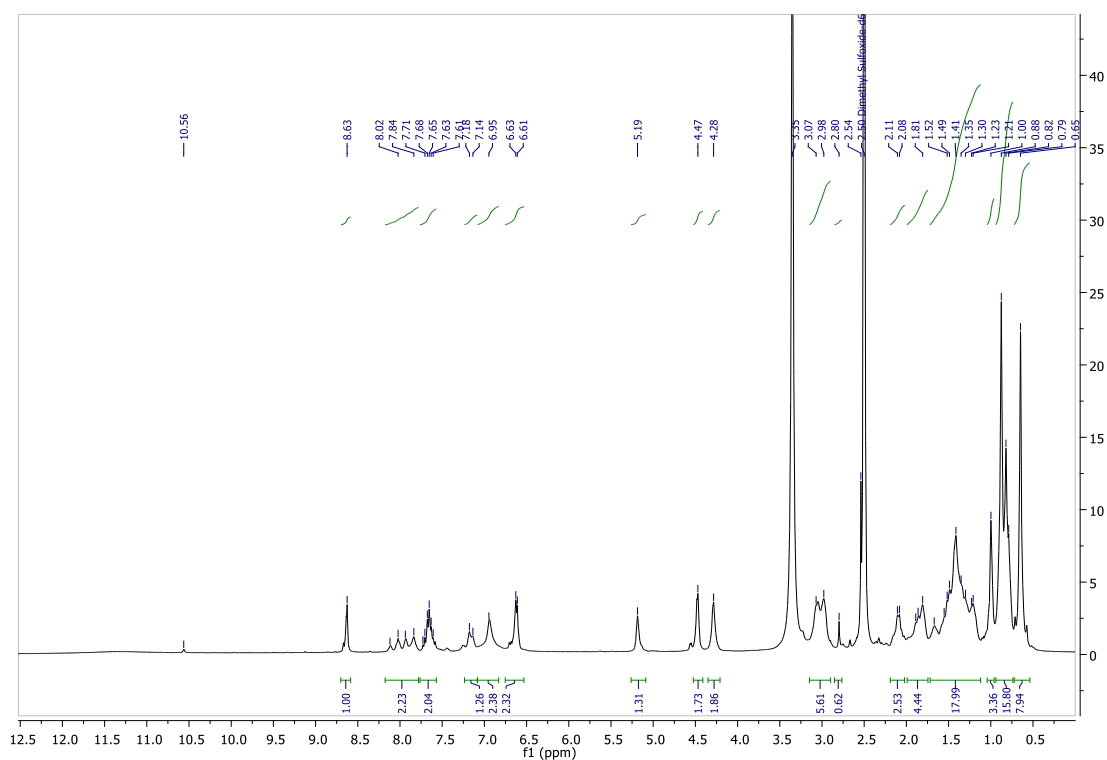


Mass Spectrum

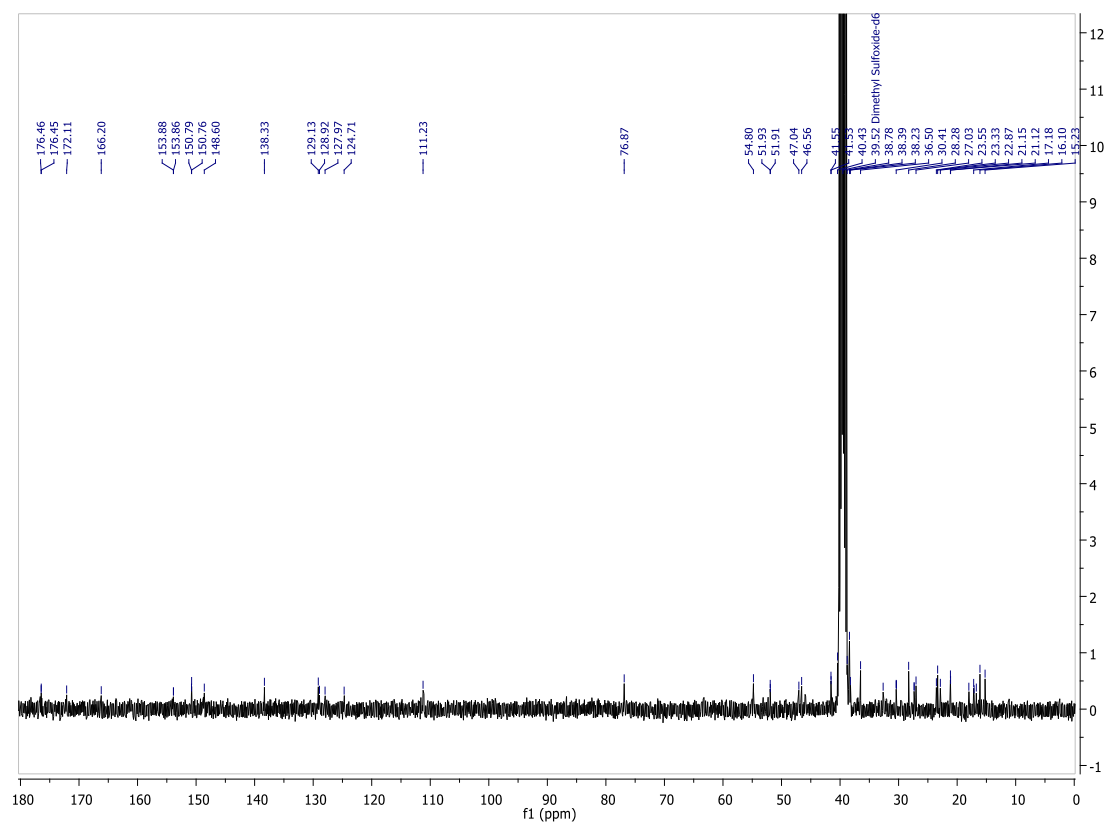


Meas. m/z	#	Ion Formula	m/z	err [mDa]	err [ppm]	rdb	N-Rule	e ⁻ Conf	mSigma
459.766753	1	C ₅₁ H ₆₉ N ₉ O ₇	459.766546	-0.2	-0.4	22.0	ok	even	6.1
920.538055	1	C ₅₁ H ₇₀ N ₉ O ₇	920.540369	2.3	2.5	21.5	ok	even	20.5

¹H NMR Spectrum (DMSO)

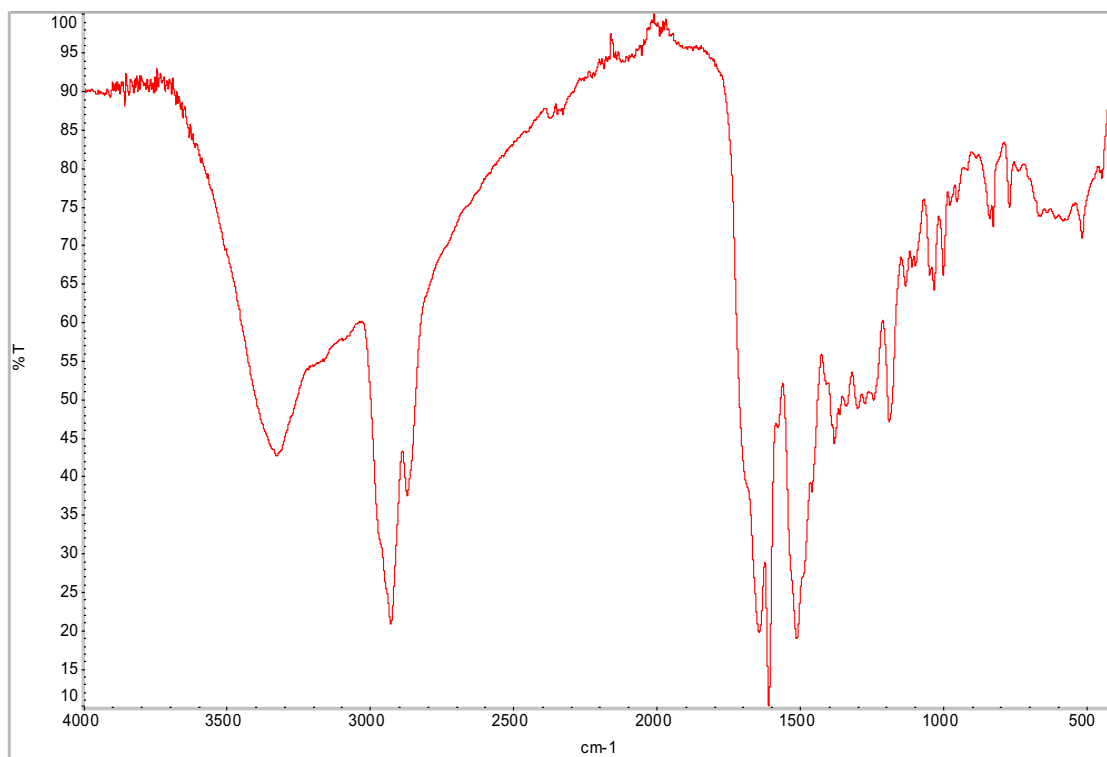


¹³C NMR Spectrum (DMSO)

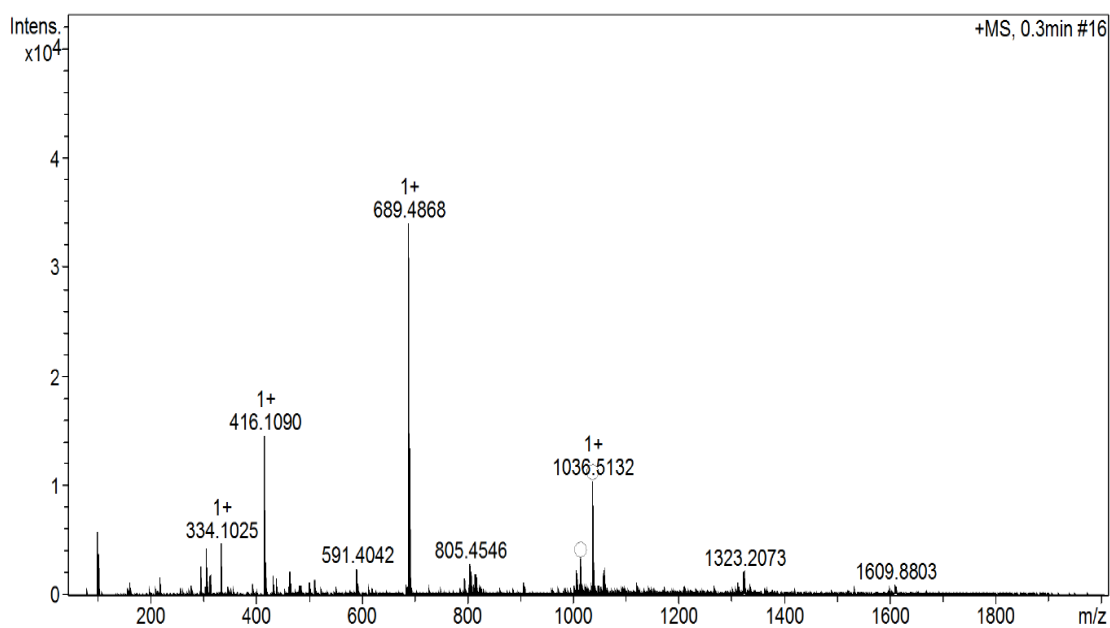


A.18 Ursolic Acid- Cystamine dihydrochloride -Folate (14)

IR Spectrum

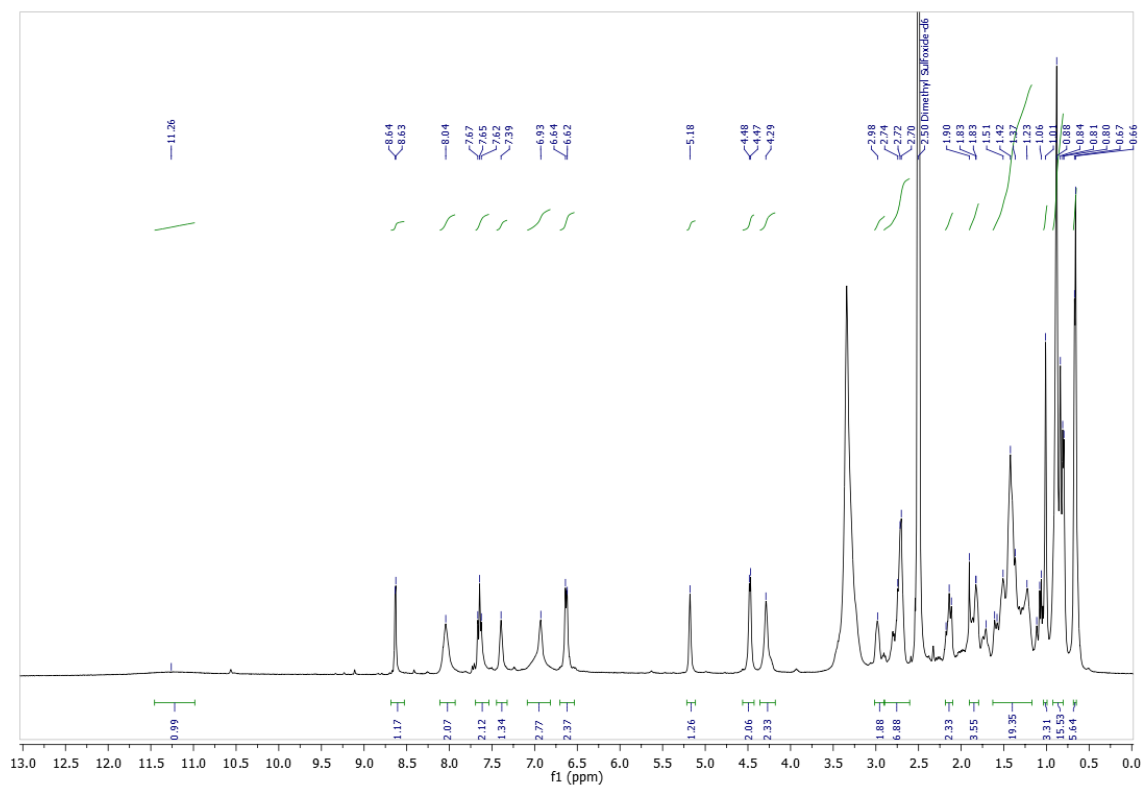


Mass Spectrum

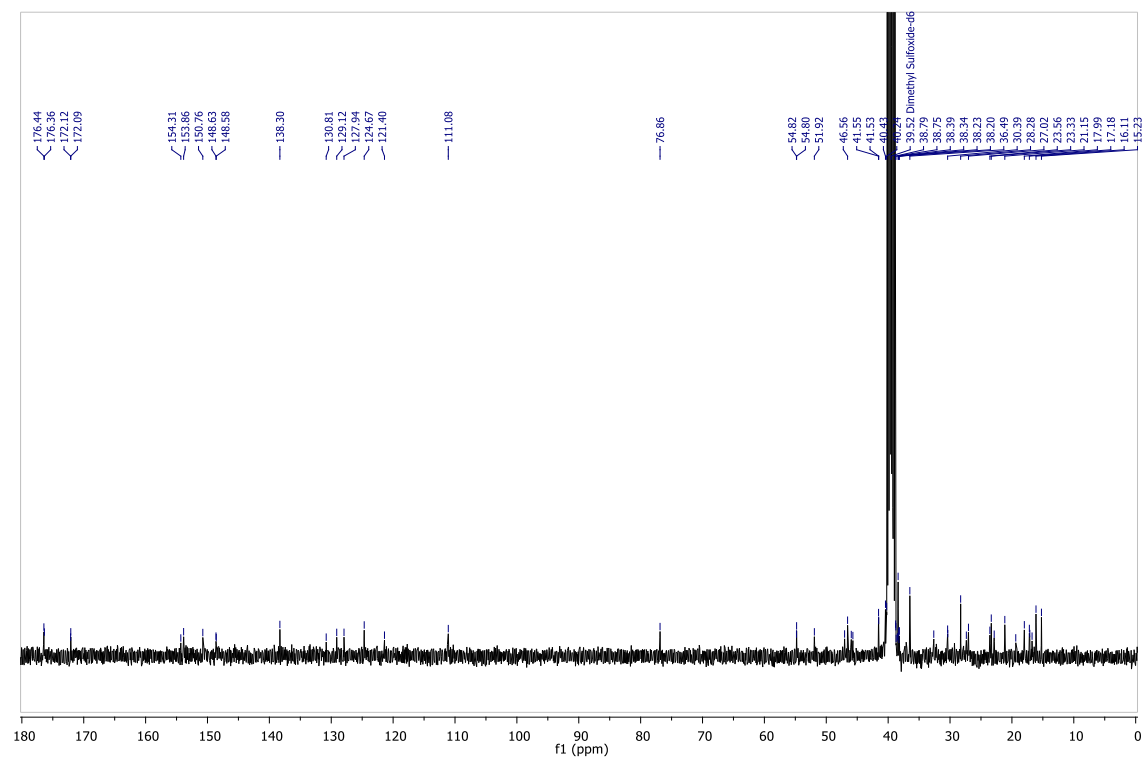


Meas. m/z	#	Ion Formula	m/z	err [mDa]	err [ppm]	rdb	N-Rule	e ⁻ Conf	mSigma
1014.527589	1	C53H76N9O7S2	1014.530364	-2.8	-2.7	20.5	ok	even	69.1
1036.513208	1	C53H75N9NaO7S2	1036.512308	-0.9	-0.9	20.5	ok	even	18.7

¹H NMR Spectrum (DMSO)



¹³C NMR Spectrum (DMSO)

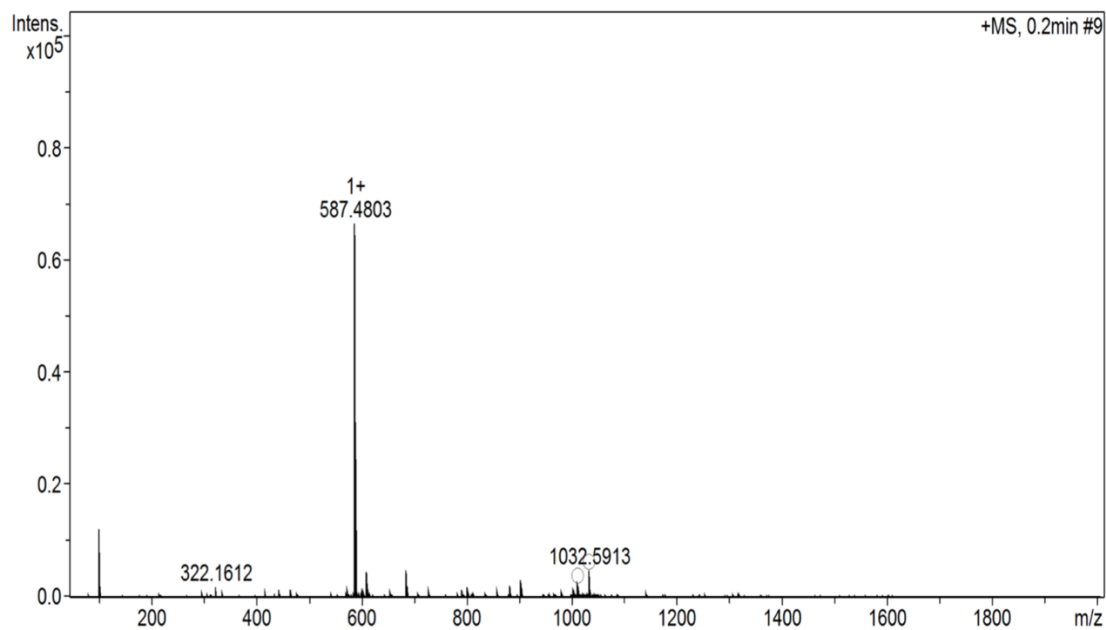


A.19 Ursolic Acid-Ethylenediamine-Folate (15)

IR Spectrum

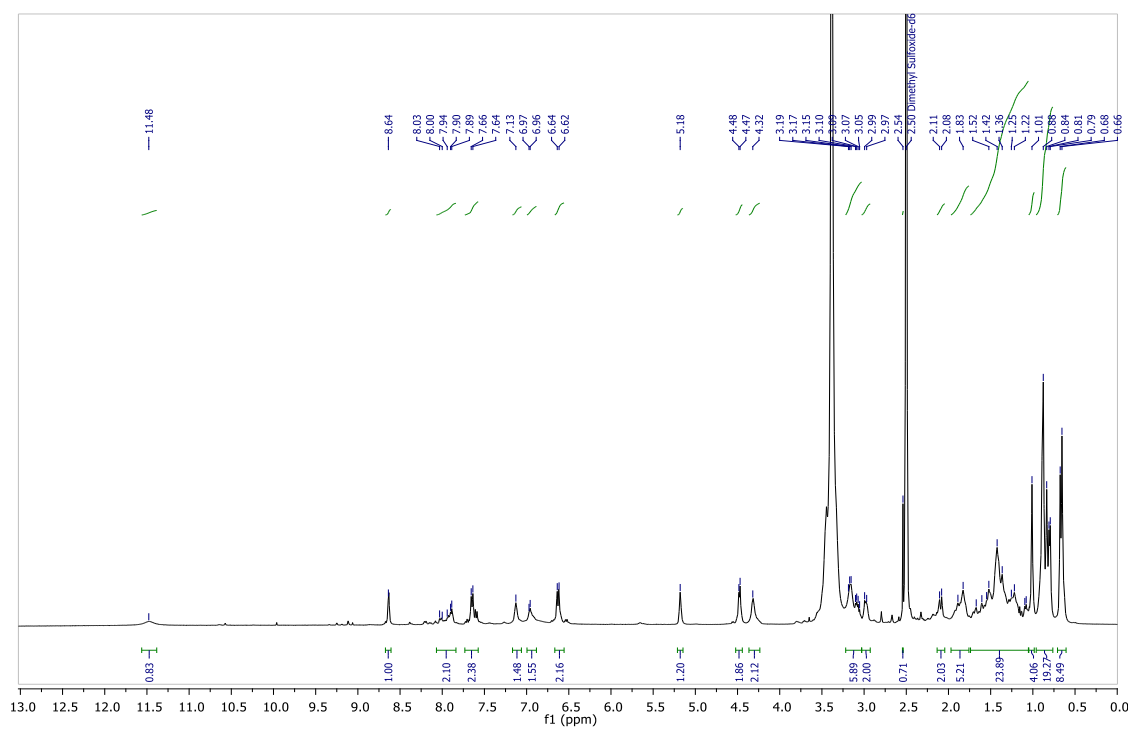


Mass Spectrum

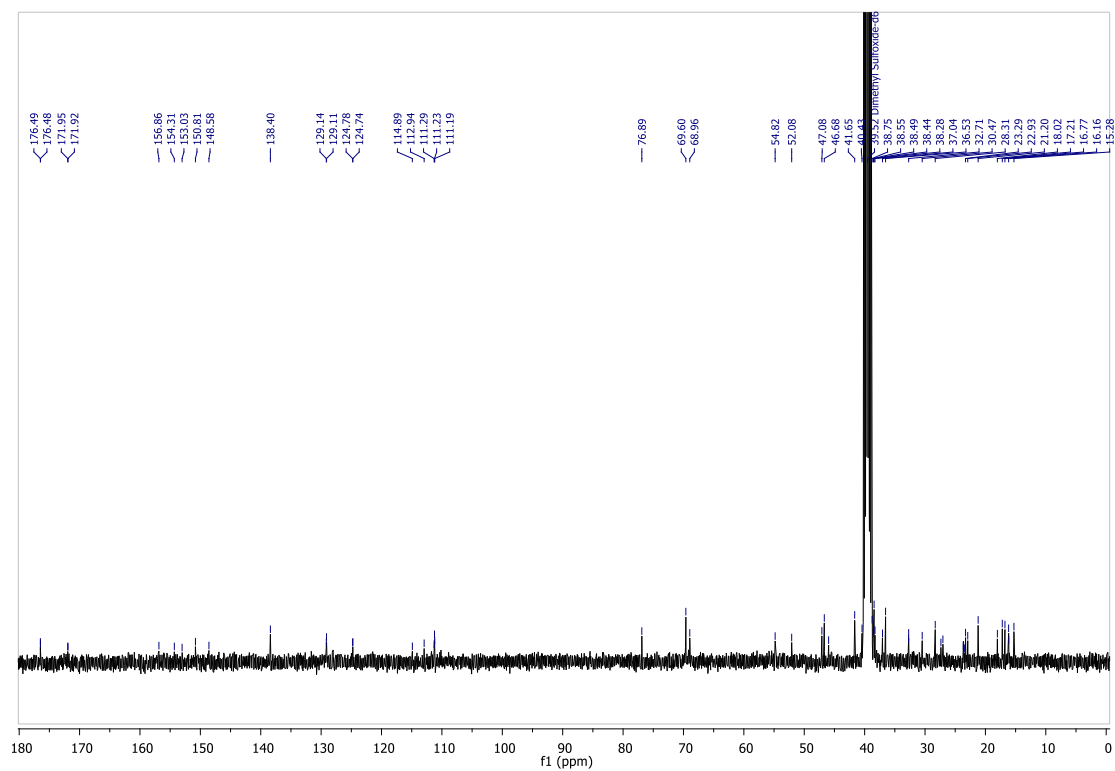


Meas. m/z	#	Ion Formula	m/z	err [mDa]	err [ppm]	rdb	N-Rule	e ⁻ Conf	mSigma
1010.607569	1	C ₅₅ H ₈₀ N ₉ O ₉	1010.607352	0.2	0.2	20.5	ok	even	73.6
1032.591264	1	C ₅₅ H ₇₉ N ₉ NaO ₉	1032.589296	2.0	1.9	20.5	ok	even	39.0

¹H NMR Spectrum (DMSO)



¹³C NMR Spectrum (DMSO)



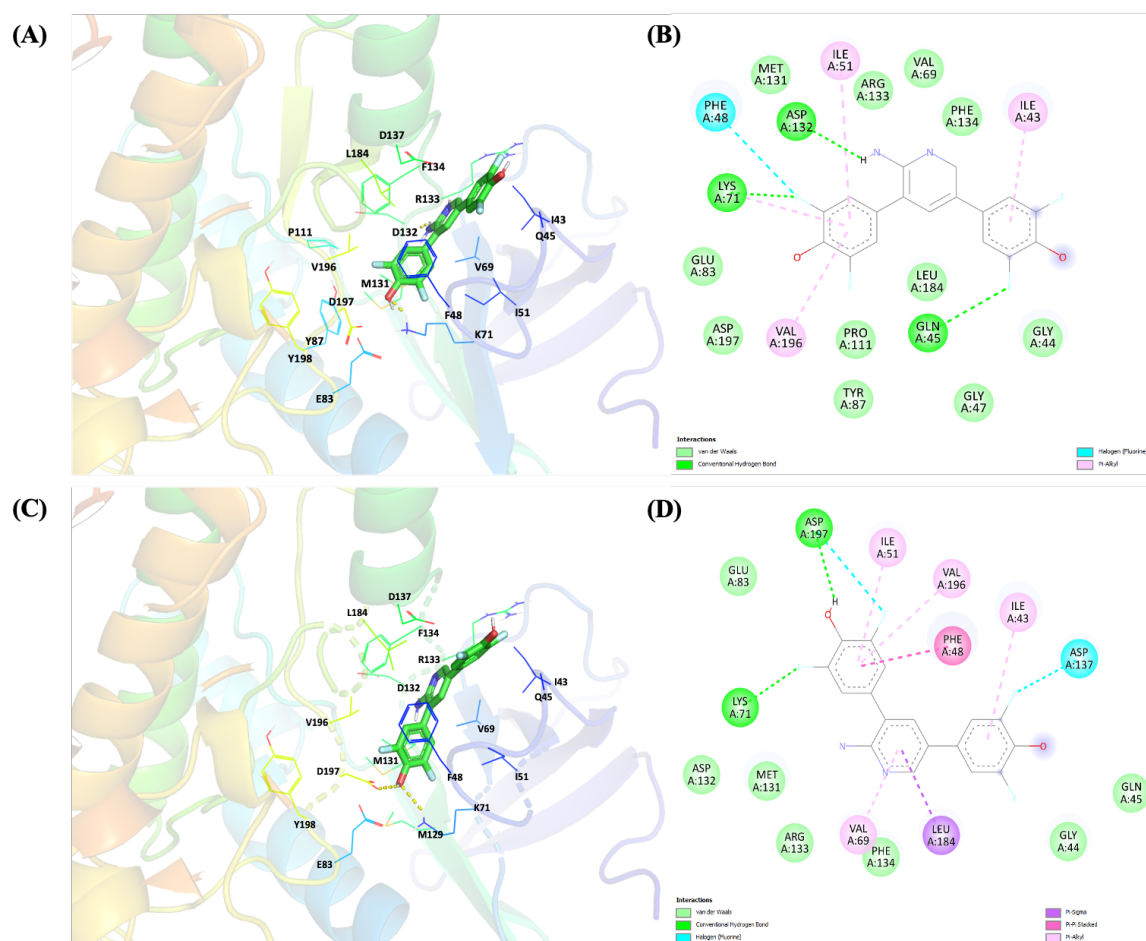
A.20

Canonical SMILES of UA and Compounds (7 – 15)

Molecule	Canonical SMILES
UA	<chem>C[C@@H]1CC[C@]2([C@@H]([C@H]1C)C1=CC[C@H]3[C@@]([C@@]1(CC2)C)(C)CCC1[C@]3(C)CC[C@@H](C1(C)C)O)C(=O)O</chem>
Compound 7	<chem>O=C(OC(C)(C)C)NCCNC(=O)[C@@]12CC[C@H]([C@@H]([C@H]2C2=CC[C@H]3[C@@]([C@@]2(CC1)C)(C)CCC1[C@]3(C)CC[C@@H](C1(C)C)O)C)C</chem>
Compound 8	<chem>O=C(OC(C)(C)C)NCCSSCCNC(=O)[C@@]12CC[C@H]([C@@H]([C@H]2C2=CC[C@H]3[C@@]([C@@]2(CC1)C)(C)CCC1[C@]3(C)CC[C@@H](C1(C)C)O)C)C</chem>
Compound 9	<chem>O=C(OC(C)(C)C)NCCOCCOCCNC(=O)[C@@]12CC[C@H]([C@@H]([C@H]2C2=CC[C@H]3[C@@]([C@@]2(CC1)C)(C)CCC1[C@]3(C)CC[C@@H](C1(C)C)O)C)C</chem>
Compound 10	<chem>NCCNC(=O)[C@@]12CC[C@H]([C@@H]([C@H]2C2=CC[C@H]3[C@@]([C@@]2(CC1)C)(C)CCC1[C@]3(C)CC[C@@H](C1(C)C)O)C)C</chem>
Compound 11	<chem>NCCSSCCNC(=O)[C@@]12CC[C@H]([C@@H]([C@H]2C2=CC[C@H]3[C@@]([C@@]2(CC1)C)(C)CCC1[C@]3(C)CC[C@@H](C1(C)C)O)C)C</chem>
Compound 12	<chem>NCCOCCOCCNC(=O)[C@@]12CC[C@H]([C@@H]([C@H]2C2=CC[C@H]3[C@@]([C@@]2(CC1)C)(C)CCC1[C@]3(C)CC[C@@H](C1(C)C)O)C)C</chem>
Compound 13	<chem>O=C(CCC(C(=O)O)NC(=O)c1ccc(cc1)NCc1cnc2c(n1)c(=O)[nH]c(n2)N)NCCNC(=O)[C@@]12CC[C@H]([C@@H]([C@H]2C2=CC[C@H]3[C@@]([C@@]2(CC1)C)(C)CCC1[C@]3(C)CC[C@@H](C1(C)C)O)C)C</chem>
Compound 14	<chem>O=C(CCC(C(=O)O)NC(=O)c1ccc(cc1)NCc1cnc2c(n1)c(=O)[nH]c(n2)N)NCCSSCCNC(=O)[C@@]12CC[C@H]([C@@H]([C@H]2C2=CC[C@H]3[C@@]([C@@]2(CC1)C)(C)CCC1[C@]3(C)CC[C@@H](C1(C)C)O)C)C</chem>
Compound 15	<chem>O=C(CCC(C(=O)O)NC(=O)c1ccc(cc1)NCc1cnc2c(n1)c(=O)[nH]c(n2)N)NCCOCCOCCNC(=O)[C@@]12CC[C@H]([C@@H]([C@H]2C2=CC[C@H]3[C@@]([C@@]2(CC1)C)(C)CCC1[C@]3(C)CC[C@@H](C1(C)C)O)C)C</chem>

A.21

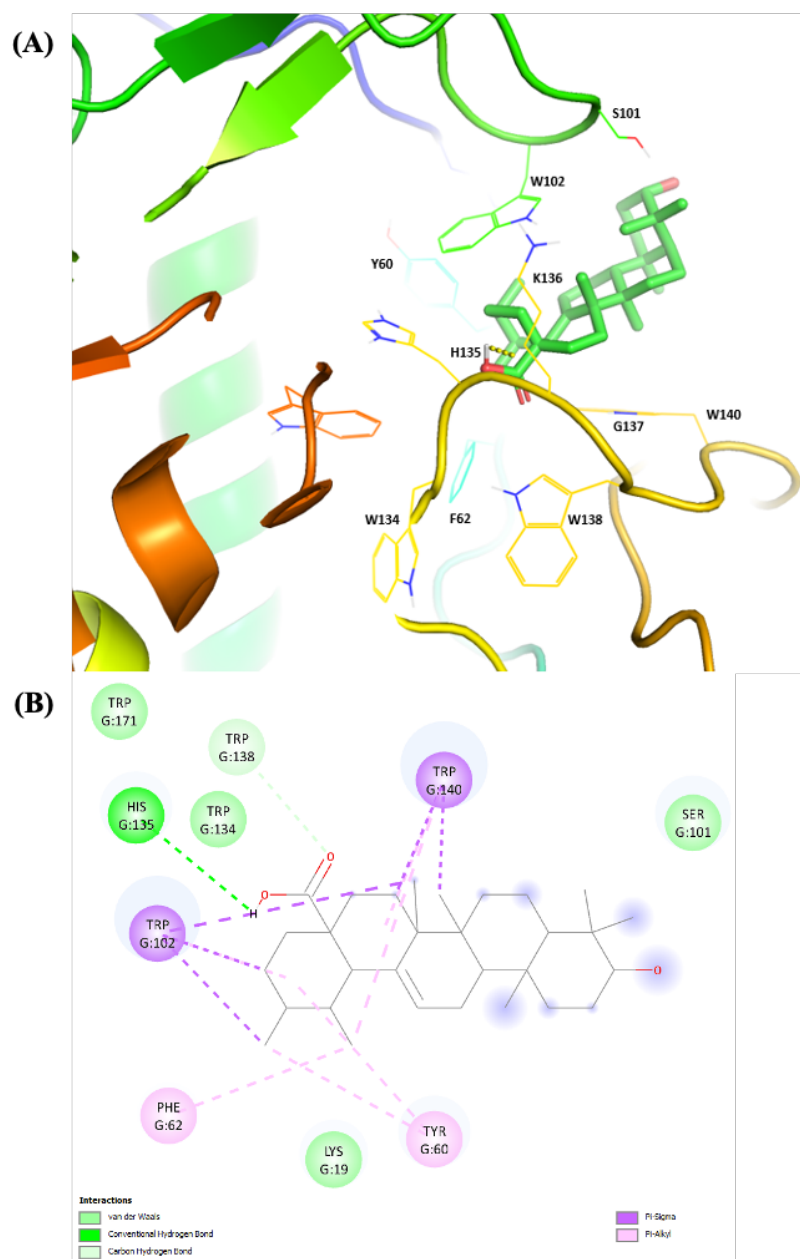
Re-docking studies of E8V to VRK1 (PDB ID: 6BU6)



The (A) 3D image and (B) 2D interaction map of E8V bound to VRK1 (PDB ID: 6BU6). The (C) 3D image and (D) 2D interaction map of docked E8V to 6BU6.

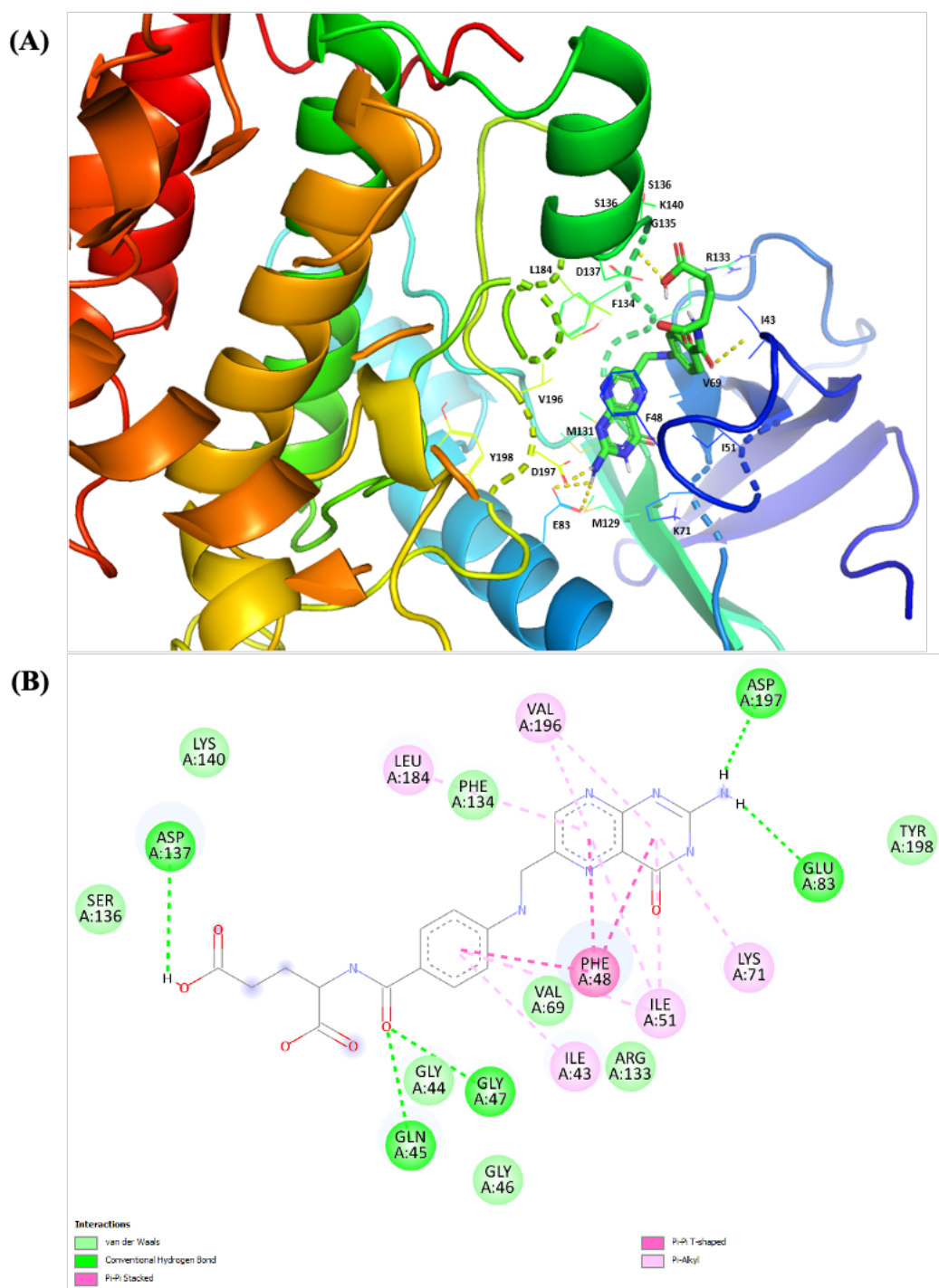
The different interactions of the co-crystallised chain A of VRK1 (6BU6) was analysed using PyMOL and Discovery Studio. It can be seen that main interactions include: conventional hydrogen bond with Lys 71, Asp 132 and Gln 45; and pi-alkyl bonds with residues Ile 51, Val 196 and Ile 43 (Couñago *et al.*, 2017). Results for the re-docked E8V to VRK1 produced 8 poses, with predicted binding affinity values between -11.0 to -8.1 kcal/mol. To select a functionally relevant docking confirmation, pose 1 was chosen with

a binding affinity of -11.0 kcal/mol. The re-docking of co-crystallised ligand (Figure x) forms specific interactions with various types of residues in the binding pocket as described in the literature. The main chemical interactions are conventional hydrogen bond with Asp 197 and Lys 71; pi-alkyl with Ile 51, Val 196, Val 69 and Ile 43; pi-pi stacked with Phe 48; and pi-sigma with Leu 184. It is noticeable that the re-docked co-crystallised ligand lost hydrogen bond interaction with Asp 132 and Gln 45 but has an interaction with Asp 197. Similarly, pi-alkyl has another interaction, Val 69, with the re-docked co-crystallised ligand, with added pi-pi stacked and pi-sigma interactions. The overlay shows that the re-docking of the ligand gives confidence to our docking protocol.



The (A) 3D image and (B) 2D interaction map of UA docked to FR α (PDB ID: 4LRH).

The predicted binding affinity was -8.6 to -6.9 kcal/mol. Image shown is the -8.6 kcal/mol score pose.



The (A) 3D image and (B) 2D interaction map of FA docked to VRK1 (PDB ID: 6BU6).

The predicted binding affinity obtained was -9.0 to -8.5 kcal/mol. Image shown is the -9.0 kcal/mol score pose.

A.24

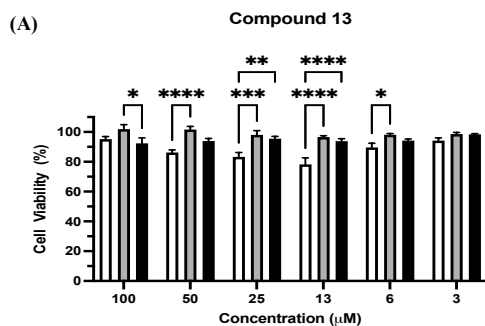
IC₅₀ of UA in different cell lines under different folate conditions

Cells	UA IC ₅₀ (μM)	
	48 hr	144 hr
Folate free medium		
U-251 MG	16.04±0.72	10.37±1.21
SKOV-3	15.82±0.83	6.36±0.25
Caco-2	10.79±0.46	4.72±0.05
MCF-7	12.51±0.90	10.32±1.07
Low folate medium		
U-251 MG	14.59±0.39	8.13±0.17
SKOV-3	11.59±0.32	12.97±462.94
MCF-7	9.14±1.62	8.51±0.44
Medium folate medium		
U-251 MG	17.36±1.00	13.61±1.65
A431	25.98±0.61	8.13±0.45
SW480	17.08±0.32	12.53±70.62
Ultrasound		
No US	17.36±1.00	12.83±0.72
5 min	16.74±0.65	10.01±0.60
10 min	17.87±1.41	9.97±0.41

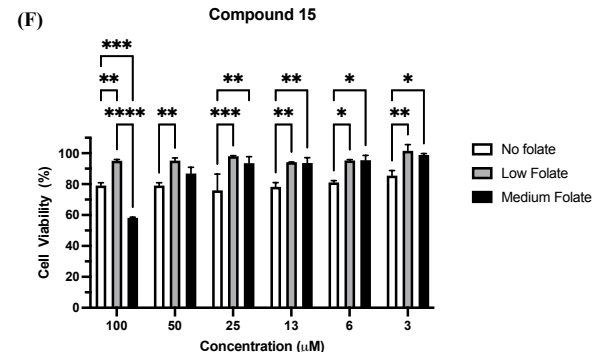
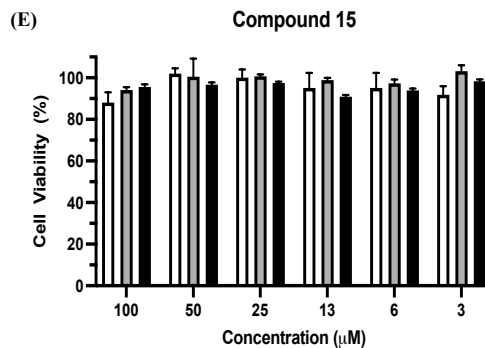
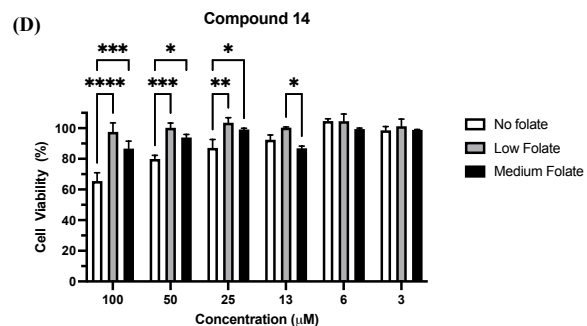
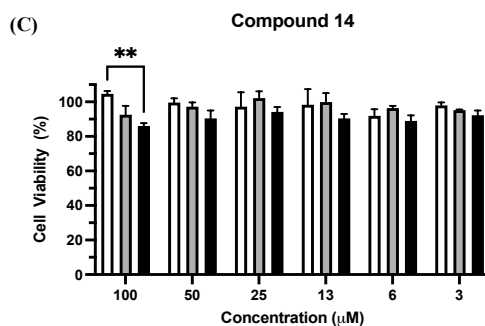
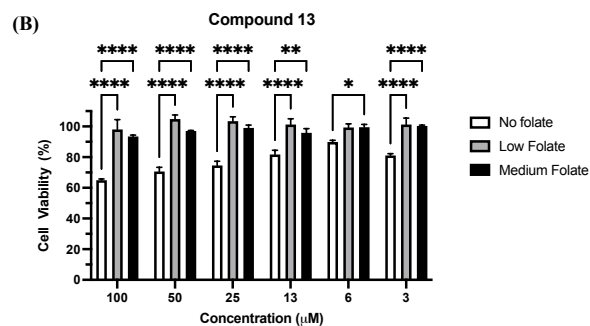
A.25 **NOAEL concentrations of novel UA derivatives (7 – 12)**

Compounds	NOAEL concentration (μM)	
	48 hr	144 hr
UA	7	7
Compound 7	13	3
Compound 8	13	6
Compound 9	6	3
Compound 10	6	3
Compound 11	13	6
Compound 12	6	3

48 hours in U-251 MG cells



144 hours in U-251 MG cells



A.27

IC₅₀ of UA and novel UA derivatives (7 – 12) in different cell lines

Compounds	U-251 MG		A431	
	48 hr	144 hr	48 hr	144 hr
UA	16.46±0.89	12.83±0.72	31.01±1.60	15.20±5.64
Compound 7	134.13±79.64	6.67±0.51	96.60±24.55	9.77±0.38
Compound 8	1374.36±1703.82	117.24±29.46	>500	102.95±3682.66
Compound 9	117.42±58.75	8.61±0.42	290.35±248.33	11.32±0.31
Compound 10	7.58±0.39	5.40±0.43	7.09±2.37	3.84±0.03
Compound 11	32.10±3.50	14.59±1.69	41.79±0.70	23.87±2248.57
Compound 12	14.22±1.02	7.66±0.63	16.87±0.69	13.08±0.58

Compounds	SKOV-3		MCF-7	
	48 hr	144 hr	48 hr	144 hr
UA	16.93±0.90	13.24±151.35	16.52±1.37	14.37±8.80
Compound 7	54.33±5.54	37.40±2.78	8.10±0.35	10.40±0.34
Compound 8	196.03±61.62	210.79±455.99	518.45±529.57	10.74±0.73
Compound 9	114.12±12.50	74.77±13.86	18.77±2.18	7.40±0.25
Compound 10	11.30±0.33	6.19±0.06	8.37±1.10	4.27±0.04
Compound 11	68.79±2.65	42.32±2.69	24.71±1.88	17.78±1.41
Compound 12	19.22±1.38	13.75±3.72	14.52±103.36	10.35±0.24

Compounds	Caco-2		HEK-293	
	48 hr	144 hr	48 hr	144 hr
UA	16.23±1.10	11.93±607.02	5.35±0.83	14.25±12.61
Compound 7	15.84±1.78	6.36±0.11	4.87±0.35	8.17±0.39
Compound 8	1382.09±1959.51	91.80±11.27	75.59±41.22	98.47±9.10
Compound 9	18.13±2.63	6.82±0.37	11.07±1.27	16.59±1.00
Compound 10	10.30±0.35	6.29±116.91	3.91±0.08	3.15±6.75
Compound 11	30.55±1.83	18.21±1.18	14.66±1.03	13.56±1.70
Compound 12	18.69±0.90	11.42±0.48	12.42±0.48	9.14±0.46